# UNIVERSIDAD DE SALAMANCA

# FACULTAD DE CIENCIAS QUÍMICAS

VNiVERSiDAD D SALAMANCA

CAMPUS DE EXCELENCIA INTERNACIONAL

# DESIGN AND VALIDATION OF NANOTECHNOLOGICAL STRATEGIES FOR HER2-POSITIVE BREAST CANCER TREATMENT

**Memoria que, para optar al grado de Doctor en Ingeniería Química (Ciencia y Tecnología Químicas) por la Universidad de Salamanca, presenta:**

**Celia Nieto Jiménez**

La **Dra. Dña. Eva Martín del Valle**, Catedrática del área de Ingeniería Química de la Universidad de Salamanca, y la **Dra. Dña. Milena Vega Moreno**, Profesora Contratado Doctor, también adscrita al Departamento de Ingeniería Química de la Universidad de Salamanca,

Certifican:

Que la presente memoria, titulada "**Diseño y validación de estrategias nanotecnológicas para el tratamiento del cáncer de mama HER2-positivo**" ("*Design and validation of nanotechnological strategies for HER2-positive breast cancer treatment*"), presentada por **Celia Nieto Jiménez** para optar al grado de Doctor en Ciencia y Tecnología Químicas por la Universidad de Salamanca, ha sido realizada bajo su dirección en el grupo de investigación Aplicaciones Biomédicas de Ingeniería Química del organismo citado.

Considerando que esta tesis reúne los requisitos científicos necesarios, autorizan su depósito y defensa. Para que así conste, firman el presente informe, en Salamanca a 28 de mayo de 2021.

Dña. Eva Martín del Valle  Dña. Milena Vega Moreno

*A la Tita, por el impulso*

# Agradecimientos

En primer lugar, gracias a mi directora, Eva Martín del Valle, por darme la oportunidad de sumergirme en el mundo de la investigación, por su dedicación, por la orientación y por la confianza depositada. De igual forma, gracias a mi co-directora, Milena Vega, por el esfuerzo, por la ayuda incesante y por haberme guiado también durante todos estos años.

En segundo lugar, gracias a mis compañeros, a los que aún están: Álvaro, Inma, Antonio, José, Chema, Audelino, Jesús, María y Belén; y a los que estuvieron: Gema, Jesús, Montaña, Sergio y Fernando. Su disposición ha facilitado mucho el camino.

Asimismo, gracias al grupo de investigación del Dr. Atanasio Pandiella, por haber aportado conocimiento, tiempo y medios. Gracias también a la Unidad de Microscopía del Centro de Investigación del Cáncer por toda la ayuda, especialmente el último año.

Del mismo modo, gracias al grupo de investigación en Biociencias de la Universidad de Aston por su acogida durante mi estancia predoctoral. En particular, gracias a la Dra. Patricia Pérez Esteban, por hacer lo que estuvo en su mano para que disfrutara de la experiencia.

Gracias a mis amigas, las de Salamanca: Carlota, Irene, Miriam, Laura, Bea y Mónica; y a las de Macotera: Cris, Alba, Bea, Teresa, Sara, Karina, Silvia y Ana. Por estar, y por sumar siempre.

A Óscar. Gracias por toda la paciencia, la compresión y el refugio.

Y, finalmente, gracias a mi familia. En especial, gracias a mi hermana, por aligerarme el peso de la mochila; y a mis padres, por su apoyo ciego y porque su esfuerzo y sacrificio ilimitados son los que han hecho posible la escritura de estas páginas.

Como afirmó un día Claude Bernard, *el Arte es "yo"; la Ciencia es "nosotros"*.

**The difference between winning and losing is most often not quitting**

Walt Disney

# General index

**List of figures and schemes** **I**
**List of tables** **XIII**
**List of equations and reactions** **XVII**
**Abstract** **XIX**

**Chapter 1. Introduction. Cancer complexity and the relevant role of nanomedicine in its treatment** **1**

***1.1.*** *What does the word "cancer" encompass?* 3
***1.2.*** *The hallmarks of cancer* 4
**1.2.1.** Initial hallmarks of cancer 4
**1.2.1.1.** Self-sufficiency in growth signals 5
**1.2.1.2.** Insensitivity to anti-growth signals 6
**1.2.1.3.** Evading apoptosis 7
**1.2.1.4.** Limitless replicative potential 8
**1.2.1.5.** Sustained angiogenesis 8
**1.2.1.6.** Tissue invasion and metastasis 9
**1.2.2.** Tumour enabling capabilities and newer hallmarks of cancer 10
**1.2.2.1.** Genome instability 11
**1.2.2.2.** Inflammation 12
**1.2.2.3.** Evading immune eradication 13
**1.2.2.4.** Energy metabolism reprogramming 14
***1.3.*** *History of chemotherapy in cancer "war"* 16
***1.4.*** *Main targeted agents for cancer therapy* 20
**1.4.1.** Antibody-based targeted cancer therapy 21
**1.4.2.** Small molecule-based targeted cancer therapy 24
**1.4.3.** Targeted cancer therapy based on vaccines 25
**1.4.4.** Gene-based targeted cancer therapy 26
**1.4.4.1.** Immunological strategies for gene-based cancer therapy 26
**1.4.4.2.** Molecular strategies for gene-based cancer therapy 27
***1.5.*** *The essential role of nanotechnology in the development of targeted cancer therapies* 27

**1.5.1.** Passive targeted cancer therapy 29
**1.5.2.** Main reported nanocarriers in cancer therapy 31
**1.5.2.1.** Polymeric drug delivery systems 32
**1.5.2.2.** Lipid drug delivery systems 34
**1.5.2.3.** Drug delivery systems of organometallic nature 35
**1.5.3.** Stimulus for drug release 37
**1.5.3.1.** Endogenous stimuli 37
**1.5.3.2.** Exogeneous stimuli 39
***1.6.*** *Published articles related to this chapter* 40
***1.7.*** *Abbreviations* 40
***1.8.*** *References* 43
***Article:*** *Trastuzumab: More than a guide in HER2-positive cancer Nanomedicine* 49

**Chapter 2. Thesis objectives** **71**

**Chapter 3. Alginate and piperazine nanoparticles conjugated with trastuzumab as targeted nanocarrier for paclitaxel** **77**

***3.1.*** *Introduction* 79
**3.1.1.** The contradictory role of HER2-overexpression 79
**3.1.2.** Trastuzumab role in HER2-positive breast cancer treatment 80
**3.1.3.** Paclitaxel: therapeutic action and major drawbacks of its administration 82
**3.1.4.** Employment of β-cyclodextrins to improve the aqueous solubility of hydrophobic drugs 84
***3.2.*** *Synthesis and characterization of alginate-piperazine nanoparticles* 86
**3.2.1.** Synthesis of nanoparticles of sodium alginate and piperazine 86
**3.2.2.** Characterization of the different alginate-piperazine nanoparticles obtained 87
**3.2.2.1.** Characterization of alginate-piperazine nanoparticle size and surface charge 87
**3.2.2.2.** Analysis of pH influence on the size and

surface charge of alginate-piperazine nanoparticles 89
**3.2.2.3.** Determination of alginate-piperazine nanoparticle stability 89
***3.3.*** *Conjugation of alginate-piperazine nanoparticles with trastuzumab and paclitaxel* 90
**3.3.1.** Obtaining of paclitaxel-*β*-cyclodextrin inclusion complexes 90
**3.3.2.** Conjugation of paclitaxel-*β*-cyclodextrin complexes and trastuzumab to alginate-piperazine nanoparticles 90
**3.3.3.** Determination of paclitaxel and trastuzumab content in alginate-piperazine nanoparticles 92
**3.3.4.** Characterization of conjugated alginate-piperazine nanoparticles 93
**3.4.** *Validation of the efficacy and HER2-selectivity of conjugated alginate-piperazine nanoparticles with conventional cell cultures* 95
**3.4.1.** Selection and culture of HER2-overexpressing and HER2-non-overexpressing human cell lines 95
**3.4.2.** Study of the internalization of conjugated alginate-piperazine nanoparticles in HER2-overexpressing cancer cells 97
**3.4.3.** Determination of HER2-specificity of conjugated alginate-piperazine nanoparticles 99
**3.4.4.** Cytotoxicity of conjugated alginate-piperazine nanoparticles as a function of the HER2 cell expression level 101
***3.5.*** *Validation of the efficacy of the conjugated alginate-piperazine nanoparticles with conventional HER2-positive tumour spheroids* 104
**3.5.1.** Development of BT474 multicellular tumour spheroids 104
**3.5.2.** Determination of the toxicity of conjugated alginate-piperazine nanoparticles to BT474 tumour spheroids 105
***3.6.*** *Conclusions* 108
***3.7.*** *Published articles related to this chapter* 109
***3.8.*** *Abbreviations* 109
***3.9.*** *References* 110
***Article:*** *Paclitaxel-trastuzumab mixed nanovehicle to target HER2-overexpressing tumours* 115

**Chapter 4. Tailored-made polydopamine nanoparticles: a potential for cancer nanomedicine** **129**

***4.1.*** *Introduction* 131
**4.1.1.** Polydopamine: a versatile bioinspired material 131
**4.1.2.** Polydopamine structure hypotheses and main synthesis approaches 132
**4.1.2.1.** Factors affecting dopamine polymerization through solution oxidation 134
**4.1.3.** Polydopamine properties and applications in cancer nanomedicine 137
***4.2.*** *Synthesis and characterization of polydopamine nanoparticles* 138
**4.2.1.** Synthesis of tailored-made polydopamine nanoparticles 138
**4.2.2.** Characterization of polydopamine nanoparticles synthesized with different ammonia concentrations and in different alcohol/water media 140
**4.2.2.1.** Effect of ammonia concentration on polydopamine nanoparticle size 140
**4.2.2.2.** Effect of the type of alcohol employed in the synthesis of polydopamine nanoparticles on their size and yield 141
**4.2.2.3.** Hansen's solubility parameter distances between dopamine and the different media employed for polydopamine nanoparticle synthesis 143
**4.2.2.4.** Effect of ammonia concentration on polydopamine nanoparticle size as a function of the alcohol used for their synthesis 145
**4.2.2.5.** Analysis of the chemical structure of polydopamine nanoparticles obtained by employing different alcohols 147
***4.3****. Selective toxicity of polydopamine nanoparticles to tumour cells* 149
**4.3.1.** Development of a protocol for the performance of MTT assays with polydopamine nanoparticles 149
**4.3.2.** Implementation of the MTT protocol developed to study polydopamine nanoparticle cytotoxicity 152
**4.3.3.** Study of polydopamine nanoparticle internalization

in cancer cells 155
***4.4.*** *Potential implication of iron affinity of polydopamine nanoparticles in their cytotoxicity* 156
**4.4.1.** Analysis of polydopamine strong metal-ion chelation ability 156
**4.4.2.** Study of the possible implication of iron affinity of polydopamine nanoparticles in their cytotoxicity 162
***4.5.*** *Influence of polydopamine nanoparticle size on their cytotoxicity* 165
***4.6.*** *Influence of the alcohol/water medium used for polydopamine nanoparticle synthesis on their cytotoxicity* 170
**4.6.1.** Influence of the synthesis medium on polydopamine nanoparticle iron adsorption capacity 171
**4.6.2.** Influence of the synthesis medium on polydopamine nanoparticle cytotoxicity 176
***4.7.*** *Conclusions* 183
***4.8.*** *Published articles related to this chapter* 184
***4.9****. Abbreviations* 184
***4.10.*** *References* 185
***Article:*** *Cytotoxicity of paramagnetic-cations loaded polydopamine nanoparticles* 191
***Article:*** *Polydopamine nanoparticles kill cancer cells* 198
***Article:*** *Size matters in the cytotoxicity of polydopamine nanoparticles in different types of tumours* 206
***Article:*** *Antineoplastic behaviour of polydopamine nanoparticles prepared in different water/alcohol media* 221

**Chapter 5. Ferric-loaded polydopamine nanoparticles charged with doxorubicin as targeted combination therapy 231**

***5.1.*** *Introduction* 233
**5.1.1.** Polydopamine-based nanomaterials in the different modalities of cancer diagnosis and therapy 233
**5.1.2.** Ferroptosis: a mechanism of regulated cell death gaining popularity in cancer therapy 233
***5.2.*** *Cytotoxicity of polydopamine nanoparticles loaded with transition metals capable of generating reactive oxygen species* 237
***5.3.*** *Cytotoxicity of ferric-chelated polydopamine nanoparticles*

*as a function of the iron-loading pH* 239
**5.3.1.** Loading of polydopamine nanoparticles with iron (III) at different pH values 239
**5.3.2.** Polydopamine nanoparticles release of iron (III) and loading of calcium (II) in the endo/lysosomal environment 243
**5.3.3.** Cytotoxicity of polydopamine nanoparticles loaded with iron (III) at different pH values 245
***5.4.*** *Enhancement of the therapeutic activity of ferric-chelated polydopamine nanoparticles with doxorubicin* 248
**5.4.1.** Doxorubicin adsorption on bare and ferric-chelated polydopamine nanoparticles 248
**5.4.2.** Cytotoxicity of bare polydopamine nanoparticles charged with doxorubicin 250
**5.4.3.** Cytotoxicity of ferric-chelated polydopamine nanoparticles charged with doxorubicin 252
**5.4.4.** *In vitro* assessment of reactive oxygen species production after treatment with doxorubicin and the different ferric-chelated polydopamine nanoparticles 256
***5.5.*** *Conclusions* 258
***5.6.*** *Published articles related to this chapter* 259
***5.7.*** *Abbreviations* 260
***5.8.*** *References* 261
***Article:*** *Tailored-made polydopamine nanoparticles to induce ferroptosis in breast cancer cells in combination with chemotherapy* 267

**Chapter 6. Polydopamine nanoparticles loaded with trastuzumab as paclitaxel targeted carrier 283**

***6.1****. Introduction* 285
**6.1.1.** Polydopamine advantages for the development of drug delivery systems 285
**6.1.2.** Drug-loading strategies in polydopamine and polydopamine-modified nanoparticles 287
**6.1.3.** Examples of currently developed drug-loaded polydopamine-based nanocarriers 288
***6.2.*** *Paclitaxel and trastuzumab loading to polydopamine nanoparticles* 290
**6.2.1.** Obtaining of polydopamine nanoparticles 290

**6.2.2.** Polydopamine nanoparticle loading with trastuzumab and paclitaxel 291
**6.2.3.** Determination of trastuzumab and paclitaxel incorporation efficiencies and content in polydopamine nanoparticles 293
***6.3**. Validation of the efficacy and HER2-selectivity of polydopamine nanoparticles loaded with trastuzumab and paclitaxel in conventional cell cultures* 294
**6.3.1.** Study of the therapeutic activity of polydopamine nanoparticles loaded with trastuzumab and paclitaxel by viability assays 294
**6.3.2.** Comparison of the anti-tumour activity and selectivity of the polydopamine and alginate-piperazine nanoparticles loaded with trastuzumab and paclitaxel 299
**6.3.3.** Validation of loaded polydopamine nanoparticles effectiveness by alive/death assays 300
**6.3.4.** Analysis of the apoptosis induced by loaded polydopamine nanoparticles through flow cytometry 301
***6.4.** Validation of the efficacy of polydopamine nanoparticles loaded with trastuzumab and paclitaxel in HER2-positive tumour spheroids* 303
**6.4.1.** Study of the interaction between polydopamine nanoparticles loaded with trastuzumab and paclitaxel and breast tumour spheroids 303
**6.4.2.** Cytotoxicity of polydopamine nanoparticles loaded with trastuzumab and paclitaxel to HER2-positive cancer spheroids 305
***6.5.** Conclusions* 308
***6.6.** Published articles related to this chapter* 309
***6.7.** Abbreviations* 309
***6.8.** References* 311
***Article:** Nature-inspired nanoparticles as paclitaxel targeted carrier for the treatment of HER2-positive breast cancer* 317

**Chapter 7. Gellan gum hydrogels loaded with paclitaxel for breast local chemotherapy** **333**

***7.1.*** *Introduction* 335
**7.1.1.** Hydrogel employment for local, post-surgical drug delivery 335
**7.1.1.1.** Hydrogels: definition, characteristics and classification 337
**7.1.2.** Gellan gum: properties and use in hydrogel preparation 339
**7.1.3.** Hydrogel chemical crosslinking through the carbodiimide chemistry 340
***7.2.*** *Synthesis of different gellan gum hydrogels* 341
***7.3.*** *Characterization of the different gellan gum hydrogels synthesized* 343
**7.3.1.** Rheological analysis of gellan gum hydrogels 343
**7.3.2.** Study of the swelling behaviour of gellan gum hydrogels 344
**7.3.3.** Analysis of the porosity of the different gellan gum hydrogels 350
**7.3.4.** Characterization of the chemical composition of the different gellan gum hydrogels 352
**7.3.5.** Thermogravimetric analysis of the different gellan gum hydrogels 353
**7.3.6.** Compression test of gellan gum hydrogels 355
**7.3.7.** Study of gellan gum hydrogel enzymatic degradation 357
***7.4.*** *Paclitaxel loading in gellan gum hydrogels* 358
**7.4.1.** Gellan gum hydrogels gelation with paclitaxel:β-cyclodextrin inclusion complexes 358
**7.4.2.** Paclitaxel release from gellan gum hydrogels 358
***7.5****. In vitro* validation of paclitaxel-loaded gellan gum hydrogels 361
**7.5.1.** *In vitro* evaluation of gellan gum hydrogel biocompatibility 361
**7.5.2***. In vitro* analysis of the anti-tumour activity of gellan gum hydrogels loaded with paclitaxel:β-cyclodextrin inclusion complexes 363
***7.6****. Conclusions* 365

***7.7.*** *Abbreviations* 367
***7.8.*** *References* 368

**Chapter 8. General conclusion** **375**

**Appendix** **381**
*Appendix I. Reagents and equipment* 383
*Appendix II* 385

# List of figures and schemes

**Figure 1.1.** Cancer incidence and mortality rates expected in following decades according to the forecasts of the GCO

**Figure 1.2.** Acquired capabilities of cancer according to Hanahan and Weinberg

**Figure 1.3.** Cell cycle clock: Growth inhibitors, under normal physiological conditions, force altered cells to become quiescent and differentiate, thus preventing them for dividing

**Figure 1.4.** Enabling characteristics and emerging hallmarks of cancer described by Hanahan and Weinberg in their second review study

**Figure 1.5.** Summary of the enabling properties (blue pictures) and hallmarks (yellow pictures) of cancer described by Hanahan and Weinberg: (**A**) Genome instability; (**B**) Inflammation; (**C**) Self-sufficiency in growth signals; (**D**) Insensitivity to anti-growth signals; (**E**) Evading apoptosis; (**F**) Limitless replicative potential; (**G**) Sustained angiogenesis; (**H**) Tissue invasion and metastasis; (**I**) Reprogramming of energy metabolism; (**J**) Evading immune eradication

**Figure 1.6.** Chronological axis showing the advances in the pharmaceutical industry that made conventional cancer chemotherapy transitioned to the age of the “targeted therapy”

**Figure 1.7.** (**A**) Structure of the most abundant mAb isotype (IgG); (**B**) Direct and indirect mechanisms of action of mAbs

**Figure 1.8.** Types of mAbs according to their origin

**Figure 1.9.** Tumour angiogenesis is responsible for the development of irregular vessels that exhibit fenestrations through which DDSs can pass. This phenomenon, along with the poor lymphatic drainage that characterises cancer tissues, contributes to the well-known EPR effect

**Figure 1.10.** Representation of the most commonly reported types of DDSs for cancer treatment

**Figure 3.1.** Molecular mechanisms that account for Tmab therapeutic activity: by specifically binding to HER2, Tmab prevents its homo- or heterodimerization with other EGF receptors. Apart from promoting a process of ADCC (**A**), Tmab is believed to be able to inhibit tumour proliferation and angiogenesis (**B**)

**Figure 3.2.** Paclitaxel chemical structure (**A**) and concentration-dependent cytotoxicity (**B**). When cells are treated with high concentrations of the taxane, mitotic arrest takes place and daughter cells die or are abnormally tetraploid. Otherwise, when PTX concentration is lower, treated cells are able to exit mitosis, but they exhibit alterations in their genetic material

**Figure 3.3.** (**A**) CD chemical structure; (**B**) PTX:βCDs inclusion complex. The hydrophobic interior cavity of the CDs allows the encapsulation of drugs with poor aqueous solubility, such as the taxane employed in this thesis

**Figure 3.4.** Scheme that summarizes the synthesis process of the APPZ, which were obtained thanks to a piperazine-mediated crosslinking of alginate chains at pH 4.6 - 4.8

**Figure 3.5.** (**A**) Size and zeta potential of APPZ as a function of the piperazine/alginate volume ratio; (**B**) Number size distribution of the smallest APPZ obtained, determined by DLS; (**C**) Size and zeta potential of APPZ (1:2 piperazine/alginate volume ratio) as a function of the suspension pH; (**D**) APPZ stability over time. All values were obtained from the mean ± SEM of three different measurements

**Figure 3.6.** Schematic representation of APPZ conjugation with Tmab and PTX:βCDs, performed by means of the carbodiimide chemistry

**Figure 3.7.** (**A**) IR absorption spectra of Tmab, APPZ, conjugated APPZ and β-CDs in the 500-4000 $cm^{-1}$ wavelength range; (**B**) Conjugated APPZ particle size distribution, determined by DLS; (**C**) Conjugated APPZ stability over time; (**D**) Image of conjugated APPZ, acquired by wet STEM

**Figure 3.8.** Study of the HER2- and pHER2-expression level in the BT474, SKBR3, OVCAR3 and HS5 cell lines. Immunoprecipitation was performed with two amounts of protein extract: 20 μg (**A**) and 1000 μg (**B**). Calnexin was employed as loading control

**Figure 3.9.** (**A**) CLSM images that revealed conjugated APPZ internalization in BT474 cells through receptor-mediated endocytosis*;* (**B**) CLSM images proving that co-localization of the HER2 and LAMP1 fluorescence signals occurred after treatment of BT474 cells with the conjugated APPZ

**Figure 3.10.** Assessment of conjugated APPZ HER2-specificity with BT474 and HS5 cell co-cultures. Both cell lines were seeded together and, after treating them with conjugated APPZ and PTX*:*βCDs complexes, optical (**A**) and confocal microscopy (**B**) images were acquired at different times. From the latter, it was determined the average number of living BT474 and HS5 cells after 48 hours of treatment (**C**)

**Figure 3.11.** Viability rates of BT474 (**A**), SKBR3 (**B**), OVCAR3 (**C**) and HS5 (**D**) cells determined by MTT assays after treatment with free PTX:βCDs complexes (7.9 μM), Tmab (0.06 nM), APPZ (1 mg/mL) or conjugated APPZ (1 mg/mL)

**Figure 3.12.** Viability rates of BT474 (**A**) and HS5 (**B**) cells determined by MTT assays after being treated with free PTX (7.9 μM), PTX:βCDs complexes (7.9 μM), Tmab (0.06 nM), APPZ (1 mg/mL), APPZ-PTX:βCDs (1 mg/mL) and APPZ-PTX:βCDs-T (1 mg/mL)

**Figure 3.13.** Optical microscopy image of one of the BT474 MCTS developed

**Figure 3.14.** (**A**) Results obtained when performing cell-counting after 48 hours of spheroid treatment with PTX:βCDs complexes (7.9 μM PTX) and conjugated APPZ (1 mg/mL); (**B**) CLSM images of BT474 spheroids acquired 48 and 72 hours after treatment with PTX*:*βCDs and conjugated APPZ concentrations similar to those employed in the cell-counting assay

**Figure 4.1.** Representation of the most widely accepted theory about PDA polymerization. It is recognized that, under basic conditions, DA is oxidized to DHI. Then, it is believed that PDA formation takes places by both covalent oxidative polymerization (left) and physical self-assembly processes (right)

**Figure 4.2.** Summary of the main factors affecting DA polymerization and, thus, PDA NP size

**Figure 4.3.** Schematic representation of the solution oxidation process carried out in basic aqueous media to synthesize PDA NPs

**Figure 4.4.** DLS number distributions, TEM images and size-range histograms of the PDA NPs prepared in EtOH/$H_2O$ (28.57% (V/V)) mixtures with different concentration of $NH_4OH$ (% (V/V)): (**A**) 2.91%; (**B**) 1.52%; (**C**) 0.84%

**Figure 4.5.** TEM images (**A**) and size-range histograms (**B**) of PDA NPs prepared in the different ROH/$H_2O$ (28.57% (V/V)) mixtures by employing a similar $NH_4OH$ concentration (0.79% (V/V))

**Figure 4.6.** (**A**) DLS intensity distribution of the PDA NPs prepared in the different ROH/$H_2O$ mixtures with various $NH_4OH$ concentrations (% (V/V)); (**B**) PDA(ROH) NP size as a function of the $NH_4OH$ concentration used in their synthesis

**Figure 4.7.** IR spectra of the different PDA(ROH) NPs obtained in the (**A**) 900-1800 $cm^{-1}$ and (**B**) 2700-3700 $cm^{-1}$ ranges

**Figure 4.8.** (**A**) UV-Vis absorption spectra of dispersions of PDA NPs of different concentration; (**B**) Overlap between the absorption spectra of the MTT reagent (purple, 0.025 mM) and that of PDA NPs (black, 0.012 mg/mL) at 550 nm; (**C**) Effect of the addition of different concentrations of PDA NPs on the MTT absorbance; (**D**) Absorbance at 550 nm of the MTT reagent (0.025 mM) plus different concentrations of PDA NPs (purple), whose absorbance was also separately determined (black)

**Figure 4.9.** Illustration of the proposed protocol to subtract PDA NP absorbance contribution at 550 nm in MTT assays and, thus, avoid getting overestimated viability results

**Figure 4.10.** DLS number distribution (**A**), TEM image and size-range histogram (**B**) of the PDA NPs that were later analysed for toxicity to BT474 and NIH/3T3 cells

**Figure 4.11.** Results of the MTT assays performed following the stablished protocol with the NIH/3T3 (**A**) and BT474 (**B**) cell lines, which were treated with different concentrations of PDA NPs; (**C**) Viability rate values of BT474 cells that would have been obtained if the procedure detailed in Figure 4.8 had not been applied

**Figure 4.12.** (**A**) CLSM images of BT474 cells incubated with fluorescent PDA NPs (100 nm, 0.05 mg/mL, blue) for 3 hours; (**B**) From left to right, bright field image of BT474 cells, fluorescent signal (blue) of PDA NPs internalized in those cells after 3 hours, fluorescent signal of BT474 stained lysosomes (red), and image obtained after merging the previous three

**Figure 4.13.** (**A**) DLS number distribution, TEM image and size-range histogram of the NPs employed to study PDA affinity for different metal cations; (**B**) DLS number distribution, DLS intensity distribution and zeta potential values of the same PDA NPs when they were re-dispersed in buffers of different pH

**Figure 4.14.** (**A**) PDA NP adsorption capacity of different $M^{n+}$, expressed as mg $M^{n+}$/g PDA NP (Q); (**B**) Q values for $Fe^{3+}$ and $Cu^{2+}$ obtained when PDA NPs were incubated with both cations simultaneously; (**C**) TEM images of the PDA NPs loaded with the different $M^{n+}$

**Figure 4.15.** (**A**) IR spectrum of bare PDA NPs; (**B**) IR spectra in the 2000-4000 $cm^{-1}$ range of PDA NPs (black) and the PDA NPs loaded with the different $M^{n+}$; (**C**) IR spectra in the 900-1800 $cm^{-1}$ range of PDA NPs (black) and the PDA NPs loaded with $Fe^{3+}$ and $Cu^{2+}$; (**D**) IR spectra in the 900-1800 $cm^{-1}$ range of PDA NPs (black) and the PDA NPs loaded with $Ca^{2+}$, $Zn^{2+}$ and $Mn^{2+}$

**Figure 4.16.** (**A**) Schematic explanation of why PDA NPs could be toxic to tumour cells: when they were internalized in cells and ended up in late endosomes/lysosomes, they could chelate the $Fe^{3+}$ existing in these organelles, causing an imbalance in Fe homeostasis and a type of cell death called ferroptosis, mediated by an excessive production of lipid ROS; (**B**) Schematic explanation of how DFO and GSH could antagonize PDA NP anti-tumour activity; (**C**) Results of the MTT assay performed 24 hours after co-treating BT474 cells with PD NPs (0.033 mg/mL) and GSH (50 μM) or DFO (0.7 μM)

**Figure 4.17.** Results of the MTT assays performed with the BT474 (**A**), HTC116 (**B**), HEPG2 (**C**), H460 (**D**) and HS5 (**E**) cell lines after treating them with different concentrations of 115 (empty bars) and 200 nm (bars with the horizontal line pattern) PDA NPs

**Figure 4.18.** Results of the MTT assays performed with BT474 (**A**), HTC116 (**B**), HEPG2 (**C**), H460 (**D**) and HS5 (**E**) cells, which were or not simultaneously treated with PDA NPs (115 nm, 0.029 mg/mL) and DFO (0.7 μM) or GSH (50 μM)

**Figure 4.19.** (**A**) Results of the MTT assay performed with the BT474 cell line after treating it with different concentrations of 420 nm PDA NPs; (**B**) CLSM images obtained 24, 48 and 72 hours after treating BT474 cells with PDA NPs (0.042 mg/mL) of 115 nm in size. 30 minutes before acquiring these images, calcein AM (green) and propidium iodide (red) were added to differentiate living cells from dead ones

**Figure 4.20.** TEM images, size range histograms and DLS number distributions of the PDA NPs prepared in aqueous media containing MeOH (**A**), EtOH (**B**), 2-PrOH (**C**), 1-PrOH (**D**) and 2-Me-2-PrOH (**E**) to analyse whether the employment of different ROHs conditioned the $Fe^{3+}$ adsorption capacity of the NPs

**Figure 4.21.** (**A**) Logarithm of the concentration of the $Fe^{3+}$ adsorbed in the PDA(ROH) NPs as a function of the logarithm of the concentration of $Fe^{3+}$ remaining in solution; (**B**) Efficiency (%) of the $Fe^{3+}$-adsorption process in the different PDA(ROH) NPs as a function of the initial concentration of

$Fe^{3+}$ used; (**C**) TEM images of PDA(EtOH) NPs before (left) and after loading them with two different initial concentrations of $Fe^{3+}$ (30 ppm (medium) and 70 ppm (right))

**Figure 4.22.** TEM images of the different PDA(EtOH) NPs, smaller in size, that were used to analyse how the ROH employed in their synthesis affected their cytotoxicity (ROH= MeOH (**A**), EtOH (**B**), 2-PrOH (**C**), 1-PrOH (**D**) and 2-Me-2-PrOH (**E**))

**Figure 4.23.** Results of the MTT assays performed with the BT474 (**A**) and HS5 (**B**) cell lines after treating them with different concentrations (0.0074 mg/mL - 0.042 mg/mL) of PDA(ROH) NPs (170 - 180 nm)

**Figure 4.24.** (**A**) Linear correlation obtained between the PD(ROH) NPs $Fe^{3+}$-loading efficiency (%) (Ci= 35 ppm) and their toxicity to BT474 cells. Cellular viabilities values represented were the ones obtained after 72 hours of treatment with different concentrations of the PDA(ROH) NPs. $R^2$ values were near to 0.9; (**B**) Results of the MTT assay performed with BT474 cells after simultaneously treating them with PDA(ROH) NPs (0.029 mg/mL) and non-toxic concentrations of DFO (0.7 μM) or GSH (50 μM)

**Figure 5.1.** Viability rate of BT474 (**A**) and NIH/3T3 (**B**) cells after treatment with the PDA NPs loaded with $Fe^{2+}$, $Fe^{3+}$, $Cu^{2+}$, and $Fe^{3+}$ plus $Cu^{2+}$. The color gradient represents the increasing range of concentrations used: 0.012, 0.031, 0.071 and 0.130 mg/mL for the BT474 cell line, and 0.015 and 0.040 mg/mL for the NIT/3T3 one

**Figure 5.2.** (**A**) DLS number distribution and (**B**) TEM image and size-range histogram of the PDA NPs that were later charged with $Fe^{3+}$ at three different pH values

**Figure 5.3.** TEM images (**A**) and IR spectra in the 900-1800 $cm^{-1}$ (**B**) and 2500-3700 $cm^{-1}$ (**C**) ranges of bare and the different $Fe^{3+}$-chelated PDA NPs.

**Figure 5.4.** (**A-B**) Viability results obtained after the performance of MTT assays with the BT474 and HS5 cell lines, which were treated with bare PDA NPs and the different PDA NPs@$Fe^{3+}$ synthesized (0.035 mg/mL); (**C**)

Graphical explanation of why the pH at which $Fe^{3+}$ was charged on PDA NPs may condition their cytotoxicity

**Figure 5.5.** Viability rates of BT474 (**A-C**) and HS5 (**B-D**) cells after treatment with free DOX (0.3 – 1 μM) and PDA NPs@$DOX_{0.3}$, PDA NPs@$DOX_{0.6}$ and PDA NPs@$DOX_1$ (0.035 mg/mL). The subscript refers to the initial DOX concentration used in the adsorption process. Bars with the line pattern represent the viability results that were obtained with the PDA NPs@$DOX^W$ (**A-B**), while the results obtained with the PDA NPs@$DOX^A$ were those of the empty bars (**C-D**)

**Figure 5.6.** Viability rates of BT474 (**A-B**) and HS5 (**C-D**) cells after treating them with all the different PDA NPs@$Fe^{3+}$/DOX (0.035 mg/mL). Results of graphs (**A-C**) (bars with the line pattern) were obtained using PDA NPs@$Fe^{3+}$/$DOX^W$ for treatment, while PDA NPs@$Fe^{3+}$/$DOX^A$ were employed to get graphs (**B-D**) (empty bars)

**Figure 5.7.** (**A**) Graphical explanation of how the synergy between $Fe^{3+}$ and DOX may occur after treatment with PDA NPs@$Fe^{3+}$/DOX; (**B-C**) Comparative BT474 viability rates obtained after treatment with bare PDA NPs, PDA NPs@$Fe_{2.5}$, PDA NPs@$DOX_{0.6}$ and PDA NPs@$Fe_{2.5}$/$DOX_{0.6}$ (0.035 mg/mL). Again, bars with the line pattern represent the viability values obtained with the PDA NPs@$DOX_{0.6}{}^W$/PDA NPs@$Fe_{2.5}$/$DOX_{0.6}{}^W$ (**B**), while the results obtained with the PDA NPs@$DOX_{0.6}{}^A$/PDA NPs@$Fe_{2.5}$/$DOX_{0.6}{}^A$ are those of empty bars (**C**)

**Figure 5.8.** Analysis of ROS production *in vitro* by FACS 48 hours after BT474 treatment without (**A**) or with (**B**) DOX (0.3 μM) and 0.035 mg/mL of (**C**) PDA NPs@$Fe_{2.5}$, (**D**) PDA NPs@$Fe_{3.1}$ and (**E**) PDA NPs@$Fe_{4.5}$

**Figure 6.1.** Main forms of PDA-based nanocarriers

**Figure 6.2.** Schematic illustration of the five strategies that can be followed to load PDA and PDA-modified NPs with anti-tumour drugs

**Figure 6.3.** (**A**) DLS number distribution and (**B**) TEM image and size-range histogram of the PDA NPs synthesized in an aqueous medium containing 2-PrOH to be loaded later with PTX and Tmab

**Figure 6.4.** Schematic representation of PDA NPs synthesis and loading with PTX and Tmab following two different procedures in the latter case: the carbodiimide chemistry (1) and physical adsorption (2)

**Figure 6.5.** Survival rates of BT474 (**A**), SKBR3 (**B**) and HS5 (**C**) cells after treatment with 0.035 and 0.042 mg/mL bare PDA NPs, PDA NPs@Tmab, PDA NPs@PTX and PDA NPs@Tmab@PTX, as well as with concentrations of free Tmab and PTX equivalent to those adsorbed in PDA NPs@Tmab@PTX

**Figure 6.6.** Survival rates of BT474 (**A**), SKBR3 (**B**) and HS5 (**C**) cells after treatment with 0.035 and 0.042 mg/mL bare PDA NPs, PDA NPs•Tmab, PDA NPs@PTX and PDA NPs•Tmab@PTX, as well as with concentrations of free Tmab and PTX equivalent to those chemically bound and adsorbed, respectively, in PDA NPs•Tmab@PTX

**Figure 6.7.** CLSM images of BT474 cells 48 and 72 hours after treatment with PTX (99.5 nM) and PDA NPs•Tmab@PTX (0.035 mg/mL). Cell viability and death were assessed by using calcein (green) and propidium iodide (red)

**Figure 6.8.** Flow cytometry analysis showing the percentage of apoptotic and necrotic BT474 cells 48 hours after treatment without (**A**) or with (**B**) PTX 99.5 (nM) and (**C**) PDA NPs•Tmab@PTX (0.035 mg/mL). The vertical axis indicates the cells labeled with 7AAD (PerCP) and the horizontal axis indicates those stained by Annexin V (FITC) (Early apoptosis: right lower, late apoptosis/necrosis: right upper)

**Figure 6.9.** SEM characterization of sections of BT474 MCTS 48 and 72 hours after treatment with PTX (99.5 nM) and PDA NPs•Tmab@PTX (0.035 mg/mL)

**Figure 6.10.** Schematic representation of how BT474 MCTS were developed and the effect that PTX (99.5 nM) vs. PDA NPs•Tmab@PTX (0.035 mg/mL) treatment had on their structure and morphology

**Figure 6.11.** CLSM images of BT474 MCTS 48 and 72 hours after treatment with PTX (99.5 nM) and PDA NPs•Tmab@PTX (0.035 mg/mL). Cell viability and death were assessed by using calcein AM (green) and propidium iodide (red), as usual

**Figure 6.12.** Percentage of living and dead cells cultured in 3D spheres determined by cell-counting 48 hours after treatment with PTX (99.5 nM), bare PDA NPs (0.035 mg/mL) and PDA NPs•Tmab@PTX (0.035 mg/mL)

**Figure 7.1.** Schematic illustration of the local vs. systemic drug delivery strategies. Main local DDS formulations include wafers, hydrogels, foams, fibres and particles. They can be administered in an injectable, implantable or sprayable way

**Figure 7.2.** Different types of hydrogels according to their size and their most common administration routes

**Figure 7.3.** The structure of native (**A**) and low-acyl (**B**) forms of GG

**Figure 7.4.** (**A**) Schematic representation of the synthesis process of the different HGGs, chemically crosslinked with L-Cys through the EDC chemistry. Crosslinking was possible thanks to L-Cys-L-Cys disulphide bonds; (**B**) Photo of three $HGG_{AB}$ patches obtained with different crosslinking degrees. They were dyed with food colouring

**Figure 7.5.** Frequency sweeps of the different $HGGs_{AB}$ and $HGGs_{PBS}$ performed at 25°C (**A-C**) and 37°C (**B-D**). Filled symbols represent G' values and, empty symbols, G'' values

**Figure 7.6.** Swelling kinetics of the three different $HGGs_{AB}$ as a function of the swelling time when immersed in solutions with different pH and ionic concentration at 25°C

**Figure 7.7.** Swelling kinetics of the three different $HGGs_{PBS}$ as a function of the swelling time when immersed in solutions with different pH and ionic concentration at 25°C

**Figure 7.8.** Morphological analysis under SEM of (**A**) $HGG_{AB}$[1.5LCys], (**B**) $HGG_{AB}$[3LCys], (**C**) $HGG_{AB}$[4.5LCys], (**D**) $HGG_{PBS}$[1.5LCys], (**E**) $HGG_{PBS}$[3LCys] and (**F**) $HGG_{PBS}$[4.5LCys] samples

**Figure 7.9.** IR spectra of L-Cys (**A**) and GG and the different HGGs in the 900 - 1800 $cm^{-1}$ (**B**) and 1800 - 4000 $cm^{-1}$ (**C**) ranges.

**Figure 7.10.** TG (**A**) and DTG (**B**) analysis of GG and the different HGGs

**Figure 7.11.** Image at the begging (**A**) and end (**B**) of the indentation of a HGG sample

**Figure 7.12.** Degradation behaviour over time of $HGGs_{AB}$[3LCys] and $HGGs_{PBS}$[3LCys]

**Figure 7.13.** Release behaviour of PTX from $HGGs_{AB}$[3LCys]@PTX and $HGGs_{PBS}$[3LCys]@PTX for 3 days at 37°C under 40 rpm agitation

**Figure 7.14.** (**A**) Results of the MTT assays performed with HS5 and BT474 cells to assess HGG biocompatibility. Cells were exposed to both $HGGs_{AB}$[3LCys] and $HGGs_{PBS}$[3LCys] (23.1% (V/V)); (**B**) CLSM images of HS5 and BT474 cells 24 hours after exposure to HGGs[3LCys] (23.1% (V/V)). Cell viability and death were assessed by using calcein AM (green) and propidium iodide (red)

**Figure 7.15.** (**A**) Results of the MTT assays performed with BT474 and SKBR3 cells to assess the therapeutic activity of the HGGs[3LCys] loaded with PTX:βCDs. Breast tumour cells were exposed to HGGs[3LCys] and HGGs[3LCys]@PTX (23.1% (V/V)), as well as to equivalent concentrations of PTX:βCDs (30.8 μM); (**B**) CLSM images of BT474 cells 48 and 72 hours after exposure to the same concentrations of HGGs[3LCys], HGGs[LCys]@PTX and PTX:βCDs than in the MTT tests. Cell viability and death were assessed by using calcein AM (green) and propidium iodide (red).

**Figure 8.1.** Major strategies developed in this thesis to improve current treatment of HER2+ breast cancer

**Box 1.1.** Main advantages of DDSs over conventional systemic-administered drugs in the clinical practise

**Box 7.1.** Main pros and cons of physically vs. chemically crosslinked hydrogels

# List of tables

**Table 1.1.** Some of the currently FDA-approved mAbs for cancer treatment

**Table 1.2.** Some of the currently FDA-approved small molecules for oncology indications

**Table 1.3.** TCVs currently approved by the FDA for cancer treatment

**Table 1.4.** Nanomedicines approved for cancer treatment to date

**Table 4.1.** Size (determined by DLS and TEM) of the PDA NPs prepared in the different ROH/$H_2O$(d) mixtures

**Table 4.2.** HSP values taken from the literature to calculate the $R_a$ values of DA and the different ROH/$H_2O$(d) mixtures

**Table 4.3.** HSP and $R_a$ values of DA and the different ROH/$H_2O$(d) mixtures (4:10, 28.57% (V/V)) estimated by using Equation 4.1 and 4.1.º

**Table 4.4.** HSP and $R_a$ values of DA and the different 1-PrOH/$H_2O$(d) mixtures obtained when different volume ratios of 1-PrOH in $H_2O$(d) were used

**Table 4.5.** HSP and $R_a$ values of DA and the different 2-Me-2-PrOH/$H_2O$(d) mixtures obtained when different volume ratios of 2-Me-2-PrOH in $H_2O$(d) were used

**Table 4.6.** Average size values ± SEM of the PDA NPs prepared in the different ROH/$H_2O$(d) mixtures with different $NH_4OH$ concentrations. $NH_4OH$ concentrations are expressed in % (V/V) and, NP sizes (determined by DLS), in nm

**Table 4.7.** $NH_4OH$ concentrations employed to prepare PDA NPs in the different ROH/$H_2O$(d) media (28.57% (V/V)) with a size less than 200 nm. NP concentration achieved in each case can be seen in the right column

**Table 4.8.** Freundlich constants (Q and 1/n) obtained after $Fe^{3+}$-adsorption in the different PDA(ROH) NPs at room temperature

**Table 4.9.** Zeta potential values of the PDA(ROH) NPs at pH 7.4, before and after loading them with $Fe^{3+}$ ($C_i$= 18 ppm).

**Table 4.10.** Size of the PDA(ROH) NPs that were later employed to perform viability *in vitro assays*, synthesized with the indicated $NH_4OH$ concentrations (% (V/V))

**Table 5.1.** Amount of the $Fe^{3+}$ released and the $Ca^{2+}$ adsorbed in the different PDA NPs@$Fe^{3+}$ suspended in a lysosome-simulator buffer (pH 4.5) containing $Ca^{2+}$. Percentage values regarding $Fe^{3+}$-release were calculated taking into account the amount of this cation that was loaded initially, and those regarding $Ca^{2+}$ adsorption were calculated taking into account the $Ca^{2+}$ initial buffer concentration (20 ppm).

**Table 5.2.** Amount of DOX charged in PDA NPs and the different PDA NPs@$Fe^{3+}$ as a function of the DOX initial concentration employed in the adsorption process. Results are expressed as ng DOX/mg PDA NPs.

**Table 5.3.** Results obtained when analyzing the intracellular ROS production by flow cytometry 48 hours after treating BT474 cells with DOX (0.3 μM) and the different PDA NPs@$Fe^{3+}$ (0.035 mg/mL)

**Table 6.1.** Examples of drug-loaded PDA NPs

**Table 6.2.** IEs (%) and Tmab and PTX content in PDA NPs (μg/mg) after PTX adsorption and/or Tmab adsorption/covalent conjugation

**Table 7.1.** pH values and ionic force (M) of the eight different media in which the HGGs were immersed to study their swelling kinetics

**Table 7.2.** Values of the swelling ratio of the different HGGs at the equilibrium ($Q_\infty$), obtained when equations were adjusted to a second-order kinetic model

**Table 7.3.** Values of the proportionality constant between the rate of swelling and the unrealized swelling capacity of the different HGGs at the equilibrium ($K_\infty$), obtained when equations were adjusted to a second-order kinetic model

**Table 7.4.** Average diameter (μm) ± SEM of the macro- and micropores of the HGGs that could be determined after analysing the morphology of the gels under SEM

**Table 7.5.** Kinetic parameters for PTX release from HGGs[3LCys]@PTX obtained when data were fitted to the different models described

# List of equations and reactions

**Equation 3.1**

**Equation 3.2**

**Equation 3.3**

**Equation 4.1**

**Equation 4.2**

**Equation 4.3**

**Equation 4.4**

**Equation 5.1**

**Equation 6.1**

**Equation 6.2**

**Equation 7.1**

**Equation 7.2**

**Equation 7.3**

**Equation 7.4**

**Equation 7.5**

**Equation 7.6**

**Equation 7.7**

**Equation 7.8**

**Equation 7.9**

**Equation 7.10**

**Equation 7.11**

**Equation 7.12**

**Equation 7.13**

# Abstract

Among the different molecular subtypes of breast cancer that are distinguished, the HER2-positive subtype is characterized, as its name indicates, by keeping the epidermal growth factor receptor-2 overexpressed. This overexpression, which occurs in 15-20% of breast cancer cases diagnosed, is related to a higher rate of cell proliferation and metastasis, so that it has long being associated with inferior outcomes for patients. Nevertheless, in recent decades, HER2-overexpression has also allowed the development of targeted therapies, which have contributed to considerably increase the disease-free survival rate of patients with HER2-positive breast cancer. Thus, today, one of the standard first-line treatments for this type of cancer consists of the combination of paclitaxel (an anti-mitotic drug) and trastuzumab (an anti-HER2 monoclonal antibody), since several trials have shown that a synergist effect occurs between this taxane and antibody. However, although paclitaxel is one the most successful anti-tumour drugs available these days and trastuzumab has proven to be very effective in inducing tumour regression, their administration entails severe side toxicity, and treatment resistances appear frequently.

Both, the apparition of adverse effects and drug resistances is mainly caused by the low bioavailability and the lack of specificity of conventional antineoplastic agents. For this reason, in the past few years, nanomedicine has aroused special interest in cancer chemotherapy, and has been applied to develop drug delivery systems to improve drug biodistribution, therapeutic activity and selectivity.

In this way, pursuing these goals, three main different nanotechnological strategies were developed in this doctoral thesis to improve the current drawbacks of HER2-positive breast cancer treatment.

The first strategy developed was focused on the design of polymeric nanoparticles, made of alginate and piperazine, that served as a targeted vehicle for paclitaxel and trastuzumab. In order to select the most suitable nanoparticles for this application, alginate and piperazine solutions were mixed in different ratios. The resulting nanosystems,

obtained thanks to the electrostatic interactions that take place between both compounds at acidic pH, were characterised. Then, the smallest nanoparticles (160 nm) were conjugated with trastuzumab and paclitaxel, previously included into β-cyclodextrins. This conjugation was carried out by means of the carbodiimide chemistry and, once the loaded nanoparticles were also characterized, their internalization in HER2-positive breast cancer cells was analysed. Subsequently, their efficacy and specificity were validated *in vitro*. Co-cultures of stromal and HER2-overexpressing breast cancer cells were treated with the conjugated nanoparticles, and conventional viability assays were performed with cell lines showing different HER2 expression levels. Results achieved in both types of experiments showed that the nanosystem developed was as effective as equivalent concentrations of paclitaxel-β-cyclodextrin complexes and even more effective than equivalent concentrations of paclitaxel. Furthermore, it reduced the viability of normal cells significantly less than the parent drug. At last, HER2-positive tumour spheroids were also developed to ascertain whether the paclitaxel-trastuzumab nanosystem obtained maintained its anti-tumour activity in these 3D biostructures mimicking human tumours. Alive/death confocal assays and cell counting were performed, and results achieved demonstrated that conjugated alginate-piperazine nanoparticles kept their anti-tumour activity when validated in 3D cell cultures.

Next, the second strategy consisted of developing new drug delivery systems based on polydopamine nanoparticles. Polydopamine, a synthetic melanin analogue, has acquired a relevant role in cancer nanomedicine in recent years thanks to its outstanding physicochemical properties. Nonetheless, despite the interest that this polymer has aroused in the scientific community, its antineoplastic activity had not been studied *in vitro* in depth yet. This is why such study was done in this thesis prior developing any polydopamine-based drug delivery system.

Thereby, for this, polydopamine nanoparticles were synthesized by dopamine solution oxidation in alkaline media containing different types of alcohols (ethanol, methanol, 2-propanol, 1-propanol and 2-methyl-2-propanol). Besides, with the aim of modulating the size (100 - 450 nm) of the polydopamine nanoparticles prepared, the $NH_4OH$ concentration used was modified in the synthesis media. Then, the

cytotoxicity of the different nanosystems obtained was determined by performing viability assays with several malignant and normal cell lines. A new protocol was stablished to subtract polydopamine absorbance when carrying out MTT experiments. By following this procedure, it was noticed that polydopamine nanoparticle size conditioned their cytotoxicity: the smaller the diameter, the greater the anti-tumour activity of the nanoparticles, which was more marked to malignant cells than to stromal cells. Likewise, it was observed that polydopamine nanoparticle cytotoxicity was also conditioned by the type of alcohol employed to synthesize them, which also influenced the well-known ability of these nanoparticles to chelate $Fe^{3+}$. As a consequence, and since it was proven that polydopamine nanoparticles were internalized in the cellular endo/lysosomes using confocal microscopy, it was hypothesized that their cytotoxicity may be related to their ability to chelate the $Fe^{3+}$ existing in these organelles. This hypothesis was later verified, when further viability assays were performed after treating different cell lines with polydopamine nanoparticles plus an iron chelator or an antioxidant compound. Both compounds antagonized polydopamine nanoparticle toxicity, so it was revealed that a disequilibrium of the intracellular Fe homeostasis could be responsible for the customizable, intrinsic anti-tumour activity of these nanoparticles.

Once at this point, a second drug delivery system was designed: polydopamine nanoparticles (150 nm) loaded with $Fe^{3+}$ and doxorubicin.

On one hand, $Fe^{3+}$ was loaded to polydopamine nanoparticles in order to target HER2-positive breast tumour cells, which overexpress the transferrin receptor-1, and to enhance the ferroptosis process that these nanoparticles may produce by themselves. Since the pH determines if $Fe^{3+}$ is a free cation or is forming $Fe(OH)_3$, $Fe^{3+}$ was loaded to polydopamine nanoparticles at different pH values to find the nanosystem with the greatest antineoplastic activity and selectivity. The different $Fe^{3+}$-loaded nanoparticles obtained were characterized and, when MTT assays were performed with them, it was proven that the anti-tumour activity and specificity of polydopamine nanoparticles were more remarkable when charged with more free $Fe^{3+}$ than $Fe(OH)_3$.

On the other hand, as doxorubicin is capable of inducing cell apoptosis and also ferroptosis as a side effect, this drug was loaded to

polydopamine nanoparticles to achieve a synergist effect with the $Fe^{3+}$ charged while reducing its side toxicity. Different concentrations of doxorubicin were adsorbed directly to polydopamine nanoparticles loaded with or without $Fe^{3+}$, which were or not later isolated in order to perform two different types of viability assays. When the latter were carried out, polydopamine nanoparticles transporting doxorubicin showed great anti-tumour activity and less toxicity to stromal cells than the parent drug. Furthermore, when nanoparticles were charged with both $Fe^{3+}$ and doxorubicin, synergy occurred between them. In addition, the importance of the pH value at which the $Fe^{3+}$-loading was carried out was again revealed, since those nanoparticles charged with more free $Fe^{3+}$ instead of $Fe(OH)_3$ were more efficacious, even despite having charged less amount of doxorubicin. In this way, this drug delivery system could be tailored-made by adjusting the $Fe^{3+}$-loading pH and the amount of doxorubicin charged depending on the potential clinical objectives pursued (increased therapeutic activity *vs.* reduced side toxicity).

Subsequently, taking into account the good results that were achieved *in vitro* with the alginate-piperazine nanoparticles conjugated with paclitaxel and trastuzumab, loading this drug and antibody to polydopamine nanoparticles (180 nm) for the first time was determined in order to develop an even more efficient drug delivery system thanks to polydopamine advantages.

Since it was previously observed that 2-propanol was the alcohol that conferred the highest anti-tumour activity to polydopamine nanoparticles, these were synthesized with this alcohol. Next, paclitaxel was directly adsorbed in polydopamine nanoparticles, without the need to include it previously in β-cyclodextrins. Trastuzumab was both directly loaded and covalently bound through the carbodiimide chemistry to compare the results obtained following both strategies. The anti-tumour activity and selectivity of the resulting loaded polydopamine nanoparticles were evaluated by means of MTT assays performed again with HER2-positive breast cancer cells and stromal cells. As a result, it was observed that the two types of conjugated polydopamine nanoparticles had great therapeutic activity, and that they were more effective than the alginate-piperazine nanosystem developed previously. Furthermore, loaded

polydopamine nanoparticles proved to be less toxic to normal cells than equivalent concentrations of paclitaxel.

Of the two types of loaded nanoparticles designed, the one in which trastuzumab was covalently bound showed to be slightly more effective and selective, so it was chosen to perform further studies. Thereby, results achieved in the MTT experiments were corroborated with the performance of alive/death confocal assays. Likewise, as was done with the previous paclitaxel-trastuzumab nanocarrier, the antineoplastic activity of the polydopamine nanoparticles selected was validated by employing HER2-positive breast tumour spheroids. The interaction between the nanoparticles and the 3D biostructures was analysed by scanning electron microscopy, further alive/death assays and cell counting. Results achieved with the different techniques allowed to reach the same conclusion: this third drug delivery system developed also maintained their efficacy in 3D cell cultures.

In the end, to finish this thesis, a third strategy was carried out to improve HER2-positive breast cancer treatment, developing macroscopic gellan gum hydrogels loaded with paclitaxel for local, post-surgery chemotherapy applications. These hydrogels were synthesized in both acetate buffer and phosphate buffer and were crosslinked at different degrees with L-cysteine. Once obtained, the hydrogels were extensively characterized by means of rheological analysis, swelling capacity studies, morphological and chemical analysis, thermogravimetric analysis and compression measurements. The results obtained after the characterization process led to select the hydrogels with an intermediate crosslinking degree to be loaded with paclitaxel, as they were shown to have a more suitable pore size for the desired application. Thus, once their biodegradability and biocompatibility were verified, these hydrogels were loaded with paclitaxel-β-cyclodextrin complexes, again developed to improve the solubility of the taxane. Paclitaxel release from the hydrogels was studied and, finally, the anti-tumour effect of the loaded gels was validated *in vitro*. Both MTT assays and alive/death confocal assays were performed with different HER2-positive breast cancer cell lines, and results obtained proved that loaded gellan gum hydrogels had great anti-tumour activity. In addition, they proved to be a good strategy to achieve a paclitaxel sustained release, which in fact may be tailored to potentially

complement other systemic anti-tumour therapies by modifying the synthesis medium of the hydrogels and their degree of crosslinking.

# CHAPTER 1

## INTRODUCTION. CANCER COMPLEXITY AND THE RELEVANT ROLE OF NANOMEDICINE IN ITS TREATMENT

## 1.1. What does the word “cancer” encompass?

According to the data that can be found in the Global Cancer Observatory (GCO), a web-based platform of the World Health Organization (WHO), cancer is the second leading cause of mortality and morbidity worldwide. In 2018, almost 18.1 million new cases were diagnosed, and this disease was responsible for the death of about 9.6 million people. More specifically, cancer had an incidence of 4.2 million cases in Europe and, on our continent, caused the death of almost 2 million people. In addition, although these figures already give food for thought, the future is not very encouraging, since cancer is expected to have even higher incidence and mortality rates in coming decades, as can be seen in **Figure 1.1** [1].

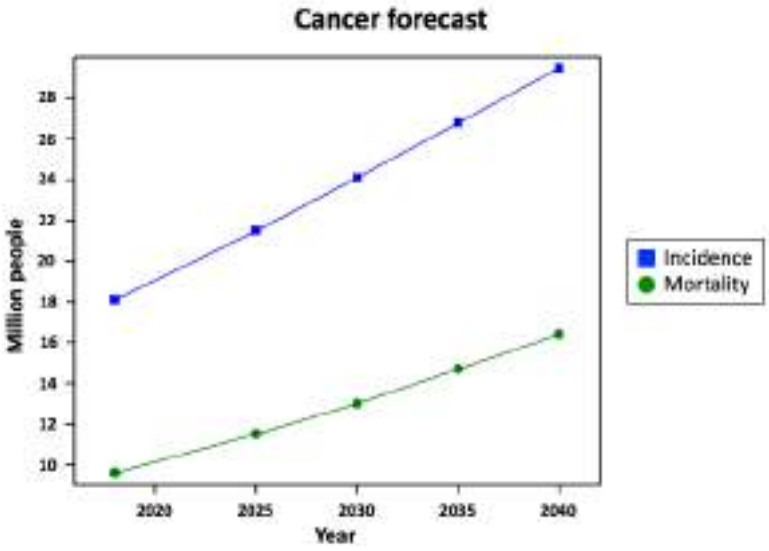


**Figure 1.1**. Cancer incidence and mortality rates expected in following decades according to the forecasts of the GCO.

Although cancer is considered as a single disease when these global data are collected, it is a very broad term. There are more than 200 different types of cancer and each of them has particular characteristics. Sometimes, these characteristics differ so much among the different sorts of cancer that these can even be regarded as independent diseases [2].

Moreover, molecular subtypes of tumours can be found within specific organs, further complicating the understanding and treatment of this disease.

Nevertheless, after more than a quarter century of rapid advances, some global rules that govern the transformation of normal human cells into malignant neoplasms have been accepted by the scientific community. As Hanahan and Weinberg described in 2000, all mammalian cells carry similar molecular machinery regulating their proliferation, differentiation and death, and tumour development proceeds via a process that can be compared to Darwinian evolution. Thereby, according to these authors, a succession of genetic changes confers some type of growth advantage to the cells and allows them to progressively become malignant tumours [3]. Thus, cancer is a disease involving dynamic changes in the genome, since there are mutations that produce oncogenes with dominant gain of function and tumour suppressor genes with recessive loss of function. In this manner, Hanahan and Weinberg firstly suggested that the vast catalogue of cancer genotypes was a manifestation of six essential alterations in cell physiology. Then, eleven years later, they added two more alterations to their list of hallmarks of cancer, as well as two tumour enabling characteristics [3-6]. All of them have been briefly described below.

## 1.2. The hallmarks of cancer

### *1.2.1. Initial hallmarks of cancer*

In their first review article, Hanahan and Weinberg highlighted the existence of six hallmarks of cancer, which have been summarized in **Figure 1.2**: self-sufficiency in growth signals, insensitivity to anti-growth signals, evading apoptosis, limitless replicative potential, sustained angiogenesis and tissue invasion and metastasis [3,5].

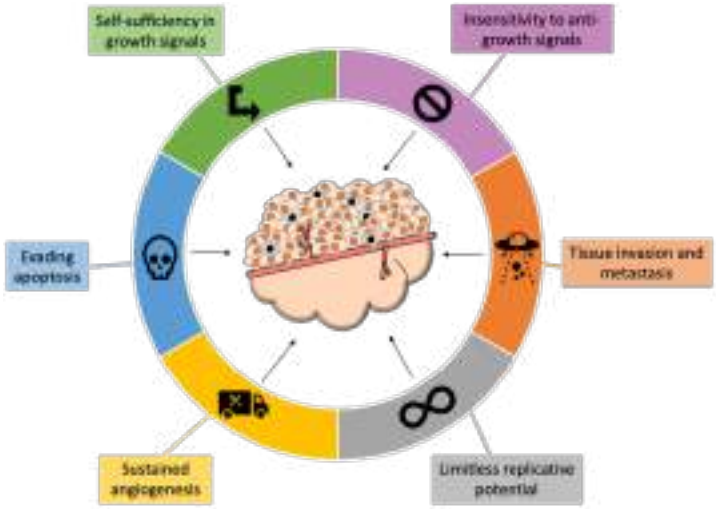


**Figure 1.2.** Acquired capabilities of cancer according to Hanahan and Weinberg [3].

#### 1.2.1.1. Self-sufficiency in growth signals

Regarding the first of these hallmarks, it should be noted that normal cells require the transmission of signalling molecules (diffusible growth factors, extracellular matrix (ECM) components and/or cell to cell interaction molecules) to move from a quiescent state into an active proliferative state. Conversely, cancer cells show much less dependency on exogeneous growth stimulation. In this way, these cells can achieve autonomy by means of three different strategies: modification of the extracellular growth signals, alteration of the transcellular transducers of these signals, and transformation of the intracellular circuits responsible for translating such signals into action [3,7].

Thereby, some malignant cells are able to accomplish an autocrine proliferation stimulation through their own production of growth factors, while others overexpress or switch their surface/ECM receptors favouring the transmission of pro-growth signals [3,7]. For instance, dysregulation of the platelet-derived growth factor (PDGF)-mediated signalling has been stablished as basis of cancer development [8], as well as alterations in the tumour necrosis factor (TNF)-α inflammatory network [9]. Similarly, it has been demonstrated that the overactivation of several receptor tyrosine

kinases (RTKs), such as the fibroblast growth factor (FGF) and the epidermal growth factor (EGF) receptors, makes cells act in an oncogenic fashion to promote the progression of different types of carcinomas in multiple steps [10,11]. Also, as mentioned before, malignant cells can disturb their intracellular signaling pathways in order to maintain an elevated proliferation rate. In this case, the modification of the PI3K-Akt and Ras-MAPK pathways plays a central role in cancer progression [12], inasmuch as a great percentage of solid tumours bear mutant *ras* and *PI3K* oncogenes [3,12-14]. Last but not least, malignant cells are not only capable of altering their own signaling, but also have the ability to induce normal neighbors to release abundant growth-stimulating signals, making the surrounding stroma essential to promote tumorigenesis [3,15].

1.2.1.2. Insensitivity to anti-growth signals

Otherwise, there are growth inhibitors that, like their positively acting counterparts, are received by transmembrane receptors in order to maintain normal tissue homeostasis. Such anti-growth signals, which are as a rule associated with the cell cycle clock (**Figure 1.3**), can block proliferation in two ways: by forcing cells to become quiescent and enter into the $G_o$ phase, or by forcing them to relinquish their proliferative potential, differentiate and enter into postmitotic states [3].

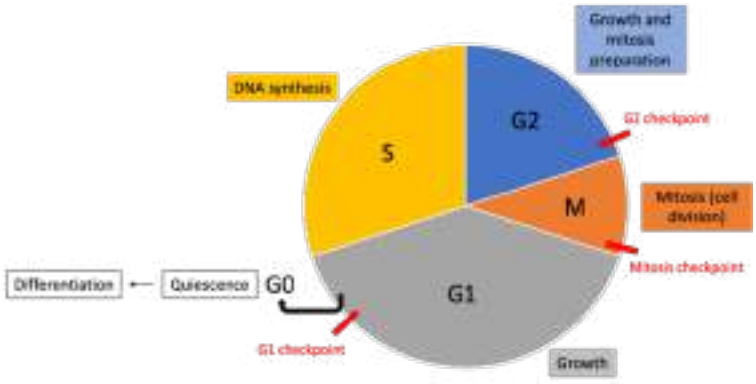


**Figure 1.3.** Cell cycle clock: Growth inhibitors, under normal physiological conditions, force altered cells to become quiescent and differentiate, thus preventing them for dividing.

Most anti-proliferative signals are funnelled through the retinoblastoma protein (pRb) which, when hypophosphorylated, can prevent the progression from $G_1$ into the S phase of the cell cycle [3]. In this way, inactivation of the pRB pathway is a mandatory event for the development of all human cancers, and malignant cells can pursue different strategies to achieve it [16,17]. Since the transforming growth factor (TGF)-β is the main soluble signalling molecule responsible for avoiding pRb phosphorylation, some tumour cells downregulate or exhibit mutant or dysfunctional TGF-β receptors, while others eliminate the transducers of the ligand-activated TGF-β receptors (like Smad4 or CDK4) through mutations [3,18]. Moreover, cancer cells are also capable of preventing terminal differentiation by overexpressing the oncogene *c-myc*, which is essential to promote cell growth [3,19].

1.2.1.3. Evading apoptosis

However, cell growth and tumour expansion not only depend on cell proliferation, but also on cell attrition, which is intimately related to programmed cell death. For this reason, all types of cancer cells tend to acquire apoptosis resistance. This phenomenon was the third hallmark of cancer described by Hanahan and Weinberg [3].

Apoptosis is present in all human cell types and is normally triggered by a variety of physiological or pathological situations (DNA damage, signalling imbalance, hypoxia…) that cause series of very defined steps to occur at the molecular level. These steps involve the action of two types of machinery: apoptosis sensors, which monitor the extra- and intracellular environments for abnormalities that determine whether a cell should live or die, and apoptosis effectors, which are cell surface receptors that bind survival (insulin growth factor (IGF)-1/2, interleukin (IL)-3) or death factors (FAS, TNF-α). Both, sensors and effectors, are controlled by an apoptotic gene family, of which two major genes are involved in programmed cell death: *bcl-2* and *p53*. The first of them, *bcl-2,* belongs to a family of anti-apoptotic genes. Its translocation has been linked to *c-myc* activation and clonal expansion of malignant immortalized cells. Just the opposite, *p53* is a tumour suppressor gene known as “the guardian of the genome”. Loss of its function, which occurs in more than

in 50% of human solid tumours, is involved in early neoplasia steps, since it allows the survival of cells that harbour genetic mutations [3,20-21].

In addition, *bcl-2* and *p53* genetic mutations are not only relevant for tumour expansion, but also modulate cancer cells sensitivity to radio- and chemotherapy agents that induce cell death via programmed suicide [20]. Thereby, anti-apoptotic mutations arising during tumour development can select for chemoresistant cells [21]. Nevertheless, most cellular regulatory components are present in redundant form, and this can be taken into account to develop new anti-cancer drugs that would enable a crosstalk between the still intact components of parallel apoptotic signalling pathways [3].

#### 1.2.1.4. Limitless replicative potential

Besides, a deregulated proliferation program is insufficient, on its own, to allow the generation of macroscopic tumours. Almost all types of mammalian cells carry an intrinsic program that limits their replicative potential and acts independently of the three signalling pathways described so far. Thus, normal cell populations progress through a certain number of doublings. Then, they stop growing and become senescent because they lose part of their telomeric DNA during each cell cycle. In this way, most types of tumour cells have to overcome the mortality barrier and acquire unlimited replicative potential, which is the fourth hallmark of cancer [3,22].

This infinite replicative potential is achieved by malignant cells through telomere maintenance, which is gained most of the time (in 85-90% of cases) via upregulated expression of the telomerase enzyme. Notwithstanding, it can be also got via a homologous recombination-mediated process known as ALT (alternative lengthening of telomers) (in 10-15% of cases) [23,24].

#### 1.2.1.5. Sustained angiogenesis

Apart from the replicative potential, oxygen and nutrients supplied by the vasculature are crucial for cell function and survival and, therefore, for tumour growth. Normal cells in a tissue need to be located within 100-200 µm of capillary blood vessels, which grow in a regulated manner once a

new tissue is formed. Thereby, healthy proliferating cells are supposed to have intrinsic ability to encourage blood vessel formation, except when they have aberrant lesions. In this last case, normal altered cells lack angiogenic ability to avoid their expansion, which shows that pre-malignant cells must acquire angiogenic capacity on their way to becoming cancerous [3,25].

Angiogenesis process can be encouraged or blocked by soluble factors and their corresponding receptors, which are present on the surface of endothelial cells, as well as by integrins and adhesion molecules [3]. As regards the former, more than a dozen different proteins have been identified as angiogenic activators, including the vascular endothelial growth factor (VEGF), the basic FGF, Il-8 and the already mentioned TGF-β and -α, TNF-α, EGF… Among them, the VEGF family and their receptors have received more attention in the field of neoplastic vascularization, since it has been demonstrated that hypoxia situations induce their expression via the hypoxia-inducible factor (HIF)-1α [26]. Similarly, more than a dozen angiogenesis soluble inhibitors are known, including thrombospodin-1, angiostatin, endostatin, interferon… Under normal physiological conditions, there is a balance between these inducers and inhibitors, but changes in this equilibrium are responsible for the angiogenesis switch that occurs in tumours. For instance, cancer cells, by means of *ras* activation and *p53* suppression, overexpress VEFG and FGF and stimulate pro-angiogenic integrin signalling, while they downregulate thrombospodin-1 expression [3,26]. In this way, they are capable of sustaining angiogenesis despite having malignant lesions.

#### 1.2.1.6. Tissue invasion and metastasis

Finally, regarding the sixth and last hallmark of cancer described by Hanahan and Weinberg in their first review study [3], it is important to note that angiogenesis is not only important for the supply of oxygen and nutrients. This capillary formation process is also essential for primary tumours to colonize adjacent tissues and originate metastases, which in fact are responsible for 90% of human cancer deaths. Herein, thanks to their capability of invasion, cancer cells are able to colonize new body tissues where nutrients and space are not initially limited, and secondary

tumours arise as a mixture of cancer and supporting normal cells from the host tissue.

Metastasis is such a complex process that it is even partially unknown. What is clear to date is that it takes place thanks to alterations in proteins involved in tethering the cells to their surroundings. Among these proteins, cell-cell adhesion molecules (CAMs), integrins and extracellular proteases are some of those that undergo functional modifications [3]. For example, E-cadherin, whose bridges between adjacent cells result in the transmission of anti-growth factors and invasion suppression, suffers a mutational inactivation in some cancer cells to allow them acquire metastasis capability. In the same manner, mutational changes in integrins, which link cells to ECM substrates, are frequent, since these mutations generate novel integrin subtypes that allow malignant cells to adapt to the composition of the ECM of the normal epithelium that they invade. Finally, matrix-degrading proteases, which also play a role in the other hallmark capabilities, are also upregulated in many human tumours to facilitate invasion processes [3,27].

### *1.2.2. Tumour enabling capabilities and newer hallmarks of cancer*

As mentioned at the beginning of the introduction, Hanahan and Weinberg described in a second review study two characteristics that enable tumours to acquire the hallmarks that they had previously detailed, and they added two emerging ones to their anterior list [3,4] (**Figure 1.4**).

As regards the enabling properties, these authors considered that both, genome instability and inflammation, were essential for promoting tumour development [4].

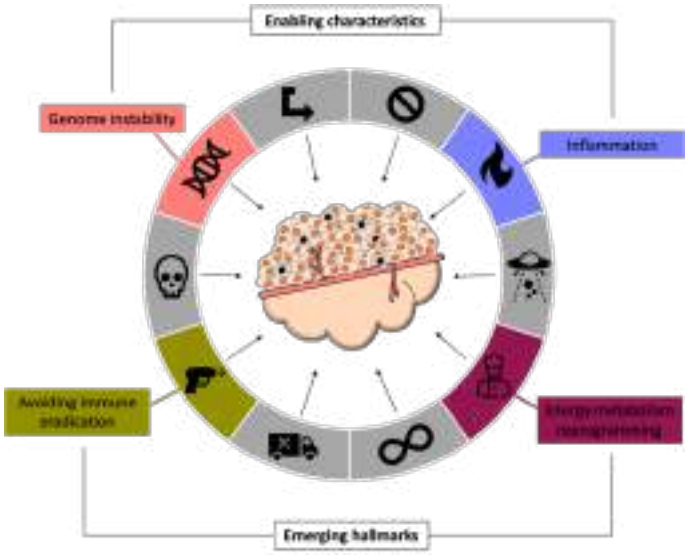


**Figure 1.4.** Enabling characteristics and emerging hallmarks of cancer described by Hanahan and Weinberg in their second review study [5].

### 1.2.2.1. Genome instability

Since certain mutant genotypes confer selective advantage on subclones of cells, genomic instability is a molecular key that enables their outgrowth and dominance in a local tissue environment, and which allows multistep tumour progression to occur through a succession of clonal expansions.

Approximately, 30% of human genes encode for proteins that regulate DNA fidelity. The extraordinary ability of the genome maintenance systems to detect and resolve defects in the DNA ensures that spontaneous mutation rates are usually very low during each cell generation. Thus, cancer cells must enhance such rates of mutation, so they increase their sensitivity to mutagenic agents, break one or several components of the genomic maintenance machinery and/or compromise the surveillance systems that monitor genomic integrity. For this reason, most cancer cells exhibit mutations in caretaker genes that detect DNA damage and activate the repair machinery, repair the DNA or inactivate mutagenic molecules before they damage the DNA. In the case of hereditary cancer syndromes, germline mutations in DNA repair genes are

responsible for the emergence of malignant tumours, while oncogene-induced DNA replication stress is believed to account for genomic instability in sporadic tumours. In any case, genome instability in both, hereditary and sporadic tumours, can be got through subtle DNA sequence changes (base substitutions, deletions or insertions and microsatellite instability), alterations in the chromosome number (CIN), chromosome translocations and gene amplifications, and it is fundamental to orchestrate all the cancer hallmark capabilities here described [4,28-29].

1.2.2.2. Inflammation

The second enabling characteristic that also orchestrate cancer hallmarks is inflammation, driven by cells of the immune system that promote tumour progression [4].

Initially, the immune response was largely though to reflect the attempt of the immune system to eradicate tumours. Nevertheless, at the end of the 21$^{st}$ century, some epidemiological studies showed that chronic inflammation predisposed individuals to various types of cancer. Thereby, it turned out that the immune system has a dual role, since it has the paradoxical effect of enhancing tumorigenesis by helping incipient neoplasms to acquire hallmark capabilities.

In this acquisition process, tumour-associated macrophages (TAMs), which are a significant component of the inflammatory infiltrate in neoplastic tissues, have demonstrated to play an important role. These immune cells are able to promote cancer progression through the supply of bioactive molecules to the tumour microenvironment, such as growth factors, survival factors, proangiogenic factors and enzymes that facilitate invasion of cancer cells. Moreover, TAMs are also responsible for the release of some chemicals, like reactive oxygen species (ROS) and nitrogen species, which are mutagenic and accelerate the genetic evolution of malignant cells. Likewise, they promote the production of migration inhibitory factors that impair p53-dependent protective processes. Furthermore, not only TAMs contribute to tumorigenesis, but also the tumour inflammatory microenvironment can facilitate the breakage of the basement membrane and assist cancer cells to migrate. Thus, all these

facts help to understand why cancer cells also produce cytokines and chemokines to attract immune cells to tumour tissues with the aim of creating conditions that facilitate cancer development, and why some authors have referred to tumours as wounds that fail to heal [4,30-32].

1.2.2.3. Evading immune eradication

Otherwise, the two emerging characteristics of tumour cells that Hanahan and Weinberg added to complete their list of hallmarks of cancer were reprogramming energy metabolism and evading immune eradication [4].

The latter, closely related to the second enabling characteristic explained in the previous point, is a still-unresolved issue. The role of the immune system in the destruction of incipient neoplasms, large-stage tumours and metastasis is not completely known yet [4].

About 10 years ago, several studies that were conducted with immunodeficient mice showed that such immune role was important not only for the great majority of the virus-induced cancers, but also for at least some forms of non-virus-induced tumours [4,33]. In this manner, Schreiber and colleagues proposed in 2011 the cancer immunoediting process, comprised by three different phases: “elimination”, “equilibrium” and “escape” [33,34]. The first of them, the elimination phase, is a cancer immune-surveillance process, in which the innate and the adaptative immune systems work together to stablish the initial effective barrier to tumorigenesis. Natural killer (NK), cytotoxic T lymphocytes (CTLs) ($CD8^+$ T cells) and helper T cells ($CD4^+$ T cells), which are possibly alerted by the expression of stress ligands on cancer cell surface, protect host against developing tumours. If they are able to completely destroy tumour cells, the elimination phase represents an endpoint of the cancer immunoediting process. On the contrary, if this does not happen and cancer cell variants survive, the equilibrium phase, in which the immune system maintains residual malignant cells in a dormancy state, starts. This equilibrium can last host lifetime, becoming the second endpoint of the immunoediting process. However, if the selective pressure exerted by the immune system has the effect of promoting the outgrowth of cancer cells

that have acquired immune-evasive mutations, such cells enter the scape phase and generate growing visible tumours. Progression from equilibrium to the escape phase can occur because tumour cells mutate in response to the immune system functions or because such immune system is supressed or deteriorated. Both changes are promoted by malignant cells through the secretion of immunosuppressive factors (TGF-β, IL-10, VEGF…), the recruitment of inflammatory cells that supress the action of the CTLs and/or by mutations in key genes of antigenic peptides that help to avoid immune recognition by CTLs [4,34-35].

1.2.2.4. Energy metabolism reprogramming

To finish the hallmarks of cancer and because uncontrolled cell proliferation involves not only a deregulated control of growth, but also a metabolism adjustment to fuel cell proliferation and division, Hanahan and Weinberg included this cancer ability in their list [4].

The first scientific evidence of cancer metabolism reprogramming was reported in 1922 by Warburg [36], who noticed that cancer cells carry out anaerobic glycolysis instead of mitochondrial oxidative phosphorylation even in the presence of oxygen ("Warburg effect"). At first glance, this metabolic adjustment, which is promoted by aberrant activation of the PI3K-AKT network and *p53* mutations [37], might seem counterproductive to neoplastic cells, since fermentation is less efficient than oxidative phosphorylation in the generation of adenosine triphosphate (ATP) molecules. However, it was later discovered that this metabolism reprogramming allows tumour cells to divert glycolytic intermediates into various biosynthetic pathways to generate nucleosides and amino acids, also essential for maintaining their exorbitant proliferation rate [4,38]. In fact, hypoxia, which operates within many tumours, accentuates glycolysis through the activation of HIF-1α. Thus, it has been shown that some tumours are composed by two symbiotic subpopulations of cells: hypoxic cells that depend on glucose for fuel and that secrete lactate as waste, and better-oxygenated cells that import this lactate to obtain energy and synthesize cellular components [4,37].

A graphic summary of all the hallmarks of cancer and tumour enabling characteristics described by Hanahan and Weinberg can be found in **Figure 1.5**.

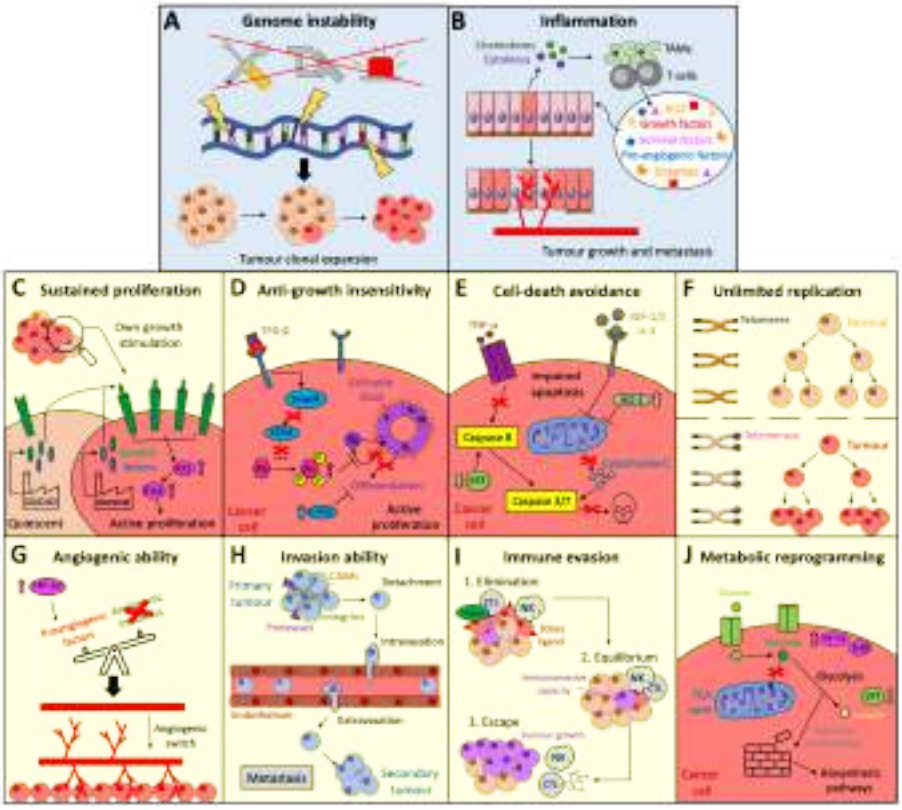


**Figure 1.5.** Summary of the enabling properties (blue pictures) and hallmarks (yellow pictures) of cancer described by Hanahan and Weinberg [3,4]: (**A**) Genome instability; (**B**) Inflammation; (**C**) Self-sufficiency in growth signals; (**D**) Insensitivity to anti-growth signals; (**E**) Evading apoptosis; (**F**) Limitless replicative potential; (**G**) Sustained angiogenesis; (**H**) Tissue invasion and metastasis; (**I**) Reprogramming of energy metabolism; (**J**) Evading immune eradication.

## 1.3. History of chemotherapy in cancer “war”

Hanahan and Weinberg defined the different hallmarks of cancer thanks to all the molecular and genetic approaches that were made in the 1980s to understand cell biology, and that enabled to discover that some signalling networks are radically altered in cancer cells [39]. In addition, this discovery also brought about fundamental advances in the pharmaceutical industry, which made conventional chemotherapy transitioned to the age of the “targeted therapy” [39,40] (**Figure 1.6**).

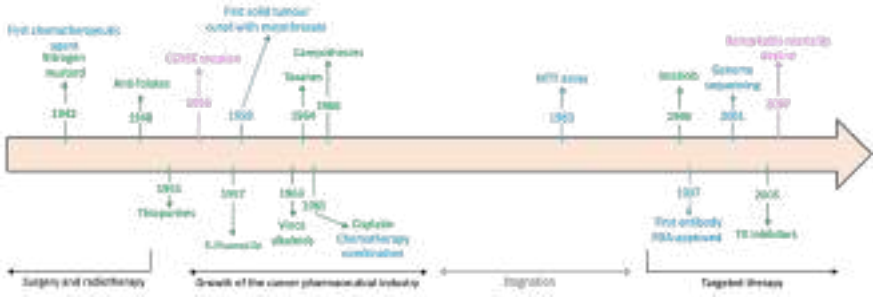

**Figure 1.6.** Chronological axis showing the advances in the pharmaceutical industry that made conventional cancer chemotherapy transitioned to the age of the “targeted therapy”.

Until the 1960s, surgery and radiotherapy dominated the field of cancer therapy, allowing to control local and regional disease. Nevertheless, it became clear that effective treatment for most patients needed to reach every organ in the body, since surgery and radiotherapy could not eradicate micrometastasis. From that point on, cancer chemotherapy became the focus to cure this complex disease [39,40].

The beginning of the modern era of cancer chemotherapy can be traced directly to the discovery of nitrogen mustard. It was developed for chemical warfare but, in 1942, this compound was ascertained to be effective in cancer treatment. Goodman and Gilman injected nitrogen mustard into the bloodstream of a patient with advanced non-Hodgkin’s lymphoma and noted that it achieved tumour regression, although this positive effect stayed only for a few weeks. In later studies, these pharmacologists found out that the molecular anti-tumour action of the

mustard compound was based on the generation of an alkylating intermediate that formed covalent bonds between DNA strains and that induced cell apoptosis. Such finding, in addition to show that systemic administration of drugs could represent a good strategy to fight against cancer, led to the development of novel and improved alkylating agents in the following 20 years. Among them, for instance, cyclophosphamide and chlorambucil stood out due to their efficacy. They began to be part of the regimens that were used to treat patients with non-solid tumours but, unfortunately, scientists noticed that cancer cells quickly became resistant to these drugs [39-41].

A second approach of cancer chemotherapy started after the Second World War, when Farber realized that folic acid stimulated the proliferation of acute lymphoblastic leukaemia (ALL). He and his collaborators synthesized folate analogues (aminopterin and, later, the now well-known methotrexate) that blocked the function of a folate-requiring enzyme, the dihydrofolate reductase (DHFR). These compounds were able to successfully induce a brief remission in children with ALL and, in subsequent decades, methotrexate (MTX) started to acquire a relevant role in cancer chemotherapy. The reason was that its administration managed to cure the first human solid tumour (a choriocarcinoma) in 1958. Later, the employment of this folate analogue in combination with leucovorin stablished the principle of the adjuvant therapy. Besides, MTX was the first drug for which pharmacokinetic analysis were performed to monitor its clearance and, in this way, to identify patients at risk of severe toxicity. It is still clinically administered to treat patients who suffer from ALL, certain lymphomas and osteosarcomas, and studies of MTX provided important understanding of the resistance mechanisms to other agents [39,42].

Little by little, results obtained with the administration of nitrogen mustard and MTX stimulated the synthesis of further chemotherapeutic drugs. Thereby, the same year that Farber showed the antifolate activity of MTX in childhood leukaemia, Hitchings and Elion isolated a compound that blocked adenine metabolism. Then, in the early 1950s, they developed two drugs from that compound which later became essential for the treatment of acute leukaemia: 6-thioquanine and 6-

mercaptopurine (6-MP). With these thiopurines, Elion and colleagues demonstrated that small changes in a compound needed by the cells (adenine in their case) could inhibit tumour growth [43]. In fact, they won the Nobel Prize in Medicine in 1988 because these thiopurines started to be widely used for the treatment of other non-neoplastic diseases [39,40].

In the same decade, the pharmaceutical company Eli Lilly discovered that *Vinca* alkaloids, employed as anti-diabetic agents, were able to inhibit microtubule polymerization and, therefore, cell division. Some years later, vincristine, one of these natural *Vinca* alkaloids, was used in combination with MTX, 6-MP and prednisone (an immune system suppressant) to treat childhood leukaemia. Such combination, stablished by three American scientists as the VAMP regimen [44], proved that combining drugs with a different site of action was the most effective manner to prevent the apparition of tumour resistances [39].

On the other hand, also in the 1950s, Heidelberger and collaborators developed a drug that was aimed at non-hematologic cancers: 5-fluorouracil (5-FU). These authors realized that rat hepatoma metabolism showed greater dependence on uracil relative to normal tissue, and they "targeted" this biochemical pathway by attaching a fluorine atom to uracil. 5-FU was found to have broad-spectrum activity against a wide range of solid tumours, and it is still a key piece in the treatment of colorectal cancer these days [40,45]. Moreover, 5-FU can be considered as the first example of targeted therapy, although the target was a biochemical pathway and not a specific biomolecule.

The success in treating ALL, together with the availability of novel animal tumour screening models, led to the creation of the first federal programme in the U.S. to promote drug discovery for cancer in 1955: The Cancer Chemotherapy National Service Centre (CCNSC). Although it was often criticized, this programme changed the face of cancer drug development worldwide, since it provided a sole resource to test, develop and produce drugs, and gave birth to the current multibillion-dollar cancer pharmaceutical industry [39,40]. For instance, one broad programme of the CCNSC that was established to find and test new natural compounds allowed the discovery of taxanes and camptothecins in 1964 and 1966,

respectively. At the begging, both types of drugs encountered problems in development. Paclitaxel (Taxol®), an antimitotic agent, could only be obtained from the bark of the Pacific Yew tree and [46], in addition, it was so insoluble that needed to be formulated in a lipid emulsion that caused hypersensitivity to patients on many occasions. It was not until 23 years after its discovery that it was found to be effective in ovarian cancer treatment. From that moment, the production of paclitaxel (PTX) began to move billions of dollars. Even the government had to think about establishing price controls. Similarly, camptothecin, which was extracted from a Chinese ornamental tree and inhibits DNA replication, showed little antitumour activity in early clinical trials even though very positive results were obtained with its administration in preclinical assays. Moreover, due to its pH instability, camptothecin was toxic to kidneys. In this case, developing a stable camptothecin analogue, irinotecan (CPT-11), took 20 years [47]. After that long period of time, CPT-11 was finally approved by the U.S. Food and Drug Administration (FDA) to treat colon cancer and, later, lung and ovarian tumours, too [39].

Between the 1970s and 1990s, few pharmaceutical companies dared to look for new anti-cancer drugs, since its discovery was associated with high risk and little chance of efficacy. Only 10% of the novel anti-tumour drugs that entered clinical trials were approved by the FDA, partly because available mouse models were unreliable in predicting clinical success. It is true that there were some hits, including the development of cisplatin (with proven efficacy in the treatment of testicular cancer) and its derivative carboplatin (less toxic and with greater action spectrum), nitrosoureas, fluoradabine phosphate, anthracyclines and epidophyllotoxins. However, progress in cancer chemotherapy was slow and the biggest drawback of the few successful compounds that were synthesized came later, as patients were cure from their primary tumours. These drugs encountered significant problems because of the acute and long-term toxicities that generated in almost all body organs and that, in the end, started to be accepted by oncologists as a price for controlling a fatal disease [39].

Therefore, in the early 1980s, the efforts made by the scientific community were not very successful in identifying new promising anti-

cancer drugs, but it is worth mentioning that improvements were made in the screening methodology. The U.S. National Cancer Institute (NCI) adopted a screen based on testing compounds against a panel of 60 human tumour cell lines that cover both, leukaemia and solid tumours. The use of such cell lines led to the development of a rapid colorimetric assay for cell viability analysis: the MTT assay [39,48]. Moreover, computer techniques were also developed to identify patterns of cytotoxicity and the apparition of resistances [39].

At last, in the late 1980s, while major attempts were still being made to discover novel cytotoxic agents, more knowledge began to be acquired, from a molecular and a genetic point of view, of the signalling pathways that are altered in cancer cells. This fact, as commented at the begging of this chapter point, enabled the targeted therapy revolution to start [39].

In this manner, in the early 1990s, cancer drug development went from a low budget to a multibillion-dollar industry. A wide variety of compounds started to be developed to target growth factors, cell-cycle proteins, signalling molecules, molecules that promote angiogenesis and apoptosis-modulators. Simply, as a general rule, these targeted compounds should meet three requirements: being metabolically stable, being well-adsorbed after oral administration and having a favourable toxicity profile at effective doses [39,49].

## 1.4. Main targeted agents for cancer therapy

Broadly speaking, it can be said that targeted cancer therapies are those that take advantage of the expression of tumour antigens or the anormal signalling that characterises cancer cells to exercise their therapeutic action in a more specific and efficient manner. Among the targeted agents that meet the requirements mentioned above, monoclonal antibodies (mAbs) and small molecules have received more attention since the revolution of the targeted cancer therapy began. Nevertheless, in recent years, therapeutic cancer vaccines and gene-based cancer therapies are also making headway in this research field [49,50].

### *1.4.1. Antibody-based targeted cancer therapy*

Antibodies are bloodstream glycoproteins used by our immune system to detect and neutralize foreign agents. The most abundant isotype of natural occurring antibodies is the immunoglobulin (IgG) one, which is a heterotetramer composed of two heavy and two light chains. IgGs are integrated by a variable fragment (Fv), which houses the complementarity determining regions (CDRs) that decide antibody binding diversity, and by a crystallisable fragment (Fc), which binds serum proteins or cells and is essential for antibody effector functions [51,52] (**Figure 1.7.A**).

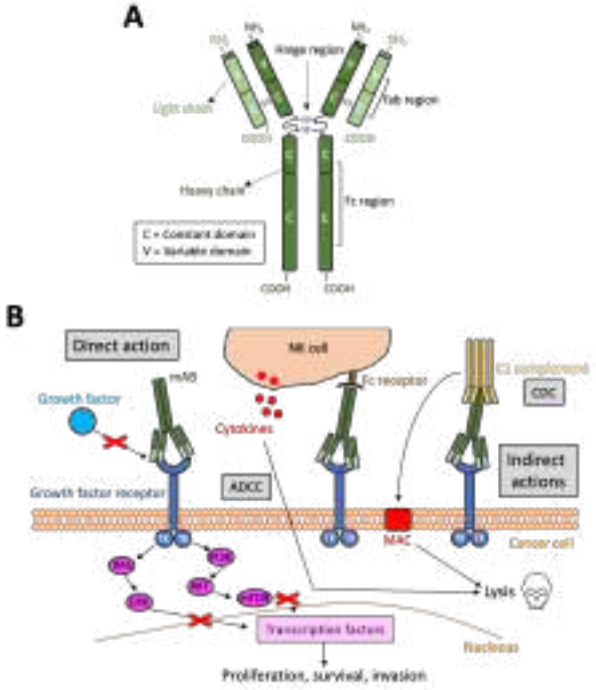


**Figure 1.7**. (**A**) Structure of the most abundant mAb isotype (IgG); (**B**) Direct and indirect mechanisms of action of mAbs.

Regarding these, it should be noted that mAbs were initially viewed as targeting "missiles" in cancer therapy. Notwithstanding, they have proven to have more complex properties and to mediate their therapeutic action through direct or indirect mechanisms after targeting tumour cells. The formers occur when, by binding to cell surface receptors or antigens, mAbs alter the signalling networks of cancer cells and help to

induce programmed death. On the other hand, indirect mechanisms involve the recruitment of effector cells or other components of the immune system that attack or induce apoptosis in cancer cells previously "marked" by mAbs. These indirect mechanisms are known as antibody-dependent cellular cytotoxicity (ADCC) and complement-dependent cytotoxicity (CDC), respectively, and are fundamental for the destruction of malignant cells [49,51] (**Figure 1.7.B**).

Such destruction, in addition, can be notably potentiated when mAbs, which have shown to be well-tolerated and to have long serum half-lives, function as carriers of cytotoxic compounds, such as radioisotopes, toxins and drugs [50,51]. These immunoconjugates are really effective in inhibiting tumour growth, and this fact, along with the good results obtained in clinical trials with antibodies, have made mAbs-based therapies a major strategy in cancer medicine. Actually, almost a third of the biotechnological products developed today are antibodies, and 24 mAbs targeting a total of 16 different antigens are currently approved by the FDA for cancer treatment [50,53]. Most of them are directed against antigens expressed on B lymphocytes (CD20, CD30 and CD52), the EGF receptor (EGFR), the human epidermal growth factor receptor-2 (HER2), the VEGF/VEGF receptor-2 (VEGFR2) and the programmed cell death protein 1 (PD-1). Otherwise, most recently approved antibodies target the cytotoxic T-lymphocyte antigen 4 (CTLA-4), disialoganglioside (GD2), CD38… [53,54] More information on the mAbs most commonly used in the clinical setting for cancer treatment can be found in **Table 1.1**.

**Table 1.1.** Some of the currently FDA-approved mAbs for cancer treatment.

| mAb | Brand name | Target | Technology | Cancer indication | Approval |
|---|---|---|---|---|---|
| Rituximab | Rituxan | CD20 | Hybridoma | Non-Hodking Lymphoma | 1997 |
| Trastuzumab | Herceptin | HER2 | Hybridoma | Breast<br>Gastric | 1998<br>2011 |
| Alemtuzumab | Campath | CD52 | Hybridoma | CML[1] | 2001 |
| Ibritumomab tiuxetan | Zevalin | CD20 | Hybridoma | Non-Hodking Lymphoma | 2002 |
| Cetuximab | Erbitux | EGFR | Hybridoma | Colorectal | 2004 |
| Bevacizumab | Avastin | VEGF-A | Hybridoma | Colorectal | 2004 |
| Panitumumab | Vectibix | EGFR | Transgenic mice | Colorectal | 2006 |

| | | | | | |
|---|---|---|---|---|---|
| Ofatumumab | Arzerra | CD20 | Transgenic mice | CLL[2] | 2009 |
| Ipilimumab | Yervoy | CTLA-4 | Transgenic mice | Metastatic melanoma | 2011 |
| Pertuzumab | Perjeta | HER2 | Hybridoma | Breast | 2012 |
| Obinutuzumab | Gazyva | CD20 | Hybridoma | CLL | 2013 |
| Ramucirumab | Cyramza | VEGFR2 | Phage display | Gastric | 2014 |
| Pembrolizumab | Keytruda | PD-1 | Hybridoma | Melanoma | 2014 |
| Necitunumab | Portrazza | EGFR | Phage display | NSCLC[3] | 2015 |
| Dinutuximab | Unituxin | GD2 | Hybridoma | Neuroblastoma | 2015 |
| Daratumumab | Darzalex | CD38 | Transgenic mice | Multiple myeloma | 2015 |
| Inotuzumab ozogamicin | Besponsa | CD22 | Hybridoma | ALL | 2017 |
| Durvalumab | Imfinzi | PD-L1 | Transgenic mice | Bladder | 2017 |

[53,54] [1]CML - Chronic myeloid leukaemia; [2]CLL – Chronic lymphoblastic leukaemia; [3]NSCLC – Non-small cell lung cancer.

As can be seen in such table, IgGs approved are human, murine, chimeric or humanized. The difference between these last two types is that chimeric mAbs are obtained by combining sequences of a murine variable domain with a human constant region domain while, in humanized mAbs, non-human CDR sequences are transplanted into a human framework sequence in order to maintain targeted specificity [54] (**Figure 1.8**).

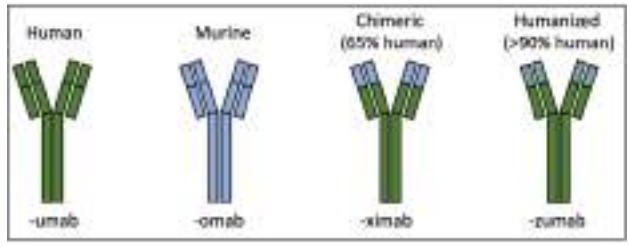


**Figure 1.8**. Types of mAbs according to their origin.

On the other hand, all these mAbs can be produced with the hybridoma or the phage display technologies, or they can be obtained from transgenic mice. The firstly introduced and the most used technique nowadays to produce antibodies is the hybridoma one [55], in which host animals are immunized with a desired antigen to generate mature B cells.

These are later merged with myeloma cells to produce hybridomas, which are screened and selected to produce the best mAbs, finally purified [54,56]. Besides, other mAbs are produced by applying the phage-display library, which constitutes a powerful tool for the rapid identification of peptides or antibody fragments. Finally, antibodies can be also generated by genetic modification of mouse lines. IgG genes are inserted in the genome of these animals, replacing their endogenous genes and making transgenic mice able to synthesize human antibodies [54].

### *1.4.2. Small molecule-based targeted cancer therapy*

Along with antibodies, small molecules are another of the most used targeted agents in cancer therapy. Antibodies exhibit great selectivity, but their targets have to be often restricted to cell surface and they require intravenous or subcutaneous administration because of their large molecular weight. By contrast, small molecules, with a much lower molecular weight (<900 Da), are able to penetrate into cancer cells and target specific proteins [49,57]. They were developed with the aim of achieving therapeutic action at the molecular level and, thus, avoiding the adverse effects that are often caused by conventional chemotherapeutic agents. Currently, more than 40 small molecules inhibitors have been already approved by the FDA for oncology indications [50,57]. Many of them focus on inactivating tyrosine kinases (TKs), since abnormal protein phosphorylation is a characteristic feature of cancer biology and has been related to unnatural proliferation and angiogenesis [50]. Other approved small molecules are inhibitors of proteasomes, cyclin-dependent kinases (CDKs) and the poly ADP-ribose polymerase (PARP). They active cell-cycle checkpoints, trigger apoptosis and coordinate DNA repair in cancer cells [49]. Information on the inhibitors most commonly used in the clinical setting can be seen in **Table 1.2**.

**Table 1.2.** Some of the currently FDA-approved small molecules for oncology indications.

| Small molecule | Classification | Target | Cancer indication |
|---|---|---|---|
| Erlotinib | TK inhibitor | EGFR, HER | NSCLC, pancreatic |
| Lapatinib | TK inhibitor | EGFR, HER2 | Breast |
| Sorafenib | TK inhibitor | VEGFR, RAF, PDGFR[1] | Renal, hepatocellular |
| Gefitinib | TK inhibitor | EGFR | NSCLC |
| Sunitinib | TK inhibitor | VEGFR, PDGFR | Gastrointestinal, renal, pancreatic |
| Imatinib | TK inhibitor | PDGFR, ABL | Leukaemia, gastrointestinal |
| Crizotinib | TK inhibitor | ALK[2] | NSCLS |
| Carfilzomib | Proteasome inhibitor | Proteasome | Multiple myeloma |
| Ribociclib | CDK inhibitor | CDK4, CDK6 | Breast |
| Rucaparib | PARP inhibitor | PARP-1, PARP-2 | Ovarian, peritoneal |
| Olaparib | PARP inhibitor | PARP-1, PARP-2 | Ovarian, breast, peritoneal |

[49,57] [1]PDGFR – Platelet-derived growth factor receptor; [2]ALK – Anaplastic lymphoma kinase

### *1.4.3. Targeted cancer therapy based on vaccines*

Treating cancer with vaccines has been a challenging research field for decades. Unlike the vaccines developed to combat infectious diseases, which are mostly prophylactic in nature, the design of therapeutic cancer vaccines (TCVs) seeks to educate patients' immune system to identify and eliminate tumours [58]. Thus, the goal of these TCVs is enhancing anti-tumour immunity by means of the activation and expansion of $CD8^+$ and $CD4^+$ T cells, which can elicit a specific immune response against two types of antigens: tumour-specific antigens (TSAs) and tumour associated antigens (TAAs) [59,60].

While TAAs are shared between healthy and tumour cells but are overexpressed by cancer cells, TSAs are only expressed in tumour cells and are absent in healthy tissues [61]. For this reason, TSAs, which are mutant proteins, are theoretically the ideal target for cancer immunotherapy. However, the somatic mutations that give rise to TSAs are almost unique to each tumour, and TCVs based on them have to be personalized and developed for individual patients. In contrast, TAAs are commonly overexpressed by tumours with the same histology and allow the design of vaccines for many individuals. Although they generate more weak immune responses because they are often recognised as self-antigens,

they have been preferred to design TCVs, which have been developed using various strategies during the last decades [59]. In this way, nowadays, cell-based, DNA/RNA-based, vector-based and protein/peptide-based vaccines against TAAs can be found in advanced clinical trials. Even the administration of three TCVs, which have been summarized in **Table 1.3**, has already been approved by the FDA [59,62]. Moreover, an exponential growth in this research field has occurred recently with the employment of various delivery approaches for cancer vaccines, such as nanoparticles and scaffolds, with which promising preclinical results are being obtained these days [63].

**Table 1.3.** TCVs currently approved by the FDA for cancer treatment.

| Brand name | Strategy | Cancer indication | Approval |
|---|---|---|---|
| TheraCys® | Bacterial vector-based | Urothelial carcinoma | 1990 |
| PROVENGE | Cell-based | Castration-resistant prostate cancer | 2010 |
| T-VEC | Viral vector-based | Advanced melanoma | 2015 |

[59,62]

### *1.4.4. Gene-based targeted cancer therapy*

Gene therapy attempts to introduce genetic material (either DNA or RNA) into cancer cells to inhibit their proliferation or to directly destroy them. This goal can be mainly achieved in two ways: either by directly replacing mutated tumour genes by normal genes to restore regular cell function, or by indirectly sensitizing malignant cells towards treatments to which they have become resistant [49]. Due to cancer complexity, numerous strategies have had to be developed when it comes to follow these two paths, which can be broadly categorized into immunological and molecular strategies [64].

#### 1.4.4.1. Immunological strategies for gene-based cancer therapy

As regards the former, since cancer cells are able to evade the immune system [4], it should be noted that these strategies seek for boosting the T cell-mediated immune response against cancer. Thus, for instance, several genetic immunotherapies involve the transfer of genes that encode the production of immune-stimulant molecules (such as

cytokines), *in vitro* manipulation of antigen presenting cells to allow them to perform their function correctly, or vaccination with antigen-encoding genes that induce the production of antigens that later trigger an immune response [64].

#### 1.4.4.2. Molecular strategies for gene-based cancer therapy

On the other hand, molecular genetic strategies aim to reset oncogenes and tumour-suppressor genes that harbour mutations in malignant cells. For example, treatment with suicide genes relies on the conversion of pro-drugs into active compounds by means of non-mammalian enzymes that are overexpressed on cancer cells as a result of a transfection with the proper genes. Administration of anti-oncogenes, which are oligonucleotides that bind to a specific DNA or RNA sequence, is useful to inhibit oncogene activity, just like the activity of *bcl-2*, *c-myc* or K-*ras*. On the contrary, transfection of wild-type tumour-suppressor genes, such as *p53*, has also proven to be an effective strategy to fight against cancer development, as well as the introduction of genes that inhibit angiogenesis or prevent side effects of antineoplastic agents and help to overcome dose-limiting toxicities [64].

## 1.5. The essential role of nanotechnology in the development of targeted cancer therapies

Although targeted agents described in the previous point have shown to have excellent therapeutic action, many times this is not enough to completely eradicate the disease. It is the case of antibodies, for example, which are normally administered as adjuvant therapy along with conventional cytotoxic agents [53]. Moreover, although some would be effective enough, limitations in their delivery exist other times, as occurs with gene-based therapies and TCVs [63,65-66]. Thus, in either case, for both the development of combined therapies and the specific delivery of anti-tumor (conventional and targeted) agents, nanotechnology has become essential by means of the synthesis of nanocarriers or drug delivery systems (DDSs).

The concept of nanotechnology was firstly predicted by Feynman, who suggested in his famous lecture "There is plenty of room at the bottom" in 1959 that matter manipulation at the atomic level could have exceptional applications [67]. About 40 years after his prediction, cancer nanotechnology emerged as a field of interdisciplinary research (in which biology, chemistry, engineering and medicine are combined), ready to revolutionize cancer diagnosis and treatment [65]. At the beginning, cancer nanomedicine (the medical application of nanotechnology) appeared timidly but, in the last two decades, it has undergone such development that only since the year 2000 more than 42,200 publications related to this field can be found in the PubMed database [68]. In general, in these published works, nanocarriers have been developed to address four challenges of formal cancer therapies: (i) non-specific systemic distribution of anti-tumour agents; (ii) unsuitable drug concentrations reaching the tumour site; (iii) intolerable cytotoxicity; (iv) apparition of multiple drug resistance (MDR). Thereby, DDSs exhibit several advantages over conventional systemic administration of the drugs, which can be found summarized in **Box 1.1** [69].

**Box 1.1.** Main advantages of DDSs over conventional systemic-administered drugs in the clinical practise.

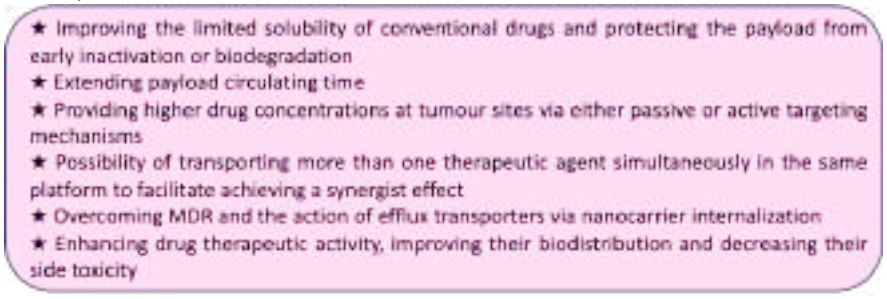


[65,69]

Among the different nanocarriers that display the benefits showed in **Box 1.1**, the most commonly designed are nanoparticles (NPs) (polymeric, inorganic or metallic), liposomes, micelles and dendrimers, which reach tumour tissues by means of both passive and active targeting mechanisms, as well as hydrogels [65,69]. Active targeting mechanisms are based on driving drug-carrying nanosystems to cancer cells such as guided missiles thanks to the action of the targeted agents described above. Nevertheless, active targeting cannot be separated from the

passive, since it only takes place after passive accumulation of DDSs in tumour tissues [70]. Since the most relevant targeted agents were already commented in the previous point of this chapter, only the passive targeted mechanism has been detailed below, along with the main properties of the most reported nanocarriers.

### *1.5.1. Passive targeted cancer therapy*

About 30 years ago, Matsumura and Maeda observed that macromolecules larger than 30 KDa were preferentially distributed to the tumour interstice and remained there for prolonged periods of time [71,72]. Such observation was ascribed to tumour angiogenesis, in which a rapid development of new and irregular blood vessels occurs, as already described. These vessels display a discontinuous epithelium and lack the basal membrane of normal vascular structures. In this way, they exhibit fenestrations in capillaries that range from 10-1000 μm and that offer little resistance to the extravasation of macromolecules to the tumour interstice [73,74]. In addition, while normal tissues keep the extracellular fluid constantly drained to lymphatic vessels, this lymphatic function is defective in tumours. In this way, in malignant tissues, molecules smaller than 4 nm can diffuse back to blood circulation, but larger nanoparticles or macromolecules accumulate because they are not efficiently cleared [73]. Thus, both the presence of fenestrations in the imperfect tumour vessels and the poorly lymphatic drainage of these tissues are responsible for the observation that was made by Matsumura and Maeda in the mid 80's. This observation has been coined as enhanced permeability and retention (EPR) effect, and it has become the engine for many scientists to delivery nanomedicines to tumours [71] (**Figure 1.9**).

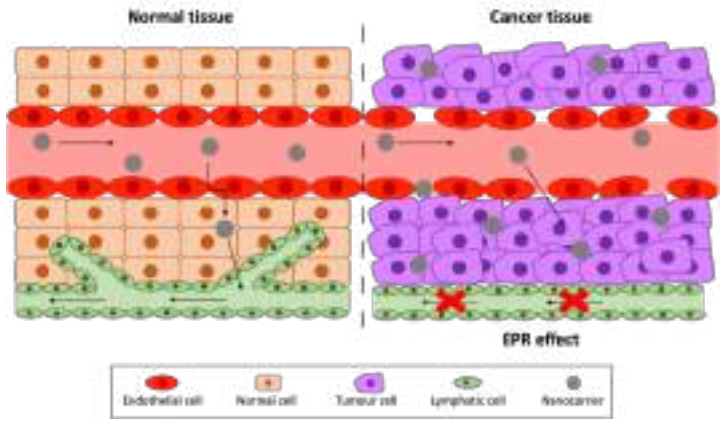


**Figure 1.9**. Tumour angiogenesis is responsible for the development of irregular vessels that exhibit fenestrations through which DDSs can pass. This phenomenon, along with the poor lymphatic drainage that characterises cancer tissues, contributes to the well-known EPR effect.

Apart from the EPR effect, other two factors enhance the arrival of bigger nanocarriers to malignant tissues: the high tumour interstitial fluid pressure (IFP) and the high microvasculature pressure. The former hinders transcapillary transport in tumours and decreases conventional drug delivery to them. Moreover, since IPF is higher in the tumour periphery than in the central region, cancer cells from the tumour "nucleus" are often spared drug action. Conversely, since nanomedicines have greater size, their extravasation is not only less affected by the high IFP, but it is also facilitated by the elevated tumour microvasculature pressure, which is one or two orders of magnitude higher than in normal tissues [73].

On the other hand, with the aim of making the extravasation process optimal, three properties of the nanocarriers have to be taken into account for their design:

- Size: the ideal diameter of cancer nanomedicines should be somewhere between 70 and 200 nm. To be able to extravasate through tumour fenestrations, nanocarrier size must be inferior to 400 nm and, to avoid kidney filtration, larger than 20 - 30 nm [75].
- Charge: nanomedicines should exhibit neutral or anionic charge to avoid renal elimination [73].

- Shape: elongated nanocarriers are preferred over spherical ones because it has been shown that they have better extravasation rate and diffuse deeper in tumour masses [71].

Nonetheless, even though these three properties are adequate, passive delivery of nanocarriers is sometimes limited. Passive targeting depends on tumour vasculature and angiogenesis and, thus, varies among tumour types and anatomical sites. For instance, prostate and pancreatic carcinomas are hypovascularized, and targeting them by only focusing on the EPR effect can be complicated. Furthermore, the high IPF of tumours occasionally avoids the successful uptake and the homogeneous distribution of nanocarriers smaller than 100 nm, and it can promote MDR if drugs are accumulated at the tumour site for long periods of time [73,74]. For this reason, the combination of both, the active targeting previously detailed and the passive targeting of tumours is often the best therapeutic strategy to follow.

### *1.5.2. Main reported nanocarriers in cancer therapy*

The most ordinary anti-cancer nanocarriers or DDSs are synthesized using a variety of materials including polymers (polymer-drug conjugates, micelles, dendrimers or hydrogels), lipids (liposomes) and organometallic compounds (carbon nanotubes, silica NPs or metallic NPs) (**Figure 1.10**) [76].

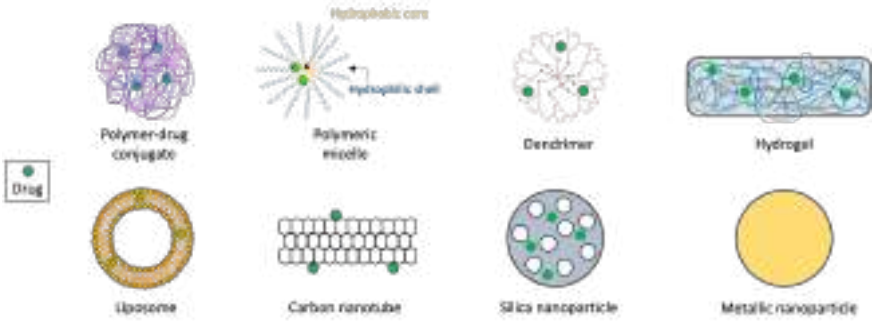


**Figure 1.10**. Representation of the most commonly reported types of DDSs for cancer treatment.

*1.5.2.1. Polymeric drug delivery systems*

Polymeric DDSs are submicron-sized colloidal particles (100-350 nm) in which the anti-cancer agent is either physically entrapped in or covalently bound to a polymeric matrix. Such matrix can be formed from natural, semi-synthetic or synthetic polymers, and the resulting therapeutic nanosystems can have the structure of capsules (polymer-drug conjugates), amphiphilic NPs (micelles), hyperbranched macromolecules (dendrimers) or polymer networks (hydrogels) [76]. Compared to lipid and organometallic nanocarriers, polymer-based DDSs have received more attention because they (i) have an intrinsically stealthy surface that allows their decoration with targeted molecules (mAbs, aptamers, peptides…); (ii) have shown an enhanced *in vivo* stability and are safer (and, sometimes, even biodegradable); (iii) can be tailored-made to achieve diverse polymer structures, molecular weights and compositions to meet the requirements of a particular drug or application [77]. Their synthesis, in general, is achieved through chemical approaches such as emulsification and solvent evaporation/extraction, nanoprecipitation, salting-out, spray-drying or the supercritical antisolvent method [78].

Regarding polymer-drug conjugates, it should be noted that albumin, chitosan, heparin, cyclodextrins and alginate are some of the natural occurring polymers often chosen for the delivery of drugs, DNA, antigens, oligonucleotides… in NP systems [79-82]. Otherwise, the most widely used synthetic polymers for this application are *N*-(2-hydroxypropyl)-methacrylamide (HPMA) and polyethylene glycol (PEG), which are non-biodegradable, and poly-L-glutamic acid (PGA) and poly(lactic-co-glycolic acid) (PLGA), which are biodegradable [76]. Several DDSs synthesized with both natural and synthetic polymers are being evaluated in clinical trials (Xyotax, CT-2106…), and clinical administration of a human serum albumin (HSA)-based nanocarrier (Abraxane®) was already approved by the main regulatory organisms several years ago. This nanocarrier harbors the already mentioned drug PTX and, at the moment, it is indicated for the treatment of MBC, NSCLL and pancreatic cancer (**Table 1.4.**) [69,76].

**Table 1.4.** Nanomedicines approved for cancer treatment to date.

| Product | Drug | Size | Indications | Manufacturer | Approval |
|---|---|---|---|---|---|
| Doxil® | DOX | 80-90 nm | Ovarian carcinoma, MBC and multiple MM[1] | Jonhson & Jonhson | FDA 1995 EMA 1996 |
| Myocet® | DOX | 150 nm | MBC | Teva | EMA 2000 |
| Abraxane® | PTX | 130 nm | MBC, NSCLL, pancreatic carcinoma | Abraxis Bioscience | FDA 2005 EMA 2009 |
| Mepact® | Mifamurtide | - | Osteosarcoma | Takeda Pharmaceutical | EMA 2009 |
| Marqibo® | Vincristine | 115 nm | ALL | Talon Therapeutics | FDA 2012 |
| Onivyde® | Irinotecan | 110 nm | Pancreatic carcinoma | Mennimack Pharmaceuticals | FDA 2015 EMA 2016 |
| Vyxeos® | Cytarabine daunorubicin | 100 nm | AML | Jazz Pharmaceuticals | FDA 2017 EMA 2018 |
| Apealea® | PTX | 20-30 nm | Ovarian, fallopian tube carcinomas | Oasmia Pharmaceutical | EMA 2018 |

[69] [1]MM – Multiple myeloma

Secondly, polymeric micelles (PMs) are nanocarriers synthesized with amphiphilic block copolymers that self-assemble to form nanosized core/shell structures in aqueous media when the critical micelle concentration is reached [76,83]. Their hydrophobic core serves as reservoir for hydrophobic drugs, while their hydrophilic shell makes them water-soluble and enables their intravenous administration [76]. However, this hydrophilic shell does not confer sometimes sufficient solubility and stability to PMs, which have to be modified (for instance, through a PEGylation process) in order to exhibit a better circulation half-live. Some PEG-modified block copolymers used to form micelles are, for example, distearoylphosphatidylethanolamine (DSPE), poly(lactic acid) (PLA) and poly(acrylic acid) (PAA). PMs modified with them are able to delivery one or more drugs, and can be decorated by different ligands, as polymer-drug conjugates, to increase their internalization rate in cancer cells [83]. As can be seen in **Table 1.4**, several PMs (NK911, NK105, NC-6004, SPI049C…) have already reached clinical trials, too [69,83], and Apealea® has been the last nanomedicine approved by the European Medicines Agency (EMA) for the treatment of ovarian and fallopian tube carcinomas with a PTX formulation [69].

Thirdly, dendrimers are synthetic macromolecules of nanometer dimensions, composed of multiple highly branched monomers that emerge radially from a central core [76]. They exhibit a homogeneous and monodispersed structure, which enables them to simultaneously deliver hydrophobic and hydrophilic drugs (doxorubicin (DOX), 5-FU, MTX, camptothecin…), as well as be easily functionalized with different ligands (folic acid, aptamers…) [83]. The most used dendrimers are those made up of polyamidoamine (PAMAM). Just like PMs, they can also be PEGylated to improve their solubility and biodistribution [71,83].

Finally, to end with the DDSs synthesized from polymers, it should be highlighted that those of hydrophilic nature can also be crosslinked and used to prepare hydrogels in which drugs of different nature can be embedded to be later topically released. Such crosslinking can be performed physically or chemically, and resulting 3D networks, which have excellent water adsorption capacity, can be directly deposited on tumours. In this manner, the toxicity that normally accompanies systemic administration of chemotherapeutics is limited within the localized area where cancer cells lie. In addition, the obstacle that the low solubility of many drugs represents can be overcome by increasing the amount of the anti-tumour agent that reaches the tumour site [84,85]. According to their response to external stimuli, hydrogels can be classified as ordinary or smart. The latter receive this denomination when they show a sol-gel phase transition upon injection in response to external stimuli (temperature, pH, light…), which makes them suitable for the delivery of many drugs (DOX, PTX, vincristine, 5-Fu, camptothecin…) in a more selective manner [85].

#### 1.5.2.2. Lipid drug delivery systems

Liposomes are self-assembling spherical vesicles that consist of one or more bilayers of phospholipids that surround a central aqueous space [76]. They can be generated from cholesterol and natural or synthetic phospholipids, and there are numerous methods available for preparing them, such as the thin film hydration method (Bangham method), membrane extrusion, detergent dialysis, reverse phase

evaporation, micro-emulsification, the solvent-injection technique, the supercritical anti-solvent method… [70].

Among the most reported nanocarriers, liposomes were the first nanotechnology product that was approved for a therapeutic application. Nowadays, there are a total of six liposomal formulations approved by the FDA and/or the EMA for the treatment of several cancer indications (**Table 1.4.**). The reason is that liposomes are biodegradable, biocompatible, little toxic and capable of encapsulating both hydrophilic and hydrophobic drugs [70,83]. However, liposomes have also some drawbacks, such as a short circulating life span, limited stability and drug loading capacity, and rapid drug release. But, just as with some of the previous nanocarriers, these issues can be improved through PEGylation. In addition, surface engineering techniques can be employed to attach different ligands (peptides, mAbs, aptamers, small molecules…) to liposomes to actively transport encapsulated drugs to specific tumour tissues [83].

1.5.2.3. Drug delivery systems of organometallic nature

Among the different types of nanocarriers of organic or metallic nature, carbon nanotubes (CNTs), mesoporous silica nanoparticles (MSNs) and metallic NPs are among the most widely used.

The first of these DDSs, the CNTs, are a class of carbon allotropes obtained when graphene sheets are rolled up into seamless, hollow cylindrical tubes. They can be synthesized by electric arc discharges, the chemical vapor deposition method or the laser ablation method and, according to the number of graphene sheets that compose them, CNTs can be classified into single-walled or multiwalled. Single-walled CNTs are more efficient in drug delivery thanks to their better-defined wall but, in any case, both types of CNTs have very attractive properties that have aroused great interest in medicine over the last decade [83,86-87]. Thus, for example, they have high drug-loading capacity, good tissue-penetrability thanks to their nanoneedle shape and great photothermal ablation capacity [83,87]. However, they are insoluble, quite cytotoxic and, in this way, poorly biocompatible, so physical and/or chemical functionalization of CNTs is required to make them smart [76,83]. Once functionalized, CNTs have shown promise not only in drug delivery

applications, but also in cancer imaging, photothermal therapy and gene therapy [86,87].

Secondly, MSNs are nanomaterials containing pores with diameters between 2-50 nm, which can be hollow or rattle-type [86]. Since they were firstly fabricated by Kresge et al. in 1992 [88], MSNs have been widely studied because of their tunable size (50-300 nm), uniform and modulable pore size (which allows drugs of different molecular shapes to be loaded), high surface area, high pore density and biocompatibility. They can be prepared by the soft or the hard template method and, as the DDSs previously described, MSNs can be PEGylated to improve their behavior *in vivo*. Moreover, their surface can be modified using folate, mannose, transferrin, peptides… for active targeting, and grafting MSN pores with co-polymers has demonstrated to be a good practice to avoid premature release of the drugs loaded. Apart from being designed to develop novel DDSs, MSNs are also prepared for cancer imaging and gene therapy [86,88].

Finally, among the different metallic nanocarriers, gold nanoparticles (AuNPs) are matter of significant interest because they are relatively biologically non-reactive compared to other metallic NPs, such as silver or cadmium NPs [89]. Besides, they have stronger optical properties, exhibit an easily controllable surface chemistry that enables versatility in adding functional groups, and they can be easily synthesized with customizable size and shape [86,89]. Likewise, AuNPs are stable in biological media and are biocompatible and, as CNTs, they are able to achieve thermal ablation of cancer cells. AuNPs can be prepared via chemical, physical or biological routes and, apart from drugs, they can also transport other biomacromolecules (proteins, DNA, RNA…). Moreover, their surface can be modified with different types of ligands, like transferrin or folic acid, for targeted drug delivery applications, too [86].

### *1.5.3. Stimulus for drug release*

So far, the characteristics of the most reported DDSs and how they achieve to target cancer cells through passive and active mechanisms have already been discussed. Thus, to finish this first chapter, what remains to be done is briefly describing how smart nanocarriers are able to release their payload in tumour tissues.

For this, it must be pointed first that there are two types of stimuli to which DDSs can respond: endogenous and exogeneous. In the case of endogenous or intrinsic stimuli, the triggering signal to release the anti-cancer drug comes from the body, while in exogeneous stimuli, such signal is extra-corporal [86].

#### 1.5.3.1. Endogenous stimuli

The most well-known examples of endogenous stimuli are pH changes, redox reactions, temperature modifications and enzyme transformations.

According to the Warburg effect, tumour cells carry out enhanced glycolysis followed by extra lactic acid fermentation [3]. This phenomenon, along with the poor blood flow, the hypoxia and the impaired elimination of metabolism wastes that characterize malignant tissues with abnormal angiogenesis, contributes to the accumulation of hydrogen ions in the tumour interstice [70,86]. For this reason, while normal tissues have an intracellular pH ($pH_i$) close to 7.2 and an extracellular pH ($pH_e$) approximately equal to 7.4, tumour tissues exhibit lower $pH_e$ (in the range of 6.5 - 7.2) and more basic $pH_i$ (superior to 7.4) [86,90]. Furthermore, apart from this difference in the $pH_i$ and $pH_e$, there is also a pH gradient among cellular organelles, since that of lysosomes is much more acidic (close to 4.7 - 5.0) than the pH of other organelles [86].

Thereby, pH-responsive DDSs, which have to be stable in the pH range of 5 - 7, are those which are prepared to store anti-cancer drugs at physiological pH, but which can release them by undergoing physical and/or chemical changes when exposed to more acidic pH environments [86,91]. This pH-sensitivity can be achieved, for instance, by means of the

introduction of weak acid or basic ionizable chemical groups (amines, phosphoric acid, carboxyl groups…) in nanocarriers, which in this manner become able to limit systemic concentrations of toxic drugs [86,91]. pH-sensitive DDSs have been studied in a variety of forms (hydrogels, polymer-drug conjugates, micelles, dendrimers…) and [91], generally, they constitute a good strategy when they are aimed to be internalized in endo/lysosomal cellular parts [70].

Apart from being responsible for the acidic $pH_e$ of tumour sites, enhanced cancer glycolysis is also the cause, together with the high proliferation rate of malignant tissues, of their increased temperature (40 - 42°C). In this manner, thermosensitive nanocarriers can be built to alter the tumour structure by releasing drugs in response to a rise in the temperature at tumour sites. This strategy is carried out more frequently with liposomes, but temperature-responsive polymeric-drug conjugates and PMs can also be found in the literature [70,92].

On the other hand, another aspect that characterizes malignant cells is their elevated intracellular concentration of glutathione sulfhydryl (GSH), which is a highly effective antioxidant that controls reductive microenvironments [86]. Its concentration in tumours is at least four times higher than in normal cells and, in addition, it is one thousand times higher in the intracellular medium than in the bloodstream. Thus, differences in the concentration of this antioxidant compound can be used to reduce the disulphide bonds of redox-sensitive DDSs, such as PMs, to release encapsulated drugs in a controlled manner [70,86].

Last, the surface of endogenous stimuli-responsive nanocarriers can be also modified to make it sensitive to the biocatalytic action of enzymes that are overexpressed in the extracellular tumour environment, like metalloproteinases, proteases, phospholipases and glycosidases [70,86,91]. These enzyme-responsive DDSs can protect their payload from degradation during transport to the target and have an increased EPR effect and site-specific delivery. Nonetheless, they have the inconvenience of not being applicable for intracellular drug release since enzymatic concentrations are similar inside cancer and normal cells [86,91]. Among these DDSs, liposomes and MSNs with polymer or lipopeptide protease-

sensitive coatings have been already developed, as well as PEGylated liposomes or metallic NPs in which matrix-metalloproteinase peptides have been employed as links between their surface and PEG chains [70,86].

1.5.3.2. Exogenous stimuli

The exogenous stimuli most frequently employed in drug delivery applications are magnetic fields, light irradiation, ultrasounds and electric fields [86,91].

Regarding the former, magnetic field-responsive nanocarriers are those designed to produce heat in the surrounding medium when they are placed under oscillating magnetic fields, since heat brings changes in their structure [86]. Liposomes and micelles coated with silica or containing $Fe_3O_4$ superparamagnetic iron oxide NPs (SPIONs), which can induce conformational changes or pore formation in polymers surrounding them, are ideal candidates for magnetic stimulus, for instance [86,91].

Otherwise, light irradiation is other attractive option for the controlled release of drugs, since it permits to accomplish it in a non-invasive manner but with great spacial and temporal precision. The most commonly used light-responsive agents include spiropyrans and azobenzenes, which change their chemical state upon ultraviolet (UV) irradiation and can produce, for example, the disassembly of PMs. Up to now, such UV light-responsive systems have been commonly employed to induce drug release because most of them respond to shorter wavelengths of light. However, they have primary limitations, such as poor tissue penetration and harmful effects to normal tissues [91]. For this reason, scientists are shifting the focus towards the development of near-infrared (NIR) or visible light-sensitive DDSs. Thanks to their capacity of adsorbing light and converting it in heat, AuNPs and CNTs are good candidates for this development, especially for light-triggered stimuli in the NIR range [86,91].

AuNPs, apart from being suitable applicants to produce photo-sensitive nanocarriers, are also adequate to generate ultrasound-

responsive DDSs along with liposomes and hydrogels [86,91]. Ultrasound-stimulus is under intense investigation these days because, as UV-light irradiation, does not require invasive procedures. In addition, it has deep body penetration and is non-ionizing. By using it, both, thermal and mechanical effects can be induced in acoustic-sensitive nanocarriers to release loaded drugs [86].

Finally, due to their easy generation and control, electric fields are also being used as exogenous stimulus [86]. For such purpose, several nanocarriers, such as hydrogels and CNTs, are being modified with electroactive polymers, such as polypyrole, polyaniline, polythiophene… [86,91] Conducting DDSs synthesized with these polymers are able to change their shape or volume upon stimulation with an electric current. In addition, such current can also be used to enhance cellular uptake of drugs or nanocarriers by a process known as electropermeabilization [91,93].

## 1.6. Published articles related to this chapter

· Nieto C, Vega MA, Martín del Valle, EM. Trastuzumab: more than a guide in HER2-positive cancer nanomedicine. Nanomaterials 2020; 10:1674.

## 1.7. Abbreviations

ADCC – Antibody-dependent cellular cytotoxicity
ALK – Anaplastic lymphoma kinase
ALL – Acute lymphoblastic leukaemia
ALT – Alternative lengthening of telomers
ATP – Adenosine triphosphate
AuNPs – Gold nanoparticles
CAM – Cell adhesion molecule
CCNSC – Cancer Chemotherapy National Service Centre
CDC – Complement-dependent cellular cytotoxicity
CDK – Cyclin-dependent kinase
CDR – Complementary determining region
CIN – Chromosomal instability

CLL – Chronic lymphoblastic leukaemia
CML – Chronic myeloid leukaemia
CNT – Carbon nanotube
CPT-11 - Irinotecan
CTL – Cytotoxic T lymphocyte
CTLA-4 – Cytotoxic T lymphocyte antigen-4
DDS – Drug delivery system
DHFR – Dihydrofolate reductase
DNA – Deoxyribonucleic acid
DOX - Doxorubicin
DSPE - Distearoylphosphatidylethanolamine
ECM- Extracellular matrix
EGF – Epidermal growth factor
EGFR - Epidermal growth factor receptor
EMA – European Medicines Agency
EPR – Enhanced permeability and retention
Fc – Crystallisable fragment
FDA – U.S. Food and Drug Administration
FGF – Fibroblast growth factor
Fv – Variable fragment
GCO – Global Cancer Observatory
GD2 – Disialoganglioside
GSH - Glutathione
HER2 – Human epidermal growth factor receptor-2
HIF – Hypoxia-inducible factor
HPMA – N-(2-hydroxypropyl)-methacrylamide
HSA – Human serum albumin
IFP – Interstitial fluid pressure
IGF – Insulin growth factor
IgG - Immunoglobulin
IL – Interleukin
mAb – Monoclonal antibody
MDR – Multidrug resistance
MM – Multiple myeloma
MSN – Mesoporous silica nanoparticle
MTX - Methotrexate
NCI – U.S. National Cancer Institute

NIR – Near-infrared
NK – Natural killer
NP - Nanoparticle
NSCLC – Non-small cell lung cancer
PAA – Poly(acrylic acid)
PAMAM - Polyamidoamine
PARP – Poly ADP-ribose polymerase
PD-1 – Programmed cell death protein-1
PDGF – Platelet-derived growth factor
PDGFR - Platelet-derived growth factor receptor
PEG – Polyethylene glycol
PGA – Poly-L-glutamic acid
$pH_e$ – Extracellular pH
$pH_i$ – Intracellular pH
pRb – Retinoblastoma protein
PLA – Poly(lactic acid)
PLGA – Poly(lactic-co-glycolic acid)
PM – Polymeric micelle
PTX - Paclitaxel
ROS – Reactive oxygen species
RNA – Ribonucleic acid
RTK – Receptor tyrosine kinase
SPION – $Fe_3O_4$ superparamagnetic iron oxide nanoparticle
TAA – Tumour-associated antigen
TAM – Tumour-associated macrophages
TCV – Therapeutic cancer vaccine
TGF – Transforming growth factor
TK – Tyrosine kinase
TNF – Tumour necrosis factor
TSA – Tumour specific antigen
UV - Ultraviolet
VEGF – Vascular endothelial growth factor
VEGFR2 – Vascular endothelial growth factor receptor-2
WHO – World Health Organization
5-FU – 5-fluorouracil
6-MP – 6-mercaptopurine

## 1.8. References

[1] Global Cancer Observatory (GCO). Available online: https://gco.iarc.fr/ (accessed on 17th September 2020).

[2] Asociación Española Contra el Cáncer (AECC). Available online: https://www.aecc.es/ (accessed on 17th September 2020).

[3] Hanahan D, Weinberg RA. The hallmarks of cancer. Cell 2000; 100:57-70.

[4] Hanahan D, Weinberg RA. Hallmarks of cancer: the next generation. Cell 2011; 144:646-74.

[5] Caon I, Bartolini B, Parnigoni A, Caravà E, Moretto P, Viola M, Karousou E, Vigetti D, Passi A. Revisting the hallmarks of cancer: the role of hyaluronan. Seminars in Cancer Biology 2020; 62:9-19.

[6] Cooper GM. The Cell: A molecular approach. 2nd. ed. Sunderland (MA): Sinauer Associates; 2000. The development and causes of cancer.

[7] Goustin AS, Leof EB, Shipley GD, Moses HL. Growth factors and cancer. Cancer Res. 1986; 46(3):1015-29.

[8] Farooqi AA, Siddik ZH. Platelet-derived growth factor signalling in cancer: rapidly emerging signalling landscape. Cell Biochem Funct. 2015; 33(5):257-65.

[9] Balkwill F. TNF-α in promotion and progression of cancer. Cancer Metastasis Rev. 2006; 25:409-16.

[10] Wesche J, Haglund K, Haugsten EM. Fibroblast growth factors and their receptors in cancer. Biochem J. 2011; 437(2):199-213.

[11] Normanno N, De Luca A, Bianco C, Strizzi L, Mancino M, Maiello MR, Carotenuto AC, De Feo G, Caponigro F, Salomon DS. Epidermal growth factor receptor (EGFR) signalling in cancer. Gene 2006; 366(1):2-16.

[12] Sever R, Brugge JS. Signal transduction in cancer. Cold Spring Harb Perspect Med. 2015; 5(4):a006098.

[13] Martini M, De Santis MC, Braccini L, Gulluni F, Hirsch E. PI3K/AKT signaling pathway and cancer: an updated review. Ann Med. 2014; 46(6):372-83.

[14] Fernández-Medarde A, Santos E. Ras in cancer and developmental diseases. Genes Cancer 2011; 2(3):344-58.

[15] Tlsty TD, Hein PW. Know thy neighbor: stromal cells can contribute oncogenic signals. Curr Opin Genet Dev. 2001; 11:54-9.

[16] Bracken AP, Pasini D, Capra M, Prosperini E, Colli E, Helin K. *EZH2* is downstream of the pRb-E2F pathway, essential for proliferation and amplified in cancer. EMBO J. 2003; 22(20):5323-35.

[17] Hickman ES, Moroni MC, Helin K. The role of p53 and pRb in apoptosis and cancer. Curr Opin Genet Dev. 2002; 12:60-6.

[18] Derynck R, Akhurst RJ, Balmain A. TFG-β signaling in tumor suppression and cancer progression. Nat Genet. 2001; 29:117-29.

[19] Miller DM, Thomas SD, Islam A, Muench D, Sedoris K. c-Myc and cancer metabolism. Clin Cancer Res. 2012; 18(20):5546-53.

[20] Bold RJ, Termuhlen PM, McConkey DJ. Apoptosis, cancer and cancer therapy. Surg Oncol. 1997; 6(3):133-42.

[21] Lowe SW, Lin AW. Apoptosis in cancer. Carcinogenesis 2000; 21(3):485-95.

[22] Shay JW, Wright WE. Role of telomeres and telomerase in cancer. Semin Cancer Biol. 2011; 21:349-53.

[23] Heaphy CM, Subhawong AP, Hong S-M, Goggings MG, Montgomery EA, Gabrielson E, Netto GJ, Epstein JI, Lotan TL, Westra WH et al. Prevalence of the alternative lengthening of telomeres telomere maintenance mechanism in human cancer subtypes. Am J Pathol. 2011; 179(4):1608-15.

[24] Bryan TM, Englezou A, Dalla-Pozza L, Dunham MA, Reddel RR. Evidence for an alternative mechanism for maintaining telomer length in human tumors and tumor-derived cell lines. Nat Med. 1997; 3(11):1271-74.

[25] Carmeliet P, Jain RK. Angiogenesis in cancer and other diseases. Nature 2000; 407:249-57.

[26] Nishida N, Yano H, Nishida T, Kamura T, Kojiro M. Angiogenesis in cancer. Vasc Health Risk Manag. 2006; 2(3):213-19.

[27] Gupta GP, Massagué J. Cancer metastasis: building a framework. Cell 2006; 127:679-95.

[28] Grady W. Genome instability and colon cancer. Cancer metastasis rev. 2004; 23:11-27.

[29] Negrini S, Gorgoulis VG, Halazonetis TD. Nat Rev. 2010; 11:220-28.

[30] Mantovani A, Allavena P, Sica A, Balkwill F. Cancer-related inflammation. Nature 2008; 454:436-44.

[31] Coussens LM, Werb Z. Inflammation and cancer. Nature 2002; 420:860-67.

[32] Lu H, Ouyang W, Huang C. Inflammation, a key event in cancer development. Mol Cancer Res. 2006; 4(4):221-33.

[33] Corthay A. Does the immune system naturally protect against cancer? Front Immunol. 2014; 5(197):1-8.

[34] Schreiber RD, Old LJ, Smyth MJ. Cancer immunoediting: integrating immunity's roles in cancer suppression and promotion. Science 2011; 331:1565-70.

[35] Gonzalez H, Hagerling C, Werb Z. Roles of the immune system in cancer: from tumour initiation to metastatic progression. Genes Dev. 2018; 32:1267-84.
[36] Ferreira LMR. Cancer metabolism: the Warburg effect today. Exp Mol Pathol. 2019; 89(3):372-80.
[37] DeBerardinis RJ, Chandel NS. Fundamentals of cancer metabolism. Sci Adv. 2016; 2(5):e1600200.
[38] Vander Heiden MG, Cantley LC, Thompson CB. Understading the Warburg Effect: the metabolic requirements of cell proliferation. Science 2009; 324:1029-33.
[39] Chabner BA, Roberts TG. Chemotherapy and the war on cancer. Nat Rev. 2005; 5:65-73.
[40] DeVita VT, Chu E. A history of cancer chemotherapy. Cancer Res. 2008; 68(21):8643-54.
[41] Singh RK, Kumar S, Prasad DN, Bhardwaj TR. Therapeutic journey of nitrogen mustard as alkylating anticancer agents: historic to future perspectives. Eur J Med Chem. 2018; 151:401-33.
[42] Frei E, Jaffe N, Tattersall HM, Pitman S, Parker L. New approaches to cancer therapy with methotrexate. N Engl J Med. 1975; 292:846-51.
[43] Lennard L. The clinical pharmacology of 6-mercaptopurine. Eur J Clin Pharmacol. 1992; 43:329-39.
[44] Freireich EJ, Wiernik PH, Steensma DP. The leukemias: a half-century of discovery. J Clin Oncol. 2014; 32(31):3463-69.
[45] Goodwin RA, Asmis TR. Overview of systemic therapy of colorectal cancer. Clin Colon Rectal Surg. 2009; 22(4):251-56.
[46] Shankar Naik B. Developments in taxol production through endophytic fungal biotechnology: a review. OPEM 2019; 19:1-13.
[47] Thomas CJ, Rahier NJ, Hecht SM. Camptothecin: current perspectives. Bioorg Med Chem. 2004; 12(7):1585-604.
[48] Mosmann T. Rapid colorimetric assay for cellular growth and survival: application to proliferation and cytotoxicity assays. J Immunol Methods 1983; 65(1-2):55-63.
[49] Lee YT, Tan YJ, Oon CE. Molecular targeted therapy: treating cancer with specificity. Eur J Pharmacol. 2018; 834:188-96.
[50] Wu HC, Chang DK, Huang CT. Targeted therapy of cancer. J Cancer Mol 2006; 2(2):57-66.
[51] Sharkey RM, Goldenberg DM. Targeted therapy of cancer: new prospects for antibodies and immunoconjugates. CA Cancer J Clin. 2006; 56(4):226-43.

[52] Conroy PJ, Law RHP, Caradoc-Davies TT, Whisstock JC. Antibodies: from novel repertoires to defining and refining the structure of biologically important targets. Methods 2017; 116:12-22.
[53] Baldo BA. Monoclonal antibodies approved for cancer therapy. Cham (Switzerland): Springer International Publishing; 2016. Safety of biologics therapy.
[54] Lu RM, Hwang YC, Liu IJ, Lee CC, Tsai HZ, Li HJ, Wu HC. Development of therapeutic antibodies for the treatment of diseases. J Biomed Sci. 2020; 27:1.
[55] Köhler G, Milstein C. Continuous cultures of fused cells secreting antibodies of predefined specificity. Nature 1975; 256:495-97.
[56] Zaroff S, Tan G. Hybridoma technology: the preferred method for monoclonal antibody generation for in vivo applications. BioTechniques 2019; 67:90-92.
[57] Bedard PL, Hyman DM, Davids MS, Siu LL. Small molecules, big impact: 20 years of targeted therapy in oncology. Lancet 2020; 395:1078-88.
[58] Jahanafrooz Z, Baradaran B, Mosafer J, Hashemzaei M, Rezaei T, Mokhtarzadeh A, Hamblin MR. Comparison of DNA and mRNA vaccines against cancer. Drug Discov Today 2020; 25(3):552-60.
[59] Vergati M, Intrivici C, Huen N-Y, Schlom J, Tsang KY. Strategies for cancer vaccine development. J Biomed Biotechnol. 2010; 2010:596432.
[60] Shemesh CS, Hsu JC, Hosseini I, Shen B-Q, Rotte A, Twomey P, Girish S, Wu B. Personalized cancer vaccines: clinical landscape, challenges and opportunities. Mol Ther. 2021; 29(2):555-70.
[61] Calvo Tardón M, Allard M, Dutoit V, Dietrich P-Y, Walker PR. Peptides as cancer vaccines. Curr Opin Pharmacol. 2019; 47:20-26.
[62] DeMaria PJ, Bilusic M. Cancer vaccines. Hematol Oncol Clin North Am. 2001; 15(4):741-73.
[63] Zhang R, Billingsley MM, Mitchell MJ. Biomaterials for vaccine-based cancer immunotherapy. J Control Release 2018; 292:256-76.
[64] El-Anned A. Current strategies in cancer gene therapy. Eur J Pharmacol. 2004; 498:1-8.
[65] Misra R, Acharya S, Sahoo SK. Cancer nanotechnology: application of nanotechnology in cancer therapy. Drug Discov Today 2010; 15(19-20):842-50.
[66] Gu W, Meng F, Haag R, Zhong Z. Actively targeted nanomedicines for precision cancer therapy: concept, construction, challenges and clinical translation. J Control Release 2021; 329:676-95.
[67] Hassanzadeh P, Fullwood I, Sothi S, Aldulaimi D. Cancer nanotechnology. Gastroenterol Hepatol Bed Bench. 2011; 4(21):63-9.

[68] PubMed. Available online: https://pubmed.ncbi.nlm.nih.gov/?term=nanoparticles+cancer&filter=years.2001-2021 (accessed on 23th November 2020).
[69] Norouzi M, Amerian M, Amerian M, Atyabi F. Clinical application of nanomedicine in cancer therapy. Drug Discov Today 2020; 25(1):107-25.
[70] Huda S, Alam MA, Sharma PK. Smart nanocarriers-based drug delivery for cancer therapy: an innovative and developing strategy. J Drug Deliv Sci Tech. 2020; 6:102018.
[71] Bertrand N, Wu J, Xu X, Kamaly N, Farokhzad OC. Cancer nanotechnology: the impact of passive and active targeting in the era of modern cancer biology. Adv Drug Deliv Rev. 2014; 66:2-25.
[72] Matsumura Y, Maeda H. A new concept for macromolecular therapeutics in cancer chemotherapy: mechanism of tumoritropic accumulation of proteins and the antitumor agent smancs. Cancer Res. 1986; 46:6387-92.
[73] Danhier F, Feron O, Préat V. To exploit the tumor-microenvironment: Passive and active tumor targeting of nanocarriers for anti-cancer drug delivery. J Control Release 2010; 148:135-146.
[74] Marques AC, Costa PJ, Velho S, Amaral MH. Functionalizing nanoparticles with cancer-targeting antibodies: a comparison of strategies. J Control Release 2020; 320:180-200.
[75] Gaumet M, Vargas A, Gunny R, Delie F. Nanoparticle for drug delivery: the need for precision in reporting particle size parameters. Eur J Pharm Biopharm. 2008; 69:1-9.
[76] Cho K, Wang X, Nie S, Chen Z, Shin DM. Therapeutic nanoparticles for drug delivery in cancer. Clin Cancer Res. 2008; 14:1310-16.
[77] Zhong Y, Meng F, Deng C, Zhong Z. Ligand-directed active tumor-targeting polymeric nanoparticles for cancer chemotherapy. Biomacromolecules 2014; 15:1955-69.
[78] Masood F. Polymeric nanoparticles for targeted drug delivery system for cancer therapy. Mater Sci Eng C 2016; 60:569-78.
[79] Hoogenboezem EN, Duvall CL. Harnessing albumin as a carrier for cancer therapies. Adv Drug Deliv Rev 2018; 130:73-89.
[80] Zhang E, Xing R, Liu S, Qin Y, Li K, Li P. Advances in chitosan-based nanoparticles for oncotherapy. Carbohydr Polym. 2019; 222:115004.
[81] Yang X, Du H, Liu J, Zhai G. Advanced nanocarriers based on heparin and its derivatives for cancer management. Biomacromolecules 2015; 16(2):423-36.

[82] Eroglu MS, Oner ET, Mutlu EC, Bostan MS. Sugar based biopolymers in nanomedicine; New emerging era for cancer imaging and therapy. Curr Top Med Chem. 2017; 17(13):1507-20.

[83] Liao Z, Wong SW, Yeo HY, Zhao Y. Smart nanocarriers for cancer treatment. Clinical impact and safety. NanoImpact 2020; 20:100253.

[84] Fan D-Y, Tian Y, Liu Z-J. Injectable hydrogels for localized cancer therapy. Front Chem. 2019; 7:675.

[85] Norouzi M, Nazari B, Miller DW. Injectable hydrogel-based drug delivery systems for local cancer therapy. Drug Discov Today 2016; 21(11):1835-49.

[86] Hossen S, Hossain MK, Basher MK, Mia MNH, Rahman MT, Uddin MJ. Smart nanocarrier-based drug delivery systems for cancer therapy and toxicity studies: A review. J Adv Res. 2019; 15:1-8.

[87] Sanginario A, Miccoli B, Demarchi D. Carbon nanotubes as an effective opportunity for cancer diagnosis and treatment. Biosensors 2017; 7:9.

[88] Dang Y, Guan J. Nanoparticle-based drug delivery systems for cancer therapy. Smart materials in Medicine 2020; 1:10-19.

[89] Lim ZZJ, Li JEJ, Ng CT, Yung LYL, Bay BH. Gold nanoparticles in cancer therapy. Acta Pharmacol Sin. 2011; 32:983-90.

[90] Webb BA, Chimenti M, Jacobson MP, Barber DL. Dysregulated pH: a perfect storm for cancer progression. Nat Rev Cancer 2011; 11:671-77.

[91] Wells CM, Harris M, Choi L, Murali VP, Guerra FD, Jennings JA. Stimuli-responsive drug release from smart polymers. J Funct Biomater. 2019; 10:34.

[92] Shao P, Wang B, Wang Y, Li J, Zhang Y. The application of thermosensitive nanocarriers in controlled drug delivery. J Nanomater. 2011; 2011:389640.

[93] Rabussay DP, Nanda GS, Goldfarb PM. Enhancing the effectiveness of drug-based cancer therapy by electroporation (electropermeabilization). Technol Cancer Res Treat. 2002; 1(1):71-82.

nanomaterials

*Review*

# Trastuzumab: More than a Guide in HER2-Positive Cancer Nanomedicine

**Celia Nieto *, Milena A. Vega and Eva M. Martin del Valle ***

Departamento de Ingeniería Química, Facultad de Ciencias Químicas, Universidad de Salamanca, 37008 Salamanca, Spain; mvega@usal.es

* Correspondence: celianieto@usal.es (C.N.); emvalle@usal.es (E.M.M.d.V.); Tel.: +34-923294500 (E.M.M.d.V.)

Received: 2 August 2020; Accepted: 24 August 2020; Published: 26 August 2020

**Abstract:** HER2 overexpression, which occurs in a fifth of diagnosed breast cancers as well as in other types of solid tumors, has been traditionally linked to greater aggressiveness. Nevertheless, the clinical introduction of trastuzumab has helped to improve HER2-positive patients' outcomes. As a consequence, nanotechnology has taken advantage of the beneficial effects of the administration of this antibody and has employed it to develop HER2-targeting nanomedicines with promising therapeutic activity and limited toxicity. In this review, the molecular pathways that could be responsible for trastuzumab antitumor activity will be briefly summarized. In addition, since the conjugation strategies that are followed to develop targeting nanomedicines are essential to maintaining their efficacy and tolerability, the ones most employed to decorate drug-loaded nanoparticles and liposomes with trastuzumab will be discussed here. Thus, the advantages and disadvantages of performing this trastuzumab conjugation through adsorption or covalent bindings (through carbodiimide, maleimide, and click-chemistry) will be described, and several examples of targeting nanovehicles developed following these strategies will be commented on. Moreover, conjugation methods employed to synthesized trastuzumab-based antibody drug conjugates (ADCs), among which T-DM1 is well known, will be also examined. Finally, although trastuzumab-decorated nanoparticles and liposomes and trastuzumab-based ADCs have proven to have better selectivity and efficacy than loaded drugs, trastuzumab administration is sometimes related to side toxicities and the apparition of resistances. For this reason also, this review focuses at last on the important role that newer antibodies and peptides are acquiring these days in the development of HER2-targeting nanomedicines.

**Keywords:** HER2 overexpression; trastuzumab; targeted nanoparticles; targeted liposomes; antibody-drug conjugates; conjugation

## 1. Introduction

Today, it is well known that cancer is one of the most important public health problems worldwide, since it is the second leading cause of death [1]. Globally, about 1 in 6 deaths is caused by cancer and, in 2018, this complex disease affected almost 20 million people and was responsible for the death of 9.5 million [1,2].

Among the different types of cancer, breast cancer has the second highest incidence, and about 11–12% of the total of new cancer cases that were diagnosed in 2018 were from this tissue [2]. Although there are manifold phenotypes of this disease, approximately 15–20% of breast cancer cases present an overexpression of the human epidermal growth factor receptor-2 (HER2) [3,4], which in addition is also overexpressed in other types of solid tumors [5]. On one hand, the increased expression of this tyrosine kinase receptor is related to cell proliferation, migration, and invasion and, thus, to a poor prognosis for patients and a higher risk of disease recurrence [4,6]. Nevertheless, on the other

hand, it has offered the possibility of developing guided-treatment approaches [4], solving one major drawback of conventional chemotherapy: its lack of specificity.

The employment of cytotoxic compounds, either alone or combined with other strategies (surgery or radiotherapy), is the most common first-line treatment against cancer. However, most of these agents exhibit a variable absorption rate and cannot be orally administered. As a consequence, due to its limited effectiveness, chemotherapy must be performed using the systemic route, which is much more uncomfortable for patients. Moreover, since chemotherapy agents are not specifically distributed because of their lack of selectivity, they harm both tumor and normal cells, causing dose-limiting toxicity with severe side effects, such as liver and kidney damage [7,8] (Figure 1). Furthermore, the absence of specificity is also responsible for the apparition of multidrug resistance (MDR) after prolonged exposure to cytotoxic agents, this being one of the most challenging limiting factors of conventional chemotherapy today [7–9].

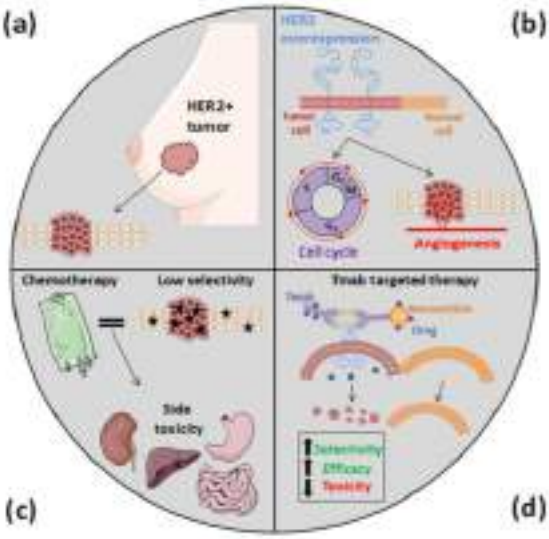


**Figure 1.** HER2 overexpression, which occurs in almost a fifth of breast cancer cases (**a**) as well as in other types of solid tumors, is related to cell proliferation and invasion and makes cancer cells more aggressive (**b**). However, this overexpression has also allowed us to develop novel nanomedicines that are more specific than conventional cytotoxic agents, which often cause acute toxicities (**c**). In the development of these new nanomedicines, since Tmab specifically recognizes HER2, it has been attached to different types of DDS, improving their efficacy and selectivity and, thus, reducing their side effects (**d**).

For these reasons, nanotechnology has acquired an essential role during recent years by means of the development of drug delivery systems (DDS), with which it aims to address the downsides of chemotherapy [5]. Thereby, the synthesis of nanomedicines based on viral vectors, drug conjugates, and lipid and polymer nanocarriers has aroused tremendous interest. Among these DDS, nanoparticles (NPs) and liposomes have been preferred for designing nanocarriers due to their advantageous properties. NPs have proven to be more easily soluble in water, increasing the stability and bioavailability of the delivered compounds, and are readily chemically modifiable [10,11]. Therefore, polymeric (chitosan, dextran, pullulan, albumin-based ... ), ceramic (silica-based or hydroxyapatite), and metallic (mainly gold) NPs have already been used as platforms for the development of new

DDS [12–15]. Similarly, liposomes have been shown to be biocompatible, have little toxicity, and are capable of promoting a controlled drug release [16].

Thanks to the characteristic properties of cancer tissues, there are two mechanisms by which NPs and liposomes can deliver drugs to tumors: passive targeting and active targeting [17]. The passive accumulation process is a direct consequence of the enhanced permeability and retention (EPR) effect, induced by the leaky blood vasculature and impaired lymphatic system of the solid tumors. NPs with an appropriate size (100–400 nm) and superficial charge (preferably negative) can achieve lengthy blood circulation times and accumulate at tumoral sites by diffusion and convection processes. Nonetheless, this passive delivery has its own issues, since the EPR effect does not occur in every tumor (as in those in which there is a great hypoxia), and vessel permeability is not usually homogeneous [8,17,18]. Besides, passive targeting can promote MDR apparition due to its lack of control and the consequent undue drug accumulation in cancer cells, a fact which, on the contrary, can be overcome by active targeting [17]. This second delivery process accomplishes a specific recognition of tumor cells that favors controlled DDS internalization in them, increasing their therapeutic efficiency [19]. Such targeting can be attained by chemical changes in the NP and liposome surface, making it more reactive to the tumor microenvironment, or with ligands that specifically recognize overexpressed receptors or proteins in cancer cells, such as several peptides, aptamers, and antibodies [17–20]. Among these three targeting molecules, peptides and aptamers are smaller, less immunogenic, more easily chemically modifiable, and more temperature-stable than antibodies. However, antibody properties have been more extensively characterized, making them indispensable for cancer research, diagnosis, and therapy [21,22].

Furthermore, aside from the synthesis of DDS, antibodies have also aroused interest in cancer nanomedicine because of the development of antibody-drug conjugates (ADCs), which have also been designed to increase the efficacy of conventional chemotherapy [23,24].

Among these antibodies, the most commonly used in the treatment against HER2+ tumors are pertuzumab and trastuzumab, two recombinant humanized monoclonal antibodies [25,26]. Of these, trastuzumab (Herceptin™, Genentech/Roche, San Francisco, FL, USA) (Tmab) specifically binds to the extracellular domain IV of the aforementioned HER2 and has allowed the survival rate of patients who suffer from HER2-positive (HER2+) breast cancer to increase [6]. For this reason, this antibody has been extensively used for both the development of guided NPs and liposomes and for the development of ADCs, and is the protein on which this review study is focused (Figure 1).

Thereby, this article summarizes how the clinical employment of Tmab has helped to improve the outcome of patients who suffer from HER2+ breast cancer, as well as the molecular mechanisms that could be behind its antineoplastic activity. Moreover, the main covalent and non-covalent strategies that are followed in the nanomedicine field to decorate NPs and liposomes with this antibody have been examined in detail, along with the ones employed to synthesize Tmab-based ADCs. At the end, the future role of Tmab in the development of novel anti-HER2 nanomedicines is also discussed.

## 2. Trastuzumab: More Than a Guide for Nanomedicines

The clinical utilization of Tmab was firstly approved by the US Food and Drug Administration (FDA) and the European Medicines Agency (EMA) in 1998 and in 2000, respectively, to treat patients with HER2+ metastatic breast cancer (MBC). Several years later (in 2006 and 2011), these two organisms also authorized the employment of this recombinant antibody as adjuvant therapy for patients with HER2+ early breast cancer (EBC) and, finally, in 2015 Tmab was added to the Essential Medicines List of the World Health Organization (WHO) [27]. Such addition was the outcome of the beneficial effects that Tmab has proven to have for women with HER2+ MBC and EBC when it is administered with chemotherapy, slowing down tumor progression, inducing tumor regression, and increasing patients' overall survival rate [28]. For instance, when Tmab is administered in the first-line treatment of MBC, it induces tumor regression in 30–35% of patients and increases patients' disease-free survival rate after five years by 10% in comparison with only the administration of conventional cytotoxic drugs [28,29].

Moreover, Tmab is able to reduce their risk of disease recurrence by 50% when it is given to patients who suffer from EBC, too [28,30].

However, the molecular pathways that are behind these positive results are not completely known and remain an active research area [31]. Among them, three main mechanisms have been proposed to be responsible for Tmab antitumor activity: (I) cell cycle arrest triggered by the inhibition of the MAPK and PI3K signaling cascades; (II) antibody-dependent cellular cytotoxicity (ADCC); and (III) the increased production of anti-angiogenic factors (Figure 2) [31,32]. The aberrant activation of the PI3K/AKT/mTOR and MEK/ERK pathways has been linked to an induction of cellular proliferation and survival rate, while the in vivo inhibition of such pathways has shown to reduce tumor growth [33]. In this way, since Tmab administration inhibits transforming signals downstream of HER2, this antibody can trigger cell cycle arrest and induce cancer cell apoptosis (Figure 2a) [34]. Otherwise, targeted cells opsonized by immunoglobulin (IgG)-based monoclonal antibodies, such as Tmab, are able to bind and activate FcγR-bearing immune effector cells, like the NK cells, and this fact results in a target cell lysis (Figure 2b) [35]. Finally, it has also been demonstrated that, through the mentioned inhibition of the PI3K/AKT/mTOR pathway, Tmab decreases the expression of some proangiogenic factors like the vascular endothelial growth factor (VEGF) and interleukin-8 (IL-8) (Figure 2c) [36].

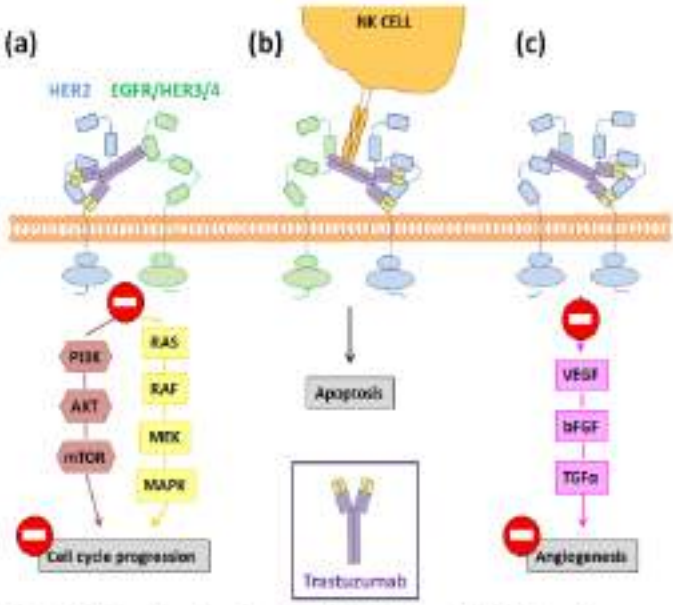


**Figure 2.** Potential molecular pathways involved in the Tmab-mediated inhibition of tumor progression once this antibody binds to the domain IV of HER2, blocking its homo- and hetero-dimerization. Such pathways are: (a) the inhibition of the MAPK and PI3K signaling cascades; (b) ADCC; (c) the blockage of the angiogenesis process.

Thereby, such three mechanisms could be implicated in the Tmab-mediated active targeting of NPs and liposomes decorated by this antibody on their surface and of Tmab-based ADCs, achieving not only a guided treatment but also a synergy between Tmab and the delivered drugs. For this reason and also because Tmab has been used in the clinic for almost two decades with the approval of the main drug regulatory agencies, a large number of NPs and liposomes have been already conjugated to

this antibody to improve conventional chemotherapy efficacy, and even a Tmab-ADC is already being commercialized [23,37].

## 3. Nanoparticle and Liposome Functionalization with Trastuzumab: Usual Strategies

The different strategies that have been pursued to anchor Tmab to the surface of sundry types of NPs and liposomes can be classified into two main groups, depending on whether or not the antibody-binding is covalent. In this way, works in which Tmab has been adsorbed on several particulate nanosystems can be found in the literature, while in other studies the antibody has been covalently attached to NPs and liposomes following several strategies, such as with carbodiimide, maleimide, or click-chemistry [17,38].

### 3.1. Functionalization through Trastuzumab Adsorption

Adsorption immobilization comprises physical and ionic bindings. In the first sort of adsorption, electrostatic and hydrophobic interactions as well as the hydrogen binding are comprised. On the other side, ionic binding occurs when the antibody and the NP surface have opposite charges (Figure 3a). In any case, both adsorptions are reversible and the non-covalent functionalization with them is rapid and simple, since it does not require any chemical modification [17]. Taking advantage of physical adsorption, Liu et al. [39] developed polylactide-*b*-α-tocopheryl polyethylene glycol succinate (PLA-TPGS) NPs loaded with docetaxel and decorated by Tmab, and demonstrated that a synergist effect could be achieved when the drug and the antibody were simultaneously administered. In the same manner and thanks to electrostatic interactions, Yu et al. [40] and Zhang et al. [41] functionalized with Tmab the surface of polyethylenimine/poly(lactic-co-glycolic acid) (PEI/PLGA) NPs that transported paclitaxel and docetaxel, respectively, to specifically treat HER2+ breast cancer cells. Likewise, Sun et al. [42] adsorbed Herceptin™ to their PLGA/montmorillonite (MTT) NPs, which also carried paclitaxel to breast tumor cells overexpressing HER2.

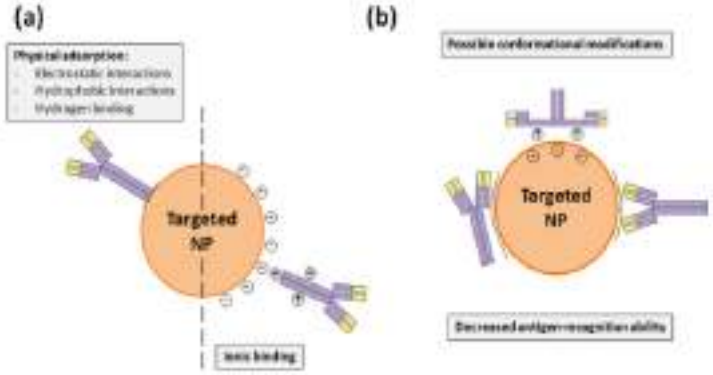


**Figure 3.** (**a**) Non-covalent binding alternatives to attach Tmab to the NP surface. (**b**) Potential conformational changes that Tmab can suffer in physical and ionic bindings and which can hinder its antigen-recognition capacity.

Nevertheless, DDS functionalization through adsorption methods is less stable than covalent bindings and requires high amounts of antibodies, which makes the conjugation process more expensive. Besides this, the adsorbed antibody can suffer conformational changes that would decrease its antigen recognition capacity and make the functionalization process less reproducible (Figure 3b) [17]. This fact was precisely demonstrated by Choi et al. [43], who compared how the employed Herceptin™- functionalization method conditioned the antiproliferative activity of

docetaxel-PLGA NPs. These authors modified the mentioned NP surface with Tmab through adsorption, charged adsorption, and bio-conjugation. As a result, they found that this last covalent conjugation process was more efficient and that bio-conjugated NPs had a greater stability, cell internalization rate, and cytotoxicity than the NPs that were functionalized through the adsorption processes [43].

### 3.2. Trastuzumab-Functionalization through Covalent Bindings

As it has been before mentioned, Tmab covalent binding can be achieved with different strategies, the most common ones being carbodiimide chemistry, maleimide chemistry, and click-chemistry.

The first one, carbodiimide chemistry [44], is probably the most used one. It requires the employment of 1-ethyl-3-(3-dimethylaminopropyl) carbodiimide (EDC), a zero-length crosslinking agent that allows the binding of the carboxyl groups present in the DDS surface with the primary amine functional groups of antibodies. When EDC reacts in one-step with carboxyl groups, O-acylisourea esters, which are highly reactive, are generated. Then, such intermediate compounds react with primary amines, and amide bonds are finally formed. The inconvenient aspect is that O-acylisourea esters are not stable enough, and intra- and inter-molecular bindings can take place between antibody functional groups. In order to avoid this fact, N-hydroxysulfosuccinimide (NHS) is usually incorporated in the carbodiimide chemistry, although its use is not mandatory [45]. With its addition, the reaction takes place in two steps with an increased efficiency, since O-acylisourea esters become semi-stable esters (Figure 4a) [17,46].

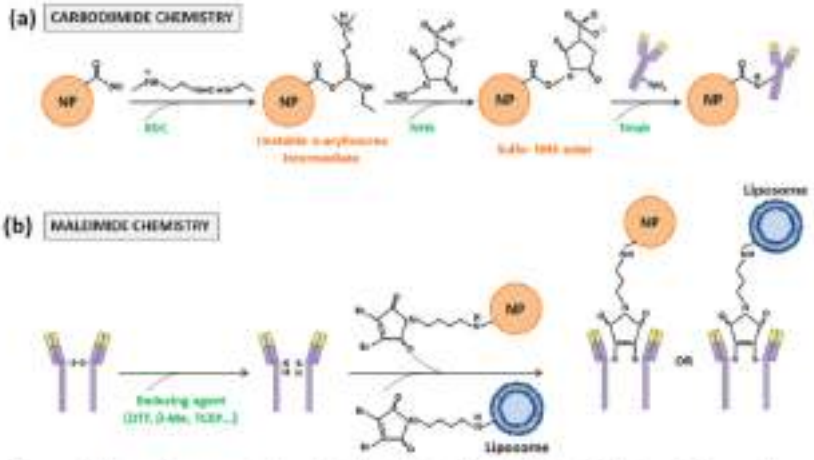


**Figure 4.** Schematic representation of the **(a)** carbodiimide and **(b)** maleimide coupling reactions between the Tmab, NP, and liposome systems.

The main advantage of this sort of covalent functionalization, which explains its large use, is its simplicity. Primary amine groups are abundant in the antibody surface and no chemical modification of the NPs is required to carry it out [17]. Because of that, carbodiimide chemistry has been widely utilized in the literature to anchor Tmab to different particle nanosystems. For instance, Choi et al. chose it to make the comparative study that was aforementioned [42]. Similarly, Zhou et al. [47], Mehata et al. [6], and Nieto et al. [48] decorated the surface of their synthesized NPs with Tmab by taking advantage of this method to treat HER2+ breast carcinoma cells. The first authors [47] developed PLGA-poly-L-histidine (Phis)-polyethylene glycol (PEG) NPs and loaded them with doxorubicin. Mehata et al. [6] obtained TPGS-g-chitosan NPs that carried docetaxel to the mentioned cells and,

finally, Nieto el al. [48] synthesized alginate-piperazine NPs to improve and guide paclitaxel treatment. In addition, these last authors also proved that their nanosystem was able to reduce the rate of survival of other types of cancer cells that also overexpress HER2, such as ovarian tumor cells. In the same way, Domínguez-Ríos et al. [49] conjugated Tmab to the surface of PLGA NPs to treat a HER2+ ovarian cancer cell line, and Arya et al. [50] did this with chitosan NPs to treat HER2+ pancreatic tumors. Furthermore, carbodiimide chemistry has not only been used to create Herceptin™-DDS, but also to develop NPs with which the bio-separation, selective radiotherapy, and hyperthermia of HER2+ cancer cells could be performed [51–53].

As it can be checked, carbodiimide chemistry has been employed to modify the surface of NPs of a very different composition, but it presents a handicap. Carbodiimide chemistry is not a really selective coupling method, since primary amine groups can be found anywhere in the antibody surface. Thus, it lacks control of antibody orientation, and as consequence other covalent functionalization methods which are more site-specific have been preferred by other researchers [17].

Functionalization performed with maleimide chemistry, which is based on bindings through the sulfhydryl or thiol groups of antibodies, is one of such methods [54]. These groups are less abundant on the antibody surface than primary amines, and generally they are oxidized and present in form of disulfide bonds that couple pairs of cysteines. These amino acids, which are essential for the formation of the tertiary or quaternary structure of proteins, are the most reactive nucleophiles in them. Nonetheless, antibody conjugation only can occur through free or reduced sulfhydryl groups, which have to be introduced. This introduction can be achieved through reaction with primary amines or through the reduction of disulfide bonds, which can be cleaved with different reducing agents, such as dithiothreitol (DTT) or 2-Mercaptoethanol (β-ME). Once obtained, reactive sulfhydryl groups can react towards maleimide, α-haloacetyls, and pyridyl disulfides [17,55]. With the first two compounds, an irreversible thioether linkage is formed, but maleimide-activate crosslinkers present a higher selectivity for the sulfhydryl side chain of cysteines and more rapid ligation kinetics in aqueous conditions and have received more attention [17,56] (Figure 4b). Thus, for such maleimide activation, two different strategies can be pursued: (i) DDS functionalization, introducing thiol groups or maleimides; or (ii) the employment of hetero- or homobifunctional linkers with one or two maleimides at the ends, respectively. Both strategies have been followed in order to conjugate NPs and liposomes with Tmab.

For example, the first option was the one followed by Taheri et al. in their study [57]. These authors conjugated methotrexate (MTX) to human serum albumin (HSA) and, after the crosslinking such protein, they obtained NPs that were decorated by Tmab to treat HER2+ breast cancer. To achieve this decoration, Taheri et al. introduced thiol functional groups in the NPs that they synthesized, and activated the anti-HER2 antibody with 4-maleimidobutyric acid-N hydroxysuccinimide (GMBS). After allowing them to react, they obtained covalent Tmab-attached MTX-HSA NPs [57]. In addition, this strategy was the one employed by Nguyen et al. and Amin et al., too [58,59], to attach Tmab to liposomes. All these authors synthesized liposomes with a maleimide-terminated PEG lipid conjugate (DSPE-PEG-Mal) and thiolated Tmab in order to perform a covalent conjugation. Thereby, Nguyen et al. managed to develop PEGylated liposomes in which they included rapamycin and polypyrrole ($PPy$) NPs for the targeted chemo-photothermal therapy of HER2+ breast cancer cells [58], while Amin et al. created Tmab-conjugated liposomes to specifically deliver idarubicin to the same sort of tumor cells [59].

On the other hand, the second option was chosen in works such as those of Chiang et al. [60], Jang et al. [61], Kesavan et al. [62], Steinhauser et al. [63], and Kubota et al. [64]. The first authors, in order to trigger the same type of tumors as the previous researchers [57–59], developed double emulsion nanocapsules (DENCs) in which they simultaneously encapsulated paclitaxel and doxorubicin. Then, on their surface they attached a magnetic targeting and Tmab in order to achieve a combined therapy and, for the antibody conjugation, followed the succinimidyl-4-(*N*-maleimidomethyl)-cyclohexane-1-carboxylate (SMCC) method. Thereby, they carried out a thiol-functionalization of their nanocapsules and a maleimide-activation

of the antibody with the SMCC Pierce™, a heterobifunctional crosslinker that contains NHS ester and maleimide groups [60]. Similarly, Jang et al. prepared liposomes encapsulating silica-core-shell magnetic NPs and attached Tmab on their surface through the SMCC method to treat HER2+ breast tumors using magnetic resonance imaging (MRI) monitoring. Briefly, these authors formed an amide bond from the primary amine of their particles employing sulfo-SMCC and, later, thiolated Tmab with Traut's reagent, proving that their conjugated liposomes accumulated in detectable amounts in tumors overexpressing HER2 [61]. In the same manner, Kesavan et al. introduced maleimide groups in Tmab and attached such antibodies to the surface of polyamidoamine dendrimer–cisplatin NPs that had been also functionalized with diglycolamic acid to treat HER2-overexpressing ovarian tumor cells. To achieve this goal, Kesavan et al. conjugated the amine groups of their NPs with LC-SPDP, another heterobifunctional crosslinker, and carried out a reduction reaction with DTT to obtain reactive thiol groups on the surface of the NPs that could react with Tmab-maleimide groups [62]. Just the opposite, Steinhauser et al. performed a thiolation of Tmab with the use of 2-iminothiolane and activated the HSA NPs that they had been previously obtained with a heterobifunctional crosslinker (NHS-PEG5000-Mal) with similar terminal functional groups to those of SMCC Pierce™. In this way, these authors were able to develop a HER2-guided drug carrier system [63]. Finally, Kubota et al. synthesized gold NPs decorated with Tmab to treat HER2+ gastric cancer cells that were resistant to this antibody [64]. To anchor Tmab to their surface, these authors employed a linker that consisted of a short PEG chain terminated at one end by a hydrazide moiety and at the other end by two thiol groups [65], and added methoxyPEG-SH to cap any remaining bare surfaces of the gold NPs [64].

Although conferring site-specific conjugation to cysteine residues, NP and liposome functionalization through maleimide chemistry also has proven disadvantages: maleimide can react with thiol groups present in serum proteins (like albumin) and, as a consequence, resulting bioconjugates have been shown to be inherently unstable in vivo. In addition, this strategy involves the loss of a covalent bond between the antibody chains. As a solution, other forming antibody-NP/liposome conjugates strategies, such as click-chemistry, have appeared [17,66].

The click-chemistry term, which was firstly proposed by Kolb et al. in 2001 [67], refers to a group of powerful chemical reactions which are orthogonal with other functional groups (amines, thiols, carboxylic acids ... ), simple to perform, favorable in aqueous conditions, with high yields, and that generate minimal byproducts [68–70]. The first reaction that was called click-chemistry, which is the most widely used today in nanomedicine, was the copper-catalyzed cycloaddition between azides and alkynes that generates 1,2,3-triazoles (CuAAC). Later, cycloadditions between strain-promoted alkynes and azides (SPAAC) enabled copper-free click-chemistry and started to be preferred to CuAAC to functionalize DDS to prevent copper bioaccumulation [68]. In the end, the inverse-demand Diels–Alder reaction with 1,2,4,5-tetrazine (Tz) and trans-cyclooctene (TCO) (IEDDA) provided an ungraded reaction rate and also began to be applied in biomedicine (Figure 5) [68,71]. As examples of the application of the click-chemistry in the development of Tmab-nanoconjugates, the works of Greene et al. [66], Yoo et al. [72], and Keinänen et al. [73] can be highlighted.

Foremost, Greene et al. described in an anterior study a new approach to insert pyridazinedione moieties bearing reactive handles into antibody-reduced disulfide bonds for enabling the incorporation of click-domains without losing covalent linkages between the antibody chains [74]. Then, in the work quoted here, these authors took advantage of such an approach to site-selectively modify the F(ab) domain of Tmab to bear a strained alkyne handle distal to the paratope and to conjugate it to azide-functionalized PLGA NPs. For such a purpose, they incorporated a complementary azide moiety into the NPs and synthesized a heterobifunctional linker to conjugate the Tmab-F(ab) disulfide to them. In such linker, Greene et al. included a strained alkyne bicyclononyne (BCN) and employed SPAAC to develop guided NPs for the treatment of HER2+ breast cancer cells, showing that the click-chemistry that they used was more efficient than the NHS ester one [66]. Secondly, Yoo et al. chose the inverse-demand Diels–Alder reaction between Tz and TCO to perform a two-step treatment of HER2+ cancer cells with Tmab and liposomes that had been loaded with the anticancer drug

SN38. They performed the conjugation of Tmab with TCO by means of a linker (TCO-PEG4-NHS ester) and modified the surface of their liposomes with the Tz groups. Later, these authors treated cancer cells with the TCO-modified Tmab, allowing the TCO groups to remain exposed on the tumor cell surface, and performed the second step of the treatment with the Tz-modified SN38-liposomes, which bound the TCO groups via click-chemistry, achieving a chemotherapy enhancement [72]. Finally, Keinänen et al. also employed the same iEDDA methodology to Yoo et al., but with a different aim: in vivo tracing the internalization of Tmab with a fluorine-18 labelled-Tz tracer. Thus, they modified the antibody with TCO and injected it in mice with HER2+ breast cancer tumors, and successfully visualized it by positron emission tomography (PET) imaging [73].

A summary of all the Tmab-guided DDS, developed following the different non-covalent and covalent strategies explained here, can be found in Table 1.

**Table 1.** Tmab-functionalized DDS developed following different non-covalent and covalent strategies to target several sorts of HER2+ cancers.

| Strategy | Type of DDS | Payload | Targeted Type of HER2+ Cancer | Reference |
|---|---|---|---|---|
| Physical adsorption | NPs (PLGA-TPGS) | Docetaxel | Breast | Liu et al. [39] |
| | NPs (PEI/PLGA) | Paclitaxel | Breast | Yu et al. [40] |
| | NPs (PEI/PLGA) | Docetaxel | Breast | Zhang et al. [41] |
| | NPs (PLGA/MIT) | Paclitaxel | Breast | Sun et al. [42] |
| Physical and ionic adsorption and carbodiimide chem. | NPs (PLGA) | Docetaxel | Breast | Choi et al. [43] |
| Carbodiimide chemistry | NPs (PLGA-Plur-PEG) | Doxorubicin | Breast | Zhou et al. [47] |
| | NPs (TPGS-g-chitosan) | Docetaxel | Breast | Mehata et al. [48] |
| | NPs (Alginate-piperazine) | Paclitaxel | Breast, ovarian | Nieto et al. [51] |
| | NPs (PLGA) | Cisplatin | Ovarian | Domínguez-Ríos et al. [49] |
| | NPs (Chitosan) | Gemcitabine | Pancreatic | Anjo et al. [50] |
| | NPs (Magnetic) | - | Breast | Alnaidi et al. [53] |
| Maleimide chemistry | NPs (BSA) | Methotrexate | Breast | Taheri et al. [57] |
| | Liposomes | Rapamycin, PPy NPs | Breast | Nguyen et al. [58] |
| | Liposomes | Idarubicin | Breast | Amin et al. [59] |
| | DENCs | Paclitaxel, doxorubicin | Breast | Chung et al. [60] |
| | Liposomes | Magnetic NPs | Breast | Jung et al. [61] |
| | NPs (Polyamidoamine dendrimers) | Cisplatin | Ovarian | Rasoulzadeh et al. [62] |
| | NPs (BSA) | - | Amyotic | Steinhauser et al. [63] |
| | NPs (Gold) | - | Gastric | Kolhatkar et al. [64] |
| Click-chemistry (IEDAAC) | NPs (PLGA) | - | Breast | Greene et al. [66] |
| Click-chemistry (IEDDA) | Liposomes | SN38 | Amyotic | Yoo et al. [72] |
| | - | Fluorine-18 | Breast | Keinänen et al. [73] |

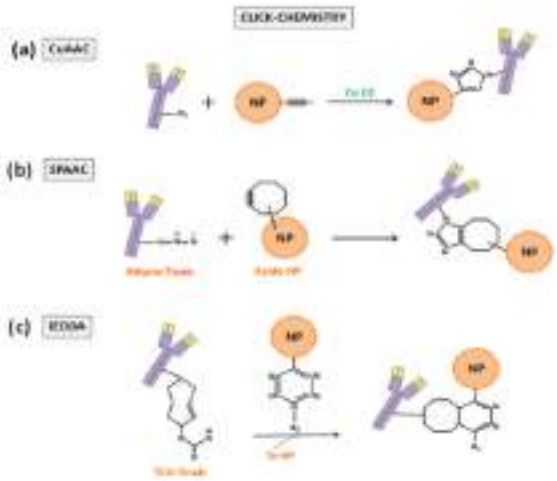


Figure 5. Schematic representation of the three most widely used click-chemistry reactions to anchor Tmab to NP or liposome surfaces: (a) CuAAC, (b) SPAAC, and (c) iEDDA.

## 4. Trastuzumab Role in Antibody-Drug Conjugates Development

As reported in the introduction section, antibodies have also become relevant in nanomedicine thanks to the development of ADCs. These glycoproteins present an insufficient clinical activity themselves and ADCs emerged to empower their antiproliferative effect [75,76]. Thereby, such conjugates are produced with the objective of selectively ablating cancer cells by combining the action of a highly potent cytotoxic compound with antibody specificity for a target antigen, with these two compounds being conjugated through a linker [24,75]. In this way, after binding it, the ADC-antigen complex is internalized and transported to cellular organelles (generally lysosomes) where the release of the attached drug can take place [75]. To improve its therapeutic activity without compromising safety, ADCs must limit the exposure of normal tissues to the transported drugs and only deliver the payload to the tumor cells that express the chosen antigen [75,76]. For this reason, linker technologies that ensure an adequate stability of the drug in ADCs are required so that the drug release does not occur in circulation [76]. Besides, the method employed in ADC conjugation conditions the drug loading stoichiometry and homogeneity and determines its anti-tumor activity, efficacy, and tolerability [76,77].

For such conjugations, at the beginning of ADC development, acid-labile hydrazone linkers that can be cleaved in the acid environment of endosomes and thus allow the release of the ADC payload in these organelles were selected. However, disulfide-based linkers demonstrated later to be a better choice because they were more stable at a physiological pH, and nowadays they are normally preferred to anchor cytotoxic compounds to antibodies [75]. When they are employed, the conjugation of linker drugs to an antibody occurs at accessible reactive amino acids derived from the reduction of its interchain disulfide bonds, and three main methods for achieving such accessibility can be distinguished: (i) the acylation of lysines, (ii) the alkylation of the reduced interchain-disulfides of cysteines, and (iii) the alkylation of genetically engineered cysteines [75,76,78].

In the majority of ADCs that have been developed and are in clinical trials, drug molecules have been covalently bound through lysine and cysteine linkers, following the first two aforementioned strategies (Figure 6a) [24]. Between both of them, the alkylation of reduced interchain-disulfides of cysteines has been normally chosen, since there are more much lysines present in the antibody surface than interchain-cysteines (40 lysines per antibody versus 8 exposed cysteine sulfhydryl groups), and the heterogeneity of the reaction is reduced when cysteines are selected to anchor the cytotoxic

compounds [24,76,78]. In any case, maleimide chemistry is usually chosen to synthesize both types of disulfide-based ADCs, and the employed linkers can be either cleavable or non-cleavable.

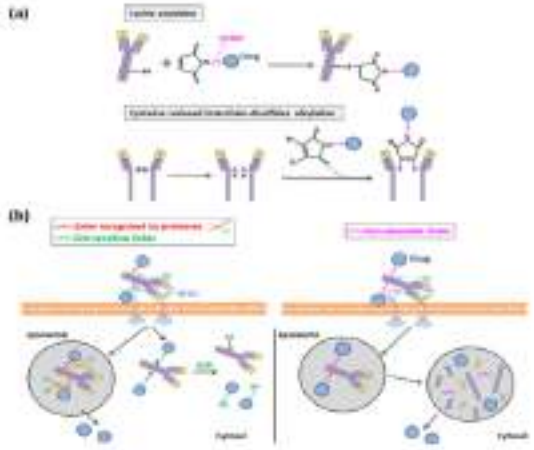


**Figure 6.** (a) Acylation and alkylation of lysine and cysteine residues, respectively, performed to develop Tmab-based ADCs. (b) Representation of the drug release that occurs in disulfide-based Tmab-based ADCs and depends on the type of linker used (cleavable vs. non-cleavable).

The first ones, the cleavable linkers, include an engineered lysosomal specific protease or are disulfide-bond-based glutathione (GSH)-sensitive, since the intracellular concentration of this molecule is much higher than it is in circulation. Otherwise, non-cleavable thioether linkers are those that make necessary a post-internalization degradation in lysosomes of the ADC to release the payload (Figure 6b) [24]. They have a better stability in the bloodstream and longer half-lives and, hence, a smaller risk of off-target toxicity than that of cleavable linkers [24,79]. For this reason, this sort of linker was the one that was employed to synthesize ado-trastuzumab emtansine (T-DM1) [80], which was the first anti-HER2 ADC that started to be commercialized in 2013 (Kadcyla®) [23].

Thus, T-DM1 is integrated by a non-cleavable linker that allows the attachment of a derivative of maytansine (DM1) to Tmab [24,81]. Maytansine, which is a natural inhibitor of tubulin polymerization, was selected to be part of this ADC because it has a great stability and an appropriate aqueous solubility. In addition, it was shown to be orders of magnitude more potent than other clinically used anticancer drugs. Notwithstanding, although natural maytansine has proper biological and biochemical properties, it lacks a suitable functional group to be conjugated to an antibody, and a thiol group had to be introduced in its structure [82,83]. Structure activity relationships (SAR) studies were carried out in order to determine the most proper modification site to avoid an alteration of maytansine potency, and in the end a thiol group was introduced in the aminoacyl side chain C3 of the drug. Then, the heterobifunctional crosslinking agent SMCC was chosen to attach DM1 to Tmab through its lysine residues by means of the formation of a thioether binding [82]. As a result, an average of 3.5 DM1 molecules were linked per antibody, and the resulting conjugate maintained good biochemical properties [82,83]. After extensive preclinical and clinical evaluations of its biological activity, pharmacokinetics, metabolism, and tolerability, the FDA finally approved T-DM1 administration seven years ago to treat patients with HER2+ MBC, previously treated with Tmab and taxanes [82]. Furthermore, the encouraging results that were obtained during the T-DM1 evaluations have caused the development of novel ADCs in which the antibody Tmab has been maintained,

but different cytotoxic drugs have been coupled to it through different linkers [82,83]. Several examples can be found in the works of Xu et al. [83], Robinson et al. [84–86], and Shen et al. [77].

The review study of Xu et al. is focused in the main properties of two different Tmab-based ADCs, SYD98 and Tmab deruxtecan (DS-8201a), which were developed with the purpose of reducing T-DM1 resistance and improving its efficacy in heterogeneous tumors [83]. The first one, SYD98, was synthesized by Elgersma et al. in 2015 [87], where they chose a duocarmycin derivative (Seco-DUBA) that has a better solubility and stability than the parent alkylating drug to be attached to Tmab. For such an attachment, they selected a peptide linker that conjugated Seco-DUBA molecules to Tmab through the hydroxyl groups present in their DNA-alkylating moiety. This linker, unlike the T-DM1 one, can be cleavable by cathepsin B, a lysosome cysteine-protease present in cells [83,87]. Similarly, Ogitani et al., who obtained DS-8201a in 2016 [88], also preferred a cleavable linker to be part of their Tmab-based ADC. These authors linked a maleic acid to Tmab and, through it, joined the commercially available linker BOC-GGFG-OH that is selectively cleaved by lysozymes. As a cytotoxic drug, Ogitani et al. decided to employ a camptothecin derivative (DXd) that was developed to improve the solubility and biological activity of the original camptothecin, a topoisomerase poison [83,88]. Both of them, SYD98 and DS-8201a, are now in clinical trials in which their suitability for the treatment of HER2+ breast, gastric, and lung cancers is being evaluated with promising results [83].

Otherwise, Robinson and co-workers demonstrated that site-selective disulfide bridging with small molecules, such as next-generation maleimides (NGMs) [84,86] and pyridazinediones (PDs) [85], constitutes a proper conjugation strategy to develop stable ADCs. In order to attach the potent anticancer drug monomethyl auristatin E (MMAE) to Tmab, they reduced the antibody native interchain disulfide-bonds with tris-2-carboxyethylphosphine (TCEP). Next, they performed a functional re-bridging with either an NGM or a PD molecule and conjugated NGM-MMAE and PD-MMAE to Tmab, obtaining efficient ADCs [84,85]. In addition, in an anterior study these authors followed the same strategy with NGMs to synthesize a Tmab-ADC with loaded doxorubicin, anticipating that the NGM platform could have considerable utility for the development of ADCs [86].

At last, Shen et al. also built Tmab-ADCs loaded with MMAE but, to assess the impact of the conjugation site, they engineered cysteines at three different Tmab sites, differing in solvent accessibility and local charge. Once obtained, they attached MMAE to them through maleimide chemistry with a maleimido-caproyl-valine-citrulline-p-amino-benzyloxy carbonyl (MC-vc-PAB) linker, and showed not only the linker choice conditions ADC biological activity, but also the conjugation site [77].

Since, in some studies, it has been shown that the location of attached compounds is not as relevant as their stoichiometry and that heavily loaded conjugates are quickly removed from the circulation, recombinant methods have begun to acquire more importance in this nanotechnology field [24,76]. ADC conjugation through the alkylation of genetically engineered cysteines arose for this reason. Mentioned above, it is the most recent strategy to attach cytotoxic compounds to antibodies and is based on protein-engineering alterations that allow the binding of a particular number of drug molecules per ADC. Antibody modifications can be performed through enzymatic conjugation and through the insertion of reactive cysteines or chemoselective functional groups of unnatural amino acids in its structure, but there are still many challenges concerning these approaches, and any ADC developed following them has reached the clinic yet [78].

## 5. Current and Future Situation of Trastuzumab-Based Nanomedicine

As has been stated, conventional adjuvant chemotherapy with Tmab results in a significant prolongation of disease-free and overall survival rates and has revolutionized the treatment of HER2+ breast cancer [89,90]. As consequence and since HER2 is not only overexpressed in this type of cancer, many studies in the preliminary stages have proposed the administration of this adjuvant therapy to treat other types of HER2+ tumors, including ovarian, bladder, and lung ones [91]. In this way, the Tmab-decorated NPs developed to target these solid tumors other than breast tumors can be already found in the literature [48–50,62,64].

However, the clinical administration of Tmab does not only have advantages. Some adverse effects, such as gastrointestinal and pulmonary symptoms, hematologic deficiencies, and especially cardiac toxicity, have been linked to Tmab use. Moreover, between 15 and 25% of the patients who have received Tmab therapy experience disease recurrence [90,92]. Manifold mechanisms of primary and treatment-emergent resistance to this antibody have been purposed, including compensatory signaling from either HER family members or other receptor types (such as epidermal growth factor or vascular endothelial growth factor receptors (EGFR and VEGFR)) [92]. For this reason, other antibodies and peptides that are able to block HER2 dimerization with other HER family members or that inhibit simultaneously other receptors have been developed [31]. Among them, two antibodies have been already approved by the FDA to treat HER2+ advanced breast cancer: pertuzumab (Perjeta®) and lapatinib (Tykerb™) [31,90]. On one hand, pertuzumab is a humanized recombinant antibody that interferes with the HER3-dimerization domain of HER2, inhibiting cancer cell proliferation by blocking the HER3-dependent signaling pathway. Even though this antibody has shown a modest anti-HER2 efficacy when it is administered alone, it has been demonstrated to have a synergistic effect with Tmab. Because of this, the FDA approved its utilization, in combination with Tmab and docetaxel, to treat HER2+ MBC, and new regimens are being studied to improve the pertuzumab efficacy and toxicity. On the other hand, lapatinib is the single tyrosine-kinase inhibitor (TKI) whose use has been approved to block HER2 and EGFR receptors together. It presents a great cancer inhibitory effect and enhances Tmab activity, too [31,90]. In addition, apart from these two antibodies whose clinical employment is already permitted, many other anti-HER2 antibodies have been developed and are now in the advanced stages of clinical trials: neratinib, pyrotinib, afatinib, pazopanib, ertumaxomab, hertuzumab, etc. [5,31,90].

With the growth of novel antibodies and peptides that target HER2, the development of new guided NPs, liposomes, and ADCs conjugated to them has also been propitiated. Regarding NPs, studies of different authors who have encapsulated lapatinib in them can be easily found. For example, Wan et al. and Zhang et al. [93,94], taking into account the high binding efficiency of lapatinib to HSA, obtained NPs based on this protein that they functionalized with the mentioned antibody to increase its low aqueous solubility. Both nanosystems were able to inhibit HER2+ breast cancer cell proliferation. In a similar manner, Mobaserri et al. [95], with the aim of improving lapatinib solubility and bioavailability, encapsulated it in dextran-chitosan NPs that were also demonstrated to have an anti-HER2+ cell growth activity. On the other hand and regarding liposomes, Singh et al. synthesized chitosan-modified liposomes and decorated them with an anti-HER2 tumor homing peptide (THP) (WNLPWYYSVSPTC) to specifically transport the pro-drug capecitabine to HER2+ breast cancer cells [96]. Otherwise, MM-302 is an HER2-targeted liposome encapsulating doxorubicin in its core, with single chain anti-HER2 antibodies (scFv) conjugated to its surface. It is already being evaluated in phase II clinical trials to treat HER2+ MBC, and is under consideration for additional oncology indications [97,98]. Finally, as regards ADCs, several examples of conjugates integrated by an anti-HER2 antibody other than trastuzumab can be encountered in the literature [89,99]. One of them is RC48-ADC, an ADC integrated by the antibody hertuzumab covalently conjugated to MMAE molecules through a cleavable dipeptide linker (hertuzumab-Val-Cit-MMAE) via cysteine residue release [100]. Its therapeutic activity against HER2+ breast carcinoma is being evaluated in phase II trials, but also some authors such as Li et al. [101] and Jiang et al. [5] have showed its efficacy as a targeted therapy for HER2+ gastric and ovarian cancers, respectively. Other examples of anti-HER2 ADCs whose antiproliferative activity is being evaluated in clinical trials for the treatment of HER2+ cancers are ARX788, TAK-522, A116, Tmab Duocarmizine, ALT-P7, DHES0815A, MED64276, and Tmab Deruxtecan [89,99,102–105]. More information about them, as well as about SYD98 and Tmab deruxtecan [83], can be found in Table 2.

**Table 2.** Examples of novel anti-HER2 ADCs, different from the well-known T-DM1, whose efficacy and safety are already being evaluated in clinical trials.

| ADC | IgG | Payload | Clinical Trial Phase [a] | Indication | Developer |
|---|---|---|---|---|---|
| RC48-ADC [1-4] | IgG1 (Hertuzumab) | MMAE | Phase I | Solid tumors | Regeneron |
| ARX788 [2,5,6] | Engineered IgG1 | MMAF | Phase I | Breast, stomach cancers | Ambrx |
| TAK-522 (MEI-1022) [2,5,7] | IgG1 (4D5) | AF-HPA | Phase I | NSCLC, breast, gastric cancers | Mersana |
| A166 [1] | Not disclosed | Not disclosed | Phase I | Breast cancer | Klus Pharma |
| Trastuzumab Emtansine (SYD985) [1,2,8] | IgG1 | Seco-DUBA | Phase II | Endometrial cancer | Synthon |
| A11P7 [2] | IgG1 (HMI, Trastuzumab) | MMAE | Phase I | Breast cancer | Allergen |
| DHES0815A [1] | IgG1 | PBD-MA | Phase I | Breast cancer | Genentech |
| MEDI4276 [2,5] | Bi-specific IgG1 (Trastuzumab) | AZ13599185 | Phase III | Breast, gastric cancers | MedImmune |
| Trastuzumab Deruxtecan (DS-8201a) [1,2,9] | IgG1 | DNA | Phase II | Breast cancer | Daiichi Sankyo |

[1] [83], [2] [84], [3] [99], [4] [100], [5] [104], [6] [105]. AF-HPA: auristatin F-hydroxypropylamide; NSCLC: non-small cell lung carcinoma; PBD-MA: pyrrolo[2,1-c][1,4]benzodiazepine monoamide.

Thus, the development of NPs, liposomes, and ADCs targeting HER2 represents a strategy of increasing interest to improve Tmab efficacy and to avoid the apparition of resistances and undesirable adverse effects. Surely, as new anti-HER2 antibodies and peptides are synthesized and their clinical administration is approved, new HER2-targeting nanosystems will emerge with enhanced therapeutic activity and reduced toxicity.

## 6. Conclusions and Future Directions

Today, it is well known that cancer is the leading cause of premature death worldwide. The conventional treatment of this complex disease involves chemotherapy, radiotherapy, and surgery, but more efficient and tolerable treatments are strongly needed to improve patient outcomes and quality of life [106].

These novel treatment strategies should be focused on the hallmarks of cancer that differentiate tumor cells from normal ones in order to reduce the apparition of side toxicology. One of such hallmarks is the overexpression of HER2 that occurs in 15–20% of breast cancers that are diagnosed, and also in other types of solid tumors, such as gastric, ovarian, or lung carcinomas [3–8,91]. HER2 overexpression has been associated with more aggressive tumors and a worse prognosis for patients for a long time but, since Tmab development, it has also offered a way to upgrade treatment specificity [4].

Tmab is a humanized monoclonal antibody that specifically binds one of the extracellular domains of HER2 [6]. Its clinical adjuvant administration, which is usually performed with traditional chemotherapy drugs, has positively revolutionized HER2+ breast cancer treatment since its use was approved [89,90]. Thus, nanotechnology, taking advantage of the antiproliferative activity of this antibody, has played an essential role in the production of novel HER2-guided cancer nanomedicines, and this review has focused on targeted NPs, liposomes, and ADCs. In these nanosystems, the simultaneous presence of Tmab together with a potent cytotoxic agent allows the achievement of a synergist effect that helps to reduce the needed drug dose and its secondary effects. Furthermore, acting as guided nanovehicles for chemotherapy agents, targeting NPs, liposomes, and ADCs also enhances their bioavailability, which is quite limited as a rule [10].

In order to get all these beneficial effects, the choice of a proper Tmab-anchoring strategy is crucial, especially to avoid the release of cytotoxic molecules into the circulation [17,76]. For this reason, part of the scientific community is addressing important efforts towards the development of novel covalent conjugation chemistries. In addition, with the aim of increasing Tmab efficacy and overcoming the apparition of resistances, numerous efforts are also dedicated to the synthesis of novel anti-HER2 antibodies that can be later conjugated for creating guided therapeutic nanovehicles [31,90]. As a consequence, tremendous investment is being made in this field, and increasing numbers of such nanotherapeutics are reaching clinical stages or even being commercialized in recent years [23,89,107,108].

In conclusion, it can be stated that nanotechnology holds a great promise for the apparition of combinatorial-based (drug plus antibody) cancer therapies that help to improve conventional ones, and that better manufacturing technologies enabling the synthesis of reproducible and safe systems will be fundamental in the near future [109].

**Author Contributions:** Conceptualization, C.N. and E.M.M.d.V.; writing—original draft preparation, C.N.; writing—review and editing, C.N., M.A.V., and E.M.M.d.V. All authors have read and agreed to the published version of the manuscript.

**Funding:** This research was funded by the Spanish Ministry of Science and Innovation (grant number PID2019-108994RB-I00). C.N. is recipient of a predoctoral contract from the Junta de Castilla y León, co-funded by the European Social Foundation (EDU/602/2016).

**Conflicts of Interest:** The authors declare no potential conflict of interest.

## Abbreviations

| | |
|---|---|
| ADC | Antibody drug conjugate |
| ADCC | Antibody-dependent cellular cytotoxicity |
| AF-HPA | Auristatin F-hydroxypropylamide |
| BCN | Bicyclononyne |
| β-Me | 2-mercaptoethanol |
| DDS | Drug delivery system |
| DENC | Double emulsion nanocapsule |
| DTT | Dithiothreitol |
| EBC | Early breast cancer |
| EDC | 1-ethyl-3-[3-dimethylaminopropyl] |
| EGFR | Epidermal growth factor receptor |
| EMA | European Medicines Agency |
| EPR | Enhanced permeability and retention |
| FDA | U.S. Food and Drug Administration |
| GMBS | 4-maleimidobutyric acid-N hydroxysuccinimide |
| GSH | Glutathione |
| HER | Human epithermal growth factor receptor |
| HSA | Human serum albumin |
| IgG | Immunoglobulin |
| MBC | Metastatic breast cancer |
| MDR | Multidrug resistance |
| MMA | Monomethyl auristatin |
| MRI | Magnetic resonance imaging |
| MTT | Montmorillonite |
| MTX | Methotrexate |
| NGM | Next-generation maleimide |
| NHS | N-hydroxysulfosuccinimide |
| NPs | Nanoparticles |
| NSCLC | Non-small cell lung carcinoma |
| PBD-MA | Pyrrolo[2,1-c][1,4]benzodiazepine monoamide |
| PD | Pyridazinedione |
| PEG | Polyethylene glycol |
| PEI | Polyethylenimine |
| PET | Positron Emission Tomography |
| Phis | Poly-L-histidine |
| PLA | Polylactide |
| PLGA | Poly(lactic-co-glycolic acid) |
| PPy | Polypyrrole |
| SMCC | Succinimidyl-4-(N-maleimidomethyl)-cyclohexane-1-carboxylate |

| | |
|---|---|
| TCEP | Tris-2-carboxyethylphosphine |
| TCO | Trans-cyclooctene |
| THP | Tumor homing peptide |
| TKI | Tyrosine-kinase inhibitor |
| Tmab | Trastuzumab |
| TPGS | Tocopheryl polyethylene glycol succinate |
| Tz | 1,2,4,5-tetrazine |
| VEGFR | Vascular endothelial growth factor receptor |
| WHO | World Health Organization |

## References


1. World Health Organization (WHO). Available online: https://www.who.int/news-room/fact-sheets/detail/cancer (accessed on 18 April 2020).
2. Bray, F.; Ferlay, J.; Soerjomataram, I.; Siegel, R.L.; Torre, L.A.; Jemal, A. Global cancer statistics 2018: GLOBOCAN estimates of incidence and mortality worldwide for 36 cancers in 185 countries. *CA Cancer J. Clin.* **2018**, *68*, 394–424. [CrossRef] [PubMed]
3. Meisel, J.L.; Zhao, J.; Suo, A.; Zhang, C.; Wei, Z.; Taylor, C.; Aneja, R.; Krishnamurti, U.; Li, Z.; Nahta, R.; et al. Clinicopathologic factors associated with response to neoadjuvant anti-HER2-directed chemotherapy in HER2-positive breast cancer. *Clin. Breast Cancer* **2020**, *20*, 19–24. [CrossRef] [PubMed]
4. Marchió, C.; Annaratone, L.; Marques, L.; Casorzo, L.; Berrino, E.; Sapino, A. Evolving concepts in HER2 evaluation in breast cancer: Heterogeneity, HER2-low carcinomas and beyond. *Semin. Cancer Biol.* **2020**, in press. [CrossRef]
5. Jiang, J.; Dong, L.; Wang, L.; Wang, L.; Zhang, J.; Chen, F.; Zhang, X.; Huang, M.; Li, S.; Ma, W.; et al. HER2-targeted antibody drug conjugates for ovarian cancer therapy. *Eur. J. Pharm. Sci.* **2016**, *93*, 274–286. [CrossRef] [PubMed]
6. Mehata, A.K.; Bhartic, S.; Singhb, P.; Viswanadha, M.K.; Kumaria, L.; Agrawald, P.; Singha, S.; Kochb, B.; Muthua, M.S. Trastuzumab decorated TPGS-g-chitosan nanoparticles for targeted breast cancer therapy. *Colloid Surf. B* **2019**, *173*, 366–377. [CrossRef] [PubMed]
7. Dang, Y.; Guan, J. Nanoparticle-based drug delivery systems for cancer therapy. *Smart Mater. Med.* **2020**, *1*, 10–19. [CrossRef]
8. Khan, H.; Mirzaei, H.R.; Amiri, A.; Akkol, E.K.; Halimi, S.M.A.H.; Mirzaei, H. Glyco-nanoparticles: New drug delivery systems in cancer therapy. *Semin. Cancer Biol.* **2020**, in press. [CrossRef]
9. Correia, A.L.; Bissell, M.J. The tumor microenvironment is a dominant force in multidrug resistance. *Drug Resist. Update* **2012**, *15*, 39–49. [CrossRef]
10. Raj, S.; Khurana, S.; Choudhari, R.; Kesari, K.K.; Kamal, M.A.; Garg, N.; Ruokolainen, J.; Das, B.C.; Kumar, D. Specific targeting cancer cells with nanoparticles and drug delivery in cancer therapy. *Semin. Cancer Biol.* **2019**, in press. [CrossRef]
11. Xu, C.H.; Ye, P.J.; Zhou, Y.C.; He, D.X.; Wei, H.; Yu, C.Y. Cell membrane-camouflaged nanoparticles as drug carriers for cancer therapy. *Acta Biomater.* **2020**, *105*, 1–14. [CrossRef]
12. Yih, T.C.; Al-Fandi, M. Engineered nanoparticles as precise drug delivery systems. *J. Cell. Biochem.* **2006**, *97*, 1184–1190. [CrossRef] [PubMed]
13. Elzoghby, A.O.; Samy, W.M.; Elgindy, N.A. Albumin-based nanoparticles as potential controlled release drug delivery system. *J. Control. Release* **2012**, *157*, 168–182. [CrossRef] [PubMed]
14. Duncan, B.; Kim, C.; Rotello, V.M. Gold nanoparticle platforms as drug and biomacromolecule delivery systems. *J. Control. Release* **2010**, *148*, 122–127. [CrossRef]
15. Liu, Z.; Jiao, Y.; Wang, Y.; Zhou, C.; Zhang, Z. Polysaccharides-based nanoparticles as drug delivery systems. *Adv. Drug Deliv. Rev.* **2008**, *60*, 1650–1662. [CrossRef] [PubMed]
16. Deshpande, P.; Biswas, S.; Torchilin, V.P. Current trends in the use of liposomes for tumor targeting. *Nanomedicine (Lond.)* **2013**, *8*, 1509–1528. [CrossRef]
17. Marques, A.C.; Costa, P.J.; Velho, S.; Amaral, M.H. Functionalizing nanoparticles with cancer-targeting antibodies: A comparison of strategies. *J. Control. Release* **2020**, *320*, 180–200. [CrossRef]

18. Bellfiore, L.; Saunders, D.N.; Ranson, M.; Thurecht, K.J.; Storm, G.; Vine, K.L. Towards clinical translation of ligand-functionalized liposomes in targeted cancer therapy: Challenges and opportunities. *J. Control. Release* **2018**, *277*, 1–13. [CrossRef] [PubMed]
19. Nava Andrade, K.; Puebla Pérez, A.M.; Carbajal Arizaga, G.G. Passive and active targeting strategies in hybrid layered double hydroxides nanoparticles for tumor bioimaging and therapy. *Appl. Clay Sci.* **2019**, *181*, 105214. [CrossRef]
20. Alibakhshi, A.; Kahaki, F.A.; Ahangarzadeh, S.; Yaghoobi, H.; Yarian, F.; Arezumand, R.; Ranjbari, J.; Mokhtarzadeh, A.; de la Guardia, M. Targeted cancer therapy through antibody fragments-decorated nanomedicines. *J. Control. Release* **2017**, *268*, 323–334. [CrossRef] [PubMed]
21. Reverdatto, S.; Burz, D.S.; Shekhtman, A. Peptide aptamers: Development and applications. *Curr. Top. Med. Chem.* **2015**, *15*, 1082–1101. [CrossRef]
22. Banerjee, J.; Nilsen-Hamilton, M. Aptamers: Multifunctional molecules for biomedical research. *J. Mol. Med.* **2013**, *2*, 1333–1342. [CrossRef] [PubMed]
23. Zhao, P.; Zhanga, Y.; Lia, W.; Jiantya, C.; Xiangb, G.; Dong, Y. Recent advances of antibody drug conjugates for clinical applications. *Acta Pharm. Sin. B* **2020**, in press. [CrossRef]
24. Parslow, A.C.; Parakh, S.; Lee, F.T.; Gan, H.K.; Scott, A.M. Antibody–drug conjugates for cancer therapy. *Biomedicines* **2016**, *4*, 14. [CrossRef] [PubMed]
25. Herta, E.; Bongiorno, C.; Ezzeddine, M.; Neil, E.C. Neurotoxicity of antibodies in cancer therapy: A review. *Clin. Neurol. Neurosurg.* **2020**, *188*, 105566–105574. [CrossRef] [PubMed]
26. Nahta, R.; Hung, M.C.; Esteva, F.J. The HER2-targeting antibodies trastuzumab and pertuzumab synergistically inhibit the survival of breast cancer cells. *Cancer Res.* **2004**, *64*, 2343–2346. [CrossRef] [PubMed]
27. Blackwell, K.; Gligorov, J.; Jacobs, I.; Twelves, C. The global need for a trastuzumab biosimilar for patients with HER2-positive breast cancer. *Clin. Breast Cancer* **2018**, *18*, 95–113. [CrossRef] [PubMed]
28. Collins, D.; Hill, A.D.K.; Young, L. Lapatinib: A competitor or companion to trastuzumab? *Cancer Treat. Rev.* **2009**, *35*, 574–581. [CrossRef] [PubMed]
29. Vogel, C.L.; Cobleigh, M.A.; Tripathy, D.; Gutheil, J.C.; Harris, L.N.; Fehrenbacher, L.; Slamon, D.J.; Murphy, M.; Novotny, W.F.; Burchmore, M.; et al. Efficacy and safety of trastuzumab as a single agent in first-line treatment of HER2-overexpressing metastatic breast cancer. *J. Clin. Oncol.* **2002**, *20*, 719–726. [CrossRef] [PubMed]
30. Slamon, D.; Eiermann, W.; Robert, N.; Pienkowski, T.; Martin, M.; Press, M.; Mackey, J.; Glaspy, J.; Chan, A.; Pawlicki, M.; et al. Adjuvant trastuzumab in HER2-positive breast cancer. *N. Engl. J. Med.* **2011**, *365*, 1273–1283. [CrossRef]
31. Zhang, X.; Chen, J.; Wang, Z.; Li, Q.; Zhao, L.; Yu, N.; Dong, L.; Xu, W.; Yang, Y.; Zhu, Z.; et al. A new anti-HER2 antibody that enhances the anti-tumor efficacy of trastuzumab and pertuzumab with a distinct mechanism of action. *Mol. Immunol.* **2020**, *119*, 48–58. [CrossRef]
32. Nahta, R.; Esteva, F.J. Molecular mechanisms of trastuzumab resistance. *Breast Cancer Res.* **2006**, *8*, 215. [CrossRef] [PubMed]
33. Hassan, G.; Du, J.; Afify, S.M.; Seno, A.; Seno, M. Cancer stem cell generation by silenced MAPK enhancing PI3K/AKT signaling. *Med. Hypotheses* **2020**, *141*, 109742–109747. [CrossRef] [PubMed]
34. Dubska, L.; Andrlra, L.; Sheard, M.A. HER2 signaling downregulation by trastuzumab and suppression of the PI3K/Akt pathway: An unexpected effect of TRAIL-induced apoptosis. *FEBS Lett.* **2005**, *579*, 4149–4158. [CrossRef] [PubMed]
35. Kamen, L.; Tsukurta, T.; Myneni, S.; Zheng, K., Chung, S. Development of a kinetic antibody-dependent cellular cytotoxicity assay. *J. Immunol. Methods* **2019**, *468*, 49–54. [CrossRef] [PubMed]
36. Wen, X.F.; Yang, G.; Mao, W.; Thornton, A.; Liu, J.; Bast, R.C.; Le, X.F. HER2 signaling modulates the equilibrium between pro- and antiangiogenic factors via distinct pathways: Implications for HER2-targeted antibody therapy. *Oncogene* **2006**, *25*, 6986–6996. [CrossRef] [PubMed]
37. Colombo, M.; Corsi, F.; Foschi, D.; Mazzantini, E.; Mazzucchelle, S.; Morasso, C.; Occhipinti, E.; Polito, L.; Prosperi, D.; Rinchi, S.; et al. HER2-targeting as a two-side strategy for breast cancer diagnosis and treatment: Outlook and recent implications in nanomedical approaches. *Pharmacol. Res.* **2010**, *62*, 150–165. [CrossRef] [PubMed]

38. Oliveira, J.P.; Prado, A.R.; Keijok, W.J.; Antunes, P.W.P.; Yapuchura, E.R.; Guimarães, M.C.C. Impact of conjugation strategies for targeting of antibodies in gold nanoparticles for ultrasensitive detection of 17β-estradiol. *Sci. Rep.* **2019**, *9*, 13859. [CrossRef]
39. Liu, Y.; Feng, S.S. The synergistic effect of Herceptin and docetaxel in polylactide-D-α-tocopheryl polyethylene glycol succinate (PLA-TPGS) nanoparticles. *J. Control. Release* **2011**, *152*, e1–e132. [CrossRef]
40. Yu, K.; Zhao, J.; Zhang, Z.; Gao, Y.; Zhou, Y.; Tang, L.; Li, Y. Enhanced delivery of Paclitaxel using electrostatically-conjugated Herceptin-bearing PEI/PLGA nanoparticles against HER-positive breast cancer cells. *Int. J. Pharm.* **2016**, *497*, 78–87. [CrossRef]
41. Zhang, X.; Liu, J.; Li, X.; Li, F.; Lee, R.J.; Sun, F.; Li, Y.; Liu, Z.; Teng, L. Trastuzumab-coated nanoparticles loaded with docetaxel for breast cancer therapy. *Dose-Response* **2019**, *17*, 1–12. [CrossRef]
42. Sun, B.; Ranganathan, B.; Feng, S.S. Multifunctional poly(D,L-lactide-co-glycolide)/montmorillonite (PLGA/MTT) nanoparticles decorated by Trastuzumab for targeted chemotherapy of breast cancer. *Biomaterials* **2008**, *29*, 475–486. [CrossRef] [PubMed]
43. Choi, J.S.; Jang, W.S.; Park, J.S. Comparison of adsorption and conjugation of Herceptin on poly(lactic-co-glycolic acid) nanoparticles—Effect on cell internalization in breast cancer cells. *Mat. Sci. Eng. C Mater.* **2018**, *92*, 496–507. [CrossRef] [PubMed]
44. Nakajima, N.; Ikada, Y. Mechanism of amide formation by carbodiimide for bioconjugation in aqueous media. *Bioconjug. Chem.* **1995**, *6*, 123–130. [CrossRef] [PubMed]
45. Shirshahi, V.; Shamsipour, F.; Hassan Zamani, A.; Verdi, J.; Saber, R. Active targeting of HER2-positive breast cancer cells by Herceptin-functionalized organically modified silica nanoparticles. *Cancer Nanotechnol.* **2013**, *4*, 27–37. [CrossRef] [PubMed]
46. Hadi Jazayeri, M.; Amani, H.; Akbar Pourfatollah, A.; Pazoki-Toroudi, H.; Sedighimoghaddam, B. Various methods for gold nanoparticles (GNPs) conjugation to antibodies. *Sens. Biosens. Res.* **2016**, *9*, 17–22. [CrossRef]
47. Zhou, Z.; Badkas, A.; Stevenson, M.; Lee, J.Y.; Leung, Y.K. Herceptin conjugated PLGA-PHis-PEG pH sensitive nanoparticles for targeted and controlled drug delivery. *Int. J. Pharm.* **2015**, *487*, 81–90. [CrossRef] [PubMed]
48. Nieto, C.; Centa, A.; Rodríguez-Rodríguez, J.A.; Pandiella, A.; Martín del Valle, E.M. Paclitaxel-trastuzumab mixed nanovehicle to target HER2-overexpressing tumors. *Nanomaterials* **2019**, *9*, 948. [CrossRef]
49. Domínguez-Ríos, R.; Sánchez-Ramírez, D.R.; Ruiz-Saray, K.; Ocegueda-Bautista, P.E.; Almadab, M.; Juárez, J.; Zepeda-Moreno, A.; Del Toro-Arreola, A.; Topete, A.; Daneri-Navarro, A. Cisplatin-loaded PLGA nanoparticles for HER2 targeted ovarian cancer therapy. *Colloid Surface B* **2019**, *178*, 199–207. [CrossRef]
50. Arya, G.; Vandana, M.; Acharya, S.; Sahoo, S.K. Enhanced antiproliferative activity of Herceptin (HER2)-conjugated gemcitabine-loaded chitosan nanoparticle in pancreatic cancer therapy. *Nanomed. Nanotechnol.* **2011**, *7*, 859–870. [CrossRef]
51. Haghighia, A.H.; Faghihb, Z.; Taghi Khorasanic, M.; Farjadian, F. Antibody conjugated octo surface modified magnetic nanoparticles for separation of HER2+ breast cancer cells. *J. Magn. Magn. Mater.* **2019**, *490*, 165479. [CrossRef]
52. Dziawer, L.; Majkowska-Pilip, A.; Gawel, D.; Godlewska, M.; Pruszynski, M.; Jastrzebski, J.; Bogdan Was, B.; Bilewicz, A. Trastuzumab-modified gold nanoparticles labeled with 211At as a prospective tool for local treatment of HER2-positive breast cancer. *Nanomaterials* **2019**, *9*, 632. [CrossRef] [PubMed]
53. Almaki, J.H.; Nasiri, Z.; Idris, A.; Nasiri, M.; Majid, F.A.A.; Lusic, D. Trastuzumab-decorated nanoparticles for in vitro and in vivo tumor-targeting hyperthermia of HER2+ breast cancer. *J. Mater. Chem. B* **2017**, *5*, 7369–7383. [CrossRef] [PubMed]
54. Martin, F.J.; Papahadjopoulos, D. Irreversible coupling of Immunoglobulin fragments to preformed vesicles. An improved method for liposome targeting. *J. Biol. Chem.* **1982**, *257*, 286–288. [PubMed]
55. Martínez-Jothar, L.; Doulkeridou, S.; Schiffelers, R.M.; Sastre Torano, J.; Oliveira, S.; van Nostrum, C.F.; Hennink, W.E. Insights into maleimide-thiol conjugation chemistry: Conditions for efficient surface functionalization of nanoparticles for receptor targeting. *J. Control. Release* **2018**, *282*, 101–109. [CrossRef]
56. Akkapeddi, P.; Azizi, S.A.; Freedy, A.M.; Cal, P.M.S.D.; Gois, P.M.P.; Bernardes, G.J.L. Construction of homogeneous antibody-drug conjugates using site-selective protein chemistry. *Chem. Sci.* **2016**, *7*, 2954–2963. [CrossRef] [PubMed]

57. Taheri, A.; Dinarvand, R.; Atyabi, F.; Ghahremani, M.H.; Ostad, S.N. Trastuzumab decorated methotrexate-human serum albumin conjugated nanoparticles for targeted delivery to HER2 positive tumor cells. *Eur. J. Pharm. Sci.* **2012**, *47*, 331–340. [CrossRef] [PubMed]
58. Nguyen, H.T.; Tran, T.H.; Thapa, R.K.; Phung, C.D.; Shin, B.S.; Jeong, J.H.; Choi, H.G.; Yong, C.S.; Kim, J.O. Targeted co-delivery of polypyrrole and rapamycin by trastuzumab-conjugated liposomes for combined chemo-photothermal therapy. *Int. J. Pharm.* **2017**, *527*, 61–71. [CrossRef]
59. Amin, M.; Pourshohod, A.; Khetrollah, A.; Afrakhteh, M.; Gholami-Borujeni, F.; Zeinali, M.; Jamalan, M. Specific delivery of idarubicin to HER2-positive breast cancerous cell line by trastuzumab-conjugated liposomes. *J. Drug Deliv. Sci. Technol.* **2018**, *47*, 209–214. [CrossRef]
60. Chiang, C.S.; Hu, S.H.; Liao, B.J.; Chang, Y.C.; Chen, S.Y. Enhancement of cancer therapy efficacy by trastuzumab-conjugated and pH-sensitive nanocapsules with the simultaneous encapsulation of hydrophilic and hydrophobic compounds. *Nanomed. Nanotechnol.* **2014**, *10*, 99–107. [CrossRef]
61. Jang, M.; Yoon, Y.I.; Kwon, Y.S.; Yoon, T.J.; Lee, H.J.; Hwang, S.I.; Yun, B.L.; Kim, S.M. Trastuzumab-conjugated liposome-coated fluorescent magnetic nanoparticles to target breast cancer. *Korean J. Radiol.* **2014**, *15*, 411–422. [CrossRef]
62. Kesavan, A.; Ilaiyaraja, P.; Sofi, Beaula, W.; Veena Kumari, V.; Sagin Lal, J.; Arunkumar, C.; Anjana, G.; Srinivas, S.; Ramesh, A.; Kumar Rayala, S.; et al. Tumor targeting using polyamidoamine dendrimer-cisplatin nanoparticles functionalized with diglycolamic acid and Herceptin. *Eur. J. Pharm. Biopharm.* **2018**, *96*, 255–263. [CrossRef] [PubMed]
63. Steinhauser, I.; Spankuch, B.; Strebhardt, K.; Langer, K. Trastuzumab-modified nanoparticles: Optimization of preparation and uptake in cancer cells. *Biomaterials* **2006**, *27*, 4975–4983. [CrossRef] [PubMed]
64. Kubota, T.; Kuroda, S.; Kanaya, N.; Morihiro, T.; Aoyama, K.; Kakiuchi, Y.; Kikuchi, S.; Nishizaki, M.; Kagawa, S.; Tazawa, H.; et al. HER2-targeted gold nanoparticles potentially overcome resistance to trastuzumab in gastric cancer. *Nanomed. Nanotechnol.* **2018**, *14*, 1919–1929. [CrossRef] [PubMed]
65. Kumar, S.; Aaron, J.; Sokolov, K. Directional conjugation of antibodies to nanoparticles for synthesis of multiplexed optical contrast agents with both delivery and targeting moieties. *Nat. Protoc.* **2008**, *3*, 314–320. [CrossRef] [PubMed]
66. Greene, M.K.; Richards, D.A.; Nogueira, J.C.F.; Campbell, K.; Smyth, P.; Fernandez, M.; Scott, C.J.; Chudasama, V. Forming next-generation antibody–nanoparticle conjugates through the oriented installation of non-engineered antibody fragments. *Chem. Sci.* **2018**, *9*, 79. [CrossRef] [PubMed]
67. Kolb, H.C.; Finn, M.G.; Sharpless, K.B. Click chemistry: Diverse chemical function from a few good reactions. *Angew. Chem. Int. Ed. Engl.* **2001**, *40*, 2004–2021. [CrossRef]
68. Yi, G.; Son, J.; Yoo, J.; Park, C.; Koo, H. Application of click chemistry in nanoparticle modification and its targeted delivery. *Biomater. Res.* **2018**, *22*, 13. [CrossRef]
69. Hein, C.D.; Liu, X.M.; Dong, W. Click chemistry, a powerful tool for pharmaceutical sciences. *Pharm. Res.* **2008**, *25*, 2216–2230. [CrossRef]
70. Takayama, Y.; Kusamori, K.; Nishikawa, M. Click chemistry as a tool for cell engineering and drug delivery. *Molecules* **2019**, *24*, 172. [CrossRef]
71. Devaraj, N.K.; Weissleder, R. Biomedical applications of tetrazine cycloadditions. *Acc. Chem. Res.* **2011**, *44*, 816–827. [CrossRef]
72. Yoo, J.; Choi, S.; Son, J.; Yi, G.; Kim, E.; Koo, H. Click chemistry-mediated tumor-targeting of SN38-loaded nanoparticles using trastuzumab. *Biochem. Biophys. Res. Commun.* **2019**, *515*, 207–213. [CrossRef] [PubMed]
73. Keinänen, O.; Fung, K.; Pourat, J.; Jallinoja, V.; Vivier, D.; Kishore Pillarsetty, N.; Airaksinen, A.J.; Lewis, J.S.; Zeglis, B.M.; Sarparanta, M. Pretargeting of internalizing trastuzumab and cetuximab with a 18F-tetrazine tracer in xenograft models. *EJNMMI Res.* **2017**, *7*, 95. [CrossRef] [PubMed]
74. Lee, M.T.W.; Maruani, A.; Richards, D.A.; Baker, J.R.; Caddick, S.; Chudasama, V. Enabling the controlled assembly of antibody conjugates with a loading of two modules without antibody engineering. *Chem. Sci.* **2017**, *8*, 2056. [CrossRef] [PubMed]
75. Sievers, E.L.; Senter, P.D. Antibody-drug conjugates in cancer therapy. *Annu. Rev. Med.* **2013**, *64*, 15–29. [CrossRef] [PubMed]
76. Alley, S.C.; Okeley, N.M.; Senter, P.D. Antibody-drug conjugates: Targeted drug delivery for cancer. *Curr. Opin. Chem. Biol.* **2010**, *14*, 529–537. [CrossRef] [PubMed]

77. Shen, B.Q.; Xu, K.; Liu, L.; Raab, H.; Bhakta, S.; Kenrick, M.; Parsons-Reponte, K.L.; Tien, J.; Yu, S.F.; Mai, E.; et al. Conjugation site modulates the in vivo stability and therapeutic activity of antibody-drug conjugates. *Nat. Biotechnol.* **2012**, *30*, 184–191. [CrossRef] [PubMed]
78. Panowski, S.; Bhakta, S.; Raab, H.; Polakis, P.; Junutula, J.R. Site-specific antibody drug conjugates for cancer therapy. *mAbs* **2014**, *6*, 34–45. [CrossRef]
79. Erickson, H.K.; Park, P.U.; Widdison, W.C.; Kovtun, Y.V.; Garrett, L.M.; Hoffman, K.; Lutz, R.J.; Goldmacher, V.S.; Blättler, W.A. Antibody-maytansinoid conjugates are activated in targeted cancer cells by lysosomal degradation and linker-dependent intracellular processing. *Cancer Res.* **2006**, *66*, 4426–4433. [CrossRef]
80. Lewis Phillips, G.D.; Li, G.; Dugger, D.L.; Crocker, L.M.; Parsons, K.L.; Mai, E.; Blättler, W.A.; Lambert, J.M.; Chari, R.V.J.; Lutz, R.J.; et al. Targeting HER2-positive breast cancer with trastuzumab-DM1, an antibody–cytotoxic drug conjugate. *Cancer Res.* **2008**, *68*, 9280–9290. [CrossRef]
81. Lopus, M. Antibody-DM1 conjugates as cancer therapeutics. *Cancer Lett.* **2011**, *307*, 113–118. [CrossRef] [PubMed]
82. Lambert, J.M.; Chary, R.V.J. Ado-trastuzumab emtansine (T-DM1): An antibody–drug conjugate (ADC) for HER2-positive breast cancer. *J. Med. Chem.* **2014**, *57*, 6949–6964. [CrossRef] [PubMed]
83. Xu, Z.; Guo, D.; Jiang, Z.; Tong, R.; Jiang, P.; Bai, L.; Chen, L.; Zhu, Y.; Guo, C.; Shi, J.; et al. Novel HER2-targeting antibody-drug conjugates of trastuzumab beyond T-DM1 in breast cancer: Trastuzumab deruxtecan (DS-8201a) and (Vic-)trastuzumab duocarmazine (SYD985). *Eur. J. Med. Chem.* **2019**, *183*, 111682. [CrossRef] [PubMed]
84. Nunes, J.P.M.; Morais, M.; Vassileva, V.; Robinson, E.; Rajkumar, V.S.; Smith, M.E.B.; Pedley, R.B.; Caddick, S.; Baker, J.R.; Chudasama, V. Functional native disulfide bridging enables delivery of a potent, stable and targeted antibody–drug conjugate (ADC). *Chem. Commun.* **2015**, *51*, 10624. [CrossRef] [PubMed]
85. Robinson, E.; Nunes, J.P.M.; Vassileva, V.; Maruani, A.; Nogueira, J.C.F.; Smith, M.E.B.; Pedley, R.B.; Caddick, S.; Baker, J.R.; Chudasama, V. Pyridazinediones deliver potent, stable, targeted and efficacious antibody–drug conjugates (ADCs) with a controlled loading of 4 drugs per antibody. *RSC Adv.* **2017**, *7*, 9073. [CrossRef]
86. Schumacher, F.F.; Nunes, J.P.M.; Maruani, A.; Chudasama, V.; Smith, M.E.B.; Chester, K.A.; Baker, J.R.; Caddick, S. Next generation maleimides enable the controlled assembly of antibody–drug conjugates via native disulfide bond bridging. *Org. Biomol. Chem.* **2014**, *12*, 7261. [CrossRef] [PubMed]
87. Elgersma, R.C.; Coumans, R.G.E.; Huijbregts, T.; Menge, W.M.P.B.; Joosten, J.A.F.; Spijker, H.J.; de Groot, F.M.H.; van der Lee, M.M.C.; Ubink, R.; van den Dobbelsteen, D.J.; et al. Design, synthesis, and evaluation of linker-duocarmycin payloads: Toward selection of HER2-targeting antibody–drug conjugate SYD985. *Mol. Pharm.* **2015**, *12*, 1813–1835. [CrossRef]
88. Ogitani, Y.; Aida, T.; Hagihara, K.; Yamaguchi, J.; Ishii, C.; Harada, N.; Soma, M.; Okamoto, H.; Oitate, M.; Arakawa, S.; et al. DS-8201a, a novel HER2-targeting ADC with a novel DNA topoisomerase I inhibitor, demonstrates a promising antitumor efficacy with differentiation from T-DM1. *Clin. Cancer Res.* **2016**, *22*, 5097–5108. [CrossRef]
89. Rinnerthaler, G.; Gampenrieder, S.P.; Greil, R. HER2 directed antibody-drug-conjugates beyond T-DM1 in breast cancer. *Int. J. Mol. Sci.* **2019**, *20*, 1115. [CrossRef]
90. Gradishar, W.J. Emerging approaches for treating HER2-positive metastatic breast cancer beyond trastuzumab. *Ann. Oncol.* **2013**, *24*, 2492–2500. [CrossRef]
91. Leyland-Jones, B.; Arnold, A.; Gelmon, K.; Verma, S.; Ayoub, J.P.; Seidman, A.; Dias, R.; Howell, J.; Rakhit, A. Pharmacologic insights into the future of trastuzumab B. *Ann. Oncol.* **2001**, *12*, S43–S47. [CrossRef]
92. Wang, J.; Xu, B. Targeted therapeutic options and future perspectives for HER2-positive breast cancer. *Signal Transduct. Target. Ther.* **2019**, *4*, 34. [CrossRef] [PubMed]
93. Wan, X.; Zheng, X.; Pang, X.; Zhang, Z.; Zhang, Q. Incorporation of lapatinib into human serum albumin nanoparticles with enhanced anti-tumor effects in HER2-positive breast cancer. *Colloids Surf. B* **2015**, *136*, 817–827. [CrossRef] [PubMed]
94. Zhang, L.; Zhang, S.; Ruan, S.B.; Zhang, Q.Y.; He, Q.; Gao, H.L. Lapatinib-incorporated lipoprotein-like nanoparticles: Preparation and a proposed breast cancer-targeting mechanism. *Acta Pharmacol. Sin.* **2014**, *35*, 846–852. [CrossRef] [PubMed]

95. Mohasseri, R.; Karimi, M.; Tian, L.; Naderi-Manesh, H.; Ramakrishna, S. Hydrophobic lapatinib encapsulated dextran-chitosan nanoparticles using a toxic solvent free method: Fabrication, release property & in vitro anti-cancer activity. *Mater. Sci. Eng. C Mater.* **2017**, *74*, 413–421.
96. Singh, M.K.; Pindiprolu, S.K.S.S.; Sanapalli, B.K.R.; Yele, V.; Ganesh, G.N.K. HER2 targeted biological macromolecule modified liposomes for improved efficacy of capecitabine in breast cancer. *Int. J. Biol. Macromol.* **2020**, *150*, 631–636. [CrossRef]
97. Engelin, C.W.; Leonard, S.C.; Geretti, E.; Wickham, T.; Hendriks, B.S. Dual HER2 targeting with trastuzumab and liposomal-encapsulated doxorubicin (MM-302) demonstrates synergistic antitumor activity in breast and gastric cancers. *Cancer Res.* **2016**, *76*, 1517:1527. [CrossRef]
98. Miller, K.; Cortes, J.; Hurvitz, S.A.; Krop, I.E.; Tripathy, D.; Verma, S.; Riahi, K.; Reynolds, J.G.; Wickham, T.J.; Molnar, I.; et al. HERMIONE: A randomized phase 2 trial of MM-302 plus trastuzumab versus chemotherapy of physician's choice plus trastuzumab in patients with previously treated, anthracycline-naive, HER2-positive, locally advanced/metastatic breast cancer. *BMC Cancer* **2016**, *16*, 352–363. [CrossRef]
99. Hamblett, K.J. HER2-Targeted ADCs: At the forefront of ADC technology development. In *Innovations for Next-Generation Antibody-Drug Conjugates*, 1st ed.; Damelin, M., Ed.; Humana Press: Cham, Switzerland, 2018; pp. 163–186.
100. Yao, X.; Jiang, J.; Wang, X.; Huang, C.; Li, D.; Xie, K.; Xu, Q.; Li, H.; Li, Z.; Lou, L.; et al. A novel humanized anti-HER2 antibody conjugated with MMAE exerts potent anti-tumor activity. *Breast Cancer Res. Treat.* **2015**, *153*, 123–133. [CrossRef]
101. Li, H.; Yu, C.; Jiang, J.; Huang, C.; Yao, X.; Xu, Q.; Yu, F.; Lou, L.; Fang, J. An anti-HER2 antibody conjugated with monomethyl auristatin E is highly effective in HER2-positive human gastric cancer. *Cancer Biol. Ther.* **2016**, *17*, 346–354. [CrossRef]
102. Humphreys, C.R.C.; Kirtely, J.; Hewit, A.; Biroc, S.; Knudsen, N.; Skidmore, L.; Wahl, A. Abstract 639: Site specific conjugation of ARX-788, an antibody drug conjugate (ADC) targeting HER2, generates a potent and stable targeted therapeutic for multiple cancers. *Cancer Res.* **2015**, *75*, 639.
103. Li, J.Y.; Perry, S.R.; Muniz-Medina, V.; Wang, X.; Wetzel, L.K.; Rebelatto, M.C.; Hinrichs, M.J.; Bezabeh, B.Z.; Fleming, R.L.; Dimasi, N.; et al. A biparatopic HER2-targeting antibody-drug conjugate induces tumor regression in primary models refractory to or ineligible for HER2-targeted therapy. *Cancer Cell* **2016**, *29*, 117–129. [CrossRef] [PubMed]
104. Clinical Trials. Available online: https://clinicaltrials.gov/ct2/home (accessed on 21 August 2020).
105. Costa, R.L.B.; Czerniecki, B.J. Clinical development of immunotherapies for HER2+ breast cancer: A review of HER2-directed monoclonal antibodies and beyond. *NPJ Breast Cancer* **2020**, *6*, 10. [CrossRef] [PubMed]
106. Mahjub, R.; Jatana, S.; Em Lee, S.; Qin, Z.; Pauli, G.; Soleimani, M.; Madadi, S.; Li, S.D. Recent advances in applying nanotechnologies for cancer immunotherapy. *J. Control. Release* **2018**, *288*, 259–263. [CrossRef] [PubMed]
107. Sun, Y.; Ma, W.; Yang, Y.; He, M.; Li, A.; Bai, L.; Yu, B.; Yu, Z. Cancer nanotechnology: Enhancing tumor cell response to chemotherapy for hepatocellular carcinoma therapy. *Asian J. Pharm. Sci.* **2019**, *14*, 581–594. [CrossRef]
108. Kim, K.Y. Nanotechnology platforms and physiological challenges for cancer therapeutics. *Nanomed. Nanotechnol.* **2007**, *3*, 103–110. [CrossRef] [PubMed]
109. Matos, A.I.; Carreira, B.; Peres, C.; Moura, L.I.F.; Conniot, J.; Fourniols, T.; Scomparin, A.; Martínez-Barriocanal, A.; Arango, D.; Conde, J.P.; et al. Nanotechnology is an important strategy for coenbinational innovative chemo-immunotherapies against colorectal cancer. *J. Control. Release* **2019**, *307*, 108–138. [CrossRef]


© 2020 by the authors. Licensee MDPI, Basel, Switzerland. This article is an open access article distributed under the terms and conditions of the Creative Commons Attribution (CC BY) license (http://creativecommons.org/licenses/by/4.0/).

# CHAPTER 2

## THESIS OBJECTIVES

The project developed in this thesis is part of one of the research lines carried out by the group *Aplicaciones Biomédicas de Ingeniería Química*, focused on the design of novel cancer nanotherapies.

Specifically, its **main objective** is trying to achieve the development and validation of three different strategies to improve the current treatment of HER2-overexpressing breast cancer, enhancing its effectiveness and reducing its side toxicity. This project began as a result of a collaboration with the research group led by Dr. Atanasio at the *Instituto de Biología Molecular y Celular del Cáncer*, and to accomplish the general objective, the following **specific objectives** will be pursued:

***First strategy***

· First, the synthesis and characterization of an alginate and piperazine nanocarrier for trastuzumab (Tmab) and PTX will be carried out. This antibody and drug are part of the first-line treatment of metastatic HER2-positive (HER2+) breast cancer, and improving their biodistribution, efficiency and selectivity will be intended by means of their nanovehiculization.

· PTX will be included into β-cyclodextrins (β-CDs) to improve its aqueous solubility. The consequential complexes, along with Tmab, will be covalently attached to the most advantageous alginate-piperazine nanoparticles (NPs) of those obtained, once characterised.

· The resulting conjugated nanovehicle will be again characterised, and its internalization in HER2+ breast cancer cells will be analysed. Then, its efficacy and selectivity will be validated in both, conventional cell cultures and tumour spheroids.

***Second strategy***

· In second place, with the purpose of further improving the main drawbacks of traditional HER2+ breast tumour chemotherapy, polydopamine (PDA) NPs will be used to design novel drug delivery systems. These nanoparticles will be prepared by dopamine solution

oxidation in aqueous media containing $NH_4OH$ and different types of alcohols.

· The effect of the $NH_4OH$ concentration and the type of alcohol used on the properties of the PDA NPs obtained will be studied. In addition, it will be investigated how these two parameters determine their cytotoxicity, which will be analysed for several cell lines.

· Besides, PDA NP internalization in breast cancer cells will be studied, and it will be tried to elucidate if their great iron affinity could be involved in their intrinsic cytotoxicity.

· Next, to upgrade the own antineoplastic activity of PDA NPs and achieve an excessive production of ROS in breast cancer cells, these NPs will be loaded with $Fe^{2+}$, $Fe^{3+}$ and $Cu^{2+}$. The resulting NPs will be characterised and analysed for cytotoxicity.

· According to the results obtained, an attempt will be made to set the $Fe^{3+}$ adsorption process in order to induce ferroptosis more efficiently and selectively in HER2-overexpressing breast tumour cells.

·The potential mechanism by which $Fe^{3+}$ would be released from PDA NPs and thus induce ferroptosis in cancer cells will be investigated.

· Moreover, to enhance PDA NP therapeutic activity while reducing DOX side effects, different concentrations of this anthracycline will be also loaded to the NPs. The cytotoxicity and selectivity of the resulting nanosystem will be determined by means of viability assays, and it will be studied whether there is a synergist effect between the $Fe^{3+}$ and DOX loaded.

· Subsequently, taking advantage of PDA great properties, especially of its intrinsic anti-tumour effect and its capability of adsorbing drugs, PDA NPs will be also synthesized as a nanovehicle for Tmab and PTX. For their preparation, the $NH_4OH$ concentration and the type of alcohol that will be observed to give them the best antineoplastic effect will be chosen.

· Later, PTX will be directly adsorbed in PDA NPs, and Tmab will be both adsorbed and covalently bound to them. The efficiency and selectivity of the NPs prepared will be assayed in different cell lines, and the best Tmab-loading strategy will be selected to perform further studies.

· In these studies, the capacity of PDA NPs to induce apoptosis will be verified, and their therapeutic activity will be also analysed in tumour spheroids. The results achieved will be compared to with those obtained when using the alginate and piperazine NPs.

***Third strategy***

· Finally, macroscopic hydrogels of gellan gum will be prepared for local, post-surgery breast cancer chemotherapy as a potential adjunct to a systemic therapy. They will be developed in both acetate and phosphate buffer with different degrees of chemical crosslinking, and they will be extensively characterized.

· The biodegradability and biocompatibility of the hydrogels will be investigated, and they will be loaded with PTX, which will be also previously included in β-CDs to improve its solubility.

· The release kinetics of the taxane from the hydrogels will be studied and, at last, the therapeutic activity of the loaded hydrogels will be analysed by employing HER2+ breast tumour cell lines.

# CHAPTER 3

## ALGINATE AND PIPERAZINE NANOPARTICLES CONJUGATED WITH TRASTUZUMAB AS TARGETED NANOCARRIER FOR PACLITAXEL

## 3.1. Introduction

### *3.1.1. The contradictory role of HER2-overexpression*

As already mentioned in the first introductory chapter, one main hallmark of cancer is the self-sufficiency in growth signals. Tumour cells are force to achieve this autonomy to maintain their elevate proliferation rate and, for this, they can follow several strategies. One of them is overexpressing surface receptors of growth factors, such as several RTKs [1]. Among these RTKs, one receptor that is overexpressed in 15-20% of breast tumours that are diagnosed, as well as in other types of solid tumours (like ovarian or gastric carcinomas), is HER2 [2-5].

HER2/ErbB2/Neu, which is encoded by a gene located in the chromosomal region 17q12-21, is a member of the EGFR family of the homologous transmembrane RTKs, along with HER3 and HER4 [6,7]. Unlike these last two receptors, HER2 has not ligand, but it is able to signal upon homo- or heterodimerization with other EGFR family members, affecting their downstream signalling [6]. This signalling determines multiple processes, including cell proliferation, survival and invasiveness. For this reason, HER2-overexpression has been traditionally associated with worse prognosis and inferior outcomes for patients suffering from HER2+ breast cancer. However, over the last years, therapeutic advances have improved clinical treatment of HER2+ tumours. In this way, overexpression of this receptor has enabled patients with HER2+ breast cancer benefit from targeted therapies based on antibodies, antibody-drug conjugates and small-molecule TK inhibitors [6,7].

Among the antibodies that target HER2, the most commonly used in the clinical setting are Tmab and pertuzumab. They are two recombinant, humanized mAbs that bind to distinct regions of the extracellular domain (ECD) of HER2: at the juxtamembrane domain IV and the dimerization domain II, respectively [2,6]. Their clinical administration to treat HER2+ breast tumours was approved by the FDA and EMA several years ago, as can be seen in Table 1.1 (Chapter 1, page 22) [2]. Perhaps because pertuzumab is approved to be jointly used with docetaxel and

Tmab, the employment of this last antibody, which is normally produced with the hybridoma technique, has been more extensive in a wide range of therapeutic strategies.

### *3.1.2. Trastuzumab role in HER2-positive breast cancer treatment*

Clinical administration of Tmab (Herceptin™) for the treatment of metastatic (MBC) and early (EBC) breast cancer was approved by both the FDA and EMA between 1998 and 2011 [8]. Later, in 2015, this mAb began to be part of the WHO Essential Medicines List as a consequence of the beneficial effects that it had shown when used in adjuvant therapies. These benefits included induction of tumour regression and increment of patients' disease-free survival rate [2].

Molecular mechanisms responsible for Tmab therapeutic activity are not fully understood yet [2]. Nonetheless, it has been generally accepted by the scientific community that this antibody inhibits HER2 activity through both, promotion of ADCC and intrinsic effects [6] (**Figure 3.1**). Among the latter, it is known that Tmab can arrest cell cycle by inhibiting the MAPK and PI3K signalling cascades and by decreasing the production of pro-angiogenic factors, such as VEGF and IL-8 [2].

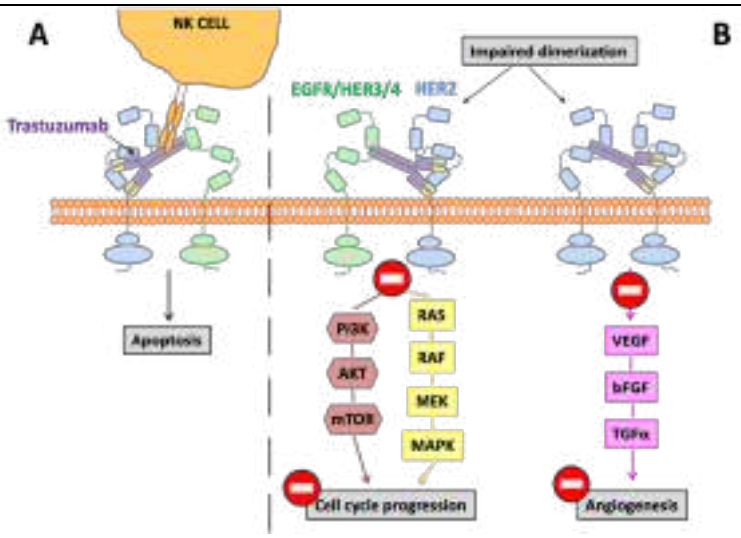


**Figure 3.1.** Molecular mechanisms that account for Tmab therapeutic activity: by specifically binding to HER2, Tmab prevents its homo- or heterodimerization with other EGF receptors. Apart from promoting a process of ADCC (**A**), Tmab is believed to be able to inhibit tumour proliferation and angiogenesis (**B**).

Tmab effective anti-tumour activity has prompted its use not only as adjuvant treatment, but also for the development of novel nanomedicines. In them, the antibody has two functions: targeting HER2-overexpressing cancer cells and enhancing the therapeutic activity of the drugs delivered [2]. Among these nanomedicines, the antibody-drug conjugate (ADC) ado-trastuzumab emtansine (T-DM1) may be the best known, given that its clinical administration was already approved by the FDA in 2013 [9]. Nevertheless, numerous nanocarriers can be found in literature which have been also conjugated with this antibody [2,10]. For example, PLGA, chitosan, HSA, gold and iron oxide NPs have been already decorated by Tmab, as well as dendrimers, MSNs and liposomes [2,10-14]. All of these resulting DDSs have served as a vehicle for numerous drugs, including PTX and docetaxel [15,16]. These two drugs have constituted for many years the standard first-line treatment of HER2+ MBC along with Tmab on the basis of the trial performed by Slamon and colleagues, in which it was demonstrated that there was a synergist effect between the anti-HER2 mAb and the taxanes [17,18].

Of both taxanes, PTX has been the one chosen in the current study to develop a novel HER2-targeting nanocarrier since, despite the fact that both drugs have similar efficacy, when balancing it and their toxicity *in vitro*, paclitaxel was favoured [19]. In addition, in a study in which a comparative cost-effectiveness analysis was performed between PTX and docetaxel, it was concluded that the latter had worse cost-effect ratio for MBC treatment [20]. Besides, PTX use for the development of particulate systems in recent years has been notably greater than that of docetaxel. Thus, the number of results found when searching for "paclitaxel nanoparticles" is much higher than that obtained when searching for "docetaxel nanoparticles" in databases such as PubMed (2424 *vs*. 830 results from 2010 to 2020) [21,22].

### *3.1.3. Paclitaxel: therapeutic action and major drawbacks of its administration*

PTX (**Figure 3.2.A**) was extracted for the first time from the bark of Pacific yew tree (*Taxus brevifolia*) in 1962 thanks to a plant screening program that was carried out by the U.S. NCI. Almost ten years later, in 1971, this taxane entered the NCI drug developing programme after showing cytotoxicity *in vitro*. Finally, in 1984, the drug entered clinical trials after demonstrating efficacy in mouse tumour models. Such was the subsequent demand for PTX that, since it could only be extracted from the slow-growing *T. brevifolia*, this specie had to be declared endangered and the taxane started to be produced synthetically in order to remain accessible [23].

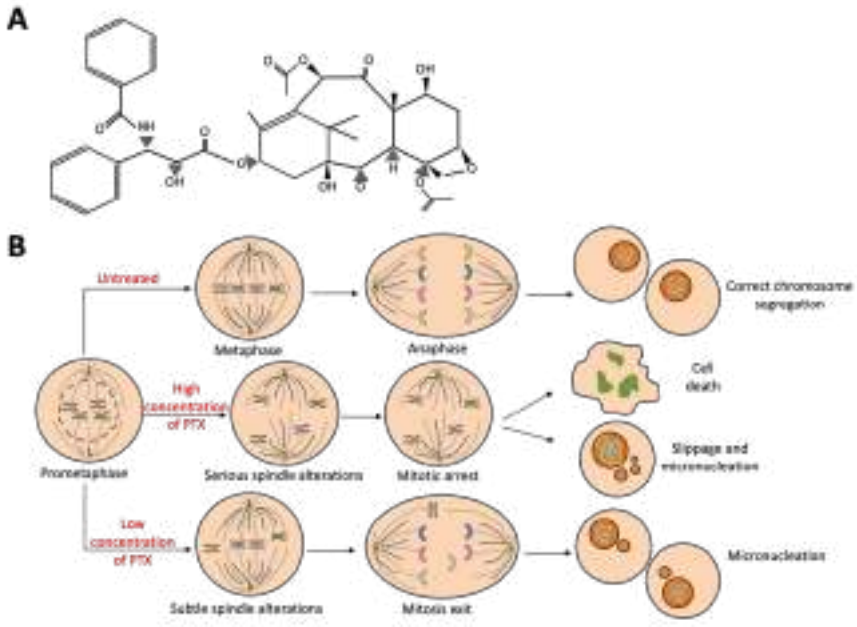


**Figure 3.2.** Paclitaxel chemical structure (**A**) and concentration-dependent cytotoxicity (**B**). When cells are treated with high concentrations of the taxane, mitotic arrest takes place and daughter cells die or are abnormally tetraploid. Otherwise, when PTX concentration is lower, treated cells are able to exit mitosis, but they exhibit alterations in their genetic material.

Regarding its cytotoxicity, it has been shown that PTX arrests cancer cells in mitosis and activates the mitotic checkpoint *in vitro* in a concentration-dependent manner. This mitotic checkpoint is a cell cycle control mechanism that delays chromosome separation until sister chromatids make stable attachments to both poles of the mitotic spindle. In this manner, it ensures that each daughter cell receives one copy of every chromatid. Such stable attachments are generated when chromatids connect to the spindle microtubules through their kinetochores. However, high PTX concentrations avoid this kinetochore attachment to take place through microtubule stabilization, and they induce a signal transduction cascade that retards mitotic progression. Then, malignant cells arrested in mitosis either die or generate abnormal tetraploid cells that end up dying or being arrested again. Otherwise, low concentrations of the taxane cause small spindle alterations that allow

cells to exit mitosis. Notwithstanding, instead of a correct chromosome segregation, micronucleation occurs [23,24] (**Figure 3.2.B**).

Its unique mechanism of action has made PTX one of the most successful natural anti-tumour drugs available today, widely used in the treatment of breast, ovarian, colorectal and urinary cancers [24]. Nevertheless, its administration involves some complications. PTX is highly lipophilic and practically insoluble in water (< 0.03 mg/mL), and its bioavailability is poor when it is orally administered. As a consequence, it normally follows systemic administration, but the taxane is rapidly eliminated through hepatic metabolism and suffers from significant MDR [25]. For these reasons, many attempts have been made to overcome PTX aqueous insolubility, and the result of one of these attempts was Taxol®. This first commercialised PTX formulation, which is prepared by dissolving the drug in a 1:1 mixture of polyoxyethylated castor oil (Cremophor EL), has solved the problem regarding its insolubility, but the use of the mentioned mixture has been related to severe side toxicities [23,25].

Thereby, with the aim of targeting HER2-overexpressing cancer cells with Tmab and PTX, while improving the pharmacokinetics of the taxane, sodium alginate and piperazine NPs were prepared in this project as a novel targeted nanocarrier for both, the antibody and the drug, which was previously included into β-cyclodextrin molecules to improve its solubility [26].

### *3.1.4. Employment* of *β-cyclodextrins to improve the aqueous solubility of hydrophobic drugs*

Cyclodextrins (CDs) are cyclic oligosaccharides formed by the linkage of 6, 7 or 8 glucose units through *α*-1,4 glycosidic bonds, called α-, β- *or* γ-CDs, respectively [27] *(***Figure 3.3.A**). These molecules show a hollow truncate cone-shaped structure in the space and, while their outside is hydrophilic, their inside cavity is slightly hydrophobic and allows the encapsulation of poor-soluble drugs, like PTX (**Figure 3.3.B**). As a result of this encapsulation, inclusion complexes, which improve the bioavailability of hydrophobic drugs, are formed by non-covalent interactions and without complex chemical reactions. For this reason and

also because of they are non-toxic, CDs have been approved by pharmacopeia in many countries as excipients for the manufacture of pharmaceutical preparations and are playing an important role in the development of new anti-cancer therapies. Thus, numerous examples of CD-based DDSs (micelles, nanoparticles, liposomes…) with good therapeutic action can be found in the literature [28,29].

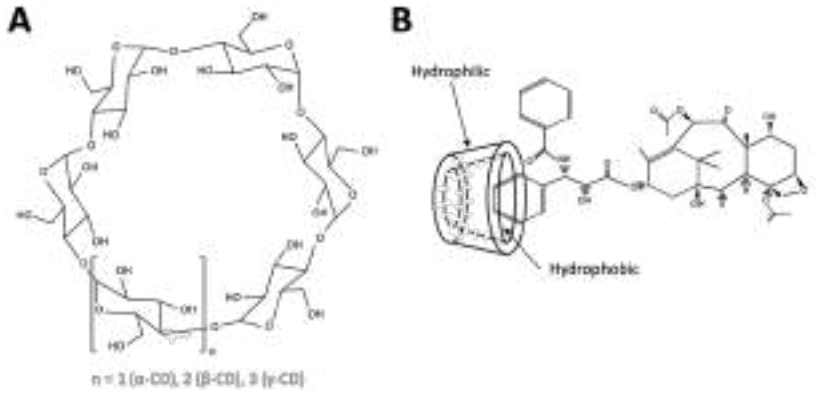


**Figure 3.3.** (**A**) CD chemical structure; (**B**) PTX:βCDs inclusion complex. The hydrophobic interior cavity of the CDs allows the encapsulation of drugs with poor aqueous solubility, such as the taxane employed in this thesis.

Among the three different types of CDs, β-CDs are the most popular (and possibly the best studied) thanks to their easiest accessibility, lowest toxicity and lowest price. Apart from in the pharmaceutical industry, they are also used in food and cosmetics and [27,30], for all these motives, they were the ones chosen in this work to prepare PTX inclusion complexes (PTX:βCDs).

The preparation of these complexes, as well as the synthesis of the alginate and piperazine nanoparticles, their characterization, conjugation and *in vitro* validation can be found throughout the remainder of this chapter.

## 3.2. Synthesis and characterization of alginate-piperazine nanoparticles

### *3.2.1. Synthesis of nanoparticles of sodium alginate and piperazine*

When synthesizing the new DDS for PTX and Tmab, sodium alginate was chosen because it is a harmless anionic polysaccharide, biocompatible and biodegradable. In fact, it is widely used in the food and cosmetic industries as gelling agent [26,31]. Moreover, alginate had already been used with chitosan to develop other NPs with anti-tumour activity [31]. On the other hand, piperazines are nitrogen-containing heterocyclic compounds with potent antioxidant activity. Thanks to their properties, they have been traditionally used to develop antifungal, antibacterial and antimalarial agents. More recently, piperazine derivates have been synthesized as alternative anti-cancer agents [26,32]. For this reason, this compound was chosen to perform chemical crosslinking of sodium alginate chains by means of electrostatic interactions to obtain NPs that act as targeted vehicle for Tmab and PTX.

In order to carry out such alginate crosslinking and according to a previous work of the research group [33], aqueous solutions of alginate and piperazine were prepared with a 1 and 2 mg/mL concentration, respectively. Then, their pH was decreased until 4.6 - 4.7 by dropping HCl (37% (V/V)), and the piperazine solution was dropped over the alginate solution in different molar ratios (1:8 - 1.5:1). Since mannuronic and guluronic acids of sodium alginate chains have a $pK_a$ of 3.4 and 3.7, and $pK_a$ values of piperazine are close to 5.7 and 9.7, the working pH was set at 4.6 - 4.7. At such pH value, carboxyl acid groups of alginate chains were expected to be deprotonated, while both amino groups of piperazine molecules were expected to be protonated. In this way, after a short stir, electrostatic interactions could take place between both compounds, and NPs were obtained thanks to the piperazine-mediated reticulation of the alginate chains. This phenomenon was favoured by the employment of alginate and piperazine solutions of low concentration [26,33] (**Figure 3.4**).

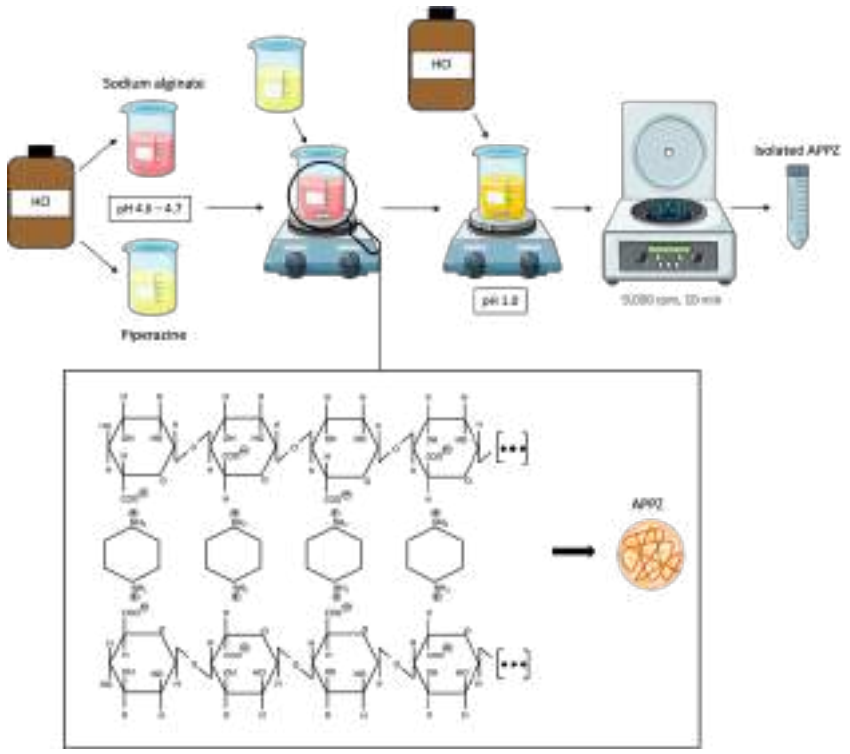


**Figure 3.4.** Scheme that summarizes the synthesis process of the APPZ, which were obtained thanks to a piperazine-mediated crosslinking of alginate chains at pH 4.6 - 4.8.

Later, in order to isolate the alginate-piperazine NPs (APPZ) obtained, the pH of the resulting mixture was decreased to 1.0 by dropping HCl. At such pH value, carboxyl groups of the sodium alginate chains were protonated, and this fact allowed the formation of aggregates of increased size that could be separated by centrifugation (9000 rpm, 10 minutes) [26,33].

### *3.2.2. Characterization of the different alginate-piperazine nanoparticles obtained*

#### 3.2.2.1. Characterization of alginate-piperazine nanoparticle size and surface charge

With the aim of characterizing the resulting NPs and determining the most appropriate piperazine/alginate molar ratio to synthesize them, isolated APPZ were again suspended in deionized water ($H_2O$(d)) after

determining their mass. The pH of the suspension was adjusted to 4.7 with few drops of NaOH (1 M) [26], and NP size and surface charge (zeta potential) were determined by using a Zetasizer equipment. This equipment, by means of dynamic light scattering (DLS), yields particle diffusion coefficient (*D*) with a 90° fixed angle detector. Then, it calculates particle hydrodynamic diameter using the Stokes-Einstein equation (**Equation 3.1**), where d(H) is the mentioned spherical diameter, k is Boltzmann's constant ($1.3807 \cdot 10^{-23}$ J/K), T represents absolute temperature and η is the dynamic viscosity of the medium.

$$d(H) = \frac{KT}{3\pi\eta D} \qquad \textbf{(Equation 3.1)}$$

APPZ average diameter was analysed from suspensions with a concentration close to 1% (WT), employing the Cumulants methods to obtain the correlation functions. Size values, as well as zeta potential values, which were calculated from particle electrophoretic mobility, were obtained as the average of three parallel measurements. The mean results obtained for both parameters ± standard error (SEM) have been represented as function of the piperazine/alginate volume ratio in **Figure 3.5**.**A**.

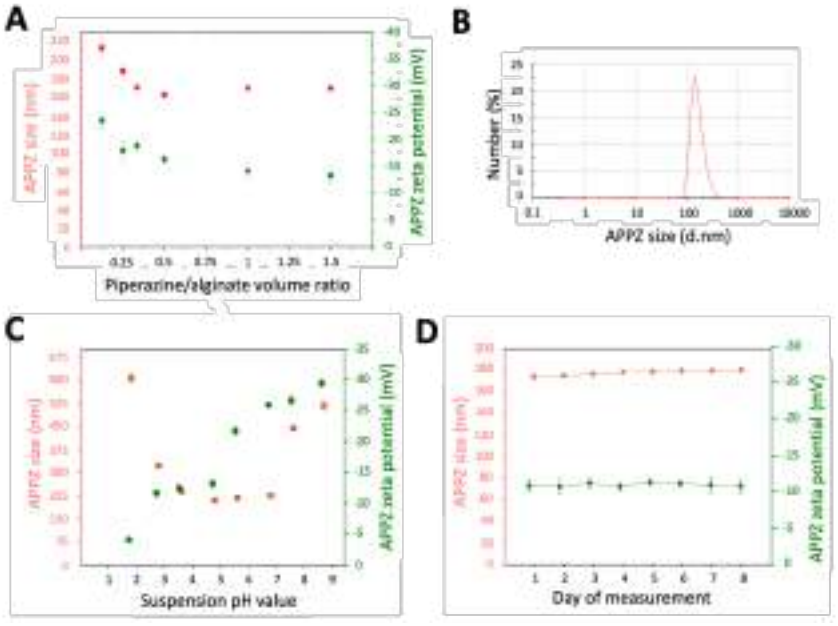


**Figure 3.5.** (**A**) Size and zeta potential of APPZ as a function of the piperazine/alginate volume ratio; (**B**) Number size distribution of the smallest APPZ obtained, determined by

DLS; (**C**) Size and zeta potential of APPZ (1:2 piperazine/alginate volume ratio) as a function of the suspension pH; (**D**) APPZ stability over time. All values were obtained from the mean ± SEM of three different measurements.

In **Figure 3.5**, it can be observed that the smallest APPZ (162.5 ± 34 nm (polydispersity index (PDI) = 0.25) were obtained with a 1:2 piperazine/alginate volume ratio (**Figure 3.5.B**). Since these NPs exhibited a suitable negative zeta potential (-16.2 ± 1.3 mV) for the application intended [34], they were the ones chosen to perform further characterization and conjugation studies.

### 3.2.2.2. Analysis of pH influence on the size and surface charge of alginate-piperazine nanoparticles

Continuing with the characterization, the influence of the pH of the suspension on NP average size and zeta potential was analysed. Thus, the pH was modified with the addition of drops of HCl or NaOH, and the diameter and surface charge of the APPZ were again determined at the different pH values (**Figure 3.5**.**C**). As a result, it was observed that, regarding the size of the NPs, there was no significant variation when the pH oscillated between 3 and 6. Nevertheless, outside this range, APPZ diameter increased, possibly as a consequence of the loss of electrostatic interactions between the alginate chains and piperazine molecules. Otherwise, it was seen that APPZ surface charge became closer to zero as the pH was more acidic. In this case, this phenomenon could be explained by the protonation of the alginate carboxyl groups [34].

### 3.2.2.3. Determination of alginate-piperazine nanoparticle stability

Finally, with the aim of determining if the APPZ obtained were stable over time, their size and zeta potential were analysed during 8 consecutive days, preserving the NPs at room temperature in an aqueous suspension of pH 4.7 - 4.8. Throughout this period and as can be seen in **Figure 3.5.D**, it was found that the nanosystem was quite stable, since neither its size nor zeta potential varied significantly (± 15.6 nm and ± 1.6 mV, respectively). Moreover, to determine the properties that the APPZ would display in a medium more similar to the physiological one, these two parameters were also analysed after suspending the NPs in phosphate

buffered saline (PBS) (1x, pH 7.4). They turned out to be approximately 214 ± 55 nm (PDI = 0.4) and -19.8 ± 1.1 mV [26].

## 3.3. Conjugation of alginate-piperazine nanoparticles with trastuzumab and paclitaxel

### *3.3.1. Obtaining of paclitaxel-β-cyclodextrin inclusion complexes*

As said in the point 3.1.3 (page 82) of this Chapter, including PTX into β-CD molecules was decided before carrying out APPZ conjugation with the taxane and Tmab to improve its aqueous solubility and stability [26].

In order to obtain these inclusion complexes (PTX:βCDs), the freeze-drying method described by Alcaro et al. in 2002 was followed [35]. Briefly, PTX (1 mg) was dissolved in pure ethanol (EtOH, 1.2 mL) and β-CDs (1.2 mg) were dissolved in $H_2O$(d) (1.4 mL). Next, the aqueous solution obtained was added to the alcoholic one, and the resulting hydroalcoholic solution (with a 1.3:1 PTX/βCDs molar ratio) was kept under agitation for 5 hours, at room temperature and in dark conditions (since PTX is photosensitive). After that time, the solution was frozen at -80°C and freeze-dried. The resulting white powder was re-suspended in $H_2O$(d) and PTX inclusion efficiency was determined through chromatography and mass spectrometry by the Service of Elemental Analysis-NUCLEUS of the University of Salamanca. For this, the experimental conditions described by Hamada et al. (mobile phase: 65:35 methanol/$H_2O$; flow rate: 1 mL/minute; column temperature: 35°C; detector: UV 230 nm) were followed [36], and PTX:βCDs inclusion efficiency was found to be close to 79% (W/W).

### *3.3.2. Conjugation of paclitaxel-β-cyclodextrin complexes and trastuzumab to alginate-piperazine nanoparticles*

Once PTX:βCDs inclusion complexes were obtained, APPZ surface was decorated by them, along by the antibody Tmab, through the carbodiimide chemistry [2].

Among the different covalent strategies that can be pursued to functionalize DDSs with mAbs, the carbodiimide chemistry is probably the most used one because of its simplicity. It requires the employment of a zero-crosslinking agent: 1-ethyl-3-(3-dimethyalminopropyl) carbodiimide (EDC), which allows the binding of antibodies through their primary amine groups to carboxyl groups in nanocarriers [2,26]. When EDC reacts in one-step with carboxyl groups, highly reactive O-acylisourea esters are generated. Later, these intermediate compounds can react with primary amine groups, which are abundant on the antibody surface, and amide bonds are finally formed. Nevertheless, resulting O-acylisourea esters are not stable enough and, to avoid unwanted intra- and inter-molecular bindings occurring among the antibody functional groups, carbodiimide chemistry is usually performed in two steps, adding N-hydroxysulfoxuccinimide (NHS) to transform O-acylisourea esters into semi-stable esters [2].

Thereby, in order to carry out APPZ conjugation, both compounds, EDC and NHS, were employed. Isolated APPZ (500 mg) were resuspended in $H_2O$(d) (5 mL), and the suspension pH was set at 4.5 - 4.7 because carbodiimide chemistry is more efficient at acidic pH values [26,37]. Then, EDC (193 mg/mL, 50 µl) and NHS (58 mg/mL, 50 µl) solutions were incorporated [33] and, after keeping the mixture stirred for 40 minutes (50 rpm), Tmab was firstly added (1.37 µM, 60 µl). The resulting suspension was kept under stirring for 3 more hours and, after that time, PTX:βCDs inclusion complexes were incorporated (92.5 µM PTX, 300 µl). The final mixture, in which Tmab was expected to be anchored through amide bonds and PTX:βCDs complexes were expected to be linked via ester bonds to the APPZ, was kept in agitation (50 rpm) in the dark overnight [26] (**Figure 3.6**). Finally, next day, conjugated APPZ were isolated by decreasing the pH of the suspension to 1.0 and by centrifuging them (9000 rpm, 10 minutes). APPZ supernatant was preserved in order to determine the amount of Tmab and PTX loaded in the NPs.

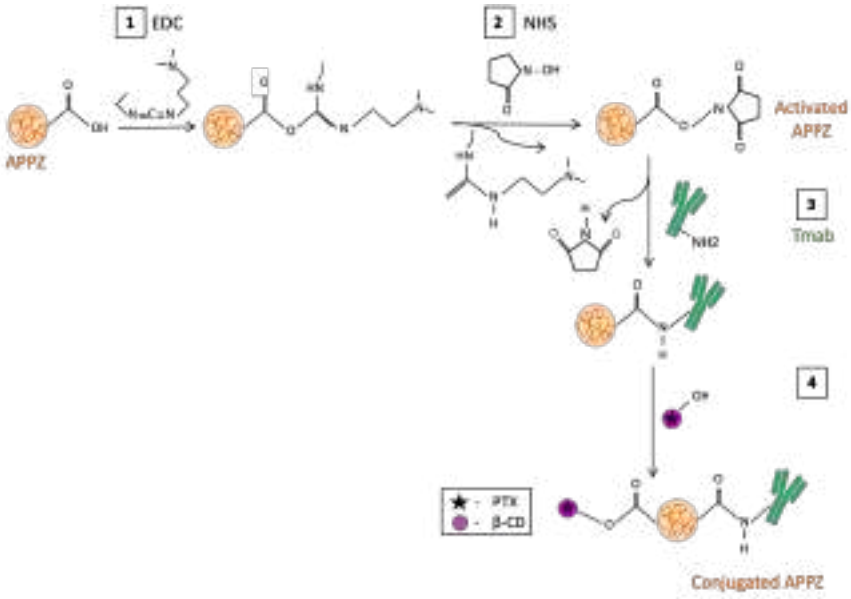


**Figure 3.6.** Schematic representation of APPZ conjugation with Tmab and PTX:βCDs, performed by means of the carbodiimide chemistry.

### *3.3.3. Determination of paclitaxel and trastuzumab content in alginate-piperazine nanoparticles*

The amount of PTX and Tmab incorporated in the APPZ was determined indirectly by difference, by analysing their concentration in the supernatant once the conjugated NPs were isolated. On one hand, PTX concentration was again determined by the Service of Elemental Analysis-NUCLEUS of the University of Salamanca by high-performance liquid chromatography (HPLC) and mass spectrometry. On the other hand, Tmab concentration in APPZ supernatant was obtained using the Bradford method.

The Bradford method, first described in 1976 [38], is based on the absorbance variation that occurs when the Coomassie brilliant blue existing in the Bradford reagent binds to basic amino acids (histidine, arginine and lysine). Such absorbance variation is proportional to the amount of dye that is bound to proteins and, consequently, allows determining in a very simple way the protein concentration in a solution.

Thereby, in order to determine Tmab concentration in APPZ supernatant, it (100 µl) was mixed with the Bradford reagent (1 mL) and, after 5 minutes, the absorbance of the mixture was measured at 595 nm. The same protocol was previously followed with albumin solutions of different concentration and, from the calibration curve obtained, Tmab concentration in APPZ supernatant was estimated [33].

Once the concentration of Tmab and PTX in APPZ supernatant was known, the amount of both compounds loaded to the nanosystem was calculated with **Equation 3.2**. As a result, it was found that 8 ng of Tmab and 6.8 µg of PTX were bound per mg of APPZ.

$$IE = \frac{Initial\ concentration - supernatant\ concentration}{APPZ\ concentration} \qquad \textbf{(Equation 3.2)}$$

### *3.3.4. Characterization of conjugated alginate-piperazine nanoparticles*

In order to verify that Tmab and PTX:βCDs inclusion complexes were covalently attached to APPZ, the infrared (IR) absorption spectra of the conjugated APPZ (APPZ-PTX:βCD-T), APPZ, Tmab and β-CDs were performed in the 500-4000 $cm^{-1}$ wavelength range and compared. All samples were frozen and freeze-dried. Then, they were prepared as pellets in dried KBr in a 1:4 weight ratio, since this ratio did not cause saturation in the absorption bands. Comparing the spectrum obtained for the APPZ-PTX:βCD-T with that of bare APPZ, it could be noticed that main changes appeared at 1232, 1704 and 3600-4000 $cm^{-1}$ (**Figure 3.7.A**) [26]. The first shift may correspond to β-CD conjugation to APPZ through ester bonds, while the other two shifts could be related to Tmab binding. Thus, the shift at 1704 $cm^{-1}$ may be assigned to amide bond vibrations, which would be also detected in the 1570-1670 $cm^{-1}$ region if the alginate signal did not mask them [39].

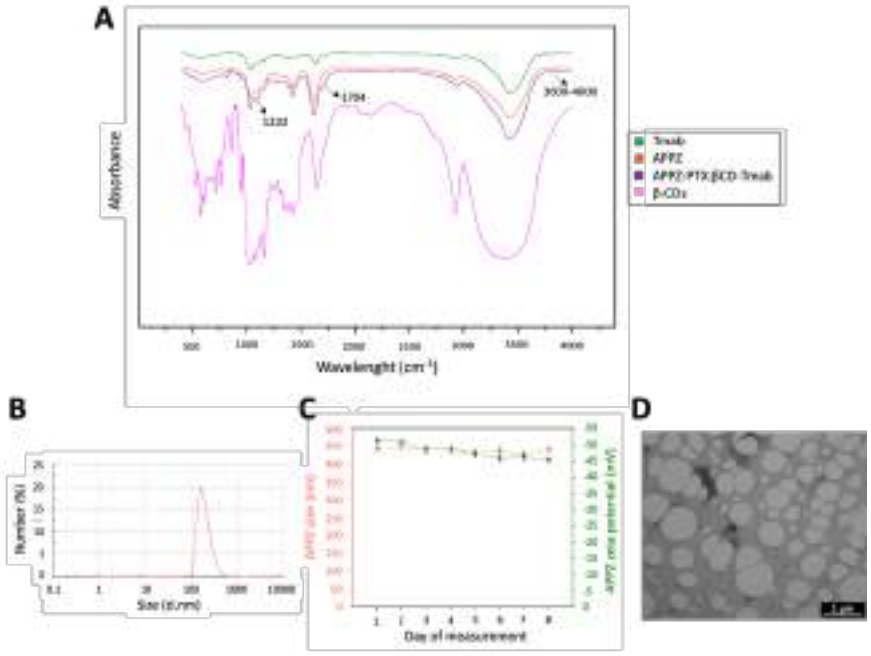


**Figure 3.7.** (**A**) IR absorption spectra of Tmab, APPZ, conjugated APPZ and β-CDs in the 500-4000 $cm^{-1}$ wavelength range; (**B**) Conjugated APPZ particle size distribution, determined by DLS; (**C**) Conjugated APPZ stability over time. All values were obtained again from the mean ± SEM of three different measurements*;* (**D**) Image of conjugated APPZ, acquired by wet STEM.

Otherwise, size and surface charge of conjugated APPZ were also determined at both, the conjugation (4.5 - 4.7) and physiological (7.4) pH. In the latter case, APPZ were suspended in PBS. APPZ hydrodynamic size and zeta potential were 296 ± 50 nm (PDI = 0.4) and -24 ± 1.4 mV in the acidic aqueous suspension (**Figure 3.7.B**). In the saline buffer, they were found to be 359 ± 60 nm (PDI = 0.45) and -26.2 ± 2.1 mV*,* respectively. In addition, both properties were determined during 8 consecutive days to analyze the stability of the conjugated APPZ. Again, it was found that neither the diameter nor the surface charge varied significantly in that period of time (± 23.9 nm and ± 5.9 mV, respectively*)* when the nanocarrier was kept at room temperature (**Figure 3.7.C**) [26].

Finally, to close this section, it should be noted that a sample of the conjugated APPZ was sent to the Advanced Microscopy Laboratory of the Nanoscience Institute of Aragon to acquire images by scanning transmission electron microscopy (STEM). One of the images obtained can be seen in **Figure 3.7.D.**

## 3.4. Validation of the efficacy and HER2-selectivity of conjugated alginate-piperazine nanoparticles with conventional cell cultures

### *3.4.1. Selection and culture of HER2-overexpressing and HER2-non-overexpressing human cell lines*

With the aim of studying the cellular internalization and the anti-tumour activity of the conjugated APPZ, as well as their HER2-selectivity, four distinct human cell lines were selected. BT474 and SKBR3 cells were chosen among the different human breast cancer cell lines which were found to overexpress HER2 in the literature [40,41]. Moreover, an additional HER2+ human ovarian carcinoma cell line was chosen (OVCAR3) [42]. Ultimately, human HS5 stromal cells were selected as negative control for the biological assays.

All the aforementioned cell lines were grown in Dulbecco's modified Eagle's medium (DMEM), supplemented with foetal bovine serum (FBS, 10% (V/V)) and antibiotics (100 U/mL penicillin and 100 mg/mL streptomycin) in a 95:5 air/$CO_2$ atmosphere at 37°C.

Next, their HER2 and active phosphorylated-HER2 (pHER2) expression was determined by means of protein isolation and western blotting. For this purpose, all cells were doubly washed with PBS and incubated for 10 minutes with ice-cold lysis buffer. After scraping the cells from the dishes, they were centrifuged at 4°C at 12,000 rpm for 10 minutes to obtain protein extracts, which were later quantified. These protein extracts were immunoprecipitated, mixing the necessary amount of protein (20 and 1000 μg) with loading buffer and incubating it with Tmab and A-Sepharose at 4°C for at least 2 hours. Immune complexes were

recovered by short centrifugation, followed by three washes with cold lysis buffer. To separate the proteins, samples were then boiled in loading buffer for 7 minutes and resolved in 6% polyacrylamide gels at a 200 V constant voltage using electrophoresis buffer. Once separated, proteins were transferred to a polyvinylidene fluoride (PVDF) membrane in transference buffer for 70 minutes at 500 mA. The membrane was kept in agitation for 1 hour in TBST buffer supplemented with bovine serum albumin (BSA). Then, it was incubated with a solution of Tmab in TBST buffer for another hour at room temperature. After that, the membrane was triply washed with TBST buffer for 7 minutes and incubated with an anti-mouse secondary antibody conjugated with horseradish peroxidase (HRP) for 30 minutes. Finally, the membrane was washed again and, to visualize western blot bands, the membrane was incubated in revealing buffer with $H_2O_2$ for 1 minute. Calnexin was selected as loading control and ImageJ 1.44 Software was employed to quantify the bands obtained. All this procedure can be found described in Cabrera et al. and Montero et al [43,44]. Both works can be consulted for more information about the composition, volume and concentration of the buffers that were used.

Regarding the results obtained, it was noted that total HER2 and pHER2 were great overexpressed in the BT474 and SKBR3 cell lines (**Figure 3.8.A**). OVCAR3 and HS5 cells also expressed this receptor, but to a much lesser extent, as it could be verified when the overexposed western blot (with 1000 µg of protein) was carried out (**Figure 3.8.B**) [26].

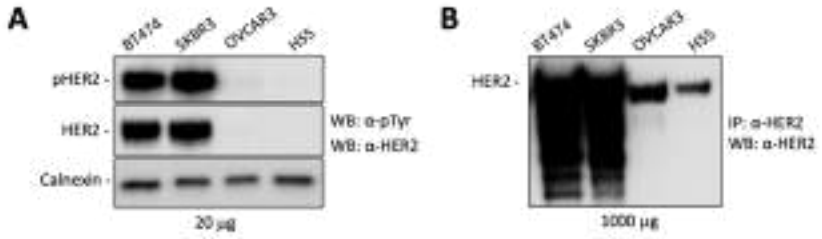


**Figure 3.8.** Study of the HER2- and pHER2-expression level in the BT474, SKBR3, OVCAR3 and HS5 cell lines. Immunoprecipitation was performed with two amounts of protein extract: 20 µg (**A**) and 1000 µg (**B**). Calnexin was employed as loading control.

### *3.4.2. Study of the internalization of conjugated alginate-piperazine nanoparticles in HER2-overexpressing cancer cells*

To study conjugated APPZ internalization in HER2+ cells, the BT474 cell line was chosen. However, before carrying out these assays, the median lethal dose (LD50) of the nanocarrier was determined for these cells, as well as that of the PTX:βCDs complexes.

Thereby, BT474 cells were grown under the conditions already mentioned, and they were seeded into 24-well plates (12,000 cells/well). Next day, once cells were attached, they were treated with different concentrations of APPZ (0.1 - 4.5 mg/mL), conjugated APPZ (0.05 - 3.5 mg/mL) and PTX:βCDs complexes (0.12 - 8.78 µM PTX), keeping some cells untreated as control. Their viability was determined through the performance of MTT assays 48 hours after treatment [45].

This type of assay is widely used to assess cell viability due to its simplicity. It is based on the enzymatic reduction of 3-[4,5-dimethylthiazole-2-yl]-2,5-diphenyltetrazolium bromide (MTT) to MTT formazan, which is catalysed by the mitochondrial succinate dehydrogenase of viable cells. MTT formazan salts are insoluble but, if a detergent solution is employed, cells can be lysed, and the coloured crystals can be solubilized. Then, colorimetric detection can be carried out at 550 - 595 nm and, since the amount of colour produced is directly proportional to the number of viable cells, this number can be inquired [45].

Thus, to calculate the LD50 of the APPZ, conjugated APPZ and PTX:βCDs complexes, MTT reagent (5 mg/mL in PBS) was added to the plate wells (110 µL/well). Cells were incubated at 37°C for 1 hour. Next, culture medium in the wells was discarded and dimethylsulfoxide (DMSO, 500 µL/well) was employed to solubilize the formazan salts generated. Plates were kept under gently agitation for 10 minutes and, finally, well absorbance was determined at 550 nm using a microplate reader. Relative cell viability (%) was calculated from the mean of three replicas according to **Equation 3.3**. The LD50 of the different treatment conditions was

determined with GraphPad Prism software. It was found to be 3.9 mg/mL for APPZ, 1.2 mg/mL for conjugated APPZ and 0.47 nM for free PTX:βCDs complexes.

$$Cell\ viability\ (\%) = \frac{Treated\ cells_{Absorbance}}{Control\ cells_{Absorbance}} \times 100 \qquad \textbf{(Equation 3.3)}$$

Once conjugated APPZ LD50 was known for the BT474 cell line, it was determined whether the nanocarrier cell internalization took place by receptor-mediated endocytosis, as expected because of Tmab anchoring.

For this purpose, breast cancer cells were cultured on coverslips and incubated with DMEM (supplemented with FBS (10%)) and chloroquine (50 µM*)* at 37°C for 1 hour to inhibit lysosomal acidification*.* Later, BT474 cells were treated with a concentration of conjugated APPZ slightly lower than the LD50 (1 mg/mL). HER2 localization was analysed by confocal laser scanning microscopy (CLSM) 0.5, 4, 24 and 48 hours after treatment by employing an anti-HER2 secondary antibody (anti-human Alexa 488). The immunofluorescence assay was performed as described by Esparís-Ogando et al. [46]. As can be seen in **Figure 3.9.A**, the immunofluorescence assay allowed to corroborate that treatment with conjugated APPZ caused progressive accumulation of HER2 in intracellular sites after 4 hours, possibly because of the binding of this membrane receptor to the Tmab loaded to the NPs [26].

In addition, a second immunofluorescence assay was carried out using a secondary antibody against the lysosomal-associated membrane protein-1 (LAMP1). The objective was verifying whether the HER2 fluorescent signal (green), once the conjugated APPZ were internalized, co-localized with that of the lysosomal marker LAMP1 (red). As a result, it was observed that such signal co-localization (orange) occurred, especially after 24 hours of treatment. Therefore, APPZ transporting Tmab and PTX, once endocyted, ended up in breast cancer cell lysosomes (**Figure 3.9.B**) [26].

In both immunofluorescence assays, 4',6-diamidino-2-phenylindole (DAPI) (blue) (0.3 µM) was used to stain cell nucleus.

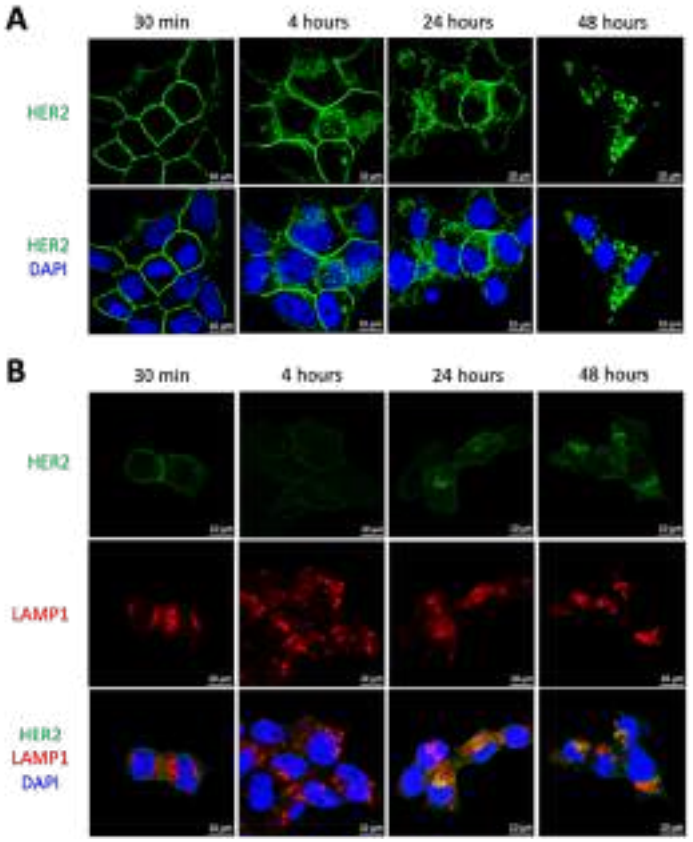


**Figure 3.9**. (**A**) CLSM images that revealed conjugated APPZ internalization in BT474 cells through receptor-mediated endocytosis; (**B**) CLSM images proving that co-localization of the HER2 and LAMP1 fluorescence signals occurred after treatment of BT474 cells with the conjugated APPZ.

### *3.4.3. Determination of HER2-specificity of conjugated alginate-piperazine nanoparticles*

In order to determine if conjugated APPZ had greater HER2-selectivity than the free PTX:βCDs complexes, BT474 and HS5 cells were co-cultured together and treated with both systems. Before carrying out this co-culture, the two human cell lines were grown separately and stained with CellTracker™ Green CMFDA (BT474 cells) and CellTracker™ Red CMPTX (HS5 cells) (20 µM). After 24 hours, BT474 and HS5 cells were

seeded together into 6-well plates, in a 1:2 number ratio (150,000:300,000 BT474/HS5 cells) due to its different proliferation rate. Next day, co-cultures were treated with conjugated APPZ (1 mg/mL) and with PTX:βCDs complexes, maintaining a PTX equivalent concentration (7.9 μM). Regular optical microscopy images were taken 24, 48 and 72 hours after treatment (10x) (**Figure 3.10.A**). In addition, stained cells were also imaged by CLSM with an excitation/detection of 492/517 (CellTracker™ Green) and 577/602 (CellTracker™ Red) nm once 24 and 48 hours elapsed (**Figure 3.10.B)**. The number of living BT474 and HS5 cells was determined from 12 CLSM images, and their average viability rate ± SEM was finally calculated to make comparisons between the two treatment conditions (conjugated APPZ *vs*. free PTX:βCDs complexes).

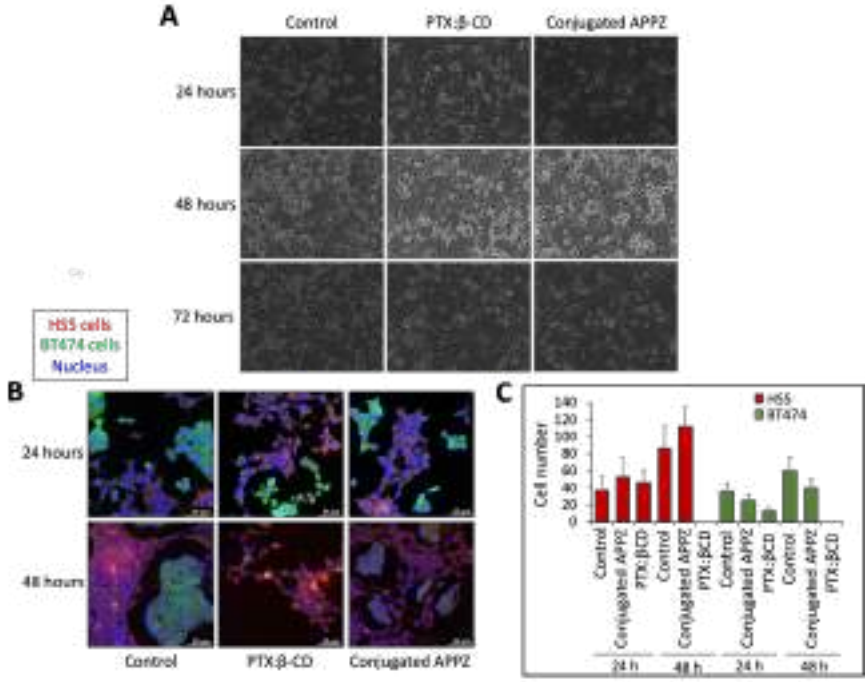


**Figure 3.10.** Assessment of conjugated APPZ HER2-specificity with BT474 and HS5 cell co-cultures. Both cell lines were seeded together and, after treating them with conjugated APPZ and PTX:βCDs complexes, optical (**A**) and confocal microscopy (**B**) images were acquired at different times. From the latter, it was determined the average number of living BT474 and HS5 cells after 48 hours of treatment (**C**).

Results showed that PTX:βCDs complexes were very effective in reducing the viability of HER2+ tumour cells, especially after 48 hours, when practically no BT474 cells were alive. Nevertheless, these inclusion complexes also significantly affected the viability rate of stromal cells, of which none survived after 48 hours. Conversely, after that time, conjugated APPZ managed to reduce HER2+ cell viability rate by a third, approximately, but barely affected that of HS5 cells. In fact, compared to the control, the number of these living cells increased after both, 24 and 48 hours of treatment, perhaps because when BT474 suffered from apoptosis, HS5 cells had greater surface area available to proliferate [26].

### *3.4.4. Cytotoxicity of conjugated alginate-piperazine nanoparticles as a function of the HER2 cell expression level*

Selectivity of conjugated APPZ was re-analysed, together with their anti-tumour activity, with the performance of further MTT assays, which were carried out with the four cell lines mentioned in point 3.4.1 of this Chapter (page 95).

In this manner, after being grown, BT474, SKBR3, OVCAR3 and HS5 cells were seeded into 24-well plates (12,000 cells/mL, except for the OVCAR3 line, from which 18,000 cells/mL were seeded). Next day, the culture media of the wells was replaced by supplemented medium containing PBS (for the control), PTX:βCDs complexes (7.9 μM PTX), Tmab (0.06 nM), APPZ (1 mg/mL) and conjugated APPZ (1 mg/mL). Again, a concentration of conjugated APPZ slightly lower than the LD50 for the BT474 line at 48 hours was chosen to perform these assays, in which the viability of the different cells was determined each 24 hours for a total of 72 hours. All MTT assays were performed as before, measuring the absorbance of the wells at 550 nm. Taking as reference a control of untreated cells, viability data for the different treatment conditions was determined by employing **Equation 3.3** (page 98). Results obtained can be seen in **Figure 3.11**, in which the average viability values ± SEM of four replicas for each treatment have been represented. Henceforth, in order to assess the significance of the cytotoxicity observed among the different treatment conditions in MTT assays, unpaired two-tailed Student t-tests

were conducted. *p*-values less than 0.05 were considered statistically significant.

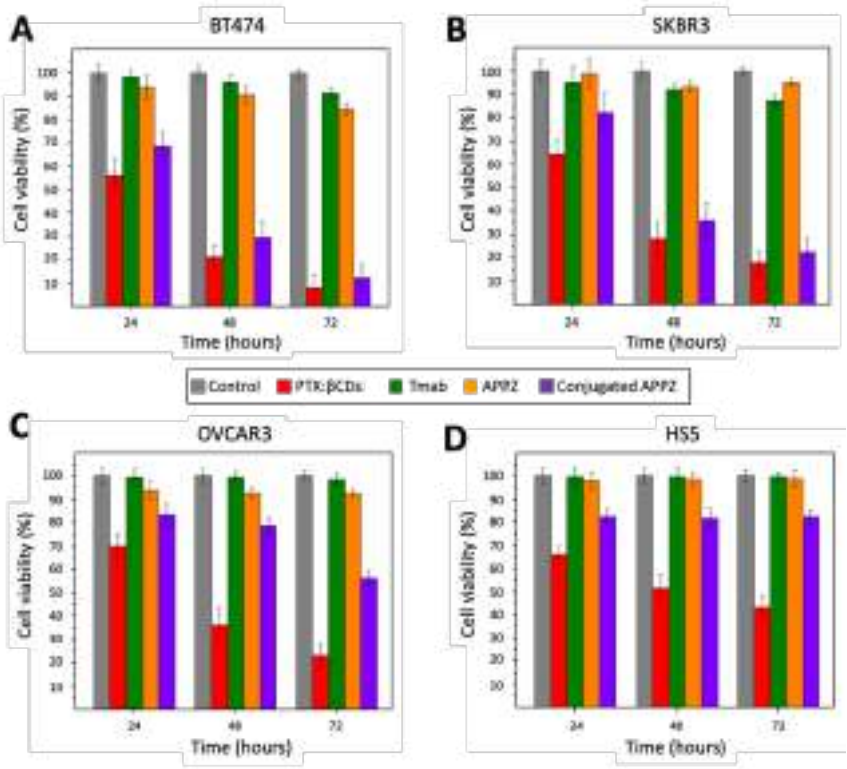


**Figure 3.11.** Viability rates of BT474 (**A**), SKBR3 (**B**), OVCAR3 (**C**) and HS5 (**D**) cells determined by MTT assays after treatment with free PTX:βCDs complexes (7.9 μM), Tmab (0.06 nM), APPZ (1 mg/mL) or conjugated APPZ (1 mg/mL).

As can be seen in **Figure 3.11**, treatment with bare APPZ did not significantly affect the viability of any cell line, except that of BT474 cells, which was reduced by approximately 20% after 72 hours. Otherwise, the free-administered antibody only affected the survival rate of HER2+ breast cancer cells. Furthermore, since a very low Tmab concentration was used, the cytotoxic effect of the antibody was mild. At last, conjugated APPZ were shown to be almost as efficient as the free PTX:βCDs complexes when they were administered to BT474 and SKBR3 cells, in which HER2 was clearly overexpressed. However, these NPs were not as toxic to the OVCAR3 and HS5 lines, which did not exhibit such HER2 overexpression. In point of fact, APPZ-PTX:βCD-T influenced especially little the survival of stromal cells. Therefore, the nanocarrier was shown to be highly effective

in inhibiting the growth of HER2-overexpressing tumours, while having greater selectivity than the inclusion complexes of the parent drug ($p < 0.05$) [26].

Finally, further MTT assays were carried out but, this time, only with the BT474 and HS5 cell lines. The objective of performing these last viability assays was comparing the antiproliferative activity of conjugated APPZ with that of free PTX, as well as verifying if NP decoration by Tmab made APPZ more selective.

Thereby, BT474 and HS5 cells were treated with the same systems as before and, in addition, with free PTX (not included into β-CDs) (7.9 µM) and APPZ conjugated only with PTX:βCDs complexes (1 mg/mL). The same procedure as before was followed to perform MTT assays. Results obtained on this occasion have been included in the **Figure 3.12**. Again, the average viability values ± SEM of four replicas for each treatment have been represented.

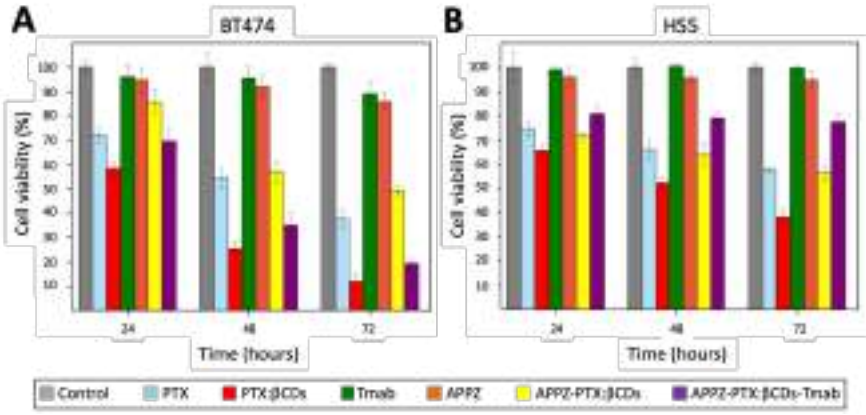


**Figure 3.12.** Viability rates of BT474 (**A**) and HS5 (**B**) cells determined by MTT assays after being treated with free PTX (7.9 µM), PTX:βCDs complexes (7.9 µM), Tmab (0.06 nM), APPZ (1 mg/mL), APPZ-PTX:βCDs (1 mg/mL) and APPZ-PTX:βCDs-T (1 mg/mL).

As can be corroborated in **Figure 3.12**, conjugated APPZ had more remarkable anti-tumour activity than the taxane ($p < 0.05$), which had greater therapeutic activity when included into β-CDs. Besides, Tmab binding to APPZ conferred them great properties, since the NPs that were

not loaded with the antibody reduced the viability of the HER2+ cancer cells in a less notable manner and were more toxic to stromal cells [26].

## 3.5. Validation of the efficacy of the conjugated alginate-piperazine nanoparticles with conventional HER2-positive tumour spheroids

To close this chapter, the anti-cancer activity of the conjugated APPZ was also studied in HER2+ tumour spheroids.

Solid tumours grow in a three-dimensional (3D) spatial conformation, resulting in a diffusion-limited distribution of oxygen, nutrients, metabolites and signalling molecules that is not mimicked in two-dimensional (2D) monolayer cell cultures. In addition, 3D cell-cell and cell-ECM interactions determine cell structure, adhesion and signalling and, consequently, general cell function. For this reason, 3D models are being specifically used in cancer research as intermediates between *in vitro* cancer cell line cultures and *in vivo* tumours. They are employed to study, for instance, chemo- and radiotherapy cell responses, tumorigenicity, and migration and invasion processes [47].

Among the numerous 3D spherical cancer models that can be developed, multicellular tumour spheroids (MCTS) were the ones generated to assess conjugated APPZ effectiveness. The reason was that it has been firmly stablished that MCTS mimic drug sensitivity behaviour of *in vivo* tumours in a more accurate manner than cancer cells cultured under monolayer conditions, and that they are suitable for high throughput screening assays [47,48].

### *3.5.1. Development of BT474 multicellular tumour spheroids*

Popularly, MCTS are generated in non-adherent conditions from single-cell suspensions after 1 to 7 days of culture, and they can attain 1 to 3 mm in diameter [47]. The most employed techniques used to achieve MCTS growth are the hanging-drop method, suspension cultures and the

liquid overlay technique [47,49], being the latter the one chosen in this work to generate BT474 spheroids.

First, cells from this line, which was preferred because SKBR3 cells are able to form loose aggregates but not spheroids [50], were grown in monolayer. Subsequently, BT474 cells were seeded into 96-well, U-shape-bottom plates (2,000 cells/well) treated by the manufacturer to offer low-cell attachment. Then, they were incubated for 3 days, without renewing their culture medium [49]. After that time, spheroid size and morphology were analysed by optical microscopy (4x) after transferring cells to slides carefully. It was found that these bio-structures, with a diameter slightly greater than 1 mm, had a perfect round shape (**Figure 3.13**).

**Figure 3.13.** Optical microscopy image of one of the BT474 MCTS developed.

### *3.5.2. Determination of the toxicity of conjugated alginate-piperazine nanoparticles to BT474 tumour spheroids*

Once BT474 spheroids were obtained, the anti-tumour activity of the conjugated APPZ was validated with them, comparing it with that of the PTX:βCDs complexes. For this, after having allowed the MCTS to grow for 3 days, the medium in the wells was replaced by fresh medium containing PBS (control), PTX:βCDs complexes (7.9 μM) or conjugated APPZ (1 mg/mL). Thus, the same treatment concentrations that in the 2D assays were employed. Cell viability was studied in two different ways: by cell-counting after 48 hours of treatment, and by CLSM after 48 and 72 hours of treatment.

For the first type of assays, culture medium was removed from the wells and spheroids were washed with PBS (100 µl/well) 48 hours after cell treatment. Later, PBS was discarded, and spheroids were incubated with trypsin (1x) (50 µl/well), which was used to disaggregate the 3D cell structures, at 37°C. After 4 minutes, fresh medium was added to inactivate trypsin (150 µl/well) and spheroids were transferred to Eppendorfs. They were centrifuged (1400 rpm, 4 minutes) and disaggregated cells were re-suspended in fresh media. Finally, samples of the resulting cellular suspensions (100 µl) were mixed with trypan blue in a 1:1 volume ratio. The number of living and dead BT474 cells for each treatment condition was determined with an automated cell counter *(***Figure 3.14.A**).

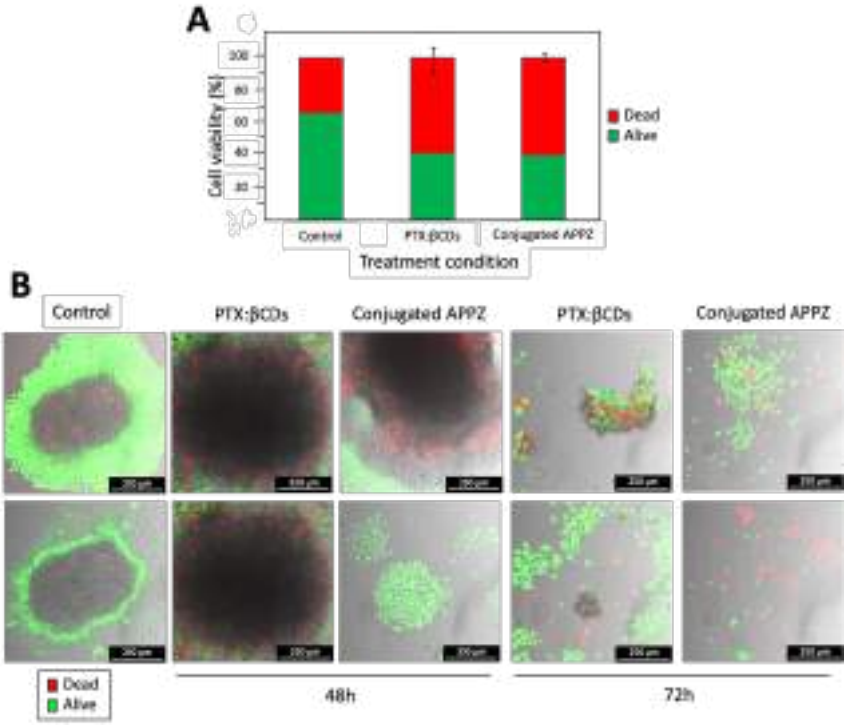


**Figure 3.14.** (**A**) Results obtained when performing cell-counting after 48 hours of spheroid treatment with PTX:βCDs complexes (7.9 µM PTX) and conjugated APPZ (1 mg/mL); (**B**) CLSM images of BT474 spheroids acquired 48 and 72 hours after treatment with PTX:βCDs and conjugated APPZ concentrations similar to those employed in the cell-counting assay.

In large MCTS (> 500 μm diameter), a necrotic core is surrounded by a viable rim, with an inner layer of quiescent cells and an outer layer of proliferating cells. This tumour cell heterogeneity is due to growth factor deprivation, nutrient and oxygen gradients, and catabolite accumulation, and explains why control spheroids showed about 66% viability [47]. Regarding the viability of the BT474 spheroids that were treated with the PTX:βCDs complexes and the conjugated APPZ, it should be noted that it was practically the same (41-42%) and, as expected, higher than that shown by BT474 cells after 48 hours of treatment in the 2D MTT assays (close to 30%). In any case, conjugated APPZ effectiveness was also revealed in 3D cell cultures.

Finally, regarding the alive/dead CLSM assays, it should be highlighted that they were performed 48 and 72 after spheroid treatment, using calcein AM (1 μM) and propidium iodide (3 drops/dish) to distinguish the living cells from the dead ones. Thereby, spheroids were transferred to glass-bottom dishes 24 hours before treatment and, 30 minutes before acquiring CLSM images, cells were stained with the mentioned dyes. They were imaged with an excitation/detection of 494/517 (calcein AM) and 535/617 (propidium iodide) nm (**Figure 3.14.B**).

In the images that were obtained, especially those of the controls, the necrotic core, characteristic of large MCTS, could be well appreciated. Likewise, it could be observed that treatment with the PTX:βCDs complexes increased the number of BT474 cells dead after 48 hours. This increase was not so remarkable after conjugated APPZ treatment, but it was showed these NPs were able to disaggregate BT474 spheroids and decrease their size. At last, after 72 hours of treatment, both PTX:βCDs complexes and conjugated APPZ were capable of disintegrating the 3D cellular structures and reducing the viability of the HER2+ cancer cells in a similar manner, so the effectiveness of the conjugated APPZ in 3D cell cultures was again proven [26].

## 3.6. Conclusions

· Different sodium alginate and piperazine NPs were obtained thanks to the electrostatic interactions that occurred between both compounds at pH 4.6 – 4.8. These APPZ were characterized, and the smallest ones (162.5 nm, -16.2 mV) were selected for further characterization and conjugation.

· When the pH of the APPZ suspension oscillated between 3 and 6, NP size did not undergo significant modifications. However, above and below these pH values, APPZ diameter increased considerably. Besides, the more acidic the pH of the NP suspension, the more positive their zeta potential.

· The APPZ obtained were stable for 8 days when preserved at room temperature, since neither their size nor their surface charge varied significantly.

· PTX was included into β-CD molecules to improve its pharmacokinetics. The resulting complexes, along with Tmab, were covalently bound to APPZ by means of the carbodiimide chemistry. The amount of Tmab and PTX found to be loaded was 8 ng and 6.8 µg/mg APPZ, respectively.

· Conjugated APPZ had a 296 nm size and -24 mV zeta potential when suspended in $H_2O$(d) and, like bare APPZ, were stable for 8 days at room temperature.

· Conjugated APPZ were internalized in HER2+ breast carcinoma cells by receptor-mediated endocytosis after 4 hours of treatment. After 24 hours, they could be found in the lysosomes of the treated cells.

· When validated in conventional cell cultures, APPZ-PTX:βCD-T reduced the viability of HER2+ breast tumour cells in a similar manner than equivalent free PTX:βCDs complexes, and even greater than free PTX. Furthermore, conjugated APPZ were significantly more selective than the taxane complexes, since they were not as toxic to stromal cells.

· When validated in 3D HER2+ MCTS, APPZ-PTX:βCD-T maintained their therapeutic activity: concentrations of conjugated APPZ lower than the

LD50 for BT474 monolayer cultures were capable of notably reducing the viability of HER2+ tumours spheroids and disaggregate them.

## 3.7. Published articles related to this chapter

· Nieto C, Centa A, Rodríguez-Rodríguez JA, Pandiella A, Martín del Valle EM. Paclitaxel-trastuzumab mixed nanovehicle to target HER2-overexpressing tumours. Nanomaterials 2019; 9:948.

## 3.8. Abbreviations

ADC – Antibody-drug conjugate
ADCC – Antibody-dependent cellular cytotoxicity
APPZ – Alginate-piperazine nanoparticles
APPZ-PTX:βCDs-T – Alginate-piperazine nanoparticles covalently conjugated with paclitaxel:β-cyclodextrin inclusion complexes and trastuzumab
BSA – Bovine serum albumin
CD – Cyclodextrin
CLSM – Confocal laser scanning microscopy
DAPI – 4',6-amidino-2-phenylindole
DDS – Drug delivery system
DLS – Dynamic light scattering
DMEM – Dulbecco's modified Eagle's Medium
DMSO - Dimethylsulfoxide
EBC – Early breast cancer
ECD – Extracellular domain
ECM – Extracellular matrix
EGFR – Epidermal growth factor receptor
EMA – European Medicines Agency
FBS – Foetal bovine serum
FDA – U.S. Food and Drug Administration
HER – Human epidermal growth factor receptor
HER2+ - Human epidermal growth factor receptor-2-positive
HPLC – High-performance liquid chromatography
HRP – Horseradish peroxidase

HSA – Human serum albumin
$H_2O$(d) – Deionized water
IR – Infrared
LAMP-1 – Lysosomal-associated membrane protein-1
LD50 – Median lethal dose
mAb – Monoclonal antibody
MBC – Metastatic breast cancer
MCTS – Multicellular tumour spheroids
MDR – Multidrug resistance
MSN – Mesoporous silica nanoparticle
MTT – 3-[4,5-dimethylthiazol-2-yl]-2,5-diphenyltetrazolium bromide
NCI – U.S. National Cancer Institute
NP – Nanoparticle
PBS – Phosphate buffered saline
PDI – Polydispersity index
pHER2 – phosphorylated human epidermal growth factor receptor-2
PLGA – Poly(lactic-co-glycolic acid)
PTX – Paclitaxel
PVDF – Polyvinylidene difluoride
RTK – Receptor tyrosine kinase
SEM – Standard error of mean
STEM – Scanning transmission electron microscopy
T-DM1 – Ado-trastuzumab emtansine
Tmab – Trastuzumab
WHO – World Health Organization
2D – Two-dimensional
3D – Three-dimensional

## 3.9. References

[1] Hanahan D, Weinberg RA. The hallmarks of cancer. Cell 2000; 100:57-70.
[2] Nieto C, Vega MA, Martín del Valle, EM. Trastuzumab: more than a guide in HER2-positive cancer nanomedicine. Nanomaterials 2020; 10:1674.
[3] Shen G, Gao G, Liu F, Zhang Y, Dai M, Zhao T, Cheng M, Xu T, Jin P, Yin W et al. The Wnt3a/β-catenin/TCF7L2 signalling axis reduces the sensitivity of HER2-

positive epithelial ovarian cancer to trastuzumab. Biochem Biophys Res Commun. 2020; 523(3):685-91.

[4] Xiang R, Han X, Ding K, Wu Z. CMIP promotes Herceptin resistance of HER2 positive gastric cells. Pathol Res Pract. 2020; 216(2):152776.

[5] Oh D-Y, Bang Y-J. HER2-targeted therapies – a role beyond breast cancer. Nat Rev Clin Oncol. 2020; 17:33-48.

[6] Connell CM, Doherty GJ. Activating HER2 mutations as emerging targets in multiple solid cancers. ESMO Open 2017; 2:e000279.

[7] Godoy-Ortiz A, Sánchez-Muñoz A, Chica Parrado MR, Álvarez M, Ribelles N, Rueda Domínguez A, Alba E. Deciphering HER2 breast cancer disease: biological and clinical implications. Front Oncol. 2019; 9:1124.

[8] Blackwell K, Gligorov J, Jacobs I, Twelves C. The global need for a trastuzumab biosimilar for patients with HER2-positive breast cancer. Clin Breast Cancer 2018; 18:95–113

[9] Rinnerthaler G, Gampenrieder SP, Greil R. HER2 directed antibody-drug-conjugates beyond TDM-1 in breast cancer. Int J Mol Sci. 2019; 20(5):1115.

[10] Kulhari H, Pooja D, Rompicharla SVK, Sistla R, Adams DJ. Biomedical applications of trastuzumab: as a therapeutic agent and a targeting ligand. Med Res Rev. 2015; 35(4):849-76.

[11] Zhou Z, Badkas A, Stevenson M, Lee J-Y, Leung Y-K. Herceptin conjugated PLGA-Phis-PEG pH sensitive nanoparticles for targeted and controlled drug delivery. Int J Pharm. 2015; 487(1-2):81-90.

[12] Mehata AK, Bharti S, Singh P, Viswanadh MK, Kumari L, Agrawal P, Singh S, Koch B, Muthu MS. Trastuzumab decorated TPGS-g-chitosan nanoparticles for targeted breast cancer therapy. Colloids Surf B 2019; 173:366-77.

[13] Kubota T, Kuroda S, Kanaya N, Morihiro T, Aoyama K, Kakiuchi Y, Kikuchi S, Nishizaki M, Kagawa S, Tazawa H et al. HER2-targeted gold nanoparticles potentially overcome resistance to trastuzumab in gastric cancer. Nanomedicine 2018; 14(6):1919-29.

[14] Amin M, Pourshohod A, Kheirollah A, Afrakhteh M, Gholami-Borujeni F, Zeinali M, Jamalan M. Specific delivery of idarubicin to HER2-positive breast cancerous cell line by trastuzumab-conjugated liposomes. J Drug Deliv Sci Tech. 2018; 47:209-14.

[15] Cortes J, Saura C. Nanoparticle albumin-bound (*nab*$^{TM}$)-paclitaxel: improving efficacy and tolerability by targeted drug delivery in metastatic breast cancer. EJC Suppl. 2010; 8(1):1-10.

[16] Sun B, Ranganathan B, Feng S-S. Multifunctional poly(D-L-lactide-co-glycolide) montmorillonite (PLGA/MMT) nanoparticles decorated by trastuzumab for targeted chemotherapy of breast cancer. Biomaterials 2008; 29(4):475-86.

[17] Loibl S, Gianni L. HER2-positive breast cancer. Lacet 2017; 389(10087):2415-29.

[18] Slamon DJ, Leyland-Jones B, Shak S, Fuchs H, Paton V, Bajamonde A, Fleming T, Eiermann W, Wolter J, Pegram M et al. Use of chemotherapy plus a monoclonal antibody against HER2 for metastatic breast cancer that overexpress HER2. N Eng J Med. 2001; 344:783-92.

[19] Carbognin L, Sperduti I, Nortilli R, Brunelli M, Vicentini C, Pellini F, Pollini GP, Giannarelli D, Tortora G, Bria E. Balancing activity and tolerability of neoadjuvant paclitaxel- and docetaxel-based chemotherapy for HER2-positive early-stage breast cancer: sensitivity analysis of randomized trials. Cancer Treat Rev. 2015; 41:262-70.

[20] Ferriols Lisart F, Ferriols Lisart R, Magraner Gil J. Evaluación farmacoeconómica del docetaxel versus paclitaxel en el tratamiento del cáncer de mama metastásico. Farm Hosp. 2000, 24(4):226-40.

[21] PubMed Database. Available online: https://pubmed.ncbi.nlm.nih.gov/?term=paclitaxel+nanoparticles&filter=years.2010-2020 (accessed on 31th March 2021).

[22] PubMed Database. Available online: https://pubmed.ncbi.nlm.nih.gov/?term=docetaxel+nanoparticles&filter=years.2010-2020 (accessed on 31th March 2021).

[23] Weaver BA. How Taxol/paclitaxel kills cancer cells. MBoC 2014; 25:2677-81.

[24] Zhu L, Chen L. Progress in research on paclitaxel and tumor immunotherapy. Cell Mol Biol Lett. 2019; 24:40.

[25] Khalifa AM, Elsheikh MA, Khalifa AM, Elnaggar YSR. Current strategies for different paclitaxel-loaded nano-delivery systems towards therapeutic applications for ovarian carcinoma: a review article. J Control Release 2019; 311-12:125-37.

[26] Nieto C, Centa A, Rodríguez-Rodríguez JA, Pandiella A, Martín del Valle EM. Paclitaxel-trastuzumab mixed nanovehicle to target HER2-overexpressing tumours. Nanomaterials 2019; 9:948.

[27] Martín del Valle, EM. Cyclodextrins and their uses: a review. Process Biochem. 2004; 39:1033-46.

[28] Zhang D, Lv P, Zhou C, Zhao Y, Liao X, Yang B. Cyclodextrin-based delivery systems for cancer treatment. Mater Sci Eng. C 2019; 96:872-86.

[29] Tian B, Hua S, Liu J. Cyclodextrin-based delivery systems for chemotherapeutic anticancer drugs: a review. Carbohydr Polym. 2020; 232:115805.

[30] Song S, Gao K, Niu R, Yi W, Zhang J, Gao C, Yang B, Liao X. Binding behaviour, water solubility and in vitro toxicity of inclusion complexes between ursolic acid and amino-appended *β-cyclodextrins. J Mol Liq. 2019; 296:111993.*

[31] Sorasitthiyanukarn FN, Muangnoi C, Bhuket PRN, Rojsitthisak P, Rojsitthisak P. Chitosan/alginate nanoparticles as a promising approach for oral delivery of curcumin diglutaric acid for cancer treatment. Mater Sci Eng C Mater Biol Appl. 2018; 93:178-90.

[32] Samie N, Muniandy S, Kanthimathi MS, Haerian BS, Azudin RER. Novel piperazine core compound induces death in human liver cancer cells: possible pharmacological properties. Sci Rep. 2016; 6:24172.

[33] Román JV, Rodríguez-Rodríguez JA, Martín del Valle EM, Galán MA. Synthesis of a new nanoparticle system based on electrostatic alginate-piperazine interactions. Polym Adv Tecnol. 2016; 27:623-29.

[34] Bhattacharjee S. DLS and zeta-potential – what they are and what they are not? J Control Release 2016; 235:337-51.

[35] Alcaro S, Ventura CA, Paolino D, Battaglia D, Ortuso F, Cattel L, Puglisi G, Fresta M. Preparation, characterization, molecular modeling and in vitro activity of paclitaxel-cyclodextrin complexes. Bioor Med Chem Lett. 2002; 12:1637-41.

[36] Hamada H, Ishihara K, Masuoka N, Mikuni K, Nakajima N. Enhancement of water-solubility and bioactivity of paclitaxel using modified cyclodextrins. J Biosci Bioeng. 2006; 102(4):369-71.

[37] Madison SA, Carnali JO. pH optimization of amidation via carbodiimides. Ind Eng Chem Res. 2013; 52:13547-55.

[38] Bradford MM. A rapid and sensitive method for the quantitation of microgram quantities of protein utilizing the principle of protein-dye binding. Anal Biochem. 1976; 72(1-2):248-54.

[39] Hua J, Li Z, Xia W, Yang N, Gong J, Zhang J, Qiao C. Preparation and properties of EDC/NHS mediated crosslinking poly (gamma-glutamic acid)/ epsilon-polylysine hydrogels. Mater Sci Eng. C 2016; 61:879-92.

[40] Subik K, Lee J-F, Baxter L, Strzepek T, Costello D, Crowley P, Xing L, Hung M-C, Bonfiglio T, Hicks DG et al. The expression patterns of ER, PR, HER2, CK5/6, EGFR, Ki-67 and AR by immunohistochemical analysis in breast cancer cell lines. Breast Cancer 2014; 4:35-41.

[41] Neve RM, Chin K, Fridlyand J, Yeh J, Baehner F, Fevr T, Clark L, Bayani N, Coppe J-P, Tong F et al. A collection of breast cancer cell lines for the study of functionally distinct cancer subtypes. Cancer Cell 2006; 10(6):515-27.

[42] Lanitis E, Dangaj D, Hagemann IS, Song D-G, Best A, Sandaltzopoulos R, Coukos G, Powell DJ. Primary human ovarian epithelial cancer cells broadly express HER2 at immunologically-detectable levels. PLoS One 2012; 7(11):e49829.

[43] Montero JC, Seoane S, Ocaña A, Pandiella A. P-Rex1 participates in neuregulin-ErbB signal transduction and its expression correlates with patient outcome in breast cancer. Oncogene 2011; 30:1059-71.

[44] Cabrera N, Díaz-Rodríguez E, Becker E, Martín-Zanca D, Pandiella A. TrkA receptor ectodomain cleavage generates a tyrosine-phosphorylated cell-associated fragment. J Cell Biol. 1996; 132(3):427-36.

[45] Mosmann T. Rapid colorimetric assay for cellular growth and survival: application to proliferation and cytotoxicity assays. J Immunol Methods 1983; 65:55-63.

[46] Esparís-Ogando A, Díaz-Rodríguez E, Montero JC, Yuste L, Crespo P, Pandiella A. Erk5 participates in neuregulin signal transduction and is constitutively active in breast cancer cells overexpressing Erb2. Mol Cell Biol. 2002; 22:270-85.

[47] Weiswald L-B, Bellet D, Dangles-Marie V. Spherical cancer models in tumour biology. Neoplasia 2015; 17(1):1-15.

[48] Nath S, Devi GR. Three-dimensional culture systems in cancer research: focus on tumour spheroid model. Pharmacol Ther. 2016; 163:94-108.

[49] Froehlich K, Haeger J-D, Heger J, Pastuschek J, Photini SM, Yan Y, Lupp A, Pfarrer C, Mrowka R, Schleuner et al. Generation of multicellular breast cancer tumor spheroids: comparison of different protocols. J Mammary Gland Biol Neoplasia 2016; 21(3-4):89-98.

[50] Ivascu A, Kubbies M. Diversity of cell-mediated adhesions in breast cancer spheroids. Int J Oncol. 2007; 31(6):1403-13.

nanomaterials

MDPI

Article

# Paclitaxel-Trastuzumab Mixed Nanovehicle to Target HER2-Overexpressing Tumors

**Celia Nieto [1], Ariana Centa [1], Jesús A. Rodriguez-Rodriguez [1], Atanasio Pandiella [2], Eva M. Martin del Valle [1,*]**

[1] Departamento de Ingeniería Química y Textil, Facultad de Ciencias Químicas, Universidad de Salamanca, 37008 Salamanca, Spain

[2] Instituto de Biología Molecular y Celular del Cáncer (IBMCC), CSIC, CIBERONC-IBSAL, 37007 Salamanca, Spain

* Correspondence: emvalle@usal.es; Tel.: +34-923294479

Received: 10 June 2019; Accepted: 28 June 2019; Published: 29 June 2019

**Abstract:** Paclitaxel is one of the most widely used chemotherapeutic agents thanks to its effectiveness and broad spectrum of antitumor activity. However, it has a very poor aqueous solubility and a limited specificity. To solve these handicaps, a novel paclitaxel-trastuzumab targeted transport nanosystem has been developed and characterized in this work to specifically treat cancer cells that overexpress the human epidermal growth factor receptor-2 (HER2). Methods: Alginate and piperazine nanoparticles were synthetized and conjugated with paclitaxel:β-cyclodextrins complexes and trastuzumab. Conjugated nanoparticles (300 nm) were characterized and their internalization in HER2-overexpressing tumor cells was analyzed by immunofluorescence. Its specific antitumor activity was studied *in vitro* using human cell lines with different levels of HER2-expression. Results: In comparison with free paclitaxel:β-cyclodextrins complexes, the developed conjugated nanovehicle presented specificity for the treatment of HER2-overpressing cells, in which it was internalized by endocytosis. Conclusions: It seems that potentially avoiding the conventional adverse effects of paclitaxel treatment could be possible with the use of the proposed mixed nanovehicle, which improves its bioavailability and targets HER2-positive cancer cells.

**Keywords:** targeted nanoparticles; paclitaxel; trastuzumab; HER2-specificity; sodium alginate; piperazine

## 1. Introduction

Cancer therapy improvement has become one of the most important health challenges for the time being due to the high incidence of this disease. Systemic chemotherapy is the necessary choice when cancer is late diagnosed and, unfortunately, it is often accompanied by severe side effects [1,2]. As most employed cytotoxic agents affect cell cycle progression, not only cancer cells are killed by antitumor drugs, but also normal cells that proliferate rapidly [3,4].

Such side effects are present, for instance, in paclitaxel (PTX)-containing treatments. This taxane diterpenoid drug targets β-tubulin in cells and arrests them in the G2/M cell cycle phase [5]. Due to its broad spectrum of antitumor activity and high effectiveness, it is normally employed to treat breast, ovarian, and non-small cell lung cancers [6]. In this manner, PTX is one of the three most administered chemotherapy agents today, but it presents an important handicap. Its aqueous solubility is very limited (0.3–0.5 μg/mL) and intravenous PTX's formulations have had to be developed [7]. Among them, they are only two that are approved to be used in clinic and the major drawback is that, in the most used one [5], PTX is dissolved into a chemical solvent mixture that

entails important side effects. Thus, such mixture reduces the taxane effectiveness and limits the doses that can be administered to patients [6].

In this context, the need of novel PTX's therapeutic systems and the relevance of the nanomedicine field in this task are understood. Nowadays, PTX inclusion complexes with cyclodextrins as well as PTX polymeric nanoparticles, liposomes, micelles, and polymeric conjugates can be found in the literature [6,8–11]. All of them look for an improved vehiculization of the taxane and this fact can be achieved by the addition of a specific monoclonal antibody (mAb) to the nanosystems. mAbs are excellent targeting proteins and their inclusion in drug delivery vehicles could enhance their endocytosis and lysosomal degradation, with the resulting release of the cytotoxic agent [12].

One humanized mAb approved by the U.S. Food and Drug Administration (FDA) is trastuzumab. It binds to the extracellular domain of the HER2/neu receptor, inhibits downstream signaling and activates immune mechanisms that ultimately contribute to its antitumor effect [13]. HER2 is overexpressed in a variety of carcinomas, like breast, ovarian, lung, and gastric tumors [14,15]. Among them, trastuzumab administration is allowed to treat HER2-positive metastatic breast cancers and HER2-positive stomach tumors and it has transformed the complicated prognosis of these subtypes of carcinomas [16]. Nevertheless, although this mAb has demonstrated a proper antitumor efficacy, it is normally administered in combination with chemotherapeutic drugs, like taxanes, to enhance the effect of both of them [14,17]. However, one of the limitations of trastuzumab-taxane therapies is their toxicity.

Given everything here mentioned, the objective of the present work has been the development, characterization, and validation of a novel administration PTX's nanovehicle, consisting of sodium alginate and piperazine nanoparticles (APPZ) [18]. In such nanosystem, PTX has been included into β-cyclodextrins molecules (βCD) to improve its water-solubility. Moreover, trastuzumab has also been attached to APPZ surface. The aim of the addition of this antibody was to favor specific targeting of HER2-overexpressing cancer cells.

Of the chemical compounds named above, sodium alginate is a harmless anionic polysaccharide that is commonly used as a gelling agent for cosmetic and food products [19]. As for piperazine, it is a heterocyclic compound having two nitrogen atoms at opposite positions in a six membered ring that confer it a potent antioxidant power [20]. Piperazine derivatives have been developed in recent years as a basis for alternative antitumor agents and, in our case, such chemical compound allowed a chemical crosslinking of the sodium alginate chains and, thus, the formation of nanoparticles [18,21]. Finally, βCD are cyclic oligosaccharides with a hydrophobic interior. These molecules are able to form inclusion complexes with a variety of lipophilic molecules and are used for many pharmaceutical applications [22]. Besides, βCD have become commonly employed in nanoparticle-based drug delivery systems thanks to their benefits [23–25] and some nanovehicles based on βCD-PTX complexes have been already describe in literature [26,27].

## 2. Materials and Methods

### 2.1. APPZ Synthesis and Characterization

APPZ were synthesized by preparing sodium alginate (1 mg/mL) and piperazine (2 mg/mL) solutions with a 4.7 pH value [18]. Different amounts of the piperazine solution were dropped over the alginate one. The mixture was magnetically stirred and suspensions of APPZ with different properties were obtained. To isolate them, pH of the suspensions was dropped to 1.0 and APPZ were centrifuged.

In order to characterize them, APPZ were re-suspended in deionized water (1 mg/mL). The pH of these suspensions was set again at 4.7. APPZ sizes and zeta potentials were measured by Light Scattering (DLS) and Laser Doppler Electrophoresis (LDE) with a 90° fixed angle detector, using a 633 nm wavelength laser (ZetaSizer Nano ZS90, Malvern Instruments Inc., Royston, Hertfordshire, UK). APPZ with the best size/surface charge values were selected and pH effect over both parameters was studied with them. Variation of their diameter and zeta potential was

over 8 consecutive days to determine APPZ stability over time. In addition, such properties were also studied at pH 7.2, re-suspending selected APPZ in PBS.

### 2.2. Preparation of PTX:βCD Inclusion Complexes

PTX:βCD complexes were prepared by means of a freeze-dying method. PTX was dissolved in pure ethanol (0.8 mg/mL) in dark conditions, whereas βCD were dissolved in deionized water (0.9 mg/mL). βCD aqueous solution was added to the PTX one (1:1 molar ratio) and the resulting hydroalcoholic solution was mechanically stirred for 5 hours. Then, it was freeze-dried and dissolved in deionized water [28,29]. PTX inclusion efficiency in βCD was analyzed by mass spectrometry (LC 2795 chromatograph connected to a ZQ-4000 mass spectrometer, Waters Corporation, Milford, MA, USA) [30].

### 2.3. APPZ Conjugation with Trastuzumab and PTX:βCD Complexes and Conjugated APPZ Characterization

1-Ethyl-3-(3-dimethylaminopropyl)carbodiimide/N-hydroxysuccinimide (EDC/NHS) coupling chemistry was the one selected to conjugate APPZ with trastuzumab and the obtained PTX:βCD complexes. EDC (193 mg/mL) and NHS (58 mg/mL) aqueous solutions were prepared and added to an APPZ suspension (100 mg/mL, pH 4.7). The mixture was stirred for 40 minutes and a trastuzumab (3.2 µg/mL) aqueous solution was later joined. The suspension was again stirred for 3 h and PTX:βCD complexes (0.8 mg/mL PTX equivalent) were added to it. Final suspension was kept in agitation in the dark overnight [31–34]. Conjugated APPZ were isolated by decreasing suspension pH value until 1.0 and by centrifuging them [18]. Supernatant was preserved to determine PTX:βCD and trastuzumab conjugation efficiencies (CEs) on APPZ.

To finish, conjugated APPZs were characterized. Their size and zeta potential were measured at the conjugation and at the physiological pH values in deionized water and phosphate buffered saline (PBS), respectively. Moreover, these parameters were determined over 8 consecutive days at pH 4.7 to study conjugated APPZ stability, too.

### 2.4. Determination of PTX and Trastuzumab Conjugation Efficiencies on APPZ

The amount of PTX:βCD and trastuzumab present in APPZ supernatant were analyzed by mass spectrometry and the Bradford method, respectively. In this last case, APPZ supernatant (100 µL) was mixed with Bradford reagent (1 mL). After 5 min, the absorbance of the mixture was measured at 595 nm (UV-1800 spectrophotometer, Shimadzu Corporation, Soraku-gun, Kyoto, Japan) [35]. Once trastuzumab amount present in APPZ supernatant was known, the antibody and the drug CEs were determined by difference, according to equation (1):

$$CE = (\text{PTX/trastuzumab initial amount} - \text{supernatant PTX/trastuzumab})/\text{nanoparticles amount} \quad (1)$$

### 2.5. Cell Culture

BT474, SKBR3, OVCAR3, and HS5 cell lines were cultured with medium supplemented with FBS (10%), containing high glucose (4500 mg/L) and antibiotics (penicillin 100 U/mL streptomycin 100 mg/mL). Cell lines were cultured at 37 °C in a humidified atmosphere in the presence of $CO_2$ (5%).

### 2.6. Determination of BT474, SKBR3, OVCAR3, and HS5 Cellular Levels of HER2-Expression

To determine HER2 and phosphorylated-HER2 (pHER2)-expression in the BT474, SKBR3, OVCAR3 and HS5 cell lines a western blot was carried out. Calnexin was selected as a loading control. Detailed procedures for the protein extraction, quantification, and immunoprecipitation, as well as for the western blotting, can be consulted in Montero et al. [36].

### 2.7. Conjugated APPZ Internalization in HER2-Overexpressing Cancer Cells

BT474 cells were cultured on coverslips and incubated with culture medium supplemented with FBS (10%) and chloroquine (50 μM) for 1 h. Cells were treated with conjugated APPZ (6.8 μg PTX-equivalent/mL medium) for 30 minutes, 4, 24, and 48 h. Dilutions (1:100) of the anti-LAMP1 antibody were employed for analyzing the HER2 and cellular lysosomes co-localization.

After conjugated APPZ treatment, an immunofluorescence assay was performed according as it was described in Esparis-Ogando et al. and analyzed by confocal laser scanning microscopy (CLSM) (Leica TCS SP5, Leica Microsystems, L'Hospitalet de Llobregat, Spain) [37].

### 2.8. Conjugated APPZ Specificity: Targeting HER2-Positive Cancer Cells

A BT474 and HS5 cell lines' co-culture was treated with conjugated APPZ in order to demonstrate their specificity. BT474 and HS5 cell lines were stained with CellTracker™ Green CMFDA and CellTracker™ Red CMPTX, respectively. After 24 h, both cell lines were seed together in 6-well plates in a 150,000:300,000 BT474:HS5 cellular ratio. Next day, cells were treated with PTX:βCD complexes (6.8 μg PTX-equivalent/mL) and conjugated APPZ (6.8 μg PTX-equivalent/mL) for 48 h. The effect of both systems was analyzed each 24 h by immunofluorescence [37]. In order to compare the specificity of the free PTX:βCD complexes and the conjugated APPZ, the number of cells of the BT474 and HS5 cell lines was counted in 12 different images for each treatment and the mean ± SD was calculated.

### 2.9. Conjugated APPZ Cytotoxic Effect According to Cellular Levels of HER2-Expression

Antitumor activity of PTX:βCD complexes and trastuzumab conjugated APPZ (APPZ-PTX:βCD-T) was studied through 3-(4,5-Dimethylthiazol-2-yl)-2,5-Diphenyltetrazolium Bromide (MTT) assays [38]. Cells from the BT474, SKBR3, OVSCAR3, and HS5 cell lines were seed in 24 well-plates and cultured with medium, supplemented with FBS (10%), overnight. The next day, culture medium was replaced by supplemented medium containing PBS (control), free PTX:βCD complexes (6.8 μg PTX-equivalent/mL), trastuzumab (T) (8 ng/mL), APPZ (1 mg/mL), and APPZ-PTX:βCD-T (1 mg/mL, 6.8 μg PTX-equivalent/mL). Free PTX (6.8 μg/mL), previously dissolved in PBS, and APPZ-PTX:βCD (1 mg/mL, 6.8 μg PTX-equivalent/mL) were also tested in the BT474 and HS5 cell lines. In all cases, cell proliferation was analyzed for 4 days, each 24 h. Shown results are the mean ± SD of four replicas for each different treatment.

### 2.10. Statistical Analyses

Data shown in APPZ characterization, regarding to their size and zeta potential, is the mean ± SD of three different measurements. Results of the MTT assays have been represented as the mean ± SD of four replicas for each treatment of three different experiments and results were considered statistically significant were $p < 0.05$. Otherwise, the quantification of the bands obtained in the western blot assay was carried out with the ImageJ 1.44 software (National Institutes of Health, Bethesda, MD, USA). The intensity of each band was determined with regard to the control values and data has been represented as the percentage of the maximum value obtained for each experiment.

## 3. Results

### 3.1. Stable APPZ Synthesis and Characterization

As it was mentioned before, APPZ were synthesized by dropping a piperazine aqueous solution over a sodium alginate one, in different molar ratios, at pH 4.7. Mannuronic and guluronic acid units from sodium alginate chains have a pKa of 3.4 and 3.7, respectively [39]. Piperazine pKa values are, approximately, 5.7 and 9.7 [40]. In this manner, at the working pH, electrostatic interactions took place between both compounds and nanoparticles were formed due to a sodium alginate chains' chemical crosslinking (Figure 1a [18].

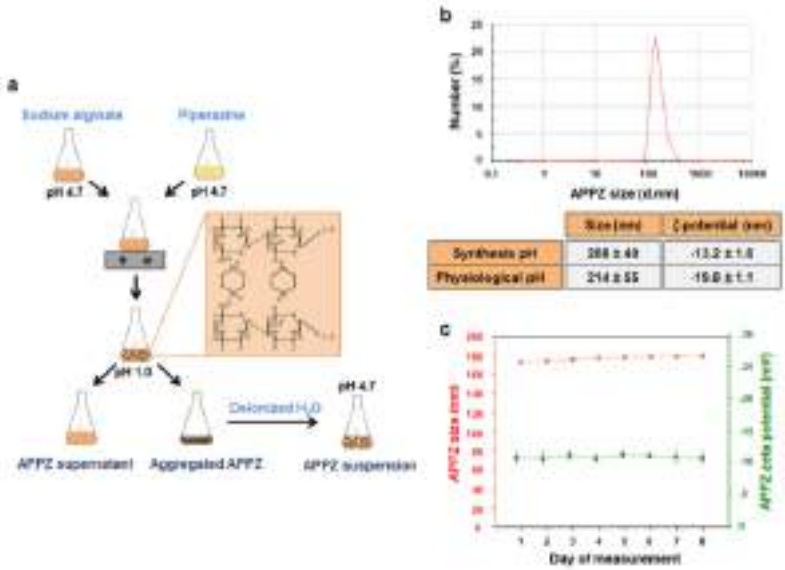


**Figure 1.** APPZ synthesis and characterization. (**a**) APPZ development. (**b**) APPZ size and ζ potential at the synthesis (4.7) and physiological (7.2) pH values in deionized water and PBS, respectively. These parameters were determined by DLS and LDE as the mean ± SD of three measurements. The diagram corresponds to APPZ mean size at pH 4.7. (**c**) APPZ diameter and surface charge stability over 8 consecutive days. All the values are the mean ± SD of three measurements, too.

Once obtained, APPZ were isolated, re-suspended in deionized water and characterized. Size and zeta potential of the APPZ synthetized with different piperazine:alginate molar ratios were determined (Figure S1a). The best size/surface charge relationship was achieved with a 0.25 piperazine:alginate molar ratio and APPZ developed in this manner were selected for further characterization. First, their size and superficial charge were determined at the synthesis pH, finding values of 208 ± 40 nm (PDI = 0.3) and −13.2 ± 1.6 mV, respectively (Figure 1b). Next, pH influence over both parameters was analyzed (Figure S1b). As it is shown, APPZ size did not vary significantly at pH values between 3.0 and 6.0. However, it increased due to the loss of the electrostatic interactions between the alginate chains and piperazine at very acid or basic pH values. As for the APPZ zeta potential, it had more positive values at acid pH values due to the protonation of the –COOH alginate groups. APPZ stability over time was also studied. Variation of their diameter and zeta potential was determined over 8 consecutive days, preserving APPZ at room temperature (Figure 1c).Over this period, size only varied a 3.5% ± 0.27% in respect of the first measurement obtained, while superficial charge changed a 5.4 ± 0.3% among the different days of the study. Finally, APPZ properties were analyzed when they were re-suspended in PBS at pH 7.2 and, in this case, they showed a 214 ± 55 nm mean diameter (PDI = 0.4) and a −19.8 ± 1.1 mV superficial charge.

### 3.2. *APPZ Conjugation with Trastuzumab and PTX:βCD Complexes and Later Characterization*

Before starting with APPZ conjugation, PTX inclusion efficiency in βCD was analyzed by High-Performance Liquid Chromatography (HPLC) and mass spectrometry. It was found that such inclusion efficiency was about a 0.79 mg PTX/mg βCD [30].

Then, once APPZ were isolated after being synthetized, trastuzumab and the obtained PTX:βCD complexes were covalently attached to their surface (Figure 2a). EDC, in a non-cytotoxic concentration (0.01M) [34], was employed to transform alginate carboxylic groups into stable O-acylurea intermediates. Besides, NHS was added to improve EDC stability [33]. Later, O-acylurea intermediates reacted with trastuzumab amine groups from lysine residues to form amide bonds when the antibody was joined [12,14]. In the same manner, PTX:βCD complexes were added to the active APPZ suspension and βCD molecules were attached to them through ester bonds.

Non-attached trastuzumab and PTX:βCD complexes were discarded by a second APPZ isolation through centrifugation. The amount of the antibody and the antitumor drug present in conjugated APPZ supernatant was analyzed. CEs were found to be 8 ng trastuzumab/mg APPZ and a 6.8 μg PTX/mg APPZ, which were adequate results according to the doses of these compounds that have to be administered in vivo [41,42]. Likewise, trastuzumab and PTX:βCD complexes attachment to APPZ was proved with a Fourier Transform-Infrared Spectroscopy (FT-IR) analysis in the 500–4000 $cm^{-1}$ region (Figure 2c). Compared with the APPZ, the main changes in the APPZ-PTX:βCD-T spectra appeared at 1232, 1704, and 3500–4000 $cm^{-1}$. The first shift could correspond to the βCD conjugation through an ester bond, while the other two demonstrated trastuzumab attachment. Thus, the shift from 1704 $cm^{-1}$ could be assigned to an amide bond vibration and there could be more amide shifts in the 1570–1670 $cm^{-1}$ region that would be masked by the wide alginate signal [34].

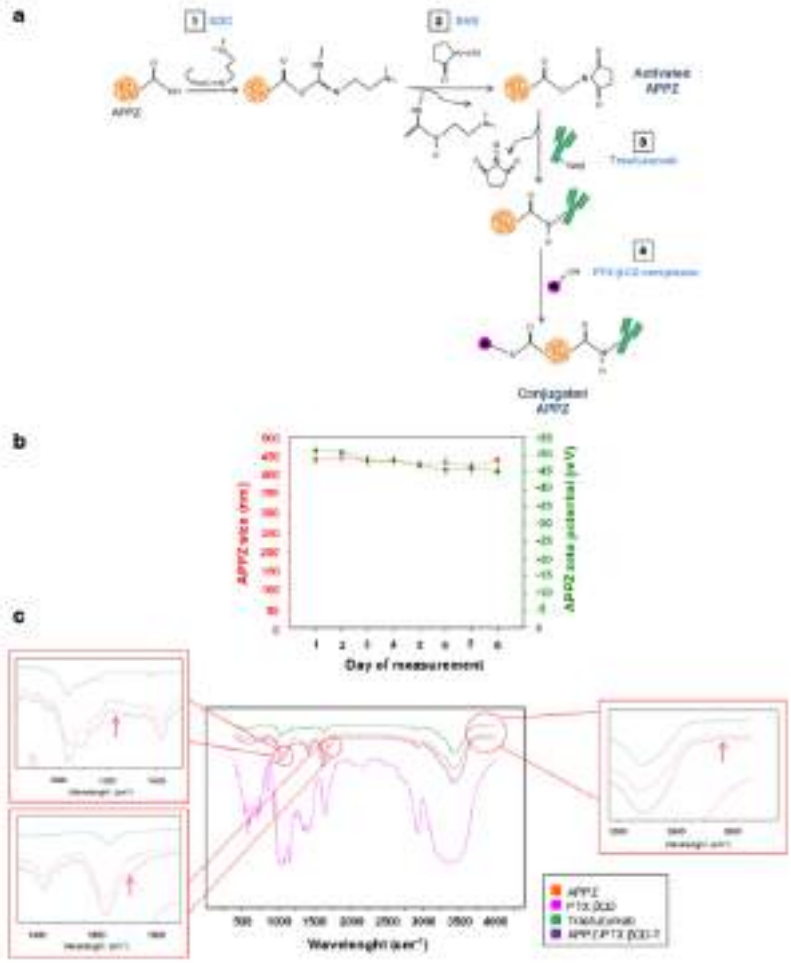


**Figure 2.** APPZ conjugation and later characterization. (a) APPZ conjugation with trastuzumab and PTX:βCD complexes. (b) Conjugated APPZ diameter and surface charge stability over 8 consecutive days. All the values are the mean ± SD of three measurements. (c) Results of the FT-IR analysis that corroborate APPZ conjugation.

To finish with conjugated APPZ characterization, their size and zeta potential were determined. At the conjugation pH value, their size was near 296 ± 50 nm (PDI = 0.4), while their superficial charge was about −24 ± 1.4 mV (Figure S2). Otherwise, when they were re-suspended in PBS, the values of these parameters were 359 ± 60 nm (PDI = 0.45) and −26.2 ± 2.1 mV at the physiological pH (7.2). Conjugated APPZ stability was also studied for 8 consecutive days at pH 4.7 (Figure 2b). Variations in their diameter and superficial charge were determined and it was found that first property varied a 2.25% ± 0.84 % in respect of the first day measurement. On the other hand, superficial charge changed a 3.13% ± 0.27 % among the different performed measurements.

*3.3. Conjugated APPZ are Internalized in HER2-Overexpressing Cancer Cells by Endocytosis*

Different cell lines expressing distinct HER2 levels were selected to study conjugated APPZ biological properties. As described in the literature [43,44], it was found that total HER2 and pHER2 were great overexpressed in the BT474 and SKBR3 cell lines. OVCAR3 and HS5 cells also expressed HER2, although to a much lesser extent. This fact can be noticed in the overexposed western blot (Figure 3a).

Conjugated APPZ internalization was studied in BT474 cells. Thanks to the presence of trastuzumab in the APPZ surface, it was expected that APPZ would be internalized in HER2-overpressing cells through an endocytosis process. In addition, it was also considered that part of the administered PTX could pass through the cellular membrane and arrived directly to the microtubules, its therapeutic center of action (Figure 3b). The first fact was proven by means of immunofluorescence and CLSM. BT474 cells were incubated with conjugated APPZ for different times and the location of trastuzumab was visualized using a secondary antibody. Incubation with APPZ resulted in progressive accumulation of trastuzumab in intracellular sites (Figure 3c). Furthermore, a co-staining of trastuzumab and the cellular lysosomes was carried out, using a LAMP1 marker, to check whether APPZ were targeted to lysosomes. There was a co-localization of both markers that proved that APPZ would end up in such organelles in treated cells (Figure 3d).

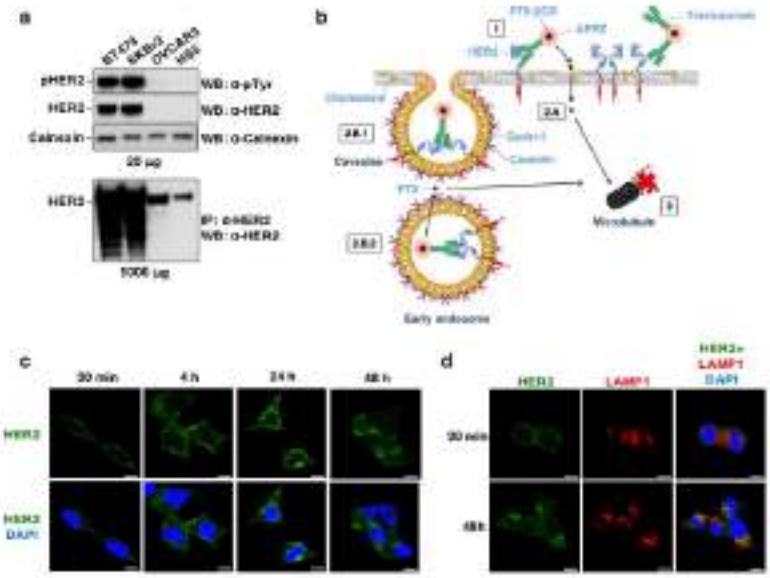


**Figure 3.** Conjugated APPZ internalization in BT474 cells. (**a**) Study of the HER2 and pHER2 expression levels in the BT474, SKBR3, OVCAR3, and HS5 cell lines. Calnexin was employed as loading control. (**b**) Expected conjugated APPZ internalization into HER2-overexpressing cancer cells. (**c**) HER2 internalization into BT474 cells' cytoplasm after treatment with conjugated APPZ. Scale bar, 10 µm. (**d**) Co-localization (orange) between HER2 and LAMP1 staining after conjugated APPZ treatment. Scale bar, 10 µm.

### *3.4. Conjugated APPZ Present HER2-Overexpressing Specificity*

In order to compare conjugated APPZ specificity with that of the free PTX:βCD complexes, a co-culture of the HER2-overexpressing BT474 and the human stromal HS5 cell lines was performed. Both cell lines were separately stained and once they were cultured together, they were treated with conjugated APPZ (Figure 4a). CLSM images were taken 24 and 48 h after such treatment (Figure 4b). It could be seen that free PTX:βCD complexes really affect to BT474 cells' viability, but they also

notably reduced HS5 cells' survival, especially after 48 h. By contrast, conjugated APPZ achieved to reduce BT474 cells' viability without affecting HS5 cells' survival in an analogous manner (Figure 4c).

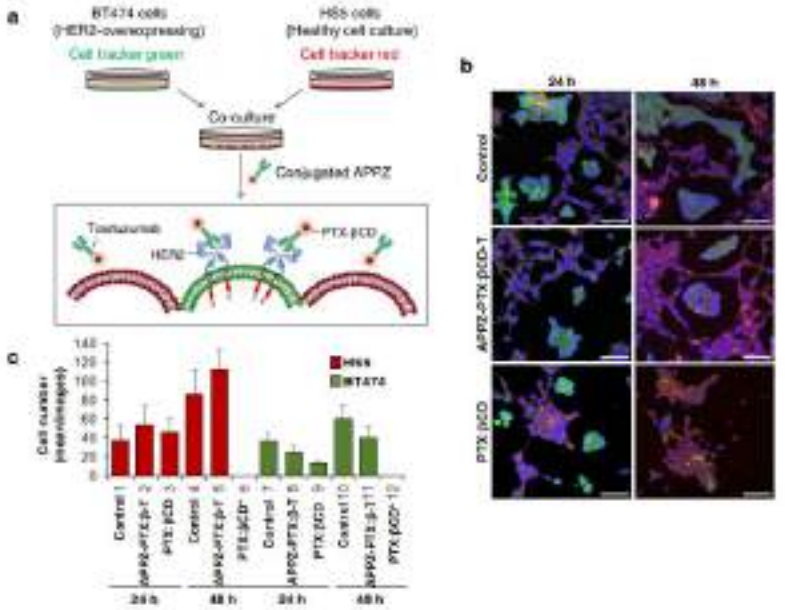


**Figure 4.** Targeting HER2-overexpressing cells with conjugated APPZ. (a) BT474 and HS5 cells were co-culture and treat equivalent free PTX:βCD complexes and conjugated APPZ. (b) Obtained results after the treatment of the co-cultured BT474 (green) and HS5 (red) cells, stained with DAPI (blue). Scale bar, 50 μm. (c) Living BT474 and HS5 cells from 12 different confocal images were counted in order to analyze the specificity of the conjugated APPZ. Results are the mean of these 12 images ± SD.

### *3.5. Conjugated APPZ Have Different Cytotoxic Effect According to Cellular Levels of HER2-Expression*

Conjugated APPZ antiproliferative activity was analyzed through MTT assays with the BT474, SKBR3, OVCAR3, and HS5 cell lines. As it was shown before, BT474 and SKBR3 cells presented a HER2-overexpression, while such expression was lower in the OVCAR3 and HS5 cell lines, respectively (Figure 3a). Thus, conjugated APPZ resulted almost as efficient as equivalent free PTX:βCD complexes in the first two HER2-overpressing cell lines (Figure 5a,b). Nevertheless, their antitumor effect decreased in the non HER2-overexpressing cells in comparison with the free PTX:βCD complexes activity (Figure 5c,d). This difference proved again the specificity of the targeted nanosystem. In addition, it could be seen that non-conjugated APPZ decreased tumor cells' proliferation rate, possible due to piperazine anticoxidant effect [45], but that such treatment did not affect non-HER2-overexpressing cells' survival rate.

With the aim of demonstrating that the specificity of the targeted nanovehicle was favored by the conjugation of trastuzumab, APPZ-PTX:βCD effect over cellular viability was also tested in BT474 and HS5 cells. As result, it was proven that APPZ-PTX:βCD decreased BT474 cells' survival rate in a lesser extent than APPZ-PTX:βCD-T did, probably because of a minor endocytosis rate, non-receptor mediated. On the contrary, APPZ-PTX:βCD were responsible for a further reduction in HS5 cells' viability in comparison with APPZ-PTX:βCD-T (Figure S3).

At last, improvement of PTX aqueous solubility with its inclusion into βCD was shown with MTT experiments with BT474 and HS5 cell lines, too. Free PTX was tested in both types of cells and it was not as much efficient as PTX:βCD complexes were. Even conjugated nanoparticles had a more remarkable effect over BT474 cellular viability (Figure S3).

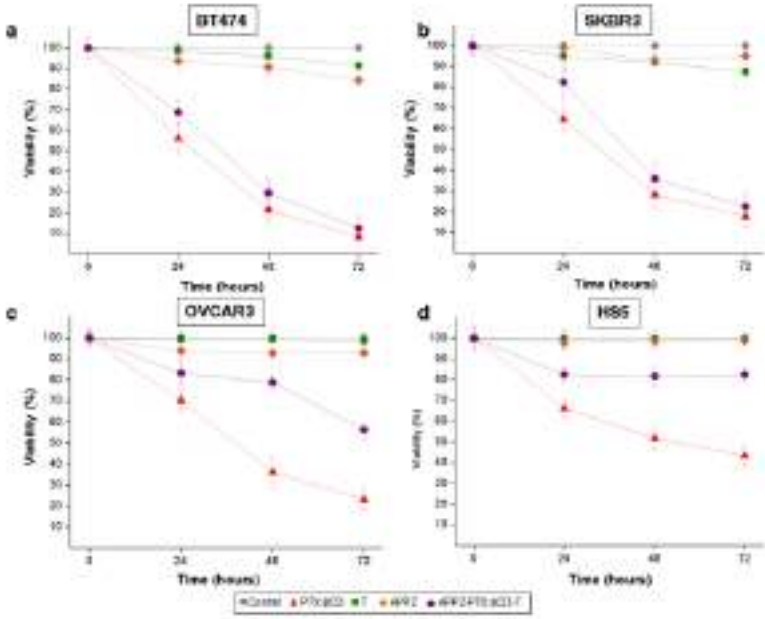


**Figure 5.** Conjugated APPZ antiproliferation effect in (**a**) BT474; (**b**) SKBR3; (**c**) OVCAR; and (**d**) HS5 cells. Shown results are the mean ± SD of four replicas for each different treatment.

## 4. Discussion

In spite of being one of the most employed chemotherapy drugs these days, PTX has a very limited aqueous solubility. As consequence, it is normally administered with solvents that add more toxicity to the taxane and limit their bioavailability. Besides, PTX inhibits microtubules' depolymerization and presents a restricted tumor-selectivity and all these handicaps confine its possible given doses [6,7].

Herein, the scientific community is making great efforts in order to reduce these PTX disadvantages and [7,8], in this work, such drawbacks' reduction was the main aim.

In this manner, a novel PTX targeted nanovehicle, which had been synthetized in previous works to transport other conventional drugs [18], was developed. Integrated by piperazine and sodium alginate nanoparticles, such nanovehicles were obtained thanks to the electrostatic interactions that took place between both biocompatible compounds at acid pH values. Once obtained, the PTX transport nanosystem was characterized at the development pH value. Moreover, their size and superficial charge were determined at other pH values, like the physiological pH. In any case, APPZ showed zeta potential values that guaranteed their colloidal stability and that, along with their mean size values and stability, were adequate for a potential in vivo administration of the nanoparticles [46].

On the developed nanovehicle's surface, trastuzumab and PTX, included in βCD molecules, were attached thanks to the EDC/NHS chemistry, previously employed in literature to anchor proteins on other nanoparticles and hydrogels [33,34]. PTX was included in βCD with the objective of improving its solubility in aqueous media [22] and the used of trastuzumab was intended to

target HER2-overexpressing cells. Their attachment to the APPZ surface was proven with a FT-IR analysis and the CEs of both, the antibody and the PTX:βCD complexes, were suitable according to the doses of these compounds that have to be administered to achieve a therapeutic effect. Once conjugated, APPZ were again characterized and anew presented a proper size, zeta potential, and stability to potentially be in vivo administered [47].

For the next step, conjugated APPZ internalization was studied in the BT474 HER2-overexpressing cell line. As expected [46], it was demonstrated with an immunofluorescence assay and CLSM that conjugated APPZ were internalized into cellular cytoplasm by endocytosis. Thus, it could be seen that trastuzumab fluorescence signal was displaced from the cellular membrane to the cytoplasm only after 4 h of treatment and that such signal overlapped with the one of the lysosomal marker LAMP1 [48].

Finally, conjugated APPZ specificity and antitumor activity was in vitro validated to check if the main objective of the work was accomplished. For the first fact, a co-culture between the BT474 and the HS5 cell lines was carried out and treated with the targeted nanovehicle and with equivalent free PTX:βCD complexes. As result, it was shown that while the free PTX:βCD complexes reduced both the HER2-overexpressing and the non-HER2-overexpressing cellular viability in a notable manner, conjugated APPZ were more specific. They were almost as much efficient as PTX:βCD complexes killing BT474 cells after 48 h, but they did not reduce HS5 viability in the same way. Even the number of such healthy cells was increased in comparison with the control 48 h after being treated with the conjugated APPZ, possibly due to higher space availability in the culture wells.

Furthermore, conjugated APPZ specificity was afresh demonstrated when their antiproliferative activity was analyzed with MTT assays. When HER2-overpressing cell lines (BT474 and SKBR3) were treated with them, conjugated APPZ almost had the same viability effect as the free PTX:βCD complexes. However, in the cell lines that had a lower HER2-expression (OVCAR3 and HS5), there was a significant difference between the targeted nanosystem and the PTX:βCD complexes activity. Hence, it was shown that PTX aqueous solubility, bioavailability, and specificity conferred by the presence of trastuzumab, were improved and that the aim of the study was attained.

## 5. Conclusions

On the whole, a novel and targeted PTX nanovehicle has been developed in this work with the aim of improving its bioavailability and specificity for the treatment of HER2-positive tumors. Integrated by piperazine and sodium alginate nanoparticles, the surface of such nanovehicles was properly activated by means of the EDC/NHS chemistry to covalently attach to it trastuzumab and PTX, included in β-cyclodextrin molecules to improve its water-solubility.

Once conjugated, the nanosystem showed a proper size, surface charge, and stability to be potentially in vivo administered. In vitro, it was demonstrated that the targeted nanovehicle was internalized into the cytoplasm of HER2-overexpressing tumor cells through an endocytosis mechanism and that it ended up entering their lysosomes. Moreover, the specificity of the conjugated nanoparticles in comparison with that of the free drug was twice proven. Firstly, a co-culture of HER2- and non-HER2-overexpressing cells was performed and, secondly, MTT assays with cell lines with a different level of HER2-expression were carried out. In both cases, the obtained results were similar. While the conjugated nanoparticles were almost as efficient as the free administered PTX:βCD in reducing HER2-overexpressing cancer cells' viability, they did not affect non-HER2-overexpressing survival rate in the same manner. Such specificity was consequence of the conjugation of trastuzumab to the nanosystem, as additional MTT assays showed. Hence, the employment of the PTX-trastuzumab nanovehicle that is here proposed could help to reduce its frequent adverse effects, being more specific and efficient for the treatment of any HER2-positive tumor.

**Supplementary Materials:** The following are available online at www.mdpi.com/2079-4991/9/7/948/s1, Figure S1: APPZ synthesis and characterization. Figure S2: Conjugated APPZ size and zeta potential determination at the conjugation-pH value. Figure S3: Results of the additional MTT experiments performed with the (a) BT474 and the (b) HS5 cell lines. They showed that conjugated APPZ specificity was favoured by trastuzumab conjugation and that PTX inclusion into βCD improved its aqueous solubility. Shown results are the mean ± SD of four replicas for each different treatment.

**Author Contributions:** Conceptualization, A.P. and E.M.M.d.V.; Funding acquisition, A.P. and E.M.M.d.V.; Investigation, C.N. and A.C.; Methodology, C.N. and A.C.; Supervision, J.A.R.-R., A.P., and E.M.M.d.V.; Writing—original draft, C.N.; Writing—review & editing, A.C., J.A.R.-R., A.P., and E.M.M.d.V.

**Funding:** This work was supported by a UE ERC Starting Grant (MYCAP, Development of a technology to produce microcapsules, based on the formation of drops from viscous non-Newtonians liquids sprayed through fan-jet nozzles, to use in cancer therapy), by the Spanish Ministry of Economy and Competitiveness (BFU2012-39151, BFU2015-71371R, CTQ2016-78988-R, PI15/00684, and FEDER), the CRIS Cancer Foundation and the Scientific Foundation of the Spanish Association Against Cancer (AECC). CN is recipient of a predoctoral contract from the Junta de Castilla y León, co-funded by the European Social Foundation (EDU/602/2016) and AC was supported by a doctoral fellowship from Coordination for the Improvement of Higher Education Personnel (CAPES) from the Ministry of Education of Brazil.

**Acknowledgments:** The authors would like to thank all the funding sources that have made possible this work.

**Conflicts of Interest:** Part of this work (the nanosystem development and characterization, and its cytotoxicity for the BT474 cell line) was presented at the AIChE Annual Meeting 2016 Conference (San Francisco, USA) and at the BIOTEC2017 Conference (Murcia, Spain) as an oral communication with interim finding.

## References

1. Luzzati, T.; Parenti, A.; Rughi, T. Economic growth and cancer incidence. *Ecol. Econ.* **2018**, *146*, 381–396.
2. Dickens, E.; Ahmed, S. Principles of cancer treatment chemotherapy. *Surgery* **2017**, *36*, 134–138.
3. Krukiewicz, K.; Zak, J.K. Biomaterial-based regional chemotherapy: Local anticancer drug delivery to enhance chemotherapy and minimize its side-effects. *Mater. Sci. Eng. C* **2016**, *62*, 927–942.
4. Abandansari, H.S.; Absali, M.; Nabid, M.R.; Niknejad, H. Enhance chemotherapy efficacy and minimize anticancer drug side effects by using reversible pH- and redox- responsive cross-linked unimolecular micelles. *Polymer* **2017**, *116*, 16–26.
5. Wang, F.; Porter, M.; Konstantopoulos, A.; Zhang, P.; Cui, H. Preclinical development of drug delivery systems for paclitaxel-based cancer chemotherapy. *J. Control. Release* **2017**, *267*, 100–118.
6. Bernabeu, E.; Cagel, M.; Lagomarsino, E.; Moretton, M.; Chiappetta, D.A. Paclitaxel: What has been done and the challenges remain ahead. *Int. J. Pharm.* **2017**, *526*, 474–495.
7. Sofias, A.M.; Dunne, M.; Storm, G.; Allen, C. The battle of nano-paclitaxel. *Adv. Drug Deliv. Rev.* **2017**, *122*, 20–30.
8. Du, X.; Khan, A.R.; Fu, M.; Ji, J.; Yu, A.; Zhai, G. Current development in the formulations of non-injection administration of paclitaxel. *Int. J. Pharm.* **2018**, *542*, 242–252.
9. Khuroo, T.; Verma, D.; Khuroo, A.; Ali, A.; Iqbal, Z. Simultaneous delivery of paclitaxel and erlotinib from dual drug loaded PLGA nanoparticles: Formulation development, thorough optimization and in vitro release. *J. Mol. Liq.* **2018**, *257*, 52–68.
10. Gupta, D.; Kumar, M.; Tyagi, P.; Kapoor, S.; Tyagi, A.; Barman, T.K.; Kharbanda, S.; Kufe, D.; Singh, H. Concomitant delivery of paclitaxel and NullCP-9 peptide for synergistic enhancement of cancer therapy. *Nanomedicine* **2018**, *14*, 1303–1313.
11. Chowdhury, P.; Negesh, P.K.B.; Hatami, E.; Wagh, S.; Dan, N.; Tripathi, M.K.; Khan, S.; Hafrez, B.B.; Meibohm, B.; Chauhan, S.C. et al. Tannic acid-inspired paclitaxel nanoparticles for enhanced anticancer effects in breast cancer cells. *J. Colloid Interface Sci.* **2019**, *535*, 133–148.
12. Huang, R.; Wang, Q.; Zhang, X.; Zhu, J.; Bi, Sun. Trastuzumab-cisplatin conjugates for targeted delivery of cisplatin to HER2-overexpressing cancer cells. *Biomed. Pharmacother.* **2018**, *72*, 17–23.
13. Nguyen, H.T.; Tran, T.H.; Thapa, R.K.; Phung, C.D.; Shin, B.S.; Jeong, J.H.; Choi, H.G.; Yong, C.S.; Kim, J.O. Targeted co-delivery of polypyrrole and rapamycin by trastuzumab-conjugated liposomes for combined chemo-photothermal therapy. *Int. J. Pharm.* **2017**, *527*, 61–71.

14. Huang, R.; Sun, Y.; Zhang, X.Y.; Sun, B.W.; Wang, Q.C.; Zhu, Z. Biological evaluation of a novel Herceptin-platinum (II) conjugate for efficient and cancer cell specific delivery. *Biomed. Pharmacother.* **2015**, *73*, 116–122.
15. Morimura, O.; Minami, T.; Kijima, T.; Koyama, S.; Otsuka, T.; Kinehara, Y.; Ota, A.; Higashiguchi, M.; Miyake, K.; Nagatomo, I. et al. Trastuzumab emtansine suppresses the growth of HER2-positive small-cell lung cancer in preclinical models. *Biochem. Biophys. Res. Commun.* **2017**, *488*, 596–602.
16. Daniels, B.; Kiely, B.E.; Lord, S.J.; Houssami, N.; Lu, C.Y.; Ward, R.L.; Pearson, S.A. Trastuzumab for metastatic breast cancer: real world outcomes from an Australian whole-of-population cohort (2001-2006). *Breast* **2018**, *38*, 7–13.
17. Baselga, J.; Manikhas, A.; Cortés, J.; Llombart, A.; Roman, L.; Semiglazov, V.F.; Byakhov, M.; Lokanatha, D.; Forenza, S.; Goldfarb, R.H. et al. Phase III trial of nonpegylated liposomal doxorubicin in combination with trastuzumab and paclitaxel in HER2-positive metastatic breast cancer. *Ann. Oncol.* **2014**, *25*(3).
18. Sánchez, J.V.; Rodríguez-Rodríguez, J.A.; Martín del Valle, E.M.; Galán, M.A. Synthesis of a new nanoparticle system based on the electrostatic alginate-piperazine interactions. *Polym. Adv. Technol.* **2016**, *27*, 623–629.
19. Huang, J.; Li, J.; Feng, Y.; Li, K.; Yan, H.; Gao, P.; Xiao, T.; Wang, C. Aggregation behavior of derivatives of sodium alginate and N-octyl-D-glucopyranoside in aqueous solutions. *Colloids Surf. A* **2015**, *478*, 11–17.
20. Shah, A.; Shah, A.M.; Parveen, N.; Rehman, Z.; Khan, S.Z.; Rana, U.A.; Khan, S.U.; Nisar, J.; Lashin, A.; Qureshi, R. Synthesis and electrochemical investigations of piperazines. *Electrochim. Acta* **2016**, *220*, 705–711.
21. Fytas, C.; Zoidis, G.; Tsotinis, A.; Fytas, G.; Khan, M.A.; Khtar, S.A. Novel1-(2-aryl-2-adamantyl) piperazine derivatives with antiproliferative activity. *Eur. J. Med. Chem.* **2015**, *93*, 281–290.
22. Martín del Valle, E.M. Cyclodextrins and their uses: a review. *Process. Biochem.* **2004**, *39*, 1033–1046.
23. Shelley, H.; Babu, R.J. Role of cyclodextrins in nanoparticle-based drug delivery systems. *J. Pharm. Sci.* **2018**, *107*, 1741–1753.
24. Oroujeni, M.; Kaboudin, B.; Xia, W.; Jönsson, P.; Ossipov, D.A. Conjugation of cyclodextrin to magnetic $Fe_3O_4$ nanoparticles via polydopamine coating for drug delivery. *Prog. Org. Coat.* **2018**, *114*, 154–161.
25. Basha, R.Y.; Kumar, S.; Doble, M. Dual delivery of tuberculosis drugs via cyclodextrin conjugated curdlan nanoparticles to infect macrophages. *Carbohydr. Polym.* **2019**, *218*, 53–62.
26. Shah, M.; Shah, V.; Ghosh, A.; Zhang, Z.; Minko, T. Molecular inclusion complexes of β-cyclodextrins derivatives enhance aqueous solubility and cellular internalization of paclitaxel: Preformulation and in vitro assessments. *J. Pharm. Pharmacol.* **2015**, *2*(2), 8.
27. Bhatt, P.; Lalani, R.; Vhora, I.; Patil, S.; Amrutiya, J.; Misra, A.; Mashru, R. Liposomes encapsulating native and cyclodextrin enclosed paclitaxel: Enhanced loading efficiency and its pharmacokinetic evaluation. *Int. J. Pharm.* **2018**, *536*(1), 95–107.
28. Alcaro, S.; Ventura, C.A.; Paolino, D.; Battaglia, D.; Ortuso, F.; Cattel, L.; Puglisi, G.; Fresta, M. Preparation, characterization, molecular modelling and in vitro activity of paclitaxel-cyclodextrins complexes. *Bioorg. Med. Chem. Lett.* **2002**, *12*, 1637–1641.
29. Hamada, H.; Ishihara, K.; Matsuoka, N.; Mikuni, K.; Nakajima, N. Enhancement of water-solubility and bioactivity of paclitaxel using modified cyclodextrins. *J. Biosci. Bioeng.* **2006**, *102*, 369–371.
30. Badea, I.; Ciutaru, D.; Lazar, L.; Niculescu, D.; Tudose, A. Rapid HPLC method for the determination of paclitaxel in pharmaceutical forms without separation. *J. Pharm. Biomed.* **2004**, *34*, 501–507.
31. Chung, W.J.; Lee, D.Y.; Yoo, S.Y. Chemical modulation of M13 bacteriophage and its functional opportunities for nanomedicine. *Int. J. Nanomed.* **2014**, *9*, 5825–5836.
32. Campuzano, S.; Yáñez-Sedeño, P.; Pingarrón, J.M. Electrochemical affinity biosensors in food safety. *Chemosensors* **2017**, *5*, 8.
33. Kelestemur, S.; Altunbek, M.; Culha, M. Influence of EDC/NHS coupling chemistry on stability and cytotoxicity of ZnO nanoparticles modified with proteins. *Appl. Surf. Sci.* **2017**, *403*, 455–463.
34. Hua, J.; Li, Z.; Xia, W.; Yang, N.; Gong, J.; Zhang, J.; Qiao, C. Preparation and properties of EDC/NHS mediated crosslinking poly (gamma-glutamic acid)/ epsilon-polylysine hydrogels. *Mater. Sci. Eng. C* **2016**, *61*, 879–892.
35. Bradford, M.M. A rapid and sensitive method for the quantitation of microgram quantities of protein utilizing the principle of protein-dye binding. *Anal. Biochem.* **1976**, *72*, 248–254.

36. Montero, J.C.; Seoane, S.; Ocaña, A.; Pandiella, A. P-Rex1 participates in neuregulin- ErbB signal transduction and its expression correlates with patient outcome in breast cancer. *Oncogene* **2011**, *30*, 1059–1071.
37. Esparís-Ogando, A.; Díaz-Rodríguez, E.; Montero, J.C.; Yuste, L.; Crespo, P.; Pandiella, A. Erk5 participates in neuregulin signal transduction and is constitutively active in breast cancer cells overexpressing ErbB2. *Mol. Cell. Biol.* **2002**, *22*, 270–285.
38. Mosmann, T. Rapid colorimetric assay for cellular growth and survival: Application to proliferation and cytotoxicity assays. *J. Immunol. Methods* **1983**, *65*, 55–63.
39. Haug, A.; Larsen, B. Separation of uronic acids by paper electrophoresis. *Acta Chem. Scand.* **1961**, *15*, 1395–1396.
40. Khalili, F.; Henni, A.; East, A.L.L. pKa values of some piperazines at (298, 303, 313 and 323) K. *J. Chem. Eng. Data* **2009**, *54*, 2914–2917.
41. Kaufman, P.A.; Wildiers, H.; Freyer, G.; Kennecy, M.; Gonçalves, A.; Jerusalem, G. et al. Phase 1b study of tribananib plus paclitaxel and trastuzumab in patients with HER2-positive locally recurrent or metastatic breast cancer. *Clin. Breast Cancer* **2019**, *19*(1), 47–57.
42. Van Ramshorst, M.S.; van Werkhoven, E.; Mandjes, I.A.M.; Schot, M.; Wesseling, J.; Vrancken Peeters, M.T.F.D.; Meerum Terwogt, J.M.; Bos, M.E.M.; Oosterkamp, H.M.; Rodenhuis, S. et al. Trastuzumab in combination with weekly paclitaxel and carboplatin as neo-adjuvant treatment for HER2-positive breast cancer: the TRAIN study. *Eur. J. Cancer* **2017**, *74*, 47–54.
43. Subik, K.; Lee, J.F.; Baxter, L.; Strzepek, T.; Costello, D.; Crowley, P.; Xing, L.; Hung, M.C.; Bonfiglio, T.; Hicks, D.G. et al. The expression patterns of ER, PR, HER2, CK5/6, EGFR, Ki-67 and AR by immunohistochemical analysis in breast cancer cell lines. *Breast Cancer* **2010**, *4*, 35–41.
44. He, J.; Jing, Y.; Li, W.; Qian, X.; Xu, Q.; Li, F.S.; Liu, L.Z.; Jiang, B.H.; Jiang, Y. Roles and mechanism of miR-199a and miR-125b in tumor angiogenesis. *Plos One* **2013**, *8*, e56647.
45. Patel, R.V.; Park, S.W. An evolving role of Piperazine moieties in drug design and discovery. *Mini-Rev. Med. Chem.* **2013**, *13*, 1579–1601.
46. Donahue, N.D.; Acar, H.; Wilhelm, S. Concepts of nanoparticle cellular uptake, intracellular trafficking, and kinetics in nanomedicine. *Adv. Drug Deliv. Rev.* 2019, In press.
47. Mohanraj, V.J.; Chen, Y. Nanoparticles – A review. *Trop. J. Pharm. Res.* **2006**, *5*, 561–573.
48. Alessandrini, F.; Pezzè, L.; Ciribilli, Y. LAMPs: Shedding light on cancer biology. *Semin. Oncol.* **2017**, *44*(4), 239-253.


© 2019 by the authors. Licensee MDPI, Basel, Switzerland. This article is an open access article distributed under the terms and conditions of the Creative Commons Attribution (CC BY) license (http://creativecommons.org/licenses/by/4.0/).

# CHAPTER 4

## TAILORED-MADE POLYDOPAMINE NANOPARTICLES: A POTENTIAL TOOL FOR CANCER NANOMEDICINE

## 4.1. Introduction

### *4.1.1. Polydopamine: a versatile bioinspired material*

Among the main reported cancer-related DDSs, it was already remarked in the first chapter that those of polymeric nature have received more attention because of their safety, the possibility of customizing them and their potential decoration with targeting molecules [1]. These nanocarriers can be synthesized from natural or synthetic polymers and, within the latter, some of the most widely used biodegradable polymers to date when developing NPs have been PLGA, PGA, PLA and chitosan [2,3]. However, a little over a decade ago, polydopamine (PDA) began to make its way into the nanomedicine field, and it is currently gaining more and more importance for the generation of biodegradable polymeric nanocarriers [3,4].

PDA was first introduced for surface modification applications in 2007 by Lee et al. [5], who were inspired by the ability of invertebrate mussels to adhere to nearly all kind of solid surfaces. Among the different mussel adhesion proteins, Mytilus foot protein-5 (Mfp-5), which is rich in lysine and 3,4-dihydroxy-L-phenylalanine (DOPA), was found to play a key role. Indeed, DOPA is the precursor of dopamine (DA), a catecholamine capable of interacting with multiple substrates via covalent and non-covalent bindings. Herein, based on DOPA structural characteristics, Lee and colleagues reported the synthesis of PDA by means of DA self-oxidative polymerization under mild alkaline conditions. These researchers showed that the black-coloured coating material that they afforded was able to adhere to almost all inorganic and organic solid surfaces [4,6]. From that moment on, PDA emerged as an attractive and versatile coating polymer in diverse material science fields. In this way, it began to be employed to coat a wide variety of nanostructures (core/shell nanocomposites, nanotubes, nanocapsules…), since it proved to give them superior properties in comparison to other modification strategies [7,8].

Besides, as PDA shares the same precursors, synthesis mechanisms and properties than natural eumelanin pigment, it also

started to be regarded as a synthetic melanin analogue [9]. Actually, the same polymerization process that yields PDA coatings was showed to lead to the simultaneous generation of nanocolloids in the bulk solution, and these aggregates soon emerged as eumelanin-like NPs with really interesting applications in energy and environmental sciences and, specially, thanks to their outstanding physicochemical properties, in the biomedicine field [10,11].

### *4.1.2. Polydopamine structure hypotheses and main synthesis approaches*

Despite PDA extensive use in material sciences over the last decade, its exact synthesis mechanism and structure remain elusive due to the multiple chemical reaction sites that DA displays. It is well recognized that, under alkaline conditions, DA is oxidized to DA-quinone, which later forms leukodopamine-chrome after intramolecular cyclation via 1,4-Michael-type addition. Then, further oxidation of leukodopamine-chrome occurs and, after a final rearrangement, 5,6-dihydroxyindole (DHI) is formed [6,12]. Thus, disputes about PDA formation lie in its subsequent polymerization mechanism [12]. The most widely accepted theory up to now is the one proposed by Lee et al. [5], who considered that PDA formation undergoes both covalent oxidative polymerization and physical self-assembly processes [4,12]. Thereby, it is believed that the covalent oxidative pathway involves oxidative DA self-polymerization, but that some DA molecules remain unpolymerized and form trimers with DHI ($(DA)_2$/DHI) through non-covalent interactions (ionic, cation-π, π-π, hydrogen bonding (H-bonding) and quadrupole-quadrupole interactions) [4,6] (**Figure 4.1**).

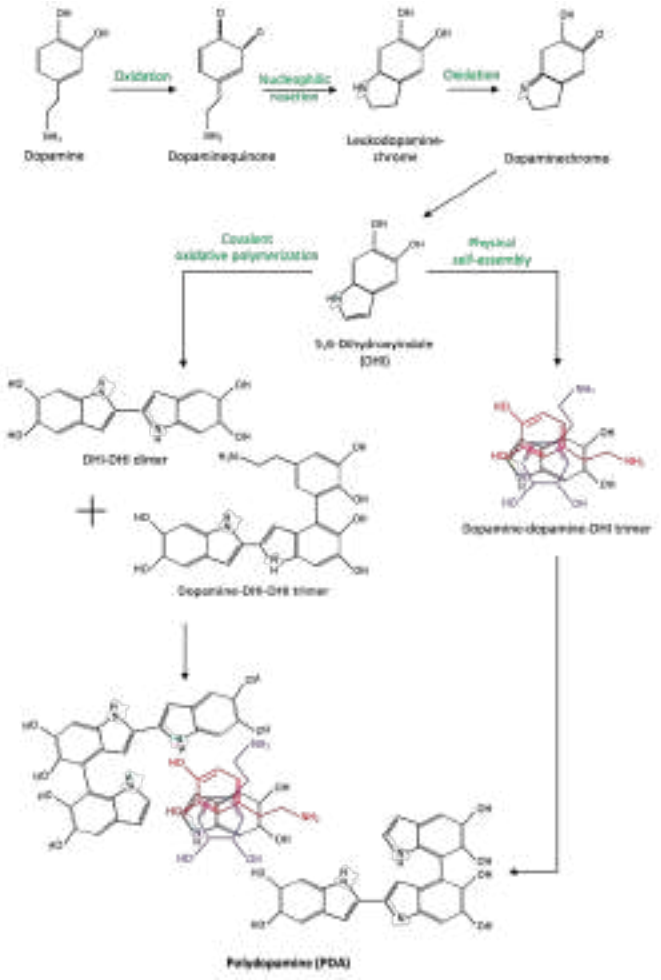


**Figure 4.1.** Representation of the most widely accepted theory about PDA polymerization. It is recognized that, under basic conditions, DA is oxidized to DHI. Then, it is believed that PDA formation takes places by both covalent oxidative polymerization (left) and physical self-assembly processes (right).

Otherwise, there are three main approaches to synthesize PDA coatings and aggregates: solution oxidation, enzymatic oxidation and electropolymerization [4,6]. The choice of one approach or another depends mostly on the subsequent PDA application, since electropolymerization is normally used to obtain thin coating surfaces of uniform roughness, while enzymatic and solution oxidations are generally employed to obtain nanocolloids, nanocapsules and core@shell

nanocomposites. Of them, although the enzymatic method is more environmental-friendly, solution oxidation is normally preferred because is simpler. The most common way to carry it out is by preparing a mixture of ammonia in EtOH and $H_2O$(d), and by later injecting a solution of DA hydrochloride into this mixture. The resulting solution, which changes from light yellow to dark brown, is then stirred under normoxic conditions for 12 hours or longer. PDA appears as a dark-black precipitate that can form NPs or coat materials immersed in the solution. Alternatively, the ammonia-EtOH mixture can be replaced by Tris-alkali or NaOH-alkali buffer. In these cases, DA hydrochloride is dissolved in a Tris-buffered solution and stirred, or is dissolved in $H_2O$(d), added to a NaOH solution and stirred. Anyway, the three solution polymerization methods are very simple and do not require complex equipment. Nevertheless, when they are employed, it is important to note that DA polymerization is sensitive to many factors (dopamine concentration, oxidant content, temperature, stirring speed…), which must be taken into account if modulating particle size or coating thickness is pretended [13,14].

#### 4.1.2.1 Factors affecting dopamine polymerization through solution oxidation

The factors that have been shown to mainly condition the DA polymerization process and, therefore, PDA NP size, which was one of most important parameters studied in this work, have been briefly described below (**Figure 4.2**) [14]. Nonetheless, to understand how they determine PDA formation, it is important to note first that there are two critical steps in the DA polymerization process, which are the initial oxidation of DA to DA-quinone (reversible), and the DA-quinone intramolecular cyclation to form leukodopamine-chrome (irreversible) [15].

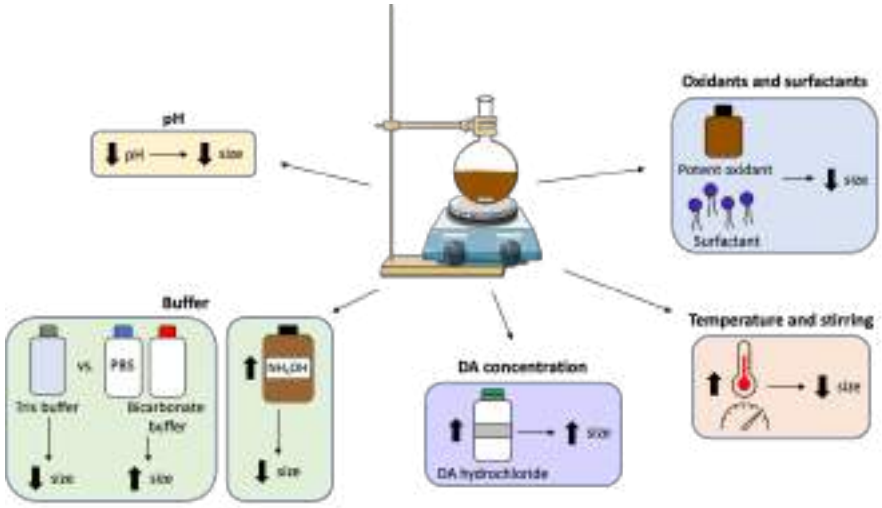


**Figure 4.2.** Summary of the main factors affecting DA polymerization and, thus, PDA NP size.

· **pH:** The most important parameters when analysing the pH effect on DA polymerization and, subsequently, on PDA NP size, are the pKa values of the DA-semiquinone and the amine group of the oxidized DA-quinone form. These pKa values are close to 4.7 and 9.6, respectively. For this reason, the effective onset pH for DA auto-oxidation is close to 5, and the reaction rate increases markedly at high pH values [15]. In this way, since protonation slows down particle growth, and increasing the pH of the synthesis media favours the obtaining of smaller PDA NPs with greater yield [14,16], DA polymerization is mostly performed at weakly alkaline pH values. Nevertheless, synthesizing PDA NPs is also possible in acidic conditions if the polymerization process is carried out under high temperature and pressure conditions, as reported by Zheng and co-workers [17].

· **Buffer solution:** When the use of various types of buffers (Tris, phosphate and bicarbonate buffers) in the synthesis of PDA NPs was compared, it was demonstrated that Tris buffer affected the nucleophilic reaction that converts DA-quinone into leukodopamine-chrome. Tris adducts were formed, and this led to particles with smaller diameter. However, no adduct formation was observed when PBS and bicarbonate buffer were employed, with which larger PDA aggregates were obtained [14]. On the

other hand, as mentioned before, DA solution oxidation can be also performed in ammonia-EtOH mixtures instead of using any buffer. In this case, ammonia acts as a catalyst in the polymerization reaction [18]. Therefore, the higher the ratio ammonia/DA, the smaller the size of the PDA NPs obtained [19], as happens when NaOH buffer is employed [14].

· **Concentration of DA:** DA hydrochloride concentration is another crucial factor that has demonstrated to condition DA polymerization mechanism. Lower concentrations of this monomer allow DA-quinone to be slowly generated and less efficiently trapped by DA and, whence, to have higher chance of intramolecular cyclation to generate leukodopamine-chrome. Conversely, when higher concentrations of DA hydrochloride are used to synthesize PDA NPs, as HCl changes the pH of the solution and decreases the polymerization reaction rate, larger NPs are generated [14].

· **Oxidants:** The employment of oxidants is essential for DA polymerization to take place. Air oxygen is usually used to obtain PDA NPs at basic pH values but, since it is a poor oxidant agent [15], other oxidant compounds, such as ammonium persulfate or sodium periodate, are occasionally employed to speed up DA polymerization [14].

· **Temperature and stirring speed:** High-speed agitation has proven to increase DA polymerization rate. Likewise, this reaction rate is also enhanced by higher temperature values, which promote DA oxidation and lead to the generation of narrow PDA NPs with increased density [14].

· **Surfactant employment:** With the aim of obtaining very small PDA NPs, of the order of a few nanometres, the employment of amphiphilic surfactants, which can interact with DA and other oxidative products, has been reported by some researchers [14].

### *4.1.3. Polydopamine properties and applications in cancer nanomedicine*

Besides its easy and low-cost polymerization, PDA has great physicochemical properties, determined by its mode of synthesis, which have made it to acquire a relevant role in nanomedicine research in recent years [20]. Some of its most notable properties are, for example [3,20-22]:

- Wide UV/Visible (Vis) absorption, ranging from the UV until IR. In addition, PDA releases the energy of the absorbed light almost entirely without radiation.
- Possibility of linking a wide range of interesting molecules (other polymers, biomolecules, metals…), since PDA contains a great variety of reactive functional groups (amino, catechol and o-quinone groups). In particular, catechol moieties provide PDA great affinity for metal ions.
- As already mentioned, ability to coat almost all type of surfaces. Its strong adhesion power is attributed to its catechol and aminoethyl groups.
- Ability to trap radicals thanks to its irregular, cross-linked polymer network.
- Electrical conductivity
- Efficiency when acting as photothermal agent
- Biocompatibility and biodegradability

These excellent properties are what have led PDA, in the specific case of cancer nanomedicine, to be used for tumour imaging, photothermal therapy, combined chemo- and photothermal therapy, and for the development of PDA-based theranostic systems and DDSs [4 6,13,23].

Regarding the application of PDA in the development of anti-tumour DDSs, which is of great importance for this thesis, it should be highlighted that the main forms of PDA-based nanocarriers than can be found in the literature are PDA nanocolloids or NPs, PDA nanocapsules or hollow NPs, PDA drug conjugates and PDA-coated (organic or inorganic) core@shell NPs [4,6,13].

Of these forms, PDA nanocolloids have been the most relevant one for the studies described in this and the following two chapters. Thereby, specifically in the current chapter, the synthesis of PDA NPs, as well as the modification of some conditions in their synthesis reaction that allowed them to be tailored-made, have been described. Likewise, the affinity of these NPs for different metal cations and their intrinsic antineoplastic activity, which are related to each other and to particle size, have been analysed. For the latter, it was necessary to develop a novel protocol that would allow to conduct viability assays with PDA-based nanomaterials, and which has also been described in this chapter.

## 4.2. Synthesis and characterization of polydopamine nanoparticles

### *4.2.1. Synthesis of tailored-made polydopamine nanoparticles*

Throughout the entire project, PDA NPs were synthesized through solution oxidation in basic aqueous media. First, an ammonia aqueous solution ($NH_4OH$, 28-30%) was mixed with an alcohol (ROH)/$H_2O$(d) (40 mL/90 mL, respectively) mixture under vigorous magnetic stirring at room temperature for 30 minutes. Later, a DA hydrochloride aqueous solution was prepared (0.05 g/mL, 10 mL) and added to the previous mixture. The polymerization reaction was left to react for 24 hours. Then, PDA NPs obtained were isolated by centrifugation and purified by at least four centrifugation-redispersion cycles in $H_2O$(d). Finally, depending on the subsequent application, these NPs were suspended in $H_2O$(d) or further washed with PBS [22,24-26] (**Figure 4.3**).

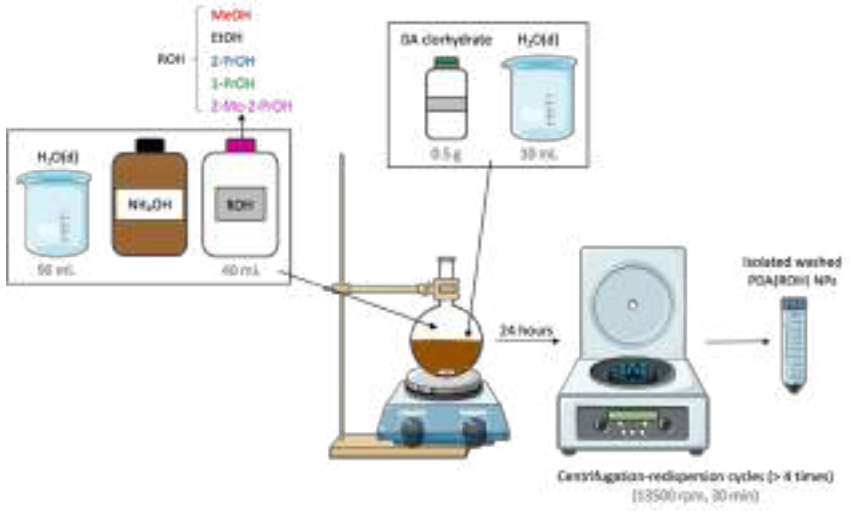


**Figure 4.3.** Schematic representation of the solution oxidation process carried out in basic aqueous media to synthesize PDA NPs.

In this synthesis process, in order to obtain NPs of different size, the $NH_4OH$ concentration used was varied (2.91, 1.52 or 0.84% (V/V)), but always keeping a constant EtOH/$H_2O$(d) volume ratio (4:10, equivalent to 28.57% (V/V)).

Besides, since PDA NPs are synthesized as a rule in EtOH/$H_2O$(d) mixtures when $NH_4OH$ is used [22,24-25,27], trying to use other ROHs with different number of carbon atoms for DA polymerization reaction was determined. In the literature, it was found that some researchers had already been able to prepare PDA NPs in aqueous media containing methanol (MeOH) and 2-propanol (2-PrOH) [28]. However, how the choice of one or the other ROH affects PDA NP properties had not been analysed yet. For this reason, to further characterize them, PDA NPs were synthesized using EtOH, MeOH and 2-PrOH. In addition, 1-propanol (1-PrOH) and 2-methyl-2-propanol (2-Me-2-PrOH) were also employed to try to produce them (**Figure 4.3**). In all cases, a fixed ROH/$H_2O$(d) volume ratio (28.57% (V/V), 140 mL) and a similar $NH_4OH$ concentration (2.79% (V/V)) were used, and it was observed that all the ROHs employed made it possible to obtain PDA NPs. Later, in order to also study the effect of the $NH_4OH$ concentration employed on NP size as a function of the ROH

chosen, additional polymerization reactions were performed by varying the $NH_4OH$ concentration in the synthesis media (0.79 - 3.01% (V/V)) [26].

### *4.2.2. Characterization of polydopamine nanoparticles synthesized with different ammonia concentrations and in different alcohol/water media*

#### 4.2.2.1. Effect of ammonia concentration on polydopamine nanoparticle size

As mentioned in the previous point, PDA NPs were firstly prepared in $EtOH/H_2O$(d) mixtures (28.57% (V/V), 140 mL) by varying the $NH_4OH$ concentration used in order to study its influence on particle size. The latter was firstly determined through DLS, on the basis of NP intensity-average distribution, after suspending PDA NPs in Trizma-base solution (50 mM, pH 10) to ensure their stability. In addition, PDA NP size was analysed, along with NP morphology, by transmission electron microscopy (TEM). In this case, all PDA NPs were dispersed in $H_2O$(d) in a concentration inferior to 0.01% (WT). Drops of these dispersions were deposited on copper grids with a collodion membrane and were allowed to dry for 24 hours. Several images were taken from each sample at an acceleration voltage of 120 kV and, after determining the diameter of at least 300 different NPs, size-range histograms were made.

As a result, when DLS was employed, it was observed that the use of higher $NH_4OH$ concentrations led to obtain smaller PDA NPs, as had already been reported in the literature [19]. In this way, when a 2.91% (V/V) $NH_4OH$ concentration was employed, PDA NPs with an average size close to 115 ± 50 nm (PDI = 0.05) were obtained. However, when this concentration was 1.52 and 0.84% (V/V), average PDA NP size was about 200 ± 50 nm and 400 ± 50 nm (PDI = 0.09 and 0.01), respectively.

This trend was also verified when TEM images were acquired, although NP average size determined by using this technique was almost 50 nm smaller than that determined by DLS, possibly because of the dehydration of the NPs, necessary when preparing TEM samples (**Figure 4.4**) [25,29].

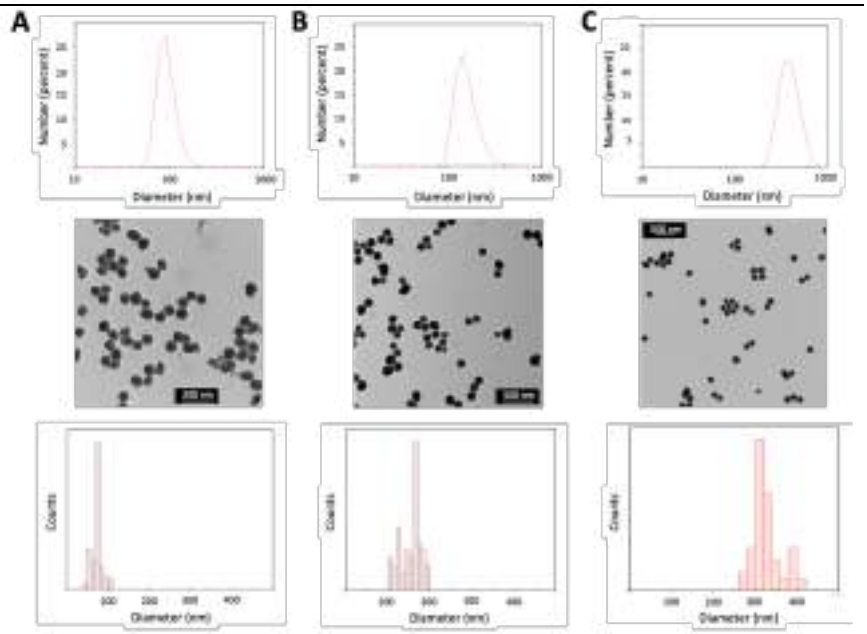


**Figure 4.4.** DLS number distributions, TEM images and size-range histograms of the PDA NPs prepared in EtOH/$H_2O$ (28.57% (V/V)) mixtures with different concentrations of $NH_4OH$ (% (V/V)): (**A**) 2.91%; (**B**) 1.52%; (**C**) 0.84%.

4.2.2.2. Effect of the type of alcohol employed in the synthesis of polydopamine nanoparticles on their size

Next, PDA NPs synthesized with the five different ROHs were also characterised by DLS and TEM, preparing the samples as described before (**Figure 4.4**). Again, NP diameters determined by TEM were smaller than those determined by DLS [29]. Anyway, both characterization methods allowed to reach the same conclusion: the type of ROH used to prepare PDA NPs conditioned their size when the $NH_4OH$ concentration and the ROH/$H_2O$(d) volume ratio employed were kept constant. Thereby, it was noticed that the higher the dielectric constant (ε) of the ROH used in the DA polymerization reaction, the larger the diameter of the PDA NPs obtained. This phenomenon was observed with all the ROHs studied, except for 1-PrOH, as can be seen in **Table 4.1**. This last ROH had the third highest ε, but its employment resulted in obtaining the smallest PDA NPs. The explanation of this fact was later found, when the Hansen's solubility parameters (HSP) distances ($R_a$ values) between DA and the different ROH/ $H_2O$(d) mixtures used were determined [26].

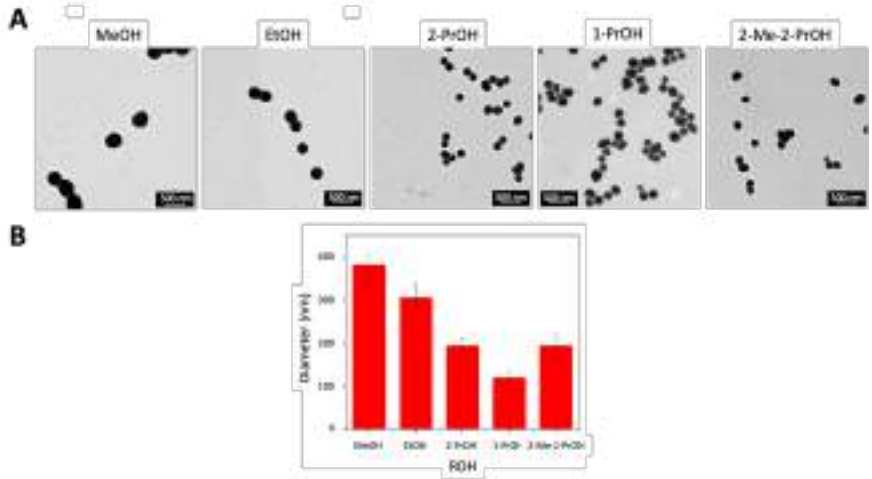


**Figure 4.5.** TEM images (**A**) and size-range histogram (**B**) of the PDA NPs prepared in the different ROH/$H_2O$ (28.57% (V/V)) mixtures by employing a similar $NH_4OH$ concentration (0.79% (V/V)).

**Table 4.1.** Size (determined by DLS and TEM) of the PDA NPs prepared in the different ROH/$H_2O$(d) mixtures. DLS particle diameters shown are the mean ± SEM of three parallel measurements.

| ROH | ε | Size (DLS) (nm) | Size (TEM) (nm) |
|---|---|---|---|
| **MeOH** | 33.1[1] | 628 ± 145 (PDI = 0.23) | 382 ± 26 |
| **EtOH** | 23.8[1] | 412 ± 120 (PDI = 0.08) | 306 ± 32 |
| **2-PrOH** | 19.2[2] | 282 ± 70 (PDI = 0.04) | 194 ± 20 |
| **1-PrOH** | 20.1[2] | 191 ± 41 (PDI = 0.23) | 119 ± 16 |
| **2-Me-2-PrOH** | 12.5[2] | 286 ± 70 (PDI = 0.21) | 194 ± 27 |

[1][25],[2][23]

4.2.2.3. Hansen's solubility parameter distances between dopamine and the different media employed for polydopamine nanoparticle synthesis

As already said, the size of PDA NPs increased as the ε of the ROHs used to synthesize them augmented, except when 1-PrOH was employed. This fact could be explained by means of the (HSP) distances ($R_a$ values) between DA and the different ROH/$H_2O$(d) mixtures prepared.

HSP theory is a semi-empirical correlation developed to explain dissolution, which is considered an adaptation between the HSP parameters of solvents and solutes. These parameters are the dispersive (D), polar (P) and H-bonding (H) solubility parameters, and HSP distances ($R_a$ values) are used to evaluate the level of the mentioned adaptation. $R_a$ values can be calculated with **Equation 4.1**. When mixed solvents are employed, as in this case, solvent composition can be taken into account with **Equation 4.2,** where Ø is the volume fraction of each component in the mixture [28]:

$$R_a = [4(D_{solv} - D_{solu})^2 + (P_{solv} - P_{solu})^2 + (H_{solv} - H_{solu})^2]^{0.5}$$

**Equation 4.1**

$$D(P,H)_{blend} = \sum \emptyset_{n,comp}\ D(P,H)_{n,comp}$$

**Equation 4.2**

Both equations had already been employed by Jiang et al. to determine the $R_a$ values between DA and mixtures of $H_2O$ and EtOH, MeOH or 2-PrOH in different volume ratios [28]. In this project, **Equations 4.1** and **4.2** were employed to analyse whether the ROH/$H_2O$ volume ratio (28.57% (V/V)) that was chosen to prepare PDA NPs in the different ROH/$H_2O$(d) mixtures was suitable. The HSP values used in such equations and the $R_a$ values that were estimated can be seen in **Table 4.2** and **4.3**.

**Table 4.2.** HSP values taken from the literature to calculate the $R_a$ values of DA and the different ROH/$H_2O$(d) mixtures.

| Chemical | D | P | H |
|---|---|---|---|
| **$H_2O$[1]** | 18.1 | 12.9 | 15.5 |
| **MeOH[1]** | 15.1 | 12.3 | 22.3 |
| **EtOH[1]** | 15.8 | 8.8 | 19.4 |
| **2-PrOH[1]** | 15.8 | 6.1 | 16.4 |
| **1-PrOH[2]** | 16 | 6.8 | 17.4 |
| **2-Me-2-PrOH[3]** | 15.1 | 5.1 | 14.7 |
| **DA[1]** | 18.2 | 9 | 17.1 |

[1][28],[2][31],[3][32]

**Table 4.3.** HSP and $R_a$ values of DA and the different ROH/$H_2O$(d) mixtures (4:10, 28.57% (V/V)) estimated by using Equation 4.1 and 4.2.

| ROH | D | P | H | $R_a$ |
|---|---|---|---|---|
| **MeOH** | 17.24 | 12.73 | 17.44 | 4.21 |
| **EtOH** | 17.28 | 11.44 | 16.89 | 3.06 |
| **2-PrOH** | 17.44 | 10.96 | 15.76 | 2.82 |
| **1-PrOH** | 17.5 | 11.16 | 16.04 | 2.78 |
| **2-Me-2-PrOH** | 17.24 | 10.67 | 15.27 | 3.13 |

The results obtained showed that the ROH/$H_2O$ volume ratio used was suitable when EtOH, MeOH and 2-PrOH were employed, since the $R_a$ values that were achieved were close to the minimum ones reported by Jiang et al. [28]. However, the $R_a$ value obtained of DA and the 1-PrOH/$H_2O$(d) (28.57% (V/V)) medium was not so adequate since, in general, the smaller the $R_a$ value, the higher the expected solubility [28].

Thereby, the optimal $R_a$ value of DA and the 1-PrOH/$H_2O$(d) mixture was determined by varying the proportion of 1-PrOH in $H_2O$(d) from 35.71% to 50% (V/V). It was found to be $R_a$ = 2.5 when the concentration of 1-PrOH in the mixture was 42.86% (V/V) (equivalent to a 6:8 ratio) (**Table 4.4**). When this volume ratio was employed, 297.5 ± 62 nm sized PDA NPs were obtained.

**Table 4.4.** HSP and $R_a$ values of DA and the different 1-PrOH/$H_2O$(d) mixtures obtained when different volume ratios of 1-PrOH in $H_2O$(d) were used.

| [1-PrOH] (V/V) | D | P | H | $R_a$ |
|---|---|---|---|---|
| **35.72%** | 17.35 | 10.72 | 16.18 | 2.59 |
| **48.26%** | 17.2 | 10.29 | 16.31 | 2.5 |
| **50%** | 17.05 | 9.85 | 16.45 | 2.54 |

Finally, regarding the employment of 2-Me-2-PrOH, which had not been reported to synthesize PDA NPs previously, it was noticed that the 2-Me-2-PrOH/$H_2O$(d) volume ratio that was initially employed (i.e., 28.57% (V/V)) was the optimal one. Lower and higher 2-Me-2-PrOH volume concentrations led to more elevated $R_a$ values, as can be observed from **Table 4.5** [26].

**Table 4.5.** HSP and $R_a$ values obtained of DA and the different 2-Me-2-PrOH/$H_2O$(d) mixtures when different volume ratios of 2-Me-2-PrOH in $H_2O$(d) were used.

| [2-Me-2-PrOH] (V/V) | D | P | H | $R_a$ |
|---|---|---|---|---|
| **14.28%** | 17.67 | 11.79 | 15.39 | 3.44 |
| **21.43%** | 17.46 | 11.23 | 15.33 | 3.21 |
| **35.75%** | 17.03 | 10.11 | 15.21 | 3.21 |

### 4.2.2.4. Effect of ammonia concentration on polydopamine nanoparticle size as a function of the alcohol used for their synthesis

Based on the $R_a$ values of DA and the aqueous solutions containing the five ROHs studied that were obtained, $NH_4OH$ concentration in the solvent mixture was varied to determine its influence on PDA NP size as a function of the ROH employed in the synthesis process. As mentioned before, the ROH/$H_2O$(d) volume ratio was kept constant (28.57% (V/V)) in this case, and polymerization reactions were performed with $NH_4OH$ concentrations ranging between 0.79% and 3.01% (V/V), depending on the type of ROH used. The diameter of all the resulting NPs (PDA(ROH) NPs) was determined by DLS (**Figure 4.6.A**) after suspending the NPs in Trizma-base solution. In **Figure 4.6.B**, average size values obtained have been represented as a function of the $NH_4OH$ concentration employed for each ROH/$H_2O$(d) medium.

As had happened before and as expected, in all the systems studied, an increase of the $NH_4OH$ concentration in the medium led to smaller PDA NPs since, as said, pH conditions DA oxidation and polymerization [14,16]. In general, the biggest NPs were obtained with MeOH and, the smallest ones, with 1-PrOH, and it was observed that when larger amounts of $NH_4OH$ were employed, the differences in size among the different PDA(ROH) NPs were less noticeable. In order to facilitate the comparison of the $NH_4OH$ concentration effect on PDA(ROH) size, diameter values represented in the **Figure 4.6.B** have also been summarized in **Table 4.6**.

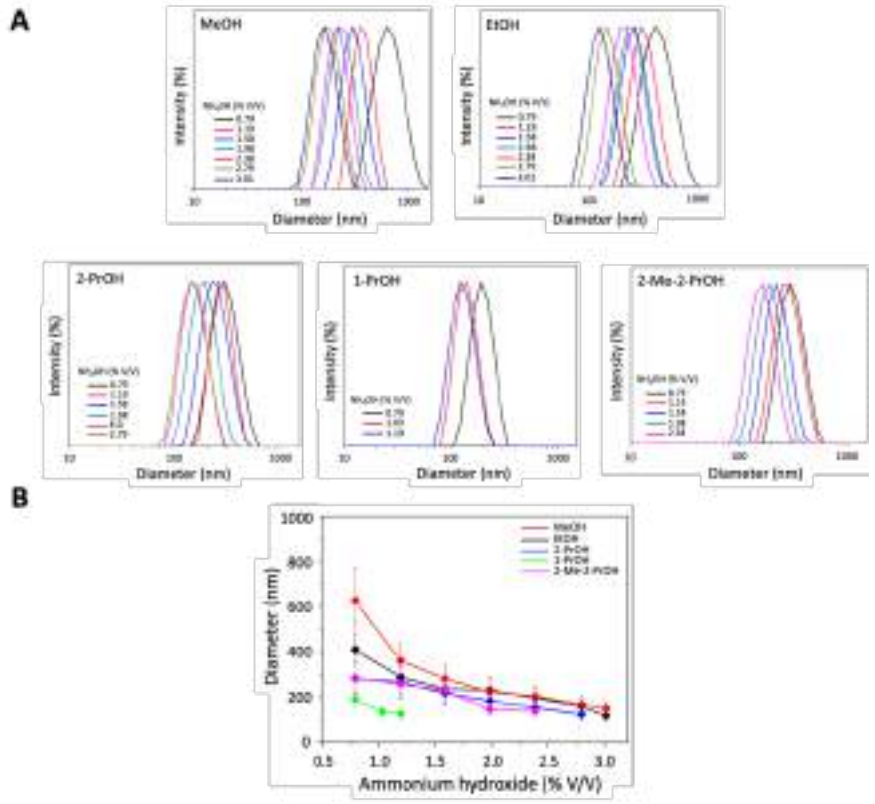


**Figure 4.6.** (**A**) DLS intensity distribution of the PDA NPs prepared in the different ROH/$H_2O$ mixtures with various $NH_4OH$ concentrations (% (V/V)); (**B**) PDA(ROH) NP size as a function of the $NH_4OH$ concentration used for their synthesis.

**Table 4.6.** Average size values ± SEM of the PDA NPs prepared in the different ROH/$H_2O$(d) mixtures with different $NH_4OH$ concentrations. $NH_4OH$ concentrations are expressed in % (V/V) and, NP sizes (determined by DLS), in nm.

| | **[$NH_4OH$]** | | | |
|---|---|---|---|---|
| **ROH** | **0.79** | **1.03** | **1.19** | **1.58** |
| **MeOH** | 628.2 ± 145 | - | 362.4 ± 82 | 382.3 ± 66 |
| **EtOH** | 411.6 ± 120 | - | 289.3 ± 76 | 237 ± 56 |
| **2-PrOH** | 282.5 ± 64 | - | 268.3 ± 67 | 218 ± 55 |
| **1-PrOH** | 191.5 ± 41 | 134.4 ± 25 | 125.2 ± 24 | - |
| **2-Me-2-PrOH** | 286.2 ± 70 | - | 259.1 ± 69 | 230.9 ± 59 |

| **ROH** | **1.98** | **2.38** | **2.79** | **3.01** |
|---|---|---|---|---|
| **MeOH** | 224.5 ± 53 | 204.7 ± 43 | 168.3 ± 35 | 149.6 ± 30 |
| **EtOH** | 231.7 ± 55 | 198 ± 45 | 158.6 ± 33 | 117.4 ± 22 |
| **2-PrOH** | 184.1 ± 39 | 154.1 ± 31 | 123 ± 26 | - |
| **1-PrOH** | - | - | - | - |
| **2-Me-2-PrOH** | 145.4 ± 29 | 138.2 ± 27 | - | - |

### 4.2.2.5. Analysis of the chemical structure of polydopamine nanoparticles obtained by employing different alcohols

By last, to finish with the characterization of the PDA(ROH) NPs obtained, and to analyse whether the use of one ROH or another affected NP chemical structure, IR absorption spectra were performed in the 4000 - 400 $cm^{-1}$ wavelength range. PDA(ROH) NPs were dried overnight at 37°C and samples were prepared as pellets of PDA NPs in dried KBr. Spectra were normalized in order to compare the intensity of the different bands (**Figure 4.7**), which were assigned according to a previous characterization of melanin, since it is a natural PDA analogue [33,34].

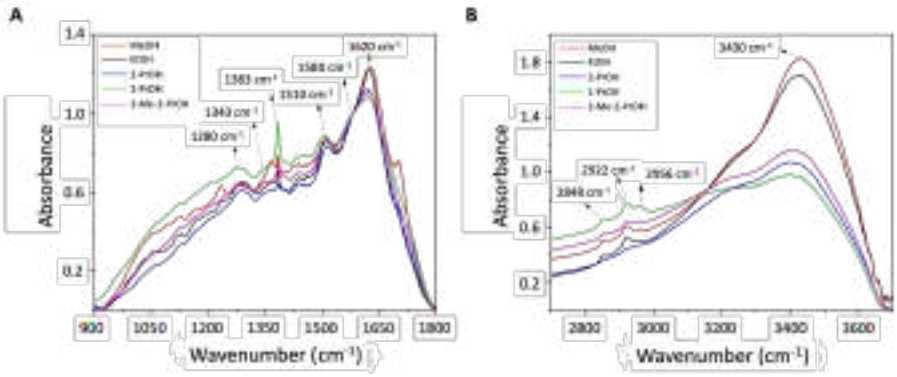


**Figure 4.7.** IR spectra of the different PDA(ROH) NPs obtained in the (**A**) 900 - 1800 $cm^{-1}$ and (**B**) 2700 - 3700 $cm^{-1}$ ranges.

According to this melanin characterization, the broad adsorption band with the maximum at 1612 $cm^{-1}$ may include the C=O stretching (non-carboxylic acid) and the C=C stretching (at 1580 $cm^{-1}$) of an aromatic system. The N-H bending in an indole ring may appear at 1510 $cm^{-1}$, while the peaks at 1345 and 1383 $cm^{-1}$ may correspond to the C-N stretching mode of an indole and a pyrrole ring, respectively. The C-OH stretching in a phenol ring appears at 1280 $cm^{-1}$, and the bands at 2956, 2922 and 2840 $cm^{-1}$ would correspond to the different vibrational modes of the aliphatic groups. Finally, the broad band that can be found at 3405 $cm^{-1}$ may include the -OH (phenol, carboxylic acid) and the -NH (in an indole ring or in a primary amine) stretching modes.

Melanin characteristic bands within the 900-1800 $cm^{-1}$ range could be distinguished in the spectra of all PDA(ROH) NPs, as well as the main bands within the 2700-3700 $cm^{-1}$ range. Nevertheless, in the latter case, the relative intensity of the band at 3430 $cm^{-1}$, associated with the -OH and -NH stretching modes, notably decreased when 1-PrOH, 2-PrOH and 2-Me-2-PrOH were employed for PDA NP synthesis [26].

## 4.3. Selective toxicity of polydopamine nanoparticles to tumour cells

### *4.3.1. Development of a protocol for the performance of MTT assays with polydopamine nanoparticles*

Once the characterization of the PDA NPs prepared was finished, their toxicity to several cell lines was studied. As mentioned in the introduction of this chapter, thanks to its outstanding properties, PDA is being used for the development of novel tumour imaging agents, photothermal therapies and DDS [3-4,13-14]. However, PDA NP cytotoxicity had not been studied *in vitro* in depth yet. Some authors had performed *in vivo* assays to show PDA biocompatibility [33,34], but this property had only been analysed *in vitro* for 24 hours in most cases. In addition, and most importantly, when conducting cell viability assays using different colorimetric techniques (such as MTT assays or assays based on the cell counting kit-8), the broad adsorption band in the UV-Vis region of the PDA NPs, which remain adhered to the bottom of the plate wells, had not been taken into account in the absorbance values obtained and, therefore, neither in viability results [19,33,35-37].

As can be seen in **Figure 4.8.A**, when the absorption of different aqueous dispersions of PDA NPs (0.006 - 0.038 mg/mL) was studied by UV-Vis spectroscopy in 100 - 1000 nm wavelength range, it was observed that PDA had maximum absorption at 280 nm. Nevertheless, PDA NP absorbance was still significant (especially when concentrations greater than 6 µg/mL were employed) at 550 nm, the wavelength at which the MTT reagent exhibits its maximum absorbance.

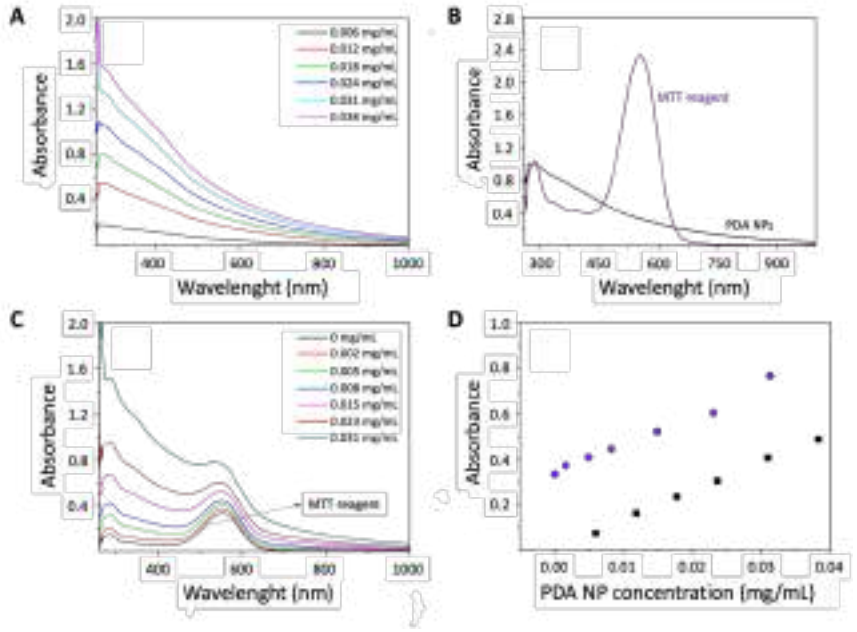


**Figure 4.8.** (**A**) UV-Vis absorption spectra of dispersions of PDA NPs of different concentration; (**B**) Overlap between the absorption spectra of the MTT reagent (purple, 0.025 mM) and that of PDA NPs (black, 0.012 mg/mL) at 550 nm; (**C**) Effect of the addition of different concentrations of PDA NPs on the MTT absorbance; (**D**) Absorbance at 550 nm of the MTT reagent (0.025 mM) plus different concentrations of PDA NPs (purple), whose absorbance was also separately determined (black).

Thus, in order to demonstrate that the absorbance of the MTT reagent and the PDA NPs could overlap at 550 nm when performing viability assays, their UV-Vis absorption spectra were obtained. For this, a MTT solution (0.025 nM) was prepared in DMSO, and PDA NPs (0.012 mg/mL) were also dispersed in this solvent, since it was the one used to solubilize formazan crystals. Spectra obtained have been represented together in **Figure 4.8.B**, in which the mentioned absorbance overlap can be seen clearly at 550 nm.

Furthermore, the effect that the addition of different concentrations of PDA NPs (0.002 - 0.031 mg/mL) had on the absorbance of the MTT reagent (0.025 mM) was also determined. First, absorption spectra of the different mixtures were obtained (**Figure 4.8.C**). Then, it could be noticed that the addition of any PDA NP dispersion to the MTT solution led to an increase in the MTT adsorption band. In this manner,

spectra obtained were the result of merging the absorption bands of the MTT solution and those of the different PDA NP dispersions. Similarly, this phenomenon could be noticed when the absorbance values of the mixtures (MTT reagent plus PDA NP dispersions) were determined at 550 nm and compared with those of the PDA NPs dispersions, measured separately (**Figure 4.8.D**). In this case, it was observed how MTT reagent absorbance increased linearly as a function of the PDA NP concentration appended, even doubling when a concentration of 0.031 mg/mL of NPs was added [22].

Conversely, when carrying out the spectrophotometry characterization of the MTT and PDA NPs, it could be also noticed that the former did not show adsorption above 700 nm (**Figure 4.8.B**). Therefore, this fact was used to develop a new protocol that would allow the performance of MTT assays with PDA-based nanomaterials without obtaining an overestimation of cell viability.

This procedure consisted of subtracting PDA contribution to sample absorbance in MTT assays by using a calibration curve that related PD concentration to its absorbance at 550 nm. This fact was achieved following the next steps, summarized in **Figure 4.9** [22]:

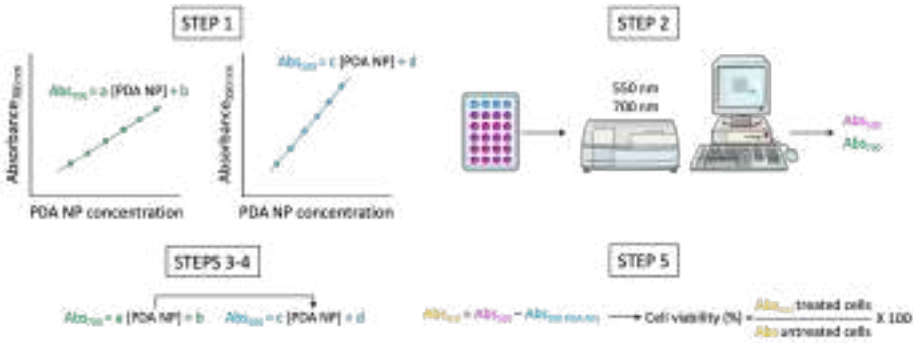


**Figure 4.9.** Illustration of the protocol proposed to subtract PDA NP absorbance contribution at 550 nm in MTT assays and, thus, avoid getting overestimated viability results.

1. Establishment of calibration curves for absorbance *vs*. PDA NP concentration (mg NPs/mL DMSO) at both 550 and 700 nm by using the microplate reader employed to perform the MTT assays.
2. Performance of the MTTs assay in the conventional way but measuring the absorbance of the wells not only at 550 nm, but also at 700 nm.
3. Since only PDA NPs absorbed at 700 nm, the absorbance values obtained at this wavelength determined the remaining PDA NP concentration adhered to the plates, which could be interpolated from the calibration curve established at 700 nm.
4. Once the remaining PDA NP concentration was known, its contribution to the absorbance at 550 nm could be interpolated from the calibration curve stablished at this wavelength.
5. Finally, in order to properly quantify cell viability, PDA NP absorbance contribution at 550 nm was subtracted from the absorbance values obtained from the samples when they were measured at such wavelength in step 2.

Fortunately, most microplate readers are able to carry out absorbance measurements in the 340 – 800 nm range, so the protocol proposed was easy to apply. In the current chapter, the steps detailed were followed to study PDA NP cytotoxicity in longer MTT assays than had been done so far in the literature (72 hours *vs*. 24 hours), as it can be seen in the oncoming points.

### *4.3.2 Implementation of the MTT protocol developed to study polydopamine nanoparticle cytotoxicity*

In order to study PDA NP cytotoxicity, the BT474 breast carcinoma cell line was chosen to perform viability assays due to its marked HER2-overexpression and its easy culture. Moreover, NIH/3T3 mouse fibroblasts were selected to compare PDA NPs toxicity to tumour and stromal cells [38,39]. Both cell lines were cultured as instructed, and once grown, they were seeded into 24-well plates (12,000 cells/mL) and were incubated for 24 hours to allow attachment. Then, culture media in the wells was replaced by DMEM containing different concentrations of PDA NPs. These NPs had been synthesized in a EtOH/$H_2O$(d) mixture with a $NH_4OH$

concentration close to 2.36% (V/V), and they had shown a 116 nm ± 20 nm (PDI = 0.04) size when they had been characterized by DLS (**Figure 4.10**) [22].

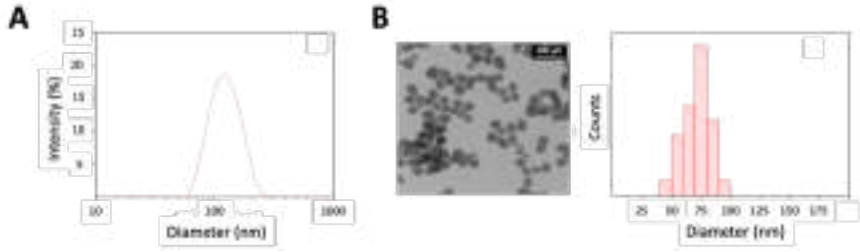


**Figure 4.10.** DLS number distribution (**A**), TEM image and size-range histogram (**B**) of the PDA NPs that were later analysed for toxicity to BT474 and NIH/3T3 cells.

To measure the absorbance of the wells 24, 48 and 72 hours after treatment, MTT reagent was added (5 mg/mL, 110 µl/well) and cells were incubated for 1 hour at 37°C, following the usual procedure. After that time, the protocol detailed in the previous point was applied. Relative cell viability was determined with Equation 3.3 (Chapter 3, page 98) by comparing the absorbance values of the cells treated with PDA NPs with the absorbance of an untreated control.

The results obtained with both cell lines, BT474 and NIH/3T3, have been included in **Figure 4.11.A-B**, where the average viability values of three parallel measurements have been represented. Furthermore, with the aim of demonstrating the importance of taking into account PDA contribution to the absorbance of the MTT reagent at 550 nm, the overestimated viability results that would be obtained with the BT474 cell line if the stablished protocol had not been followed have also been included in **Figure 4.11.C** [22].

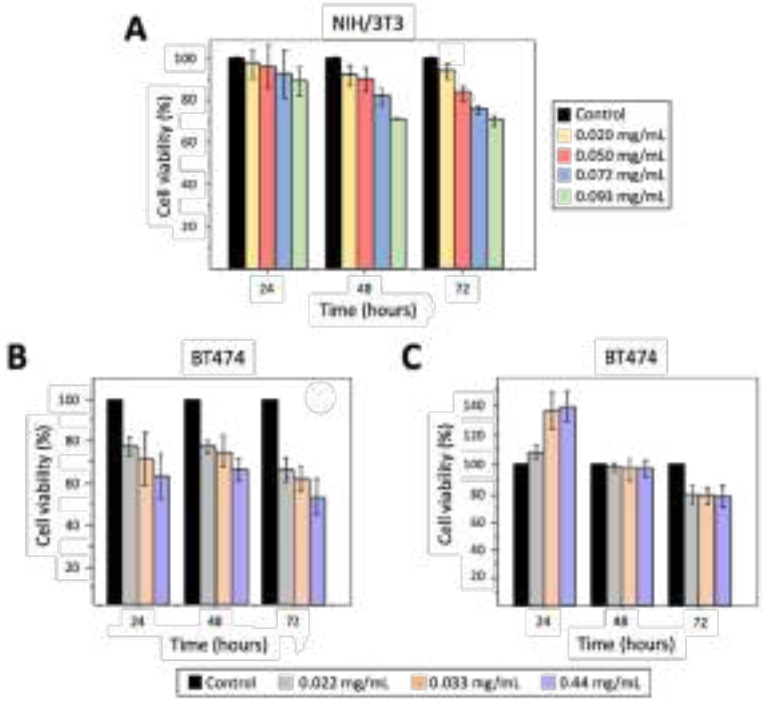


**Figure 4.11.** Results of the MTT assays performed following the stablished protocol with the NIH/3T3 (**A**) and BT474 (**B**) cell lines, which were treated with different concentrations of PDA NPs; (**C**) Viability rate values of BT474 cells that would have been obtained if the procedure detailed in Figure 4.8 had not been applied. All results shown are the average viability values ± SEM of three parallel experiments.

On one hand, regarding the results obtained with the NIH/3T3 cell line (**Figure 4.11.A**), it could be noticed that, after 24 hours of treatment, no PDA NP concentration decreased fibroblast viability below 90%. This fact was in line with the results obtained in works in which it had been affirmed that PDA was biocompatible [19,33,35-37]. After 48 hours of treatment, only the stromal cells that were treated with the highest PDA NP concentration (0.093 mg/mL) showed a viability of less than 80%. Instead, after 72 hours of exposure, the 0.072 mg/mL NP concentration also reduced fibroblast survival rate below 80%. Therefore, it was

concluded that PDA NPs were biocompatible at concentrations below 0.05 mg/mL [22].

On the other hand, when concentrations that were not toxic to fibroblasts (0.022 - 0.044 mg/mL) were used to treat breast carcinoma cells, their viability was significantly reduced ($p < 0.05$) (**Figure 4.11.B**). After 24 and 48 hours of treatment, BT474 cell survival rate was close to 77 - 64%, depending on the NP concentration employed. When 24 hours more elapsed, such rate decreased to 65 - 52%. Thus, following the procedure stablished for conducting MTT assays, it was revealed that concentrations of PDA NPs lower than 0.05 mg/mL had selective toxicity to tumour cells. On the contrary, if this protocol had not been followed and PDA contribution to absorbance values at 550 nm had not been taken into account, PDA NP anti-tumour activity would not have been detected, since the survival rate of treated cells would have been overestimated by about 30% (**Figure 4.11.C**) [22].

### *4.3.3. Study of polydopamine nanoparticle internalization in cancer cells*

Once it was verified that PDA NPs were toxic to BT474 cells, their internalization in this cell line was assessed by CLSM. For this purpose, fluorescent PDA NPs were prepared following the protocol described by Chen and colleagues [40]. Briefly, PDA NPs previously synthesized (100 nm, 0.15% (WT)) were suspended in a Tris base solution (37.5 mL) containing 177.8 mg of DA, and a second polymerization reaction was allowed to occur. NPs were kept under magnetic stirring for 1 hour and $H_2O_2$ (10 mL, 33% (V/W)) was added. Then, the reaction was left to proceed for 24 hours, and the resulting fluorescent PDA NPs were purified by four centrifugation-redispersion cycles in $H_2O$(d) plus four additional cycles in PBS [22,24].

Next, BT474 cells were seeded into glass bottom plates (8,000 cells/mL) and incubated next day with the fluorescent PDA NPs (0.05 mg/mL) at 37°C for 3 hours. After that time, CLSM images were acquired with an excitation of 405 nm. In these images, fluorescent PDA NPs could be observed in the cytoplasm of the treated cells (**Figure 4.12.A**). In addition, lysosomes of BT474 cells were stained with LysoTracker™ Red

DND-99 (50 nM) and imaged with an excitation/detection of 647/668 nm. This fact allowed to verify that the signal of these acidic organelles co-localized with that of the fluorescent PDA NPs. Herein, when PDA NPs were endocyted, they remained in the cellular late endosomes/lysosomes (**Figure 4.12.B**) [22,24].

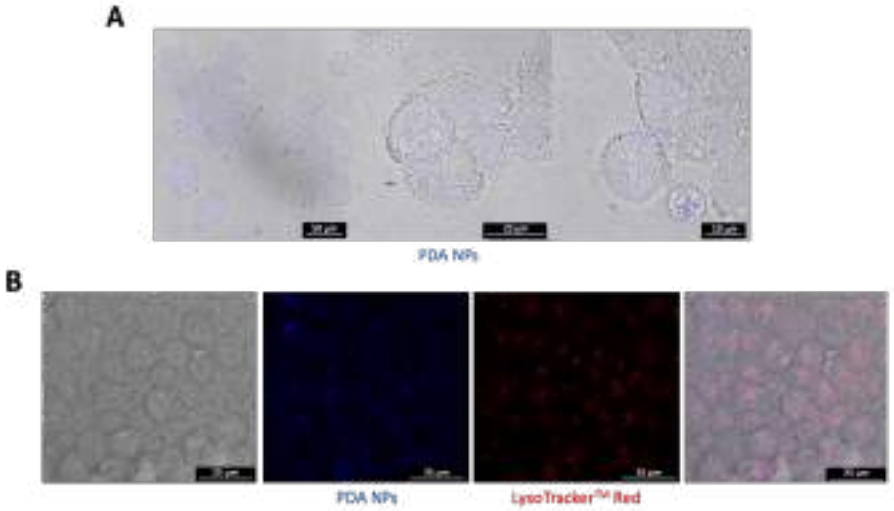


**Figure 4.12.** (**A**) CLSM images of BT474 cells incubated with fluorescent PDA NPs (100 nm, 0.05 mg/mL, blue) for 3 hours; (**B**) From left to right, bright field image of BT474 cells, fluorescent signal (blue) of PDA NPs internalized in those cells after 3 hours, fluorescent signal of BT474 stained lysosomes (red), and image obtained after merging the previous three.

## 4.4. Potential implication of iron affinity of polydopamine nanoparticles in their cytotoxicity

### *4.4.1. Analysis of polydopamine strong metal-ion chelation ability*

As already said in the introduction of this chapter, one property that has made PDA relevant in the nanomedicine field is its great variety of functional groups (catechol, amines, imines…), which allows its functionalization with a wide range of molecules [3,41]. Among these molecules, those for which PDA, like melanin [42], shows the highest affinity are metal ions [24].

With regard to the latter, it should be noted that metal ion assimilation is essential for all mammalians. Nonetheless, the availability of these ions within the cells has to be properly controlled to avoid protein inactivation and, therefore, to prevent cell malfunction [43]. Indeed, the intracellular organelles responsible for maintaining this metal ion homeostasis by storing them are the late endo/lysosomes, in which PDA NPs were found after their internalization [24,43].

This, along with results obtained in studies performed by other authors in which it had been proven than melanin is able to both protect the cells by chelating metal ions and to harm them by releasing these ions in the cytosol [42], led to think that the cytotoxicity of the PDA NPs could be related to their ability to chelate the metal ions stored in the acid organelles of the cells treated with them. In addition, some findings had also suggested that cancer cells have an enhanced secretion of the lysosomal content to the extracellular space [44], and this fact could contribute to explain the selective toxicity of PDA NPs along with other phenomena. In this manner, analysing PDA NP interaction with different metal cations, as well as their metal loading capacity at the lysosomal pH (4.5 - 5.0), was decided [24].

To study the affinity of PDA NPs for different metal cations, these NPs were firstly synthesized in a EtOH/$H_2O$(d) mixture (28.57% (V/V)), with a 1.75% (V/V) $NH_4OH$ concentration. NPs obtained were characterized by both DLS and TEM, and they showed a diameter close to 305 ± 84 nm (PDI = 0.04) and 223 ± 22 nm, respectively (**Figure 4.13.A**). In addition, the size and zeta potential of these PDA NPs were also determined at the lysosomal (4.5), physiological (7.4) and at a basic pH (8.4) value. For such purpose, they were re-suspended in acetate buffer (0.4 M), PBS (50 mM) and Tris base solution (50 mM). As a result, it was verified than PDA NPs remained well dispersed at pH = 7.4 and 8.5, at which their superficial charge (-13.4 and -20.6 mV, respectively) guaranteed their colloidal stability. However, they tended to aggregate and discompose (> 1000 nm) at pH = 4.5, at which their zeta potential was closer to zero (-6.4 mV) and, their size, much greater than at more basic pH values [24] (**Figure 4.13.B**).

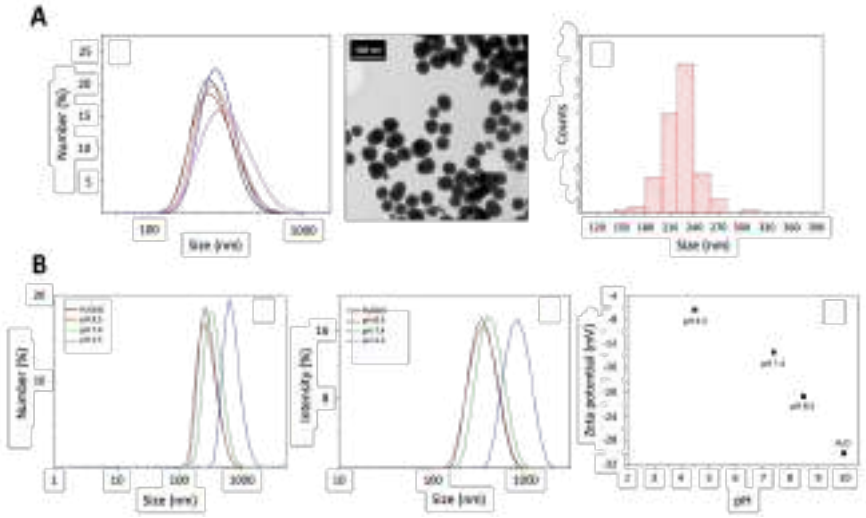


**Figure 4.13.** (**A**) DLS number distribution, TEM image and size-range histogram of the NPs employed to study PDA affinity for different metal cations; (**B**) DLS number distribution, DLS intensity distribution and zeta potential values of the same PDA NPs when they were re-dispersed in buffers of different pH.

Once characterized, PDA NPs (0.9 mL, 0.035% (WT)) were mixed in solutions (40 mL) of different metal ($Fe^{2+}$, $Fe^{3+}$, $Ca^{2+}$, $Na^{+}$, $Zn^{2+}$, $Cu^{2+}$) (70 ppm) salts prepared in acetate buffer (pH 4.5, 0.4 M). These cations were chosen for being trace elements of the human body. Otherwise, the working pH, apart from simulating that of the lysosomal interior, also guaranteed that the metals used did not have solubility problems. Suspensions were kept in agitation (100 rpm) for 16 hours at room temperature and, later, PDA NPs were isolated by centrifugation (11,000 rpm, 10 minutes). The metal content of the resulting supernatants was analysed by inductively coupled plasma atomic emission spectroscopy (ICP-OES) to determine PDA NP metal loading capacity by difference.

Results obtained allowed to verify that the metal ($M^{n+}$) concentrations employed (70 ppm) were in a large excess, since 70% of the metals remained in solution after the adsorption process. Anyway, the results obtained, which have been summarized in **Figure 4.14.A**, allowed to prove that PDA NPs were able to interact with a great variety of metallic cations. Specifically, among those studied, NPs had greater affinity for $Ca^{2+}$, $Fe^{3+}$ and $Cu^{2+}$, being capable of adsorbing 343, 314 and 283 mg/g NP

(Q) of these $M^{n+}$. The adsorption of $Zn^{2+}$, $Fe^{2+}$ and $Mn^{2+}$, although to a lesser extent, was also significant, with Q values of 248, 170 and 153 mg/g NP [24].

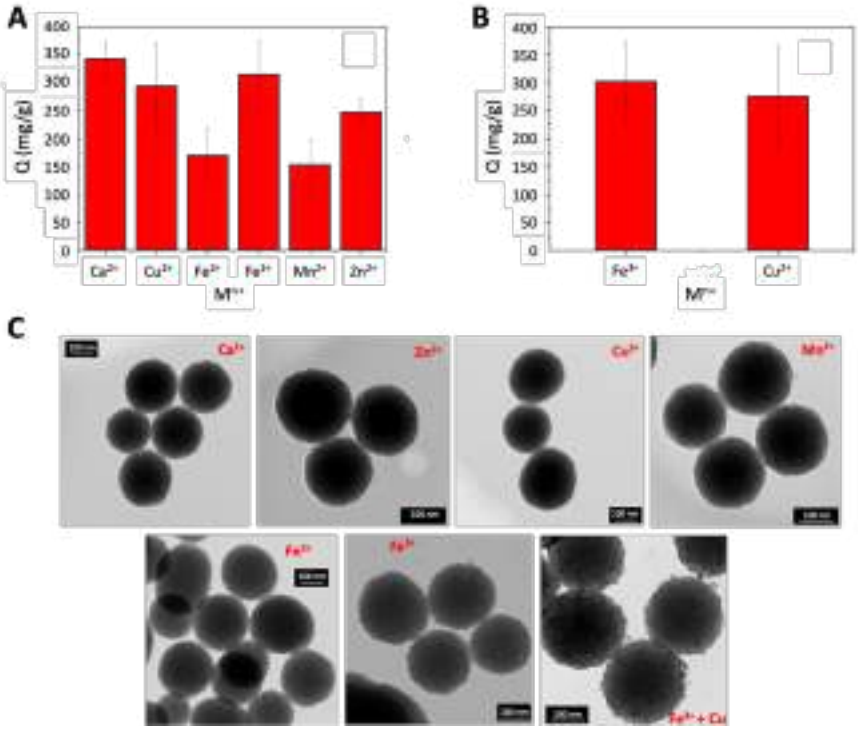


**Figure 4.14.** (**A**) PDA NP adsorption capacity of different $M^{n+}$, expressed as mg $M^{n+}$/g PDA NP (Q); (**B**) Q values for $Fe^{3+}$ and $Cu^{2+}$ obtained when PDA NPs were incubated with both cations simultaneously; (**C**) TEM images of the PDA NPs loaded with the different $M^{n+}$.

Taking note of these Q values, it was observed that the capacity of PDA NPs to adsorb $Fe^{3+}$ and $Cu^{2+}$, which were precisely the two potentially most toxic elements of those adsorbed [45], was quite similar, and performing competition assays with both cations was decided. In this way, following the same procedure as before, NPs were incubated with a solution containing salts of both $M^{n+}$. Later, the amount of $Fe^{3+}$ and $Cu^{2+}$ adsorbed was determined, and it was noticed that it was similar for both metals (around 250 - 275 mg/g NP) (**Figure 4.14.B**). Thereby, the amount of each $M^{n+}$ loaded was minor than the amount loaded for each cation independently. Nevertheless, their joint Q value (500 - 550 mg/g NPs)

greatly exceeded that of each independent ion, which meant that they probably bind to PDA NPs in different sites.

To support this conclusion, $Fe^{3+}$ and $Cu^{2+}$ were also loaded in two sequential steps. PDA NPs were firstly loaded with $Fe^{3+}$, and they exhibited a Q value close to 240 mg/g NP. Then, these NPs were isolated by centrifugation and re-suspended in acetate buffer containing $Cu^{2+}$ (80 ppm). This time, $Cu^{2+}$ was estimated to be loaded with a Q = 327 mg/g NP. Furthermore, $Fe^{3+}$ was no detected in the supernatant of the NPs when they were again isolated, which indicated that there was not cation displacement [24].

The morphology of the PDA NPs loaded with both $Fe^{3+}$ and $Cu^{2+}$, as well as the morphology of the PDA NPs loaded with the other $M^{n+}$, was later studied by TEM. No significant alteration was found in their appearance. Only those that had been loaded with $Fe^{3+}$ (with and without $Cu^{2+}$) showed a spongier surface, so this change was ascribed to a different way of coordination between the $Fe^{3+}$ and the rest of $M^{n+}$, which may modify PDA self-assembly (**Figure 3.14.C**) [24].

At last, to finish with the characterization of the $M^{n+}$-loaded PDA NPs, their IR spectra were obtained and compared to that of unloaded PDA NPs (**Figure 4.15.A**). One of the changes that was detected occurred in the broad band placed at 3405 $cm^{-1}$, which may include the -OH and -NH stretching modes. It decreased in intensity after $M^{n+}$ binding, suggesting that deprotonation took placed at pH 4.5 and that hydroxyl and amine groups could be involved in the binding of all the cations studied (**Figure 4.15.B**).

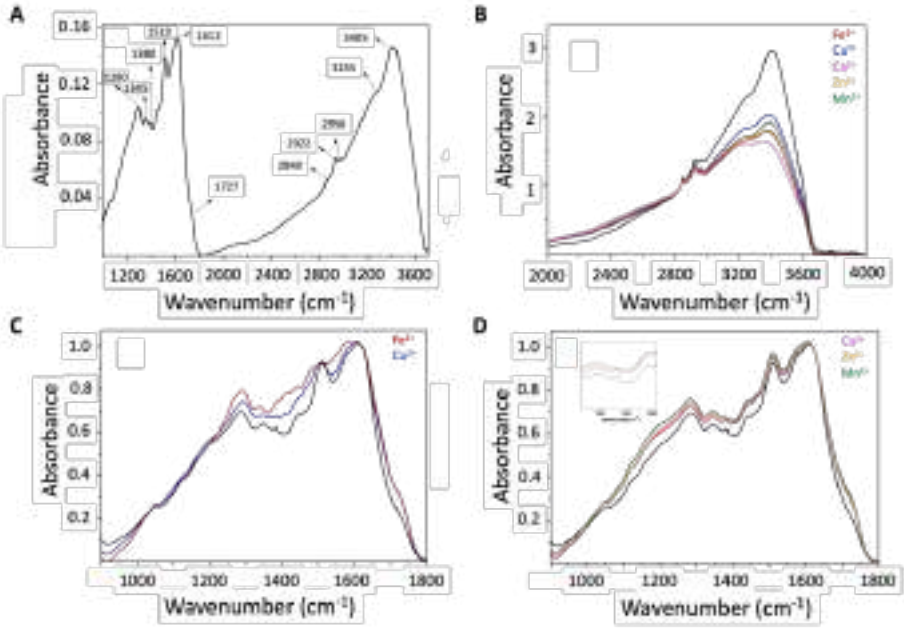


**Figure 4.15.** (**A**) IR spectrum of bare PDA NPs; (**B**) IR spectra in the 2000-4000 $cm^{-1}$ range of PDA NPs (black) and the PDA NPs loaded with the different $M^{n+}$; (**C**) IR spectra in the 900-1800 $cm^{-1}$ range of PDA NPs (black) and the PDA NPs loaded with $Fe^{3+}$ and $Cu^{2+}$; (**D**) IR spectra in the 900-1800 $cm^{-1}$ range of PDA NPs (black) and the PDA NPs loaded with $Ca^{2+}$, $Zn^{2+}$ and $Mn^{2+}$.

On the other hand, upon $Fe^{3+}$ and $Cu^{2+}$ binding, notable modifications were produced in the 1800-1000 $cm^{-1}$ region (**Figure 4.15.C**). First, the band at 1280 $cm^{-1}$, which characterizes the C-OH stretching mode in phenol rings, sift to 1284 and 1293 $cm^{-1}$ after the loading of $Fe^{3+}$ and $Cu^{2+}$, respectively. However, its position did not vary for the rest of $M^{n+}$. Second, bands located at 1510 and 1612 $cm^{-1}$ were broadened, especially after $Fe^{3+}$ binding. Otherwise, after $Zn^{2+}$ and $Mn^{2+}$ coordination (**Figure 4.15.D**), the band at 1380 $cm^{-1}$, which is assigned to the C-N stretching in pyrrole rings, disappeared when $Cu^{2+}$ was loaded to PDA NPs, as well as the bands at 1345 and 1380 $cm^{-1}$. The band at 1345 $cm^{-1}$ shifted to 1336 $cm^{-1}$ for $Fe^{3+}$ loading but, when $Ca^{2+}$ was bound, neither of these two bands changed.

Thereby, to sum up, it could be concluded that catechol and amine groups of the PDA indole ring could account for $Fe^{3+}$ and $Cu^{2+}$

complexation. In the $Cu^{2+}$ binding, pyrrole rings, which also played an important role in $Zn^{2+}$ and $Mn^{2+}$ loading, could be involved, and PDA carboxyl groups could participate in the complexation of all $M^{n+}$ [24,46].

### *4.4.2. Study of the possible implication of iron affinity of polydopamine nanoparticles in their cytotoxicity*

Among the different $M^{n+}$ with which PDA NPs were loaded, $Cu^{2+}$ and $Fe^{2+/3+}$ have a contradictory role. On one hand, they are important cofactors for many enzymes and, thus, necessary for life. However, as they are transition metals and exhibit more than one oxidation state, their redox capacity also makes them able to catalyse the generation of ROS, which can damage the biological molecules [45].

Of these two $M^{n+}$, Fe, for which PDA NPs showed a slightly higher affinity (Figure 4.14.A, page 159) and which is present in higher concentrations in the human body [47,48], had already been related to brain aging and several diseases (like Parkinson's) when interacting with DA neurotransmitter [49,50]. Thereby, it had been demonstrated that Fe can catalyse the oxidation of DA and enhance the production of $H_2O_2$ and superoxide radicals ($\bullet O_2^-$) [49]. In addition, it had been observed that DA can form a variety of complexes with Fe in its two oxidations states over a wide pH range and mobilize ferritin-bound Fe through a reduction process, causing the generation of strong oxidizing hydroxyl radicals (•OH) by means of the Fenton chemistry [50].

For this reason, it was believed that PDA NPs may sequester lysosomal $Fe^{3+}$ when they were endocyted [51], altering the intracellular homeostasis of this metal. As a consequence, abnormal concentrations of ROS may be produced that would explain NP cytotoxicity, although ROS are initially necessary to accelerate the genetic evolution of malignant cells. Late endo/lysosomes of all cells contain low mass redox-active Fe and, since their interior is acidic and rich in reducing equivalents, any low mass Fe should be likely $Fe^{2+}$. Nevertheless, since PDA NPs had higher affinity for $Fe^{3+}$ than for $Fe^{2+}$ (Figure 4.14.A, page 159), they could contribute to increase $Fe^{3+}$ intracellular concentration by chelating it in the acidic organelles. Then, thanks to the activity of the STEA3

metalloreductase, this intracellular $Fe^{3+}$ would be reduced to $Fe^{2+}$ in late endosomes, and $Fe^{2+}$ would get the cytosol of the treated cells through the divalent metal transporter-1 (DMT1). Once into the cytosol, $Fe^{2+}$ may finally promote the generation of •OH radicals through the Fenton reaction from the $H_2O_2$ that is generated by the mitochondria (**Equation 4.3**). At the end, •OH radicals may cause the peroxidation of the cellular lipids, and their excessive production could bring about programmed Fe-dependent tumour cell death, which is known as "ferroptosis" [52] (**Figure 4.16.A**).

$$Fe^{2+} + H_2O_2 \rightleftarrows Fe^{3+} + \cdot OH + OH^- \qquad \textbf{Equation 4.3}$$

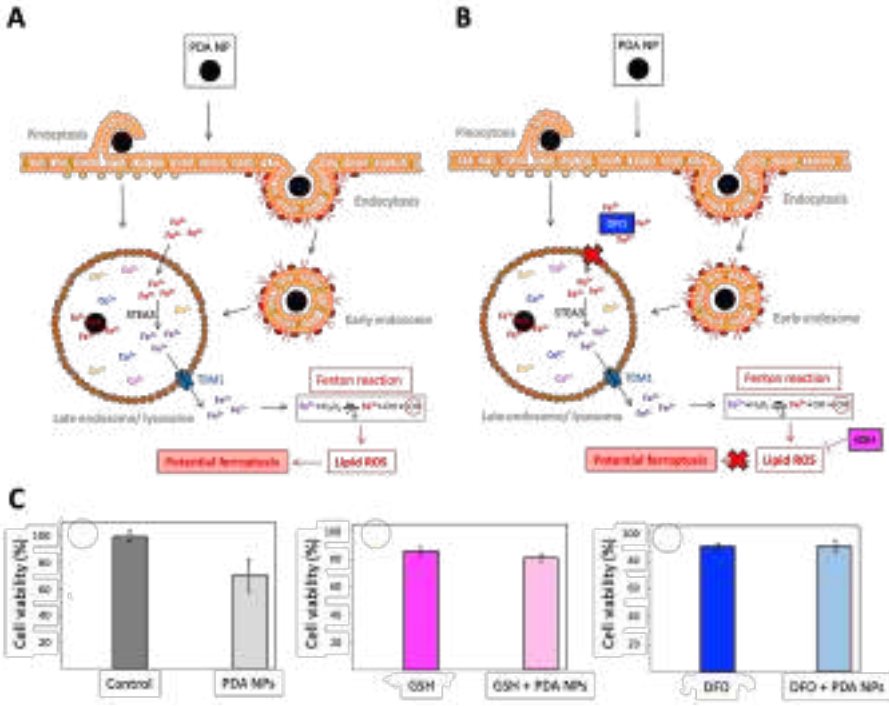


**Figure 4.16**. (**A**) Schematic explanation of why PDA NPs could be toxic to tumour cells: when they were internalized in cells and ended up in late endosomes/lysosomes, they could chelate the $Fe^{3+}$ existing in these organelles, causing an imbalance in Fe homeostasis and a type of cell death called ferroptosis, mediated by an excessive production of lipid ROS; (**B**) Schematic explanation of how DFO and GSH could antagonize PDA NP anti-tumour activity; (**C**) Results of the MTT assay performed 24 hours after co-

treating BT474 cells with PD NPs (0.033 mg/mL) and GSH (50 μM) or DFO (0.7 μM). Results shown are the average viability values ± SEM of three parallel experiments.

In order to validate this hypothesis, further MTT assays were carried out, but co-treating BT474 cells with non-toxic concentrations of either glutathione (GSH) or deferoxamine (DFO) in addition to PDA NPs. On one hand, GSH is a natural potent ROS scavenger present in malignant cells in increased concentrations, and which is depleted during ferroptosis. On the other hand, DFO is an $Fe^{3+}$ chelating agent, so the employment of both compounds sought to antagonize PDA NPs cytotoxicity (**Figure 4.16.B**) [51].

These additional MTT assays were conducted in a similar way as the previous ones, choosing an intermediate concentration of PDA NPs from those already tested (0.033 mg/mL), which was not toxic to stromal cells, to treat BT474 cells. 24 hours after being seeded into 24-well plates, HER2+ breast cancer cells, in addition to being treated with PDA NPs, were also treated with or without GSH (50 μM) or DFO (0.7 μM). Their viability rate was determined 24 hours later, following the procedure detailed in Figure 4.9 (page 151). The results that were obtained have been collected in **Figure 4.16.C**, in which it can be observed that the concentrations administered of both, GSH and DFO, were able reduce the toxicity of PDA NP treatment. Thus, after 24 hours, PDA NPs reduced BT474 survival rate about to 70%, but both GSH and DFO maintained the viability rate of the treated cells at values very similar to those of the control. While DFO could favourably compete with PDA NPs binding to $Fe^{3+}$ in the lysosomes, in which it is endocyted and remains non-degraded [53], the extra-addition of GSH could help tumour cells fight excessive lipid ROS production. Herein, in both cases, it was shown that PDA affinity for $Fe^{3+}$ could be responsible for its toxicity to breast tumour cells [22].

## 4.5. Influence of polydopamine nanoparticle size on their cytotoxicity

As already mentioned in the first introductory chapter, nanomedicine biodistribution greatly depends on the physicochemical properties of the nanocarriers, especially size [51]. Thus, size plays a critical role in modulating NP interactions with the biological milieu following administration, ranging from molecular binding, cell-NP binding, internalization, and intracellular trafficking to vascular distribution, extravasation and tissue diffusion. In this way, NP size dictates the overall delivery efficiency of nanomedicines and [51,54-55], for this reason, studying how this property affected PDA NP cytotoxicity was decided [25].

For this purpose, further MTT assays were carried out. This time, they were performed with four different tumour cell lines in order to be sure when determining the most advantageous PDA NP diameter from a therapeutic point of view. The BT474 cell line was chosen again and, along with it, cells from the human cancer lines HTC116 (colon carcinoma), HEPG2 (liver carcinoma) and H460 (lung carcinoma) were also grown. In addition, human stromal cells (HS5 cell line) were cultured, too, to be able to compare the cytotoxicity of the different NP sizes to normal and malignant cells. As before, all these cell lines were grown as instructed and, to perform the MTT assays according to the tuned protocol, cells were seed in 24-well plates (12,000 cells/well). 24 hours later, they were treated with PDA NPs of 115 and 200 ± 50 nm in size, which had been prepared in a EtOH/$H_2O$(d) mixture (28.57% (V/V)) with $NH_4OH$ concentrations of 2.91 and 1.52% (V/V), respectively. Cell treatment was carried out with four different concentrations of PDA NPs, ranging from 0.0074 mg/mL to 0.042 mg/mL, avoiding the employment of concentrations higher than 0.050 mg/mL to reduce the toxicity of the nanosystem to normal cells. Again, cell viability was determined each 24 hours for a total of 72 hours.

Results achieved have been included in **Figure 4.17**, in which it can be appreciated how the smallest PDA NPs (115 nm) had greater antineoplastic activity. This was in accordance with the global message

from the literature that reports that smaller NPs have enhanced ability to reach their target [51].

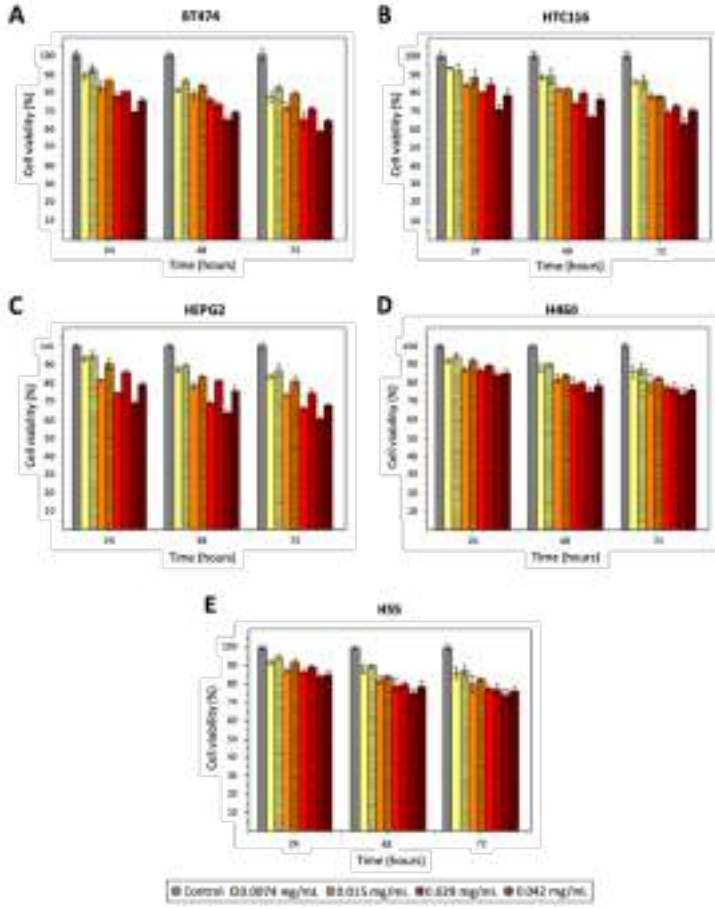


**Figure 4.17.** Results of the MTT assays performed with the BT474 (**A**), HTC116 (**B**), HEPG2 (**C**), H460 (**D**) and HS5 (**E**) cell lines after treating them with different concentrations of 115 (empty bars) and 200 nm (bars with the horizontal line pattern) PDA NPs. Results shown are again the average viability values ± SEM of three parallel experiments.

Among the four tumour cell lines, PDA NP cytotoxicity was more marked to BT474 cells, followed by HTC116 and HEPG2 cells (with which very similar results were obtained) and finally, by H460 cells, to which PDA NPs were not as cytotoxic. Perhaps, if Fe plays an important role in PDA NP cytotoxicity, this could be explained because lung cells have more protective mechanisms to avoid oxidative damage. For example, they are

covered by a thin layer of fluid containing high levels of antioxidant molecules and secrete proteins that bind Fe and maintain it in a chemically inert form [56].

Otherwise, among the different concentrations that were used, those that were able to reduce the viability of cancer cells to a greater extent were the two highest ones (0.029 and 0.042 mg/mL). In this manner, when tumour cells were treated with 0.042 mg/mL PDA NPs, their survival rate was reduced after 72 hours to 57 - 63% (BT474), 62 - 67% (HTC116), 60 - 65% (HEPG2) and 72 - 76% (H460), depending on NP size. On the contrary and positively, viability of the stromal cells was not so affected as that of the tumour cells since, except for the highest concentration, the rest of the concentrations used did not decrease the viability of the HS5 line below 80% at no time [25]. Considering again Fe affinity of PDA NP responsible for their anti-tumour activity, this fact could be explained taking into account that altered Fe metabolism is considered as a hallmark of cancer [57]. Iron plays a crucial role in tumour progression and metastasis due to its major function in cancer cell survival and reprogramming of the tumour microenvironment. Consequently, cancer cells must maintain stable, elevated Fe levels and they disturb the pathways that control the intracellular import and export of this metal [57,58]. However, normal cells are not so dependent on Fe homeostasis and, while ferroptosis may account for cancer cell death (Figure 4.16.A, page 153) [58], it may occur to a lesser extent in healthy tissues. In addition, if PDA NPs were capable of producing an imbalance in the concentration of the lysosomal Fe, it would also make sense that those of smaller size had greater anti-tumour activity since, in addition to be larger endocytosed, the total surface available for Fe chelation would be larger.

In order to indirectly verify if PDA NP ability to chelate lysosomal Fe could be related to their size and their anti-tumour activity, additional MTTs were again performed co-treating cells with GSH (50 µM) or DFO (0.7 µM), but for 72 hours this time [25]. Thus, once cells were grown, they were seeded in 24-well plates at the same density as before and, after 24 hours, treated with an intermediate concentration of PDA NPs (0.029 mg/mL, 115 and 200 nm in size), as well as with the antioxidant agent or the Fe chelator. MTT assays were performed on a regular basis. Then,

when cell viability rates were analysed, it was observed that cellular treatment with DFO or GSH decreased the antiproliferative effect of both types of PDA NPs at all measured times in all cell lines, with this phenomenon becoming more noticeable after 24 hours of treatment. The results obtained with the smallest PDA NPs (115 nm) can be found in **Figure 4.18**. The same trend in cell viability was observed when treating cells with larger NPs (200 nm), although as their cytotoxicity was less notable, so was the antagonistic effect of DFO and GSH. In any case, the results obtained with both particle sizes showed once again that Fenton chemistry may be involved in reducing the viability rate of the cancer cells treated with PDA NPs.

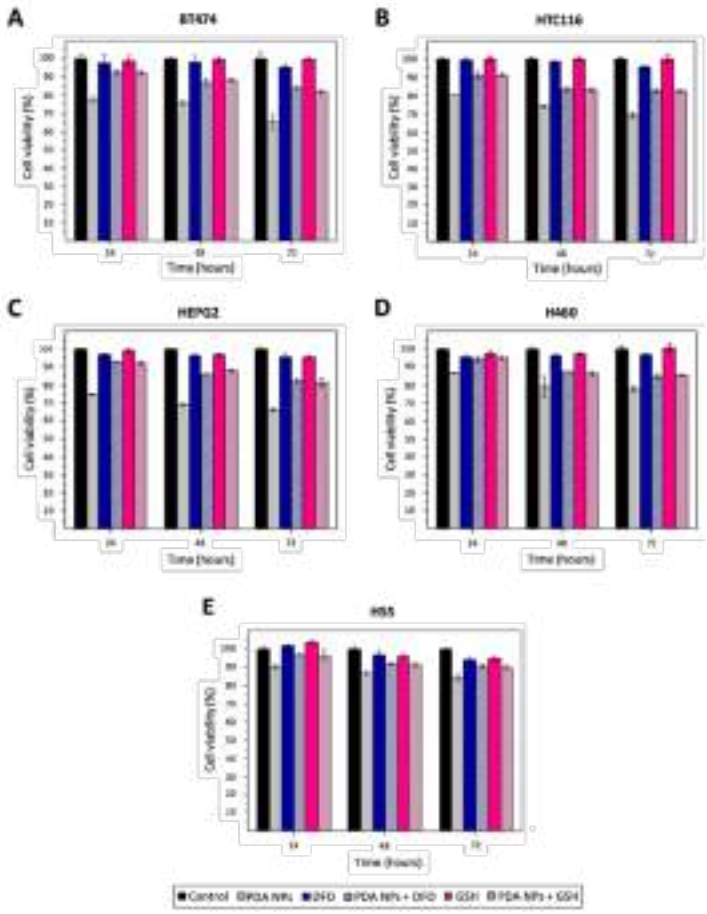


**Figure 4.18.** Results of the MTT assays performed with BT474 (**A**), HTC116 (**B**), HEPG2 (**C**), H460 (**D**) and HS5 (**E**) cells, which were or not simultaneously treated with

PDA NPs (115 nm, 0.029 mg/mL) and DFO (0.7 µM) or GSH (50 µM). Results shown represent the average viability values ± SEM of three parallel experiments, as always.

Subsequently, since it was corroborated that size conditioned PDA NP therapeutic activity, extra MTT assays were carried out, treating BT474 cells with larger NPs (420 nm) (**Figure 4.19.A**). These NPs were prepared with a $NH_4OH$ concentration of 0.84% (V/V) and their characterization can be found with that of the smaller NPs (Figure 4.4, page 141). This time, only BT474 cells were chosen to perform the new viability assays because, apart from being the most interesting cells for this project, they were also the malignant cells with which the best results were previously achieved (Figure 4.17, page 166) [25].

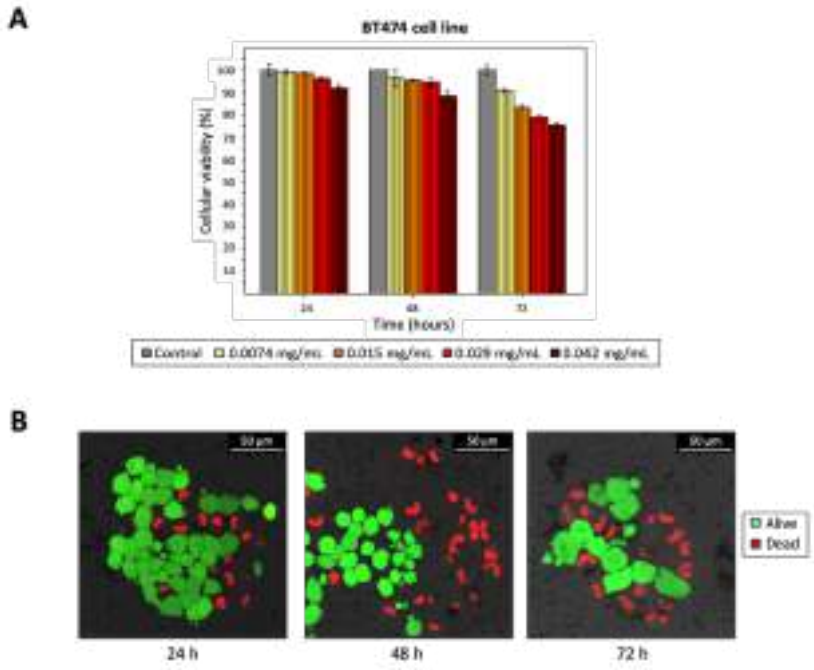


**Figure 4.19**. (**A**) Results of the MTT assay performed with the BT474 cell line after treating it with different concentrations of 420 nm PDA NPs. Results shown are anew the average viability values ± SEM of three parallel experiments; (**B**) CLSM images obtained 24, 48 and 72 hours after treating BT474 cells with PDA NPs (0.042 mg/mL) of 115 nm in size. 30 minutes before acquiring these images, calcein AM (green) and propidium iodide (red) were added to differentiate living cells from dead ones.

Using the same four concentrations of PDA NPs as in the previous studies, these NPs (420 nm) were found to have little effect on the survival rate of the breast carcinoma cell line after 24 and 48 hours of treatment. Only the highest NP concentration (0.042 mg/mL) achieved to reduce their viability rate to 92 - 88%. Nonetheless, when 72 hours had elapsed, the cytotoxicity of the 420 nm PDA NPs was more remarkable, since the three highest concentrations reduced the viability of breast tumour cells to 84, 79 and 75%, respectively. Therefore, as expected, compared to the smaller NPs, those with a 420 nm diameter had minor therapeutic activity, reducing BT474 cell survival rate by 20-25% less when 0.029 and 0.042 mg/mL PDA NP concentrations were administered.

To end this point and with the aim to visually corroborate the viability results obtained with the MTT assays, a live/dead assay was carried out by CLSM. For this purpose, BT474 cells were seeded in glass-bottom dishes (12,000 cells/mL) and treated with 0.042 mg/mL PDA NPs (115 nm), which were the NPs and the concentration that previously reduced the survival rate of the breast carcinoma cell line the furthest. 24, 48 and 72 hours after treatment, calcein AM (1 µM) and propidium iodide (3 drops/dish) were added to the plates and, after incubating cells for 30 minutes at 37°C, they were imaged by CLSM (**Figure 4.19.B**). BT474 cell viability was determined by counting the number of living cells from different images, and it was ascertained that it was reduced to 74, 63 and 52% after 24, 48 and 72 hours of treatment, respectively. These values were in accordance with those obtained in the MTT assays.

## 4.6. Influence of the alcohol/water medium used for polydopamine nanoparticle synthesis on their cytotoxicity

If a research is made in the literature, in those works in which PDA NPs have been applied for therapeutic purposes and have been synthesized by solution oxidation, this last process has always been carried out in a EtOH/$H_2O$(d) media. For this reason, since EtOH/$H_2O$(d) is the most well-known synthesis mixture, it was chosen so far in this project to prepare PDA NPs and to analyse their intrinsic antiproliferative activity.

However, at this point, as it was seen that obtaining PDA NPs with up to five different ROH/$H_2O$(d) mixtures was possible, and that these conditioned NP size, studying whether PDA NP $Fe^{3+}$ adsorption capacity and, consequently, their cytotoxicity were influenced by the type of ROH/$H_2O$(d) medium in which they were prepared was determined.

### *4.6.1. Influence of the synthesis medium on polydopamine nanoparticle iron adsorption capacity*

For the first aim, that is, to analyse whether the ROH used to synthesize PDA NPs influenced their ability to chelate $Fe^{3+}$, NPs were prepared using the five ROHs early described in this chapter (MeOH, EtOH, 2-PrOH, 1-PrOH and 2-Me-2-PrOH) with a diameter less than 200 nm and as similar as possible among them. PDA NP polymerization was performed as in previous times, maintaining the same ROH/$H_2O$(d) volume ratio (28.57% (V/V)) in all cases, but varying the $NH_4OH$ concentration employed in each medium to achieve the desired particle size. The $NH_4OH$ concentration used in each media, as well as the resulting NP diameters and concentrations have been summarized in **Table 4.7**. Otherwise, DLS number distributions, TEM images and size range histograms of the PDA(ROH) NPs that were yielded can be found in **Figure 4.20** [26].

**Table 4.7.** $NH_4OH$ concentrations employed to prepare PDA NPs in the different ROH/$H_2O$(d) media (28.57% (V/V)) with a size less than 200 nm. NP concentration achieved in each case can be seen in the right column.

| ROH | [$NH_4OH$] (% (V/V)) | PDA(ROH) NP size (DLS) (nm) | [NP] (mg/mL) |
|---|---|---|---|
| MeOH | 2.54 | 168 ± 43 (PDI = 0.026) | 2.4 |
| EtOH | 2.67 | 169 ± 37 (PDI = 0.026) | 2.4 |
| 2-PrOH | 1.97 | 187 ± 37 (PDI = 0.055) | 2.8 |
| 1-PrOH | 0.79 | 190 ± 46 (PDI = 0.044) | 2.7 |
| 2-Me-2-PrOH | 1.84 | 170 ± 47 (PDI = 0.066) | 3.9 |

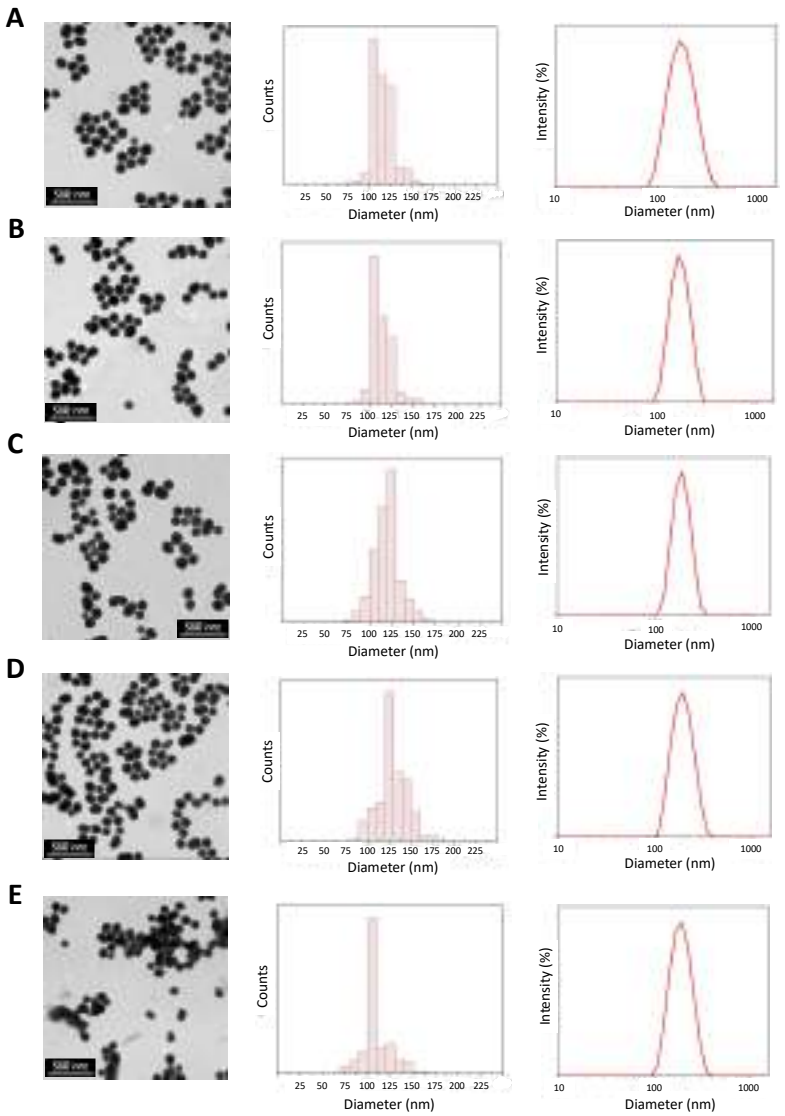


**Figure 4.20**. TEM images, size range histograms and DLS number distributions of the PDA NPs prepared in aqueous media containing MeOH (**A**), EtOH (**B**), 2-PrOH (**C**), 1-PrOH (**D**) and 2-Me-2-PrOH (**E**) to analyse whether the employment of different ROHs conditioned the $Fe^{3+}$ adsorption capacity of the NPs.

Once synthesized and characterized, the $Fe^{3+}$-adsorption capacity of the PDA(ROH) NPs was determined by mixing 1 mL of the NP suspensions with $FeCl_3$ solutions (20 mL) that were prepared in acetate buffer (0.4 M, pH 4.5) to simulate the lysosomal pH. PDA NP concentration

was kept constant in all cases, while $FeCl_3$ solutions had an initial $Fe^{3+}$ concentration ranging from 7 to 35 ppm to be able to build adsorption isotherms. Resulting mixtures were maintained under orbital shaking (100 rpm) overnight at room temperature. Then, $Fe^{3+}$-loaded PDA NPs were isolated by centrifugation (11,000 rpm, 10 minutes) and $Fe^{3+}$ concentration in the supernatants was determined by ICP-OES to analyse PDA(ROH) NPs $Fe^{3+}$-loading capacity. Equilibrium results were fitted using the linearized Freundlich isotherm (**Equation 4.4**), which is normally applied in multilayer adsorption processes on heterogeneous surfaces [26]. This isotherm relates the concentration of a solute ($Fe^{3+}$) on the surface on an adsorbent (PDA(ROH) NPs) (q) to the remaining concentration of the solute in solution at the equilibrium ($C_e$, mg/mL) [28,59]. Thus, it allowed to determine the Freundlich constants (Q and 1/n, corresponding to the adsorption capacity and intensity, respectively, of the PDA(ROH) NPs) for the different PDA(ROH) NPs.

$$\log q = \log Q + ({}^{1}/_{n}) \cdot log C_e \qquad \textbf{Equation 4.4}$$

In this way, the logarithm of the concentration of the $Fe^{3+}$ existing in the supernatants when the PDA(ROH) NPs were isolated was represented against the logarithm of the amount of $Fe^{3+}$ (mg) adsorbed per g of PDA(ROH) NPs, which was determined by difference, by taking into account the initial $Fe^{3+}$ concentrations used. Then, from the Y-interceptions and the slopes of the resulting plots, which can be seen in **Figure 4.21.A**, the different Freundlich constants were estimated (**Table 4.8**).

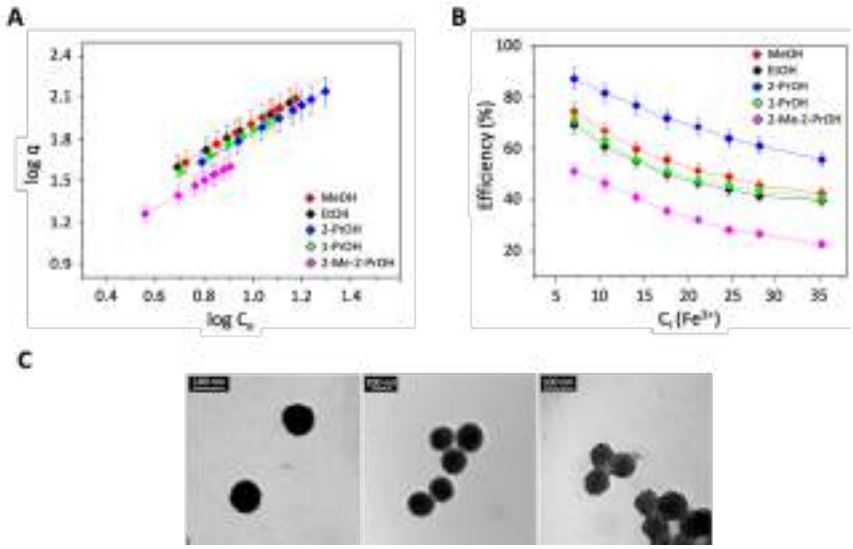


**Figure 4.21.** (**A**) Logarithm of the concentration of the $Fe^{3+}$ adsorbed in the PDA(ROH) NPs as a function of the logarithm of the concentration of $Fe^{3+}$ remaining in solution; (**B**) Efficiency (%) of the $Fe^{3+}$-adsorption process in the different PDA(ROH) NPs as a function of the initial concentration of $Fe^{3+}$ used; (**C**) TEM images of the PDA(EtOH) NPs before (left) and after loading them with two different initial concentrations of $Fe^{3+}$ (30 ppm (medium) and 70 ppm (right)).

**Table 4.8.** Freundlich constants (Q and 1/n) obtained after $Fe^{3+}$-adsorption in the different PDA(ROH) NPs at room temperature.

| ROH | Q (L/mg) | 1/n (d-less) | $R^2$ |
|---|---|---|---|
| MeOH | 8.12 ± 0.004 | 1.009 ± 0.004 | 0.999 |
| EtOH | 8.13 ± 0.045 | 1.008 ± 0.047 | 0.999 |
| 2-PrOH | 7.01 ± 0.002 | 1.005 ± 0.002 | 0.999 |
| 1-PrOH | 7.40 ± 0.007 | 0.998 ± 0.007 | 0.999 |
| 2-Me-2-PrOH | 5.15 ± 0.006 | 0.992 ± 0.007 | 0.999 |

According to the correlation coefficients ($R^2$) obtained, it could be verified that experimental data fitted Freundlich isotherm properly in the $Fe^{3+}$ concentration range studied (7- 35 ppm), which was chosen because it corresponded to the linear zone of the isotherms. Otherwise, observing the Q values obtained, it could be noticed that, depending on the ROH used to synthesize the PDA NPs, their $Fe^{3+}$-loading capacity changed, being the PDA(2-Me-2-PrOH) NPs those with a minor adsorption capacity.

Likewise, the adsorption intensity (1/n) of the PDA nanosystems was different, being greater when NPs were prepared in EtOH, MeOH and 2-PrOH (although 1/n values were close to 1 in all cases, showing that PD(ROH) NP surface was homogeneous) [26].

In addition to estimating the Freundlich constants, the $Fe^{3+}$-adsorption efficiency (%) of the different PDA(ROH) NPs was also determined as a function of the initial $Fe^{3+}$ concentration used to load them (**Figure 4.21.B**). Again, it was shown that this efficiency was conditioned by the NP synthesis media, being the efficiencies of the PDA(ROH) NPs more accentuated when higher initial $Fe^{3+}$ concentrations were used. The PDA(ROH) NPs that showed the highest $Fe^{3+}$-adsorption capacity were the ones prepared in 2-PrOH/$H_2O$(d) media, while those that adsorbed $Fe^{3+}$ in a lesser extent were the ones prepared in 2-Me-2-PrOH/$H_2O$(d) mixtures [26].

To verify whether $Fe^{3+}$-adsorption in the different PDA nanosystems affected their surface charge, PDA(ROH) NP zeta potential was determined at pH 7.4 before and after $Fe^{3+}$ ($C_i$ = 18 ppm) adsorption (**Table 4.9**). By adsorbing $Fe^{3+}$, which is positively charged, the surface charge of the PDA NPs was expected to be closer to zero, and this fact took place regardless of the synthesis medium in which PDA NPs were prepared.

**Table 4.9.** Zeta potential values of the PDA(ROH) NPs at pH 7.4, before and after loading them with $Fe^{3+}$ ($C_i$= 18 ppm). Each value is the mean of three measurements performed in parallel.

| ROH | Bare PDA NPs | $Fe^{3+}$-loaded PDA NPs |
|---|---|---|
| MeOH | -20.1 ± 1.3 mV | -10.2 ± 0.7 mV |
| EtOH | -14.9 ± 0.4 mV | -9.4 ± 0.3 mV |
| 2-PrOH | -20.1 ± 1.8 mV | -12.6 ± 0.3 mV |
| 1-PrOH | -17.0 ± 0.3 mV | -11.9 ± 2.1 mV |
| 2-Me-2-PrOH | -16.8 ± 1.1 mV | -10.9 ± 0.9 mV |

Finally, in order to verify again if the adsorption of $Fe^{3+}$ in the NPs made their surface spongier as seen previously, TEM images of the PD(EtOH) NPs loaded with initial $Fe^{3+}$ concentrations of 30 and 70 ppm

were acquired (**Figure 4.21.C**). Preparing the samples as before, it was indeed verified that $Fe^{3+}$-loading modified the morphology of the PDA NPs, and that this change was more noticeable when the highest initial concentration of $Fe^{3+}$ (70 ppm) was employed.

### *4.6.2. Influence of the synthesis medium on polydopamine nanoparticle cytotoxicity*

Once it was verified that the synthesis medium conditioned the $Fe^{3+}$-adsorption capacity of PDA NPs, it was decided to analyse whether it also determined their cytotoxicity.

Thus, since it had already been proven that smaller sizes conferred greater antiproliferative activity to PDA NPs [26], to carry out the following viability assays, NPs were again synthesized using the five different ROHs, but with increased concentrations of $NH_4OH$ to get NPs with a dehydrated size closer to 100 nm. Once prepared, PDA(ROH) NPs were characterized by DLS and TEM, too. The resulting size values and NP concentrations, along with the $NH_4OH$ concentrations that were employed this time, can be found in the **Table 4.10**. Otherwise, TEM images obtained have been included in **Figure 4.22**.

**Table 4.10.** Size of the PDA(ROH) NPs that were later employed to perform viability assays, synthesized with the indicated $NH_4OH$ concentrations (% (V/V)).

| ROH | Size (DLS) (nm) | Size (TEM) (nm) | [$NH_4OH$] | [NPs] (mg/mL) |
|---|---|---|---|---|
| MeOH | 168.5 ± 40.7 (PDI = 0.034) | 71.0 ± 8.4 | 2.79% | 1.76 |
| EtOH | 173.0 ± 51.3 (PDI = 0.067) | 71.8 ± 12.4 | 3.01% | 2.47 |
| 2-PrOH | 188.0 ± 53.0 (PDI = 0.047) | 91.1 ± 12.3 | 2.38% | 2.80 |
| 1-PrOH | 176.3 ± 50.4 (PDI = 0.052) | 90.9 ± 12.5 | 1.19% | 1.50 |
| 2-Me-2-PrOH | 170.8 ± 53.7 PDI (0.077) | 91.5 ± 16.0 | 2.38% | 1.94 |

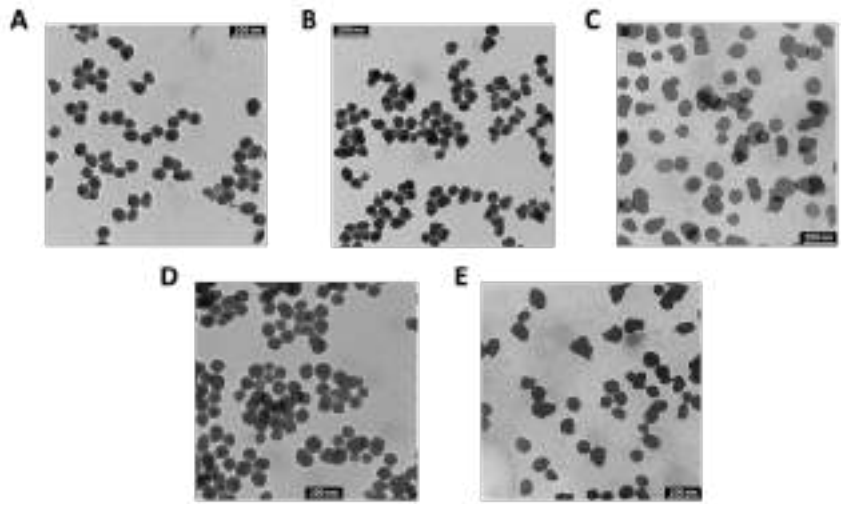


**Figure 4.22.** TEM images of the different PDA(EtOH) NPs, smaller in size, that were used to analyse how the ROH employed in their synthesis affected their cytotoxicity (ROH= MeOH (**A**), EtOH (**B**), 2-PrOH (**C**), 1-PrOH (**D**) and 2-Me-2-PrOH (**E**))**.**

After their characterization, PDA(ROH) NPs were isolated by centrifugation and re-suspended in PBS to carry out the oncoming *in vitro* assays. On this occasion, these experiments were performed again only with the BT474 and HS5 cell lines, which were cultured under the same conditions as all the previous times. Once grown, they were seeded in 24-well plates with an initial density of 12,000 BT474 cells/mL and 15,000 HS5 cells/mL (due to their different proliferation rate). Next day, the culture medium of the wells was replaced by fresh DMEM containing PBS (for the control) and different concentrations (0.074 - 0.042 mg/mL) of all PDA(ROH) NPs. To facilitate the comparison of the results, the same NP concentration range as in previous experiments was chosen, but a new value (0.035 mg/mL) was included, so that there would not be such a marked gap between the two highest concentrations administered. As usually, the viability of both cell lines was determined every 24 hours for a total of 72 hours by applying previously made calibration curves to subtract PDA contribution to the absorbance sample values [22,26]. The results obtained with both cell lines have been included in **Figure 4.23**.

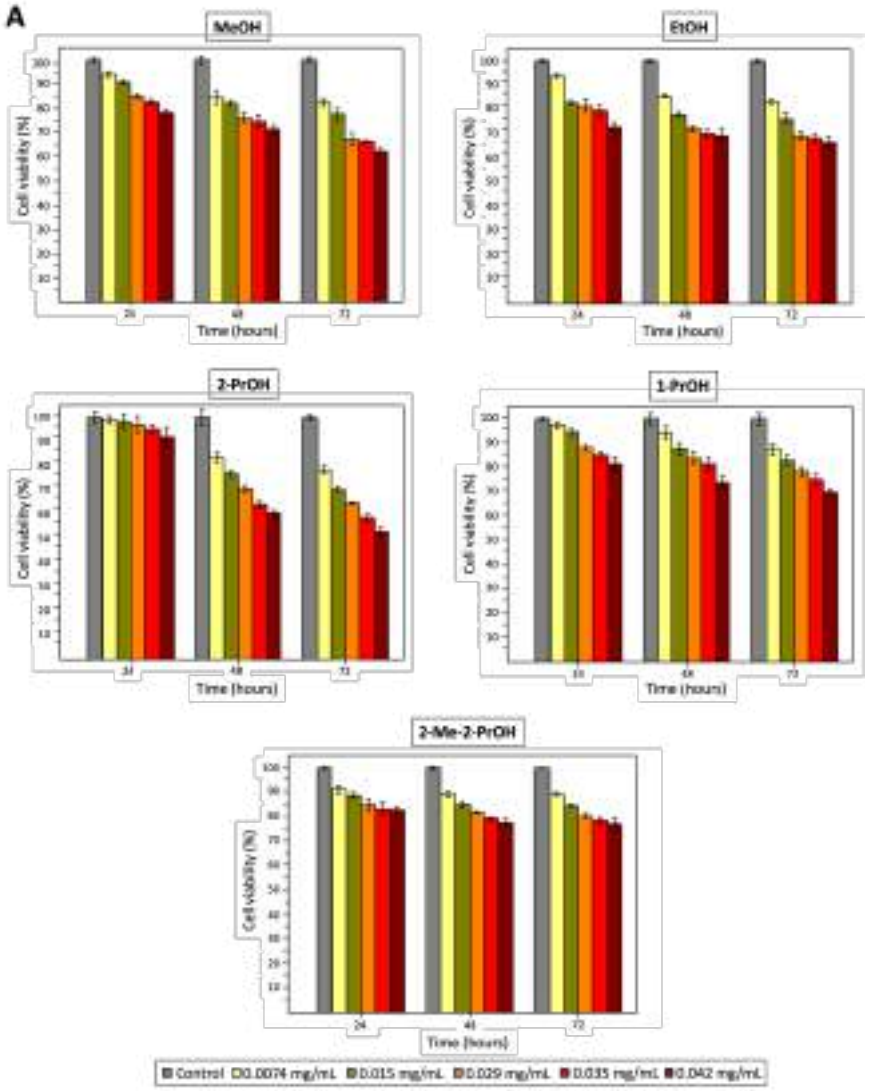
A
MeOH
EtOH
2-PrOH
1-PrOH
2-Me-2-PrOH
Cell viability (%)
Time (hours)
Control 0.0074 mg/mL 0.015 mg/mL 0.029 mg/mL 0.035 mg/mL 0.042 mg/mL

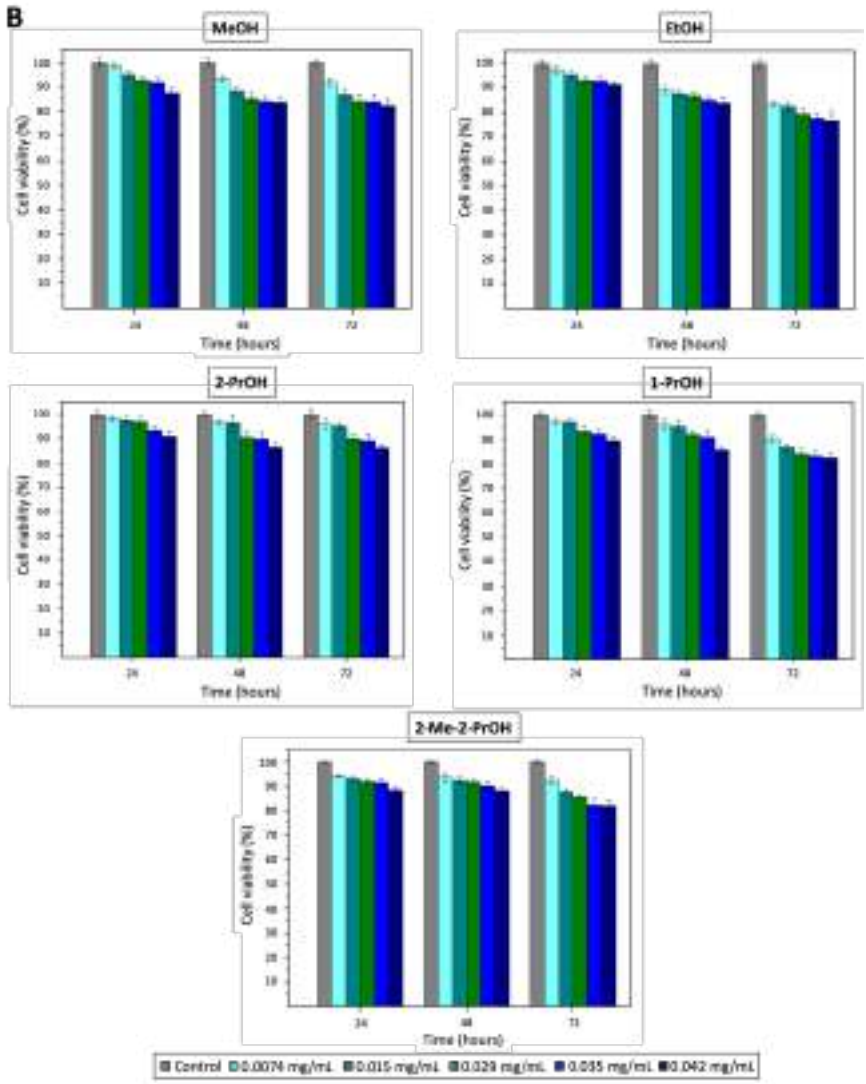


**Figure 4.23**. Results of the MTT assays performed with the BT474 (**A**) and HS5 (**B**) cell lines after treating them with different concentrations (0.0074 mg/mL - 0.042 mg/mL) of the PDA(ROH) NPs (170 - 180 nm). As in previous graphics, results shown are again the average viability values ± SEM of three parallel experiments.

With regard to the results obtained with the HER2+ breast carcinoma cell line, it should be noted that all PDA NPs, regardless of the ROH employed in their synthesis, were able to reduce BT474 viability, especially when they were employed at 0.035 and 0.042 mg/mL concentrations. After 24 hours of treatment, PDA NPs synthesized with

MeOH, EtOH and 1-PrOH exhibited practically the same level of cytotoxicity, being able to reduce by 20-25% the viability of the tumour cells when they were treated with the two highest mentioned concentrations. Nevertheless, the survival rate of these cells was slightly higher when they were treated with equivalent concentrations of PDA(2-Me-2-PrOH) NPs, and it was even more elevated when PDA(2-PrOH) NPs were administered. Notwithstanding, this pattern changed once 48 and 72 hours elapsed. After such times, the highest concentrations employed of the PDA NPs synthesized in media containing MeOH, EtOH and 1-PrOH reduced by 30-40% the viability of BT474 cells. Similar concentrations of PDA(2-Me-2-PrOH) NPs achieved to reduce the survival rate of these cells by 25-30%, and the cytotoxicity of the PDA(2-PrOH) NPs became much more marked. In this way, when 0.042 mg/mL of these NPs were added, BT474 cell viability was almost reduced to half after 72 hours.

Conversely, the toxicity of neither type of PDA(ROH) NPs was as significant to normal cells, which viability was superior to 80% after treatment with the highest concentration (0.042 mg/mL) of almost all NPs. Only PDA NPs prepared in aqueous medium containing EtOH, which turned to be the most toxic NPs to stromal cells, reduced HS5 viability under such value 72 hours after employment of 0.035 and 0.042 mg/mL concentrations to treat the fibroblasts. PDA NPs prepared with MeOH, 1-PrOH and 2-Me-2-PrOH proved to have similar toxicity to this type of cells and, contrary to what happened with BT474 cells, PDA(2-PrOH) NPs were the ones that reduced in a lesser extent the survival rate of the HS5 cells. In this manner, when 0.042 mg/mL PDA(2-PrOH) NPs were administered to stromal cells, their survival rate was only reduced by 15%, thus existing a difference of 35% with the viability rate of the BT474 cell line after equivalent treatment.

By relating the $Fe^{3+}$-adsorption capacity of the different PDA(ROH) NPs at pH 4.5 with their cytotoxicity, it could be noticed that, in general, the greater their ability to chelate $Fe^{3+}$, the greater their toxicity to cancer cells and the lower their toxicity to normal cells. In this way, PDA NPs synthesized with 2-PrOH, which were those with the greatest $Fe^{3+}$-adsorption efficiency, were also the NPs that had more marked therapeutic activity and those that proved to be less toxic to HS5 cells. On

the contrary, PDA NPs prepared in 2-Me-2-PrOH/$H_2O$(d) media were the ones that least reduced BT474 cell viability, and the NPs that adsorbed the least amount of $Fe^{3+}$. Therefore, the existence of a linear correlation between these PDA NP properties ($Fe^{3+}$ adsorption ability *vs.* anti-tumour activity and selectivity) was revealed. To show it in a clearer manner, data regarding BT474 cell survival rate 72 hours after treatment with different concentrations of the PDA(ROH) NPs was represented as a function of the $Fe^{3+}$-loading efficiency of the PDA NPs (**Figure 4.24.A**).

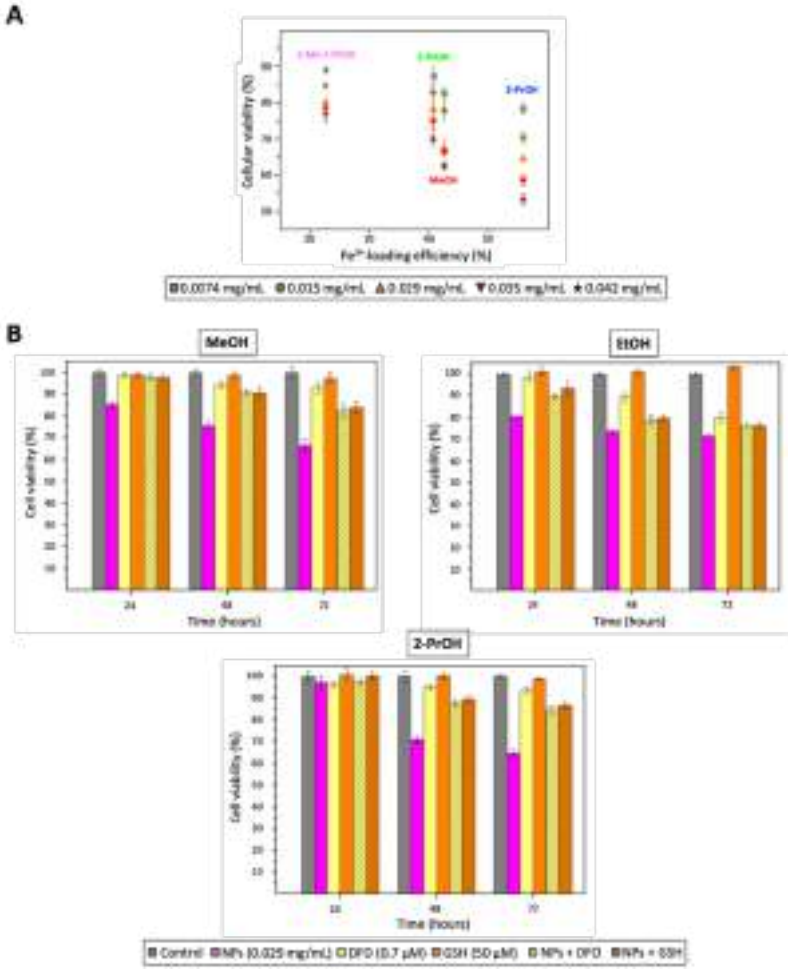


**Figure 4.24.** (**A**) Linear correlation obtained between PD(ROH) NPs $Fe^{3+}$-loading efficiency (%) (Ci= 35 ppm) and their toxicity to BT474 cells. Cellular viabilities values represented were the ones obtained after 72 hours of treatment with different concentrations of the PDA(ROH) NPs. $R^2$ values were near to 0.9; (**B**) Results of the MTT assay performed with

BT474 cells after simultaneously treating them with PDA(ROH) NPs (0.029 mg/mL) and non-toxic concentrations of DFO (0.7 μM) or GSH (50 μM). Anew, results shown are the average viability values ± SEM of three parallel experiments.

The only PDA NPs for which the correlation between their $Fe^{3+}$ adsorption capacity and their anti-tumour activity and selectivity was not fulfilled were those prepared in EtOH/$H_2O$(d) media. They turned to be the most toxic NPs to normal cells, despite not being the ones that loaded the least amount of $Fe^{3+}$. For this reason, data obtained with these NPs was not included in **Figure 4.24.A**.

Otherwise, the hypothesis that advocated that the anti-tumour activity of PDA NPs may be related to their affinity for the lysosomal $Fe^{3+}$, whose metabolism, as already commented before, is different in malignant than in healthy cells, was again revealed. In order to verify that this hypothesis could take place with all PDA(ROH) NPs and not only with the PDA(EtOH) NPs, final MTT assays were carried out. BT474 cells were grown and seeded into 24-well plates at the same density as in the previous viability studies. Next day, they were treated with PDA NPs (0.029 mg/mL) prepared in aqueous media containing 2-PrOH, MeOH and EtOH, as well as with DFO (0.7 μM) or GSH (50 μM). These three types of NPs were chosen because they were the ones with the greatest anti-tumour activity. Results obtained were those that can be seen in **Figure 4.24.B**.

As had happened in previous assays, co-treatment with both, DFO and GSH, antagonized the cytotoxicity of all PDA(ROH) NPs, maintaining cell viability above 80% in almost all cases. Since the antiproliferative activity of the PDA(ROH) NPs was more marked 72 hours after treatment, also the action of DFO and GSH was more noticeable after that time, especially when BT474 cells were treated with PDA(MeOH) and PDA(2-PrOH) NPs. The cytotoxicity of the NPs prepared in EtOH/$H_2O$(d) was also reduced with the co-treatment performed but to a lesser extent, so that, because these NPs were also the most toxic to stromal cells, other mechanisms, along with PDA $Fe^{3+}$-affinity, were supposed to be responsible for their cytotoxicity [26].

## 4.7. Conclusions

· PDA NPs were synthesized by dopamine solution oxidation, not only in basic, aqueous media containing EtOH, which is the ROH most commonly employed, but also containing MeOH, 2-PrOH, 1-PrOH and 2-Me-2-PrOH.

· The size of the PDA NPs prepared could be tuned by simply varying the $NH_4OH$ concentration and the type of ROH employed in their synthesis process.

· In order to perform viability assays, a new protocol was developed that allowed to subtract PDA contribution to the absorbance of the samples when carrying out MTT assays. In this way, overestimating cell viability could be avoided.

· By following this protocol, it was observed PDA NP size determined their cytotoxicity: the smaller their diameter, the greater their toxicity, which was more marked to malignant cells than to normal cells. Among the different tumour cell lines studied, PDA NPs anti-tumour activity was most remarkable for HER2-overexpressing breast carcinoma cells, followed by colon, liver and lung carcinoma cells.

· Not only the size of the PDA NPs determined their cytotoxicity, but also the type of ROH used to prepare them. Thus, PDA NPs prepared in aqueous media containing 2-PrOH had more remarkable anti-tumour activity than those synthesized with MeOH, EtOH, 1-PrOH and, above all, 2-Me-2-PrOH.

· Apart from conditioning their cytotoxicity, the ROH employed to prepare PDA NPs was also seen to influence its well-known ability to adsorb $Fe^{3+}$. For this reason, and because it had been observed that fluorescent PDA NPs remained in the cellular endo/lysosomes once endocyted, it was hypothesized that PDA NP cytotoxicity could be related to their ability to chelate the $Fe^{3+}$ existing in the mentioned acidic organelles.

· To verify that the selective anti-tumour activity of the PDA NPs could be linked to an imbalance of the intracellular $Fe^{3+}$ homeostasis, tumour cells were co-treated with both PDA NPs and DFO or GSH. Both compounds

antagonized PDA NP therapeutic effect, so indeed it was revealed that a ferroptosis-like process could mediate PDA NP customizable, inherent antineoplastic activity.

## 4.8. Published articles related to this chapter

· Vega MA, Nieto C, Marcelo G, Martín del Valle EM. Cytotoxicity of paramagnetic cations-loaded polydopamine nanoparticles. Colloid Surf B 2018; 167:284-90.
· Nieto C, Vega MA, Marcelo G, Martín del Valle EM. Polydopamine kills cancer cells. RSC Adv. 2018; 8:36201.
· Nieto C, Vega MA, Enrique J, Marcelo G, Martín del Valle EM. Size matters in the cytotoxicity of polydopamine nanoparticles in different types of tumours. Cancers 2019; 11:1679.
· Nieto C, Marcelo G, Vega M, Martín del Valle EM. Antineoplastic behaviour of polydopamine nanoparticles prepared in different water/alcohol media. Colloid Surf B 2021; 199:111506.

## 4.9. Abbreviations

CLSM – Confocal laser scanning microscopy
DA - Dopamine
DDS – Drug delivery system
DFO – Deferoxamine
DHI – 5,6-dihydroxyindole
DLS – Dynamic light scattering
DMEM – Dulbecco's modified Eagle's Medium
DMSO – Dimethylsulfoxide
DMT1 – Divalent metal transporter-1
DOPA – 3,4-dihydroxy-L-phenylalanine
EtOH - Ethanol
GSH – Glutathione
HER2 - Human epidermal growth factor receptor-2
H-bonding – Hydrogen-bonding
HSP – Hansen's solubility parameters

$H_2O$(d) – Deionized water
ICP-OES – Inductively coupled plasma – optical emission spectroscopy
IR – Infrared
$M^{n+}$ - Metal cation
MeOH – Methanol
Mfp-5 – Mytilus foot protein-5
MTT – 3-[4,5-dimethylthiazol-2-yl]-2,5-diphenyltetrazolium bromide
NP – Nanoparticle
PBS – Phosphate buffered saline
PDA - Polydopamine
PDI – Polydispersity index
PGA – Polyglutamic acid
PLA – Polylactic acid
PLGA – Poly(lactic-co-glycolic acid)
ROH - Alcohol
TEM – Transmission electron microscopy
Tmab – Trastuzumab
UV-Vis – Ultraviolet-visible
1-PrOH – 1-propanol
2-Me-2-PrOH – 2-methyl-2-propanol
2-PrOH – 2-propanol

## 4.10. References

[1] Zhong Y, Meng F, Deng C, Zhong Z. Ligand-directed active tumor-targeting polymeric nanoparticles for cancer chemotherapy. Biomacromolecules 2014; 15:1955-69.
[2] Cho K, Wang X, Nie S, Chen Z, Shin DM. Therapeutic nanoparticles for drug delivery in cancer. Clin Cancer Res. 2008; 14:1310-16.
[3] Ambekar RS, Kandasubramanian B. A polydopamine-based platform for anti-cancer drug delivery. Biomater Sci. 2019; 7:1776.
[4] Jin A, Wang Y, Lin K, Jiang L. Nanoparticles modified by polydopamine: working as “drug” carriers. Bioact Mater. 2020; 5(3):522-41.
[5] Lee H, Dellatore SM, Miller WM, Messersmith PB. Mussel-inspired surface chemistry for multifunctional coatings. Science 2007; 318(5849):426-30.

[6] Wang Z, Duan Y, Duan Y. Application of polydopamine in tumor targeted drug delivery system and its drug release behavior. J Control Release 2018; 290:56-74.
[7] Ryu JH, Messersmith PB, Lee H. Polydopamine surface chemistry: a decade of discovery. ACS Appl Mater Interfaces 2018; 10(9):7523-40.
[8] Lee HA, Ma Y, Zhou F, Hong S, Lee H. Material-independent surface chemistry beyond polydopamine coating. Acc Chem Res. 2019; 52(3):704-13.
[9] Hauser D, Septiadi D, Turner J, Petri-Fink A, Rothen-Rutishauser B. From bioinspired glue to medicine: polydopamine as a biomedical material. Materials 2020; 13:1730.
[10] Liu Y, Ai K, Lu L. Polydopamine and its derivative materials: synthesis and promising applications in energy, environmental and biomedical fields. Chem Rev. 2014; 114(9):5057-115.
[11] Liu H, Yang Y, Liu Y, Pan J, Wang J, Man F, Zhang W, Liu G. Melanin-like nanomaterials for advanced biomedical applications: a versatile platform with extraordinary promise. Adv Sci. 2020; 7(7):1903129.
[12] Wang Z, Yang H-C, He F, Peng S, Li Y, Shao L, Darling SB. Mussel-inspired surface engineering for water-remediation materials. Matter 2019; 1:115-55.
[13] Li H, Yin D, Li W, Tang Q, Zou L, Peng Q. Polydopamine-based nanomaterials and their potentials in advanced drug delivery and therapy. Colloid Surf B 2021; 199:11502.
[14] Batul R, Tamanna T, Khaliq A, Yu A. Recent progress in the biomedical applications of polydopamine nanostructures. Biomater Sci. 2017; 5:1204.
[15] Salomäki M, Marttila L, Kivelä H, Ouvinen T, Lukkari J. Effects of pH and oxidants on the first steps of PDA formation: a thermodynamic approach. J Phys Chem. B 2018; 122:6314-27.
[16] Ho C-C, Ding S-J. The pH-controlled nanoparticles size of polydopamine for anti-cancer drug delivery. J Mater Sci: Mater Med 2013; 24:2381-90.
[17] Zheng W, Fan H, Wang L, Jin Z. Oxidative self-polymerization of dopamine in an acid environment. Langmuir 2015; 31(42):11671-77.
[18] Ball V. Polydopamine nanomaterials: recent advances in synthesis methods and applications. Front Bioeng Biotechnol. 2018; 6:109.
[19] Liu Y, Ai K, Liu J, Deng M, He Y, Lu L. Dopamine-melanin colloidal nanospheres: an efficient near-infrared photothermal therapeutic agent for in vivo cancer therapy. Adv Mater. 2013; 25:1353-59.
[20] Liebscher J. Chemistry of polydopamine – Scope, variation and limitation. Eur J Org Chem. 2019; 4976-94.

[21] Mrówczynski R. PDA-based multifunctional (nano)materials for cancer therapy. ACS Appl Mater Interfaces 2018; 10:7541-61.
[22] C, Vega MA, Marcelo G, Martín del Valle EM. Polydopamine kills cancer cells. RSC Adv. 2018; 8:36201.
[23] Farokhi M, Mottaghitalab F, Saeb MR, Thomas S. Functionalized theragnostic nanocarriers with bio-inspired polydopamine for tumour imaging and chemo-photothermal therapy. J Control Release 2019; 309:203-19.
[24] Vega MA, Nieto C, Marcelo G, Martín del Valle EM. Cytotoxicity of paramagnetic cations-loaded polydopamine nanoparticles. Colloid Surf B 2018; 167:284-90.
[25] Nieto C, Vega MA, Enrique J, Marcelo G, Martín del Valle EM. Size matters in the cytotoxicity of polydopamine nanoparticles in different types of tumours. Cancers 2019; 11:1679.
[26] Nieto C, Marcelo G, Vega M, Martín del Valle EM. Antineoplastic behaviour of polydopamine nanoparticles prepared in different water/alcohol media. Colloid Surf B 2021; 199:111506.
[27] Yegappan R, Selvaprithiviraj V, Mohandas A, Jayakumar R. Nano polydopamine crosslinked thiol-functionalized hyaluronic acid hydrogel for angiogenic drug delivery. Colloid Surf B 2019; 177:41-9.
[28] Jiang X, Wang Y, Li M. Selecting water-alcohol mixed solvent for synthesis of polydopamine nanospheres using solubility parameter. Sci Rep. 2014; 4:6070.
[29] Lizunova AA, Loshkarev AA, Tokunov YM, Ivanov VV. Comparison of the results of measurements of the sizes of NPs in stable colloidal solutions by the methods of acoustic spectroscopy, dynamic light scattering and transmission electron microscopy. Meas Tech. 2017; 59:1151-55.
[30] Manz DH, Blanchette NL, Paul BT, Torti FM, Torti SV. Iron and cancer: recent insights. Ann NY Acad Sci. 2016; 1368:149-61.
[31] Fujiwara N, Yamamoto H. Evaluation of adsorption of organic solvents to modified hydrophobic silica adsorbents based on Hansen solubility parameter. Sep Purif Technol. 2019; 210:907-12.
[32] Smith RM, Hill RM, Denison D, Sniveley J, Ashcraft P. U.S. Patent Application No. 15/990 2019; 374.
[33] Liu X, Cao J, Li H, Li J, Jin Q, Ren K, Ji J. Mussel-inspired polydopamine: a biocompatible and ultrastable coating for nanoparticles in vivo. ACS Nano 2013; 7(10):9384-95.

[34] Hong S, Kim KY, Wook MJ, Park SY, Lee KD, Lee DY, Lee H. Attenuation of the in vivo toxicity of biomaterials by PDA surface modification. Nanomedicine 2011; 6(5):793-801.

[35] Si J, Yang H. Preparation and characterization of biocompatible $Fe_3O_4$@polydopamine spheres with core/shell nanostructure. Mater Chem Phys. 2011; 128(3):519-24.

[36] Postma A, Yan Y, Wang Y, Zelikin AN, Tjipto E, Caruso F. Self-polymerization of dopamine as a versatile and robust technique to prepare polymer capsules. Chem Mater. 2009; 21:3042-44.

[37] Cheng C, Nie S, Li S, Peng H, Yang H, Ma L, Sun S, Zhao C. Biopolymer functionalized reduced graphene oxide with enhanced biocompatibility via mussel inspired coatings/anchors. J Mater Chem. B 2013; 1:265.

[38] Mattos Dos Santos PC, Feuser PE, Barrelo Cardoso P, Trevisol Steiner B, da Silva Córneo E, Scussel R, da Cas Viegas A, Machado-de-Ávila RA, Sayer C, Hermes de Araujo PE. Evaluation of in vitro cytotoxicity of superparamagnetic poly(thioether-ester) nanoparticles on erythrocytes, non-tumor (NIH3T3), tumor (HeLa) cells and hyperthermia studies. J Biomater Sci Polym Ed. 2018; 29(16):1935-48.

[39] Cheng C, Meng Y, Zhang Z, Chen J, Zhang Q. Imine bond- and coordinate bond- linked pH-sensitive cisplatin complex nanoparticles for active targeting to tumor cells. J Nanosci Nanotechnol. 2019; 19(6):3277-87.

[40] Chen X, Yan Y, Müller M, Van Koeverden MP, Noi KF, Zhu W, Caruso F. Engineering fluorescent poly(dopamine) capsules. Langmuir 2014; 30:2921-25.

[41] Wang Z, Zou Y, Li Y, Chen Y. Metal-containing polydopamine nanomaterials: catalysis, energy and theranostics. Small 2020; 16:1907042.

[42] Karlsson O, Lindquist NG. Melanin affinity and its possible role in neurodegeneration. J Neural Transm. 2013; 120:1623-30.

[43] Blaby-Haas CE, Merchant SS. Lyososme-related organelles as mediators of metal homeostasis. J Biol Chem. 2014; 289(41):28129-36.

[44] Kallunki T, Olsen OD, Jäättelä M. Cancer-associated lysosomal changes: friends or foes? Oncogene 2013; 32:1995-2004.

[45] Brewer GJ. Risks of copper and iron toxicity during aging in humans. Chem Res Toxicol. 2010; 23:319-26.

[46] Hong L, Liu Y, Simon JD. Binding of metal ions to melanin and their effects on the aerobic reactivity. Photochem Photobiol. 2004; 80:477-81.

[47] Tapiero H, Townsed DM, Tew KD. Trace elements in human physiology and pathology. Copper. Biomed Pharmacother. 2013; 57(9):386-98.

[48] Ponka P. Cellular iron metabolism. Kidney Int. 1999; 55(69):S2-S11.
[49] Zucca FA, Segura-Aguilar J, Ferrari E, Muñoz P, Paris I, Sulzer D, Sarna T, Casella L, Zerca L. Interactions of iron, dopamine and neuromelanin pathways in brain aging and Parkinson's disease. Prog Neurobiol. 2017; 155:96-119.
[50] Sun Y, Pham AN, Waite TD. Elucidation of the interplay between Fe(II), Fe(III), and dopamine with relevance to iron solubilization and reactive oxygen species generation by catecholamines. J Neurochem. 2016; 137:955-68.
[51] Gaumet M, Vargas A, Gunny R, Delie F. Nanoparticle for drug delivery: the need for precision in reporting particle size parameters. Eur J Pharm Biopharm. 2008; 69:1-9.
[52] Kurz T, Eaton JW, Brunk UT. The role of lysosomes in iron metabolism and recycling. Int J Biochem Cell B. 2011; 43:1686-97.
[53] Kurz T, Terman A, Gustafsson B, Brunk UT. Lysosomes in iron metabolism, aging and apoptosis. Histochem Cell Biol. 2008; 199(4):389-406.
[54] Verma A, Stellacci F. Effect of surface properties on nanoparticle-cell interactions. Small 2010; 6(1):12-21.
[55] Hickey JW, Santos JL, Williford J-M, Mao H-Q. Control of polymeric nanoparticle size to improve therapeutic delivery. J Control Release 2015; 219:536-47.
[56] Neves J, Haider T, Gassmann M, Muckenthaler MV. Iron homeostasis in the lungs – A balance between health and disease. Pharmaceuticals 2019; 12:5.
[57] Brown RAM, Richardson KL, Kabir TD, Trinder D, Ganss R, Leedman PJ. Altered iron metabolism and impact in cancer biology, metastasis and immunology. Front Oncol. 2020; 10:476.
[58] Jung M, Mertens C, Tomat E, Brüne B. Iron as a central player and promising target in cancer progression. Int J Mol Sci. 2019; 20(2):273.
[59] Aristizabal C, Alvarado PN, Vargas AF. Numerical determination of the correct solvents to extract a phytochemical from coffee pulp using Hansen solubility parameters, risk assessment, sustainability evaluation, and economic analysis. DYNA 2019; 86(211):138-47.

Colloids and Surfaces B: Biointerfaces 167 (2018) 284–292

Contents lists available at ScienceDirect

Colloids and Surfaces B: Biointerfaces

journal homepage: www.elsevier.com/locate/colsurfb

# Cytotoxicity of paramagnetic cations—Loaded polydopamine nanoparticles

Milena A. Vega, Celia Nieto, Gema Marcelo*, Eva M. Martín del Valle*

Department of Chemical Engineering, IRNASA Abbreviation: IU 37008, Universidad de Salamanca, Salamanca 37, Spain

ARTICLE INFO

Article history:
Received 30 December 2017
Received in revised form 26 March 2018
Accepted 10 April 2018
Available online 12 April 2018

Keywords:
Polydopamine
Metallic cations
Cancer
In vitro
Cytotoxicity
MTT

ABSTRACT

Polydopamine (PD) is a synthetic melanin pigment of great importance in biomedicine, where its affinity for metallic cations, especially paramagnetic ions, has sparked interest in its use in the development of magnetic resonance imaging (MRI) contrast agents. In this work, we report the cytotoxicity of metal-enriched PD nanoparticles on NIH3T3, a healthy cell line and BT474, a breast cancer cell line. Remarkably, it was found that the metal- enriched PD particles ($Mn^{2+}$ > $Fe^{2+}$, $Fe^{3+}$ and $Cu^{2+}$) were highly cytotoxic to the breast cancer cells, even after 24 h of treatment. Although, this effect was not selective systems, since an acute cytotoxic effect was also observed on the healthy cell line, this systems can be considered as starting point for designing advanced antineoplastic agents.

© 2018 Elsevier B.V. All rights reserved.

## 1. Introduction

Melanins are naturally occurring pigments (biopolymers that are present in many living organisms [1]. Melanin pigments have different functions, of which UV protection of the skin is the most familiar. The role of melanins in the regulation of free metallic ion concentration is less well-known. Melanin particles can act either as reservoir or sequester of different metallic cations [2–6]. For instance, melanins can regulate the concentration free $Fe^{3+}$ in the neurons of the substantia nigra [7]. The overloading of iron in neuro-melanin has been found to be related to brain disorders such as Parkinson's disease.

Polydopamine (PD) is a synthetic melanin analogue that has acquired a central role in the field of Material Science since its discovery as a multifunctional biocompatible surface coating [8]. Likewise, PD also presents great metal affinity. So, the PD chelation of paramagnetic metallic cations has been considered for devising MRI contrast agents and even more advanced theranostic systems [9–11]. The lack of toxicity after 24 h of treatment has been reported for these metal-enriched systems, but their cytotoxicity after longer exposure times has not been explored.

Lysosomes are acid cellular compartments where PD particles are transported after they enter the cell by an endocytotic mechanism [12–14]. They are centers of degradation and intracellular cell stores for $Fe^{3+}$, $Fe^{2+}$, $Zn^{2+}$ and $Cu^{2+}$. Iron and copper catalyze the production of radical oxygen species (ROS) via Fenton chemistry, which are essential for normal cell function. However, the aberrant accumulation of metals and/or ROS is linked to degenerative diseases and immediate cell damage [15]. Hence, degradation of lysosomes by anomalous ROS production has been caused by nanosystems that carry $Fe^{2+}$ and deliver it specifically into the lysosomes [16–18].

Herein, the study of the interaction of PD particles with different cations ($Fe^{2+}$, $Fe^{3+}$, $Ca^{2+}$, $Na^{+}$, $Zn^{2+}$ and $Cu^{2+}$) at pH 4.5 (lysosomal pH) is presented and their metal loading capacity and affinity have been analyzed. Additionally, a tentative assignation of metal binding sites was performed by IR spectroscopy, and finally, the cytotoxic effects of these metal-enriched PD nanoparticles on healthy fibroblasts (NIH3T3) and breast cancer (BT474) cell using the MTT assay is described. Our main concern regarding the use of metal-enriched-PD particles for biomedical applications, such as MRI contrast agents, is the long- term toxic effect of these metal ions when they target lysosomes via the PD carrier, since they are able to catalyze ROS production and adversely affect cell survival.

* Corresponding authors.
E-mail addresses: [illegible] (G. Marcelo), [illegible] (E.M. Martín del Valle).

https://doi.org/10.1016/j.colsurfb.2018.04.027
0927-7765/© 2018 Elsevier B.V. All rights reserved.

## 2. Experimental section

### 2.1. Materials

Dopamine hydrochloride, Zinc chloride anhydrous 97%, Ammonium hydroxide A.C.S. reagent, Sodium chloride 99.8%, Tris(Hydroxymethyl) aminomethane (Trizma), Trizma – Hydrochloride 99%, phosphate buffered saline pH 7.4 (PBS) were provided by Sigma-Aldrich. Copper (II) chloride copper was provided by Riedel-de Haën, Iron (II) chloride tetrahydrate reagent grade 98% was provided by Honeywell. Iron (III) chloride anhydrous 97%, Manganese (II) chloride 4-hydrate, Ascorbic acid reagent grade, hydrogen peroxide 33% (v/w) and sodium acetate anhydrous were provided by Panreac. Calcium chloride dihydrate cell is pure was provided by Scharlau. Ethanol was supplied by GPR Rectapur.

Dulbecco's Modified Eagle's Medium (DMEM), Fetal Bovine Serum (FBS, qualified, USA origin, sterile-filtered, cell-cultured tested), thiazolyl blue tetrazolium bromide (>97.5%), phosphate buffer solution (PBS) (Biotech, Performance Certified, pH 7.4), dimethyl sulfoxide (DMSO, >99.9%) and trypsin (1x, gamma irradiated), were all supplied by Sigma-Aldrich. Penicillin/Streptomycin (5000 U/ml) and trypan blue (0.4%) were purchased from Thermo Fisher Scientific. Cells were count with the Invitrogen™ Countess™ and cellular viability was study with the ASYS Expert Plus.

### 2.2. Methods

IR absorption spectra were performed in a spectrophotometer Jasco DS-702G, operating in the wavelength range 4000–400 $cm^{-1}$. The samples were prepared as pellets of PD in KBr, the chosen weight ratio did not present saturation in the absorption bands. TEM images were taken with a Technai Spirit Twin equipment. Cell microscopy images were taken with an inverted laser scanning confocal microscope (Leica TCS-SP5) equipped with an Ar laser and a HeNe laser using the 63 × 1.2NA Objective. Dynamic light scattering (DLS) measurements were performed by using Malvern Zetasizer Nano ZS series equipment. Particles dispersed in deionized water (pH = 6) at less than 0.01 wt% were characterized. Hydrodynamic size was given as the number average size. The correlation functions were analyzed by Cumulants method. The equipment used for the metals analysis was an ICP – OES Plasma Emission Spectrometer model ULTIMA 2 of Jobin Yvon. For the equipment calibration, standardized solutions of the different metals (Panreac) of 1000 mg/L were used, grouping all the Standard solutions in a multi-elemental pattern. The range calibration used was 10–100 ppm.

### 2.3. Synthesis of polydopamine nanoparticles (PD)

The synthesis procedure was reported previously [5]. Briefly, to synthesize polydopamine nanoparticles with an average diameter of ca. 100 nm, ammonia aqueous solution (1.3 mL, $NH_4OH$, 28–30%) was mixed with ethanol (40 mL) and deionized water (90 mL) under magnetic stirring at 25 °C for 30 min. Dopamine hydrochloride (0.5 g) was dissolved in deionized water (10 mL) and then added into the above solution. The reaction was left to react for 24 h. Polydopamine nanoparticles were isolated by centrifugation and purified by at least four cycles of centrifugation–redispersion in deionized water (40 mL). Polydopamine particles with an average diameter of ca. 270 nm were prepared by decreasing the volume of ammonia aqueous solution to 2.6 mL.

For the synthesis and purification of PD with an average diameter of ca. 300 nm, the experimental procedure was the above described but the volume of ammonia aqueous solution ($NH_4OH$, 28–30%) was 2 mL.

### 2.4. Synthesis of fluorescent polydopamine nanoparticles

100 nm PD in water (40 mL, 0.15 wt%) were centrifuged and resuspended in 37.5 mL of Tris buffer (pH 10) containing 177.8 mg of dopamine. The mixture was left to react for 60 min under magnetic stirring. Subsequently, 10 mL of $H_2O_2$ were added and the reaction was left to proceed for 24 h. The particles were purified by several cycles of centrifugation–resuspension in de-ionized water.

### 2.5. Metal loading of polydopamine nanoparticles

Metal-loaded polydopamine nanoparticles were prepared by mixing ca. 0.9 mL (ca. 0.035 wt%) of the synthesized polydopamine in 40 mL of a metal salt solution (pH 4.5, acetate buffer, 0.4 M) at room temperature for 16 h. The initial metal concentration was approximately 70 ppm for all solutions. After that, the particles were isolated by centrifugation and the metal content in the supernatant was determined by inductively coupled plasma atomic emission spectroscopy (ICP-AES). The isolated metal-enriched particles for cytotoxicity studies were purified by four centrifugation–resuspension cycles in water. In the last cycle they were resuspended in PBS with a final concentration of approximately 2.4 mg/mL.

### 2.6. Particles treatment for the cytotoxicity studies

The PBS dispersion of PD and metal enriched PD particles were sonicated for four minutes. After that, they were irradiated in a home with UV light for 40 min and left in the dark for 40 min before being added to the cell culture.

### 2.7. Cell culture

Cells were cultured with regular growth medium consisting of high-glucose DMEM supplemented with 10% fetal bovine serum (FBS), 1% penicillin-streptomycin and cultured at 37 °C in a 5% $CO_2$ humidified environment.

### 2.8. Cytotoxicity studies

Cytotoxicity was performed by standard MTT assays. For the mentioned assay, BT474 cancer cells were cultured and seeded in 24-well plates (10,000 cells/mL) and 24 h later, different aliquots of a PBS dispersion of PD nanoparticles charged with $Fe^{2+}$, $Fe^{3+}$, $Cu^{2+}$ and $Fe^{2+}$ + $Cu^{2+}$ were added to the cells. The concentration range was 10–110 mg/mL. Cellular viability was determined each 24 h, during 72 h, by adding a tetrazolium bromide solution (0.55 mg/mL) and by dissolving the obtained formazan salts in DMSO (500 μL/well). Absorbance was measured at 550 nm and, based on it, cellular viability was determined. The $LD_{50}$ was estimated for the BT474 cell line at 48 h.

Finally, and once the $LD_{50}$ was known for the breast carcinoma cell line, a new MTT assay was performed with healthy fibroblasts, from the NIH3T3 cell line, with the objective of studying metal enriched polydopamine nanoparticles' cytotoxicity effect over a non-cancerous cell line. In the same conditions, NIH3T3 cells were cultured and seeded and after 24 h, different aliquots of PD nanoparticles charged with $Fe^{2+}$, $Fe^{3+}$ and $Fe^{2+}$ plus $Cu^{2+}$ were added to the 24-well plates. The final PD concentrations were 15 and 40 mg/mL. To finish, viability of fibroblasts was studied each 24 h, during 72 h, and polydopamine nanoparticles' cytotoxicity effect over this cell line was compared with the effect that they first had over the BT474 cell line.

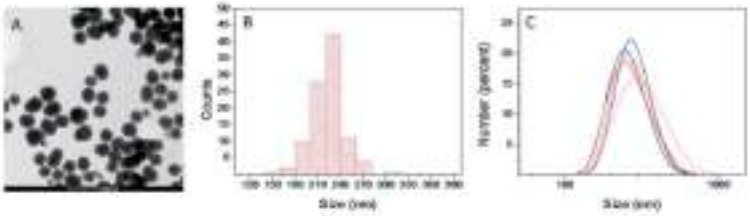


Fig. 1. A) TEM image of print in PD particles. B) Histogram that shows the PD size distribution obtained from the measurement of ca. 100 particles in different TEM images. C) DLS number distribution (the correlation function was fitted with the Cumulants method) of a dispersion of PD (black) and $M^{n+}$ loaded PD particles in deionized water (pH around 6): $M^{n+}$ = $Fe^{3+}$ (red), $Cu^{2+}$ (blue), $Ca^{2+}$ (pink) and $Zn^{2+}$ (orange). PD concentration was 0.0033 mg/mL. (For interpretation of the references in colour in this figure legend, the reader is referred to the web version of this article.)

important) PD presents a featureless and constant absorbance along the Vis spectrum that overlaps with the absorbance of formazan salts (Fig. S1, Supporting Information). In the MTT assay, when the culture medium is discarded before adding DMSO (which will solubilize formazan salts) most of the PD nanoparticles remain adhered to the bottom of the plate. To avoid interference of PD absorbance with the formazan absorbance, the DMSO (500 µL) was pipetted and placed in a clean cell-plate to make the absorbance measurement that accounts for cell viability. If the PD-formazan absorbance overlapping was not considered an overestimation of cell viability would be obtained.

## 3. Results and discussion

### 3.1. Polydopamine – $M^{n+}$ interaction

PD particles can be synthesized by oxidative polymerization of dopamine hydrochloride in a basic aqueous medium [5,18,20]. At the initial stages, the oxidation of dopamine to dopamine quinone takes place. Next, further oxidation and cyclization occur to give 5,6-dihydroxyindole. Since then, polymerization proceeds to give the black pigments emulating the properties of natural melanins. There is a disorder in monomers, reactivity and degree of polymerization, which makes extraordinary difficult the PD chemical characterization. Therefore, the PD chemical structure is still under discussion [19,21–24]. Generally, it is accepted the presence of certain functional groups in the PD structure: i) alcohol (phenolic), ii) quinone and semiquinone groups, iii) amine group (indole ring), iv) amine groups from uncycled dopamine units and v) acid groups from a small fraction of pyrrolecarboxylic acid moieties derived from the oxidative degradation of the indole units [18]. These functional groups are central in the metal binding ability of natural melanin [4]. However, the interaction of PD with diverse metallic cations is seldom explored. Natural melanins (eumelanin) and PD are structurally dissimilar because the chemical structure of their precursor is different [25]. Dopamine does not contain carboxylic acids, moreover uncyclized amine units are only presented in PD. Therefore, the characterization of the PD metal loading behavior (affinity and loading capacity) will be presented before the cytotoxicity study.

The TEM image of the PD particles as well as the size histogram are shown in Fig. 1A and B. The average size is 221 ± 22 nm. The PD particles remained stable in water with an average hydrodynamic diameter determined by DLS (from the number-averaged size distribution shown in Fig. 1C) of 305 ± 84 nm (PdI = 0.04). This value is higher than the average diameter obtained by TEM, which can be ascribed to the hydration of the particles. Colloidal stability of the PD particles with the medium pH was characterized at three different pH values, pH = 4.5 (acetate buffer, 0.4 M), 7.4 (phosphate saline buffer, 50 mM) and 8.5 (Tris-HCl buffer, 50 mM). DLS hydrodynamic diameter and zeta potential were determined at each pH (Fig. S2, Supporting Information). Particles remain dispersed with a hydrodynamic diameter of ca. 300 nm at pH = 7.4 and 8.5. The zeta-potential was negative at these pH values, being −13.4 and −20.6 mV respectively, which guarantees the colloidal stability. Contrarily, at pH = 4.5 particles tend to aggregate. Their hydrodynamic diameter was close to 1000 nm. Moreover, their zeta-potential value was smaller and close to zero, being −6.4 mV in this case.

Approximately 220 nm – PD particles were used to characterize the interaction with the following metallic cations ($M^{n+}$): $Ca^{2+}$, $Cu^{2+}$, $Fe^{3+}$, $Fe^{2+}$, $Mn^{2+}$ and $Zn^{2+}$ at pH 4.5 (acetate buffer). They were selected because they are trace elements in the human body. Besides, some of them can enhance MRI contrast. Thus, their PD enrichment ($Cu^{2+}$, $Fe^{3+}$, $Mn^{2+}$) is currently receiving attention to device cancer diagnosis systems [6–11].

The pH value for the complexation experiments was fixed at 4.5 for two reasons: i) the selected cations do not present solubility problems at pH 4.5; ii) importantly it is the pH of cell lysosomes. Besides, the cell internalization of synthetic melanins has been reported to occur via the lysosomes [12]. Thus, this pH value would rule the complexation chemistry of PD in these organelles.

PD metal loading capacity was evaluated by mixing 1 mg of PD nanoparticles with $M^{n+}$ solutions (ca. 70 ppm) at pH 4.5 (acetate buffer). After that, PD particles were isolated and the remaining metal concentration in solution was determined by ICP-AES. The metal concentration is in a large excess in all experiments, since 70% of metal remained in solution after the adsorption process.

Three different approaches were conducted to assess the interaction of PD with the different $M^{n+}$: i) the independent interaction of $M^{n+}$ and PD particles was evaluated and ii) the competitive interaction of $Fe^{3+}$ and $Cu^{2+}$ to be adsorbed on the PD particles was studied. To do that, these ions were incubated together with the PD particles. iii) $Fe^{3+}$ and $Cu^{2+}$ were loaded in two sequential steps and the loading capacity of each one was determined.

Fig. 2A shows that PD nanoparticles can interact with a great variety of metallic cations. It is remarkable the adsorption, expressed as Q (mg of $M^{n+}$/g of PD particles), of $Fe^{3+}$, $Cu^{2+}$ and $Ca^{2+}$ with Q values of 314, 283 and 341 mg/g respectively. However, although in a lesser extent the adsorption of $Zn^{2+}$, $Mn^{2+}$ and $Fe^{2+}$ was also significant, with Q values of 248, 153 and 170 mg/g respectively. As an important result, PD particles can act as carrier of diverse metallic cations showing preference for iron in its highest oxidation state.

The result of the competitive interaction between $Fe^{3+}$ and $Cu^{2+}$ towards the PD particles is shown in Fig. 2B. We can observe that

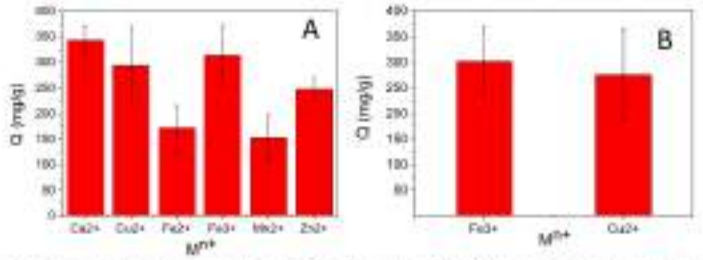


Fig. 2. A) Loading of $M^{n+}$ expressed as Q on PD. B) Competitive loading of $Fe^{3+}$ and $Cu^{2+}$ expressed as Q on PD particles (both ions were incubated together with the PD particles). The Q values are the average of the Q values obtained in three different experiments.

multiple $M^{n+}$ loading is happening, $Fe^{3+}$ and $Cu^{2+}$ are similarly loaded with Q values around 250 mg/g. The loaded amount of each cation is minor than the amount loaded of each ion independently. However, the result of loading both ions [$Q_{Fe}+Q_{Cu}=500$] greatly exceeds the Q value of each independent ion. It may mean that there are at least two different binding sites for both ions. This result would agree with a previous study dealing with the sepia melanin-$M^{n+}$ interaction. In which $Fe^{3+}$ could be loaded in melanin particles previously charged with other cations such as $Ca^{2+}$ and non-cation displacement was observed [28]. Since, $Ca^{2+}$ and $Fe^{3+}$ seemed not to share the same binding site.

To support that conclusion, $Fe^{3+}$ and $Cu^{2+}$ were loaded in two sequential steps. First, PD particles were loaded with $Fe^{3+}$ with a Q = 345 mg/g. Then, iron loaded PD particles were isolated and re-suspended in a $Cu^{2+}$ solution (aprox. 80 ppm, pH 4.5). After that, $Cu^{2+}$ was estimated to be loaded with a Q = 327 mg/g and $Fe^{3+}$ was not detected in solution, which indicates that there was not metal displacement.

Finally, PD particles loaded with either $Cu^{2+}$ or $Fe^{3+}$ were resuspended in deionized water (40 mL). After 72 h, the presence of $Cu^{2+}$ or $Fe^{3+}$ in solution was not detected.

PD particles enriched with the different $M^{n+}$ remain well-dispersed in water with similar number- averaged size distribution as the PD particles. In case of PD particles loaded with both $Ca^{2+}$ and $Cu^{2+}$ the number- averaged size distribution is slightly shifted to larger diameters as it is shown in Fig. 1C.

Morphology of PD particles after the interaction with the $M^{n+}$ was studied by TEM, Fig. 3. Particles did not change after the interaction with the different metallic cations except for $Fe^{3+}$. The direct binding of $Fe^{3+}$ or in combination with $Cu^{2+}$ made the surface become spongy. However, $Cu^{2+}$ loading did not produce such modification. Therefore, we ascribed this surface change to the different way of coordination between $Fe^{3+}$ and the rest of $M^{n+}$ that may modify the PD self-assembly [27].

IR spectroscopy has been used to characterize the different cationic metal binding sites in sepia melanin [2]. IR spectrum of PD is shown in Fig. 3A. The main bands are assigned according to the previous characterization of melanins [2,28–30]. The absorption band with the maximum at 1612 $cm^{-1}$ is very broad and intense and may include the C=O stretching (non carboxylic acid) and the C=C stretching of the aromatic system (at ca. 1580 $cm^{-1}$). Besides that, the N–H bending in an indole ring may appear at 1510 $cm^{-1}$, while the peaks at 1345 and 1383 $cm^{-1}$ may correspond with the C–N stretching mode of an indole and pyrrole ring respectively, and the C–OH stretching in a phenol ring appears at 1280 $cm^{-1}$. In the region from 4000 to 2800 $cm^{-1}$, the bands at 2956, 2922 and 2840 $cm^{-1}$ correspond to the different vibrational modes of aliphatic groups. Additionally, there is a broad band placed at 3405 $cm^{-1}$, which may include the –OH (phenol, carboxylic acid) and the –NH stretching modes (in an indole or in a primary amine) respectively.

After $M^{n+}$ binding, the main changes in the spectra (normalized at 1620 and 2840 $cm^{-1}$ for the 1800–1000 $cm^{-1}$ and 3400–2000 $cm^{-1}$ ranges respectively) are summarized as follows: the broad band placed at 3405 $cm^{-1}$ (Fig. 4A), which includes the –OH and the diverse –NH stretching modes, decreases in intensity after the $M^{n+}$ binding. This behavior suggests the deprotonation upon metal binding (Fig. 4B) and it indicates that these functional groups can be involved in the binding of all $M^{n+}$ at pH 4.5. Nevertheless, we could not determine the independent contribution of each one.

Upon $Fe^{3+}$ and/or $Cu^{2+}$ binding, notable changes in the band structure in the 1800–1000 $cm^{-1}$ region are produced (Fig. 4C). The band at 1280 $cm^{-1}$, which characterizes the C–OH stretching mode in the phenol ring, is shifted to longer wavenumbers after $Fe^{3+}$ and/or $Cu^{2+}$ loading. From 1288 $cm^{-1}$ for PD to 1293 $cm^{-1}$ for PD enriched with $Fe^{3+}$ or $Cu^{2+}$. The position of this band did not change for the rest of $M^{n+}$ (Fig. 4D). The bands placed at 1510 and 1612 $cm^{-1}$ also changed after $Fe^{3+}$ or $Cu^{2+}$ loading. These bands were broadened, and the effect was more notable in the case of $Fe^{3+}$.

After coordination of $Zn^{2+}$ and $Mn^{2+}$, the band at 1380 $cm^{-1}$, which was assigned to the C–N stretching in a pyrrole ring, disappeared as it is shown in the inset in Fig. 4D (inset). For $Cu^{2+}$ the bands at 1345 and 1380 $cm^{-1}$ have also disappeared. Nevertheless, they are not affected in case of the $Zn^{2+}$ binding. For $Fe^{3+}$, the band placed at 1345 $cm^{-1}$ is shifted to lower wavenumbers, 1336 $cm^{-1}$.

To summarize, we can conclude that for both $Fe^{3+}$ and $Cu^{2+}$, catechol and the amine in the indole ring account for most of their complexation. Additionally, the pyrrole rings seem to participate in the $Cu^{2+}$ binding. In case of the $Zn^{2+}$ and $Mn^{2+}$ binding, the pyrrole units play an important role. Probably, the carboxylate groups may be participating in the complexation of the $M^{n+}$.

### 3.2. Cytotoxicity study

One advantage of the synthetic methodology is the control on PD particle size. Reducing the volume of ammonium hydroxide from 3.3 to 2.5 mL yields PD nanoparticles of ca. 100 nm. Next, PD nanoparticles with a hydrodynamic diameter of 100 nm were loaded with the following metallic cations: $Fe^{3+}$, $Fe^{2+}$, $Cu^{2+}$ and the combination of $Cu^{2+}$ and $Fe^{3+}$. These $M^{n+}$ were selected for cyto-

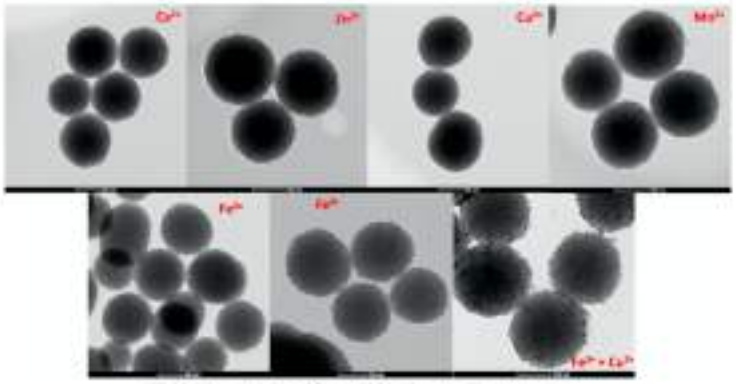

Fig. 3. TEM images of PD particles loaded with the different $M^{n+}$ and their combinations.

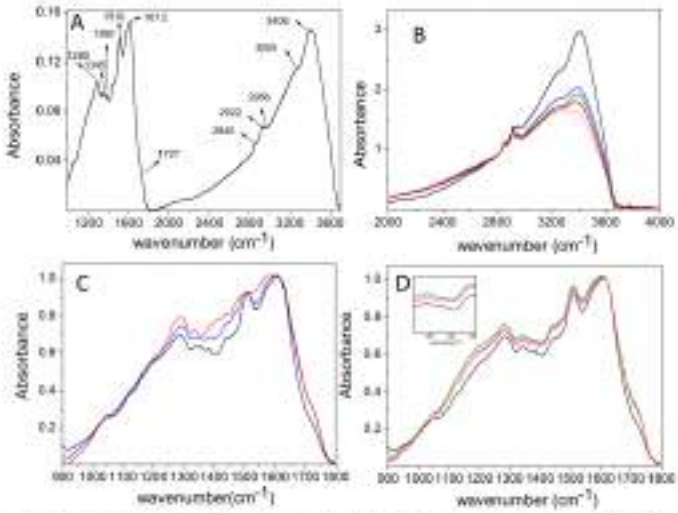


Fig. 4. A) IR spectrum of PD particles. B) IR spectra in the 2000–4000 cm$^{-1}$ range of PD (black) and PD after interaction with $Fe^{3+}$ (red), $Cu^{2+}$ (blue), $Ca^{2+}$ (pink), $Zn^{2+}$ (orange) and $Mn^{2+}$ (green). C) IR spectra in the 900–1800 cm-1 range of PD (black) and PD after interaction with $Fe^{3+}$ (red) and $Cu^{2+}$ (blue). D) IR spectra in the 900–1800 cm-1 range of PD (black) and PD after interaction with $Ca^{2+}$ (pink), $Zn^{2+}$ (orange) and $Mn^{2+}$ (green). (For interpretation of the references in colour in this figure legend, the reader is referred to the web version of this article.)

toxic studies because they have been combined with PD to design MRI contrast agents without having the consideration they could catalyze Fenton type reactions [13].

Two cell lines were selected for the cytotoxicity studies: NIH3T3 and BT-474 cell lines. Both cell lines were not arbitrary chosen. According to the American Type Cell Culture (ATCC), BT474 cell line was isolated from a solid, invasive ductal breast carcinoma. It has an epithelial morphology, expresses estrogen and progesterone receptors and has an ERBB2 amplification, that is normally associated with invasion and metastatic processes. Because of this last

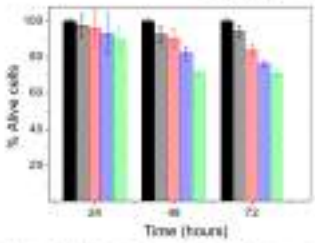


fact, it is normally used to perform assays in which an aggressive cell line is needed. On the other hand, NIH3T3 is a mouse embryonic fibroblast cell line. It is commonly chosen as healthy control.

Firstly, the cytotoxic effect of PD nanoparticles (without metal) was studied in the NIH3T3 cell line. Fig. 5 shows the percent of alive healthy cells (NIH3T3 cells), after exposure at different PD concentrations in a range of 0.04–0.09 mg/mL up to 72 h.

After 24 h, the percentage of alive cells was above 80% for all the concentration range which indicates that PD nanoparticles presented a limited cytotoxicity. After 48 h of treatment, cell viability was reduced below the 80% only for the concentration 0.093 mg/mL and after 72 h, cell viability was slightly below the 80% only for 0.0072 and 0.093 mg/mL concentrations. As conclusion, PD is a biocompatible system that does not present cytotoxic effect on healthy cells (NIH3T3), which agrees with prior work that describe the toxicity lack of PD in rats [5].

Next, the cytotoxic effect of the different metal enriched-PD nanoparticles on the NIH3T3 and BT474 cell lines was studied. Cell viabilities after treatment with different concentrations of the metal–PD systems are shown in Fig. 6. Concentration is expressed in mg of PD/mL of cell culture medium.

In general, the metal-PD systems have a severe cytotoxic effect on both cell lines in the 0.130–0.010 mg/mL range. At 72 h, the viability is reduced below the 25% for most of the $M^{n+}$ and concentrations. However, differences in the time–action relation can be noticed because cancer cell viability strongly drops 24 h after treatment (Fig. 6A), being lower than 50% for all metal systems, while healthy cell viability can be found between 55 and 90% depending on the metal and concentration (Fig. 6B).

$IC_{50}$ values (estimated at 48 h, expressed in PD concentration) of the metal-enriched PD nanoparticles for the BT474 cell line were 0.014, 0.016, 0.012 and 0.011 mg/mL for $Fe^{2+}$, $Fe^{3+}$, $Cu^{2+}$ and $Fe^{2+}$+$Cu^{2+}$ respectively. We hypothesize that the toxicity may be associated to the ROS production catalyzed by the metals via Fenton chemistry [16–18].

Finally, fluorescent PD nanoparticles [31] were prepared and their internalization in the BT474 cancer cell line was monitored. After 180 min of incubation, fluorescence of the PD particles could be observed in cell cytoplasm. Fig. 7 shows the merged images

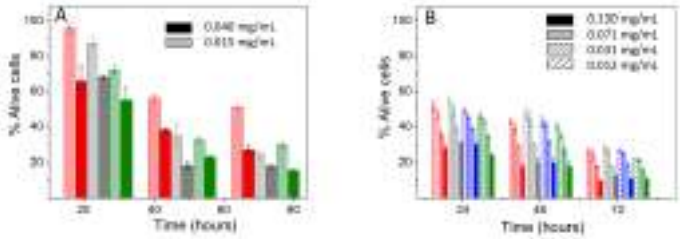

(bright field and fluorescence) of the BT474 cancer cell line after 150 min, which indicates that PD could be easily internalized.

Colocalization experiments were carried out. The results are shown in Fig. S4 (Supporting Information). After 4 h, fluorescence of PD (blue) co-localized with the chemical marker of lysosomes (red), which may indicate that PD nanoparticles target lysosomes via an endocytic mechanism.

## 4. Conclusions

The interaction of PD particles with different metallic cations, $Fe^{3+}$, $Fe^{2+}$, $Ca^{2+}$, $Na^{+}$, $Zn^{2+}$ and $Cu^{2+}$, was studied at pH 4.5. The adsorption of $Fe^{2+}$, $Cu^{2+}$ and $Ca^{2+}$ caused by PD was remarkable, producing Q values of 314, 283 and 343 mg/g respectively. The adsorption of $Zn^{2+}$, $Mn^{2+}$ and $Fe^{3+}$ was also significant, but to a lesser extent, giving Q values of 263, 121 and 221 mg/g, respectively. In addition, it was found that for $Fe^{3+}$ and $Cu^{2+}$, catechol and the amine (in the indole ring) account for most of the complexation.

Fluorescent PD particles were prepared and their internalization in BT474 cancer cells was monitored. After 4 h, fluorescence was observed in the cytoplasm, indicating that the particles were easily taken up. Co-localization experiment indicated that PD particles target the lysosomes.

The cytotoxicity of the metal-enriched PD particles (with $M^{n+}$ = $Fe^{3+}$, $Fe^{2+}$, $Cu^{2+}$, paramagnetic cations that can be involved in ROS production) was evaluated in two cell lines, BT474 and NIH3T3, for a period of up to 72 h using the MTT assay. They were found to be highly toxic systems to BT474 during the first 24 h. The $IC_{50}$ (referring to PD concentration) for the BT474 cells were 0.014, 0.016, 0.012 and 0.011 mg/mL for $Fe^{2+}$, $Fe^{3+}$, $Cu^{2+}$ and $Fe^{2+}$ + $Cu^{2+}$, respectively. Therefore, these metal-enriched PD particles can be considered as antineoplastic agents, although this system was not selective as acute toxic effect were observed in the healthy cell line NIH3T3.

## Acknowledgments

This work was supported by Junta de Castilla y León (project reference SA084U16). G.M and C.V thanks Junta de Castilla y León for the Post-Doc and predoc fellowships.

## Appendix A. Supplementary data

Supplementary data associated with this article can be found, in the online version, at https://doi.org/10.1016/j.colsurfb.2018.04.027.

## References

[1] P. Meredith, T. Sarna, The physical and chemical properties of eumelanin, Pigment Cell Res. 19 (2006) 572–594.
[2] L. Hong, P. Liu, J.D. Simon, Binding of metal ions to melanins and their effects on the aerobic reactivity, Photochem. Photobiol. 83 (2007) 417–425.
[3] L. Hong, J.D. Simon, Insight into the binding of divalent cations to synthetic melanins from IR absorption spectroscopy, Photochem. Photobiol. 82 (2006) 1283–1289.
[4] L. Hong, J.D. Simon, Current understanding of the binding sites, capacity, affinity, and biological significance of melanin to metal ions, J. Phys. Chem. B 111 (2007) 7938–7947.
[5] Y. Liu, R. Hu, J. Liu, M. Dong, Y. He, L. Lu, Dopamine-melanin colloidal nanospheres: an efficient near-infrared photothermal therapeutic agent for in vivo cancer therapy, Adv. Mater. 23 (2011) 1352–1356.
[6] A. Iacomussi, V. Lio, J.D. Simon, Characterization of the HOD-binding site in sepia melanosomes by resonance Raman excitation intensity profiles, Photochem. Photobiol. 80 (2004) 84–88.
[7] L. Zecca, M. Gallorini, V. Schünemann, A.X. Trautwein, M. Gerlach, P. Riederer, et al., Iron, neuromelanin and ferritin content in the substantia nigra of normal subjects at different ages: consequences for iron storage and neurodegenerative processes, J. Neurochem. 76 (2001) 1766–1773.
[8] H. Lee, S.M. Dellatore, W.M. Miller, P.B. Messersmith, Mussel-inspired surface chemistry for multifunctional coatings, Science 318 (2007) 426–430.
[9] S. Cho, W. Park, D.-H. Kim, Silica-coated metal-chelating melanin nanoparticles as a dual-modal contrast enhancement imaging and therapeutic agent, ACS Appl. Mater. Interfaces 9 (2017) 1181–1191.
[10] B. Ge, M. Lin, B. Li, S. Liu, W. Wang, S. Li, et al., Tyr2+-loaded polydopamine nanoparticles for magnetic resonance imaging-guided pH- and near-infrared light-stimulated thermo-chemotherapy, ACS Appl. Mater. Interfaces 9 (2017) 18308–18316.
[11] K.-T. Yu, S. Lee, J. Yun, J. Choi, J.-K. Lee, Bio-inspired development of a dual-mode nanoprobe for MRI and Raman imaging, Small 11 (2015) 84–88.
[12] Y. Huang, F. Li, Z. Hu, X. Yue, M.T. Proetto, Y. Jones, et al., Melanizing melanomas: polydopamine nanoparticles as artificial microparasols, ACS Nano Am. J. (2011) Web 868.
[13] L. Ding, K. Jiao, Y. Wang, N. Hu, X. Ling, H. Chen, et al., Intracellular fate of nanoparticles with polydopamine surface engineering and a novel strategy for exocytosis-inhibiting, lysosome impairment-based cancer therapy, Nano Lett. 17 (2017) 6798–6805.
[14] R. Silvestri, O. Vilella, G. Luciani, F. Cavagnis, A. Cossarizza, M. Lisillo, et al., Probing the nanobiotic silica interface in chemically engineered bulk hybrid nanoparticles for targeted subcellular antioxidant protection, ACS Appl. Mater. Interfaces 9 (2017) 37815–37823.
[15] S.J. Dixon, N.R. Stockwell, The role of iron and reactive oxygen species in cell death, Nat. Chem. Biol. 10 (2014) 9–17.
[16] P. Wang, J. Zhou, B. Chen, H. Hu, Y. Wang, J. Lu, et al., Core–shell metal–organic frameworks as Fe2+ suppliers for Fe2+-mediated cancer therapy under multimodality imaging, Chem. Mater. 29 (2017) 3477–3489.
[17] L.E. Ren, L. Zhang, R. Ma, M. Reynaud, P. Chen, C. Ingrosso, et al., Ultrasmall nanoparticles induce ferroptosis in nutrient-deprived cancer cells and suppress tumour growth, Nat. Nanotechnol. 13 (2018) 997.
[18] S. Tavagnin, G.J. Dawes, An iron age for cancer therapy, Nat. Nanotechnol. 13 (2018) 821.
[19] N.F. Della Vecchia, R. Luciani, A. Napolitano, E. D'Errico, E. Modica, N. Grimaldi, et al., Tris buffer modulates polydopamine growth, aggregate size and paramagnetic properties, Langmuir 30 (2014) 9811–9818.
[20] K.-T. Ju, P. Lee, S. Lee, D.K. Park, J.-K. Lee, Biomimetic polymerization of dopamine to generate melanin-like nanoparticles having an excellent free-radical-scavenging property, Biomacromolecules 12 (2011) 625–632.
[21] D.B. Kenyon, D.J. Miller, B.D. Freeman, D.R. Paul, C.W. Bielawski, Elucidating the structure of poly(dopamine), Langmuir 29 (2012) 6426–6435.
[22] S. Hong, Y.S. Na, S. Choi, I.T. Song, W.Y. Kim, H. Lee, Non-covalent self-assembly and covalent polymerization co-contribute to polydopamine formation, Adv. Funct. Mater. 22 (2012) 4711–4717.
[23] J. Liebscher, R. Mrówczyński, H.A. Scheidt, C. Filip, N.D. Hădade, R. Turcu, et al., Structure of polydopamine: a never-ending story, Langmuir 29 (2013) 10539–10548.
[24] N.F. Della Vecchia, R. Avolio, M. Alfè, M.E. Errico, A. Napolitano, M. d'Ischia, Building-block diversity in polydopamine underpins a multifunctional eumelanin-type platform tunable through a quinone control point, Adv. Funct. Mater. 23 (2013) 1331–1340.
[25] M. d'Ischia, A. Napolitano, V. Ball, C.-T. Chen, M.J. Buehler, Polydopamine and eumelanin: from structure–property relationships to a unified tailoring strategy, Acc. Chem. Res. 47 (2014) 3541–3550.
[26] P. Liu, J. Huang, K.D. Berndt, E. Wikstrom, G. Du, J.D. Simon, Ion-Exchange and adsorption of Pr[III] by sepia melanin, Pigm. Cell Res. 17 (2004) 262–266.
[27] A.A.R. Watt, J.P. Bothma, P. Meredith, The supramolecular structure of melanin, Soft Matter 5 (2009) 3754–3760.
[28] M.G. Bridelli, D. Tampellini, L. Zecca, The structure of neuromelanin and its iron binding site studied by infrared spectroscopy, FEBS Lett. 417 (1997) 19–22.
[29] S.A. Centeno, J. Shamir, Surface enhanced Raman scattering (SERS) and FTIR characterization of the sepia melanin pigment used in works of art, J. Mol. Struct. 873 (2008) 149–159.
[30] R.A. Ganeshmoorthy, T.A. Moore, M.J. Tarlov, Characterization of polydopamine thin films deposited at short times by autoxidation of dopamine, Langmuir 33 (2017) 8619–8628.
[31] E. Chen, Y. Yan, M. Müllner, M.P. van Koeverden, B.F. Noi, W. Hu, et al., Regioselective fluorescent poly(dopamine) capsules, Langmuir 30 (2014) 2831–2839.

RSC Advances

PAPER

View Article Online

# Polydopamine nanoparticles kill cancer cells

Celia Nieto, Milena A. Vega, Gema Marcelo* and Eva M. Martín del Valle*

Cite this: RSC Adv., 2018, 8, 36201

Received 29th June 2018
Accepted 8th October 2018

DOI: 10.1039/c8ra05569

rsc.li/rsc-advances

Polydopamine (PD) is a synthetic melanin analogue of growing importance in the field of biomedicine, especially with respect to cancer research, due, in part, to its biocompatibility. But little is known about the cytotoxic effects of PD on cancer cell lines. PD is a UV-vis absorbing material whose absorbance overlaps with that of formazan salts, which are used to assess cell viability in MTT assays. In this study, a protocol has been established to eliminate the contributing absorbance of PD at 550 nm, and has been applied to characterise the cytotoxicity of PD nanoparticles in both healthy and breast cancer cell lines. Once the protocol is applied, it was found that PD is per se an antineoplastic system, meaning it selectively kills cancer cells, especially those of breast cancer, but it has no toxic effect on healthy cells. The mechanism of action could be related to the production of ROS and the alteration of iron homeostasis in lysosomes. To the best of our knowledge there are only a few examples of nanoparticle systems devoid of drugs that selectively kill cancer cells.

## Introduction

Polydopamine (PD) is a synthetic melanin analogue with properties similar to those occurring in natural systems.[1,2] In cancer research, polydopamine plays a central role in devising new materials for diagnosis and/or therapy due to its: (i) biocompatibility;[3] (ii) physical properties, such as thermal deactivation[4–6] and chemical versatility,[7–9] which permits further functionalisation strategies as well as the chelation of diverse metallic cations;[9–11] and (iii) its coating ability regardless of the substrate material.[9,12]

The biocompatibility of PD has been shown by previous studies using MTT assays on different cell lines.[3,10–13] Additionally, its long-term toxicity has been examined by intravenous injection in rats, where the injected animals remain alive for one month with no abnormal effects observed.[3] However, little is known about the cytotoxic effects of PD in cancer cells.

Radical oxygen species (ROS) are produced endogenously in multiple and normal cellular metabolic processes. Lysosomes are acid cell compartments that act as centers for cell degradation, among other functions. Therefore, they are the main intracellular stores for $Fe^{3+}$, $Fe^{2+}$, $Zn^{2+}$ and $Cu^{2+}$ cations.[14–16] Many of these metals participate in the production of ROS *via* Fenton chemistry.[17] lysosomes contain certain levels of ROS, which are essential for normal cell function.[17] However, an aberrant accumulation of metals and/or ROS is linked to immediate cell damage and degenerative diseases.[16,18]

Recently, new strategies for targeting cancer treatment have emerged that are linked to the use of nanosystems/drugs capable of altering the lysosomal homeostasis of certain metallic cations, essentially iron.[19] This in turn leads to ROS production and subsequent cancer cell death.[20–24] The mechanism of these systems are thought to act differently, where nanosystems (metal-organic frameworks) can deliver $Fe^{3+}$, degrading lysosomes through the production of ROS. Additionally, salinomycin molecules sequester $Fe^{2+}$ in the lysosome leading to its depletion, which is linked to ROS production and causes cancer cell death. This latter mechanism is known as ferroptosis, and a similar mechanism occurs with the use of ultra-small (ethylene glycol)-coated silica nanoparticles.

The MTT assay is a standard test frequently used in cytotoxicity studies.[25] It is based on the fact that only metabolic active cells, *i.e.* viable cells, are able to reduce and convert the yellow water-soluble tetrazolium dye (3-[4,5-dimethyl-2-thiazolyl]-2,5-diphenyl-2*H*-tetrazolium bromide) into purple-colored formazan crystals ([1,2]-5-[4,5-dimethylthiazol-2-yl]-1,3-diphenyl-formazan) due to the action of mitochondrial dehydrogenases. The formazan product is spectrophotometrically analysed at 550 nm and its absorbance can be related to the number of viable cells. However, PD is an UV-vis absorbing material, and its broad absorption band overlaps with the absorbance band of the formazan salts. If not taken into account, this overlap would lead to the overestimation of cell viability and the real toxic effect of PD would not be correctly assessed.

Here we show that the absorbance of PD overlaps with the absorbance of formazan salts and the consequences of underestimating the true absorbance in cell viability assays. A general protocol eliminating the contribution of the absorbance of PD from the MTT absorbance measurement has been designed. Also, the toxic effect of PD on both a healthy cell line and a cancer cell line has been assessed following this proposed protocol.

(Department of Chemical Engineering, Universidad de Salamanca, Plaza de los Caídos s/n, 37008, Salamanca, Spain. E-mail: gemamarcelo@usal.es; emvalle@usal.es

Open Access Article. Published on 24 October 2018. Downloaded on 11/5/2018 9:01:15 AM.
This article is licensed under a Creative Commons Attribution-NonCommercial 3.0 Unported Licence.

Melanins have an active role in the regulation of the free iron concentration in neurons of the substantia nigra.[24] Similar to natural melanins, PD can sequester many metallic cations in the lysosomes of rapidly proliferating cancer cells which often contain more metals than normal cells. Likewise, PD may also alter metal homeostasis which could adversely affect cell survival.

## Results and discussion

### Synthesis and characterization of PD nanoparticles

PD nanoparticles were synthesized by oxidative polymerization of dopamine in a basic aqueous medium containing ethanol, water and ammonium hydroxide.[3] A TEM image and a histogram exhibiting the range of sizes are shown in Fig. 1A and B. The average size is 71 ± 11 nm. PD particles remained stable in water with an average hydrodynamic diameter of 116 ± 20 nm (PdI = 0.04), as determined by DLS (from the intensity-averaged size distribution shown in Fig. 1C).

### UV-vis spectroscopy characterization of PD nanoparticles and the MTT reagent

The interference caused by the absorption of PD together with the absorption of the MTT reagent was studied by UV-vis spectroscopy. The PD particle dispersion in water (concentrations ranging from 0.005 to 0.04 mg mL$^{-1}$) and a solution containing formazan in DMSO (0.025 mM) were used for this analysis. The absorption spectra (normalized at 260 nm) of PD (0.012 mg mL$^{-1}$) and the MTT reagent are shown in Fig. 2A. PD has a broad and featureless absorption band ranging from 280 to 1000 nm, with the maximum absorption at 280 nm. In addition, absorption at 330 nm was also shown to be significant. The variation observed in the absorption spectrum with respect to concentration is shown in Fig. 2B. The extinction coefficient at 550 nm was 12.79 mL mg$^{-1}$ cm$^{-1}$, which could not be expressed in molar units because the chemical structure of PD still remains under discussion.[10,25] Additionally, the UV-vis spectrum of the MTT reagent is characterized by an absorption band located at 564 nm, which is approximately the wavelength of absorption used in the MTT assay. Furthermore, formazan does not show absorption above 700 nm. Therefore, PD absorbance overlaps with the absorbance of the MTT reagent. The effect of the concentration of PD on the MTT absorption spectrum is shown in Fig. 2C. The addition of PD (final concentrations in the range of 0.001–0.011 mg mL$^{-1}$) to the MTT solution leads to an increase in the MTT absorption band, Fig. 1C. Thus, the final spectrum is the result of the merging absorption bands of PD and the MTT located at 564 nm spectra. The change in absorbance at 550 nm using a mixture containing the MTT reagent (at a fixed concentration, 0.025 mM) and PD at different concentrations is shown in Fig. 2D. The absorbance at 550 nm increases from 0.34 (in the absence of PD nanoparticles) to 0.77 when PD is at a concentration of 0.011 mg mL$^{-1}$. The variation observed is linear, and the slope is close to the PD extinction coefficient 12.91 mL mg$^{-1}$ cm$^{-1}$. As a result, the degree to which cellular viability would be overestimated is based on the concentration of PD. That is to say, a two-fold increase in viability would be obtained when the concentration of PD is 0.04 mg mL$^{-1}$.

Moreover, the absorbance of the mixture MTT + PD is the result of combining the absorbances of both PD nanoparticles and the MTT reagent at a particular PD concentration. Consequently, the contribution of PD can be eliminated from the absorbance determined by the MTT assay if either the PD absorbance or concentration is known.

PD particles present a great capacity for adhering to different types of materials. PD is comprised of catechol groups, which are versatile adhesives able to bind to either organic or inorganic substrates using a mechanism that is similar to the adhesion of marine mussels to surfaces.[4,26] This characteristic makes evaluating toxicity using UV-vis absorption spectroscopy difficult. It has been observed that PD remains adhered to the bottom of the cell culture plate when carrying out the MTT assay, which makes it practically impossible to eliminate PD from the cell plate when the medium is discarded. Moreover, part of the PD adhered to the plate may be re-dispersed when DMSO is added to dissolve the formazan crystals. As a result, the absorbance obtained at 550 nm would not provide a correct estimate of the quantity of viable cells, but instead would be an overestimate.

Therefore, the contribution of PD to the absorbance determined by the MTT assay could be easily removed if the

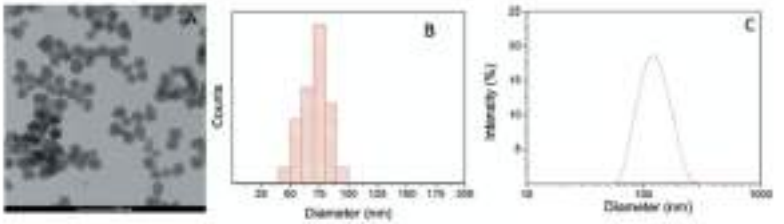


Fig. 1 (A) TEM image of PD nanoparticles. (B) Histogram of the size distribution obtained by measurement of ca. 300 particles of different TEM images. (C) Intensity-averaged size distribution of PD dispersed in deionized water (pH = 7).

Open Access Article. Published on 24 October 2016. Downloaded on 11/9/2016 9:51:18 AM.
This article is licensed under a Creative Commons Attribution-NonCommercial 3.0 Unported Licence.

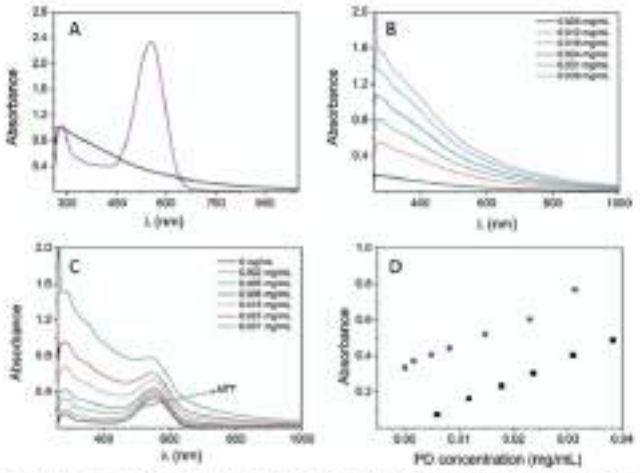


Fig. 2 (A) Normalized UV–vis absorption spectra (at 280 nm) of PD (black line) and the MTT reagent (purple line). (B) UV–vis absorption spectrum of PD at different PD concentrations. (C) The effect of PD concentrations, in range of 0.000–0.032 mg mL$^{-1}$, on the MTT absorption spectrum. (D) Absorbance variations detected at 550 nm as a function of PD concentration for a PD colloidal dispersion (black square) and a solution of the MTT reagent upon the addition of different PD aliquots (purple circle).

concentration of the PD remaining in the culture plate is known. Since absorbance could be determined from the concentration by using a calibration curve that relates PD concentration to its absorbance at 550 nm.

### Protocol for estimating cell viability using an MTT assay

First, it is necessary to determine the absorbance of PD at 550 nm, in order to eliminate its contribution from the absorption measured by the MTT assay. This allows the absorbance of formazan at 550 nm to be obtained, which gives an indication of the quantity of viable cells.

Fortunately, many of the microplate readers measure wavelengths of absorption within the range of 340 to 800 nm. The protocol proposed in this study requires that calibration curves be established for absorbance versus PD concentration (mg of PD/mL of DMSO) at both 550 and 700 nm using the microplate reader. In addition, the absorbance readings at both 550 nm and 700 nm in the MTT assay are also required.

A wavelength of 700 nm was selected because only PD absorbs and not formazan, as shown in Fig. 2A. Thus, the absorbance read at this wavelength in the MTT assay will determine the remaining concentration of PD in the plate by allowing the absorbance to be interpolated from the corresponding calibration curve of the absorbance of PD (700 nm) vs. the concentration of PD. Once the concentration of PD is known, its contributing absorbance at 550 nm can be estimated by interpolating the PD concentration in the calibration curve PD absorbance (550 nm) vs. PD concentration.

Finally, the PD absorbance value must be subtracted from the absorbance determined at 550 nm in the MTT assay before cell viability can be quantified. The proposed protocol is illustrated in Scheme 1.

### Cytotoxicity study of PD nanoparticles

The toxicity of the PD nanoparticles in a healthy cell line (NIH3T3) and a breast cancer (BT474) cell line was evaluated by performing a MTT assay. The procedure previously described for eliminating the contributing absorbance of PD from the MTT absorbance measured at 550 nm was applied to estimate cell viability.

The results obtained on the cytotoxic effect of PD (concentration range 0.015–0.070 mg mL$^{-1}$) in NIH3T3 cells during a period of 72 h are shown in Fig. 3.

After 24 h, the percentage of live cells was greater than 90% for all of the concentrations assayed, which supports the idea that PD is a biocompatible system. After 48 hours, cell viability was reduced to less than 80% but only for the concentration 0.093 mg mL$^{-1}$. After 72 hours of exposure, cell viability was slightly less than 80% for concentrations 0.072 and 0.093 mg mL$^{-1}$. Therefore, PD appears not to be cytotoxic at concentrations below 0.05 mg mL$^{-1}$, findings that agree with those of

View Article Online



Open Access Article. Published on 24 October 2016. Downloaded on 10/10/2019 9:03:17 AM.
This article is licensed under a Creative Commons Attribution-NonCommercial 3.0 Unported Licence.

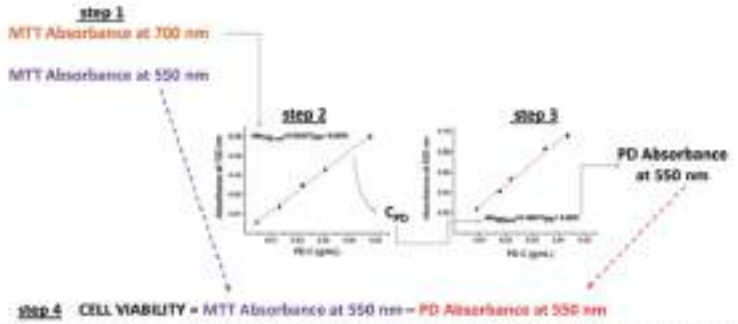


Scheme 1 Illustration of the proposed procedure to eliminate the contributing absorbance of PD at 550 nm, which is directly estimated in the MTT assay. First step: absorbance is measured at 550 and 700 nm. Second step: the absorbance at 700 nm is interpolated in the PD calibration curve (PD absorbance at 700 nm vs. PD concentration) to estimate the PD concentration ($C_{PD}$) that remains in the well. Third step: $C_{PD}$ is interpolated in the PD calibration curve (PD absorbance at 550 nm vs. PD concentration) to determine the PD absorbance at 550 nm. Fourth step: cell viability can be calculated considering the MTT absorbance at 550 nm that is measured in the first step and the PD absorbance at 550 nm.

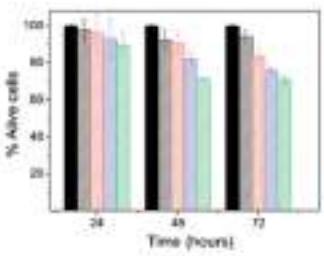


Fig. 5 The viability of the cell line MB-MTT cultured in different concentrations of PD. Green: 0.02 mg mL$^{-1}$, blue: 0.010 mg mL$^{-1}$, red: 0.002 mg mL$^{-1}$ and black: 0.093 mg mL$^{-1}$.

prior studies where PD did not prevent a toxic effect *in vitro* or *in vivo* in rats.[11,12]

The effect of PD on the BT474 cancer cell line was assessed during a period of 72 hours with a PD concentration range of 0.022–0.044 mg mL$^{-1}$. These results are shown in Fig. 4A. PD did not exhibit toxic effects on normal cells with the same concentration range. In contrast, PD particles had a significant adverse effect on BT474 cell viability. At 24 hours, cell proliferation was reduced to 77 and 62% for the lower and upper limits of the concentration range, respectively. After 48 hours, the percentage of live cells was between 37–44%, and finally at 72 hours, viability was in the range of 45–52%.

In conclusion, it can be said that PD selectively kills BT474 cancer cells in a concentration range that does not have any adverse effect on NIH3T3 healthy cells.

The adverse effect of PD on the viability of the BT474 cell line would not have been detected if the absorbance of PD had been eliminated directly from the absorbance recorded in the MTT assay. Fig. 5 shows the resulting cell viability when the developed protocol was not applied. In this case cell viability ranged between 108–143% after a 24 hours treatment.

### Cell internalization

Fluorescent PD particles[7,8] were prepared and their internalization in BT474 cancer cells was monitored. BT474 cells were cocultured with fluorescent PD particles. Fig. 6 shows that after 4 hours, the PD fluorescence (blue) co-localized with the fluorescence of the lysosome chemical marker (red), which indicates that PD targets lysosomes via an endocytic mechanism, a result that agrees with prior work reporting the same mechanism for the systematic uptake of PD.[13,19]

### PD chelation of metallic cations ($M^{n+}$)

The PD chemical structure is still under discussion.[11,19,20,21] Despite this, it is accepted the presence of certain functional groups in the PD structure such as alcohol (phenolic), quinone and semiquinone groups, amine group (indole ring), amine groups from uncycled dopamine units and acid groups from a small fraction of pyrrolecarboxylic acid moieties derived from the oxidative degradation of the indole units. $Fe^{2+}$, $Fe^{3+}$ and $Cu^{2+}$, among others, are metallic cations that can be found in lysosomes. Recently, we showed by infrared spectroscopy that these functional groups are responsible for the rich PD complexation chemistry towards many metallic cations and their loading capacity was determined.[8] Here, we again show a brief summary of the interaction of PD with $Fe^{2+}$ and $Fe^{3+}$ at pH 4.5 (which is the pH of lysosomes).[4] PD particles can load iron in both oxidative states through the complexation with

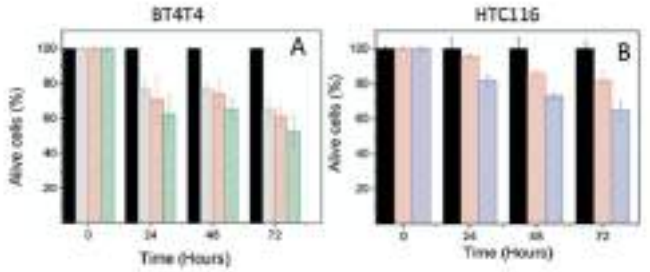


Fig. 4 (A) BT474 cell viability after treatment with different concentrations of PD. Control (black filled column). PD concentration (unfilled column): green: 0.044 mg mL$^{-1}$, red 0.033 mg mL$^{-1}$ and black: 0.022 mg mL$^{-1}$. (B) The viability of HTC116 cells after being cultured with two concentrations of PD: 0.025 mg mL$^{-1}$ (red) and 0.050 mg mL$^{-1}$ (blue). The control is represented by the solid black bar.

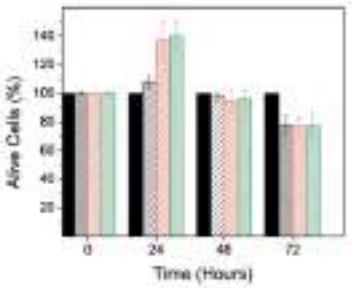


Fig. 5 Results without protocol implementation: BT474 cell viability after treatment with different concentrations of PD. Control (black filled column). PD concentration (unfilled columns): green: 0.044 mg mL$^{-1}$, red: 0.033 mg mL$^{-1}$ and black: 0.022 mg mL$^{-1}$.

catechol groups. The adsorption of $Fe^{3+}$, expressed as $Q$ (mg of $Fe^{3+}$/g of PD particles), was notable with $Q = 178$ mg g$^{-1}$, as compared to $Fe^{2+}$ with $Q = 210$ mg g$^{-1}$, which was smaller but also significant. In conclusion, these results may support the following hypothesis: PD could sequester these metal cations in lysosomes and lead to the modification of its homeostasis.

### Cytotoxicity mechanism

Lysosomes are the main intracellular stores for many metals and have an important role in the regulation of iron transport through the cell.[44] Additionally, iron is involved in the generation of ROS via Fenton reactions in lysosomes, to an abnormal concentration are toxic to the cell. In the former characterization, we showed that PD particles target lysosomes *via* an endocytic mechanism where their metal complexation chemistry may alter the homeostasis of iron.

Ferroptosis is a cell death mechanism that is related to an iron dependent ROS production that leads to oxidative damage of the membrane lipids of lysosome.[45,46] ROS are produced dependently upon modifying iron levels in lysosome. However, the precise role of iron in this mechanism is unclear. This action mechanism has been reported for salinomycin molecule and ultra-small (ethylene glycol)-coated silica nanoparticles among others.[46,47] Some evidences of this mechanism can be found upon co-treatment with either glutathione (GT) or deferoxamine (DFO). GT is selected because is a potent antioxidant involved in cellular protection against ROS[47] and DFO is a lysosomal iron chelating agent used to treat iron overload.[48] After GT/DFO co-treatment, the ferroptosis mechanism is blocked and the toxic effect of the drug is suppressed.

Now, we are going to focus our study on providing some insights that could support the idea that both iron level alteration and ROS production are closely related to the mechanism that could explain the toxicity of PD particles in breast cancer cells. To do so, we selected the PD concentration of 0.033 mg mL$^{-1}$ to study the toxic effect of PD particles in combination with either DFO or glutathione after a 24 hours treatment.

First, cell proliferation was reduced to 70% (related to the control) when they are treated only with PD particles, Fig. 7A. After that, BT474 cells were co-cultured with PD particles [0.033 mg mL$^{-1}$] and GT [50 μM]. After 24 hours, cell viability was very similar to the cell viability observed for the control (cells treated only with GT), as shown in Fig. 7B. This fact could indicate that GT protects cancer cells from the effect exerted by PD particles and suggests that the mechanism of toxicity for PD could be related to ROS production.

To evaluate if PD could alter the lysosomal iron homeostasis, we co-treated breast cancer cells with PD [0.033 mg mL$^{-1}$] and DFO (0.7 μM). The co-treatment with DFO and PD seemed to block the toxic effect of PD since cell viability was very similar to the cell viability observed for the control (cells treated only with DFO), Fig. 7C.

In sum, the toxicity of PD particles in the cancer cell line, BT474, could be related to ROS production, which may be

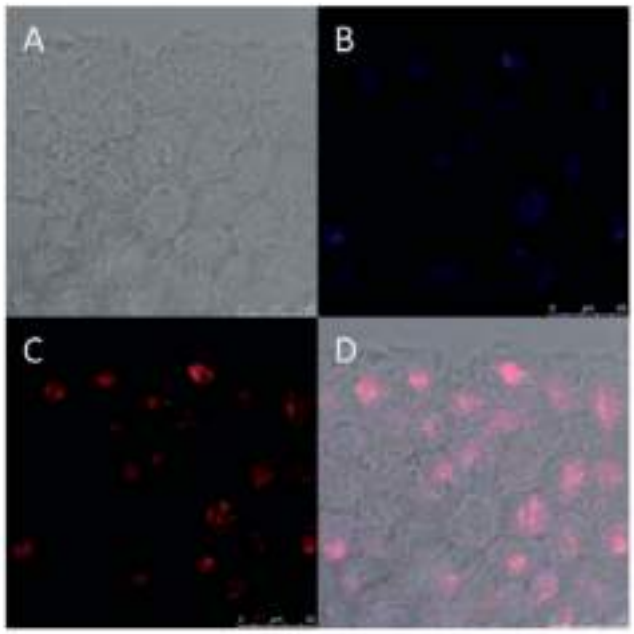


Fig. 6 (A) Bright field image of the BT474 cell line, (B) fluorescent image of the BT474 cell line after co-culturing with fluorescent PD particles (0.05 mg mL$^{-1}$) for 3 hours, with excitation at 405 nm. The fluorescence is due to the PD particles (C) lysosomes were stained with the Lyso Tracker red DND 99 marker, the excitation is at 570 nm and fluorescence is due to the lysosomes marker (D) image after merging (A–C) images.

associated with the alteration of iron homeostasis in lysosomes as it occurs in the ferroptosis mechanism. As characterized above, PD particles would be able to sequester iron in both oxidative states at lysosomal pH. Nevertheless, additional work is required to know in full the mechanism of action of PD particles.

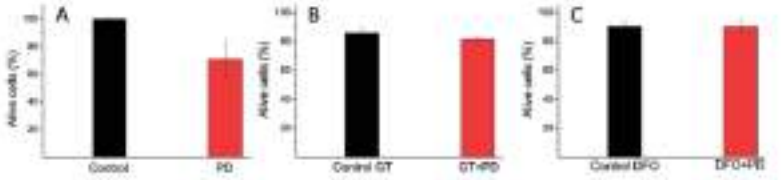


Fig. 7 The viability of BT474 cells after a 24 hours treatment for the following conditions: (A) without (black bar) and with PD particles at 0.033 mg mL$^{-1}$ (red bar); (B) reduced GT at a concentration of 50 μM (black bar) and the combination of GT (50 μM) with PD particles (0.033 mg mL$^{-1}$) (red bar); (C) DFO at a concentration of 0.7 μM (black bar) and the combination of DFO (0.7 μM) with PD particles (0.033 mg mL$^{-1}$) (red bar).

Open Access Article. Published on 02 October 2018. Downloaded on 10/5/2018 9:01:11 AM.
This article is licensed under a Creative Commons Attribution-NonCommercial 3.0 Unported Licence.

Finally, we sought to show that the toxic effect of PD is not limited only to the BT474 cancer line. Thus, we examined the toxic effect of PD in a human colorectal carcinoma (HTC116) cell line. The result of this analysis (at 15 and 50 mg $mL^{-1}$) on HTC116 cells during a 72 hours period is shown in Fig. 6B. After 24 hours, viability was reduced to 82% with a concentration of 50 mg $mL^{-1}$. After 48 hours of treatment, viability significantly decreased to 66 and 73% with the PD concentrations of 15 and 50 mg $mL^{-1}$, respectively. Finally, after 72 hours, the viability slightly decreased to values of 62 and 65% for the PD concentrations of 15 and 50 mg $mL^{-1}$, respectively.

## Conclusions

A protocol has been established for evaluating the anti-proliferative effect of PD systems on cell lines using a standard MTT assay. This procedure allows the contributing absorbance of PD at 570 nm to be eliminated from the MTT assay used to assess cell viability. This method is easy to implement, since it only requires that calibration curves for absorbance versus PD concentration be established at both 550 and 700 nm, as well as the absorbance readings at these same wavelengths for the MTT assay.

In this work, this protocol was applied to assess the cytotoxicity of PD particles in both healthy and breast cancer cell (BT474) lines by means of the MTT assay. It was found that PD kills cancer cells within the concentration range of 0.02–0.04 mg $mL^{-1}$. By contrast, PD particles were not toxic to healthy fibroblasts with this same concentration range.

It has been shown that PD particles target cellular lysosomes by an endocytic mechanism and exert an action that leads to the selective killing of cancer cells.

Furthermore, PD nanoparticles present rich metal complexation chemistry at lysosomal pH and can bind $Fe^{3+}$ and $Fe^{2+}$ with Q values of 330 and 210 mg $g^{-1}$, respectively.

The toxic effect of PD is inhibited in the presence of both DFO (iron chelating agent) and glutathione (radical scavenging agent). The results of the experiments performed using these two compounds may support the idea that the mechanism that could explain the selective toxicity of PD particles against cancer cells might be related to ROS production and an alteration of iron homeostasis in lysosomes.

These results are relevant since, to the best of our knowledge, there are only a few existing examples of nanosystems that are devoid of drugs that selectively kill cancer cells.[29]

## Experimental

### Materials and methods

TEM images were taken with a Technai Spirit Twin equipment. Dynamic light scattering (DLS) measurements were performed by using Malvern Zetasizer Nano ZS series equipment. Particles dispersed in deionized water (pH ~ 6) at less than 0.01 weight% were characterized. Hydrodynamic size was given as the number average size. The correlation functions were analyzed by cumulants method. The equipment used for the iron analysis was an ICP-OES Plasma Emission Spectrometer model ULTIMA 2 of Jobin Yvon. For the equipment calibration, standardized solutions of the different metals (Panreac) of 1000 mg $L^{-1}$ were used, grouping all the standard solutions in a multi-elemental pattern. The range calibration used was 10–100 ppm. Absorbance in the MTT assay was measured in a microplate reader EZ Reader 2000 of Biochrom. Absorbance spectra were obtained with UV 1800 Shimadzu UV-vis spectrophotometer. 1 cm quartz cuvettes were used for such characterization.

### Synthesis of polydopamine (PD) nanoparticles

An ammonia aqueous solution (1.3 mL, $NH_4OH$, 28–30%) was mixed with ethanol (40 mL) and deionized water (90 mL) under magnetic stirring at 25 °C for 30 min to synthesize polydopamine (PD) nanoparticles with an average diameter of approximately 100 nm. Dopamine hydrochloride (0.5 g) was dissolved in deionized water (10 mL) and then added to the above solution. The mixture was left to react for 24 h. PD nanoparticles were isolated by centrifugation and purified by centrifugation–redispersion in deionized water (40 mL), a procedure that was repeated at least four times. At the end of this procedure, the nanoparticles were resuspended in PBS at a final concentration of approximately 3.4 mg $mL^{-1}$.

### Cell culture

BT-474, HTC 116 and NIH/3T3 cell lines were all obtained from the American Type Culture Collection (lot numbers HTB-20, CCL-247 and CRL-1658, respectively). All of them were cultured as recommended and cells' authenticity was regularly test by short tandem repeat (STR). All of the cell lines used were cultured in a growth medium consisting of high-glucose DMEM supplemented with a 10% of fetal bovine serum (FBS) and a 1% of penicillin–streptomycin at 37 °C in a 5% $CO_2$ humidified environment.

### MTT assay

Healthy (NIH/3T3) and cancer (BT474) cell lines were cultured and seeded in 24-well plates (8000 cells per mL). After 24 hours, different aliquots of a colloidal dispersion of PD nanoparticles (in PBS, pH = 7.4) were added to the cells. The concentration of PD in the culture medium was in the range of 0.01–0.1 mg $mL^{-1}$.

Cell viability was determined every 24 hours, during a 72 hours period, by adding a tetrazolium bromide solution (0.5 mg $mL^{-1}$) and by dissolving the produced formazan salts in DMSO (500 μL per well). Absorbance was determined at 550 and 700 nm. The protocol that will be described later on in this work was applied to eliminate the contribution of the absorbance of PD at 550 nm in the MTT assay. Each result value is the average of three independent experiments.

## Conflicts of interest

The authors declare no conflict of interest.

Open Access Article. Published on 24 October 2018. Downloaded on 11/5/2018 9:01:13 AM.
This article is licensed under a Creative Commons Attribution-NonCommercial 3.0 Unported Licence.

## Acknowledgements

This work was supported by a grant from the Regional Government of Castile and Leon (project reference number SA044U16). G. M. and C. N. also thank the Regional Government of Castile and Leon and European Social Fund for being awarded a Post-doctoral and Pre-doctoral fellowship, respectively.

## References

1 P. Meredith and T. Sarna, *Pigm. Cell Res.*, 2006, **19**, 572–594.
2 M. d'Ischia, A. Napolitano, V. Ball, C.-T. Chen and M. J. Buehler, *Acc. Chem. Res.*, 2014, **47**, 3541–3550.
3 Y. Liu, K. Ai, J. Liu, M. Deng, Y. He and L. Lu, *Adv. Mater.*, 2013, **25**, 1353–1359.
4 P. Meredith and J. Riesz, *Photochem. Photobiol.*, 2004, **79**, 211–216.
5 H. Lee, J. Rho and P. B. Messersmith, *Adv. Mater.*, 2009, **21**, 431–434.
6 H. Lee, S. M. Dellatore, W. M. Miller and P. B. Messersmith, *Science*, 2007, **318**, 426–430.
7 Y. Song, G. Yu, F. Wu, Z. Wang, S. Liu, M. Kopel, Z. Wang, J. Chen, J. Wang and K. Matyjaszewski, *Chem. Mater.*, 2016, **28**, 9013–9021.
8 R. Ge, M. Lin, X. Li, S. Liu, W. Wang, S. Li, X. Zhang, Y. Liu, L. Liu, F. Shi, H. Sun, H. Zhang and B. Yang, *ACS Appl. Mater. Interfaces*, 2017, **9**, 19796–19716.
9 M. A. Vega, C. Nieto, G. Marcelo and E. M. Martín del Valle, *Colloids Surf., B*, 2018, **167**, 284–290.
10 X.-H. Miao, H. Wang, H. Yang, Z.-L. Li, L. Zhen and C.-Y. Xu, *ACS Appl. Mater. Interfaces*, 2015, **7**, 16946–16952.
11 Y. Huang, Y. Li, Z. Hu, X. Yue, M. T. Proetto, Y. Jones and N. C. Gianneschi, *ACS Cent. Sci.*, 2017, **3**, 564–569.
12 A. Postma, Y. Yan, Y. Wang, A. N. Zelikin, E. Tjipto and F. Caruso, *Chem. Mater.*, 2009, **21**, 3042–3044.
13 K.-Y. Ju, Y. Lee, S. Lee, S. B. Park and J.-K. Lee, *Biomacromolecules*, 2011, **12**, 625–633.
14 H. Xu and D. Ree, *Annu. Rev. Physiol.*, 2015, **77**, 57–80.
15 T. Kurz, J. W. Eaton and U. T. Brunk, *Int. J. Biochem. Cell Biol.*, 2011, **43**, 1686–1697.
16 S. J. Dixon and B. R. Stockwell, *Nat. Chem. Biol.*, 2014, **10**, 9–17.
17 J. D. Lambeth and A. S. Neish, *Annu. Rev. Pathol.: Mech. Dis.*, 2014, **9**, 119–145.
18 D. B. Kell, *BMC Med. Genomics*, 2009, **2**, 2.
19 A. Tarangelo and S. J. Dixon, *Nat. Nanotechnol.*, 2018, **13**, 923.
20 S. E. Kim, L. Zhang, K. Ma, M. Riegman, F. Chen, I. Ingold, M. Conrad, M. Z. Turker, M. Gao, X. Jiang, S. Monette, M. Pauliah, M. Gonen, P. Zanzonico, T. Quinn, U. Wiesner, M. S. Bradbury and M. Overholtzer, *Nat. Nanotechnol.*, 2016, **11**, 977.
21 T. T. Mai, A. Hamai, A. Hienzsch, T. Cañeque, S. Müller, J. Wicinski, O. Cabaud, C. Leroy, A. David, V. Acevedo, A. Ryo, C. Ginestier, D. Birnbaum, E. Charafe-Jauffret, P. Codogno, M. Mehrpour and R. Rodriguez, *Nat. Chem.*, 2017, **9**, 1025.
22 D. Wang, J. Zhou, R. Chen, R. Shi, G. Wang, J. Liu, G. Zhao, G. Xia, S. Zhou, Z. Liu, H. Wang, Z. Gao and Q. Chen, *Chem. Mater.*, 2017, **29**, 3477–3488.
23 M. V. Berridge, P. M. Herst and A. S. Tan, in *Biotechnology Annual Review*, Elsevier, 2005, vol. 11, pp. 127–152.
24 L. Zecca, M. Gallorini, V. Schünemann, A. X. Trautwein, M. Gerlach, P. Riederer, F. Vezzoni and D. Tampellini, *J. Neurochem.*, 2001, **76**, 1766–1773.
25 N. F. Della Vecchia, R. Avolio, M. Alfè, M. E. Errico, A. Napolitano and M. d'Ischia, *Adv. Funct. Mater.*, 2013, **23**, 1331–1340.
26 J. Liebscher, R. Mrówczyński, H. A. Scheidt, C. Filip, N. D. Hădade, R. Turcu, A. Bende and S. Beck, *Langmuir*, 2013, **29**, 10539–10548.
27 J. H. Waite, *Int. J. Adhes. Adhes.*, 1987, **7**, 9–14.
28 X. Chen, Y. Yan, M. Millner, M. P. van Koeverden, K. P. Noi, W. Zhu and F. Caruso, *Langmuir*, 2014, **30**, 2931–2938.
29 L. Ding, X. Zhu, T. Wang, B. Shi, X. Ling, H. Chen, W. Nan, A. Barrett, Z. Gao, W. Tao, J. Wu and X. Shi, *Nano Lett.*, 2017, **17**, 6790–6801.
30 N. F. Della Vecchia, A. Luchini, A. Napolitano, G. D'Errico, G. Vitiello, N. Szekely, M. d'Ischia and L. Paduano, *Langmuir*, 2014, **30**, 9511–9518.
31 D. R. Dreyer, D. J. Miller, B. D. Freeman, D. R. Paul and C. W. Bielawski, *Langmuir*, 2012, **28**, 6428–6435.
32 S. Hong, Y. S. Na, S. Choi, I. T. Song, W. Y. Kim and H. Lee, *Adv. Funct. Mater.*, 2012, **22**, 4711–4717.
33 G. K. Sukumaran, K. Dabur and D. Fraser, *Cell Biochem. Funct.*, 2004, **22**, 345–352.
34 P. Y. Bernhardt, *Dalton Trans.*, 2007, 3214–3220, DOI: 10.1039/B701531B.

cancers

MDPI

Article

# Size Matters in the Cytotoxicity of Polydopamine Nanoparticles in Different Types of Tumors

Celia Nieto [1], Milena A. Vega [1], Jesús Enrique [1], Gema Marcelo [2,*] and Eva M. Martín del Valle [1,*]

[1] Departamento de Ingeniería Química y Textil, Facultad de Ciencias Químicas, Universidad de Salamanca, 37008 Salamanca, Spain; celianieto@usal.es (C.N.); mvega@usal.es (M.A.V.); j.enrique@usal.es (J.E.)

[2] Departamento de Química Analítica, Química Física e Ingeniería Química, Facultad de Farmacia, Universidad de Alcalá, 28801 Alcalá de Henares (Madrid), Spain

* Correspondence: gema.marcelo@uah.es (G.M.); emvalle@usal.es (E.M.M.d.V.); Tel.: +34-923-294-479 (E.M.M.d.V.)

Received: 8 October 2019; Accepted: 25 October 2019; Published: 29 October 2019

**Abstract:** Polydopamine has acquired great relevance in the field of nanomedicine due to its physicochemical properties. Previously, it has been reported that nanoparticles synthetized from this polymer are able to decrease the viability of breast and colon tumor cells. In addition, it is well known that the size of therapeutic particles plays an essential role in their effect. As a consequence, the influence of this parameter on the cytotoxicity of polydopamine nanoparticles was studied in this work. For this purpose, polydopamine nanoparticles with three different diameters (115, 200 and 420 nm) were synthetized and characterized. Their effect on the viability of distinct sorts of human carcinomas (breast, colon, liver and lung) and stromal cells was investigated, as well as the possible mechanisms that could be responsible for such cytotoxicity. Moreover, polydopamine nanoparticles were also loaded with doxorubicin and the therapeutic action of the resulting nanosystem was analyzed. As a result, it was demonstrated that a smaller nanoparticle size is related to a more enhanced antiproliferative activity, which may be a consequence of polydopamine's affinity for iron ions. Smaller nanoparticles would be able to adsorb more lysosomal $Fe^{3+}$ and, when they are loaded with doxorubicin, a synergistic effect can be achieved.

**Keywords:** polydopamine nanoparticles; size; cytotoxicity; iron affinity; doxorubicin

## 1. Introduction

Nanomedicine has acquired an essential role in recent decades due to the urgent need for developing novel therapeutic strategies for cancer treatment. This multidisciplinary field, by taking advantage of nanotechnology, aims to overcome the pharmaceutical limitations of conventional chemotherapeutics. Thus, the improvement of their stability, aqueous solubility and dose limiting toxicity, as well as avoiding the apparition of multidrug resistances (MDR), are some of the objectives that are highly relevant for the scientific community today [1,2]. Moreover, with the employment of nanoparticles (NPs) for cancer treatment, increasing tumor retention of therapeutic molecules while reducing their non-specific distribution in normal tissues is being attempted [2].

In this manner, a considerable number of nanomaterials have been developed recently [3–5]. Among them, polydopamine (PD), a synthetic melanin, which is a black biopolymer produced by autoxidation of dopamine, has achieved great importance [6]. Thanks to their physical and chemical properties [5], their feasible surface functionalization, and their good degradation in vivo [7,8], PD NPs stand out for the development of new diagnosis and antiproliferative nanosystems [5,9–14].

Thus, there are only a few existing works that report nanoparticle systems devoid of drugs with an antineoplastic behavior in the literature [15,16]. However, in previous studies, it was demonstrated

that PD NPs can also constitute themselves an antitumour strategy [17,18]. Thereby, unlike the majority of developed therapeutic nanocarriers, their use could help to reduce the administration of drugs. In one of these previous works, it was found that PD by itself had an antiproliferative capacity after developing a novel protocol to evaluate its cytotoxicity [18]. Furthermore, it was reported that such antiproliferative capacity could be related to a ferroptosis mechanism, since PD cytotoxicity was reduced in the presence of an iron chelator (deferoxamine, DFO) or a potent antioxidant compound involved in cellular ROS-protection (glutathione, GSH) [18–20]. As with other melanins [17,21], PD presents a great binding affinity for free metallic ions, especially for $Cu^{2+}$ and $Fe^{3+}$ [17,22,23]. These free ions, which are more abundant in cancer cells, are stored in lysosomes and, since PD NPs end up in these organelles when they are internalized [18], their metal affinity could be related to their cytotoxicity [24–28]. Precisely because of this fact, in another previous study, the antiproliferative ability of iron-loaded PD NPs was investigated, and it was observed that such systems had a strong cytotoxicity for breast carcinoma cells [17].

On the other hand, it is well accepted for the design of therapeutic nanosystems that size may determine their endocytosis rate and, therefore, their antiproliferative activity [29–31]. Cancer endothelium is known to present leaky fenestrations between vasculature cells, and these gaps have sizes ranging from 100 to 780 nm, depending on the tumor type. As a consequence, it is generally considered that the smaller the size of the administered NPs, the higher their rate of endocytosis and their accumulation in tumor sites [30–32].

For all these reasons, the size-dependent cytotoxicity effect of PD NPs was studied in the present work. PD NPs with three different sizes (115, 200 and 420 nm) were synthetized and characterized. Their antiproliferative activity was analyzed and compared in four distinct types of human carcinomas (breast, colon, liver and lung carcinomas) and in healthy stromal cells. Moreover, it was again proven that such antiproliferative effects may be related to their metal-loading ability. To do that, their cytotoxicity was studied in co-treatment experiments of PD with either DFO (iron chelator) and GSH (antioxidant compound), conducted with all of the previous mentioned cell lines [32–34]. Finally, doxorubicin (DOX), a conventional chemotherapy drug [35,36], was adsorbed on PD NPs in a very low concentration (10.6 ng DOX/mg PD NP) with the goal of enhancing their antitumor impact while reducing the necessary DOX therapeutic doses. The antitumor effect of the resulting nanosystem over the viability of breast carcinoma cells was also studied.

## 2. Results

### 2.1. Synthesis and Characterization of 115, 200 and 420 nm PD NPs

PD NPs of different sizes were synthetized through dopamine oxidative polymerization in a basic aqueous medium [17,18,37]. It contained fixed volumes of ethanol and water and different concentrations of ammonium hydroxide, on which the size of PD NPs depends (Figure 1a). To characterize them, transmission electron microscopy (TEM) images of all PD NPs were taken and size-range histograms were obtained (Figure 1b–d). As shown, their average sizes were 75 nm, 170 nm and 340 nm. Thus, the higher the ammonium hydroxide concentration employed, the smaller the synthetized PD NPs. In trizma base solution (50 mM, pH 10), such NPs remained stable with average hydrodynamic diameters of 115 ± 50 nm (PdI = 0.047), 199 ± 50 nm (PdI = 0.085) and 417 ± 50 nm (PdI = 0.012). Such values were analyzed by dynamic light scattering (DLS) and were higher than the ones obtained by TEM because of a possible PD NPs hydration.

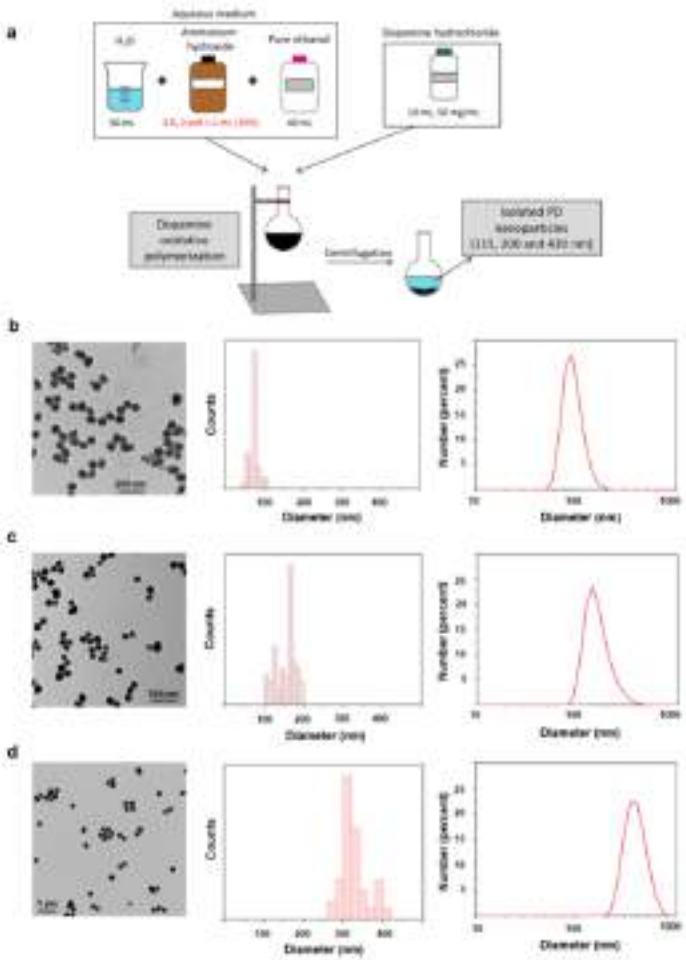


**Figure 1.** (a) Schematic representation of PD NPs synthesis by dopamine oxidative polymerization in a basic aqueous medium. (b–d) TEM images, size-range histograms and DLS number distributions of dispersions of PD NPs with three different diameters (pH = 7.0).

### 2.2. Cytotoxicity Effect of PD NPs Depends on Their Size

Since it was demonstrated that size of NPs plays an important role in their endocytosis rate and therapeutic effect [29–31], and that PD NPs are able to reduce the viability of cancer cells themselves [17,18], it was analyzed how the variation of PD NPs' diameter could affect to their cytotoxicity in different types of tumors. In this manner, BT474, HTC116, HEPG2 and H460 human cell lines were selected to carry out MTT assays with previously synthetized 115 and 200 nm PD NPs (Figure 2a–d and Figure S1a–d) [38]. Furthermore, such assays were also performed with a stromal human cell line, the HS5 one, in order to elucidate whether there were significant variations in

the viability reduction of treated cancer and healthy cells (Figure 2e and Figure S1e). Four different concentrations of PD NPs were employed (from 0.0074 mg/mL to 0.042 mg/mL), and MTT assays were performed following a protocol which was previously developed in order to avoid the strong contribution of PD NPs absorbance to formazan salts absorbance values [18].

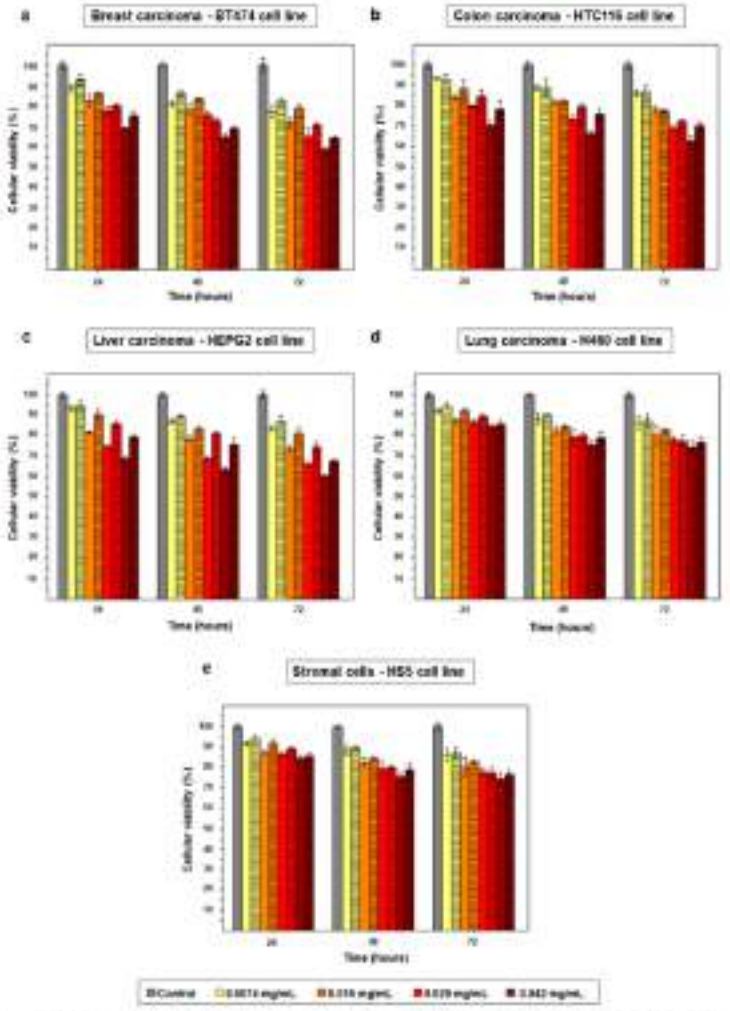


Figure 2. Obtained results in the MTT assays performed with the BT474 (a), HTC116 (b), HEPG2 (c), H460 (d) and HS5 (e) cell lines. Cells were treated with four different concentrations (0.0074, 0.015, 0.029 and 0.042 mg/mL) of PD NPs with a diameter of 115 nm (empty bars) and 200 nm (bars with the horizontal line pattern). The results shown are the mean ± SD of three replicates for each treatment.

As shown in Figure 2a and Figure S1a, when breast cancer cells (BT474 cell line) were treated with more elevated PD NPs concentrations, a more noticeable reduction in their viability was achieved. Thus, the best cytotoxic effect was obtained 72 h after treatment of the mentioned cells with 0.042 mg/mL of 100 nm PD NPs, which reduced their survival rate to 59%. The same concentration of 200 nm PD NPs decreased BT474 viability to 63% after 72 h.

In the case of the treatment of colon and liver carcinoma cells (HTC116 and HEPG2 cell lines) (Figure 2b,c and Figure S1b,c), it was analogously found that the best cytotoxic effect was accomplished when 0.042 mg/mL of 100 nm PD NPs were employed. With these experimental conditions, HTC116 survival rate was reduced to 63% after 72 h and HEPG2 viability, to 60%.

Likewise, a similar trend in the results obtained after the treatment of lung carcinoma cells (H460 cell line) can be observed in Figure 2d and Figure S1d. Nevertheless, the cytotoxicity of PD NPs was less remarkable than for the three previously mentioned tumor cell lines (BT474, HTC116 and HEPG2). Thereby, 72 h after the treatment with 0.042 mg/mL of 100 nm PD NPs, H460 survival rate decreased to 74%.

Positively, in the same manner, stromal cells' viability was not reduced as much as the carcinoma cell lines' viabilities when they were treated with PD NPs, neither those PD NPs with a size of 100 nm nor those with a size of 200 nm (Figure 2e and Figure S1e). Treatment with the highest concentration (0.042 mg/mL) of such NPs reduced, after 72 h, the viability of HS5 cells to 75–76%, but this value was higher than 80% 72 h after the treatment with the lowest concentrations of 100 and 200 nm PD NPs.

Therefore, in brief, it was found that the cytotoxicity of PD NPs was more noticeable, at all administered concentrations, for the HTC116, HEPG2 and, especially, for the BT474 cell line. The lowest concentration (0.0074 mg/mL) was barely toxic during the studied time for all treated cell lines. However, the two highest concentrations (0.029 and 0.042 mg/mL) achieved a notable decrease in cancer cell viability 72 h after a treatment of 35–40%, except for H460 viability, which was not so remarkably reduced. Furthermore, PD NPs did not decrease the viability of stromal cells in the same manner as the viability of cancer cells. In fact, the two lowest concentrations employed (0.0074 and 0.015 mg/mL) of PD NPs showed pretty specific results. Treatment with them almost had no affect on HS5 cellular viability, possibly because tumor cells present high intracellular iron levels [25,26]. Finally, it was generally observed that the smaller the diameter of the PD NPs, the more pronounced their cytotoxic effect. In comparison with the antiproliferative effect of the 200 nm PD NPs, those with a 115 nm diameter achieved a decrease in the viability of BT474 with a 3–8% improvement in efficacy, depending on the administered concentration. These differences in viability reduction, in the case of the HTC166, HEPG2, H460 and HS5 cells, were close to 2–9%, 3–12%, 2–5% and 1–11%, respectively, and could be explained by a larger endocytosis rate.

Next, since it was corroborated that size affected the therapeutic effect of PD NPs, MTT assays were again performed with synthetized 420 nm PD NPs [18]. For such assays, the BT474 cell line was chosen because the best previous MTT results were obtained with these breast carcinoma cells. As a result, and as shown in Figure 3, after the first 24 h of treatment, none of the concentrations employed were cytotoxic. The three lowest concentrations had virtually no effect on BT474 survival rate, and the highest one (0.042 mg/mL) only achieved a reduction in their viability to 92%. After 48 h of treatment, the cytotoxicity of the 420 nm PD NPs, in all concentrations, was neither pretty noticeable but, when 72 h had elapsed, it was more remarkable for the three highest chosen concentrations. In this manner, 0.015 mg/mL of PD NPs reduced breast cancer cells' survival to 84%, which was then decreased to 79% and 75% when 0.029 mg/mL and 0.042 mg/mL of PD NPs were employed for the treatment of BT474 cells. In any case, as expected, the cytotoxicity of 420 nm PD NPs was lower than that caused by the 115 and 200 nm PD NPs, with there being a difference of as high as 20–25% in cellular viability when the two most elevated NPs concentrations (0.029 and 0.042 mg/mL) were employed.

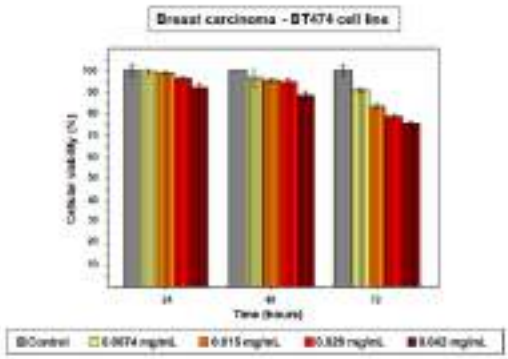


**Figure 3.** The results of the MTT assay carried out with PD NPs with a size of 420 nm (vertical lines—pattern bars) with BT474 cells. The same four concentrations (0.0074, 0.015, 0.029 and 0.042 mg/mL) of PD NPs as before were employed. The results shown are the mean ± SD of three replicates for each treatment.

Finally, in order to visually corroborate the cellular viability results obtained in the MTT assays, a live/dead assay with confocal laser scanning microscopy (CLSM) was performed. For this purpose, BT474 cells were again chosen and treated for 72 h with 0.042 mg/mL of 115 nm PD NPs, which were the NPs and the concentration that had previously reduced the survival of the breast carcinoma cell line the furthest. 24, 48 and 72 h after treatment, these cells were stained with calcein AM and propidium iodide (PI), and the resulting images are shown below in Figure 4 [39–41]. As can be observed, the survival rate of BT474 cells was reduced to 74% after the first 24 h of treatment and, after 48 and 72 h, 57% and 48% of the breast cancer cells remained alive, with these survival rates being similar to those that had been obtained when MTT assays were carried out previously (Figure 2a and Figure S1a). Thus, images of the live/dead assay corroborate the MTT results, wherein 115 nm PD nanoparticle cytotoxicity was more remarkable after 48 h of treatment.

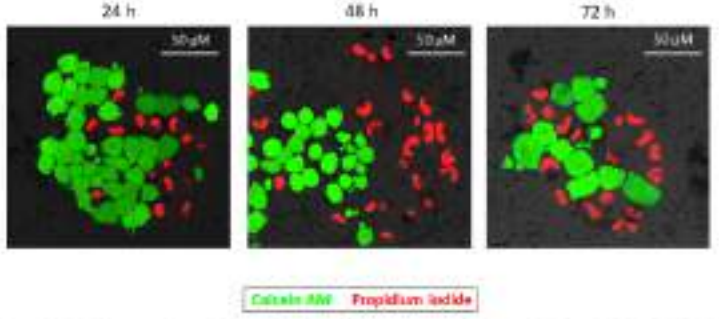


**Figure 4.** CMLS images taken 24, 48 and 72 h after the treatment of BT474 cells with 115 nm PD NPs (0.042 mg/mL). Calcein AM (in green, excited at 495 nm, indicator of cellular viability) and PI (in red, excited at 493 nm, indicator of cellular death) were selected to be performed in an alive/dead assay.

### 2.3. PD NPs Cytotoxicity in Tumor Cells Could be Related to Their Iron Affinity

PD NPs' ability to adsorb $Fe^{3+}$ has been demonstrated in previous studies, as well as the fact that when these NPs are endocyted [17,42], they end up in cellular lysosomes. Such organelles are specifically responsible for the regulation of the concentration of free metallic cations and, as a consequence, when cells are treated with PD NPs, ROS production levels may be increased due to a possible imbalance in Fenton chemistry [18,24] (Figure 5).

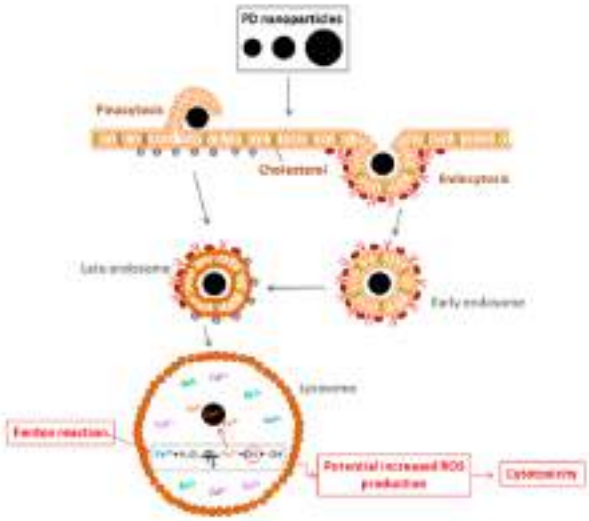


**Figure 5.** Schematic representation of the mechanism that could explain how PD NPs could be responsible for a reduction in cancer cells' viability after their cellular internalization in lysosomes.

For this reason, ferroptosis could be the process of cell death responsible for the cytotoxicity of PD NPs [32,34]. To demonstrate this fact, more MTT assays were performed with the same cell lines (BT474, HTC116, HEPG2, H460 and HS5) [17], treating cells with 115 and 200 nm PD NPs (0.029 mg/mL), but also with non-toxic concentrations of DFO (0.7 μM) and GSH (50 μM), an iron chelator and an antioxidant compound, respectively [19,20] (Figure 6a).

The results obtained with the BT474 and the HS5 cell lines when 115 nm PD NPs were employed are shown below (Figure 6b,c). It can be observed that, in both cell lines, the co-treatment with DFO and with GSH was able to decrease the antiproliferative effect of PD NPs at all measured times in all cell lines, with this fact becoming more noticeable after 24 h of treatment. For this reason, when BT474 cells were co-treated with DFO or GSH and with PD NPs, these last ones were around 12–18% less successful, depending on the time at which they were measured. In the case of the HS5 cell line, the cytotoxicity of PD NPs was reduced by 5–11%. This reduction could be lower because PD NPs were not as toxic for this cell line as for BT474 cells; however, despite this, with the administration of DFO and GSH, the toxicity of PD NPs was almost totally reduced for HS5 cells. Ultimately, with the other tumor cell lines (Figure S2) and with a co-treatment of DFO (0.7 μM) or GSH (50 μM) with 200 nm PD NPs (0.028 mg/mL), similar results as the ones obtained after the co-treatment of BT474 cells were also observed.

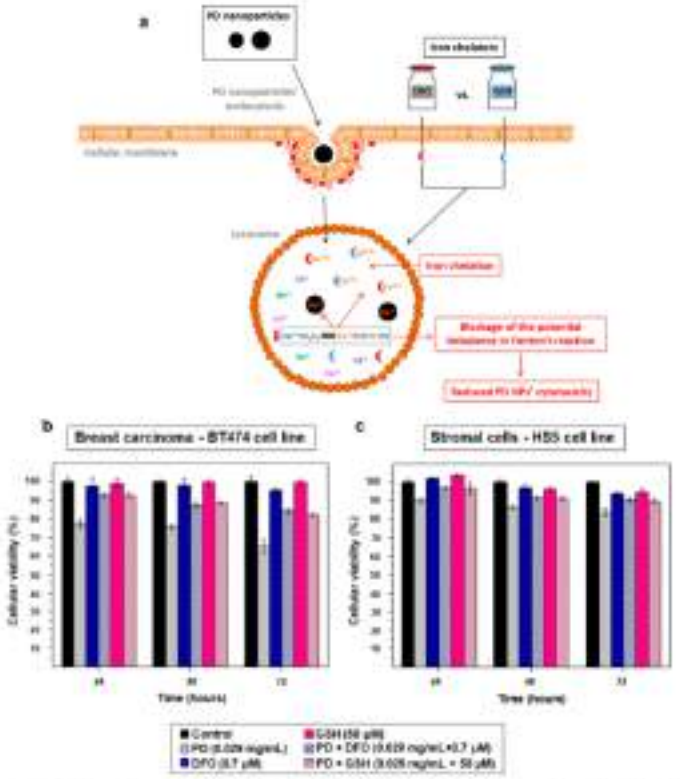


Figure 6. (a) Scheme that represents how DFO and GSH could be able to reduce the cellular death caused by the treatment with PD NPs. (b,c) Results of the MTT assays carried out with BT474 and HS5 cells after a co-treatment of 115 nm PD NPs (0.029 mg/mL, gray) with DFO (0.7 μM, blue) and GSH (50 μM, pink). The results shown are again the mean ± SD of three replicates of each treatment.

### 2.4. DOX-Adsorbed PD NPs (DOX@PD NPs) Presented a Notable Antiproliferation Activity

DOX is one of the most widely employed antineoplastic agents for the treatment of different types of cancers today, but its administration is currently limited due to the severe adverse effects that it has for patients. In this manner, many strategies are being developed to encapsulate this drug in order to improve its side toxicity [43,44]. Among these, PD-modified DOX-nanocarriers can already be found in the literature [45,46]. This issue, together with the fact that DOX is related to the formation of iron-related free radicals in cells [35,36], propitiated its selection for loading on the PD NPs synthetized here. For this purpose, 115 nm PD NPs were chosen because, as has been shown (Figure 2 and Figure S1), they present a more remarkable antiproliferative activity. In this manner, these NPs were mixed with a diluted DOX solution (10 nM), and the concentration of DOX adsorbed on PD NPs was determined by difference, by measuring the absorbance ($\lambda$ = 494 nm) of the filtered supernatant once the DOX@PD NPs were isolated. As a result, it was found that the PD NPs were able to be loaded with 10.6 ng DOX/mg PD NPs.

Based on this data, three distinct concentrations of DOX@PD NPs (0.029, 0.035 and 0.045 mg/mL) were tested in BT474 cells, which were again chosen because the best MTT assay results had been achieved with this breast carcinoma cell line. Likewise, treatment with equivalent DOX concentrations (12.9, 18.4 and 25.8 nM), which were pretty low in comparison to those employed in other works [11,44], was performed.

The results of these experiments indicated that, as shown in Figure 7, after only 24 h of treatment, DOX@PD NPs presented noticeable cytotoxicity, especially at the two highest concentrations (0.035 mg/mL + 18.4 nM and 0.042 mg/mL + 25.8 nM). While PD NPs achieved reductions in BT474 survival rate to 76%, 74% and 68%, the same concentrations of DOX@PD NPs achieved reductions of 73%, 62% and 50%, respectively. Moreover, the increase in the cytotoxicity of the two highest concentrations was more potent after 48 and 72 h of treatment. On the one hand, after 48 h had elapsed, 0.035 and 0.042 mg/mL of DOX@PD NPs decreased breast carcinoma cell viability to around 52% and 44%, while viability was approximately 72% and 64% when the same concentrations of non-loaded PD NPs were employed. On the other hand, after 72 h of treatment with the mentioned concentrations of DOX@PD NPs, BT474 viability was around 42% and 37%, while the corresponding values for similar treatment with PD NPs were 65% and 58%. In this way, at all measured times, cellular viability reduction caused by DOX@PD NPs was more remarkable than that caused by the non-loaded PD NPs, chiefly when cells were treated with 0.035 and 0.042 mg/mL of NPs. Furthermore, DOX@PD NPs were even more effective than the equivalent treatment with DOX concentrations, especially during the first 24 h. After this time, the highest concentration of free DOX only achieved a reduction in BT474 survival to 91%, and the other two presented almost no cytotoxicity. Then, 48 and 72 h after treatment, the reduction in cellular viability caused by free DOX was more noticeable but, in any case, it did not exceed that resulting from equivalent treatment with DOX@PD NPs. Such results could be explained by a likely more remarkable ferroptosis-dependent ROS production that could take place together with DOX-dependent DNA damage [35,36]. In this manner, the use of DOX@PD NPs could enhance the therapeutic activity of both PD and DOX, resulting in lower DOX doses being required for potential treatment, partially avoiding the severe adverse effects that this drug has for patients, as mentioned above [43,44].

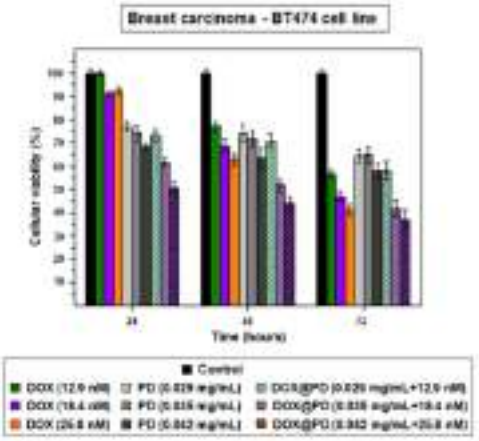


**Figure 7.** Results of the MTT assay carried out with the BT474 cell line, previously treated with free DOX (12.9 (green), 18.4 (purple) and 25.8 (orange) nM), 115 nm PD NPs (0.029, 0.035 and 0.042 mg/mL (grayscale)) and DOX@PD NPs (grayscale with colored patterns) in equivalent concentrations. The results shown are the mean ± SD of three replicates for each treatment.

## 3. Discussion

Since nanomedicine's occupation of a fundamental role in the development of novel therapeutic systems, the scientific community has been aware of the importance possessed by size in determining their effect [29–31,47]. For this reason, in the present work, the influence of size on the cytotoxicity of PD NPs, previously reported for breast and colon carcinoma cells [17,18], was studied in different tumor and stromal cell lines.

Thus, PD NPs with three different diameters (115, 200 and 420 nm) were synthetized. Once they had been characterized by TEM and DLS, the cytotoxicity of four different concentrations of the two smallest types of PD NPs (115 and 200 nm) was studied in different types (breast, colon, liver and lung) of human carcinomas and in stromal cells. Furthermore, the largest PD NPs' (420 nm) effect on cellular viability was also tested with the breast carcinoma cell line, BT474. The results obtained showed that, in all cases, the smaller the size of the NPs, the more noticeable their antiproliferative activity, with this being even more noticeable in BT474 cells. In addition, with such experiments, it could be noticed that the lowest tested concentrations of PD NPs had a tumor-selective effect. In this manner, employing low doses of these NPs could be a possible strategy for achieving greater treatment specificity and overcoming the any undesirable side effects. So far, most developed therapeutic nanosystems are vehicles for the delivery of cytotoxic drugs and, in this way, the employment of PD NPs could represent an awesome strategy for reducing the administration of chemotherapeutics [15]. Likewise, the size of PD NPs could be selected according to the antiproliferative effect that would be desired.

On the other hand, it was demonstrated that the adsorption of iron could be responsible for the cytotoxic effect of such PD NPs. Their affinity for different metallic cations has been described in numerous studies, and the ability of PD NPs to load lysosomal $Fe^{3+}$ cations once they have been endocyted could explain the death of cells treated with them by means of Fenton chemistry [17,18,24,34]. To corroborate that this ferroptosis process could take place in the present study, more viability assays were carried out, treating cells of the different carcinomas simultaneously with PD NPs and with two iron chelators, DFO and GSH. In this manner, it was demonstrated that this co-treatment affected the cytotoxicity of PD NPs, decreasing it at all measured times and in all types of treated cells.

Finally, 115 nm PD NPs were loaded with DOX. This drug was chosen because it is one of the most commonly used chemotherapeutic drugs, and because it has also been associated with ferroptosis processes in recent toxicity-related studies [35,36]. The cytotoxicity of the resulting NPs (DOX@PD NPs') was analyzed with BT474 cells and compared with the viability values obtained with equivalent concentrations of free-DOX and non-loaded PD NPs. On the basis of this comparison, it could be seen that the antiproliferative effect of DOX@PD NPs was considerably greater. Actually, these NPs were even more effective than free DOX, possibly because of the occurrence of a synergist effect. Additionally, the DOX doses employed were much lower than those used so far in literature, and this fact could be important in avoiding the side effects, too [12,20].

## 4. Materials and Methods

### 4.1. Chemicals

Dopamine Hydrochloride, Ammonium Hydroxide ($NH_4OH$), Phosphate Buffered Saline (PBS, 0.01 M, pH 7.4), Dulbecco's Modified Eagle's Medium (DMEM), Fetal Bovine Serum (FBS, USA origin), Thiazolyl Blue Tetrazolium Bromide (MTT reagent), L-glutathione Reduced (GSH) and Deferoxamine Mesilate CRS (DFO) were all supplied by Sigma-Aldrich (Darmstadt, Germany). Ethanol absolute was purchased from VWR International Eurolab S.L. (Llinars del Vallés, Barcelona, Spain). Penicillin-Streptomycin (5000 U/mL), Calcein AM, Propidium Iodide (PI) ReadyProbes™ reagent and Doxorubicin Hydrochloride Solid (DOX) were obtained from Thermo Fisher Scientific (Eugene, OR, USA).

### 4.2. Synthesis and Characterization of PD NPs of Different Sizes

PD NPs with average diameters of 115, 200 and 420 nm were synthetized by mixing distinct volumes of $NH_4OH$ aqueous solution (3.9, 2 and 1.1 mL, respectively, 28–30%) with ethanol (40 mL) and deionized water (90 mL). In all cases, the obtained mixture was left under magnetic stirring at room temperature for 30 min, and a dopamine hydrochloride aqueous solution (10 mL, 50 mg/mL) was later added. The reaction was allowed to react for 24 h. PD NPs were isolated and purified by several centrifugation-redispersion cycles in deionized water (35 mL). Finally, NPs were re-suspended in PBS at final concentrations of 2, 3.2 and 1 mg/mL, respectively [17,18,35].

To characterize them, TEM images (Tecnai Spirit Twin, Fei Company, Hillsboro, OR, USA) were taken, employing a voltage acceleration of 120 kV. The synthetized PD NPs were dispersed in deionized water (pH = 6.0) in a concentration of less than 0.01% (WT), and a drop of this dispersion was deposited on a copper grid with a collodium membrane and dried for 24 h. Images were recorded after this time, and histograms exhibiting the size ranges were obtained. To this end, the size of a minimum of 500 PD NPs in different images was determined (using ImageJ software, NIH, Bethesda, MD, USA) in order to build each histogram. Moreover, the hydrodynamic diameter of the PD NPs was analyzed using DLS (on the basis of their intensity–average size distribution) (Zetasizer Nano ZS90, Malvern Instruments Inc., Royston, Hertfordshire, UK) when they were re-suspended in a trizma base solution (pH = 10.0) in a concentration that was also less than 0.01% (WT).

### 4.3. Cell Culture

BT474, HTC116, HEPG2, H460 and HS5 cell lines were cultured with medium supplemented with FBS (10%) and antibiotics (penicillin-streptomycin) (1%) as instructed (ATCC, Wesel, Germany). All cells were cultured at 37 °C in a humidified atmosphere in the presence of $CO_2$ (5%).

### 4.4. Size-Dependent Cytotoxicity Effect of PD NPs

The antitumor activity of 115 and 200 nm PD NPs was firstly studied based on MTT assays [37]. BT474, HTC116, HEPG2, H460 and HS5 cells were seeded in 24-well plates and cultured with supplemented medium overnight. The next day, the culture medium was replaced by supplemented medium containing PBS (control) and four different concentrations (from 0.0074 mg/mL to 0.042 mg/mL) of 115 and 200 PD NPs. In addition, BT474 cells were also treated with the same concentrations of 420 nm PD NPs. In all cases, cellular survival was analyzed for 4 days (EZ Reader 2000, Biochrom, Cambridge, UK), every 24 h, following the protocol described by Nieto et al. [18]. The results shown are the mean ± SD of three replicates for each different treatment.

Secondly, the reduction of viability caused by 115 nm PD NPs was corroborated in BT474 cells by CLSM (Leica TCS SP5, Leica Microsystems, L'Hospitalet de Llobregat, Spain) with an alive/dead cellular assay [36]. The cells were seeded in crystal-bottom plates (8000 cells/mL) and cultured with supplemented medium overnight. Over the following days, the culture medium was replaced by supplemented medium containing PBS (control) and 115 nm PD NPs (0.042 mg/mL). After 24, 48 and 72 h, calcein AM (1.25 mM) and PI (1 drop/1 mL culture media) were added and, after 30 min, CLSM images were taken [37,38].

### 4.5. PD Iron-Affinity could Explain the Cytotoxicity of PD NPs in Tumor Cells

To demonstrate that the iron affinity of PD could be implicated in the cytotoxicity of cells treated with PD NPs, HTC116, HEPG2, H460, BT474 and HS5 cells were seeded in 24-well plates and cultured with supplemented medium overnight. After 24 h, the culture medium was replaced by supplemented medium containing PBS (control), DFO (0.7 μM), GSH (50 μM), 115 and 200 nm PD NPs (0.029 mg/mL) and PD NPs plus DFO and GSH at the same concentrations. Again, cell viability was analyzed every 24 h for 4 days, following the same protocol as before [18]. The results shown are also the mean ± SD of three replicates for each different treatment.

### 4.6. DOX Adsorption onto PD NPs

With the aim of adsorbing DOX onto PD NPs, an aqueous solution (1% DMSO) of the drug was prepared at a final concentration of 10 mM. PD NPs (0.75 mL, 0.035 mg/mL) with a diameter of 115 nm were mixed with DOX solution, and the mixture was kept under stirring overnight [17]. Next, DOX@PD NPs were isolated through centrifugation and re-suspended in PBS at a final concentration of 2 mg/mL. The resulting supernatant was preserved, and its DOX concentration was determined in order to quantify PD NPs DOX adsorption. To this end, the supernatant was filtered several times with 0.1 µM syringe filters (GE Healthcare Life Sciences, Buckinghamshire, UK) and its absorbance was measured at 494 nm (UV-1800 Spectrophotometer, Shimadzu Corporation, Soraku-gun, Kyoto, Japan). Finally, taking into account the absorbance value of the initial DOX solution at such wavelength, the DOX adsorption onto PD NPs was quantified.

### 4.7. Antiproliferative Activity of DOX@PD NPs

To study the reduction in tumor cells' viability caused by DOX@PD NPs, the BT474 cell line was chosen to carry out further MTT assays. Following the steps described above, the cells were again seeded in 24-well plates and, 24 h later, they were treated with medium supplemented with PBS (control), different concentrations of 115 nm DOX@PD NPs (0.029, 0.035 and 0.042 mg/mL) and equivalent adsorbed DOX concentrations (12.9, 18.4 and 25.8 nM). Cellular viability was measured every day for 72 h, always following the same protocol as before [18]. The results shown are again the mean ± SD of three replicates for each different treatment.

### 4.8. Statistical Analysis

Data related to the size of the PD NPs is the mean ± SD of three different measurements. Otherwise, results of the different MTT assays are represented as the mean ± SD of three replicates for each treatment of three different experiments, and the results were considered statistically significant where $p < 0.05$.

## 5. Conclusions

In this work, it has been demonstrated that size plays an important role in the cytotoxic effect of PD NPs. This was demonstrated on the basis of viability assays carried out with different human carcinoma cell lines and with stroma cells, in which the therapeutic action of two or three PD NPs of different sizes was analyzed (115, 200 and 420 nm). In all cell lines, and with all of the tested PD NP concentrations, it was shown that the smaller the diameter of the NPs, the more enhanced their antiproliferative activity. Therefore, the size of PD NPs could be tailored depending on the desired application.

With respect to the cytotoxic effect of PD NPs, it was observed that this may be related to a process of ferroptosis. PD NPs are able to load $Fe^{3+}$ in lysosomes, and this fact could originate an abnormal cellular ROS production. However, when either an iron chelator (DFO) or a potent antioxidant (GSH) were employed, their antiproliferative ability was notably decreased. For this reason, when PD NPs were loaded with DOX, their antiproliferative effect was enhanced. Apart from triggering DNA damage, DOX cytotoxicity is also a consequence of a process of ferroptosis which, in addition to the one potentially produced by PD NPs, may result in the achievement of a synergist effect.

**Supplementary Materials:** The following are available online at http://www.mdpi.com/2072-6694/11/11/1679/s1, Figure S1: Data corresponding to MTT results shown in Figure 2 with the BT474 (a), HTC116 (b), HEPG2 (c), H460 (d) and HS5 (e) cell lines. Shown results are the average cellular viability percentage ± SD of three replicas for each treatment; Figure S2: Results of the MTT assays carried out with HTC116 (a), HEPG2 (b) and H460 (c) cells after a co-treatment of 115 nm PD NPs (0.029 mg/mL, blue) with DFO (0.7 µM, green) and GSH (50 µM, pink). Shown results are again the mean ± SD of three replicas for each treatment.

**Author Contributions:** Conceptualization, G.M. and M.A.V.; Methodology, C.N., J.E., G.M. and M.A.V.; Investigation, C.N., J.E., G.M. and M.A.V.; Resources, E.M.M.d.V.; Writing—original draft preparation, C.N.; Writing—review and editing, C.N., G.M., M.A.V. and E.M.M.d.V.; Supervision, G.M., M.A.V. and E.M.M.d.V.; Funding acquisition, E.M.M.d.V.

**Funding:** This research has been funded by the Spanish Ministry of Economy and Competitiveness (CTQ2016-79988-R) and by the Ramón Areces Foundation ("Development and validation of an aerosol with vectorized nanoparticles to human lung cancer treatment"). In addition, C.N. is recipient of a predoctoral contract from the Junta de Castilla y León, co-funded by the European Social Foundation (EDU/602/2016).

**Acknowledgments:** The authors would like to thank all the funding sources that have made possible this work.

**Conflicts of Interest:** The authors declare no conflict of interest.

## References

1. Awasthi, R.; Roseblade, A.; Hansbro, P.M.; Rathbone, M.J.; Dua, K.; Bebawy, M. Nanoparticles in Cancer Treatment: Opportunities and Obstacles. *Curr. Drug Targets* **2018**, *19*, 1696–1709. [CrossRef] [PubMed]
2. Liu, J.; Cheng, Q.; Feng, L.; Liu, Z. Nanomedicine for tumor microenvironment modulation and cancer treatment enhancement. *Nano Today* **2018**, *21*, 55–73. [CrossRef]
3. Quader, S.; Kataoka, K. Nanomaterial-enabled cancer therapy. *Mol. Ther.* **2017**, *25*, 1501–1513. [CrossRef] [PubMed]
4. Liu, J.; Dong, J.; Zhang, T.; Peng, Q. Graphene-based nanomaterials and their potentials in advanced drug delivery and cancer therapy. *J. Control. Release* **2018**, *286*, 64–73. [CrossRef]
5. Wu, H.; Hu, H.; Wan, J.; Li, Y.; Wu, Y.; Tang, Y.; Xiao, C.; Xu, H.; Yang, X.; Li, Z. Hydroxyethyl starch stabilized polydopamine nanoparticles for cancer chemotherapy. *Chem. Eng. J.* **2018**, *349*, 129–145. [CrossRef]
6. Liu, H.; Qu, X.; Tan, H.; Song, J.; Lei, M.; Kim, E.; Payne, G.F.; Liu, C. Role of polydopamine's redox-activity on its pro-oxidant, radical-scavenging and antimicrobial activities. *Acta Biomater.* **2019**, *88*, 181–196. [CrossRef]
7. Liu, X.; Cao, J.; Li, H.; Li, J.; Jin, Q.; Ren, K.; Ji, J. Mussel-inspired polydopamine: A biocompatible and ultrastable coating for nanoparticles in vivo. *ACS Nano* **2013**, *7*, 9384–9395. [CrossRef]
8. Bettinger, C.J.; Bruggeman, J.P.; Misra, A.; Borenstein, J.T.; Langer, R. Biocompatibility of biodegradable semiconducting melanin films for nerve tissue engineering. *Biomaterials* **2009**, *30*, 3050–3057. [CrossRef]
9. Dong, Z.; Gong, H.; Gao, M.; Zhu, W.; Sun, X.; Feng, L.; Fu, T.; Li, Y.; Liu, Z. Polydopamine nanoparticles as a versatile molecular loading platform to enable imaging-guided cancer combination therapy. *Theranostics* **2016**, *6*, 1031–1042. [CrossRef]
10. Mrowczynski, R. Polydopamine-based multifunctional (nano)materials for cancer therapy. *ACS Appl. Mater. Interfaces* **2018**, *10*, 7541–7561. [CrossRef]
11. Wang, L.; Dai, W.; Yang, M.; Wei, X.; Ma, K.; Song, B.; Jia, P.; Gong, Y.; Yang, J.; Zhao, J. Cell membrane mimetic copolymer coated polydopamine nanoparticles for combined pH-sensitive drug release and near-infrared photothermal therapeutic. *Colloids Surf. B Biointerfaces* **2019**, *176*, 1–8. [CrossRef] [PubMed]
12. Lei, Z.; Mengying, Z.; Dongdong, B.; Xiaoyu, Q.; Yifei, G.; Xiangtao, W.; Meihua, H. Alendronate-modified polydopamine-coated paclitaxel nanoparticles for osteosarcoma-targeted therapy. *J. Drug Deliv. Sci. Technol.* **2019**, in press. [CrossRef]
13. Zhang, H.; Sun, Y.; Huang, R.; Cang, H.; Cai, Z.; Sun, B. pH-sensitive prodrug conjugated polydopamine for NIR-triggered synergistic chemo-photothermal therapy. *Eur. J. Pharm. Biopharm.* **2018**, *128*, 260–271. [CrossRef] [PubMed]
14. Zhou, J.; Jiang, Y.; Hou, S.; Upputuri, P.K.; Wu, D.; Li, J.; Wang, P.; Zhen, X.; Pramanik, M.; Pu, K.; et al. Compact plasmonic blackbody for cancer theranosis in the near-infrared II window. *ACS Nano* **2018**, *12*, 2643–2651. [CrossRef]
15. Kim, S.E.; Zhang, L.; Ma, K.; Riegman, M.; Chen, F.; Ingold, I.; Conrad, M.; Turker, M.Z.; Gao, M.; Jiang, X.; et al. Ultrasmall nanoparticles induce ferroptosis in nutrient-deprived cancer cells and suppress tumour growth. *Nat. Nanotechnol.* **2016**, *11*, 977–985. [CrossRef]
16. Sarna, M.; Krzykawska-Serda, M.; Jakubowska, M.; Zadlo, A.; Urbanska, K. Melanin presence inhibits melanoma cell spread. *Sci. Rep.* **2019**, *9*, 9280–9289. [CrossRef]
17. Vega, M.A.; Nieto, C.; Marcelo, G.; Martín del Valle, E.M. Cytotoxicity of paramagnetic cations-loaded polydopamine nanoparticles. *Colloids Surf. B Biointerfaces* **2018**, *167*, 284–290. [CrossRef]

18. Nieto, C.; Vega, M.A.; Marcelo, G.; Martín del Valle, E.M. Polydopamine nanoparticles kill cancer cells. *RSC Adv.* **2018**, *8*, 36201–36208. [CrossRef]
19. Liu, P.; He, K.; Song, H.; Ma, Z.; Yin, W.; Xu, L.X. Deferoxamine-induced increase in the cellular iron levels in highly aggressive breast cancer cells leads to increased cell migration by enhancing TFN-α dependent NF-κB signaling and TGF-β signaling. *J. Inorg. Biochem.* **2016**, *160*, 40–48. [CrossRef]
20. Couto, N.; Wood, J.; Barber, J. The role of glutathione reductase and related enzymes on cellular redox homeostasis network. *Free Radic. Biol. Med.* **2016**, *95*, 27–42. [CrossRef]
21. Ball, V.; Bour, J.; Michel, M. Step-by-step deposition of synthetic dopamine-eumelanin and metal cations. *J. Colloid Interface Sci.* **2013**, *405*, 331–335. [CrossRef] [PubMed]
22. Cho, S.; Park, W.; Kim, D.H. Silica-coated metal chelting-melanin nanoparticles as a dual-modal contrast enhacement imaging and therapeutic agent. *ACS Appl. Mater. Interfaces* **2017**, *9*, 101–111. [CrossRef] [PubMed]
23. Ge, R.; Lin, M.; Li, X.; Liu, S.; Wang, W.; Li, S.; Zhang, Z.; Liu, Y.; Liu, L.; Shi, F.; et al. $Cu^{2+}$-loaded polydopamine nanoparticles for magnetic resonance imaging-guided pH- and near-infrared-light-stimulated thermochemotherapy. *ACS Appl. Mater. Interfaces* **2017**, *9*, 19706–19716. [CrossRef] [PubMed]
24. Kurz, T.; Eaton, J.W.; Brunk, U.T. The role of lysosomes in iron metabolism and recycling. *Int. J. Biochem. Cell. Biol.* **2011**, *43*, 1686–1697. [CrossRef] [PubMed]
25. Zhang, X.Z.; Yang, Y.; Sun, X.; Dong, X.-P. Methods for monitoring $Ca^{2+}$ and ion channels in the lysosome. *Cell Calcium* **2017**, *64*, 20–28. [CrossRef] [PubMed]
26. Jung, M.; Mertens, C.; Tomat, E.; Brüne, B. Iron as a central player and promising target in cancer progression. *Int. J. Mol. Sci.* **2019**, *20*, 273. [CrossRef] [PubMed]
27. Manz, D.H.; Blanchette, N.L.; Paul, B.T.; Torti, F.M.; Torti, S.V. Iron and cancer: Recent insights. *Ann. N. Y. Acad. Sci.* **2016**, *1368*, 149–161. [CrossRef]
28. Liou, G.Y.; Storz, P. Reactive oxygen species in cancer. *Free Radic. Res.* **2010**, *44*, 479–496. [CrossRef]
29. Dresden, E.C.; Austin, L.A.; Mackey, M.A.; El-Sayed, M.A. Size matters: Gold nanoparticles in targeted cancer drug delivery. *Ther. Deliv.* **2012**, *3*, 457–478. [CrossRef]
30. Gaumet, M.; Vargas, A.; Gurny, R.; Delie, F. Nanoparticles for drug delivery: The need for precision in reporting particle size parameters. *Eur. J. Pharm. Biopharm.* **2008**, *69*, 1–9. [CrossRef]
31. Jo, D.H.; Kim, J.H.; Lee, T.G.; Kim, J.H. Size, surface charge and shape determine therapeutic effects of nanoparticles in brain and retinal diseases. *Nanomedicine* **2015**, *11*, 1603–1611. [CrossRef] [PubMed]
32. Mai, T.T.; Hamai, A.; Hienzsch, A.; Cañeque, T.; Müller, S.; Wicinski, J.; Cabaud, O.; Leroy, C.; David, A.; Acevedo, V.; et al. Salinomycin kills cancer stem cells by sequestering iron in lysosomes. *Nat. Chem.* **2017**, *9*, 1025–1033. [CrossRef] [PubMed]
33. Corcé, V.; Gouin, S.G.; Renaud, S.; Gaboriau, F.; Deniaud, D. Recent advances in cancer treatment by iron chelators. *Bioorg. Med. Chem. Lett.* **2016**, *26*, 251–256. [CrossRef] [PubMed]
34. Dixon, S.J.; Lemberg, K.M.; Lamprecht, M.R.; Skouta, R.; Zaitsev, E.M.; Gleason, C.E.; Patel, D.N.; Bauer, A.J.; Cantley, A.M.; Yang, W.S.; et al. Ferroptosis: An iron-dependent form of nonapoptotic cell death. *Cell* **2012**, *149*, 1060–1072. [CrossRef]
35. Zeng, X.; Cai, H.; Yang, J.; Qiu, H.; Cheng, Y.; Liu, M. Pharmacokinetics and cardiotoxicity of doxorubicin and its secondary alcohol metabolites in rats. *Biomed. Pharmacother.* **2019**, *116*, 108964. [CrossRef]
36. Kukimi, N.; Nickel, B.E.; Edel, A.L.; Fandrich, R.R.; Ravandi, A.; Kardami, E. Oxidized phospholipids in doxorubicin-induced cardiotoxicity. *Chem. Biol. Interact.* **2019**, *303*, 35–39. [CrossRef]
37. Liu, Y.; Ai, K.; Liu, J.; Deng, M.; He, Y.; Lu, L. Dopamine-melanin colloidal nanospheres: An efficient near-infrared photothermal therapeutic agent for in vivo cancer therapy. *Adv. Mater.* **2013**, *25*, 1353–1359. [CrossRef]
38. Mosmann, T. Rapid colorimetric assay for cellular growth and survival: Application to proliferation and cytotoxicity assays. *J. Immunol. Methods* **1983**, *65*, 55–63. [CrossRef]
39. Boulos, L.; Prévost, M.; Barbeau, B.; Coallier, J.; Desjardins, R. LIVE/DEAD® BacLight™: Application of a new rapid staining method for direct enumeration of viable and total bacteria in drinking water. *J. Microbiol. Methods* **1999**, *34*, 77–86. [CrossRef]
40. Li, Y.; Khuu, N.; Gevorkian, A.; Sarfinsky, S.; Therien-Aubin, H.; Wang, Y.; Cho, S.; Kumacheva, E. Supramolecular nanofibrillar thermoreversible hydrogel for growth and release of cancer spheroids. *Angew. Chem. Int.* **2016**, *55*, 1–6.

41. Chung, S.; Nguyen, V.; Lin, Y.L.; Kamen, L.; Sung, A. Thaw-and-use target cells pre-labeled with calcein AM for antibody-dependent cell-mediated cytotoxicity assays. *J. Immunol. Methods* **2017**, *447*, 37–46. [CrossRef] [PubMed]
42. Ding, L.; Zhu, X.; Wang, Y.; Bingyang, S.; Ling, X.; Chen, H.; Nan, W.; Barrett, A.; Guo, Z.; Tao, W.; et al. Intracellular fate of nanoparticles with polydopamine surface engineering and a novel strategy for exocytosis-inhibiting, lysosome impairment-based cancer therapy. *Nano Lett.* **2017**, *17*, 8790–8801. [CrossRef] [PubMed]
43. Ibsen, S.; Zahavy, E.; Wrasdilo, W.; Berns, M.; Chan, M.; Esener, S. A novel doxorubicin prodrug with controllable photolysis activation for cancer therapy. *Pharm. Res.* **2010**, *27*, 1848–1860. [CrossRef] [PubMed]
44. Chen, Y.; Wan, Y.; Wang, Y.; Zhang, H.; Jiao, Z. Anticancer efficacy enhancement and attenuation of side effects of doxorubicin with titanium dioxide nanoparticles. *Int. J. Nanomed.* **2011**, *6*, 2321–2326.
45. Bi, D.; Zhao, L.; Li, H.; Guo, Y.; Wang, X.; Han, M. A comparative study of polydopamine modified and conventional chemical synthesis method in DOX liposomes form the aspect of tumor targeted therapy. *Int. J. Pharm.* **2019**, *559*, 76–85. [CrossRef]
46. Ji, F.; Sun, H.; Qin, Z.; Zhang, E.; Cui, J.; Wang, J.; Li, S.; Yao, F. Engineering polyzwitterion and polydopamine decorated doxorubicin-loaded mesoporous silica nanoparticles as a pH-sensitive drug delivery. *Polymers* **2018**, *10*, 326. [CrossRef]
47. Win, K.-Y.; Feng, S.-S. Effects of particle size and surface coating on cellular uptake of polymeric nanoparticles for oral delivery of anticancer drugs. *Biomaterials* **2005**, *26*, 2713–2722. [CrossRef]

© 2019 by the authors. Licensee MDPI, Basel, Switzerland. This article is an open access article distributed under the terms and conditions of the Creative Commons Attribution (CC BY) license (http://creativecommons.org/licenses/by/4.0/).

Colloids and Surfaces B: Biointerfaces 199 (2021) 111506

Contents lists available at ScienceDirect

Colloids and Surfaces B: Biointerfaces

journal homepage: www.elsevier.com/locate/colsurfb

# Antineoplastic behavior of polydopamine nanoparticles prepared in different water/alcohol media

Celia Nieto [a], Gema Marcelo [b], Milena Vega [a,*], Eva M. Martín del Valle [a,*]

[a] Departamento de Ingeniería Química y Textil, Facultad de Ciencias Químicas, Universidad de Salamanca, 37008, Salamanca, Spain
[b] Departamento de Química Analítica, Química Física e Ingeniería Química, Facultad de Farmacia, Universidad de Alcalá, 28805, Alcalá de Henares (Madrid), Spain

ARTICLE INFO

*Keywords:*
Polydopamine nanoparticles
Alcohols
Iron
Iron adsorption capacity
Cytotoxicity

ABSTRACT

Polydopamine nanoparticles (PD NPs) have been synthesized in the present work through the oxidative polymerization of dopamine in aqueous media containing five different types of alcohol in a constant solvent volume ratio. We have shown that the type of alcohol, along with the ammoniacal hydroxide concentration used in the synthesis process, conditions particle size. Additionally, it has been found that the type of alcohol employed influences the well-known capacity of polydopamine nanoparticles to adsorb iron. As a consequence, since a ferroptosis-like mechanism may account for the cytotoxicity of these nanoparticles, the type of alcohol could also have a determining role in their antineoplastic activity. Here, the existence of a correlation between the ability of polydopamine nanoparticles to bind $Fe^{2+}$ and their toxic effect on breast cancer cells has been proven. For instance, nanoparticles synthesized using 2-propanol adsorbed more $Fe^{2+}$ and had the greatest capacity to reduce breast tumor cell viability. Moreover, most of the nanoparticle synthesized with the different alcohols significantly decreased normal cell survival. Cancer cells present greater iron dependence than healthy cells and this fact may explain why polydopamine nanoparticles (native), in which ferrous chemistry could be implicated, source tumor-specific.

## 1. Introduction

Polydopamine, a synthetic melanin that made its way into materials Science as a coating agent [1], has begun to gain importance for cancer diagnosis and therapy [2]. Like natural melanins, which play an essential role in our organism by regulating the concentration of free metal cations [3,4], polydopamine has also shown to have a great affinity for such ions [5]. For this reason, nanoparticles synthesized with this polymer are being developed to create novel contrast agents for imaging techniques and new photothermal therapy systems [6,7].

Likewise, it has been observed that polydopamine nanoparticles (PD NPs) have intrinsic antineoplastic activity, and this property could be also related to their affinity for a metal cation: $Fe^{2+}$. When internalized, PD NPs end up in lysosomes, the organelles that precisely store free cations in the cell, and it is though that, given their high $Fe^{2+}$-binding capacity compared to that of other cations, they may be involved in a ferroptosis-like mechanism [8–10]. Thus, it is believed that PD NPs could adsorb lysosomal iron and cause an imbalance in the $Fe^{2+}/Fe^{3+}$ concentration that may propitiate an excessive generation of reactive oxygen species (ROS) through Fenton chemistry in cancer cells [11,12]. This fact would explain why when iron chelators or antioxidant compounds are administered together with PD NPs the latter are not so cytotoxic and why the chelation of PD NPs with Fe increases their toxicity to tumor cells [8,9,13]. Moreover, as normal cells are not as dependent on iron as malignant cells [14,15], the PD-mediated ferroptosis would not notably affect to their survival rate, as it has been already shown [8,9].

On the other hand, it is relevant to mention that most of these findings related to the cytotoxicity of PD NPs have been performed by synthetizing them in a basic aqueous medium containing ethanol, in which the self-polymerization of dopamine occurs [8]. It has been reported that the use of alcohols in this chemical process can help to control PD NP size, which can range from tens to hundreds of nanometers by simply tuning the volume ratio of water to alcohol [10,11]. Among the different alcohols available, ethanol is the most frequently used possibly because it is completely miscible in water and is more polar than other types of alcohols [10,16]. Methanol and 2-propanol have also been employed to produce PD NPs [17]. However, the differences caused in PD NPs by the use of different alcohols in their synthesis have not been characterized and reported to date.

* Corresponding authors.
*E-mail addresses:* mvega@usal.es (M. Vega), emvalle@usal.es (E.M. Martín del Valle).

https://doi.org/10.1016/j.colsurfb.2020.111506
Received 14 June 2020; Received in revised form 8 November 2020; Accepted 30 November 2020
Available online 4 December 2020
0927-7765/© 2020 Elsevier B.V. All rights reserved.

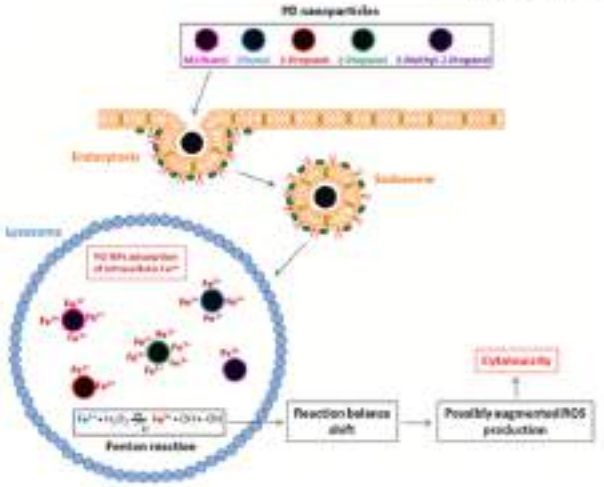


Fig. 1. Scheme representing how the type of ROH employed in the synthesis of PD NPs may determine their tumor specific toxicity. Since the ROH used seems to condition the ability of PD NPs to adsorb $Fe^{2+}$ cations, it may determine the production of ROS in treated cancer cells through the Fenton chemistry.

Therefore, in the present study, PD NPs have been synthesized in aqueous media containing water, ammonium hydroxide ($NH_4OH$) and different alcohols (ROH), such as methanol (MeOH), ethanol (EtOH), 2-propanol (2-PrOH), 1-propanol (1-PrOH) and 2-methyl-2-propanol (2-Me-2-PrOH). The first aim was to analyze how the type of ROH and the water/ROH volume ratio employed, along with the concentration of $NH_4OH$ in the medium, influence particle size. In addition, since a ferroptosis-like mechanism may be responsible for PD NP toxicity to tumor cells, the $Fe^{2+}$-loading capacity of the different PD@ROH NPs produced has been also determined and compared. As a result, it has been shown that the type of ROH employed in PD NPs synthesis determines their $Fe^{2+}$-adsorption capacity and, consequently, their cytotoxicity, which has been determined for a breast cancer cell line (Fig. 1). A correlation between both properties has been found and besides, it has been observed that such relationship is reverse for normal cells. Finally, with the co-administration of deferoxamine (DFO) and glutathione (GSH) (an iron chelator and an antioxidant compound, respectively) together with the PD NPs [13,12], it has been corroborated that Fenton chemistry may mediate the production of ROS in treated tumor cells.

## 2. Materials and methods

### 2.1. Material

Dopamine hydrochloride, ammonium hydroxide, phosphate buffered saline (PBS, 0.01 M, pH 7.4), DMEM medium, Fetal Bovine Serum (FBS), MTT reagent, L-glutathione reduced (GSH) and deferoxamine mesilate (DFO) were provided by Sigma-Aldrich. Penicillin-streptomycin (5000 U/mL) was provided by Thermo Fisher Scientific. Iron (II) chloride anhydrous ($FeCl_2$, 97 %), sodium acetate anhydrous, 1-propanol (extra pure), 2-propanol (99.5 %) and 2-methyl-2-propanol (99.5 %) were provided by Panreac. Absolute ethanol (99.5 %) and methanol (99.5 %) were supplied by VWR Chemicals.

### 2.2. Methods

IR absorption spectra were performed in a PerkinElmer Spectrum Two™ spectrometer operating in the 4000–400 $cm^{-1}$ wavelength range after preparing samples as pellets of PD NPs in potassium bromide. TEM images were acquired with a FEI Tecnai Spirit Twin at an acceleration voltage of 120 kV. PD NPs were dispersed in deionized water in a concentration less than 0.01 % (WT) and a drop of this dispersion was deposited on a copper grid with a collodion membrane and allowed to dry for 24 h. Hydrodynamic diameter of PD NPs was analyzed by dynamic light scattering (DLS) on the basis of their intensity-average size distribution with the Zetasizer Nano ZSP90. PD NPs were suspended in a Tris/urea buffer (3.6 mM, pH 10) in a concentration less than 0.01 % (WT) and their translational diffusion coefficient was calculated using the Stokes-Einstein equation (Eq. (1)), where d(H) represents the hydrodynamic diameter, D is the translational diffusion coefficient, k is the Boltzmann's constant, T is absolute temperature and $\eta$ is viscosity. Correlation functions were analyzed by the Cumulants method.

$$d(H) = \frac{kT}{3\pi\eta D} \quad (1)$$

Finally, the equipment used for the $Fe^{2+}$ analysis was the Plasma Emission Spectrometer, model ULTIMA 2 of Jobin Yvon. The calibration range used was 10–100 ppm.

#### 2.2.1. Synthesis of polydopamine nanoparticles (PD NPs)

The synthesis of the different PD NPs was carried out in a water (90 mL)/ROH (40 mL) mixture, fixing the volume of the resulting solvent at 140 mL in all cases. A $NH_4OH$ aqueous solution (28–30 %) was added to the water/ROH mixtures under magnetic stirring at 25 °C for 30 min, varying the concentration of $NH_4OH$ from 0.79 to 3.01 % (V/V) depending on the type of ROH. Finally, dopamine hydrochloride (0.5 g) was dissolved in deionized water (10 mL) and directly added to the mixed solution. All polymerization reactions were allowed to proceed

for 24 h [18].

Once obtained, PD(ROH) NPs were isolated by centrifugation and purified by at least four centrifugation-redispersion cycles in deionized water. In order to calculate dopamine conversion rate, the resulting products were oven-dried at 105 °C until reaching a constant weight.

### 2.2.2. $Fe^{3+}$-loading capacity of the PD(ROH) NPs

$Fe^{3+}$-loaded PD(ROH) NPs were prepared by mixing approximately 1 mL of PD NPs with 20 mL of a $FeCl_3$ solution (acetate buffer, 0.4 M, pH 4.3) at 25°C, in orbital shaking at 100 rpm overnight. Concentration and diameter (DLS) of NPs were: MeOH (2.4 mg/mL, 168 nm ± 43, PDI = 0.026); EtOH (2.4 mg/mL, 169 nm ± 37, PDI = 0.026); 2-PrOH (2.8 mg/mL, 187 nm ± 37, PDI = 0.055); 1-PrOH (2.7 mg/mL, 190 nm ± 46, PDI = 0.044); and 2-Me-2-PrOH (3.9 mg/mL, 170 ± 47, PDI = 0.066). Different initial $Fe^{3+}$ concentrations, from approximately 7–35 ppm, were studied for all PD(ROH) NPs. Then, loaded PD NPs were isolated by centrifugation and the $Fe^{3+}$ content of the supernatant was determined by Inductively Coupled Plasma Atomic Emission Spectroscopy (ICP-AES).

### 2.2.3. PD(ROH) NPs treatment for the cytotoxicity studies

Isolated PD(ROH) NPs were purified by four centrifugation-resuspension cycles in deionized water for carrying out the cytotoxicity studies. These PD NPs were later suspended in PBS (pH 7.4) with a final concentration and diameter (DLS) of approximately: i) MeOH (2.47 mg/mL, 173.0 ± 51.3 nm, PDI = 0.067); ii) EtOH (1.76 mg/mL, 166.5 ± 40.7 nm, PDI = 0.048); iii) 2-PrOH (2.8 mg/mL, 188.0 ± 50.0 nm, PDI = 0.047); iv) 1-PrOH (1.50 mg/mL, 176.3 ± 50.4 nm, PDI = 0.052); and v) 2-Me-2-PrOH (1.94 mg/mL, 170.0 ± 52.7 nm, PDI = 0.077).

### 2.2.4. Cell culture

BT474 and HS5 cells were cultured at 37 °C in a humidified atmosphere in the presence of carbon dioxide ($CO_2$) (5 %). Culture medium (DMEM) was supplemented with FBS (10 %) and antibiotics (1 %) as instructed (ATCC, Wesell).

### 2.2.5. Cytotoxicity studies

To study the cytotoxicity of the PD(ROH) NPs, BT474 and HS5 were seeded in 24-well plates, with a density of 12,000 and 15,000 cells/mL respectively, and grown overnight with supplemented medium. The culture medium was replaced the following day with medium containing PBS (control) and five different concentrations (from 0.0074 mg/mL to 0.042 mg/mL) of the PD(ROH) NPs. In all cases, the cellular survival rate was analyzed for 72 h (82 Reader 2000), and cellular viability was checked every 24 h through MTT assays, following a previously described protocol [8]. Each value shown is the average of three independent experiments and the results obtained were considered statistically significant when $p < 0.05$.

### 2.2.6. Effect of GSH and DFO on PD(ROH) NPs cytotoxicity

With the purpose of testing whether the capacity of PD NPs to adsorb $Fe^{3+}$ could be involved in their antiproliferative activity, additional MTT assays were performed using the BT474 cell line, seeding them in 24-well plates with at a density of 12,000 cells/mL [3,8,9]. After growing them overnight to supplemented medium, it was replaced the next day with medium containing: i) PBS (control); ii) DFO or GSH; iii) PD (MeOH) NPs; iv) PD(2-PrOH) NPs; v) PD(MeOH) NPs + DFO or GSH; and vi) PD(2-PrOH) NPs + DFO or GSH. In all cases, the concentration for PD(ROH) NPs, DFO and GSH were 0.020 mg/mL, 0.7 μM and 50 μM, respectively. The viability of the treated BT474 cells was studied again for 72 h, and the cellular survival rates were quantified every 24 h using the previously mentioned protocol [8]. Each result shown is again the average value of the three independent experiments.

**Table 1**
Size (TEM, DLS) of the PD NPs, conversion yield and Ra values of dopamine polymerization reaction as a function of the ROH employed.

| ROH | ε | TEM (nm) | DLS (nm) | Yield (%) | Ra[c] |
|---|---|---|---|---|---|
| MeOH | 33.1[a] | 392 ± 26 | 628 ± 140 (PDI: 0.223) | 22.9 | 4.23 |
| EtOH | 25.0[a] | 300 ± 32 | 452 ± 120 (PDI: 0.075) | 17.9 | 3.58 |
| 2-PrOH | 19.2[a] | 194 ± 29 | 282 ± 70 (PDI: 0.034) | 14.6 | 2.92 |
| 1-PrOH | 20.1[a] | 210 ± 18 | 193 ± 43 (PDI: 0.041) | 5.4 | 2.78 |
| 2-Me-2-PrOH | 12.47[a] | 194 ± 27 | 286 ± 70 (PDI: 0.204) | 13.8 | 3.13 |

[a] [14].
[b] [18].
[c] The calculation used for obtaining the Ra values among dopamine and the ROH mixtures can be found in the Supplementary Material.

## 3. Results and discussion

### 3.1. Effect of the different types of alcohols on the synthesis of PD NPs

PD NPs were prepared using the standard procedure of oxidative polymerization of dopamine in a basic aqueous medium containing $NH_4OH$ and ROH. In order to study the effect that the type of ROH had on this chemical process, NP synthesis was performed with five different ROHs of 1, 2, 3 and 4 carbons. In all cases, the water/ROH volume ratio (10:6, 58.59 % (V/V)) and the $NH_4OH$ concentration (0.79 % V/V) were kept constant. Resulting PD(ROH) NPs were characterized by DLS and TEM and the values of the Hansen's Solubility Parameters (HSP) distances (Ra values) between dopamine and all the water/ROHs mixtures were determined (Table 1).

As can be seen, MeOH produced the largest NPs, followed by those produced using EtOH, 2-PrOH, 2-Me-2-PrOH and, finally, 1-PrOH. PD (ROH) NPs size, as determined by TEM, ranged from 392 ± 26 nm (MeOH) to 130 ± 16 nm (1-PrOH), which indicated that the higher the alcohol dielectric constant (ε), the greater the NP diameter and the polydopamine conversion yield. By contrast, PD NPs produced with 1-PrOH were smaller despite 1-PrOH having a high ε (20.1) [18]. The values for the hydrodynamic diameter obtained by DLS were higher than those obtained by TEM possibly due to the dehydration of the NPs that was necessary to perform to prepare the samples for microscopy, but followed the same trend in both cases [18]. Moreover, obtained NP polydispersity index (PDI) values were acceptable, and those lower than 0.1 indicated that the PD(ROH) NPs were highly monodisperse [34].

According to the literature, the type of ROH used affects dopamine polymerization, being this effect explained by the HSP theory, in which Ra values refer to the three-dimensional distance between the solubility parameters of dopamine and the solvent (water/ROH mixtures) [14]. Thus, Jiang et al. had previously demonstrated that there is a relationship between dopamine conversion yield and PD NP size, in turn conditioned by the water/ROH volume ratio employed. These authors calculated the Ra values among dopamine and three different water/ROH (EtOH, MeOH and 2-PrOH) solvent mixtures and reported that the smaller the Ra value, the higher the expected dopamine solubility and the higher the polymer conversion yield achieved. In addition, they also concluded that PD NPs can be more easily obtained in weakly alkaline water/ROH solvent mixtures with smaller Ra values [18].

In this way, the Ra values determined between dopamine and the five ROHs tested in this work showed that the water/ROH volume ratio (10:6, 58.57 % (V/V)) used was suitable for synthesizing PD NPs with MeOH, EtOH and 2-PrOH because the obtained values were close to the minimum Ra values reported by Jiang et al. [18]. However, when 1-PrOH was used, the Ra value determined in this work (2.78) for the mentioned water/ROH ratio was far from being optimum. The optimal Ra value (10:6, 42.86 % (V/V)), with which a 297.1 ± 62.3 nm particle

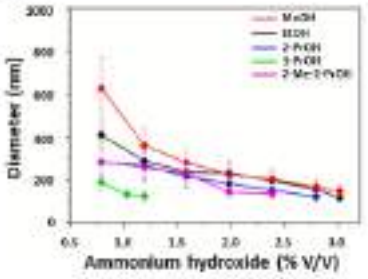


Fig. 2. Hydrodynamic diameter (nm) of the PD(ROH) NPs as a function of the $NH_4OH$ concentration used in their synthesis with each water/ROH mixture.

size was obtained, was found by varying the proportion of ROH in the solvent mixture from 35.71 % (V/V) to 50.0 % (V/V). Finally, regarding the use of 2-Me-2-PrOH, the Ra value obtained in this work (Ra = 3.13; 28.57 % (V/V)) was also appropriate, since lower and higher ROH volume ratios (from 14.28 % to 21.43 % and 35.71 % (V/V)) led to obtain higher Ra values. All the steps taken in this work to determine the described Ra values can be consulted in the Supplementary Material (Tables S1–S4).

Otherwise, in a second experiment, the effect of the $NH_4OH$ concentration on PD(ROH) NPs size was also studied. Fig. 2 and S1 show that for a fixed water/ROH volume ratio, the size of PD NPs could be altered by varying the concentration of $NH_4OH$, whose main function in the synthesis process is to create a basic medium that allows polydopamine to be oxidized.

In general, for all of the PD(ROH) systems studied, lower diameters were obtained by increasing the concentration of $NH_4OH$, since the pH of the synthesis medium conditions PD oxidation and polymerization, as it had been previously demonstrated [19,21]. When the $NH_4OH$ concentration was set at 0.79 % (V/V), the smallest PD NPs (191 nm) were obtained using 1-PrOH and the largest (628 nm) using MeOH. Also, it was interesting to find that for 1-PrOH, the diameter of the NPs varied by 200 nm when $NH_4OH$ concentration was increased from 0.79 to 1.19 % (V/V) and by 65 nm when the concentration increased from 1.19 to 1.58 % (V/V). A similar behavior in size was found, based on the $NH_4OH$ concentration, for PD NPs obtained with MeOH and EtOH. The difference in their diameter when the $NH_4OH$ concentration was increased from 1.19 to 1.58 % (V/V) was 200 and 120 nm, respectively. However, when larger amounts of $NH_4OH$ were used, such difference was not so marked, similar to what was observed when 2-PrOH and 2-Me-2-PrOH were employed. Data corresponding to the PD(ROH) NPs diameter values as a function of the $NH_4OH$ concentration employed can be found in the Supplementary Material, too (Fig. S1F).

Finally, in order to obtain PD(ROH) NPs smaller than 100 nm, which are interesting from a biomedical perspective [13,22], higher concentrations of $NH_4OH$ were tested. Fig. 3A shows the size of the PD NPs produced according to the type of ROH used and Fig. 3B-F shows the morphology of these PD(ROH) NPs smaller than 100 nm.

### 3.2. Infrared characterization of PD(ROH) NPs

IR spectroscopy has been widely used to characterize melanins [3,23,24]. Thus, main bands were here assigned according to the previous characterization of melanins and were the following: the broad absorption band with the maximum at 3412 $cm^{-1}$ may include the C=O stretching (non-carboxylic acid) and the C=C stretching of the aromatic system (at ca. 1600 $cm^{-1}$). The N–H bending in an indole ring may

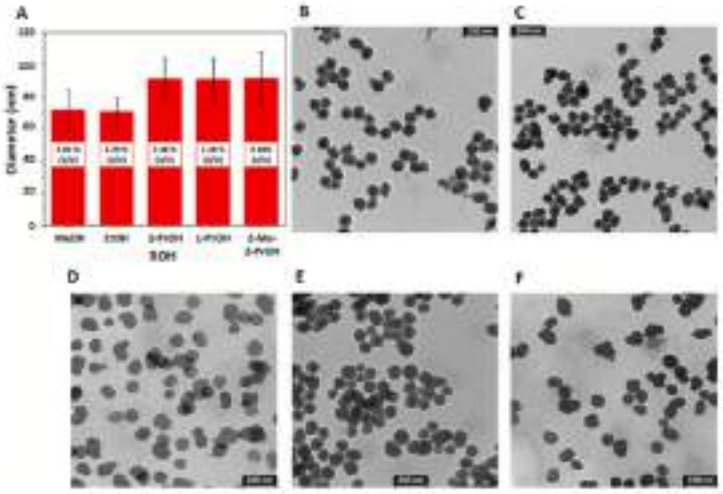


Fig. 3. Characterization of smaller PD(ROH) NPs. (A) Bar graph: Diameter vs. ROH and $NH_4OH$ concentration (inside bars) employed; TEM images of PD(ROH) NPs, showing a mean size of (B) MeOH: 71.8 ± 12.4 nm, (C) EtOH: 71 ± 9.6 nm, (D) 2-PrOH: 91.1 ± 12.3 nm, (E) 1-PrOH: 90.9 ± 12.3 nm) (F) 2-Me-2-PrOH: 91.0 ± 14 nm. Scale bars are 200 nm in all cases.

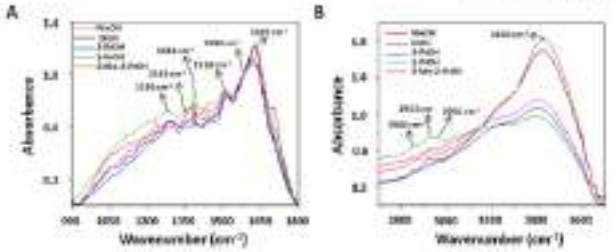


Fig. 4. IR spectra in the 900–1600 $cm^{-1}$ range (A) and in the 2700–3700 $cm^{-1}$ range (B) for all the PD(BOH) NPs.

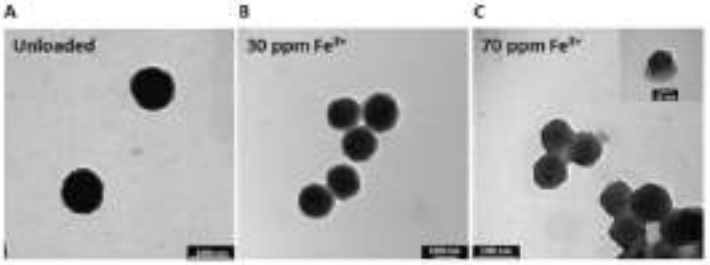


Fig. 5. TEM images of PD(BOH) NPs (A) unloaded (105.7 ± 14.4 nm), (B) after interacting with 30 ppm of $Fe^{3+}$ (95.1 ± 12.3 nm) and (C) after interacting with 70 ppm of $Fe^{3+}$ (97.8 ± 14.8 nm). Scale bars are 100 nm.

appear at 1510 $cm^{-1}$, while the peaks at 1345 and 1302 $cm^{-1}$ may correspond to the C-N stretching mode of an indole and a pyrrole ring, respectively. The C–OH stretching in a phenol ring appears at 1280 $cm^{-1}$. In the region from 4000 to 2000 $cm^{-1}$, the bands at 2930, 2922 and 2840 $cm^{-1}$ correspond to the different vibrational modes of the aliphatic groups. The broad band placed at 3405 $cm^{-1}$ may include the -OH (phenol, carboxylic acid) and the -NH stretching modes (in an indole or in a primary amine).

IR spectra of PD NPs obtained in the different water/BOH media are shown in Fig. 4. Spectra were normalized at 1580 $cm^{-1}$ in order to compare the intensity of the different bands.

The above-described characteristic bands of melanins within the 900–1600 $cm^{-1}$ range can be seen in all PD(BOH) NPs. This is also the case within the 2700–3700 $cm^{-1}$ range, but the relative intensity of the band at 3400 $cm^{-1}$ associated with -OH and -NH stretching modes notably decreased when either 1-PrOH, 2-PrOH or 2-Me-2-PrOH were used for PD NPs synthesis.

### 3.2. Influence of the use of different alcohols on PD NPs $Fe^{3+}$-adsorption capacity

Here, the $Fe^{3+}$-adsorption capacity of the PD(BOH) NPs was studied. First, changes in the morphology of PD(EtOH) NPs upon interaction with two initial $Fe^{3+}$ concentrations (30 and 70 ppm) were evaluated. TEM image in Fig. 5A shows a control of unloaded PD NPs, while the slight variation in the morphology of $Fe^{3+}$-loaded NPs can be observed in Fig. 5B-C, especially when the initial $Fe^{3+}$ concentration was higher, since the NPs seem to be spongier.

Then, PD(BOH) NP $Fe^{3+}$-loading capacity was further analyzed, fitting the equilibrium results using the Freundlich isotherm, which is applied in multilayer adsorption processes on heterogeneous surfaces [28,29]. The initial $Fe^{3+}$ concentration added varied in the range of 7–55 ppm at pH 4.5, while the concentration of the PD NPs was kept constant to allow for proper comparisons. TEM images of the NPs used to obtain the isotherms can be found in the Supplementary Material (Fig. S2). As a result, it was shown that all PD(BOH) NPs were able to adsorb this metal cation, which made their surface spongier, a fact that was in accordance with what had already been reported in the literature [11]. Nevertheless, according to the equilibrium results, $Fe^{3+}$-loading capacity varied depending on the water/BOH synthesis mixture employed. This difference was more accentuated when a higher $Fe^{3+}$ concentration (30 ppm) was used, while the differences in the adsorption capacity of the PD(BOH) NPs was negligible for a lower concentration (7 ppm). PD NPs prepared in 2-PrOH showed the highest adsorption capacity of $Fe^{3+}$ with respect to the other PD(BOH) systems and, by contrast, PD(2-Me-2-PrOH) NPs were clearly the NPs with the lowest $Fe^{3+}$-adsorption capacity. Linear fittings according to Freundlich model, $Fe^{3+}$-adsorption efficiency (%) and fitted parameters (1/n and Q) can also be consulted in the Supplementary Material (Fig. S3 and Table S4).

### 3.4. Cytotoxicity of the different PD(BOH) NPs

In this section, the cytotoxicity of the PD(BOH) NPs synthesized was analyzed. Previously, it had been reported that standard PD(EtOH) NPs were intrinsically toxic to cancer cells, especially to the breast carcinoma cell line BT474 [8,9,9]. For this reason, this human cell line was chosen to study the antitumor effect of the different PD(BOH) NPs produced in this work. Likewise, the stromal HS5 cell line was selected

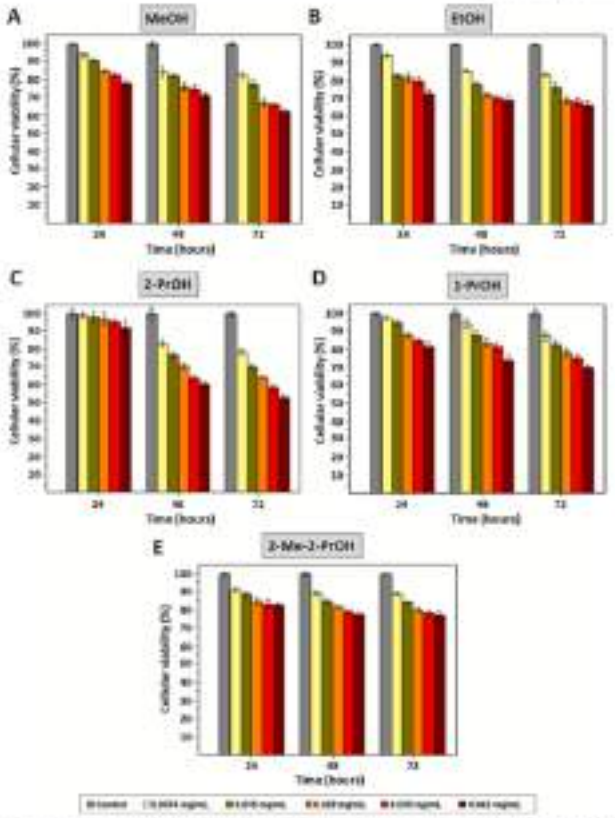


Fig. 6. Results of the MTT assay performed on the BT474 cell line treated with five different concentrations of PD(ROH) NPs: ROH = (A) MeOH, (B) EtOH, (C) 2-PrOH, (D) 1-PrOH and (E) 2-Me-2 PrOH. The results shown represent the mean ± standard deviation of three replicates done for each treatment.

for comparing PD(ROH) NPs toxicity to tumor and normal cells. The results of the viability assays carried out on both cell lines, treated with different concentrations of the PD(ROH) NPs, can be found in Fig. 6 (BT474 cells) and in Fig. 7 (HSS cells). Additionally, a table with the survival rates (%) corresponding to these figures can be found in the Supplementary Material (Fig. S5).

As shown in Fig. 6, the PD(ROH) NPs caused, in all cases, a notable reduction in the viability of BT474 cells. This result was especially apparent 72 h after the cells were treated with the highest concentrations of NPs (0.035 mg/mL and 0.042 mg/mL). Among the different types of PD NPs, those synthesized using MeOH, EtOH and 1-PrOH exhibited practically the same level of cytotoxicity. It was observed that these PD NPs were able to reduce the rate of cell survival by 20–25 % 24 h after treatment with NP concentrations of 0.035 mg/mL and 0.042 mg/mL. However, the survival rate of these cells was slightly higher when they were treated with the same concentrations of PD(2-Me-2-PrOH) NPs, and even more when PD(2-PrOH) NPs were administered. Nevertheless, this pattern changed since 48 and 72 h elapsed. After such time, the highest concentrations of PD(MeOH), PD(EtOH) and PD (1-PrOH) NPs used reduced cellular viability by around 30–40 %, while cell treatment with PD(2-Me-2-PrOH) NPs caused a viability reduction of 25–30 %. However, the cytotoxicity of the PD(2-PrOH) NPs was more marked, where BT474 cell survival rate was reduced to approximately half. In addition, it was observed that for the other PD (ROH) NP concentrations, the behavior was similar to that described for the highest concentrations, although their antitumor effect was not as marked.

Also, no significant reduction in HSS cell viability was found for any of the PD(ROH) NPs (Fig. 7). In all cases, the rates of cellular survival were higher than 82 % 72 h after treatment with the highest NP

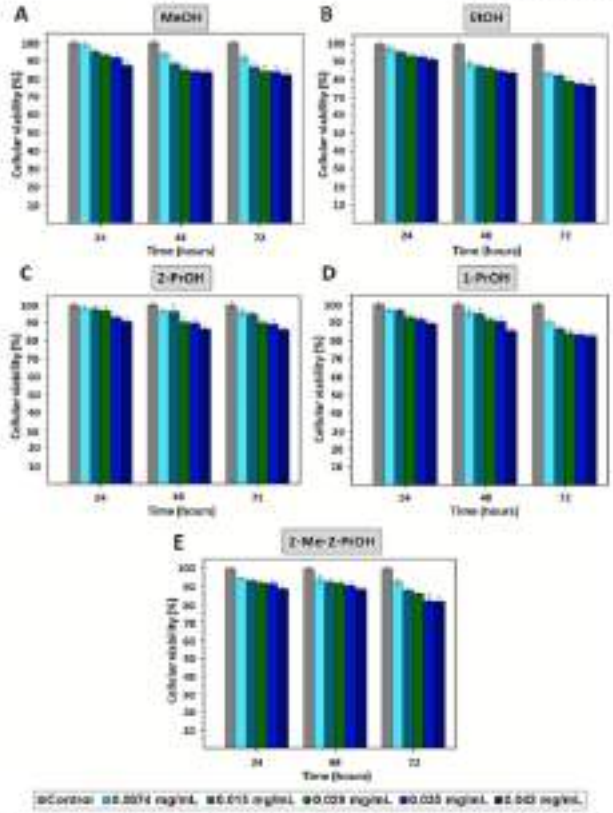


Fig. 7. Results of the MTT assays performed on the HS5 stromal cell line treated with five different concentrations of (A) PD(MeOH), (B) PD(EtOH), (C) PD(2-PrOH), (D) PD(1-PrOH) and (E) PD(2-Me-2-PrOH) NPs. The results shown represent the mean ± standard deviation of the three replicas done for each treatment.

concentrations, except when treatment was performed with PD(EtOH) NPs, which were the most toxic to stromal cells. When comparing the viability percentages of both BT474 and HS5 cell lines, treated with the same concentrations of NPs, greater differences were found after 72 h, the time point when PD NPs antitumor activity was the highest. Taking into account the results obtained, it should be mentioned that the less selective NPs were the ones prepared in 2-Me-2-PrOH, while the NPs with the most selective antitumor activity were the PD(2-PrOH) NPs.

As shown, PD(2-PrOH) NPs were the NPs that decreased BT474 cellular viability the most (to 33 % after 72 h of the treatment with a 0.043 mg/L concentration) and had the most noticeable $Fe^{3+}$-adsorption capacity (140 mg/g for Cl⁻ = 35 ppm). Conversely, PD(2-Me-2-PrOH) NPs exhibited the lowest $Fe^{3+}$-adsorption efficiency and had the lowest ability to reduce the survival rate of the BT474 cells (reduced to 73 % after 72 h of treatment with a the highest concentration). This relation between $Fe^{3+}$-loading and BT474 cell toxicity was also similar for all of the other PD(ROH) NPs, except for the PD(EtOH) NPs, with which similar results were obtained to those that had already been reported [8, 9]. As a result, a linear correlation could be established between both properties (Fig. S6). Also, this relation seemed to be inverse for HS5 cells, where a lower $Fe^{3+}$-adsorption capacity of PD NPs was accompanied by a higher toxicity to stromal cells.

Iron is an essential element for most organisms, with a fundamental role for cell growth and proliferation. However, as mentioned in the introduction, iron can also be implicated in the generation of reactive oxygen species (ROS) through its participation in Fenton's chemistry, triggering cell death [3, 13, 27]. For this reason, it was believed that PD $Fe^{3+}$-adsorption capacity could be related to PD(ROH) NPs tumor-specific toxicity and to verify this fact, additional viability assays were carried out, where breast cancer cells were co-treated with DFO or

GSH.

*3.5. Antiproliferative effect of PD(R/H/I) NPs on cancer cells co-treated with DFO or GSH*

In order to show that the $Fe^{3+}$-adsorption capacity of PD(R/H/I)D NPs could be involved in their tumor-selective toxicity, BT474 cells were co-treated with PD(MeOH, H/I)H and 2-PrOH) NPs and with non-toxic concentrations of DFO and GSH. These three types of PD(R/H/I) NPs were the ones selected to perform further viability assays because they presented greater anticancer activity. Also, DFO and GSH were chosen because they are an iron-chelating compound and an antioxidant agent, respectively [58,59]. Thus, additional MTT assays were carried out, studying BT474 cellular viability 24, 48 and 72 h after the aforementioned co-treatment [8]. As shown in Fig. S7, it could be seen that such co-treatment managed to partially block the antiproliferative activity of PD(R/H/I) NPs, since the cellular survival rate was on average higher than 80 %. Major differences between the cytotoxicity of the treatment with PD(R/H/I) NPs or with PD(R/H/I) NPs plus DFO or GSH could again be noticed after 72 h and were greater when BT474 cells were treated with PD(2-PrOH) NPs.

Consequently, it was found that the $Fe^{3+}$-binding of the PD NPs could account for their antitumor effect. Thus, when these NPs are internalized and end up in cellular lysosomes [8], they could cause an imbalance between the oxidized and reduced free iron forms and mediate an enhanced production of ROS through the Fenton reaction. In addition, since cancer cells have a greater iron-dependence than normal cells [14, 15], the viability of the latter was not so reduced by the PD NPs cytotoxicity mediated by their $Fe^{3+}$-binding capacity.

## 4. Conclusions

Throughout the present study it was shown that MeOH, EtOH, 2-PrOH, 1-PrOH and 2-Me-2-PrOH can all be used to synthesize PD NPs, which size depended on the type of ROH used. Generally, the lower their $\alpha$ of the ROH, the smaller the PD NP diameter, which also depended on the $NH_4OH$ concentration used in the synthetic process. With regard to the latter, the higher the concentration of $NH_4OH$ added, the smaller the size of the NPs produced.

In addition, it has also been proven that $Fe^{3+}$-binding capacity of PD NPs was determined by the ROH used in their synthesis. Since a ferroptosis-like mechanism may account for PD NP cytotoxicity, the ROH used may also influence the final outcome. Cancer cells present great dependence on iron and, for this reason, PD NPs that are more efficient at adsorbing $Fe^{3+}$ may cause a greater imbalance in the concentration of their lysosomal $Fe^{2+}$ and $Fe^{3+}$ when they are endocytosed and propitiate an increase in ROS production. This fact would help to explain why PD(2-PrOH) NPs, the ones with a higher $Fe^{3+}$-adsorption capacity, were the NPs that most reduced the survival rate of breast cancer cells. Finally, this fact could also explain why PD NP toxicity was partially reduced when cells were co-treated with an iron chelator or an antioxidant compound. Moreover, since non-tumor cells are not that iron-dependent, the ferroptosis-like mechanism mediated through PD NPs may shed light on why such NPs did not significantly reduce their viability.

Therefore, based on the results presented here, it is clear that PD NPs, especially those prepared using 2-PrOH, may play an important role in the development of future and novel cancer therapy strategies.

## CRediT authorship contribution statement

**Celia Nieto:** Conceptualization, Methodology, Writing - original draft, Writing - review & editing. **Gema Marcelo:** Conceptualization, Methodology, Writing - review & editing. **Milena Vega:** Conceptualization, Methodology, Supervision, Writing - original draft, Writing - review & editing. **Eva M. Martín del Valle:** Conceptualization, Writing - review & editing, Funding acquisition.

## Declaration of Competing Interest

The authors declare that they have no known competing financial interests or personal relationships that could have appeared to influence the work reported in this paper.

## Acknowledgments

This research was funded by the Spanish Ministry of Economy and Competitiveness (grant number CTQ2016-79988-R) and by the Ramón Areces Foundation. C. Nieto thanks Junta de Castilla y León for the predoc fellowship. The authors thank the Microscopy Service of the University of Salamanca for the TEM images.

## Appendix A. Supplementary data

Supplementary material related to this article can be found, in the online version, at doi:https://doi.org/10.1016/j.colsurfb.2020.111306.

## References

[1] E. Lee, J.M. Hollander, W.M. Miller, J.S. Blumenthal, Mixed tumorous surface chemistry for dual fluorescent imaging, Science Nat. (2007) 435–451.
[2] R. Mout, moyano, Nanoparticles for intracellular delivery, Chem. Soc. Rev. (2012) 2780–2799.
[3] P. Horcajada, R.C. Arnaud, J. Maser, B.E. Vaghenzender-Rampal, M.E. Tolmasov, S. Li, Metal–organic nanoscale carriers, Nature Nanotechnology for nanomedicine, Nat. Mater. 2 (2004) 37–44.
[4] J.R. Holtzinger, E.K. Wheeler, J.D. Bazak, Stabilizing terminal titanium oxo-clusters for nanomedicine, Biomaterials 47 (2015) 102–109.
[5] M.A. Vega, E. Nieto, G. Marcelo, E.M. Martín del Valle, Cytotoxicity of polydopamine-cisplatin-coated polyhydroxyalkanoate nanoparticles, Colloid Surf. B 167 (2018) 249–260.
[6] P.C.L. Black, A. Yi, P.O. Kwiatkowski, R.L. Infante-Lopez, F.B. Blumenthal, Polydopamine-modified surface-functionalization of gold nanorods for cancer cell-targeting imaging and photothermal therapy, Nanomedicine 9 (2013) 17–28.
[7] Y. Li, C. Peng, G. Zhang, F. Peng, B. Sun, B. Ai, X. Chen, L. Liu, Targeted polydopamine nanoparticles enable photoacoustic imaging guided chemo-photothermal synergic therapy of tumor, Acta Biomater. 47 (2017) 124–134.
[8] C. Nieto, M.A. Vega, G. Marcelo, E.M. Martín del Valle, Polydopamine nanoparticles kill cancer cells, RSC Adv. 9 (2019) 30202–30208.
[9] C. Nieto, M.A. Vega, J. Enrique, G. Marcelo, E.M. Martín del Valle, Size matters in the cytotoxicity of polydopamine nanoparticles in different types of tumors, Cancers 11 (2019) 1979.
[10] K.T. Ai, Y. Liu, L. Lu, X.H. Cai, J.Y. Ren, Hydrothermal synthesis of nanosized polydopamine as a novel drug delivery system with high loading capacity and controlled release, J. Mater. Chem. 21 (2011) 5196–5205.
[11] S.J. Dixon, K.M. Patel, Ferroptosis: an iron-dependent form of non-apoptotic cell death, Nat. Rev. Mol. Cell Biol. 13 (2012) 723–734.
[12] V. Cuzzocrea, G.G. Ferraro, L. Ferrazzoli, F. Sorbello, F. Amoroso, Ferroptosis enhances the efficacy of cisplatin in cervical cancer, Front. Oncol. 9 (2019) 1–12.
[13] L. Chen, Z. Liu, L. Liu, B. Huang, W. Du, H. Ge, Y. Sun, $Fe^{3+}$-$Fe^{2+}$ ions-chelated ultra-pH-sensitive polydopamine nanoparticles reduce resistance for cancer therapy, ACS Biomater. Sci. Eng. 5 (2019) 4862–4869.
[14] D.H. Wang, D.L. Hamilton, R.T. Tsai, P.M. Yuan, S.V. Yan, Iron and cancer: recent insights, Ann. NY Acad. Sci. 1368 (2016) 149–161.
[15] M. Jung, C. Mertens, R. Tomat, B. Brüne, Iron as a central player and promising target in cancer progression, Int. J. Mol. Sci. 20 (2019) 273.
[16] J. Fan, L. Yang, H.F. Liu, J. Ma, L. Lu, Y.L. Lin, Polydopamine spheres as active templates for convenient synthesis of various nanostructures, Small 9 (2013) 3384–3391.
[17] F. Shahbazi, A. Zamanian, A. Bahmanghahsi, M.R. Fathi, A facile method to synthesize organic-inorganic polydopamine nanospheres as an active template for in situ formation of biomimetic hydroxyapatite, Mater. Sci. Eng. C 94 (2019) 720–730.
[18] S. Deng, Y. Wang, M. Li, Selecting water-alcohol mixed solvent to achieve the synthesis of polydopamine nanospheres using solubility parameter, Sci. Rep. 6 (2016) 1–8.
[19] A.A. Ensafi, A.A. Amiribavar, T.M. Tabatabaei, Y.V. Lonare, Comparison of the results of measurements of thickness of nanoparticles in stable colloidal solutions by the methods of atomic spectroscopy, dynamic light scattering, and transmission electron microscopy, Meas. Tech. 59 (2017) 1111–1118.
[20] J.M. Hughes, P.M. Reed, A. Green, P. Evans, R. Thalia, J. Lewis, Highly monodisperse, hollow-core/shell polydopamine nanoparticles as potential multimodal reference materials for multi-functional "core" bio-assays, J. Appl. Polym. Sci. 132 (2015) 41806.

# CHAPTER 5

## FERRIC-LOADED POLYDOPAMINE NANOPARTICLES CHARGED WITH DOXORUBICIN AS TARGETED COMBINATION THERAPY

## 5.1. Introduction

### *5.1.1. Polydopamine-based nanomaterials in the different modalities of cancer diagnosis and therapy*

In the introduction of the previous chapter, it was already reported that PDA excellent properties, especially its easy functionalization and its ability to chelate metal ions, are allowing it to acquire an important role in cancer diagnosis and therapy these days [1-3]. Indeed, in less than a decade, the number of annual publications related to the application of this bio-inspired material in cancer nanomedicine has been multiplied by ten in the PubMed database [4].

Undoubtedly, the most frequent application to date of PDA-based materials has been the development of novel tumour imaging and photothermal therapy (PTT) nanosystems [5-7]. Nonetheless, the development of DDSs based on this melanin analogue is gradually becoming more and more relevant [8,9]. Also, as PDA DDSs have gained popularity, so has the combination of PTT and chemotherapy with PDA NPs or NPs coated with PDA [1,7,10-12]. Combining both types of therapies seeks to overcome the limitations of each monotherapy, i.e., the uneven hyperthermia distribution and the lack of selectivity and the apparition of MDR that are associated with chemotherapy [2,10,12]. In this way, PDA NPs, as well as AuNPs, MSNs and $Fe_3O_4$ NPs coated with PDA can already be found in the literature conjugated with different chemotherapy drugs (DOX, docetaxel or bortezomib) to target and induce hyperthermia in tumour tissues [2-3,10-12].

### *5.1.2. Ferroptosis: a mechanism of regulated cell death gaining popularity in cancer therapy*

However, despite the fact that chemotherapy combined with PPT has been shown to be effective in improving cancer therapeutic outcomes, drug resistance remains still an important challenge [10]. This resistance is mainly caused because almost all of the clinical applied and the currently investigated systems for cancer therapy and nanotherapy induce

programmed cell death through caspase-dependent apoptosis. Nevertheless, as explained in the introductory chapter, tumour cells are capable of developing different strategies to overcome apoptosis, and this fact causes the emergence of MDR, which is nothing more than a self-defense mechanism of malignant cells [13,14]. In addition, pro-apoptotic therapy fails to deal with *ras* mutant cancer cells, which are responsible for about 30% of the cases of resistance to conventional chemotherapeutic drugs [13].

All this highlights the urgent need to develop non-apoptotic therapies and explains the growing interest of the scientific community in targeting the unique biochemical alterations of cancer cells. This, according to recent studies, might be a feasible approach to achieve therapeutic selectivity and even prevent the development of MDR [13,15].

Among the different metabolic hallmarks of cancer, one that is sparking great interest for the development of novel non-apoptosis-based anti-tumour therapies is Fe homeostasis [13]. As described in Chapter 4, cancer cells have greater dependence on this metal, which is required for all the stages of tumour development, survival, proliferation and metastasis. For this reason, the pathways that govern the uptake, storage and efflux of Fe, which are tightly regulated under normal physiological conditions, are perturbed in tumours to maintain increased Fe levels in these tissues [16,17].

Regarding Fe metabolic pathways, it should be noted that the $Fe^{2+}$ formed by intestinal absorption or erythrocyte degradation can be oxidized by ceruloplasmin to $Fe^{3+}$, which binds to transferrin (Tf) on the cell membrane to form Tf-$Fe^{3+}$ complexes. Then, Tf-$Fe^{3+}$ binds Tf receptor-1 (TfR1), and the resulting complex is internalized in the cells by endocytosis. Once in late endosomes, as already explained before, $Fe^{3+}$ can be reduced by the six-transmembrane epithelial antigen of the prostate 3 (STEAP3) to $Fe^{2+}$, which gets the cytosol through DMT1. Most $Fe^{2+}$ is stored in ferritin, but part forms an unstable Fe pool known as LIP. At last, excess of $Fe^{2+}$ is oxidized again to $Fe^{3+}$ and pumped outside the cells by ferroportin (FPN). This recycling Fe homeostasis, with no excretory route, strictly controls the intracellular concentration of this metal and

[18], since it has to be more elevated in tumour tissues, cancer cells overexpress TfR1 and STEAP3, while reduce FPN expression [16].

With regard to the $Fe^{2+}$ that integrates the LIP, it should be mentioned that it has to remain at a moderate low level, since it can be detrimental due to its redox ability. In Chapter 4 it was already highlighted that, through Fenton's chemistry, this cation can catalyze the production of $\cdot OH^-$ from $H_2O_2$, such as the generated during mitochondrial metabolism. Thereby, when the concentration of labile $Fe^{2+}$ is excessive and ROS are accumulated and cause undue lipid peroxidation, the cellular defense system can collapse and a Fe-dependent form of regulated death can take place: ferroptosis [19,20].

This type of oxidative cell death, which may account for PDA NPs intrinsic anti-tumour activity [21-23], was firstly described in 2012 by Dixon and colleagues. It can be distinguished from the other forms of regulated cell death (RCD) by several characteristic features, just like the diminution in size and the increased membrane density of the mitochondria [24].

Nowadays, ferroptosis has become the basis for the development of novel anti-tumour therapies. At the beginning, when Fe or Fe-based NPs started to be developed for cancer nanomedicine, they attracted the attention for magnetic resonance imaging (MRI), computed tomography (CT) and PPT thanks to their excellent magnetic targeting properties. Nonetheless, as more knowledge has been gained about the relationship between Fe metabolism and ferroptosis in cancer cells, this trend has changed, and these NPs have begun to be used with the aim of inducing this type of Fe-dependent cell death [25]. The vast majority of these NPs are SPIONs, which have been already developed to induced ferroptosis in different types of tumours, such as ovarian, brain and breast tumours [25-28]. However, several Fe-doped (silicon NPs, graphene oxide NPs…) and Fe-based nanomaterials (metal-organic-frameworks, polymer micelles…) capable of inducing ferroptosis can also be found in the literature [29], as well as some non-Fe-containing nanomaterials [25,29], such as silica and zinc NPs [30,31]. Likewise, the combination of these ferroptosis-inducing nanosystems with conventional chemotherapeutic agents in a whole is a

strategy that has been already employed by several research groups to enhance the therapeutic effect of conventional drugs [25,29].

Finally, among the different non-Fe-based NPs, some that have been precisely employed in recent days to induce ferroptosis in cancer cells are Fe-chelated PDA NPs. The great affinity of these NPs for different metal cations, including $Fe^{2+}$ and $Fe^{3+}$, was already demonstrated in the previous Chapter (page 159) [32], and was used, for instance, by Chen et al. and Dong et al. to design novel PDA ferroptosis-inducing NPs [33,34].

In the same manner, the ability of PDA NPs to chelate $Fe^{3+}$ has been taken into account in this thesis to enhance the ferroptosis that these NPs may be capable of producing by themselves. Thus, the toxicity to breast cancer and stromal cells of PDA NPs chelated with metals able to generate ROS was firstly analysed and compared [32]. Then, once it was proven that these NPs could have an interesting therapeutic effect, those that had greater targeted anti-tumour activity, i.e., the $Fe^{3+}$-chelated PDA NPs, were selected to perform further studies. Until then, in all the works carried out concerning the use of $Fe^{3+}$-chelated PDA NPs to induce ferroptosis [32-34], the pH value at which the $Fe^{3+}$ was loaded to PDA NPs was not given enough importance. However, it determines if $Fe^{3+}$ is a free cation or is forming ferric hydroxide ($Fe(OH)_3$) and, consequently, it could influence the therapeutic activity of the $Fe^{3+}$-chelated PDA NPs. For this reason, loading $Fe^{3+}$ to PDA NPs at different pH values and studying later their anti-tumour activity and selectivity was decided. Furthermore, DOX was also burdened to these PDA NPs to further enhance their antineoplastic activity by achieving a synergist effect. All the methods used to achieve these objectives, as well as the results obtained, have been detailed below.

## 5.2. Cytotoxicity of polydopamine nanoparticles loaded with transition metals capable of generating reactive oxygen species

As already mentioned, the ability of PDA NPs to load different metal cations was analyzed in the anterior Chapter, since it was suspected that it could be related to their intrinsic anti-tumour activity. PDA NPs were synthesized in a basic aqueous medium containing EtOH, and to assess their metal loading capacity at the endo/lysosomal pH (pH 4.5), they were mixed with solutions of different metal salts in acetate buffer. The initial metal concentration of these solutions was set at 70 ppm because, under the working conditions employed, no salt precipitation occurred at this concentration. As a result, it was shown that PDA NPs had the greatest affinity for $Ca^{2+}$, followed by $Fe^{3+}$ and $Cu^{2+}$, but also that PDA NPs were able to load significant amounts of other metal cations, such as $Fe^{2+}$, $Mn^{2+}$ and $Zn^{2+}$ (Figure 4.14.A, page 159) [32].

Subsequently, with the use of DFO and GSH, it was indirectly elucidated that the ability of PDA NPs to chelate the $Fe^{3+}$ existing in the late endo/lysosomes of the cancer cells could account for PDA anti-tumor activity through a ferroptosis process [21-23]. Therefore, with the aim of trying to enhance this type of RCD and target HER2+ breast cancer cells, PDA NPs were prepared and loaded with both $Fe^{2+}$ and $Fe^{3+}$ at the lysosomal pH to study and compare their cytotoxicity. Due to the importance of particle size [20], small PDA NPs of about 100 nm in diameter were synthetized in EtOH/$H_2O$(d) (28.57% (V/V), 140 mL) media containing 2.3% (V/V) of $NH_4OH$. Then, once characterized, PDA NPs were kept in agitation for 16 hours with solutions of $FeCl_2$ and $FeCl_3$ (70 ppm $Fe^{2+}$/$Fe^{3+}$) in acetate buffer. Moreover, PDA NPs were also mixed with $Cu^{2+}$ solutions of similar concentration, prepared from $CuCl_2$ [32]. The reason was that this cation, like Fe, is found in higher concentrations in malignant cells than in normal cells and, because of its redox potential, it is also capable of increasing the production of intracellular ROS through a Fenton-like reaction [35-37]. Thus, $Cu^{2+}$ loaded to PDA NPs was also thought to enhance their cytotoxicity, which was analyzed together with that of the PDA NPs loaded with $Fe^{2+/3+}$. For such purpose, $M^{n+}$-loaded PDA NPs were isolated by centrifugation after the adsorption process and were

washed through four centrifugation-redispersion cycles in PBS. In the last cycle, they were resuspended with a final concentration of approximately 2.4 mg/mL. Their cytotoxicity was evaluated by MTT assays, which were performed again with the BT474 and NIH/3T3 cell lines.

Foremost, once grown, BT474 cells were seeded into 24-well plates (10,000 cells/mL) and incubated for 24 hours to allow attachment. Next day, the medium in the wells was replaced by fresh supplemented DMEM containing the PDA NPs decorated (PDA NPs@$M^{n+}$) by $Fe^{2+}$, $Fe^{3+}$, $Cu^{2+}$ and, in addition, with $Fe^{3+}$ plus $Cu^{2+}$ to see if synergy between both metal cations took place. These NPs were administered in concentrations ranging from 0.010 to 0.130 mg/mL, and cells were incubated again for 24, 48 and 72 hours. After these times, BT474 cell survival rate was determined by means of the procedure that had been previously set-up to subtract PDA contribution to sample absorbance in MTT assays [17]. The $LD_{50}$ of each nanosystem for the breast carcinoma cell line was estimated after 48 hours of treatment. It was found to be 0.014, 0.016, 0.012 and 0.011 mg/mL PDA NPs@$M^{n+}$ when $M^{n+}$ represented $Fe^{2+}$, $Fe^{3+}$, $Cu^{2+}$ and $Fe^{3+}$ plus $Cu^{2+}$, respectively. As can be seen in **Figure 5.1.A**, all the PDA NPs@$M^{n+}$ obtained were notably toxic to BT474 cells. In this way, even the lowest concentrations managed to reduce the viability of breast cancer cells below 50% after 24 hours of treatment, and their survival rate was inferior to 25% in all cases once 72 hours elapsed [32].

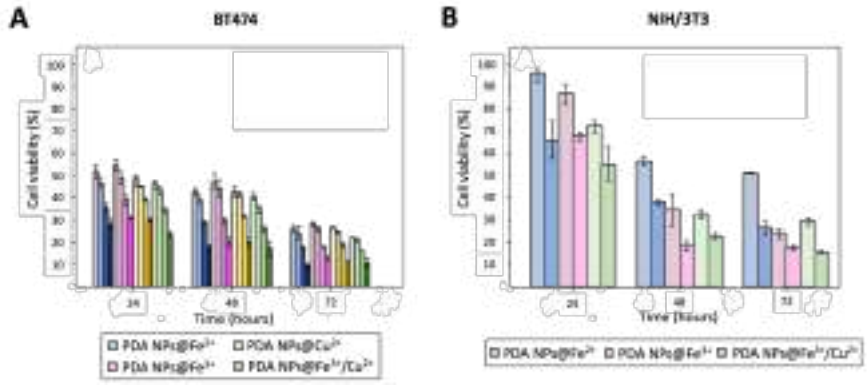


**Figure 5.1.** Viability rate of BT474 (**A**) and NIH/3T3 (**B**) cells after treatment with the PDA NPs loaded with $Fe^{2+}$, $Fe^{3+}$, $Cu^{2+}$, and $Fe^{3+}$ plus $Cu^{2+}$. The color gradient represents the increasing range of concentration used: 0.012, 0.031, 0.071 and 0.130 mg/mL for the

BT474 cell line, and 0.015 and 0.040 mg/mL for the NIT/3T3 one. Results shown are the average viability values ± SEM of three parallel measurements.

Once the results were obtained with the BT474 cell line, further MTT assays were carried out with NIH/3T3 cells. To do this, the steps detailed in the paragraph above were repeated again. Notwithstanding, fibroblasts were treated only with two intermediate concentrations (0.015 and 0.040 mg/mL) of the different PDA NPs@$M^{n+}$ given their great cytotoxicity to BT474 cells. The results obtained in these second viability assays have been summarized in **Figure 5.1.B**, where it can be observed that PDA NPs@$M^{n+}$ were not excessively toxic to normal cells after 24 hours. However, they considerably reduced their survival rate after 48 and 72 hours of treatment, especially at the highest concentration (0.040 mg/mL) [32]. Thereby, it was revealed that PDA NPs loaded with $Fe^{2+/3+}$ or/and $Cu^{2+}$ had a great potential therapeutic effect, but that further studies were needed in order to improve their tumour selectivity.

## 5.3. Cytotoxicity of ferric-chelated polydopamine nanoparticles as a function of the iron-loading pH

### *5.3.1. Loading of polydopamine nanoparticles with iron (III) at different pH values*

Precisely, with the aim of improving the tumour selectivity of the PDA NPs chelated with redox-active transition metals, carrying out subsequent studies with PDA NPs@$Fe^{3+}$ was decided. The reason was that, as already mentioned, many malignant cells, such as breast cancer cells [38], overexpress TfR1 [16]. Since this receptor binds specifically to the complexes formed by $Fe^{3+}$ and Tf, it was expected that the endocytic rate of $Fe^{3+}$-loaded nanosystems was higher and also more specific than that of the other PDA NPs@$M^{n+}$ [33,34].

On the other hand, in the previous point, it was decided to determine the cytotoxicity of the PDA NPs@$M^{n+}$ after loading the different $M^{n+}$ at pH 4.5 because it was the pH of the late endo/lysosomes, in which it had been verified that PDA NPs were internalized (Chapter 4, page 156)

[21]. Likewise, in other works in which $Fe^{3+}$-chelated PDA NPs were used to induce ferroptosis, $Fe^{3+}$-loading was carried out at alkaline pH values (pH > 8) [33,34]. Nevertheless, at both pH 4.5 and pH 8.0 - 10.0, most of the $Fe^{3+}$ existing in aqueous solutions is not found as free cation, but forming $Fe(OH)_3$. In order to verify whether loading $Fe^{3+}$ at one pH value or another conditioned the effectiveness and selectivity of the PDA NPs@$Fe^{3+}$, performing this adsorption at various pH values and comparing the cytotoxicity results obtained was decided. $Fe(OH)_3$ starts to be generated at pH 2.7 at room temperature [39], so it was decided to chelate PDA NPs with $Fe^{3+}$ at a lower pH value (2.5), at a slightly higher pH value (3.1) and, again, at pH 4.5 [40].

For this purpose, PDA NPs were synthesized in a basic aqueous medium containing EtOH (28.57% V/V) and $NH_4OH$ (2.9% V/V) following the usual procedure [21-23,32]. Oxidative polymerization of DA was allowed to run for 24 hours and the PDA NPs obtained were washed through four centrifugation-redispersion cycles in $H_2O$(d). They were finally resuspended in a concentration of 2 mg/mL and, before loading $Fe^{3+}$, PDA NPs were characterized by DLS and TEM. Their hydrodynamic diameter was found to be 154.2 ± 28.5 nm (PDI = 0.012) (**Figure 5.2.A**), while PDA NP average size determined from different TEM images turned out to be 111.2 ± 16.2 nm (**Figure 5.2.B**) [40].

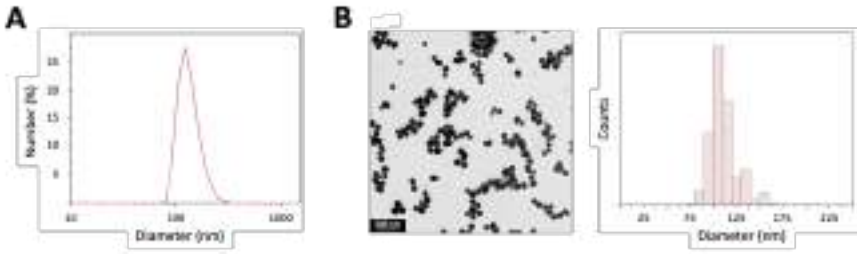


**Figure 5.2**. (**A**) DLS number distribution and (**B**) TEM image and size-range histogram of the PDA NPs that were later charged with $Fe^{3+}$ at three different pH values.

Then, once characterized, PDA NPs were loaded with $Fe^{3+}$ by mixing them (1 mL) with solutions (20 mL) of $FeCl_3$ prepared in buffers of different pH. On this occasion, the initial $Fe^{3+}$ concentration of the $FeCl_3$ solutions was set at 30 ppm. In previous assays, when this concentration was 70 ppm, PDA NPs@$Fe^{3+}$ turned out to be too toxic. Since it had been

already observed that loading PDA NPs with an initial $Fe^{3+}$ concentration of 30 ppm did not affect their morphology so noticeably (Figure 4.21.C, page 174) [23], it was decided to better work with this lower concentration. In this way, 30 ppm $Fe^{3+}$ solutions were prepared in citrate/NaOH buffer (0.1 M), whose pH was adjusted by dropping HCl (0.1 M) to load $Fe^{3+}$ at pH 2.5 and 3.1. However, to charge $Fe^{3+}$ to PDA NPs at pH 4.5, $FeCl_3$ was dissolved in acetate buffer (0.4 M), just as it had been done in the former point [32]. In all cases, PDA NPs were kept stirred within the $FeCl_3$ solutions at 100 rpm at room temperature, but the adsorption process was allowed to run for 3 hours at pH 2.5 and 3.1, while it was allowed to run overnight at pH 4.5 [40]. This time difference was due to the fact that very acidic pH values can alter PDA chemical structure and [41], as a consequence, $Fe^{3+}$-loading at pH 2.5 and 3.1 could not be extended for longer.

To determine the $Fe^{3+}$-adsorption efficiency at the different pH values, all PDA NPs@$Fe^{3+}$ were isolated by centrifugation (11,000 rpm, 10 minutes) and the metal concentration in the supernatants was analyzed by ICP-OES. As a result, it was observed that when $Fe^{3+}$ was loaded at pH 4.5, PDA NPs were able to chelate 100 mg/g NPs (equivalent to 13 mg $Fe^{3+}$/L). Nonetheless, when the adsorption process was carried out at pH 2.5 and 3.1, PDA NPs were capable of chelating 16 and 15 mg $Fe^{3+}$/g NPs (equivalent to 2.3 and 2.2. mg $Fe^{3+}$/L), respectively (**Table 5.1**). Since the critical pH at which $Fe(OH)_3$ starts to be generated is 2.7 [39], practically all the $Fe^{3+}$ adsorbed at pH 2.5 was the free cation. At pH 3.1, since it was a value close to 2.7 but slightly higher than it, a small part of the $Fe^{3+}$ loaded to the PDA NPs would also be $Fe(OH)_3$. At last, despite the fact that $Fe^{3+}$-chelation was much more remarkable at pH 4.5, possibly because the process was allowed to run for longer time, the vast majority of $Fe^{3+}$ would be $Fe(OH)_3$ at this pH value. In this way, taking into account that $Fe(OH)_3$ solubility product constant (Ksp) is 37.0 at room temperature [39], only $3.52 \cdot 10^{-5}$ mg/L $Fe^{3+}$ would be free $Fe^{3+}$ (**Equation 5.1**) [40].

$$\mathrm{Fe}(OH)_3 \downarrow \text{É } Fe^{3+} + 3OH^- \qquad \textbf{(Equation 5.1)}$$

$$[Fe^{3+}][OH^-]^3 = 10^{-37}$$

$$[Fe^{3+}] = [OH^-]^3 = a \rightarrow a^4 = 10^{37}$$

$$a = \sqrt[4]{10^{-37}} = 10^{-9.2}\, M = 3.52 \cdot 10^{-5}\, mg/L$$

Subsequently, all PDA NPs@$Fe^{3+}$ were characterized by TEM imaging to verify if $Fe^{3+}$-chelation changed their morphology. TEM samples were prepared in the same way as those of unloaded PDA NPs. The images acquired have been included in **Figure 5.3.A**. As can be seen, the adsorption of $Fe^{3+}$ made chelated PDA NPs look spongier than bare PDA NPs, as in previous assays [23,32]. When this adsorption process was carried out at pH 4.5, this fact was more remarkable than when it was performed at pH 2.5 and 3.1 [40].

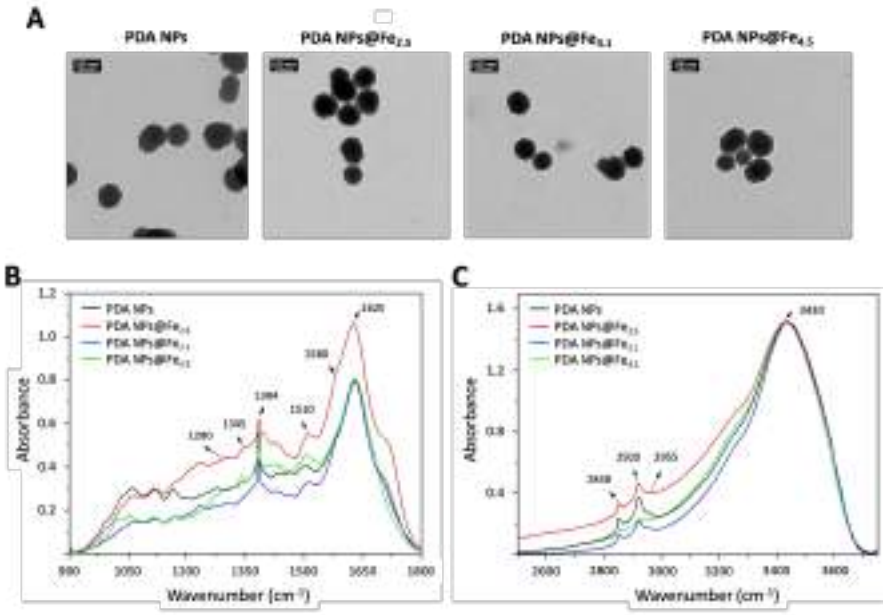


**Figure 5.3.** TEM images (**A**) and IR spectra in the 900-1800 $cm^{-1}$ (**B**) and 2500-3700 $cm^{-1}$ (**C**) ranges of bare and the different $Fe^{3+}$-chelated PDA NPs.

To finish with PDA NPs@$Fe^{3+}$ characterization, their IR spectra were obtained and compared to that of the bare PDA NPs in the 4000 - 400 $cm^{-1}$ wavelength range to ascertain whether $Fe^{3+}$-loading caused any modification in PDA NP chemical structure. All spectra were normalized to be able to compare the intensity of the main bands, which were once again assigned according to previous melanin characterizations [32]. After $Fe^{3+}$-binding, the principal changes in the 900-1800 $cm^{-1}$ range occurred in the bands at 1280 and 1620 $cm^{-1}$ (**Figure 5.3.B**). These bands may respectively include the C-OH stretching in a phenol ring and the C=O (non-carboxylic

acid) stretching, and their relative intensity was higher for the PDA NPs loaded with $Fe^{3+}$ at pH 2.5 (PDA NPs@$Fe_{2.5}$) than for the other PDA NPs. Otherwise, in the 2500-3700 $cm^{-1}$ range (**Figure 5.3.C**), the main modifications occurred at 2848, 2929 and 2955 $cm^{-1}$. These bands may correspond to the different vibrational modes of aliphatic groups and decreased in intensity for the PDA NPs with $Fe^{3+}$ chelated at pH 4.5. Adversely, they were broadened for the PDA NPs@$Fe_{2.5}$ [40].

### *5.3.2. Polydopamine nanoparticles release of iron (III) and loading of calcium (II) in the endo/lysosomal environment*

PDA NP ability to form stable complexes through coordination effects with $Fe^{3+}$ cations was already described in the previous Chapter [32,42]. Likewise, it was already proven that the two adjacent hydroxyl groups coordinating with $Fe^{3+}$ on the PDA benzene ring may competitively combine with protons in acidic environments, such as that found inside the late endo/lysosomes. Thus, this phenomenon may stimulate $Fe^{3+}$-release from the PDA NPs@$Fe^{3+}$ in these acidic organelles. By contrast, $Fe^{3+}$-release could be considerably lower at physiological pH (7.4) [33,34].

Besides, it was also demonstrated in the preceding Chapter that PDA NP affinity for $Ca^{2+}$ was even greater than for $Fe^{3+}$ (Figure 4.14, page 159) [32]. This cation is also abundant in the late endo/lysosomes, and previous investigations showed that it could mediate the deprotonation of the PDA catechol group. Since this catechol group was also believed to account for $Fe^{3+}$ complexation [42,43], it was though that $Ca^{2+}$ could also stimulate $Fe^{3+}$-release from the PDA NPs in the endo/lysosomes, along with the acidic pH of these organelles.

In this way, in order to verify this hypothesis, $Fe^{3+}$-release from all PDA NPs@$Fe^{3+}$ was analysed in a lysosome-simulator buffer (pH 4.5), in which $Ca^{2+}$ was dissolved in a concentration (20 ppm) similar to that believed in these organelles [42]. The different PDA NPs@$Fe^{3+}$ (2 mg/mL, 1 mL) were mixed with $CaCl_2$ solutions (20 mL) prepared in the mentioned buffer ($C_6H_8O_7$ 0.1 M, $Na_2HPO_4$ 0.2 M, pH 4.5) [44], and the resulting suspensions were kept in agitation (100 rpm) for 48 hours. This period of time was selected after having verified previously that the anti-tumour

activity of the PDA NPs was more noticeable after 48 hours (Figure 5.1, page 238). After such time, PDA NPs, then loaded with $Fe^{3+}$ and $Ca^{2+}$, were isolated by centrifugation (11,000 rpm, 10 minutes). The concentration of both cations existing in the supernatants was determined by ICP-OES to find out the amount of $Fe^{3+}$ released and the amount of $Ca^{2+}$ adsorbed [40].

**Table 5.1**. Amount of the $Fe^{3+}$ released and the $Ca^{2+}$ adsorbed in the different PDA NPs@$Fe^{3+}$ suspended in a lysosome-simulator buffer (pH 4.5) containing $Ca^{2+}$. Percentage values regarding $Fe^{3+}$-release were calculated taking into account the amount of this cation that was loaded initially, and those regarding $Ca^{2+}$ adsorption were calculated taking into account the $Ca^{2+}$ initial buffer concentration (20 ppm).

| pH | $Fe^{3+}$ loaded (q, mg/g) | $Fe^{3+}$ released (q, mg/g) | $Fe^{3+}$released (%) | $Ca^{2+}$ loaded (q, mg/g) | $Ca^{2+}$ loaded (%) |
|---|---|---|---|---|---|
| 2.5 | 16 | 6 | 38 | 21 | 13 |
| 3.1 | 15 | 4 | 30 | 20 | 13 |
| 4.5 | 100 | 75 | 75 | 16 | 10 |

As can be seen from the data collected in **Table 5.1**, all PDA NPs@$Fe^{3+}$ were able to release $Fe^{3+}$ and adsorb $Ca^{2+}$ after 48 hours in the lysosome-simulator environment. Regarding $Fe^{3+}$-release, it should be noted that it was greater from PDA NPs@$Fe_{4.5}$ than from PDA NPs@$Fe_{2.5}$ and PDA NPs@$Fe_{3.1}$. This fact could be due to $Fe^{3+}$ small ionic radius and charge, which may hinder the release of the free cation from the two mentioned PDA NPs@$Fe^{3+}$. Conversely, $Fe(OH)_3$ molecules, which were expected to be loaded to a greater extent at pH 4.5, are much larger and have neutral charge, and this could advantage their release, along with having loaded more $Fe^{3+}$. On the other hand, differences in $Ca^{2+}$-adsorption capacity were not so marked among the different PDA NPs@$Fe^{3+}$, but it was shown that this cation was loaded when $Fe^{3+}$ was released from the NPs. Herein, this phenomenon brought about that an ionic displacement may contribute to release $Fe^{3+}$ from the PDA NPs@$Fe^{3+}$ in the late endo/lysosomes, together with the protons existing in these organelles [40].

### *5.3.3. Cytotoxicity of polydopamine nanoparticles loaded with iron (III) at different pH values*

With the aim of finding out whether $Fe^{3+}$-chelation at pH values closer to the critical one at which $Fe(OH)_3$ starts to be formed conditioned the cytotoxicity of the PDA NPs@$Fe^{3+}$, novel MTT assays were performed with BT474 and HS5 cells. Breast cancer cells, like those of other tumours, have an altered Fe homeostasis that enhances their growth, survival and metastasis [45,46]. For instance, they overexpress TfR1 to enhance $Fe^{3+}$ uptake and ferritin to store more $Fe^{2+}$ [46]. Furthermore, as have been described along the entire project, BT474 cells also overexpress HER2, and several researchers had observed that a complex formed by Tf and artemisin (a ferroptosis-inducing compound) was capable of declining HER2 expression in this cell line [47]. Thus, all PDA NPs@$Fe^{3+}$ were expected to reduce BT474 cell viability to a greater extent than that of HS5 cells.

In order to verify this and elucidate if there were differences in PDA NP anti-tumour activity and selectivity according to the $Fe^{3+}$-loading pH, BT474 and HS5 cell were seeded into 24-well plates (12,000 cells/well) once grown. After 24 hours, the culture medium in the wells was replaced by DMEM containing PBS (control) and 0.035 mg/mL of the different PDA NPs@$Fe^{3+}$, as well as of bare PDA NPs. This concentration was chosen because it showed to be able to notably reduce malignant cell viability, but without significantly affecting the survival rate of normal cells in Chapter 4 (page 179) [23]. After treatment, cells were incubated for 24, 48 and 72 hours, and their viability was determined, as always, by applying the procedure described for carrying out MTT assays with PDA-based NPs [21,40]. Results obtained have been summarized in **Figure 5.4**.

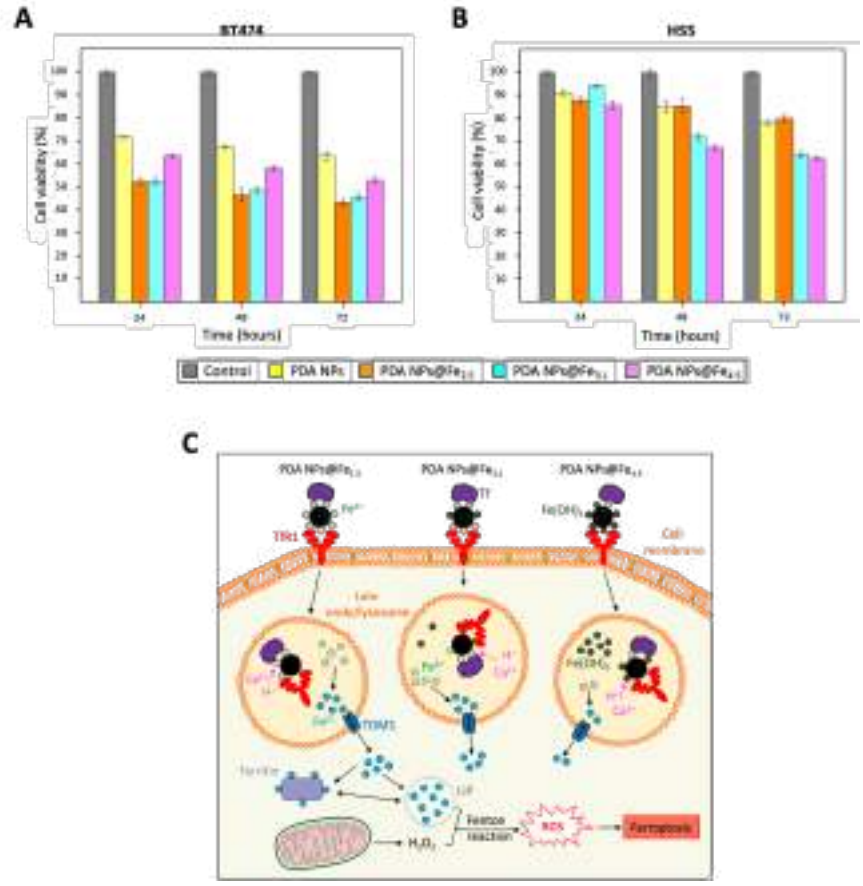


**Figure 5.4.** (**A-B**) Viability results obtained after the performance of MTT assays with the BT474 and HS5 cell lines, which were treated with bare PDA NPs and the different PDA NPs@$Fe^{3+}$ synthesized (0.035 mg/mL). Results shown are again the average viability values ± SEM of three parallel experiments; (**C**) Graphical explanation of why the pH at which $Fe^{3+}$ was charged on PDA NPs may condition their cytotoxicity.

It general, it could be observed that all PDA NPs@$Fe^{3+}$ reduced BT474 survival rate in greater order than bare PDA NPs (**Figure 5.4.A**). In this way, PDA NPs@$Fe_{4.5}$ treatment reduced breast cancer cell viability by almost a half (to 52.8 ± 1.3%) after 72 hours, i.e., 10% more than unloaded PDA NPs. This cytotoxicity increase was close to 20% when the other two PDA NPs@$Fe^{3+}$ were administered. Thereby, they reduced the survival rate of the BT474 cell line to 43.3 ± 1.4% (PDA NPs@$Fe_{2.5}$) and to 45.6 ± 1.5% (PDA NPs@$Fe_{3.1}$) at the end of the assays, while 63.6 ± 1.9% BT474 cells were alive 72 hours after treatment with bare PDA NPs [40].

Regarding HS5 cell viability (**Figure 5.4.B**), as expected, it was not as affected as that of tumour cells after treatment with any of the PDA NPs@$Fe^{3+}$. Nevertheless, as was the case with the BT474 cell line, differences could be also seen as function of the $Fe^{3+}$-adsorption pH. When PDA NPs@$Fe_{2.5}$ were used, HS5 survival rate was close to 90, 85 and 80%, which were values very similar to those obtained after treatment with uncharged PDA NPs. Thus, PDA NPs@$Fe_{2.5}$ reduced normal cell viability by 35-40% less compared to that of breast cancer cells. However, this selectivity was less remarkable for PDA NPs@$Fe_{3.1}$ and PDA NPs@$Fe_{4.5}$, which decreased HS5 survival rate most notably, especially after 48 and 72 hours of treatment. In this manner, when fibroblasts were treated with PDA NPs@$Fe_{3.1}$, 40-20% more of them survived compared to BT474 cells, and this viability difference between both cell lines was 20-10% when PDA NPs@$Fe_{4.5}$ were employed [40].

Consequently, the PDA NPs@$Fe^{3+}$ with the most remarkable therapeutic activity were the PDA NPs@$Fe_{2.5}$, which were also the less toxic to normal cells. On the contrary, PDA NPs@$Fe_{4.5}$ were those that showed an anti-tumour activity more similar to that of the uncharged PDA NPs and reduced the most the survival rate of stromal cells. As said in the two previous points, these last NPs practically only adsorbed $Fe(OH)_3$, while PDA NPs@$Fe_{2.5}$ were chelated with $Fe^{3+}$ as free cation. Thus, since free $Fe^{3+}$ is the one that binds to Tf and is endocyted and reduced in the late endo/lysosomes to the $Fe^{2+}$ that can later participate in the Fenton reaction [16,19], it made sense that the PDA NPs@$Fe^{3+}$ that adsorbed more $Fe^{3+}$ as free cation were the most efficient and selective, even despite having adsorbed less metal amount (**Figure 5.4.C**) [40].

## 5.4. Enhancement of the therapeutic activity of ferric-chelated polydopamine nanoparticles with doxorubicin

### *5.4.1. Doxorubicin adsorption on bare and ferric-chelated polydopamine nanoparticles*

As already described in the introduction, targeting the unique biochemical alterations of cancer cells can constitute a feasibly strategy to prevent the apparition of MDR. In this manner, metabolism inhibitors have been effective anti-tumour agents for decades [48]. Notwithstanding, these inhibitors are susceptible to many endogenous factors when administered alone [49]. For this reason, numerous strategies are based on combining these agents with chemotherapeutic drugs to both avoid this drawback while enhancing drug anti-tumour action, improving patients' response [50].

In the specific case of the ferroptosis-inducing nanotherapies, one of the drugs that they occasionally transport is DOX [49,51-52]. This anthracycline is widely used in the clinical setting due to its efficacy in fighting a wide range of cancers, both solid tumours and haematological diseases [53,54]. Unfortunately, despite being highly effective, DOX is not selective to cancer cells. Its most prominent adverse effect is myocardial injury, which is a major dose-limiting factor because, once developed, carries a poor prognosis and is frequently fatal [54,55].

The mechanisms of DOX therapeutic activity on tumour cells are different from those that account for its cardiotoxicity. On one hand, its anti-malignancy effects are triggered by DNA intercalation, leading to DNA damage and apoptosis induction. On the other hand, DOX cardiotoxicity is ascribed to an increased oxidative stress, which is consequence of a Fe overload in the mitochondria and, thus, to a ferroptosis process mediated by the Fenton chemistry [55-57].

Precisely for this reason, DOX can be found loaded to various ferroptosis-inducing nanoparticles in the literature [51,52], and was also charged on PDA NPs@$Fe^{3+}$ in the current project to achieve a synergist effect with the $Fe^{3+}$ chelated. Likewise, to verify that this synergy took

place, this anthracycline was also adsorbed to bare PDA NPs to make comparisons [40].

In this manner, with the purpose of later carrying out viability assays, PDA NPs and all the different PDA NPs@$Fe^{3+}$ were first washed through five centrifugation-redispersion cycles in PBS. NPs were resuspended in this saline buffer in a final concentration of 2 mg/mL. Then, they were mixed (250 µl) with three different volumes of a DOX stock solution to obtain drug working concentrations of 0.3, 0.6 and 1 µM. Since DOX $LD_{50}$ for the BT474 cell line was found to be 1 µM [58], employing a solution of this concentration to charge DOX on PDA NPs and PDA NPs@$Fe^{3+}$ was decided, as well as employing two additional lower concentrations. The adsorption process, which was carried out in duplicate, was allowed to run overnight in dark conditions, keeping NPs in orbital shaking (100 rpm). The reason why the process was done in duplicate was that some PDA NPs were isolated by centrifugation (13,500 rpm, 7 minutes) and resuspended in PBS (2 mg/mL) next day, while others were kept in suspension when the non-charged DOX. There are more and more clinical trials in which some nanotherapies are administered with free conventional anticancer drugs to achieve a plasma drug concentration peak followed by a more sustained release [59-61], and this was the aim of administering PDA NPs loaded with DOX (PDA NPs@DOX) with unbound DOX. Thereby, two different types of cytotoxicity assays were carried out. DOX concentrations in the suspensions of the non-isolated PDA NPs (PDA NPs@$DOX^{W}$ and PDA NPs@$Fe^{3+}$/$DOX^{W}$) were expected to be 0.3, 0.6 and 1 µM, while the amount of drug adsorbed in those NPs that were isolated (PDA NPs@$DOX^{A}$ and PDA NPs@$Fe^{3+}$/$DOX^{A}$) was determined by difference. DOX concentration was quantified in the resulting supernatants by UV-Vis spectrophotometry, measuring the absorbance of the samples at 480 nm. The supernatant of the DOX-uncharged PDA NPs was used as blank, and DOX concentration was determined from a previously made calibration curve with a dilution series [40]. Results obtained were those of the **Table 5.2**.

**Table 5.2**. Amount of DOX charged in PDA NPs and the different PDA NPs@$Fe^{3+}$ as a function of the DOX initial concentration employed in the adsorption process. Results are expressed as ng DOX/mg PDA NPs.

| Initial [DOX] | PDA NPs | PDA NPs@$Fe_{2.5}$ | PDA NPs@$Fe_{3.1}$ | PDA NPs@$Fe_{4.5}$ |
|---|---|---|---|---|
| **0.3 μM** | 21.4 ng/mg | 16.8 ng/mg | 19.0 ng/mg | 18.8 ng/mg |
| **0.6 μM** | 42.1 ng/mg | 33.2 ng/mg | 37.3 ng/mg | 35.7 ng/mg |
| **1 μM** | 57.9 ng/mg | 51.7 ng/mg | 55.8 ng/mg | 54.6 ng/mg |

Among the different PDA NPs, there were not remarkable gaps in terms of DOX adsorption capacity, although it was noticed that PDA NPs@$Fe^{3+}$ were capable of charging a little less amount of the anthracycline than bare PDA NPs [40].

### *5.4.2. Cytotoxicity of bare polydopamine nanoparticles charged with doxorubicin*

Subsequently, the cytotoxicity of the naked PDA NPs charged with different concentrations of DOX was first investigated through further MTT assays, which were again performed with the BT474 and HS5 cell lines. The same procedure as the one carried out to study the cytotoxicity of the PDA NPs@$Fe^{3+}$, which has been detailed above, was followed. This time, BT474 and HS5 cells were treated with the different PDA NPs@$DOX^{W}$ and PDA NPs@$DOX^{A}$ (0.035 mg/mL), as well as with equivalent concentrations of free DOX (0.3, 0.6 and 1 μM). Cell viability rates were anew determined each 24 hours for a total of 72 hours [21], performing absorbance measurements in triplicate [40]. Data obtained have been collected in **Figure 5.5**.

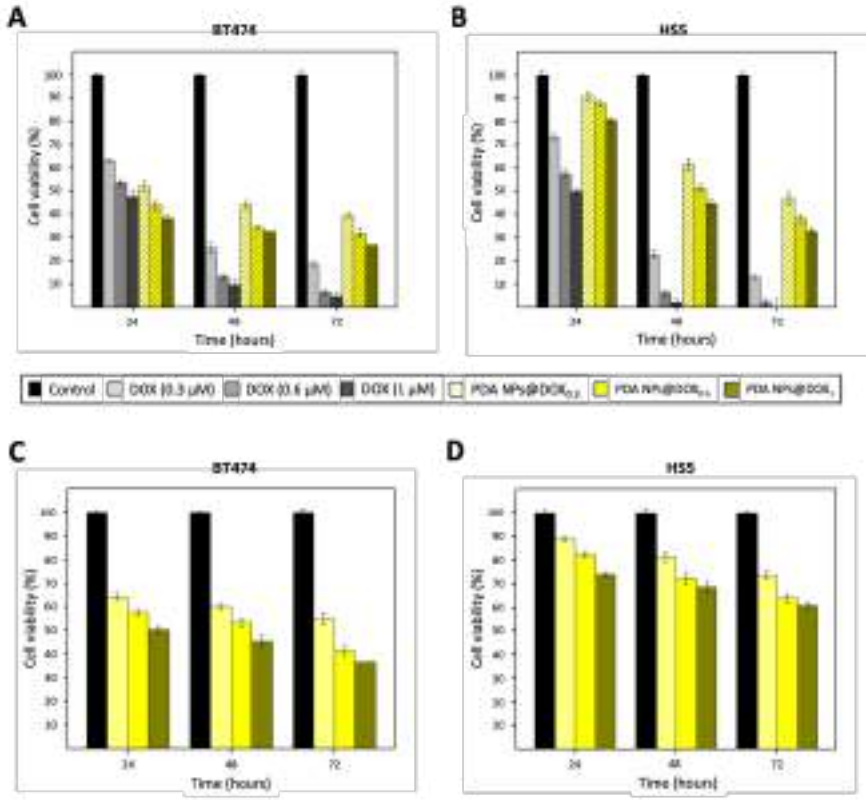


**Figure 5.5.** Viability rates of BT474 (**A-C**) and HS5 (**B-D**) cells after treatment with free DOX (0.3 – 1 μM) and PDA NPs@$DOX_{0.3}$, PDA NPs@$DOX_{0.6}$ and PDA NPs@$DOX_1$ (0.035 mg/mL). The subscript refers to the initial DOX concentration used in the adsorption process. Bars with the line pattern represent the viability results that were obtained with the PDA NPs@$DOX^W$ (**A-B**), while the results obtained with the PDA NPs@$DOX^A$ were those of the empty bars (**C-D**). Anew, all the results shown are the average viability values ± SEM of three parallel experiments.

Focusing first on the results obtained after BT474 cell treatment with all the PDA NPs@DOX that were administered together with the unbound DOX (**Figure 5.5.A**), it should be noted that this treatment was really effective. All PDA NPs@$DOX^W$ achieved to reduce breast cancer survival rate below 50% after 24 hours and, when 72 hours elapsed, they decreased BT474 cell viability by 60-75%, depending on DOX concentration. Furthermore, comparing the results of the PDA NPs@$DOX^W$ with those of the equivalent concentrations of free DOX, it was observed

that these NPs contributed to achieve a more-sustained drug release. The drawback was that, as can be seen in **Figure 5.5.B**, PDA NPs@DOX$^{W}$ also reduced the viability of the stromal cells in a similar way to that of the BT474 cells after 48 and 72 hours of treatment. Nonetheless, these NPs were certainly much less toxic than the free DOX, so that its adsorption on PDA NPs could be a good strategy to partially reduce its severe adverse effects [40].

On the other hand, when treatment of breast cancer cells was performed with the isolated PDA NPs charged with DOX (**Figure 5.5.C**), their survival rate was not so affected as with the PDA NPs@DOX$^{W}$, as expected from administering lower drug concentrations. However, this did not mean that these PDA NPs were not effective. Quite the contrary, since they reduced BT474 viability by 65-45% after 72 hours, depending on the amount of DOX charged in them. What's more, when PDA NPs@DOX$^{A}$ were employed for HS5 cell treatment (**Figure 5.5.D**), it was noticed that these NPs were not so toxic to normal cells, whose viability was 20-25% higher than that of cancer cells at all times analysed. Therefore, the difference in the antitumor activity of these nanoparticles with respect to the PDA NPs@DOX$^{W}$ could compensate if their selectivity was taken into account [40].

### *5.4.3. Cytotoxicity of ferric-chelated polydopamine nanoparticles charged with doxorubicin*

Otherwise, final MTT assays were performed in a similar manner with the BT474 and HS5 cell lines to analyse the anti-tumour activity and selectivity of the different PDA NPs@$Fe^{3+}$ charged also with DOX (PDA NPs@$Fe^{3+}$/DOX). Again, both types of cells were treated with 0.035 mg/mL of the non-isolated (PDA NPs@$Fe^{3+}$/DOX$^{W}$) and isolated (PDA NPs@$Fe^{3+}$/DOX$^{A}$) PDA NPs charged with $Fe^{3+}$ at the different pH values and with different DOX concentrations [40]. Results obtained this time were those that can be found in **Figure 5.6**.

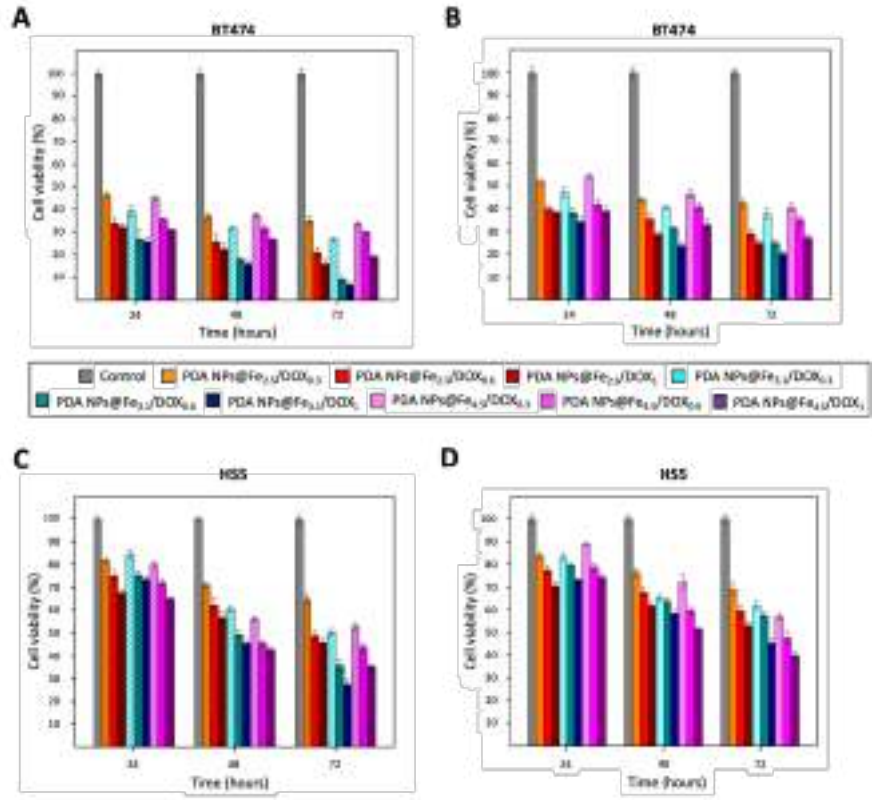


**Figure 5.6.** Viability rates of BT474 (**A-B**) and HS5 (**C-D**) cells after treating them with all the different PDA NPs@$Fe^{3+}$/DOX (0.035 mg/mL). Results of graphs (**A-C**) (bars with the line pattern) were obtained using PDA NPs@$Fe^{3+}$/$DOX^{W}$ for treatment, while PDA NPs@$Fe^{3+}$/$DOX^{A}$ were employed to get graphs (**B-D**) (empty bars). The results shown are the average viability values ± SEM of three parallel experiments.

Regardless of whether BT474 treatment was carried out with PDA NPs@$Fe^{3+}$/$DOX^{W}$ or PDA NPs@$Fe^{3+}$/$DOX^{A}$, differences in the cell viability rate could be appreciated again as a function of the $Fe^{3+}$-loading pH. PDA NPs@$Fe_{3.1}$/DOX were the ones with the most remarkable anti-tumour activity, maybe because they had been shown to be capable of adsorbing the highest amount of DOX. PDA NPs with the second more marked therapeutic effect were the PDA NPs@$Fe_{2.5}$/DOX, despite being the ones that charged less amount of the anthracycline. Possibly, this was because the $Fe^{3+}$ adsorbed in these NPs was the free cation and not $Fe(OH)_3$. At last, PDA NPs@$Fe_{4.5}$/DOX, despite having adsorbed slightly lower amounts of

DOX than the PDA NPs@$Fe_{3.1}$/DOX, reduced BT474 cell viability in a lesser extent. Anyway, all PDA NPs@$Fe^{3+}$/DOX turned to be very effective. After 72 hours of treatment, PDA NPs@$Fe^{3+}$/$DOX^{W}$ reduced malignant cell survival rate to 35-7%, in a DOX concentration-dependent manner and according to the $Fe^{3+}$-loading pH (**Figure 5.6.A**). In the case of treatment with the PDA NPs@$Fe^{3+}$/$DOX^{A}$, this percentage range was 42-20% (**Figure 5.6.B**) [40].

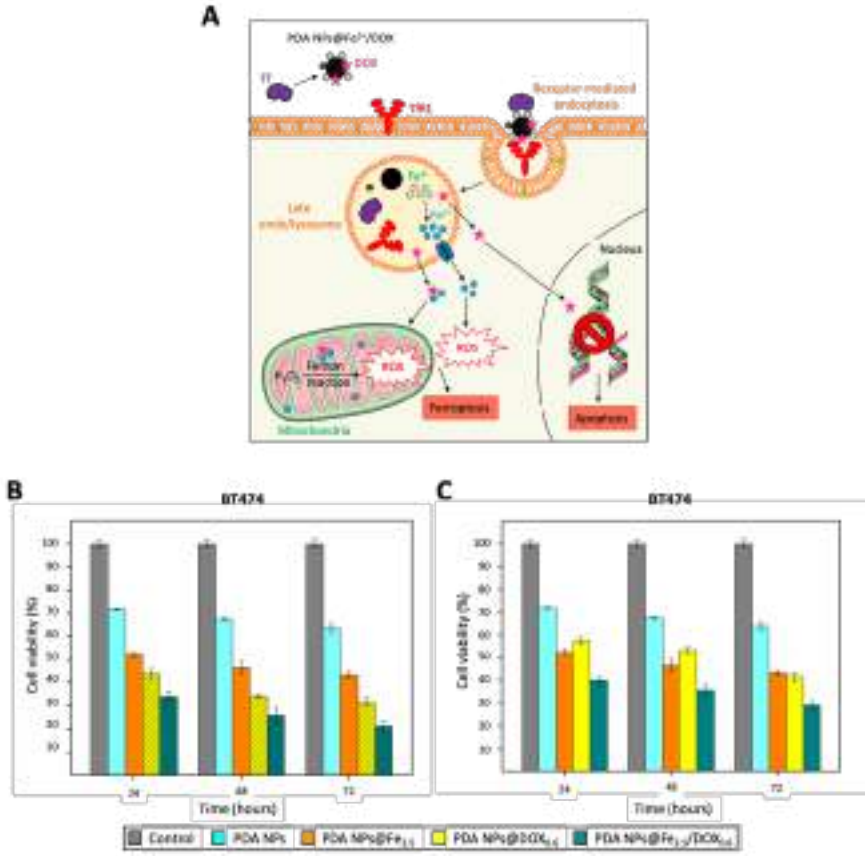


**Figure 5.7.** (**A**) Graphical explanation of how the synergy between $Fe^{3+}$ and DOX may occur after treatment with PDA NPs@$Fe^{3+}$/DOX; (**B-C**) Comparative BT474 viability rates obtained after treatment with bare PDA NPs, PDA NPs@$Fe_{2.5}$, PDA NPs@$DOX_{0.6}$ and PDA NPs@$Fe_{2.5}$/$DOX_{0.6}$ (0.035 mg/mL). Again, bars with the line pattern represent the viability values obtained with the PDA NPs@$DOX_{0.6}{}^{W}$/PDA NPs@$Fe_{2.5}$/$DOX_{0.6}{}^{W}$ (**B**), while the results obtained with the PDA NPs@$DOX_{0.6}{}^{A}$/PDA NPs@$Fe_{2.5}$/$DOX_{0.6}{}^{A}$ are those of empty bars (**C**). The results shown are the average viability values ± SEM of three parallel experiments.

Besides, PDA NPs loaded with both $Fe^{3+}$ and DOX, showed more remarkable anti-tumour activity than the PDA NPs charged only $Fe^{3+}$ or DOX. In this way, PDA NPs@$Fe^{3+}$/DOX were able to further reduce BT474 cell viability compared to PDA NPs@$Fe^{3+}$ or PDA NPs@DOX, and this brought out that there was a synergist effect between the metal cation and the anthracycline (**Figure 5.7.A**). To facilitate the visualization of this fact, viability rate vales obtained after treating BT474 cells with bare PDA NPs, PDA NPs@$Fe_{2.5}$, PDA NPs@$DOX_{0.6}$ and PDA NPs@$Fe_{2.5}$/$DOX_{0.6}$ have been collected in **Figure 5.7.B-C**. For instance, focusing on the results got after 48 hours of treatment, it could be noticed that PDA NPs@$Fe_{2.5}$/$DOX_{0.6}^{W}$ reduced BT474 viability by about 10% more than PDA NPs@$Fe_{2.5}$, and 20% more than PDA NPs@$DOX_{0.6}^{W}$ (**Figure 5.7.B**). Likewise, when breast cancer cells were treated with the isolated PDA NPs (**Figure 5.7.C**), PDA NPs@$Fe_{2.5}$/$DOX_{0.6}^{A}$ were found to be 10 and 18% more efficient in reducing BT474 viability than the PDA NPs@$Fe_{2.5}$ and PDA NPs@$DOX_{0.6}^{A}$, respectively [40].

Finally, in addition to being more effective, all PDA NPs@$Fe^{3+}$/DOX also demonstrated certain selectivity, since when normal cells were treated with them, their viability was 15-40% greater than that of the HER2+ breast malignant cells (**Figure 5.6.C-D**). The most selective NPs were the PDA NPs@$Fe_{2.5}$/DOX, followed by the PDA NPs@$Fe_{3.1}$/DOX and the PDA NPs@$Fe_{4.5}$/ DOX. Precisely, PDA NP content in free $Fe^{3+}$ and not in $Fe(OH)_3$ also followed this trend. Therefore, the results suggested that the pH value at which the $Fe^{3+}$-chelation was performed may be important to determine $Fe^{3+}$ state and, consequently, the endocytosis of the PDA NPs@$Fe^{3+}$, mediated by Tf and TfR1. Since these proteins are overexpressed in malignant phenotypes but not in normal tissues [62], this overexpression may sensitize cancer cells to ferroptosis by increasing the endocytosis rate of the nanosystems chelated with $Fe^{3+}$ [19,34], while guaranteeing certain tumour selectivity [40].

### *5.4.4. In vitro assessment of reactive oxygen species production after treatment with doxorubicin and the different ferric-chelated polydopamine nanoparticles*

To close this chapter, it was verified that treatment with both free DOX (0.3 µM) and the different PDA NPs@$Fe^{3+}$ (0.035 mg/mL) could increase ROS production through a ferroptosis process in cancer cells. Thus, the intracellular generation of radicals was evaluated by flow cytometry 48 hours after treating BT474 cells with the mentioned therapies, using a ROS-sensitive probe. As described in the manufacturer's instructions, treated BT474 cells were harvested and CellROX® Deep Red was added (5 µM, 4 µl) to cellular suspensions ($10^6$ cells/mL, 1.5 mL). Cells were incubated for 45 minutes at 37°C and then, Sytox® Blue, which allows to differentiate death cells, was incorporated (1 µM, 2 µl) to the suspensions. BT474 cells were incubated for a further 15 minutes at 37°C [63], and samples were acquired (at least 50,000 events) by the Cytometry Facility-NUCLEUS of the University of Salamanca upon excitation with 644 (CellROX®) and 444 (Sytox®) nm light. Median values of fluorescence intensity were used to provide a semiquantitative assessment of ROS production [40].

As shown in **Figure 5.8** and **Table 5.3**, a significant increase in the intracellular basal ROS levels was detected when BT474 cells were treated with 0.3 µM DOX and, especially, when NPs loaded with $Fe^{3+}$ were administered. Among these NPs, there were no major differences, since all of them increased ROS production close to double compared to the control. What could be observed was that the percentage of cells $CellROX^+/Sytox^-$ was slightly higher and the number of cells $CellROX^-/Sytox^-$ was smaller after treatment with the PDA NPs@$Fe_{2.5}$ [40].

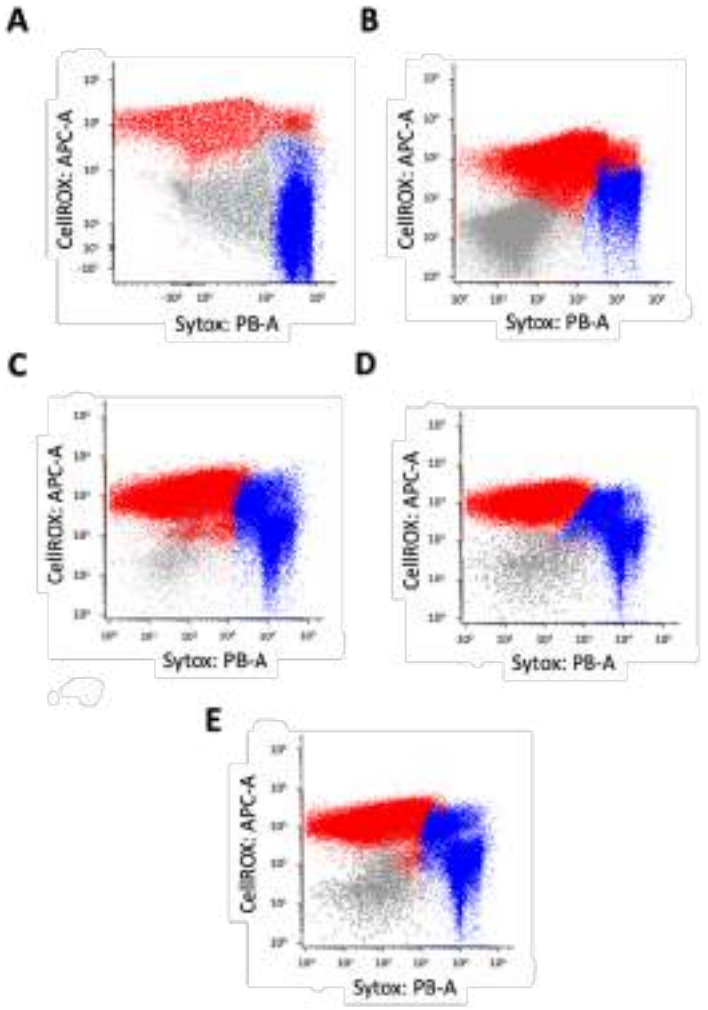


**Figure 5.8.** Analysis of ROS production *in vitro* by FACS 48 hours after BT474 treatment without (**A**) or with (**B**) DOX (0.3 µM) and 0.035 mg/mL of (**C**) PDA NPs@$Fe_{2.5}$, (**D**) PDA NPs@$Fe_{3.1}$ and (**E**) PDA NPs@$Fe_{4.5}$.

**Table 5.3**. Results obtained when analyzing the intracellular ROS production by flow cytometry 48 hours after treating BT474 cells with DOX (0.3 μM) and the different PDA NPs@$Fe^{3+}$ (0.035 mg/mL).

| Treatment | CellROX$^-$/Sytox$^-$ | CellROX$^-$/Sytox$^+$ | CellROX$^+$/Sytox$^-$ |
|---|---|---|---|
| **Control** | 42.9% | 8.5% | 48.6% |
| **DOX (0.3 μM)** | 16.8% | 6.6% | 76.6% |
| **PDA NPs@$Fe_{2.5}$** | 0.5% | 7.1% | 92.4% |
| **PDA NPs@$Fe_{3.1}$** | 4.8% | 7.3% | 87.9% |
| **PDA NPs@$Fe_{4.5}$** | 5.9% | 6.3% | 85.8% |

## 5.5. Conclusions

· First, PDA NPs were synthesized in an alkaline aqueous medium containing EtOH and chelated with $Fe^{2+}$, $Fe^{3+}$ and $Cu^{2+}$ at pH 4.5 to enhance their intrinsic therapeutic activity. An initial metal concentration of 70 ppm was used. PDA NPs@$M^{n+}$ obtained were highly toxic to breast cancer cells, but also to normal cells.

· In order to improve PDA NP@$M^{n+}$ specificity, further studies were performed by loading an initial 30 ppm $Fe^{3+}$ concentration to the PDA NPs. This was done at pH 2.5, 3.1 and 4.5 to determine if the efficacy and selectivity of the PDA NPs@$Fe^{3+}$ depended on whether they mostly contained $Fe^{3+}$ as free cation or $Fe(OH)_3$.

· When the different PDA NPs@$Fe^{3+}$ were characterized, it was observed that loading $Fe^{3+}$ at one pH or another made the NPs more or less spongy (possibly due to their distinct amount of $Fe^{3+}$ charged), and that several changes occurred in their IR spectra according to the $Fe^{3+}$-loading pH.

· Likewise, when viability assays were performed with BT474 and HS5 cells, it was proven that the pH at which $Fe^{3+}$ was loaded to PDA NPs, since it determined its chemical state, also conditioned the efficiency and tumour

selectivity of the resulting PDA NPs@$Fe^{3+}$. Thus, the more free $Fe^{3+}$ charged in the PDA NPs, the greater their therapeutic activity and the lower their toxicity to normal cells.

· To achieve a synergist effect, DOX was decided to be loaded to PDA NPs@$Fe^{3+}$. Nevertheless, different concentrations of the drug were first charged in bare PDA NPs that were or not later isolated to perform two different types of viability assays. Both PDA NPs@$DOX^{A}$ and PDA NPs@$DOX^{W}$ showed great anti-tumour activity and less toxicity to normal cells in comparison to equivalent concentrations of free DOX.

· Next, when DOX was loaded to the different PDA NPs@$Fe^{3+}$ and viability assays were again performed, synergy occurring between the $Fe^{3+}$ and DOX adsorbed was revealed. In addition, the importance of the pH value at which the $Fe^{3+}$-loading was carried out was again noticed, since those NPs charged with more free $Fe^{3+}$ and less $Fe(OH)_3$ were more selective and effective, even despite having charged less amount of DOX. In this manner, performing $Fe^{3+}$-chelation at one pH or another and adsorbing more or less amount of drug could be decided depending on the objectives pursued (more efficacy *vs.* fewer side effects).

· By flow cytometry, it was found that treatment with both DOX and the different PDA NPs@$Fe^{3+}$ notably increased ROS basal level in breast cancer cells. Thus $Fe^{3+}$ and DOX synergy, as expected, could take place because both caused an excessive ROS production.

## 5.6. Published articles related to this chapter

· Nieto C, Vega MA, Martín del Valle EM. Tailored-made polydopamine nanoparticles to induce ferroptosis in breast cancer cells in combination with chemotherapy. Int J Mol Sci. 2021; 22:3161.

## 5.7. Abbreviations

AuNPs – Gold nanoparticles
CP – Computed tomography
DA - Dopamine
DDS – Drug delivery system
DFO – Deferoxamine
DLS – Dynamic light scattering
DMEM – Dulbecco's modified Eagle's Medium
DMSO – Dimethylsulfoxide
DMT1 – Divalent metal transporter-1
DNA – Deoxyribonucleic acid
DOX - Doxorubicin
EtOH – Ethanol
FPN - Ferroportin
GSH – Glutathione
HER2 - Human epidermal growth factor receptor-2
$H_2O$(d) – Deionized water
ICP-OES – Inductively coupled plasma – optical emission spectroscopy
IR – Infrared
Ksp – Solubility product constant
$LD_{50}$ – Median lethal dose
LIP – Labile iron pool
$M^{n+}$ - Metal cation
MDR – Multidrug resistance
MRI – Magnetic resonance imaging
MSN – Mesoporous silica nanoparticle
MTT – 3-[4,5-dimethylthiazol-2-yl]-2,5-diphenyltetrazolium bromide
NP – Nanoparticle
PBS – Phosphate buffered saline
PDA – Polydopamine
PDA NPs – Polydopamine nanoparticles
PDA NPs@$DOX^A$ – Isolated polydopamine nanoparticles loaded with DOX
PDA NPs@$DOX^W$ – Non-isolated polydopamine nanoparticles loaded with DOX and administered with unbound DOX
PDA NPs@$DOX_{0.3}$ – Polydopamine nanoparticles loaded with a 0.3 μM DOX solution

PDA NPs@$DOX_{0.6}$ - Polydopamine nanoparticles loaded with a 0.6 µM DOX solution
PDA NPs@$DOX_1$ - Polydopamine nanoparticles loaded with a 1 µM DOX solution
PDA NPs@$Fe_{2.5}$ – Polydopamine nanoparticles loaded with $Fe^{3+}$ at pH 2.5
PDA NPs@$Fe_{3.1}$ – Polydopamine nanoparticles loaded with $Fe^{3+}$ at pH 3.1
PDA NPs@$Fe_{4.5}$ – Polydopamine nanoparticles loaded with $Fe^{3+}$ at pH 5.5
PDA NPs@$Fe^{3+}$/DOX - Polydopamine nanoparticles loaded with $Fe^{3+}$ and DOX
PDA NPs@$M^{n+}$ - Polydopamine nanoparticles chelated with a metal cation
PDI – Polydispersity index
PTT – Photothermal therapy
RCD – Regulated cell death
ROS – Reactive oxygen species
rpm – Revolutions per minute
SEM – Standard error mean
SPION – Superparamagnetic iron oxide nanoparticle
STEAP3 – Six-transmembrane epithelial antigen of the prostate 3
TEM – Transmission electron microscopy
Tf – Transferrin
TfR1 – Transferrin receptor-1
UV-Vis – Ultraviolet-visible

## 5.8. References

[1] Hauser D, Septiadi D, Turner J, Petri-Fink A, Rothen-Rutishauser B. From bioinspired glue to medicine: polydopamine as a biomedical material. Materials 2020; 13:1730.
[2] Hong Z-Y, Feng H-Y, Bu L-H. Melanin-based nanomaterials: the promising nanoplatforms for cancer diagnosis and therapy. Nanomedicine: NBM 2020; 28:102211.
[3] Li H, Yin D, Lin W, Tang Q, Zou L, Peng Q. Polydopamine-based nanomaterials and their potentials in advanced drug delivery and therapy. Colloid Surf B Biointerfaces 2021; 199:111502.
[4] PubMed database. Available online: https://pubmed.ncbi.nlm.nih.gov/?term=polydopamine+cancer. Accessed on 11th February 2021.

[5] Wang P, Xu X, Wang Y, Zhou B, Qu J, Li J, Shen M, Xia J, Shi X. Zwitterionic polydopamine-coated manganese oxide NPs with ultralight longitudinal relaxivity for tumor-targeted MRI imaging. Langmuir 2019; 35(12):4336-41.

[6] Zhu J, Wang Z, Xu X, Xu M, Yang X, Zhang C, Liu J, Zhang F, Shuai X, Wang W, Cao Z. Polydopamine-encapsulated perfluorocarbon for ultrasound contrast imaging and photothermal therapy. Mol Pharm. 2020; 17(3):817-26.

[7] Farokhi M, Mottaghitalab F, Saeb MR, Thomas S. Functionalized theranostic nanocarriers with bio-inspired polydopamine for tumor imaging and chemo-photothermal therapy. J Control Release 2019; 309:203-19

[8] Jin A, Wang Y, Lin K, Jiang L. Nanoparticles modified by polidopamine: working as “drug” carriers. Bioact Mater. 2020; 5:522-41.

[9] Wang Z, Duan Y, Duan Y. Application of polydopamine in tumor targeted drug delivery systems and its drug release behaviour. J Control Release 2018; 290:56-74.

[10] Wang W, Tang Z, Zhang Y, Wang Q, Liang Z, Zeng X. Mussel-inspired polydopamine: the bridge for targeting drug delivery system and synergist cancer treatment. Macromol Biosci 2020; 20:2000222.

[11] Ni G, Yang G, He Y, Li X, Du T, Xu L, Zhou S. Uniformly sized hollow microspheres loaded with PDA NPs and doxorubicin for local chemo-photothermal combination therapy. Chem Eng J. 2020; 379:122317.

[12] Chen H, Chen H, Wang Y, Bai Y, Yuan P, Che Z, Zhang L. A novel self-coated polydopamine nanoparticle for synergist photothermal-chemotherapy. Colloid Surf B Biointerfaces 2021; 200:111596.

[13] Liu T, Liu W, Zhang M, Yu W, Gao F, Li C, Wang S-B, Feng J, Zhang X-Z. Ferrous-supply-regeneration nanoengineering for cancer-cell-specific ferroptosis in combination with imaging guided photodynamic therapy. ACS Nano 2018; 12:12181-92.

[14] Brown JM, Attardi LD. The role of apoptosis in cancer development and treatment response. Nat Rev Cancer 2005; 5:231-37.

[15] Trachoatham D, Alexandre J, Huang P. Targeting cancer cells by ROS-mediated mechanisms: a radical therapeutic approach? Nat Rev. 2009; 8:579-91.

[16] Forcinitti S, Greco L, Grizzi F, Malesci A, Laghi L. Iron metabolism in cancer progression. Int J Mol Sci. 2020; 21:2257.

[17] Jung M, Mertens C, Tomat E, Brüne B. Iron as a central player and promising target in cancer progression. Int J Mol Sci. 2019; 20:273.

[18] Li J, Cao F, Yin H-L, Huang Z-J, Lin Z-T, Mao N, Sun B, Wang G. Ferroptosis: past, present and future. Cell Death Dis. 2020; 11:88.

[19] Battaglia AM, Chirillo R, Aversa I, Sacco A, Costanzo F, Biamonte F. Ferroptosis and cancer: mitochondria meet the “iron maiden” cell death. Cells 2020; 9:1505.
[20] Bebber CM, Müller F, Clement LP, Weber J, Von Karstedt S. Ferroptosis in cancer biology. Cancers 2020; 12:164.
[21] Nieto C, Vega MA, Marcelo G, Martín del Valle, EM. Polydopamine nanoparticles kill cancer cells. RSC Adv. 2018; 8:36201.
[22] Nieto C, Vega MA, Enrique J, Marcelo G, Martín del Valle EM. Size matters in the cytotoxicity of polydopamine nanoparticles in different types of tumors. Cancers 2019; 11:1679.
[23] Nieto C, Marcelo G, Vega MA, Martín del Valle EM. Antineoplastic behaviour of polydopamine nanoparticles prepared in different water/alcohol media. Colloid Surf B Biointerfaces 2021; 199:111506.
[24] Dixon SJ, Lemberg KM, Lamprecht MR, Skouta R, Zaitsev EM, Gleason CE, Patel DN, Bauer AJ, Cantley AM, Yang WS et al. Ferroptosis: an iron-dependent form of non-apoptotic cell death. Cell 2012; 149(5):1060-72.
[25] Wang S, Luo J, Zhang Z, Dong D, Shen Y, Fang Y, Hu L, Liu M, Dai C, Peng S et al. Iron and magnetic: new research direction of the ferroptosis-based cancer therapy. Am J Cancer Res. 2018; 8(10):1933-46.
[26] Huang Y, Lin J, Xiong Y, Chen J, Du X, Liu Q, Liu T. Superparamagnetic iron oxide nanoparticles induce ferroptosis of human ovarian cancer stem cells by weaking cellular autophagy. J Biomed Nanotechnol. 2020; 16(11):1612-22.
[27] Shen Z, Liu T, Li Y, Lau J, Yang Z, Fan W, Zhou Z, Shi C, Ke C, Bregadze VI et al. Fenton-reaction-accelerateble magnetic nanoparticles for ferroptosis therapy of orthotopic brain tumors. ACS Nano 2018; 12(11):11355-65.
[28] Jiang Q, Wang K, Zhang X, Ouyang B, Liu H, Pang Z, Yang W. Platelet membrane-camouflaged magnetic nanoparticles for ferroptosis-enhanced cancer immunotherapy. Small 2020; 16(22):e2001704.
[29] Liu M, Liu B, Liu Q, Du K, Wang Z, He N. Nanomaterial-induced ferroptosis for cancer specific therapy. Coord Chem Rev. 2019; 382:160-80.
[30] Kim SE, Zhang L, Ma K, Riegman M, Chen F, Ingold I, Conrad M, Turker MZ, Gao M, Jiang X et al. Ultrasmall nanoparticles induce ferroptosis in nutrient-deprived cancer cells and suppress tumour growth. Nat Nanotechnol. 2016; 11(11):977-85.
[31] Zhang C, Liu Z, Zhang Y, Ma L, Song E, Song Y. “Iron free” zinc oxide nanoparticles with ion-leaking properties disrupt intracellular ROS and iron homeostasis to induce ferroptosis. Cell Death Dis. 2020; 11:183.

[32] Vega MA, Nieto C, Marcelo G, Martín del Valle EM. Cytotoxicity of paramagnetic cations-loaded polydopamine nanoparticles. Colloid Surf B Biointerfaces 2018; 167:284-90.

[33] Chen L, Lin Z, Liu L, Zhang X, Shi W, Ge D, Sun Y. $Fe^{2+}$/$Fe^{3+}$ ions chelated with ultrasmall polydopamine nanoparticles induce ferroptosis for cancer therapy. ACS Biomater Sci Eng. 2019; 5(9):4861-69.

[34] Dong L, Wang C, Zhen W, Jia X, An S, Xu Z, Zhang W, Jiang X. Biodegradable iron-coordinated hollow polydopamine nanospheres for dihydroartemisin delivery and selective enhanced therapy in tumor cells. J Mater Chem B 2019; 7:6172.

[35] Pham AN, Xing G, Miller CJ, Waite TD. Fenton-like copper redox chemistry revisited: hydrogen peroxide and superoxide mediation of copper-catalyzed oxidant production. J Catal. 2013; 301:54-64.

[36] Zafar A, Singh S, Ahmad S, Khan S, Siddiqi MI, Naseem I. Interaction of C20-substituted derivative of pregnenolone acetate with copper (II) leads to ROS generation, DNA cleavage and apoptosis in cervical cancer cells: therapeutic potential of copper chelation for cancer treatment. Bioorg Chem. 2019; 87:276-90.

[37] Denoyer D, Masaldan S, La Fontaine S, Cater MA. Targeting copper in cancer therapy: 'copper that cancer'. Metallomics 2015; 7:1459.

[38] Lamy PJ, Durigova A, Jacot W. Iron homeostasis and anemia markers in early breast cancer. Clin Chim Acta 2014; 434:34-40.

[39] Buriel Marti F, Lucena Conde F, Hernández Méndez J, Arribas Jimeno S. Química analítica cuantitativa. 18th. ed. Madrid: Paraninfo; 2006.

[40] Nieto C, Vega MA, Martín del Valle EM. Tailored-made polydopamine nanoparticles to induce ferroptosis in breast cancer cells in combination with chemotherapy. Int J Mol Sci. 2021; 22:3161.

[41] Chen W, Nie J, Xu Lv, Liang C, Peng Y, Liu G, Wang T, Mei L, Huang L, Zeng X. pH-sensitive delivery vehicle based on folic acid-conjugated polydopamine-modified mesoporous silica nanoparticles for targeted cancer therapy. ACS Appl. Mater. Interfaces 2017; 9:18462-73.

[42] Raffaelo A, Mammucari C, Gherardi G, Rizzuto R. Calcium at the center of cell signalling: interplay between endoplasmic reticulum, mitochondria, and lysosomes. Trends Biochem Sci. 2016; 41(12):1035-49.

[43] Klosterman L, Bettinger CJ. Calcium-mediated control of polydopamine film oxidation and iron chelation. Int J Mol Sci. 2017; 18:14.

[44] Carreira AC, de Almeida RFM, Silva LC. Development of lysosome-mimicking vesicles to study the effect of abnormal accumulation of sphingosine on membrane proteins. Sci Rep. 2017; 7:3949.
[45] Cheng M, Liu P, Lu LX. Iron promotes breast cancer cell migration via IL-6/JAK2/STAT3 siganlling pathways in a paracrine or autocrine IL-6-rich inflammatory environment. J Inorg Biochem. 2020; 210:111159.
[46] Lamy PJ, Durigova A, Jacot W. Iron homeostasis and anemia markers in early breast cancer. Clin Chim Acta 2014; 434:34-40.
[47] Gong Y, Gallis BM, Goodlett DR, Yang Y, Lu H, Lacoste E, Lai H, Sasaki T. Effects of transferrin conjugates of artemisin and artemisin dimer on breast cancer cell lines. Anticancer Res. 2013; 33:123-32.
[48] Luengo A, Gui DY, Vander Heiden MG. Targeting metabolism for cancer therapy. Cell Chem Biol. 2017; 24(9):1161-80.
[49] Xue C-C, Li M-H, Zhao Y, Zhou J, Hu Y, Cai K-Y, Zhao Y, Yu S-H, Luo Z. Tumor microenvironment activatable Fe-doxorubicin preloaded amorphous $CaCO_3$ nanoformulation triggers ferroptosis in target tumor cells. Sci Adv. 2020; 6(18):eaax1346.
[50] Zhao Y, Butler EB, Tan M. Targeting cellular metabolism to improve cancer therapeutics. Cell Deat Dis. 2013; 4:e532.
[51] Yao X, Yang P, Jin Z, Jiang Q, Guo R, Xie R, He Q, Yang W. Multifunctional nanoplatform for photoacoustic imaging-guided combined therapy enhanced by CO induced ferroptosis. Biomaterials 2019; 197:268-83.
[52] Yang R, Li Y, Wang X, Yan J, Pan D, Xu Y, Wang L, Yang M. Doxorubicin loaded ferritin nanoparticles for ferroptosis enhanced targeted killing of cancer cells. RSC Adv. 2019; 9:28548-53.
[53] Carvalho C, Santos RX, Cardoso S, Correia S, Oliveira PJ, Santos MS, Moreira PI. Doxorubicin: the good, the bad and the ugly effect. Curr Med Chem. 2009; 16(25):3267-85.
[54] Meredith AM, Dass CR. Increasing role of the cancer chemotherapeutic doxorubicin in cellular metabolism. J Pharm Pharmacol. 2016; 68:729-41.
[55] Chatterjee K, Zhang J, Honbo N, Karliner JS. Doxorubicin cardiomyopathy. Cardiology 2010; 115:155-62.
[56] Liu Y, Zeng L, Yang Y, Chen C, Wang D, Wang H. Acyl-CoA thioesterase I prevents cardiomyocytes from doxorubicin-induced ferroptosis via shaping the lipid composition. Cell Death Dis. 2020; 11:756.

[57] Tadokoro T, Ikeda M, Ide T, Deguchi H, Ikeda S, Okabe K, Ishikita A, Matsushima S, Koumura T, Yamada K-I et al. Mitochondria-dependent ferroptosis plays a pivotal role in doxorubicin cardiotoxicity. JCI Insight 2020; 5(9):e132747.

[58] Wen S-H, Su S-C, Liou B-H, Lin C-H, Lee K-R. Sulbactam-enhanced cytotoxicity of doxorubicin in breast cancer cells. Cancer Cell Int. 2018; 18:128.

[59] Loibl S, Weber KE, Timms KM, Elkin EP, Hahnen E, Fasching PA, Lederer B, Denkert C, Schneeweiss A, Braun S et al. Survival anañysis of carboplatin added to an anthracycline/taxane-based neoadjuvant chemotherapy and HRD score as predictor of reponse-final results from GeparSixto. Ann Oncol. 2018; 29:2341-47.

[60] Pujade-Lauraine E, Wagner U, Aavall-Lundquist E, Gebski V, Heywood M, Vasey PA, Volgger B, Vergote I, Pignata S, Ferrero A et al. Pegylated liposomal doxorubicin and carboplatin compared with paclitaxel and carboplatin for patients with platinum-sensitive ovarian cancer in late relapse. J Clin Oncol. 2010; 28(20):3323-29.

[61] Sparano JA, Makhson AN, Semiglazov VF, Tjulandin SA, Balashova OI, Bondarenko IN, Bogdanova NV, Manikhas GM, Oliynychenko GP, Chatikhine VA et al. Pegylated liposomal doxorubicin plus docetaxel significantly improves time to progression without additive cardiotoxicity compared to docetaxel monotherapy in patients with advanced breast cancer previously treated with neoadjuvant-adjuvant anthracycline therapy: results from a randomized phase III study. J Clin Oncol. 2009; 27(27):4522-29.

[62] Rouault TA. The role of iron regulatory proteins in mammalian iron homeostasis and disease. Nat Chem Biol. 2006; 2:406-14.

[63] Anticoli S, Amatore D, Matarrese P, De Angelis M, Palamara AT, Nencioni L, Ruggieri A. Counteraction of HCV-induced oxidative stress concurs to establish chronic infection in liver cell cultures. Oxid Med Cell Longev. 2019; 2019:6452390.

International Journal of Molecular Sciences

MDPI

Article

# Tailored-Made Polydopamine Nanoparticles to Induce Ferroptosis in Breast Cancer Cells in Combination with Chemotherapy

Celia Nieto, Milena A. Vega * and Eva M. Martín del Valle *

Departamento de Ingeniería Química y Textil, Facultad de Ciencias Químicas, Universidad de Salamanca, 37008 Salamanca, Spain; celianieto@usal.es

* Correspondence: mvegamartin@usal.es (M.A.V.); emvalle@usal.es (E.M.M.d.V.); Tel.: +34-923294500 (E.M.M.d.V.)

**Abstract:** Ferroptosis is gaining followers as mechanism of selective killing cancer cells in a non-apoptotic manner, and novel nanosystems capable of inducing this iron-dependent death are being increasingly developed. Among them, polydopamine nanoparticles (PDA NPs) are arousing interest, since they have great capability of chelating iron. In this work, PDA NPs were loaded with $Fe^{3+}$ at different pH values to assess the importance that the pH may have in determining their therapeutic activity and selectivity. In addition, doxorubicin was also loaded to the nanoparticles to achieve a synergist effect. The in vitro assays that were performed with the BT474 and H55 cell lines showed that, when $Fe^{3+}$ was adsorbed in PDA NPs at pH values close to which Fe(OH)$_3$ begins to be formed, these nanoparticles had greater antitumor activity and selectivity despite having chelated a smaller amount of $Fe^{3+}$. Otherwise, it was demonstrated that $Fe^{3+}$ could be released in the late endo/lysosomes thanks to their acidic pH and their $Ca^{2+}$ content, and that when $Fe^{3+}$ was co-transported with doxorubicin, the therapeutic activity of PDA NPs was enhanced. Thus, reported PDA NPs loaded with both $Fe^{3+}$ and doxorubicin may constitute a good approach to target breast tumors.

**Keywords:** breast cancer; polydopamine nanoparticles; iron; ferroptosis; reactive oxygen species; doxorubicin

**Citation:** Nieto, C.; Vega, M.A.; Martín del Valle, E.M. Tailored-Made Polydopamine Nanoparticles to Induce Ferroptosis in Breast Cancer Cells in Combination with Chemotherapy. Int. J. Mol. Sci. 2021, 22, 3161. https://doi.org/10.3390/ijms22063161

Academic Editor: Salvatore Gallo and Francesca Boso

Received: 23 February 2021
Accepted: 17 March 2021
Published: 19 March 2021

**Publisher's Note:** MDPI stays neutral with regard to jurisdictional claims in published maps and institutional affiliations.

**Copyright:** © 2021 by the authors. Licensee MDPI, Basel, Switzerland. This article is an open access article distributed under the terms and conditions of the Creative Commons Attribution (CC BY) license (http://creativecommons.org/licenses/by/4.0/).

## 1. Introduction

In recent decades, extensive efforts have been made by the scientific community to find novel, more efficient, effective, and tolerable cancer therapies [1]. In the pursuit of this major goal, nanomedicine is playing a fundamental role in trying to improve the therapeutic activity and selectivity of anticancer agents, focusing on those biological aspects of malignancy that differentiate tumor from normal cells [1,2]. However, most developed nanotherapies are only focused on inducing programmed death of cancer cells and these are able to combat the apoptosis pathway many times, so that multidrug resistance (MDR) occurs more frequently than desired [3]. For this reason, recent studies have suggested that targeting biochemical alterations in cancer cells, in combination or not with the employment of pro-apoptotic agents, may be a feasible and efficacious approach to selectively treat cancer and prevent the apparition of MDR [2,4]. In fact, this combinatorial strategy (metabolic targeting plus conventional drug) is even being used for the therapy of other diseases, such as neurodegenerative disorders [5].

Among the biochemical hallmarks of cancer, one that is sparking great interest for the development of new non-apoptosis-based therapies is iron (Fe) metabolism [3]. Fe is an indispensable element for both malignant and normal cells but, since it is essential for cell proliferation and growth, cancer cells exhibit a stronger dependence on it [6]. In this way, the import, storage and export pathways of Fe, which are tightly regulated in healthy

cells (with no excretory route for excess Fe), are perturbed in tumors to maintain increased Fe levels in these tissues [7].

Regarding Fe cellular pathways, it should be noted that this metal binds transferrin (Tf) in the plasma and the resulting complex is taken into cells by transferrin receptor-1 (TfR1)-mediated endocytosis [6,8]. Then, $Fe^{3+}$ is reduced to $Fe^{2+}$ and exported to the cytosol. The majority of cytoplasmic $Fe^{2+}$ is stored within ferritin, but a small pool of $Fe^{2+}$ remains free (LIP) and can be detrimental due to its redox ability, since it can directly catalyze free radical formation via Fenton reaction [9]. When the amount of free $Fe^{2+}$ is excessive and the production of free radicals collapses the cellular defense system [10], a Fe-dependent form of regulated cell death takes places: Ferroptosis [9,11].

Thus, in recent years, nanoparticles (NPs) capable to induce a Fe-dependent cell death are being developed for cancer treatment. In the vast majority of cases, they are FeOx NPs combined or not with chemotherapeutic agents, although gold, silver or silica NPs transporting Fe to induce ferroptosis can also be found in the literature [12]. In any case, all the NPs developed with this intention to date are metallic in nature, with one exception: Polydopamine (PDA) NPs [13–15].

PDA, which is a nature-inspired polymer, has many interesting properties, such as high affinity to a wide range of metal cations, especially to $Fe^{3+}$, $Fe^{2+}$, and $Ca^{2+}$ [13,16]. This phenomenon was shown in previous works [13], as well as that PDA NP capability to load the $Fe^{2+}$ naturally present in late endo/lysosomes may be related to their intrinsic toxicity to tumor cells [17–19]. Based on their ability to chelate $Fe^{3+}$, PDA NPs have begun to be used to transport it and induce ferroptosis in malignant cells [13–15]. However, in all studies carried out to date, the pH at which the $Fe^{3+}$-loading was performed was not been given enough importance, and it is essential because determines if $Fe^{3+}$ is free or forming $Fe(OH)_3$ and therefore, it can condition nanosystem effectiveness and selectivity.

For that reason, in the current work, $Fe^{3+}$-adsorption in PDA NPs was performed at three different pH values (2.5, 3.1, and 4.5) in order to analyze which of the resulting nanosystems was more effective in selectively inducing ferroptosis in breast cancer cells. Likewise, a mechanism involving $Ca^{2+}$ was proposed that could explain the release of $Fe^{3+}$ from PDA NPs in late endo/lysosomes. Finally, $Fe^{3+}$-burden PDA NPs (PDA NPs@Fe) were also charged with doxorubicin (DOX) to enhance their therapeutic activity. The capacity of this widely used drug to cause mitochondrial Fe accumulation and increase the production of reactive oxygen species (ROS) is well-known [20,21]. For this motive, it was chosen to produce a synergist effect with the chelated $Fe^{3+}$ and cause ROS overproduction [21]. As a result, it was found that when $Fe^{3+}$ was loaded to PDA NPs at the two most acidic pH values (2.5 and 3.1), resulting PDA NPs were more toxic to breast tumor cells but more selective, possibly because most of the loaded $Fe^{3+}$ was in a free form and was not $Fe(OH)_3$. Otherwise, it was seen that treatment with all different PDA NPs@Fe increased ROS production in breast cancers cells. Thus, this fact indicated that a process of ferroptosis could be occurring. At last, the antitumor activity of these PDA NPs was enhanced with DOX-loading, and it was demonstrated that a synergist effect took place between the chelated $Fe^{3+}$ and the drug. In this way, when both $Fe^{3+}$ and DOX were charged on PDA NPs (PD NPs@Fe/DOX), the nanosystem obtained reduced breast cancer cell viability in a more remarkable manner. Fortunately, PDA NPs@Fe/DOX did not affect normal cell survival rate in the same extent.

## 2. Results

### 2.1. Preparation and Characterization of PDA NPs

PDA NPs were prepared using the standard procedure of oxidative polymerization of dopamine in a basic aqueous medium containing ethanol (27.7% V/V) and $NH_4OH$ (2.9% V/V) [13,17,18]. Once synthesized, PDA NPs were characterized by TEM and a size-range histogram was obtained, from which it was determined that NPs had an average

size of 111.2 ± 16.2 nm (Figure 1a). Moreover, PDA NP hydrodynamic size was determined by DLS and it was found to be 154.2 ± 28.5 nm (PDI = 0.012) (Figure 1b). Possibly, this last value obtained from PDA NPs in suspension was higher than the average size determined through TEM because of the dehydration that is necessary to prepare TEM samples [22].

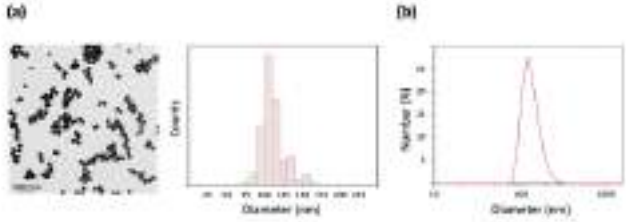


**Figure 1.** (a) TEM image and size-range histogram of the polydopamine nanoparticles (PDA NPs) synthesized; (b) DLS number distribution of a suspension of the obtained PDA NPs in Tricma base solution (pH 10.0).

### 2.2. pH Effect on the $Fe^{3+}$-Adsorption Capacity of PDA NPs

In prior research in which the $Fe^{3+}$-chelation capacity of the PDA NPs was studied, $Fe^{3+}$-adsorption was performed at pH 4.5, since it was a similar value to that of acidic cell organelles (late endosomes and lysosomes) [13,19]. However, the critical pH for $Fe^{3+}$ to form $Fe(OH)_3$ in aqueous solutions is 2.7 [23], so most of $Fe^{3+}$ would be as $Fe(OH)_3$ at pH 4.5. Thus, to see if carrying out $Fe^{3+}$-adsorption at pH values closer to 2.7 conditioned PDA NP cytotoxicity by guaranteeing the existence of more free $Fe^{3+}$, this metal was also adsorbed at pH 2.5 and 3.1 in the current work.

For this purpose, $Fe^{3+}$-adsorption was performed with $FeCl_3$ solutions with an approximate initial $Fe^{3+}$ concentration of 30 mg/L in all cases. As a result, it was observed that when $Fe^{3+}$ was loaded to PDA NPs at pH 4.5, PDA NPs adsorbed 100 mg $Fe^{3+}$/g NPs (equivalent to 13 mg $Fe^{3+}$/L). Nevertheless, when the adsorption process was carried out at pH 2.5 and 3.1, PDA NPs were able to adsorb 16 and 15 mg $Fe^{3+}$/g NP (equivalent to 2.3 and 2.2 mg $Fe^{3+}$/L), respectively (Table 1). At pH 2.5, most of the $Fe^{3+}$ loaded would be as free cation while, at pH 3.1, since it was a value close to 2.7 but higher than it, part of the $Fe^{3+}$ loaded to the PDA NPs would also be as $Fe(OH)_3$. Finally, even though $Fe^{3+}$-loading was much more remarkable at pH 4.5 (possibly because the process was allowed to run for longer time), the vast majority of $Fe^{3+}$ would be as $Fe(OH)_3$ at this pH value. Thus, taking into account that $Fe(OH)_3$ solubility product constant ($K_{sp}$) is 37.0 at room temperature, only $3.52 \times 10^{-9}$ mg/L $Fe^{3+}$ would be as free cation. More information regarding this calculation can be consulted in the Supplementary Material.

**Table 1.** Amount of the $Fe^{3+}$ released and the $Ca^{2+}$ adsorbed in the different PDA NPs@Fe suspended in lysosomal buffer (pH 4.5) containing $Ca^{2+}$ (20 mg/L). The percentage values regarding $Fe^{3+}$-release were calculated taking into account the amount of this cation that was loaded initially, and those regarding $Ca^{2+}$-adsorption were calculated taking into account $Ca^{2+}$ initial concentration in the buffer.

| pH | $Fe^{3+}$ Loaded (q) | $Fe^{3+}$ Released (q) | $Fe^{3+}$ Released (%) | $Ca^{2+}$ Loaded (q) | $Ca^{2+}$ Loaded (%) |
|---|---|---|---|---|---|
| 2.5 | 16 mg/g | 6 mg/g | 38 | 21 mg/g | 13 |
| 3.1 | 15 mg/g | 4 mg/g | 30 | 20 mg/g | 13 |
| 4.5 | 100 mg/g | 75 mg/g | 75 | 16 mg/g | 10 |

Next, all PDA NPs@Fe were again characterized by TEM and IR spectroscopy to see if changes in their morphology and chemical structure occurred after $Fe^{3+}$-adsorption. Both characterization techniques were chosen because they complement each other well, although other methods, such as small-angle X-ray scattering (SAXS) [24], also allow obtaining relevant information on the structure of nanoparticle systems.

Regarding TEM characterization, it was noticed that $Fe^{3+}$-loading at pH 2.5 and 3.1 caused PDA NPs@Fe to become slightly spongier in comparison to bare PDA NPs, a change that was even more noticeable at pH 4.5 (Figure 2).

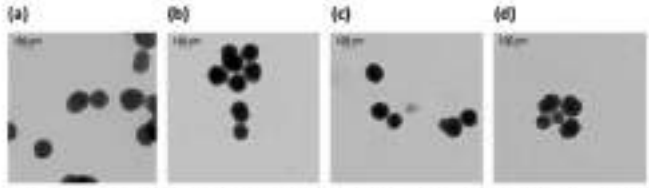


Figure 2. TEM images of (a) bare PDA NPs (114.9 ± 17.6 nm); (b) PDA NPs@$Fe_{2.5}$ (112.2 ± 19.1 nm); (c) PDA NPs@$Fe_{3.1}$ (106.2 ± 17.5 nm) and (d) PDA NPs@$Fe_{4.5}$ (111.8 ± 51.1 nm). As shown, $Fe^{3+}$-loading made PDA NPs spongier, especially when the metal adsorption was performed at pH 4.5.

On the other hand, the main bands of the IR spectra were assigned according to previous characterizations of melanins [13]. After $Fe^{3+}$-binding, the principal changes in the 900–1800 $cm^{-1}$ range occurred in the bands at 1280 and 1620 $cm^{-1}$ (Figure S1a). These bands may include the C-OH stretching in a phenol ring and the C=O stretching (non-carboxylic acid), respectively, and their relative intensity was higher for the PDA NPs with $Fe^{3+}$ loaded at pH 2.5 (PDA NPs@$Fe_{2.5}$) than for the rest of PDA NPs. In the 2500–3700 $cm^{-1}$ range (Figure S1b), the main changes occurred at 2848, 2920, and 2955 $cm^{-1}$. These bands may correspond to the different vibrational modes of aliphatic groups and decreased in intensity for the PDA NPs with $Fe^{3+}$ loaded at pH 4.5 (PDA NPs@$Fe_{4.5}$), while they were broadened, for instance, for the PDA NPs@$Fe_{3.1}$.

### 2.3. $Fe^{3+}$-Release and $Ca^{2+}$-Loading from/to the Different PDA NPs@Fe

In previous works, it was already described that PDA formed stable complexes through coordination effects with $Fe^{3+}$ cations [25]. However, under acidic environments, such as those inside late endo/lysosomes, the two adjacent hydroxyl groups coordinating with $Fe^{3+}$ on the PDA benzene ring may competitively combine with protons. This fact could stimulate the release of $Fe^{3+}$ from PDA NPs, which, on the contrary, would be considerably lower at physiological pH (7.4) [14,15]. Further, it was also shown that PDA NPs had great affinity for other cations apart from $Fe^{3+}$. In fact, even though $Fe^{3+}$ was one of the cations for which PDA NPs had the highest affinity, its affinity for $Ca^{2+}$, which is also abundant in the endo/lysosomes [25], was even greater [13]. Since previous investigations demonstrated that $Ca^{2+}$ cations could mediate the deprotonation of the PDA catechol group [26], which accounts for $Fe^{3+}$-complexation [13], it was thought that $Ca^{2+}$ existing in the endo/lysosomes may also stimulate the release of the $Fe^{3+}$ charged in PDA NPs along with the acidic pH.

For this reason, $Fe^{3+}$-release from PDA NPs@Fe was analyzed by using a lysosome-simulator buffer (pH 4.5) [27], which contained $Ca^{2+}$ in a concentration (20 mg/L) similar to that believed in these organelles [25]. All PDA NPs@Fe were suspended in this buffer for 48 h and, after such time, they were isolated to determine the concentration of $Fe^{3+}$ and $Ca^{2+}$ present in the supernatant and, thus, to find out the amount of $Fe^{3+}$ that was released and the $Ca^{2+}$ that was adsorbed.

As can be seen from the data collected in Table 1, $Fe^{3+}$ was released from all PDA NPs@Fe after 48 h and all of them were able to adsorb $Ca^{2+}$. Regarding $Fe^{3+}$-release, it should be noted that it was greater from PDA NPs@$Fe_{4.5}$ than from NPs@$Fe_{2.5}$ and NPs@$Fe_{1.1}$. This fact could be consequence of the $Fe^{3+}$ small ionic radius (0.64 Å) and ionic charge, which may hinder its release. Conversely, $Fe(OH)_3$ molecules, which were expected to be loaded at pH 4.5, are much larger and neutral, and this fact could make their release easier.

Otherwise, the differences in $Ca^{2+}$-adsorption capacity were not so marked among the different PDA NPs@Fe. In any case, it was shown that this cation was loaded at the same time that $Fe^{3+}$ was released from the NPs, so an ionic displacement may contribute to the release of the loaded $Fe^{3+}$ from PDA NPs in the endolysosomes.

### 2.4. Therapeutic Activity of PDA NPs@Fe as Function of the $Fe^{3+}$-Loading pH

As it has been described before, one of the aims of this work was to verify if loading $Fe^{3+}$ at pH values closer to the critical pH at which $Fe(OH)_3$ is formed affected to the cytotoxicity of the PDA NPs@Fe. Herein, the viability of BT474 and HS5 cells after treating them with all the PDA NPs@Fe synthesized was evaluated by MTT assays and compared to that obtained after treating them with bare PDA NPs. BT474 cell line was selected because it had been shown that breast cancer cells have an altered Fe homeostasis that enhances their growth, survival, and metastasis [28,29]. For instance, they overexpress ferritin to store more Fe and TfR1 to enhance its uptake [29]. Accurately, the overexpression of this receptor sensitizes cells to ferroptosis by increasing $Fe^{3+}$-loaded nanosystem endocytosis rate [9,15]. In addition, BT474 cells overexpress HER2, and researchers observed that a complex of Tf with a ferroptosis-inducing compound was capable of declining HER2 expression in this cell line [30]. On the other hand, HS5 stromal cells were chosen to compare PDA NPs@Fe toxicity to malignant and normal cells.

Thus, HS5 and BT474 cells were treated with 0.035 mg/mL PDA NPs and PDA NPs@Fe. The mentioned NP concentration was chosen because in a previous work it was demonstrated that it reduced tumor cell viability but without significantly affecting the survival of healthy cells [19]. Likewise, to load PDA NPs with $Fe^{3+}$ at the different pH values, a solution with an initial 30 mg/L $Fe^{3+}$ concentration was prepared because in an anterior study, when a solution with a higher metal concentration was employed, obtained $Fe^{3+}$-loaded PDA NPs turned out to be toxic to normal fibroblasts [13].

The results obtained in these first MTT assays have been represented in the Figure 3 and, to facilitate their comparison, the corresponding viability rate values have been included in the Table S1. In general, it can be said that all PDA NPs@Fe reduced the survival rate of BT474 cells (Figure 3a) in greater order than unloaded PDA NPs. In this manner, PDA NPs@$Fe_{4.5}$ treatment increased the death of breast cancer cells by approximately 10% compared to naked PDA NPs at all times, reducing their viability by almost half (to 52.8 ± 1.3%) after 72 h. This cytotoxicity increase was close to 20% in the case of the treatment with the other two PDA NPs@Fe, so that the viability of BT474 cells was reduced to 43.3 ± 1.4% (PDA NPs@$Fe_{2.5}$) and 45.6 ± 1.5% (PDA NPs@$Fe_{1.1}$) at the end of the assays, while 63.6 ± 1.9% of BT474 cells were alive 72 h after treatment with unloaded PDA NPs.

Regarding HS5 cell viability (Figure 3b), it was not as affected as that of malignant cells after treatment with any of the PDA NPs@Fe. Their survival rate after treating them with unloaded PDA NPs was close to 90%, 85%, and 80% after 24, 48, and 72 h, and these percentages were very similar to those obtained after PDA NPs@$Fe_{2.5}$ treatment. Thereby, in this case, HS5 cell viability was affected by 35–40% less compared to breast cancer cell viability. PDA NPs@$Fe_{1.1}$ and PDA NPs@$Fe_{4.5}$ were less selective and decreased stromal cell survival rate most notably, especially after 48 and 72 h. Thus, compared to BT474 cells, when HS5 cells were treated with PDA NPs@$Fe_{4.5}$ 40–20% more of them survived and, when they were treated with PDA NPs@$Fe_{4.5}$, this percentage range was 20–10%.

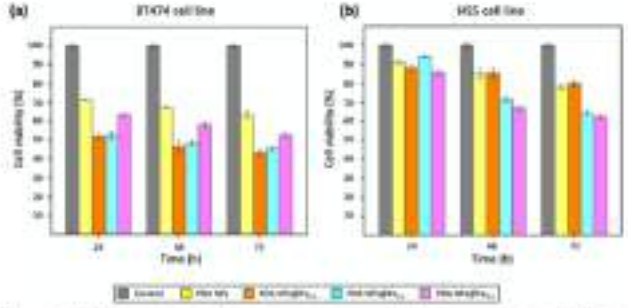


**Figure 3.** Viability results obtained after the performance of MTT assays with the (a) BT474 and (b) HS5 cell lines, which were treated with 0.036 mg/mL PDA NPs, PDA NPs@$Fe_{III}$, PDA NPs@$Fe_{III}$ and PDA NPs@$Fe_{II}$.

Consequently, the $Fe^{3+}$-loaded PDA NPs with the most remarkable therapeutic activity were the PDA NPs@$Fe_{III}$ which were also the most selective. On the contrary, PDA NPs@$Fe_{III}$ were those that showed an antitumor activity more similar to that of bare PDA NPs and reduced the most the survival rate of the normal cells. As already mentioned, practically all the $Fe^{3+}$ loaded to PDA NPs@$Fe_{III}$ was $Fe(OH)_3$, while PDA NPs@$Fe_{III}$ had both free $Fe^{3+}$ and $Fe(OH)_3$ and PDA NPs@$Fe_{II}$ had only free $Fe^{3+}$. Since free $Fe^{3+}$ is the one that binds to Tf and is reduced in late endo/lysosomes to the $Fe^{2+}$ that can later participate in Fenton chemistry (Equation (1)) [6–9], it made sense that PDA NPs with the highest charged amount of free cation were the most efficient and selective, even despite having adsorbed less amount of Fe.

$$Fe^{2+} + H_2O_2 \leftrightarrow Fe^{3+} + HO^- + HO \quad (1)$$

### 2.3. Therapeutic Activity of PDA NPs@Fe/DOX

To enhance the antitumor activity of PDA NPs@Fe, loading them also with DOX was decided. This drug exerts part of its therapeutic activity through the accumulation of intramitochondrial Fe and the production of ROS. For this reason, PDA NPs were also loaded with it in order to achieve a synergist between $Fe^{3+}$ and DOX [20,21], while trying to reduce DOX severe side effects [31]. In this manner, in order to verify if these two phenomena took place, both PDA NPs and PDA NPs@Fe were loaded with three different concentrations of DOX (0.3, 0.6, and 1 μM). Since the LD50 of this drug for the BT474 cell line was found to be 1 μM [32], it was decided to employ a solution of this concentration to absorb DOX in PDA NPs and PDA NPs@Fe, as well as two solutions with a concentration lower than it. Moreover, there are more and more clinical trials in which some therapeutic nanosystem is administered with some free conventional antitumor drug to achieve a peak of drug concentration in the plasma followed by a more sustained release [33–35]. For this reason, it was decided both to isolate the PDA NPs/PDA NPs@Fe once the adsorption process was finished to study their efficacy and selectivity, but also to analyze the cytotoxicity of the whole suspensions (PDA NPs@DOX and PDA NPs@Fe/DOX + unloaded DOX), in which DOX concentrations were expected to be therefore 0.3, 0.6, and 1 μM.

In those NPs that were isolated (PDA NPs@DOX$^{ads}$), the amount of DOX that was loaded was determined by measuring the concentration of the drug present in the supernatants by UV-Vis. Results obtained were those of the Table 2. Among the different PDA

NPs, there were not remarkable differences in terms of DOX adsorption capacity, although it was noticed that PDA NPs@Fe were capable of adsorbing a little less amount of drug than unloaded PDA NPs.

**Table 2.** Amount of DOX adsorbed to PDA NPs and PDA NPs@Fe as a function of the DOX initial concentration employed in the adsorption process. Results are expressed as ng DOX/mg PDA NPs.

| Initial [DOX] | PDA NPs | PDA NPs@$Fe_{3.5}$ | PDA NPs@$Fe_{5.5}$ | PDA NPs@$Fe_{7.5}$ |
|---|---|---|---|---|
| 0.3 μM | 21.4 ng/mg | 16.8 ng/mg | 19.0 ng/mg | 18.8 ng/mg |
| 0.6 μM | 42.1 ng/mg | 33.2 ng/mg | 37.3 ng/mg | 35.7 ng/mg |
| 1 μM | 57.9 ng/mg | 51.7 ng/mg | 55.8 ng/mg | 54.6 ng/mg |

Then, the effect of both PDA NPs@DOX$^{A}$ and PDA NPs@DOX that were kept with unloaded DOX (PDA NPs@DOX$^{W}$) on the viability of BT474 and HS5 cells was firstly analyzed and compared to that of equivalent concentrations of DOX.

Focusing first in the results obtained after PDA NPs@DOX$^{W}$ treatment of the BT474 cell line (Figure 4a), it could be seen that it was very effective, especially after 72 h, when it decreased their viability by 60–75%. Moreover, it could be also noticed that the employment of this nanosystem helped to achieve a more-sustained drug release. The drawback was PDA NPs@DOX$^{W}$ also reduced the viability of HS5 cells in a similar way to that of BT474 cells after 48 and 72 h (Figure 4c). Nonetheless, these NPs were certainly much less toxic than equivalent concentrations of free DOX, so PDA NPs@DOX$^{W}$ administration could contribute to reduce DOX severe side effects.

On the other hand, when treatment of breast tumor cells was performed with PDA NPs@DOX$^{A}$ (empty bars) (Figure 4b), their survival rate was not so affected, as expected from working with lower DOX concentrations. However, these NPs were also considerably effective, and reduced BT474 viability by 45–65% after 72 h. In addition, when PDA NPs@DOX$^{A}$ were employed for HS5 cell treatment (Figure 4d), it was observed that these NPs were not so toxic to normal cells, whose viability was 20–25% higher than that of cancer cells at all the times analyzed.

Otherwise, final MTT assays were carried out with the BT474 and HS5 cell lines to determine the antitumor activity and selectivity of the different PDA NPs@Fe loaded also with DOX. Again, both types of cells were treated with isolated and non-isolated PDA NPs@Fe/DOX (PDA NPs@Fe/DOX$^{A}$ and PDA NPs@Fe/DOX$^{W}$), and the results obtained were those of Figure 5.

Regardless of whether BT474 cell treatment was carried out with PDA NPs@Fe/DOX$^{A}$ or PDA NPs@Fe/DOX$^{W}$, differences in their viability rate could be appreciated again as a function of the $Fe^{3+}$-loading pH. PDA NPs@$Fe_{3.5}$/DOX were the ones with the most remarkable antitumor activity, maybe because they had been shown to be capable of adsorbing more DOX than the other nanosystems. The NPs with a second more marked therapeutic activity, despite being the ones that adsorbed least DOX, were PDA NPs@$Fe_{7.5}$/DOX, possibly because the $Fe^{3+}$ loaded to these NPs was the free cation and not $Fe(OH)_3$. At last, PDA NPs@$Fe_{5.5}$/DOX, despite having DOX adsorption efficiencies very similar to those of PDA NPs@$Fe_{7.5}$/DOX, reduced BT474 cell viability in a lesser extent. Nevertheless, all PDA NPs@Fe/DOX turned to be very effective. After 72 h of treatment, PDA NPs@Fe/DOX$^{W}$ reduced tumor cell viability to 7–35% (Figure 5a), according to the type of PDA NPs@Fe and in a DOX concentration-dependent manner and, in the case of PDA NPs@Fe/DOX$^{A}$, this percentage range was 20–42% (Figure 5b).

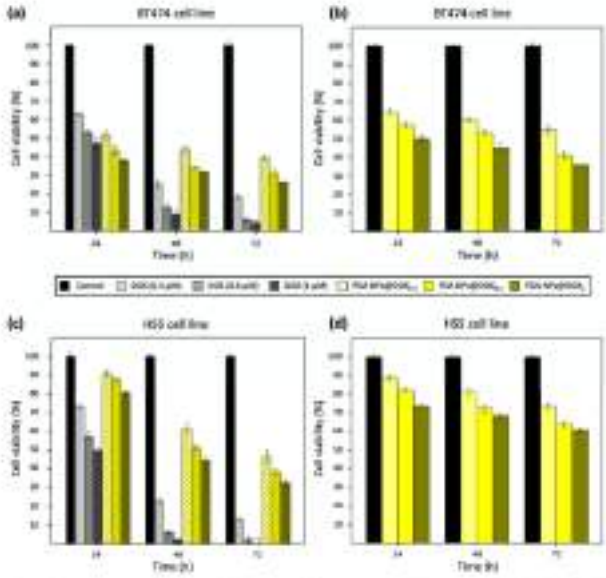

**Figure 4.** Viability results obtained after the performance of MTT assays with the (**a**,**b**) BT474 and (**c**,**d**) HS5 cell lines, which were treated with DOX (0.3–1 μM) and PDA NPs@DOX$_{0.3}$, PDA NPs@DOX$_{0.6}$ and PDA NPs@DOX$_{1}$ (0.108 mg/mL). Bars with the line pattern represent the viability results that were obtained after using PDA NPs@DOX$^{W}$ (**a**–**c**), while the results obtained with PDA NPs@DOX$^{A}$ were those of the empty bars (**b**–**d**).

Besides, PDA NPs loaded with both $Fe^{3+}$ and DOX, showed more noticeable therapeutic activity than PDA NPs loaded only with $Fe^{3+}$ or DOX. Thus, PDA NPs@Fe/DOX were able to further reduce the viability of BT474 cells compared to PDA NPs@Fe and PDA NPs@DOX, and this demonstrated that there was a synergist effect between the metal cation and the drug. To facilitate understanding this fact, viability rate values obtained after BT474 treatment with bare PDA NPs, PDA NPs@Fe$_{1.5}$, PDA NPs@DOX$_{0.6}$, and PDA NPs@Fe$_{1.5}$/DOX$_{0.6}$ have been collected in Figure 6. For instance, after 48 h of treatment, when PDA NPs with adsorbed DOX were administered with unloaded DOX (Figure 6a), PDA NPs@Fe$_{1.5}$/DOX$_{0.6}{}^{W}$ reduced BT474 viability by about 10% more than PDA NPs@Fe$_{1.5}$ and 20% more than PDA NPs@DOX$_{0.6}{}^{W}$. Likewise, when breast cancer cells were treated with PDA NPs with only loaded DOX (Figure 6b), PDA NPs@Fe$_{1.5}$/DOX$_{0.6}{}^{A}$ were 10% and 18% more efficient than PDA NPs@Fe$_{1.5}$ and PDA NPs@DOX$_{0.6}{}^{A}$, respectively, in reducing BT474 viability.

Finally, in addition to being effective, all PDA NPs@Fe/DOX also demonstrated certain selectivity, since when HS5 cells were treated with them (Figure 5c,d), their viability was 15–40% greater than that of BT474 cells. The most selective NPs were PDA NPs@Fe$_{1.5}$/DOX, followed by PDA NPs@Fe$_{1.5}$/DOX and PDA NPs@Fe$_{0.3}$/DOX. Precisely, the content in free $Fe^{3+}$ and not in $Fe(OH)_3$ also followed this trend, so that results suggested again that the pH value at which $Fe^{3+}$-adsorption was performed may be important to determine $Fe^{3+}$ state and, therefore, PDA NPs@Fe endocytosis mediated by Tf and TfR1, which are overexpressed in malignant phenotypes but not in normal tissues [36].

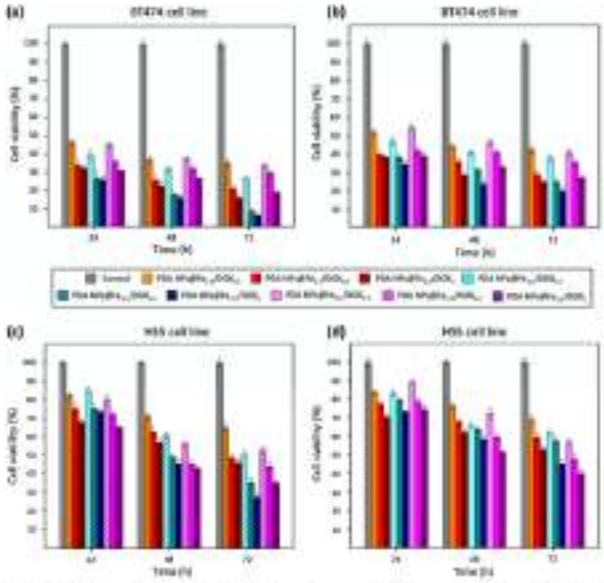

Figure 5. Viability results obtained after the performance of MTT assays with the (a,b) BT474 and (c,d) H69 cell lines, which were treated with all the different PDA NPs@Fe/DOX (0.005 mg/mL). Results of the graphs (a,c) were obtained after using PDA NPs@Fe/DOX$^{x}$, while PDA NPs@Fe/DOX$^{\wedge}$ were employed to obtain graphs (b,d).

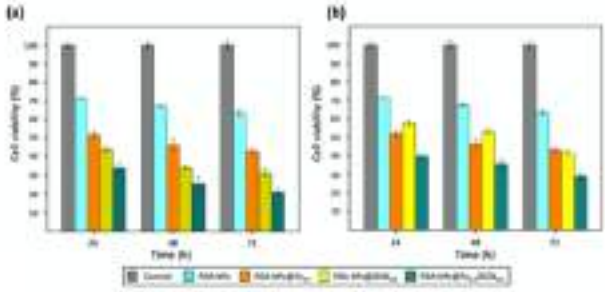

Figure 6. BT474 cell viability rates obtained after the performance of different MTT assays that showed that there was a synergist effect between the $Fe^{3+}$ and doxorubicin (DOX) charged on PDA NPs. Again, bars with the line pattern represent the viability values obtained after BT474 cell treatment with PDA NPs@DOX$^{x}$ (a), while the results obtained with the PDA NPs@DOX$^{\wedge}$ are those of the empty bars (b).

All the different viability values represented in Figures 4 and 5 have also been included in the Supplementary Material (Tables S2 and S3).

*2.6. In Vitro ROS Production after Treatment with PDA NPs and PDA NPs@Fe*

To verify that both DOX and PDA NPs@Fe treatment increased ROS production, the generation of radicals was evaluated 48 h after administering them to BT474 cells by FACS, using a ROS-sensitive probe. As shown in Figure S2, a significant increase in intracellular ROS levels was detected when BT474 cells were treated with DOX and, especially, when NPs loaded with $Fe^{3+}$ were administered. Furthermore, the overproduction of ROS followed the same trend as the viability reduction of breast cancer cells, so that PDA NPs@$Fe_{III}$ caused a slightly higher ROS increase than the rest of PDA NPs@Fe, and the population of cells CellROX$^+$ Sytox$^-$ was smaller after this treatment.

## 3. Discussion

The fundamental work that nanomedicine is carrying out in the search for novel therapies against cancer is indisputable. In recent years, given the frequent appearance of MDR, this research is moving to the development of nanosystems targeting the biochemical aspects that differentiate tumor from normal cells instead of only developing pro-apoptotic nanomedicines [2,37]. One of these biochemical hallmarks of cancer, which is arousing great interest, is Fe homeostasis. Since Fe is essential for cell growth and proliferation, tumor cells are more dependent on this metal and overexpress the proteins that mediate its uptake and cellular internalization [3,6,7,37]. Based on this fact, the number of nanosystems that are being synthesized to induce targeted Fe-dependent death, known as ferroptosis [9–11], is growing considerably [12].

PDA NPs constitute one of such nanosystems. It is believed that their great Fe affinity could be related to their intrinsic antitumor activity [17–19], and some works can be found in the literature in which $Fe^{3+}$ has been loaded to these NPs to improve their therapeutic effect [13–15]. However, in these studies, the pH at which $Fe^{3+}$-adsorption was carried out was not given the importance it deserves, since the pH is essential when determining whether $Fe^{3+}$ is a free cation or $Fe(OH)_3$.

For this reason, in this work, it was decided to analyze how the loading pH affected to PDA NPs $Fe^{3+}$-adsorption efficiency and cytotoxicity. Thus, $Fe^{3+}$-adsorption was carried out at the late endolysosomal pH (4.5), but also at 2.5 and 3.1, since these pH values were closer to the critical pH at which $Fe(OH)_3$ starts to be formed. When $Fe^{3+}$-adsorption was performed at pH 4.5, the amount of $Fe^{3+}$ loaded to PDA NPs was greater than at pH 2.5 and 3.1, perhaps because adsorption was allowed to run during less time at more acidic pH values. Similarly, PDA NPs@$Fe_{III}$ showed an enhanced $Fe^{3+}$-release, which could be promoted by the acidic lysosomal pH and the $Ca^{2+}$ existing in these organelles. Nevertheless, despite exhibiting a larger amount of $Fe^{3+}$ loaded and released, PDA NPs@$Fe_{III}$ reduced the viability rate of breast cancer cells in a lesser extent than the other PDA NPs@Fe. The explanation could lie in the fact that these NPs practically entirely loaded $Fe(OH)_3$, while PDA NPs@$Fe_{III}$ would have loaded both free $Fe^{3+}$ and $Fe(OH)_3$, and PDA NPs@$Fe_{III}$ would only have loaded free $Fe^{3+}$. In this way, although the efficiency of $Fe^{3+}$-adsorption at pH 2.5 and 3.1 was smaller, since the amount of free $Fe^{3+}$ loaded to PDA NPs was greater, so was their therapeutic activity, possibly because their Tf and TfR1-mediated endocytosis may be enhanced [14] (Figure 7a). In addition, since Tf and TfR1 are overexpressed in tumor cells but not under normal physiological conditions, this explanation would also help to understand why PDA NPs@$Fe_{III}$ and PDA NPs@$Fe_{III}$ were less toxic to stromal cells than PDA NPs@$Fe_{III}$.

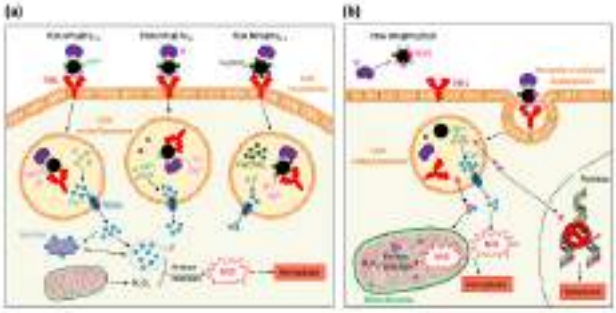


Figure 7. Graphical representation of (a) how the pH at which $Fe^{3+}$ was adsorbed may condition the cytotoxicity of the PDA NPs@Fe and of (b) the synergist effect that could take place between $Fe^{3+}$ and DOX when both of them were loaded to PDA NPs.

Otherwise, with the aim of enhancing PDA NPs@Fe antitumor activity, loading them with different concentrations of DOX, while trying to reduce the severe adverse effects of this drug, was determined. Following assays were performed in two different manners. On one hand, PDA NPs@DOX and PDA NPs@Fe/DOX were isolated to study their cytotoxicity and, on the other hand, they were administered as combination therapy with unbound DOX. In both cases, PDA NPs@DOX showed more sustained DOX release and less toxicity than equivalent concentrations of the parent drug. Their antitumor activity increased as function of DOX concentration and, as expected, combination therapy was more effective, but also less selective, than treatment with isolated PDA NPs@DOX[4]. This phenomenon also occurred with PDA NPs@Fe/DOX, which exhibited a more remarkable antineoplastic activity than the PDA NPs in which only $Fe^{3+}$ or DOX had been adsorbed. Such fact showed that there was a synergist effect between the metal and the drug, which was precisely chosen among the different antitumor agents for causing ROS-overproduction, as occurs in the ferroptosis process (Figure 7b). This synergy was evident for all PDA NPs@Fe/DOX, but differences in their cytotoxicity could also be appreciated. In general, the NPs that reduced breast cancer cell viability the most were PDA NPs@$Fe_{1.0}$/DOX, while the most selective were PDA NPs@$Fe_{0.5}$/DOX. The first were the PDA NPs that adsorbed the greatest amount of DOX and, PDA NPs@$Fe_{0.5}$/DOX were the particles with less loaded drug. This, along with the fact that these PDA NPs had more free $Fe^{3+}$ loaded than the PDA NPs@$Fe_{1.0}$/DOX, would help to understand their cytotoxic behavior. Finally, PDA NPs@$Fe_{1.5}$/DOX, despite having more DOX burdened than PDA NPs@$Fe_{1.0}$/DOX and more $Fe^{3+}$ loaded than both PDA NPs@$Fe_{0.5}$/DOX and PDA NPs@$Fe_{1.0}$/DOX, were not the most effective, but were the least selective. Such phenomenon revealed once again that the pH at which $Fe^{3+}$-adsorption was performed may condition the efficacy and side toxicity of the resulting PDA nanosystems, which could be potentially chosen or alternatively administered depending on the objectives pursued (more efficacy vs. fewer side effects) and the response of the patients.

## 4. Materials and Methods

### 4.1. Synthesis and Characterization of PDA NPs

PDA NPs were synthesized by the oxidation and self-polymerization of dopamine in a basic aqueous medium. Briefly, deionized $H_2O$ ($H_2O$(d), 90 mL) was mixed with pure ethanol (40 mL) and $NH_4OH$ (25–28%, 4.2 mL), and the resulting mixture was kept under vigorous stirring for 30 min. Then, dopamine hydrochloride (0.5 g) was dissolved in

$H_2O$(d) (10 mL) and this solution was added to the previous mixture. The polymerization reaction was allowed to proceed for 24 h and after that time, PDA NPs obtained were isolated by centrifugation [15,17,18]. Next, four centrifugation–redispersion cycles in $H_2O$(d) were performed to eliminate any residue, and washed PDA NPs were finally re-suspended in $H_2O$(d) in a final concentration of 2 mg/mL.

To characterize them, TEM images were taken (Tecnai Spirit Twin, Fei Company, Hillsboro, OR, USA) with a voltage acceleration of 120 kV. PDA NPs were resuspended in $H_2O$(d) in a concentration inferior to 0.01% WT, and drops of this dispersion were deposited on copper grids with a collodium membrane. They were allowed to dry for 24 h, TEM images were taken and size-range histograms were obtained after determining the size of at least 300 different PDA NPs (ImageJ software, NIH, Bethesda, MD, USA). In addition, PDA NP hydrodynamic diameter was also determined by DLS (Zetasizer Nano ZS90, Malvern Instruments Inc., Royston, Hertfordshire, UK) on the basis of their intensity-average size distribution. On this occasion, PDA NPs were dispersed in Trizma base solution (pH 10.0), also in a concentration lower than 0.01% WT.

### 4.2. $Fe^{3+}$-Loading to PDA NPs at Different pH Values

To load PDA NPs with $Fe^{3+}$, NPs (1 mL, 2 mg/mL) were mixed with solutions of $FeCl_3$ (30 mg/L, 20 mL) that were prepared in buffers of different pH values. Thus, to load $Fe^{3+}$ to PDA NPs at pH 2.5 and 3.1, $FeCl_3$ solutions were prepared in citrate/NaOH buffer (0.1 M), whose pH was adjusted to the mentioned values by dropping HCl (0.1 M). Nevertheless, to load $Fe^{3+}$ to PDA NPs at pH 4.5, $FeCl_3$ was dissolved in acetate buffer (0.4 M), just as it had been done in previous works [13,19]. In all cases, PDA NPs were kept stirred within the $FeCl_3$ solutions at 100 rpm at room temperature but, at pH 2.5 and 3.1, the adsorption process was allowed to run for 3 h, while it was allowed to run overnight at pH 4.5. This time difference was due to the fact that very acidic pH values can alter PDA chemical structure and as a consequence, $Fe^{3+}$-loading at pH 2.5 and 3.1 could not be extended for longer.

To determine the $Fe^{3+}$-adsorption efficiency, PDA NPs@Fe were isolated by centrifugation and the concentration of $Fe^{3+}$ existing in the different supernatants was analyzed by ICP-OES (ULTIMA 2 emission spectrometer, Horiba Jobin Yvon, Unterhaching, Germany). Subsequently, all PDA NPs@Fe were characterized by TEM imaging, preparing the samples in the same way as in the previous point. Moreover, to verify if any modification occurred in the chemical structure of PDA NPs after $Fe^{3+}$-adsorption, IR spectra of PDA NPs@Fe were obtained (SpectrumTwo™, PerkinElmer, Waltham, MA, USA) and compared to bare PDA NP spectrum in the 4000–400 $cm^{-1}$ wavelength range. Samples were prepared as pellets of PDA NPs@Fe in KBr, choosing a weight ratio that did not present saturation in the absorption bands. All spectra were normalized at 1580 $cm^{-1}$ to be able to compare the intensity of the bands.

### 4.3. $Fe^{3+}$-Release and $Ca^{2+}$-Loading from/to the Different PDA NPs@Fe

To later preform in vitro cytotoxicity assays, bare PDA NPs and all PDA NPs@Fe were washed again through five centrifugation–redispersion cycles in PBS (0.01 M, pH 7.4), being finally resuspended in this buffer in a final concentration of 2 mg/mL. Then, PDA NPs@Fe (1 mL) were mixed with $CaCl_2$ solutions (20 mg/L, 20 mL) prepared in a lysosomal simulator buffer (0.1 M $C_6H_8O_7$, 0.2 M $Na_2HPO_4$, pH 4.5) [27], and the resulting suspensions were kept in agitation (100 rpm) for 48 h. After such time, PDA NPs@Fe/Ca were isolated again by centrifugation and the concentrations of $Fe^{3+}$ and $Ca^{2+}$ existing in the supernatants were determined by ICP-OES.

### 4.4. DOX-Loading to PDA NPs and the Different PDA NPs@Fe

Once PDA NPs (with and without loaded $Fe^{3+}$) were resuspended in PBS, DOX-adsorption was carried out. For this, three different volumes of a stock solution of the drug

were added to PDA NP suspensions (250 µL, 2 mg/mL) in order to obtain DOX working concentrations of 0.3, 0.6, and 1 µM. The adsorption process was allowed to run overnight in dark conditions, keeping the NPs in agitation (100 rpm). Next day, PDA NPs of some suspensions were isolated by centrifugation and resuspended in PBS (2 mg/mL). However, other suspensions were not centrifuged, and PDA NPs were kept with non-adsorbed DOX to perform two different types of cytotoxicity assays.

In those PDA NPs that were isolated, the amount of DOX adsorbed was determined by difference, quantifying DOX concentration in the supernatants by UV-Vis spectrophotometry (UV-1800, Shimadzu Corporation, Kioto, Japan). The absorbance of the samples was measured at 480 nm, using the supernatant of the DOX-unloaded PDA NPs as blank. Subsequently, DOX concentration was determined from a previously made calibration curve.

### 4.5. Cell Culture

BT474 and HS5 cell lines (ATCC, Wesel, Germany) were cultured as instructed. They were grown in DMEM, supplemented with FBS (10% V/V) and antibiotics (100 U/mL penicillin and 100 mg/mL streptomycin) in a 95:5 air/$CO_2$ humidified atmosphere at 37 °C.

### 4.6. In Vitro Cytotoxicity

First, the cytotoxicity of PDA NPs and the different PDA NPs@Fe was compared using BT474 and HS5 cells by the MTT assay. BT474 and HS5 cells, once grown, were seeded into 24-well plates (12,000 cells/well) and incubated for 24 h to allow attachment. Then, culture medium in the wells was replaced by fresh supplemented DMEM containing PBS (for the control), PDA NPs, PDA NPs@$Fe_{III}$, PDA NPs@$Fe_{II}$, or PDA NPs@$Fe_{0}$ (0.035 mg/mL), and cells were incubated again for 24, 48 and 72 h. A total of 110 µL MTT solution (5 mg/mL) were added to each well and cell incubation was performed for 1 h. Formazan crystals were dissolved by adding DMSO (500 µL/well), and the optical density value of each well was determined by applying a procedure that was previously set-up to subtract PDA contribution to sample absorbance [17]. This absorbance was measured in a microplate reader (Zetasizer Nano ZS90, Malvern Instruments Inc., Royston, UK).

Next, the same protocol was followed to assess the cytotoxicity of PDA NPs@DOX and PDA NPs@Fe/DOX, which was compared to that of free DOX (0.3, 0.6 and 1 µM). In all cases, BT474 and HS5 cells were treated with 0.035 mg/mL PDA NPs but, as mentioned before, these assays were performed in two different manners: On one hand, cells were treated with PDA NPs@DOX or PDA NPs@Fe/DOX that were isolated after the DOX adsorption process and, on the other hand, they were treated with the complete suspension, in which PDA NPs@DOX or PDA NPs@Fe/DOX were kept with unloaded DOX. Again, the viability of BT474 and HS5 cells was analyzed each 24 h, for a total of 72 h, following the same steps as before.

### 4.7. In Vitro ROS Detection

ROS production was evaluated 48 h after BT474 treatment with DOX (0.3 µM) and PDA NPs@Fe (0.035 mg/mL) by using CellROX® Deep Reagent (Thermo Fisher, C10491). As described in the manufacturer's instructions, BT474 cells were harvested and CellROX® (0.5 µM) was added to the suspension (1 mL, $10^6$ cells/mL). Cells were incubated for 45 min at 37 °C and Sytox® (1 µM) was incorporated when 30 min elapsed. Samples were acquired (at least 50,000 events) with a FACSAria™ III cytometer (BD Biosciences, San José, CA, USA) and data obtained were analyzed using CellQuest software (BD Biosciencies). Median values of fluorescence intensity were used to provide a semiquantitative assessment of ROS production [38].

### 4.8. Statistical Analysis

Data concerning MTT assays were analyzed using an unpaired two-tailed Student t-test. p-values less than 0.05 were considered to be statistically significant. Displayed viability results are the average ± SEM of three replicates per treatment condition that were obtained in two parallel experiments.

## 5. Conclusions

In conclusion, the importance that the pH has when $Fe^{3+}$ is loaded to PDA NPs to induce ferroptosis in tumor cells has become clear throughout this work. This pH value determines $Fe^{3+}$ state and, therefore, the selectivity and therapeutic activity of the resulting $Fe^{3+}$-loaded PDA NPs. Such antitumor activity can be enhanced by co-loading other agents that also increase ROS production in cancer cells, like DOX, and PDA NPs with different concentrations of $Fe^{3+}$ and drugs could be tailored-synthesized and administered depending on the therapeutic need.

**Supplementary Materials:** The following are available online at www.mdpi.com/1422-0067/22/4/2161/s1. Figure S1: IR spectra of PDA NPs and all PDA NPs@$Fe_3$. Figure S2: In vitro ROS production analysis by FACS. Table S1: Viability rate values corresponding to Figure 3, Table S2: Viability rate values corresponding to Figure 4, Table S3: Viability rate values corresponding to Figure 5.

**Author Contributions:** Conceptualization, C.N. and M.A.V.; methodology, C.N. and M.A.V.; software, M.A.V.; validation, C.N. and M.A.V.; investigation, C.N. and M.A.V.; writing—original draft preparation, C.N.; writing—review and editing, C.N., M.A.V., and E.M.M.d.V.; supervision, M.A.V. and E.M.M.d.V.; project administration, E.M.M.d.V.; funding acquisition, E.M.M.d.V. All authors have read and agreed to the published version of the manuscript.

**Funding:** This research was funded by SPANISH MINISTRY OF SCIENCES, INNOVATION AND UNIVERSITIES, grant number PID2019-108899RB100.

**Institutional Review Board Statement:** Not applicable.

**Informed Consent Statement:** Not applicable.

**Data Availability Statement:** The data that support the findings of this study are available from the corresponding authors upon reasonable request.

**Acknowledgments:** C.N. thanks to Junta de Castilla y León for her predoctoral fellowship and all the authors thank the Electron Microscopy Facilities-NUCLEUS of the University of Salamanca for the TEM images.

**Conflicts of Interest:** The authors declare no conflict of interest.

## Abbreviations

| | |
|---|---|
| DOX | Doxorubicin |
| LIP | Labile iron pool |
| MDR | Multidrug resistance |
| PDA NPs | Polydopamine nanoparticles |
| PDA NPs@$Fe_{2.5}$ | Polydopamine nanoparticles loaded with $Fe^{3+}$ at pH 2.5 |
| PDA NPs@$Fe_{3.1}$ | Polydopamine nanoparticles loaded with $Fe^{3+}$ at pH 3.1 |
| PDA NPs@$Fe_{4.5}$ | Polydopamine nanoparticles loaded with $Fe^{3+}$ at pH 4.5 |
| PDA NPs@$DOX_{0.3}$ | Polydopamine nanoparticles loaded with a 0.3 μM DOX solution |
| PDA NPs@$DOX_{0.6}$ | Polydopamine nanoparticles loaded with a 0.6 μM DOX solution |
| PDA NPs@$DOX_{1}$ | Polydopamine nanoparticles loaded with a 1 μM DOX solution |
| PDA NPs@$DOX^{A}$ | Isolated DOX-loaded polydopamine nanoparticles |
| PDA NPs@$DOX^{W}$ | Whole suspension of DOX-loaded polydopamine nanoparticles plus unloaded DOX |
| PDA NPs@$Fe_3DOX$ | Polydopamine nanoparticles loaded with $Fe^{3+}$ and DOX |
| ROS | Reactive Oxygen Species |
| Tf | Transferrin |
| TfR1 | Transferrin receptor-1 |

**References**


1. Kwon, S.; Ko, H.; You, D.G.; Kataoka, K.; Park, J.H. Nanomedicines for reactive oxygen species mediated approach: An emerging paradigm for cancer treatment. *Acc. Chem. Res.* **2019**, *52*, 1771–1782.
2. Trachootham, D.; Alexandre, J.; Huang, P. Targeting cancer cells by ROS-mediated mechanisms: A radical therapeutic approach? *Nat. Rev.* **2009**, *8*, 579–591.
3. Liu, T.; Liu, W.; Zhang, M.; Yu, W.; Gao, F.; Li, C.; Wang, S.-B.; Feng, J.; Zhang, X.-Z. Ferrous-supply-regeneration nanoengineering for cancer-cell-specific ferroptosis in combination with imaging-guided photodynamic therapy. *ACS Nano* **2018**, *12*, 12181–12192.
4. Hartleben, G.; Schorpp, K.; Kwon, Y.; Betz, B.; Tsokanos, F.-F.; Dantes, Z.; Schäfer, A.; Rothenaigner, I.; Kuhn, J.M.M.; Mongiry, F.; et al. Combination therapies induce cancer cell death through the integrated stress response and disturbed pyrimidine metabolism. *EMBO Mol. Med.* **2021**, *Mar 3*, e12461.
5. Angelova, A.; Angelov, B. Dual and multi-drug delivery nanoparticles towards neuronal survival and synaptic repair. *Neural. Regen. Res.* **2017**, *12*, 886–889.
6. Fonseniti, S.; Greco, L.; Grizzi, F.; Malesci, A.; Laghi, L. Iron metabolism in cancer progression. *Int. J. Mol. Sci.* **2020**, *21*, 2257.
7. Jung, M.; Mertens, C.; Tomat, E.; Brüne, B. Iron as a central player and promising target in cancer progression. *Int. J. Mol. Sci.* **2019**, *20*, 273.
8. Mitchell, K.K.P.; Sandoval, S.; Cortes-Marcos, M.J.; Alfaro, J.G.; Kummel, A.C.; Trogler, W.C. Self-assembled targeting of cancer cells by iron(III)-doped, silica nanoparticles. *J. Mater. Chem. B Mater. Biol. Med.* **2014**, *2*, 8017–8025.
9. Battaglia, A.M.; Chirillo, R.; Aversa, I.; Sacco, A.; Costanzo, F.; Biamonte, F. Ferroptosis and cancer: Mitochondria meet the "iron maiden" cell death. *Cells* **2020**, *9*, 1505.
10. Bebber, C.M.; Müller, F.; Clemente, L.P.; Weber, J.; von Karstedt, S. Ferroptosis in cancer cell biology. *Cancers* **2020**, *12*, 164.
11. Dixon, S.J.; Lemberg, K.M.; Lamprecht, M.R.; Skouta, R.; Zaitsev, E.M.; Gleason, C.E.; Patel, D.N.; Bauer, A.J.; Cantley, A.M.; Yang, W.S.; et al. Ferroptosis: An iron-dependent form of non-apoptotic cell death. *Cell* **2012**, *149*, 1060–1072.
12. Wang, S.; Luo, J.; Zhang, Z.; Dong, D.; Shen, Y.; Fang, Y.; Hu, L.; Liu, M.; Dai, C.; Peng, S.; et al. Iron and magnetic: New research direction of the ferroptosis-based cancer therapy. *Am. J. Cancer Res.* **2018**, *8*, 1933–1946.
13. Vega, M.A.; Nieto, C.; Marcelo, G.; Martín del Valle, E.M. Cytotoxicity of paramagnetic cations-loaded polydopamine nanoparticles. *Colloids Surf. B Biointerfaces* **2018**, *167*, 284–290.
14. Chen, L.; Lin, Z.; Liu, L.; Zhang, X.; Shi, W.; Ge, D.; Sun, Y. $Fe^{2+}$/$Fe^{3+}$ ions chelated with ultrasmall polydopamine nanoparticles induce ferroptosis for cancer therapy. *ACS Biomater. Sci. Eng.* **2019**, *5*, 4861–4869.
15. Dong, L.; Wang, C.; Zhen, W.; Jia, X.; An, S.; Xu, Z.; Zhang, W.; Jiang, X. Biodegradable iron-coordinated hollow polydopamine nanospheres for dihydroartemisinin delivery and selective enhanced therapy in tumor cells. *J. Mater. Chem. B* **2019**, *7*, 6172.
16. Wang, Z.; Zou, Y.; Li, Y.; Cheng, Y. Metal-containing polydopamine nanomaterials: Catalysis, energy and theranostics. *Small* **2020**, *16*, e1907042.
17. Nieto, C.; Vega, M.A.; Marcelo, G.; Martín del Valle, E.M. Polydopamine nanoparticles kill cancer cells. *RSC Adv.* **2018**, *8*, 36281.
18. Nieto, C.; Vega, M.A.; Enrique, J.; Marcelo, G.; Martín del Valle, E.M. Size matters in the cytotoxicity of polydopamine nanoparticles in different types of tumors. *Cancers* **2019**, *11*, 1679.
19. Nieto, C.; Marcelo, G.; Vega, M.A.; Martín del Valle, E.M. Antineoplastic behaviour of polydopamine nanoparticles prepared in different water/alcohol media. *Colloids Surf. B Biointerfaces* **2021**, *198*, 111506.
20. Ichikawa, Y.; Ghanefar, M.; Bayeva, M.; Wu, R.; Khechaduri, A.; Prasad, S.V.N.; Mutharasan, R.K.; Naik, T.J.; Ardehali, H. Cardiotoxicity of doxorubicin is mediated through mitochondrial iron accumulation. *J. Clin. Investig.* **2014**, *124*, 617–630.
21. Li, X.-J.; Li, W.-T.; Li, Z.-H.-R.; Zhang, L.P.; Gai, C.C.; Zhang, W.F.; Ding, D.J. Iron-chelated polydopamine decorated doxorubicin-loaded nanodevices for reactive oxygen species enhanced cancer combination therapy. *Therapy. Front. Pharmacol.* **2019**, *10*, 75.
22. Umnova, A.A.; Loshkarev, A.A.; Tokunov, Y.M.; Ivanov, U.V. Comparison of the results of measurements of the sizes of nanoparticles in stable colloidal solutions by the methods of acoustic spectroscopy, dynamic light scattering, and transmission electron microscopy. *Mem. Tech.* **2017**, *59*, 1151–1155.
23. Bartel Marti, F.; Lucena Conde, F.; Hernández Méndez, J.; Arribas Jimeno, S. *Química Analítica Cuantitativa*, 18th ed.; Paraninfo: Madrid, Spain, 2006; p. 1090.
24. Dong, Y.-D.; Boyd, B.J. Applications of X-ray scattering in pharmaceutical science. *Int. J. Pharm.* **2011**, *417*, 101–111.
25. Raffaello, A.; Mammucari, C.; Gherardi, G.; Rizzuto, R. Calcium at the center of cell signaling: Interplay between endoplasmic reticulum, mitochondria, and lysosomes. *Trends Biochem. Sci.* **2016**, *41*, 1035–1049.
26. Klosterman, L.; Bettinger, C.J. Calcium-mediated control of polydopamine film oxidation and iron chelation. *Int. J. Mol. Sci.* **2017**, *18*, 14.
27. Carreira, A.C.; de Almeida, R.F.M.; Silva, L.C. Development of lysosome-mimicking vesicles to study the effect of abnormal accumulation of sphingosine on membrane properties. *Sci. Rep.* **2017**, *7*, 3949.
28. Cheng, M.; Liu, P.; Lu, L.X. Iron promotes breast cancer cell migration via IL-6/JAK2/STAT3 signalling pathways in a paracrine or autocrine IL-6-rich inflammatory environment. *J. Inorg. Biochem.* **2020**, *210*, 111159.
29. Lamy, P.-J.; Durigova, A.; Jacot, W. Iron homeostasis and anemia markers in early breast cancer. *Clin. Chim. Acta* **2014**, *436*, 34–40.
30. Gong, Y.; Gallis, B.M.; Goodlett, D.R.; Yang, Y.; Lu, H.; Lacomis, E.; Lai, H.; Sasaki, T. Effects of transferrin conjugates of artemisinin and artemisinin dimer on breast cancer cell lines. *Anticancer Res.* **2013**, *33*, 123–132.

31. Thorn, C.F.; Oshiro, C.; Marsh, S.; Hernandez-Boussard, T.; McLeod, H.; Klein, T.E.; Altman, R.B. Doxorubicin pathways: Pharmacodynamics and adverse effects. *Pharmacogenet. Genom.* **2011**, *21*, 440.
32. Wen, S.-H.; Su, S.-C.; Liou, B.-H.; Lin, C.-H.; Lao, K.-R. Sulbactam-enhanced cytotoxicity of doxorubicin in breast cancer cells. *Cancer Cell Int.* **2018**, *18*, 128.
33. Loibl, S.; Weber, K.E.; Timms, K.M.; Elkin, E.P.; Hahnen, E.; Fasching, P.A.; Lederer, B.; Denkert, C.; Schneeweiss, A.; Braun, S.; et al. Survival analysis of carboplatin added to an anthracycline/taxane-based neoadjuvant chemotherapy and HRD score as predictor of response-final results from GeparSixto. *Ann. Oncol.* **2018**, *29*, 2341–2347.
34. Pujade-Lauraine, E.; Wagner, U.; Aavall-Lundqvist, E.; Gebski, V.; Heywood, M.; Vasey, P.A.; Volgger, B.; Vergote, I.; Pignata, S.; Ferrero, A.; et al. Pegylated liposomal doxorubicin and carboplatin compared with paclitaxel and carboplatin for patients with platinum-sensitive ovarian cancer in late relapse. *J. Clin. Oncol.* **2010**, *28*, 3323–3329.
35. Sparano, J.A.; Makhson, A.N.; Semiglazov, V.F.; Tjulandin, S.A.; Bálint Lahat, O.I.; Bondarenko, I.N.; Beiglarova, N.V.; Manikhas, G.M.; Olivynchenko, G.P.; Chatikhine, V.A.; et al. Pegylated liposomal doxorubicin plus docetaxel significantly improves time to progression without additive cardiotoxicity compared with docetaxel monotherapy in patients with advanced breast cancer previously treated with neoadjuvant-adjuvant anthracycline therapy: Results from a randomized phase III study. *J. Clin. Oncol.* **2009**, *27*, 4522–4529.
36. Rouault, T.A. The role of iron regulatory proteins in mammalian iron homeostasis and disease. *Nat. Chem. Biol.* **2006**, *2*, 406–414.
37. Pavlova, N.N.; Thompson, C.B. The emerging hallmarks of cancer metabolism. *Cell Metab.* **2016**, *23*, 27–47.
38. Anticoli, S.; Amatore, D.; Matarrese, P.; De Angelis, M.; Palamara, A.T.; Nencioni, L.; Ruggieri, A. Counteraction of HCV induced oxidative stress concurs to establish chronic infection in liver cell cultures. *Oxid. Med. Cell Longev.* **2019**, *2019*, 6452390.

# CHAPTER 6

## POLYDOPAMINE NANOPARTICLES LOADED WITH TRASTUZUMAB AS PACLITAXEL TARGETED CARRIER

## 6.1. Introduction

### *6.1.1. Polydopamine advantages for the development of drug delivery systems*

As described in the general introduction and as has been highlighted in previous Chapters, despite the fact that the knowledge acquired on cancer molecular biology has greatly improved the diagnosis and treatment of this disease, chemotherapy remains the most commonly applied strategy in cancer therapy [1,2]. To date, very effective anti-tumour compounds have been discovered. However, their administration is not always easy, mainly because many of them have limited aqueous solubility [3]. Furthermore, another relevant disadvantage of these broad-spectrum compounds is their lack of selectivity. These drugs have practically the same effect on killing normal cells while attacking tumour tissues [1], and this imposes major limitations in their clinical efficacy and safety [3]. In addition, long-term chemotherapy frequently leads to the development of MDR, which in turn causes tumour recurrence and makes it difficult for patients to overcome the disease [1,4].

Fortunately, nanotechnology has brought novel strategies to the biomedical field, especially nanoparticle-based anti-tumour therapies, which have shed light in cancer treatment [5]. Since pathological features of the majority of solid tumours differ from those of normal tissues, nano-delivery systems can transport chemotherapeutic drugs to tumours in a more specific manner thanks, among other phenomena, to the EPR effect [1,6]. In this manner, as has been said on several occasions, these DDSs, in comparison to conventional chemotherapy agents, can reduce the exposure of drugs to non-targeted sites, limiting their side toxicity and the apparition of MDR, and even lowering the economic costs of chemotherapy [1].

Over the last few years, numerous types of NP systems of different nature have been developed as vehicles for anti-tumour drugs, including micelles, liposomes, polymeric NPs, inorganic NPs, carbon nanotubes… [1] The development of all of them has been possible thanks to the advances

in material sciences, which have occurred at a rate that was previous unthinkable and have provided biomedicine with biocompatible and biodegradable compounds with extraordinary applications [7]. Among them, one of the nanomaterials that has aroused great interest for the development of advantageous DDSs, as already described in Chapter 4 and 5, is PDA [1,8-9].

This mussel-inspired versatile polymer can be used to synthesize PDA NPs and PDA hollow NPs or nanocapsules, as well as to coat and modify NPs prepared from other organic and inorganic materials, and to develop PDA-drug conjugates [1,9] (**Figure 6.1**).

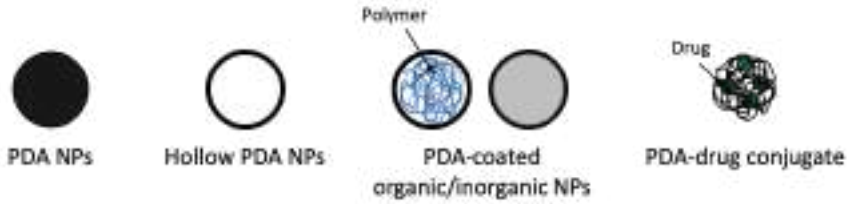


**Figure 6.1**. Main forms of PDA-based nanocarriers.

Compared to other nanomaterials employed in the biomedicine field, PDA has very convenient characteristics that have made it gain great popularity since it was first described in 2007 [10]. These properties have already been highlighted previously [11], especially in Chapter 4 (page 137), and in order to not be repetitive, only the three that are especially interesting for the development of drug nanocarriers have been here summarized. The first one is that the synthesis of PDA NPs and coatings is simple and does not require organic solvents or complicated instrumentation [1,9,12]. In alkaline media, DA produces PDA aggregates with good polydispersity, and in addition, PDA NP size and PDA coating thickness can be modulated by varying the synthesis conditions [1,9], which even allows controlling the intrinsic antineoplastic effect of the NPs prepared from this polymer [13,14]. Secondly, due to its chemical structure, PDA is capable of adsorbing drugs with high loading rates [15]. Its richness of catechol and quinone moieties offers the potential to anchor anti-tumour compounds with an anthraquinone structure by physical bonding via π-π stacking or hydrogen bonds [1,9,15]. Besides, when DA is self-polymerized, phenolic groups, amino groups and other

reactive sites remain in PDA surface and allow secondary chemical modifications with compounds containing thiol or amino groups through Michael addition or Schiff base reactions [1,9,16]. Lastly, PDA is highly sensitive to pH. NPs and coatings made up with this polymer can promote the release of drug molecules in acidic and high GSH-concentration conditions while reducing their release at the physiological pH because of its zwitterionic property. In this manner, employing PDA for the development of DDSs can contribute to make them pH-responsive [9,17,18].

### *6.1.2. Drug-loading strategies in polydopamine and polydopamine-modified nanoparticles*

Taking into account the advantages provided by PDA structure, several strategies can be followed to load drugs in PDA-based NPs (**Figure 6.2**) [9]:

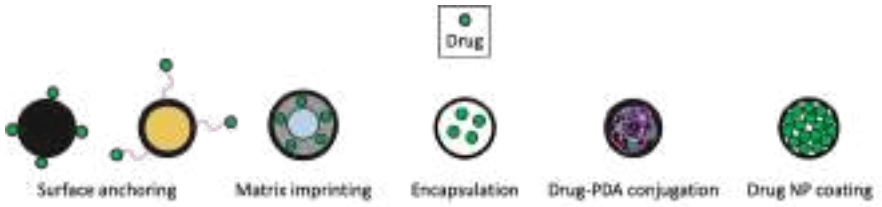


**Figure 6.2**. Schematic illustration of the five strategies that can be followed to load PDA and PDA-modified NPs with anti-tumour drugs.

i) Loading them onto PDA surface through physical adsorption (van der Waal's forces and hydrogen bonds) or chemical bonding (Michael addition or Schiff base reactions). This strategy is the most frequently used with PDA NPs and organic/inorganic NPs coated with PDA.

ii) Embedding and imprinting the drugs in a matrix, either via physical adsorption or chemical bonding. This approach is normally utilized in multi-layer PDA-modified NPs.

iii) Encapsulating the drugs in PDA hollow NPs or loading them to MSNs where PDA is used as "gate keeper".

iv) Forming PDA-drug conjugates via chemical linking.

v) Self-assembling drugs like DOX or PTX in NPs where possible and coating them with PDA in order to enhance their stability.

### *6.1.3. Examples of currently developed drug-loaded polydopamine-based nanocarriers*

Of the three types of PDA-based nanocarriers that can be synthesized, those most used up to now for the development of new DDSs have been the PDA-coated organic and inorganic NPs [1,9]. In these nanosystems, PDA-coating, apart from being carried out to anchor bioactive molecules, perform secondary modifications or achieve an on-demand drug release, is also performed to improve the hydrophilicity, biocompatibility and biodegradability of the modified nanocarriers [9]. Thus, pursuing these objectives, NPs of organic nature, such as those made up by PLGA, have been modified with PDA to transport DOX [19,20]. Likewise, inorganic NPs such as MSNs, AuNPs and $Fe_3O_4$ NPs have been coated with PDA to act as vehicles for adsorbed or encapsulated DOX, DM1 or cisplatin [1,12]. In addition, in some of these DDSs, PDA-coating has also served to anchor biomolecules (like cetuximab [19,21], folic acid (FA) [20,22] or some peptides [23]) to target cancer cells overexpressing certain receptors.

On the other hand, despite having been less employed for the development of DDSs, several examples of PDA NPs acting as drug carriers can be also found in the literature. In most cases, these NPs transported adsorbed DOX, but PDA NPs physically loaded with CPT, cisplatin and/or 7-ethyl-10-hydroxycamptothecin (SN-38) have been designed by certain research groups in recent years, too. Some of the drug-loaded PDA NPs developed have been collected in **Table 6.1**.

**Table 6.1.** Examples of drug-loaded PDA NPs.

| Nanoparticle | Adsorbed drug | Secondary functionalization | Targeted cancer | Reference |
|---|---|---|---|---|
| PDA | CPT | - | Lung, cervical | [24] |
| PDA-PEG[a] | DOX, SN38 | - | Breast, lung | [25] |
| PDA-PEG | DOX | TPP[b] | Breast | [26] |
| PDA | DOX | RGDC[c] peptide | Cervical | [27] |
| PDA-PEG | DOX | ICG[d], $Mn^{2+}$ | Breast, cervical | [28] |
| PDA-PEG | DOX | - | Cervical | [29] |
| PDA-PEG | DOX | $^{131}I$ | Breast | [30] |
| PDA | SN38 | SCM[e] | Bone | [31] |
| PDA | Bortezomib | Glucosyl ligands | Breast | [32] |
| Mesoporous PDA | DOX | TPGS[f] | Breast | [33] |

[a]PEG – Polyethylene glycol; [b]TPP – Triphenylphosphonium; [c]RGDC – Arginine-glycine-cysteine acid; [d]ICG – Indocyanine green; [e]SCM – Stem cell membrane; [f]TPGS – D-α-tocopheryl polyethylene glycol 1000 succinate.

As can be seen from **Table 6.1**, PDA NPs have not been loaded with PTX to date. Thereby, if a cross-search of the terms "PDA" and "PTX" is done, only three research works can be encountered. In one of them, PTX NPs were obtained and subsequently coated with PDA [34]. In another, PLGA microspheres were tailored with PDA and loaded with PTX and gold NPs and [35], in the last work, mesoporous PDA NPs were modified with PEG and loaded with PTX [36]. Therefore, in no study the taxane has been directly adsorbed in PDA NPs.

Similarly, no work has been found published in which PDA NPs have been functionalized with an antibody. As already mentioned, PDA-coated NPs have been modified with various peptides, FA and the antibody cetuximab to target cancer cells [1,37]. Likewise, lipid PDA hybrid NPs have been decorated by an anti-claudin 3 Ig [38]. However, no antibody has been hitherto directly anchored to the surface of PDA NPs.

For these reasons, and since in Chapter 3 APPZ were developed as nanocarriers for PTX and Tmab [39], charging PDA NPs with this taxane and this anti-HER2 antibody for the first time was decided in order to compare the results obtained with those of the conjugated APPZ. Since PDA NPs have been shown to have intrinsic antineoplastic activity [11,13-14], the main objective of loading them with PTX and Tmab was further

improving the effectiveness and selectivity shown by the conjugated APPZ, employing also this time 2D and 3D cell cultures for the *in vitro* validation of the loaded PDA NPs.

## 6.2. Paclitaxel and trastuzumab loading to polydopamine nanoparticles

### *6.2.1. Obtaining of polydopamine nanoparticles*

Given that results obtained in Chapter 4 (page 178) allowed to observe that PDA NPs prepared in an aqueous medium containing 2-PrOH had greater antineoplastic activity than those synthesized with other ROHs [14], using 2-PrOH was determined to obtain the nanosystem with the greatest possible anti-tumour effect. Likewise, as in that Chapter (page 166) it was also shown that size influenced the cytotoxicity of PDA NPs [13], NPs with a diameter inferior to 200 nm were decided to be prepared.

In this way, as usual, PDA NPs were obtained by the oxidation and self-polymerization of DA in a basic aqueous medium containing 2-PrOH (28.1% (V/V)) and $NH_4OH$ (1.75% (V/V)). The polymerization reaction was allowed to proceed for 24 hours, and PDA NPs obtained were isolated, washed and resuspended in $H_2O$(d) in a 2 mg/mL concentration [2].

Later, before loading them with PTX and Tmab, PDA NPs were characterized (**Figure 6.3**). Their hydrodynamic diameter was determined by DLS, and it was found to be 179.3 ± 41 nm (PDI = 0.07) (**Figure 6.3.A**). In addition, their zeta potential, which was -27.4 ± 0.5 mV, was also determined, and the morphology and size of the NPs were examined by TEM (**Figure 6.3.B**). Again, images of at least 300 different PDA NPs were acquired to make a NP size-range histogram. According to it, PDA NPs obtained had an average diameter of 124.3 ± 19.2 nm.

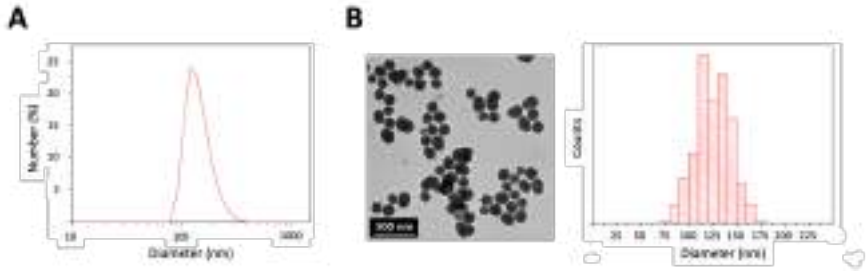


**Figure 6.3.** (**A**) DLS number distribution and (**B**) TEM image and size-range histogram of the PDA NPs synthesized in an aqueous medium containing 2-PrOH to be loaded later with PTX and Tmab.

### *6.2.2. Polydopamine nanoparticle loading with trastuzumab and paclitaxel*

Then, in order to subsequently carry out *in vitro* studies, PDA NPs were washed with PBS before being charged with Tmab and PTX. Regarding the loading of the taxane, it should be noted that in Chapter 3, to improve its limited aqueous solubility, PTX had to be included into β-CDs, and that the resulting complexes were the ones loaded to APPZ along with Tmab through the carbodiimide chemistry [39]. Nevertheless, given PDA great adsorption capacity, PTX was decided to be directly adsorbed into PDA NP surface this time [2]. In this manner, the size of the system was prevented from increasing considerably more and, in addition, the loading process could be more productive.

Otherwise, Tmab loading was performed following two different procedures, which have been schematized in **Figure 6.4**.

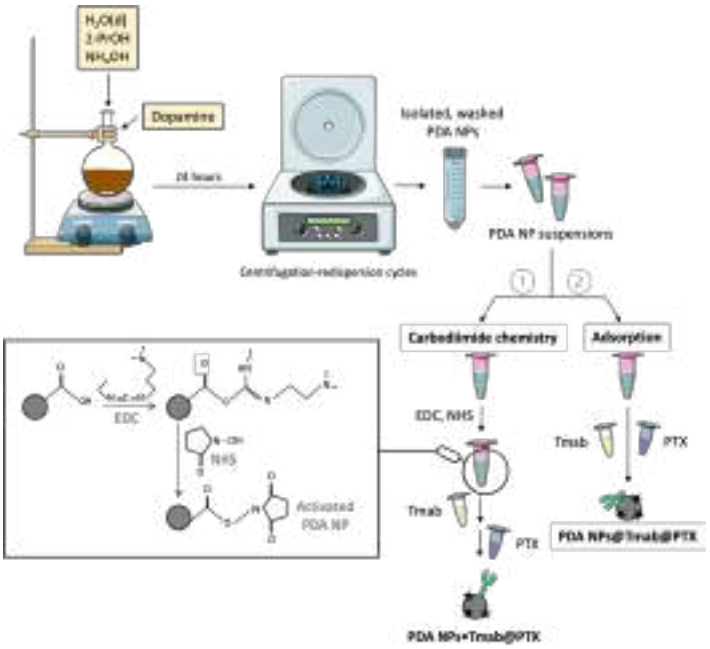


**Figure 6.4.** Schematic representation of PDA NPs synthesis and loading with PTX and Tmab following two different procedures in the latter case: the carbodiimide chemistry (1) and physical adsorption (2).

On one hand, like PTX, Tmab was physically adsorbed in PDA NPs. In this case, solutions of the antibody (1.37 µM, 17.5 µL) and the taxane (0.52 µM, 20.2 µL, 2:1 $H_2O$(d)/DMSO) were incorporated to PDA NP suspensions (2 mg/mL, 350 µL), which were later kept under orbital shaking (100 rpm) in dark conditions overnight.

On the other hand, Tmab was covalently attached to PDA NPs through the carbodiimide chemistry, as was done with the APPZ, to verify whether this procedure enhanced loaded PDA NP effectiveness and selectivity. For this purpose, the pH of the PDA NP suspensions (2 mg/mL, 1 mL) was adjusted to 4.7 - 4.8 by dropping HCl to make the amidation reaction more efficient [40]. Then, solutions of EDC (193 mg/mL, 10 µL) and NHS (58 mg/mL, 10 µL) were added to the NP suspensions to activate PDA carboxyl groups, and the resulting mixtures were kept under orbital shaking (100 rpm) for 40 minutes. After that time, a Tmab solution was

incorporated (1.37 µM, 50 µL), and NP suspensions were kept agitated for a further 3 hours. Ultimately, a PTX solution (0.52 µM, 58 µL, 2:1 $H_2O$(d)/DMSO) was also added, and the mixtures obtained were left shaking in dark conditions overnight. Working concentrations of the anti-HER2 antibody and the drug employed were the same in the adsorption and amidation procedures and, in both cases, loaded PDA NPs (PDA NPs@Tmab@PTX and PDA NPs•Tmab@PTX, respectively) were isolated by centrifugation next day [2].

Furthermore, in order to later be able to make comparisons when conducting *in vitro* viability assays, PDA NPs loaded only with PTX (PDA NPs@PTX) and only with Tmab (PDA NPs@Tmab and PDA NPs•Tmab) were also prepared following the same procedures.

### *6.2.3. Determination of trastuzumab and paclitaxel incorporation efficiencies and content in polydopamine nanoparticles*

In all nanosystems, Tmab and PTX loading efficiencies were found out by difference, by determining their concentration in the supernatants of the different loaded PDA NPs. This determination was done by UV-Vis spectrophotometry once these NPs were isolated. While PTX concentration was quantified at 227 nm, the amount of Tmab in the supernatants was determined using the Pierce™ BCA Protein Assay Kit, following the instructions detailed by the manufacturer. This protein detection kit is more sensitive than the Bradford method and [41], in addition, exhibits less protein-to-protein variation, so it was preferred to determine Tmab concentration in the samples.

Tmab and PTX incorporation efficiencies (IEs) (%) and content (W/W) in loaded PDA NPs were found applying **Equation 6.1** and **6.2** [44].

$$EI\ (\%) = \frac{Weight\ of\ Tmab\ or\ PTX\ found\ loaded}{Weight\ of\ total\ Tmab\ or\ drug\ used} \times\ 100 \qquad \textbf{(Equation 6.1)}$$

$$Content\ (W/W) = \frac{Weight\ of\ Tmab\ or\ PTX\ found\ loaded}{Weight\ of\ loaded\ PDA\ NPs} \times\ 100 \qquad \textbf{(Equation 6.2)}$$

Results, obtained according to the two methods followed to carry out Tmab loading, have been collected in **Table 6.2**.

**Table 6.2.** IEs (%) and Tmab and PTX content in PDA NPs (μg/mg) after PTX adsorption and/or Tmab adsorption/covalent conjugation.

| | PTX | | Tmab | |
|---|---|---|---|---|
| | **IE** | **NP content** | **IE** | **NP content** |
| PDA NPs@PTX | 24.2% | 3.1 μg/mg NPs | - | - |
| PDA NPs@Tmab | - | - | 61.3% | 3.1 μg/mg NPs |
| PDA NPs•Tmab | - | - | 53.7% | 2.7 μg/mg NPs |
| PDA NPs@Tmab@PTX | 18.0% | 2.3 μg/mg NPs | 27.4% | 1.4 μg/mg NPs |
| PDA NPs•Tmab@PTX | 19.1% | 2.4 μg/mg NPs | 37.8% | 1.9 μg/mg NPs |

As can be seen in **Table 6.2**, there were not very significant differences between PTX IE values when both PTX and Tmab were loaded to PDA NPs. Nonetheless, it was observed that in the absence of the antibody, PDA NPs were capable of adsorbing a slightly higher amount of the taxane. Otherwise, Tmab loading efficiency, which was also more remarkable when PTX was not charged, was greater when the carbodiimide chemistry was employed.

## 6.3. Validation of the efficacy and HER2-selectivity of polydopamine nanoparticles loaded with trastuzumab and paclitaxel in conventional cell cultures

### *6.3.1. Study of the therapeutic activity of polydopamine nanoparticles loaded with trastuzumab and paclitaxel by viability assays*

First, in order to evaluate and compare the anti-tumour activity and selectivity of the two types of loaded PDA NPs obtained, MTT assays were carried out with two breast carcinoma cell lines overexpressing HER2 (BT474 and SKBR3 lines) and with stromal cells (HS5 cell line). All of them were used before for the *in vitro* validation of the conjugated APPZ and [39], as usual, were cultured as instructed by the American Type Culture Collection (ATCC).

Once grown, for the performance of the MTT assays, BT474, SKBR3 and HS5 cells were seeded into 24-well plates (12,000 cells/well)

and incubated for 24 hours to allow attachment. Next day, culture medium in the wells of some plates was replaced by supplemented DMEM containing PBS (control), PDA NPs (0.035 and 0.042 mg/mL), PTX (99.5 and 119.5 nM), Tmab (0.45 and 0.54 nM), PDA NPs•Tmab (0.035 and 0.042 mg/mL), PDA NPs@PTX (0.035 and 0.042 mg/mL) and PDA NPs•Tmab@PTX (0.035 and 0.042 mg/mL) [2]. 0.035 and 0.042 mg/mL PDA NP concentrations were employed because it was demonstrated that they had a remarkable intrinsic antineoplastic activity in Chapter 4 (page 179) [14]. Likewise, the same concentrations of PDA NPs charged with PTX and/or Tmab were administered to the cells, which were also treated with concentrations of the antibody and the taxane similar to those chemically bound and adsorbed in PDA NPs, respectively.

Culture medium in the wells of other plates was otherwise replaced by DMEM containing the same concentrations (0.035 and 0.042 mg/mL) of PDA NPs, PDA NPs@Tmab, PDA NPs@PTX and PDA NPs@Tmab@PTX and, this time, PTX (94.9 and 113.6 nM) and Tmab (0.33 and 0.42 nM) concentrations equivalent to those physically adsorbed in PDA NPs [2].

In both cases, cells were later incubated for 24, 48 and 72 hours and, after those times, MTT assays were performed by applying the procedure previously set-up to subtract PDA contribution to sample absorbance values [11]. Results achieved after cell treatment with PDA NPs in which Tmab was adsorbed can be found in **Figure 6.5**, while those obtained after the administration of PDA NPs to which Tmab was covalently bound have been summarized in **Figure 6.6**.

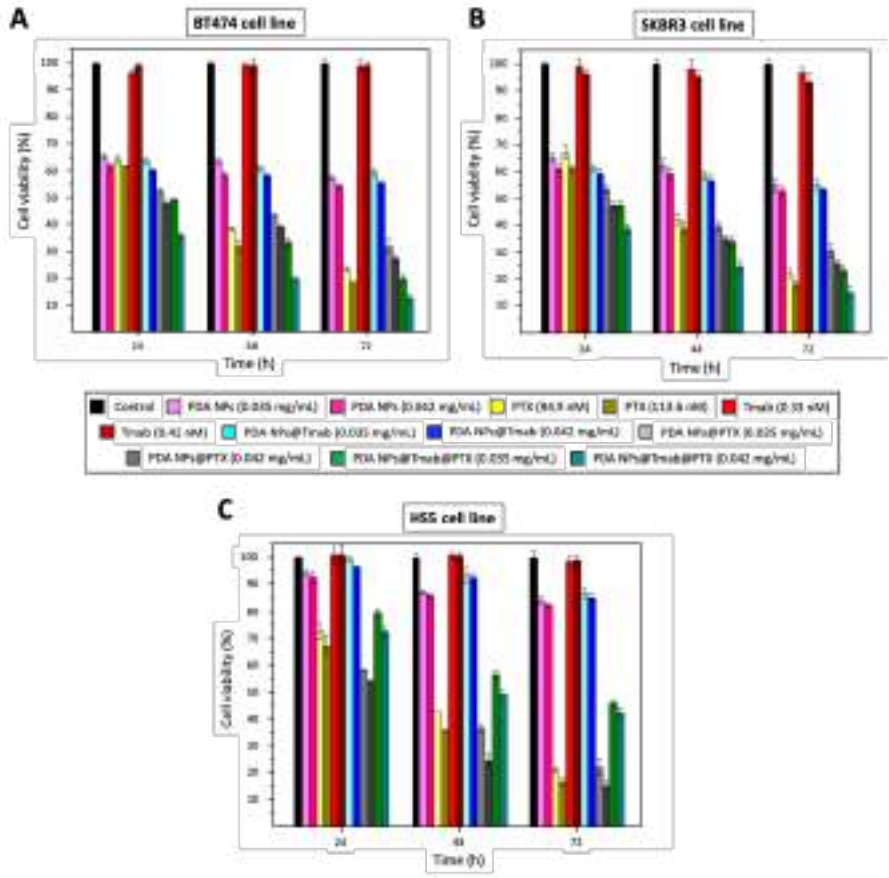


**Figure 6.5.** Survival rates of BT474 (**A**), SKBR3 (**B**) and HS5 (**C**) cells after treatment with 0.035 and 0.042 mg/mL bare PDA NPs, PDA NPs@Tmab, PDA NPs@PTX and PDA NPs@Tmab@PTX, as well as with concentrations of free Tmab and PTX equivalent to those adsorbed in PDA NPs@Tmab@PTX. All data were obtained in triplicate and results shown are the mean ± SEM.

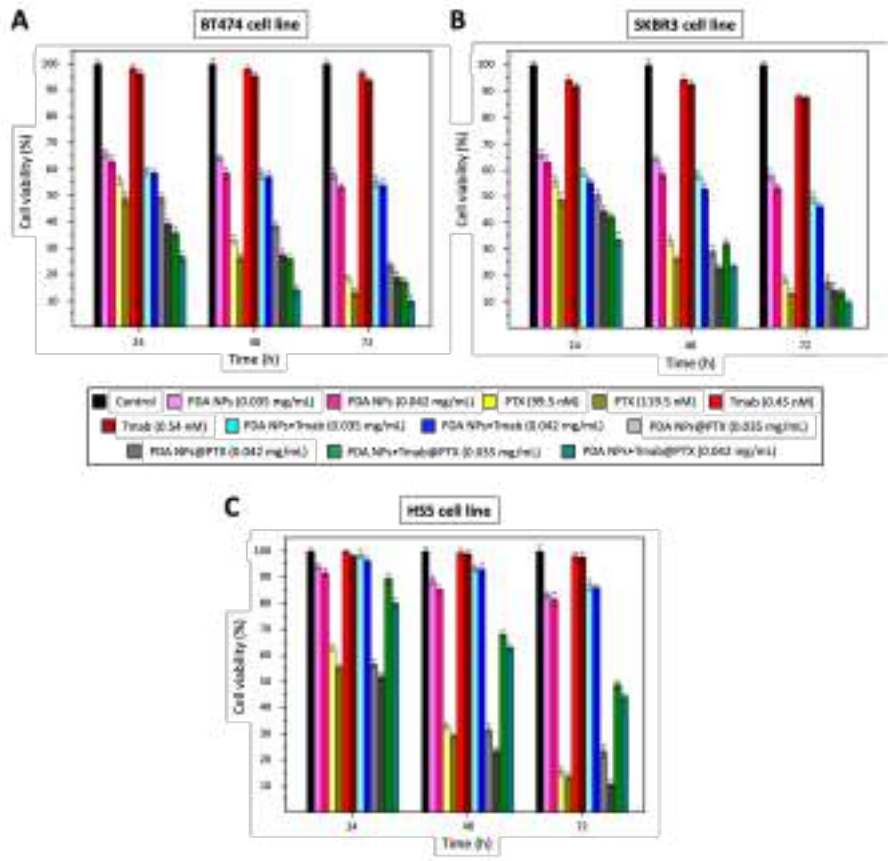


**Figure 6.6.** Survival rates of BT474 (**A**), SKBR3 (**B**) and HS5 (**C**) cells after treatment with 0.035 and 0.042 mg/mL bare PDA NPs, PDA NPs•Tmab, PDA NPs@PTX and PDA NPs•Tmab@PTX, as well as with concentrations of free Tmab and PTX equivalent to those chemically bound and adsorbed, respectively, in PDA NPs•Tmab@PTX. Also, results shown are the average viability values ± SEM of three parallel experiments.

As can be noticed in both figures, bare PDA NPs were not excessively toxic to normal cells. Nevertheless, they notably reduced the viability rate of the two HER2+ breast cancer cell lines, being these results in line with those obtained in prior Chapters [11,13-14].

Otherwise, both PDA NPs@Tmab@PTX and PDA NPs•Tmab@PTX were found to have great antineoplastic activity, since they even reduced BT474 and SKBR3 viability rate to a slightly greater extent than equivalent concentrations of free PTX (between 5 and 10% more) in most of the conditions studied ($p < 0.05$). Herein, when BT474 cells were treated with

PDA NPs@Tmab@PTX, only 19 and 13% of them survived after 72 hours (depending on NP concentration), while these percentages were 17 and 10% when PDA NPs•Tmab@PTX were employed for cell treatment. Regarding the viability of the SKBR3 cell line, it was close to 23-15% and 14-10% 72 hours after treatment with PDA NPs@Tmab@PTX and PDA NPs•Tmab@PTX, respectively. Besides, it was observed that when Tmab was adsorbed or covalent bound to PDA NPs, their anti-tumour effect was enhanced, since it was greater when NPs were charged with both the antibody and the drug than when they were solely loaded with the taxane. In this manner, PDA NPs@Tmab@PTX and PDA NPs•Tmab@PTX diminished BT474 and SKBR3 cell viability rates between 5-15% more than PDA NPs@PTX (depending on NP concentration and treatment time), so Tmab loading could favor the internalization of the Tmab-charged NPs in HER2+ tumour cells [2].

Aversely, Tmab loading to PDA NPs made them less toxic to stromal cells, a fact that revealed that Tmab adsorption and chemical conjugation may enhance the selectivity of the PDA NPs. When HS5 cells were treated with PDA NPs@Tmab@PTX and PDA NPs•Tmab@PTX their survival rate was 23-30% higher than when similar concentrations of PDA NPs@PTX were used for treatment. Furthermore, in comparison to free PTX, PDA NPs loaded with both Tmab and PTX reduced stromal cell viability by about 25-34% less and, compared to breast tumour cells subjected to the same treatment, about 26-36% more HS5 cells survived. In fact, Tmab loading even slightly improved the intrinsic toxicity of bare PDA NPs to HS5 cells [2].

### *6.3.2. Comparison of the anti-tumour activity and selectivity of the polydopamine and alginate-piperazine nanoparticles loaded with trastuzumab and paclitaxel*

When comparing the viability of the BT474 and SKBR3 cells treated with the conjugated APPZ (Figure 3.11, Chapter 3, page 102) and the PDA NPs@Tmab@PTX or PDA NPs•Tmab@PTX (Figure 6.5 and 6.6, pages 296-297), it might seem like there was not a remarkable difference when one nanosystem or the other was used. Thus, loaded PDA NPs reduced the viability rate of HER2+ breast cancer cells more rapidly, but a similar number of these cells (10-20%) survived 72 hours after treatment with both types of nanoparticulate systems. However, it should be noted that the concentration of the loaded PDA NPs administered to treat malignant cells was almost 30 times lower than that of conjugated APPZ, and that the amount of PTX that they transported was two orders of magnitude smaller than that charged in the APPZ. Therefore, PDA NPs@Tmab@PTX and PDA NPs•Tmab@PTX proved to be more effective.

Furthermore, it is noteworthy that although the marked cytotoxicity of the loaded PDA NPs may be due to PTX transport (as will be verified later), also a part of it, responsible for the cytotoxicity of bare PDA NPs, could be mediated by a ferroptosis mechanism. In this way, since PDA NPs charged with Tmab and PTX may be capable of inducing both apoptosis and ferroptosis mechanisms, the employment of these NPs may prevent the potential appearance of treatment resistances even to a greater extent than the administration of conjugated APPZ. What's more, PDA NPs ability to induce ferroptosis could be modulable. As described in Chapter 4, it could be adjusted simply by modifying the type of ROH and the $NH_4OH$ concentration used in PDA NP synthesis, so that the anti-tumour activity of this nanosystem could be partially increased or reduced depending on the clinical needs.

The downside of PDA NPs@Tmab@PTX and PDA NPs•Tmab@PTX use compared to conjugated APPZ employment is that the former NPs turned out to be less selective (possibly due to their intrinsic toxicity), thereby reducing the viability of HS5 cells to a greater extent than loaded APPZ.

### *6.3.3. Validation of loaded polydopamine nanoparticles effectiveness by alive/death assays*

Even though the differences in terms of efficacy and selectivity between PDA NPs@Tmab@PTX and PDA NPs•Tmab@PTX were not statistically significant ($p > 0.05$), those NPs that had the antibody covalently bound decreased BT474 and SKBR3 viability 1.2 - 13.5% more, (depending on concentration and time) than PDA NPs@Tmab@PTX. Likewise, PDA NPs•Tmab@PTX affected HS5 survival rate 2.2 - 15.9% less than PDA NPs@Tmab@PTX (Figure 6.5 and 6.6, pages 296 - 297). For this reason, PDA NPs•Tmab@PTX were the NPs chosen to perform further *in vitro* studies.

Thus, their therapeutic effect was also verified by live/death CLSM assays, which were carried out with the BT474 cell line. These HER2-overexpressing cells, once grown, were seeded in glass-bottom dishes (24,000 cells/dish) and incubated for 24 hours at 37°C. Subsequently, BT474 cells were treated with or without PDA NPs•Tmab@PTX (0.035 mg/mL) and PTX in a similar concentration to that adsorbed in the NPs (99.5 nM), and they were incubated again for 48 and 72 hours. After that time, calcein AM (1 μM) and propidium iodide (2 drops/dish) fluorescent dyes were added to the dishes, and cells were incubated for 15 minutes. At last, BT474 cells stained were imaged by CLSM with an excitation/detection of 494/517 (calcein AM) and 535/617 nm (propidium iodide). Images acquired can be seen collected in **Figure 6.7**.

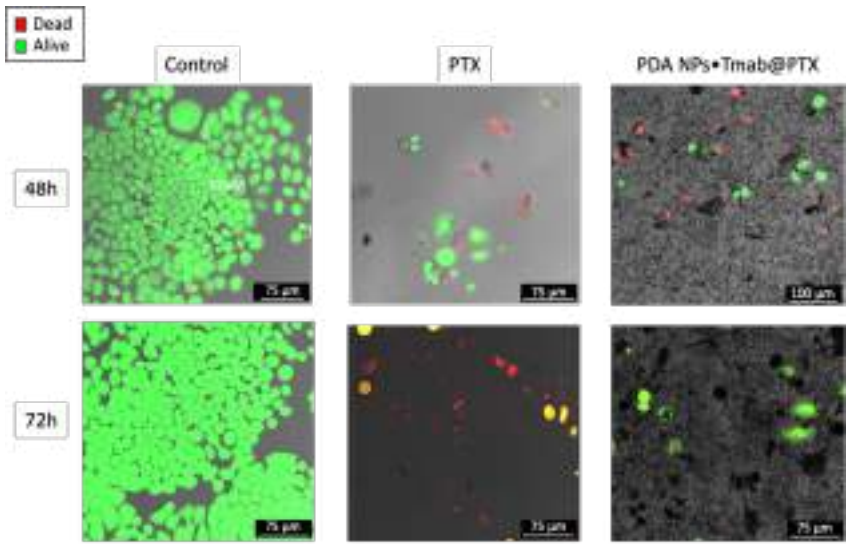


**Figure 6.7.** CLSM images of BT474 cells 48 and 72 hours after treatment with PTX (99.5 nM) and the PDA NPs•Tmab@PTX (0.035 mg/mL). Cell viability and death were assessed by using calcein (green) and propidium iodide (red).

From at least 5 of these images, the average percentage of living and dead cells was determined for each treatment condition. While 36.1% and 16.7% of BT474 cells remained alive 48 and 72 hours after treatment with free PTX, 36.3% and 14.3% of them survived when treated with 0.035 mg/mL PDA NPs•Tmab@PTX for 48 and 72 hours, respectively. Thereby, results of these CLSM assays proved, along with those achieved in the MTT experiments, that PDA NPs•Tmab@PTX were highly effective [2].

### *6.3.4. Analysis of the apoptosis induced by loaded polydopamine nanoparticles through flow cytometry*

Next, in order to verify that PTX adsorption in PDA NPs did not affect its pharmacological activity, which is mediated by the induction of apoptosis in tumour cells [43], the number of early and late apoptotic BT474 cells was determined by flow cytometry 48 hours after treatment with PDA NPs•Tmab@PTX and free PTX.

Flow cytometry data were obtained by using an annexin V apoptosis detection kit with 7AAD according to manufacturer's instructions. Briefly, once grown, BT474 cells were cultured in dishes

(12,000 cells/mL), treated with or without free PTX (99.5 nM) or the PDA NPs•Tmab@PTX (0.035 mg/mL) and incubated at 37°C for 48 hours. Once this time elapsed, cells were collected, centrifuged and resuspended in warm PBS. Soon, they were washed by warm PBS twice and resuspended in annexin binding buffer (1x) in a $10^6$ cells/mL concentration. Annexin V (5 µl) and 7AAD (5 µl) were added to cell samples ($10^5$ cells/mL, 100 µl), which were incubated in dark conditions at room temperature for 15 minutes [44]. Stained cells (at least 50,000 events) were analysed by flow cytometry by the Cytometry Facility-NUCLEUS of the University of Salamanca, using FITC (green) for annexin V and PerCP (red) for 7AAD. As a result, it was observed that the PDA NPs•Tmab@PTX treatment increased the number of early apoptotic ($7AAD^-$/Annexin $V^+$) BT474 cells in a similar manner than the equivalent free PTX treatment. Therefore, PTX therapeutic activity remained unchanged upon loading to PDA NPs (**Figure 6.8**) [2].

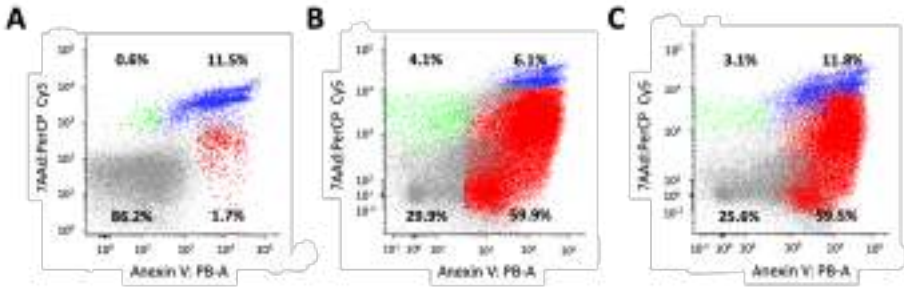


**Figure 6.8.** Flow cytometry analysis showing the percentage of apoptotic and necrotic BT474 cells 48 hours after treatment without (**A**) or with (**B**) PTX (99.5 nM) and (**C**) PDA NPs•Tmab@PTX (0.035 mg/mL). The vertical axis indicates the cells labeled with 7AAD (PerCP) and the horizontal axis indicates those stained by Annexin V (FITC) (Early apoptosis: right lower, late apoptosis/necrosis: right upper).

## 6.4. Validation of the efficacy of polydopamine nanoparticles loaded with trastuzumab and paclitaxel in HER2-positive tumour spheroids

### *6.4.1. Study of the interaction between polydopamine nanoparticles loaded with trastuzumab and paclitaxel and breast tumour spheroids*

Finally, as was done with the APPZ conjugated with PTX and Tmab in Chapter 3, the effectiveness of PDA NPs•Tmab@PTX was also analysed in HER2+ breast cancer spheroids [2], since they mimic the behaviour of human solid tumours better than conventional monolayer cell cultures [45].

In this way, as was done previously, MCTS derived from the BT474 cell line were developed to further evaluate the antineoplastic activity of the PDA NPs•Tmab@PTX [2]. For this, breast tumour cells were seeded (10,000 cells/mL) in U-shaped bottom microplates. By day 3 of growth, they had formed compact multicellular spheres about 1 mm in diameter, which were then treated with or without PDA NPs•Tmab@PTX (0.035 mg/mL) and PTX in a concentration equivalent to that adsorbed in the NPs (99.5 nM). Then, 48 and 72 hours after treatment, SEM was employed to characterize the interaction between the doubly-loaded PDA NPs and the 3D BT474 cell cultures. To prepare the samples, MCTS were carefull sectioned by the Electron Microscopy Facilities-NUCLEUS of the University of Salamanca, and deposited on filter paper treated with poly-L-lysine. Spheroid sections were fixed overnight at 8°C in PBS with glutaraldehyde (25%) and, next day, they were washed by PBS three times. Subsequently, PBS with osmium (1%) was added to the samples and, 1 hour later, MCTS sections were washed by $H_2O$(d) three times and progressively dehydrated by a gradient concentration of acetone series. Critical point drying was achieved with $CO_2$, and samples were observed after gold coating by SEM in a secondary electron mode [46]. Images acquired can be found in **Figure 6.9**.

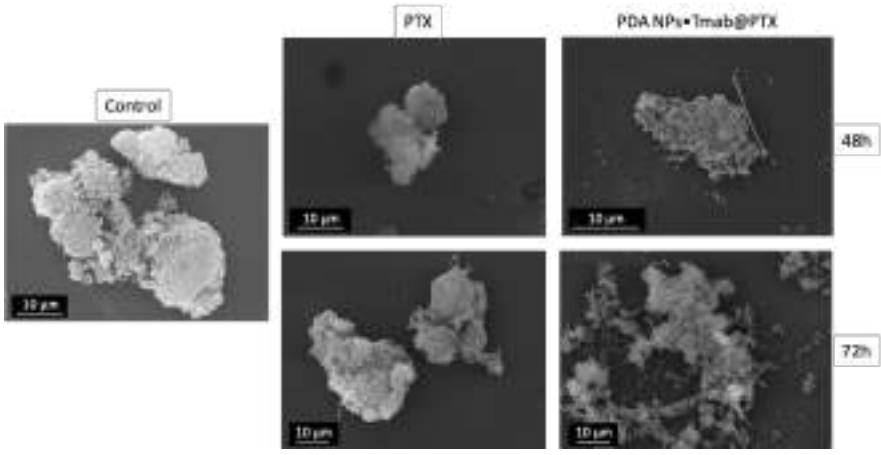


**Figure 6.9.** SEM characterization of sections of BT474 MCTS 48 and 72 hours after treatment with PTX (99.5 nM) and PDA NPs•Tmab@PTX (0.035 mg/mL).

Morphological differences between the control spheroids and the spheroids treated with both free PTX and loaded PDA NPs could be detected, especially when 72 hours elapsed. In this way, after treatment with the taxane, BT474 spheroids became smaller and disaggregated. This reduction in size and the structural disorganization with loss of integrity could be already noticed after exposure to the PDA NPs•Tmab@PTX, with which spheroids acquired a grape bunch-shape in which individual cells could be better distinguished (**Figure 6.10**). Moreover, in both the images obtained from the spheroids treated with free PTX and the PDA NPs•Tmab@PTX, filamentous-like structures were observed that may correspond to PTX crystals formed in solution (**Figure 6.9**) [2,47].

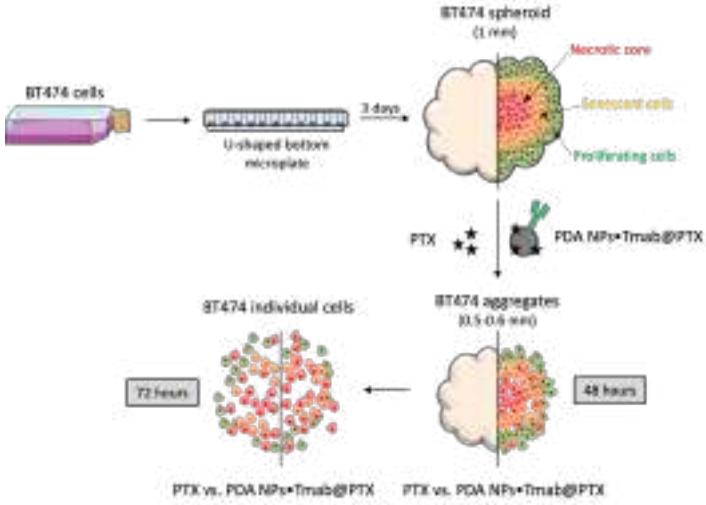


**Figure 6.10.** Schematic representation of how BT474 MCTS were developed and the effect that PTX (99.5 nM) *vs.* PDA NPs•Tmab@PTX (0.035 mg/mL) treatment had on their structure and morphology.

### *6.4.2. Cytotoxicity of polydopamine nanoparticles loaded with trastuzumab and paclitaxel to HER2-positive cancer spheroids*

To close this chapter, the viability of B474 tumour spheroids after treatment with PDA NPs•Tmab@PTX was also assessed in two different manners.

On one hand, MCTS were developed again as indicated in the previous point, and additional live/death CLSM assays were performed in the same way as it was done with the 2D monolayer cell cultures. Thereby, once grown, BT474 spheroids were carefully deposited in glass-bottom dishes and were treated with PDA NPs•Tmab@PTX (0.035 mg/mL) and PTX in an equivalent concentration to that adsorbed in the NPs (99.5 nM) once 3.5 hours elapsed to allow cell attachment. Next, 48 and 72 hours after this treatment, living cells were stained with calcein AM (1 µM) and, death ones, with propidium iodide (3 drops/dish). Spheroids were incubated for 15 minutes to finally acquire confocal images. The cells stained were imaged by employing the same excitation/detection wavelengths mentioned in point 6.3.3 (page 300) (**Figure 6.11**).

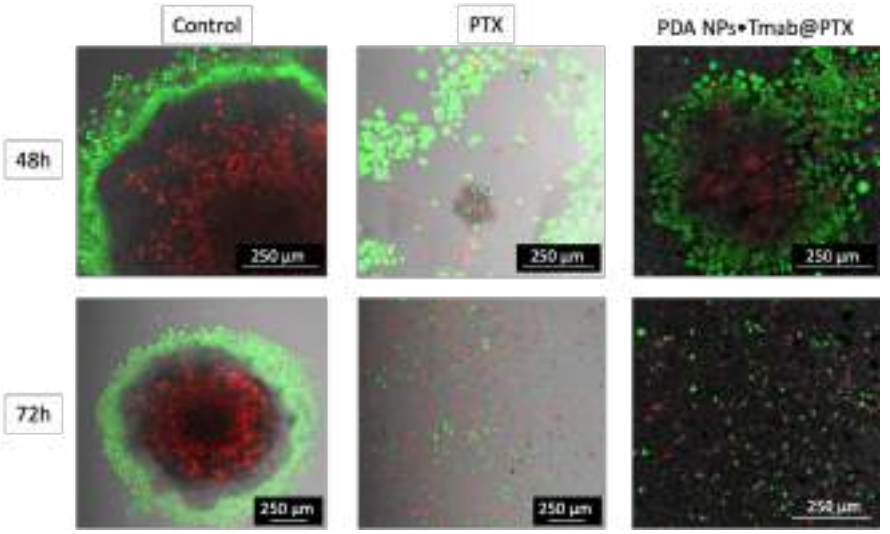


**Figure 6.11.** CLSM images of BT474 MCTS 48 and 72 hours after treatment with PTX (99.5 nM) and PDA NPs•Tmab@PTX (0.035 mg/mL). Cell viability and death were assessed by using calcein AM (green) and propidium iodide (red), as usual.

Images of BT474 control spheroids allowed to appreciate how they had a necrotic core surrounded by a viable rim with an inner layer of quiescent cells and an outer layer of proliferating cells also this time. As already mentioned in Chapter 3 (page 107), the existence of these cellular subpopulations, caused by a gradient of oxygen, nutrients and waste, is characteristic of large MCTS (> 500 µm) [48]. Otherwise, the loss of integrity of treated spheroids that was observed by SEM could be corroborated with this live/death assay. Thereby, it could be noticed that both free PTX and the PDA NPs•Tmab@PTX were able to reduce the size of the developed 3D cellular structures and to disaggregate them, especially after 72 hours [2].

On the other hand, the viability of the BT474 cells integrating the MCTS was determined by cell-counting, too. Thereof, tumour spheroids were afresh grown and, by day 3, they were treated with or without free PTX (99.5 nM), PDA NPs•Tmab@PTX (0.035 mg/mL) and, in addition, with bare PDA NPs (0.035 mg/mL). Subsequently, after 48 hours, MCTS were washed by warm PBS, disaggregated with trypsin, collected in fresh,

supplemented DMEM and centrifuged (1400 rpm, 4 minutes). Cells were again resuspended in DMEM and their viability was determined after mixing the suspension with trypan blue (1:1 (V/V)). Results obtained can be found in **Figure 6.12**, where the average of the viability values of three replicas ± SEM have been represented.

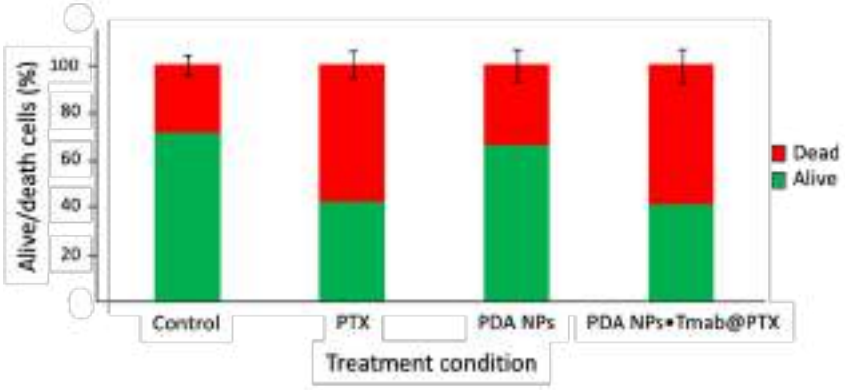


**Figure 6.12.** Percentage of living and dead cells cultured in 3D spheres determined by cell-counting 48 hours after treatment with PTX (99.5 nM), bare PDA NPs (0.035 mg/mL) and PDA NPs•Tmab@PTX (0.035 mg/mL).

As can be seen, the viability of the control spheroids was close to 71 ± 4% due to the existence of the necrotic core described before. The average survival rate of the MCTS treated with unloaded PDA NPs was about 65 ± 5% while, when free PTX and the PDA NPs•Tmab@PTX were administered, spheroid viability diminished to 58 ± 5% and 59 ± 6%, respectively. Therefore, it was proven that loaded PDA NPs were not only effective in inducing apoptosis of HER2+ breast cancer cells in monolayer cultures, but also when these cells were forming 3D structures, to which they showed a cytotoxicity similar to that of the parent drug despite, surely, spread worse [2,49].

## 6.5. Conclusions

· Newly, PTX and Tmab were loaded in PDA NPs about 180 nm in size, prepared with 2-PrOH, to target HER2+ breast cancer cells. While PTX was directly adsorbed in the NPs, Tmab loading was carried out by following two different procedures. On one hand, like the taxane, the antibody was directly charged to the PDA nanosystem. On the other hand, carbodiimide chemistry was employed to covalently bind Tmab to the PDA NPs, and thus try to improve their efficacy and selectivity.

· Next, Tmab and PTX content in the two types of loaded PDA NPs was determined by employing UV-Vis spectrophotometry. It was found to be 1.4 µg Tmab/mg NPs and 2.3 µg PTX/mg NPs in PDA NPs@Tmab@PTX, and 1.9 µg Tmab/mg NPs and 2.4 µg PTX/mg NPs in PDA NPs•Tmab@PTX.

· Subsequently, the anti-tumour activity and selectivity of both PDA NPs@Tmab@PTX and PDA NPs•Tmab@PTX were analysed through MTT assays, which were performed with BT474, SKBR3 and HS5 cells. As a result, it could be observed that the two types of loaded PDA NPs significantly reduced the viability of HER2+ breast tumour cells, and that they were more effective than the conjugated APPZ developed in Chapter 3. In addition, stromal cell survival rate was not so affected by the administration of these PDA-based NPs, which proved to be more selective than equivalent concentrations of the parent drug.

· Since PDA NPs•Tmab@PTX were slightly more effective and selective than PDA NPs@Tmab@PTX, they were chosen to perform further *in vitro* studies. Thereby, their antineoplastic activity was determined and compared to that of free PTX by means of alive/death CLSM assays performed with BT474 cells. These assays proved that practically no breast cancer cells survived 48 and 72 hours after treatment neither with the taxane nor with the charged NPs, which were as or more effective than the taxane in monolayer cultures.

· Furthermore, to be sure that PTX pharmacological activity was not altered when loaded to the NPs, the number of BT474 early and late apoptotic cells was determined 48 hours after treatment with PDA

NPs•Tmab@PTX and compared to that achieved after equivalent free PTX administration. Both treatments induced apoptosis in a similar way, so PTX pharmacological activity remained unchanged after its adsorption in PDA NPs.

· Then, the anti-tumour activity of the PDA NPs•Tmab@PTX was validated by employing HER2+ breast tumour spheroids. First, the interaction of PDA NPs•Tmab@PTX with BT474 3D spheres was studied by SEM, finding that loaded PDA NPs were able to reduce the size of the MCTS and disaggregate them, especially after 72 hours. Its effect was similar to that of free PTX, despite surely diffusing worse in these 3D cell cultures.

· The similarity in terms of efficacy between free PTX and PDA NP•Tmab@PTX MCTS treatments was also corroborated later by additional alive/death CLSM assays and, ultimately, by cell counting. Therefore, PDA NPs•Tmab@PTX were shown to have improved antineoplastic activity and selectivity in monolayer cell cultures in comparison to free PTX, while maintaining their efficacy in 3D tumour structures.

## 6.6. Published articles related to this chapter

· Nieto C, Vega MA, Martín del Valle EM. Nature-inspired nanoparticles as paclitaxel targeted carrier for the treatment of HER2-positive breast cancer. Cancers 2021, 13:2526.

## 6.7. Abbreviations

APPZ – Sodium alginate-piperazine nanoparticles
ATCC – American Type Culture Collection
AuNP – Gold nanoparticle
CD - Cyclodextrin
CLSM – Confocal laser scanning microscopy
CPT - Camptothecin
DA - Dopamine

DDS – Drug delivery system
DLS – Dynamic light scattering
DMEM – Dulbecco's Modified Eagle's Medium
DMSO – Dimethylsulfoxide
DM1 – Emtansine
DOX - Doxorubicin
EDC - N-(3-Dimethylaminopropyl)-N'-ethylcarbodiimide hydrochloride
EGFR – Epidermal growth factor receptor
EPR -Enhanced permeability and retention
EtOH - Ethanol
FA – Folic acid
FBS – Foetal bovine serum
GSH – Glutathione
HER2 – Human epidermal growth factor receptor-2
HER2+ – HER2-positive
$H_2O$(d) – Deionized $H_2O$
ICG – Indocyanine green
IE – Incorporation efficiency
Ig – Immunoglobulin
MBC – Metastatic breast cancer
MCTS – Multicellular tumour spheroids
MDR – Multi-drug resistance
MSN – Mesoporous silica nanoparticle
NHS - N-hydroxysuccinimide
NP – Nanoparticle
PBS – Phosphate buffered saline
PDA – Polydopamine
PDA NPs – Polydopamine nanoparticles
PDA NPs@PTX – Polydopamine nanoparticles loaded with paclitaxel
PDA NPs•Tmab - Polydopamine nanoparticles covalently loaded with trastuzumab
PDA NPs@Tmab - Polydopamine nanoparticles loaded with trastuzumab
PDA NPs•Tmab@PTX – Polydopamine nanoparticles covalently loaded with trastuzumab and charged with paclitaxel
PDA NPs@Tmab@PTX - Polydopamine nanoparticles loaded with trastuzumab and paclitaxel
PDI – Polydispersity index

PEG – Polyethylene glycol
PLGA - Poly(lactic-co-glycolic acid)
PTX - Paclitaxel
RGDC – Arginine-glycine-cysteine acid
ROH - Alcohol
SCM – Stem cell membrane
SEM – Scanning electron microscopy
SEM – Standard error of mean
SN38 - 7-ethyl-10-hydroxycamptothecin
TEM – Transmission electron microscopy
Tmab – Trastuzumab
TPGS - D-α-tocopheryl polyethylene glycol 1000 succinate
TPP- Triphenylphosphonium
UV-Vis – Ultraviolet-visible
2-PrOH – 2-propanol

## 6.8. References

[1] Wang Z, Duan Y, Duan Y. Application of polydopamine in tumor targeted drug delivery system and its drug release behaviour. J Control Release 2018; 290:56-74.
[2] Nieto C, Vega MA, Martín del Valle EM. Nature-inspired nanoparticles as paclitaxel targeted carrier for the treatment of HER2-positive breast cancer. Cancers 2021, 13:2526.
[3] Dragojevic S, Ryu JS, Raucher D. Polymer-based prodrugs: improving tumor targeting and the solubility of small molecules in cancer therapy. Molecules 2015, 20:21750-69.
[4] Zhou L, Wang H, Li Y. Stimuli-reponsive nanomedicines for overcoming cancer multidrug resistance. Theranostics 2018, 8(4):1059-74.
[5] Wang X, Yang L, Chen Z, Shin DM. Application of nanotechnology in cancer therapy and imaging. CA Cancers J Clin. 2008, 58:97-110.
[6] Maeda H, Wu J, Sawa T, Matsumura Y, Hori K. Tumor vasculature permeability and the EPR effect in macromolecular therapeutics: a review. J Control Release 2000, 65:271-84.

[7] Mitragotri S, Anderson DG, Chen X, Chow EK, Ho D, Kabanov AV, Karp JM, Kataoka K, Mirkin CA, Petrosko SH et al. Accelerating the translation of nanomaterials in biomedicine. ACS Nano 2015, 9(7):6544-54.

[8] Wu H, Hu H, Wan J, Li Y, Wu Y, Tang Y, Xiao C, Xu H, Yang X, Li Z. Hydroxyethyl starch stabilized polydopamine nanoparticles for cancer therapy. Chem Eng J. 2018, 349:129-45.

[9] Jin A, Wang Y, Lin K, Jiang L. Nanoparticles modified by polydopamine: working as “drug” carriers. Bioact Mater. 2020, 5:522-41.

[10] Lee H, Dellatore SM, Miller WM, Messersmith PB. Mussel-inspired surface chemistry for multifunctional coatings. Science 2007, 318(5849):426-30.

[11] Nieto C, Vega MA, Marcelo G, Martín del Valle, EM. Polydopamine nanoparticles kill cancer cells. RSC Adv. 2018, 8:36201.

[12] Batul R, Tamanna T, Khaliq A, Yu A. Recent progress in the biomedical applications of polydopamine nanostructures. Biomater Sci. 2017, 5:1204.

[13] Nieto C, Vega MA, Enrique J, Marcelo G, Martín del Valle, EM. Size matters in the cytotoxicity of polydopamine nanoparticles in different types of tumors. Cancers 2019, 11:1679.

[14] Nieto C, Marcelo G, Vega MA, Martín del Valle, EM. Antineoplastic behaviour of polydopamine nanoparticles prepared in different water/alcohol media. Colloid Surf B Biointerfaces 2021, 199:111506.

[15] Wang W, Tang Z, Zhang Y, Wang Q, Liang Z, Zeng X. Mussel-inspired polydopamine: the bridge for targeting drug delivery system and synergist cancer treatment. Macromol Biosci. 2020, 20:2000222.

[16] Li L, Xie C, Xiao X. Polydopamine modified $TiO_2$ nanotube arrays as a local drug delivery system for ibuprofen. J Drug Deliv Sci Tecnol. 2020, 56:101537.

[17] Chang D, Gao Y, Wang L, Liu G, Chen Y, Wang T, Tao W, Mei L, Huang L, Zeng X. Polydopamine-based surface modification of mesoporous silica nanoparticles as pH-sensitive drug delivery vehicles for cancer therapy. J Colloid Interface Sci. 2016, 463:279-87.

[18] Pan H, Shen X, Tao W, Chen S, Ye X. Fabrication of polydopamine-based curcumin nanoparticles for chemical stability and pH-responsive delivery. J Agric Food Chem. 2020, 68:2795-802.

[19] He H, Markoutsa E, Zhan Y, Zhang J, Xu P. Mussel-inspired PLGA/polydopamine core-shell nanoparticles for light induced cancer thermochemotherapy. Acta Biomater. 2017, 59:181-91.

[20] Park J, Brust TF, Lee HJ, Lee SC, Walts VJ, Yeo Y. Polydopamine-based simple and versatile surface modification of polymeric nano drug carriers. ACS Nano 2014, 8:3347-56.
[21] Mu X, Zhang F, Kong C, Zhang H, Zhang W, Ge R, Liu Y, Jiang J. EGFR-targeted delivery of DOX-loaded $Fe_3O_4$@polydopamine multifunctional nanocomposites for MRI and antitumor chemo-photothermal therapy. Int J Nanomedicine 2017, 12:2899-911.
[22] Cheng W, Nie J, Xu L, Liang C, Peng Y, Liu G, Wang T, Mei L, Huang L, Zeng X. pH-sensitive delivery vehicle based on folic acid-conjugated polydopamine modified mesoporous silica nanoparticles for targeted cancer therapy. ACS Appl Mater Interfaces 2017, 9:18462-73.
[23] Zhang L, Su H, Cai J, Cheng D, Ma Y, Zhang J, Zhou C, Liu S, Shi H, Zhang Y, Zhang C. A multifunctional platform for tumor angiogenesis-targeted chemothermal therapy using polydopamine-coated gold nanorods. ACS Nano 2016, 10, 10404-417.
[24] Ho CC, Ding SJ. The pH-controlled nanoparticle size of polydopamine for anti-cancer drug delivery. J Mater Sci: Mater Med. 2013, 24(10):2381-90.
[25] Wang X, Zhang J, Wang Y, Wang C, Xiao J, Zhang Q, Cheng Y. Multi-responsive photothermal-chemotherapy with drug-loaded melanin-like nanoparticles for synergistic tumor ablation. Biomaterials 2016, 81:114-24.
[26] Li W-Q, Wang Z, Hao S, He H, Wan Y, Zhu C, Sun L-P, Cheng G, Zheng S-Y. Mitochondria-targeting polydopamine nanoparticles to delivery doxorubicin for overcoming drug resistance. ACS Appl Mater Interfaces 2017, 9(20):16793-802.
[27] Li Y, Jiang C, Zhang D, Wang Y, Ren X, Ai K, Chen X, Lu L. Targeted polydopamine nanoparticles enable photoacoustic imaging guided chemo-photothermal synergist therapy of tumor. Acta Biomater. 2017, 47, 124-34.
[28] Dong Z, Gong H, Gao M, Zhu W, Sun X, Feng L, Fu T, Li Y, Liu Z. Polydopamine nanoparticles as a versatile molecular loading platform to enable imaging-guide cancer combination therapy. Theragnostics 2016, 6(7):1031-42.
[29] Zhu Z, Su M. Polydopamine nanoparticles for combined chemo- and photothermal cancer therapy. Nanomaterials 2017, 7(7):160.
[30] Zhong X, Yang K, Dong Z, Yi X, Wang Y, Ge C, Zhao Y, Liu Z. Polydopamine as a biocompatible multifunctional nanocarrier for combined radioisotope therapy and chemotherapy of cancer. Adv Funct Mater. 2015, 25, 7327-36.
[31] Zhang M, Zhang F, Liu T, Shao P, Duan L, Yan Y, Mu X, Jiang J. Polydopamine nanoparticles camouflaged by stem cell membranes for synergistic chemo-

photothermal therapy of malignant bone tumors. Int J Nanomedicine 2020, 15:10183-97.

[32] Li Y, Hong W, Zhang H, Zhang TT, Chen Z, Yuan S, Peng P, Xiao M, Xu L. Photothermally triggered cytosolic drug delivery of glucose functionalized polydopamine nanoparticles in response to tumor microenvironment for the $GLUT_1$-targeting chemo-phototherapy. J Control Release 2020, 10(317):232-245.

[33] Xing Y, Zhang J, Chen F, Liu J, Cai K. Mesoporous polydopamine nanoparticles with co-delivery function for overcoming multidrug resistance via synergistic chemo-photothermal therapy. Nanoscale 2017, 9:8781-90.

[34] Zhao L, Bi D, Qu X, Guo Y, Yue F, Wang X, Han M. Polydopamine-based surface modification of paclitaxel nanoparticles for osteosarcoma targeted therapy. Nanotecnology 2019, 30:255101.

[35] Banstola A, Pham TT, Jeong JH, Yook S. Polydopamine-tailored paclitaxel-loaded polymeric microspheres with adhered NIR-controllable gold nanoparticles for chemo-phototherapy of pancreatic cancer. Drug Deliv. 2019, 26(1):629-40.

[36] Zhang L, Yang P, Guo R, Sun J, Xie R, Yang W. Multifunctional mesoporous polydopamine with hydrophobic paclitaxel for photoacoustic imaging-guided chemo-photothermal synergistic therapy. Int J Nanomed. 2019, 14:8647-63.

[37] Ambekar RS, Kandasubramanian B. A polydopamine-based platform for anti-cancer drug delivery. Biomater Sci. 2019, 7:1776.

[38] Yang H, Le Q-V, Shim G, Oh Y-K, Shin YK. Molecular engineering of antibodies for site-specific conjugation to lipid polydopamine hybrid nanoparticles. Acta Pharm Sin B, 2020, 10(11):2212-26.

[39] Nieto C, Centa A, Rodríguez-Rodríguez JA, Pandiella A, Martín del Valle EM. Paclitaxel-trastuzumab mixed nanovehicle to target HER2-overexpressing tumours. Nanomaterials 2019, 9:948.

[40] Madison SA, Carnali JO. pH optimization of amidation via carbodiimides. Ind Eng Chem Res. 2013, 52(38):13547-55.

[41] Huang T, Long M, Huo B. Competitive binding to cuprous ions of protein and BCA in the Bicinchoninic acid protein assay. Open Biomed Eng J. 2010, 4:271-8.

[42] Yousefpour P, Atyabi F, Vasheghani-Farahani E, Movahedi A.-A. M., Dinarvand R. Targeted delivery of doxorubicin-utilizing chitosan nanoparticles surface-functionalized with anti-HER2 trastuzumab. Int J Nanomed. 2011, 6:1977-90.

[43] Weaver BA. How Taxol/paclitaxel kills cancer cells. MBoC 2014; 25:2677-81.

[44] Park J, Kim H-D, Lee S-H, Kwak C-H, Chang Y-C, Lee Y-C, Chung T-W, Magae J, Kim C-H. Ascochlorin induces caspase-independent necroptosis in LSP-stimulated RAW 264.7 macrophages. J Ethnopharmacol. 2019, 39:111898.
[45] Ishiguro T, Ohata H, Sato A, Yamawaki K, Enomoto T, Okamoto K. Tumor-derived spheroids: relevance to cancer stem cells and clinical applications. Cancer Sci. 2017, 108(3):283-89.
[46] Mollo V, Scognamiglio P, Marino A, Ciofani G, Santoro F. Probing the ultrastructure of spheroids and their uptake of magnetic nanoparticles by FIB-SEM. Adv Mater Technol. 2020, 5:1900687.
[47] Castro JS, Tapia LV, Silveyra RA, Martínez CA, Deymier PA. Negative impact of paclitaxel crystallization in hydrogels and novel approaches for anticancer drug delivery systems. In: Ozdemir O, editor. Current cancer treatment: novel beyond conventional approaches. Rijeka, Croatia: IntechOpen; 2011. pp. 767-82.
[48] Weiswald L-B, Bellet D, Dangles-Marie V. Spherical cancer models in tumour biology. Neoplasia 2015, 17(1):1-15.
[49] Tchoryk A, Taresco V, Argent RH, Ashford M, Gellert PR, Stolnik S, Grabowska A, Garnett MC. Penetration and uptake of nanoparticles in 3D tumor spheroids. Bioconjugate Chem. 2019; 30:1371-84.

cancers

MDPI

Article

# Nature-Inspired Nanoparticles as Paclitaxel Targeted Carrier for the Treatment of HER2-Positive Breast Cancer

**Celia Nieto *, Milena A. Vega and Eva Martín del Valle ***

Chemical Engineering Department, Faculty of Chemical Sciences, University of Salamanca, 37008 Salamanca, Spain; mvega@usal.es
* Correspondence: celianm@usal.es (C.N.); emvalle@usal.es (E.M.d.V.); Tel.: +34-923294500 (E.M.d.V.)

**Simple Summary:** Great advances have been made in the treatment of an aggressive subtype of breast cancer, known as HER2-positive subtype. However, the antitumor therapy most widely employed in the clinical fight against it has severe side effects, and the apparition of treatment resistances is frequent. To overcome these drawbacks, nano-sized particles had already been developed as targeted vehicles for the drug and the antibody that are usually administered as first-line treatment for this subtype of breast cancer. These nanoparticles showed better results than the drug that they transported. Nevertheless, to further reduce the drug effective dose and its toxicity to normal tissues, other nanoparticles, more advantageous than the previous ones, were developed in the current work. Compared to the previous nanoparticles, those prepared here proved to be more efficacious, and their potential administration may constitute an excellent approach to improve the outcomes of patients suffering from HER2-positive breast cancer.

Citation: Nieto, C.; Vega, M.A.; Martín del Valle, E. Nature-Inspired Nanoparticles as Paclitaxel Targeted Carrier for the Treatment of HER2-Positive Breast Cancer. Cancers 2021, 13, 2526. https://doi.org/10.3390/cancers13112526

Academic Editors: Ana Isabel Torres-Suárez and Ana Isabel Fraga-Sánchez

Received: 13 April 2021
Accepted: 10 May 2021
Published: 21 May 2021

**Publisher's Note:** MDPI stays neutral with regard to jurisdictional claims in published maps and institutional affiliations.

**Copyright:** © 2021 by the authors. Licensee MDPI, Basel, Switzerland. This article is an open access article distributed under the terms and conditions of the Creative Commons Attribution (CC BY) license (http://creativecommons.org/licenses/by/4.0/).

**Abstract:** Despite the advances made in the fight against HER2-positive breast cancer, the need for less toxic therapies and strategies that avoid the apparition of resistances is indisputable. For this reason, a targeted nanovehicle for paclitaxel and trastuzumab, used in the first-line treatment of this subtype of breast cancer, had already been developed in a previous study. It yielded good results in vitro but, with the aim of further reducing paclitaxel effective dose and its side effects, a novel drug delivery system was prepared in this work. Thus, polydopamine nanoparticles, which are gaining popularity in cancer nanomedicine, were novelty loaded with paclitaxel and trastuzumab. The effectiveness and selectivity of the nanoparticles obtained were validated in vitro with different HER2-overexpressing tumor and stromal cell lines. These nanoparticles showed more remarkable antitumor activity than the nanosystem previously designed and, in addition, to affect stromal cell viability rate less than the parent drug. Moreover, loaded polydopamine nanoparticles, which notably increased the number of apoptotic HER2-positive breast cancer cells after treatment, also maintained an efficient antineoplastic effect when validated in tumor spheroids. Thereby, these bioinspired nanoparticles charged with both trastuzumab and paclitaxel may represent an excellent approach to improve current HER2-positive breast cancer therapies.

**Keywords:** breast cancer; HER2-overexpression; drug delivery system; polydopamine nanoparticles; paclitaxel; trastuzumab

## 1. Introduction

Throughout 2020, more than 2.2 million new cases of breast cancer (BC) were diagnosed worldwide and nearly 0.7 million people died from this complex disease, which was the type of cancer with the highest incidence last year [1].

Among the new cases of BC that are diagnosed, around 15–20% overexpress the human epidermal growth factor receptor-2 (HER2) [2]. HER2, also overexpressed in other types of solid tumors [3,4], can dimerize with other members of its receptor family,

and this fact leads to cancer cell proliferation and survival, angiogenesis and metastasis [4]. In this way, HER2-overexpression may result in more aggressive clinical behavior and has been linked to worse patient outcomes [2]. However, as the overexpression of this tyrosine kinase (TK) receptor does not occur under normal physiological conditions [3], on the other hand, it has allowed the development of anti-HER2 targeted agents that have dramatically improved the survival rate of patients suffering from HER2-positive (HER2+) BC [2]. Undoubtedly, the most widely used HER2-targeted agent to date has been trastuzumab (Herceptin®, Basilea, Switzerland), a humanized monoclonal antibody (mAb) approved by the major drug regulatory agencies for the past two decades for the treatment of both early and metastatic BC [5]. Trastuzumab (Tmab) has been shown to induce tumor regression through different molecular mechanisms and to significantly increase overall survival of patients in multiple trials [6,7]. For this reason, it is nowadays an established part of adjuvant HER2+ BC treatment along with taxanes [6,8]. Nonetheless, Tmab intravenous administration also has some downsides. The two most important ones are its inherent cardiotoxicity and the apparition of acquired Tmab resistances, which cause 15% of patients to relapse after treatment [7,9].

Likewise, these two drawbacks (severe side effects and apparition of drug resistances) are also characteristic of conventional chemotherapy agents, mainly due to their poor specificity towards neoplastic tissues [10,11]. For instance, paclitaxel (PTX), which is frequently administered as adjuvant therapy with Tmab for the treatment of HER2+ BC [12], is very effective in stabilizing the microtubules of cancer cells and triggering subsequent apoptosis. Nevertheless, it has very poor aqueous solubility and low bioavailability, and the PTX formulation that is normally administered in the clinical setting (Taxol®, NY, USA) has severe adverse effects [13,14]. Thereby, the targeted delivery of this antimitotic compound is a major necessity [11,14], and it constitutes one of the main goals that nanotechnology is trying to achieve by means of the development of novel drug delivery systems (DDS) [13–15].

With regard to the latter and given that the combination of PTX plus Tmab is regulated and widely employed in the clinical setting, a DDS composed of alginate and piperazine nanoparticles (NPs) was already developed as vehicle for both the mAb and the taxane in a previous work to target HER2+ cancer cells. To enhance PTX aqueous solubility, this drug was previously included in β-cyclodextrin molecules. The resulting complexes along with Tmab were attached to the mentioned NPs, which were not toxic to human tumor or healthy cells. The nanosystem developed showed greater effectiveness and selectivity than the parent drug [16]. Nonetheless, with the aim of further improving the antitumor activity of the taxane, reducing its effective dose and lowering its adverse effects in an even more remarkable manner, a new DDS for Tmab and PTX was developed in the current work.

This DDS is composed of polydopamine (PDA) NPs, which have acquired great relevance in cancer nanomedicine in recent years thanks to their excellent physicochemical properties [17,18]. More specifically, PDA is biocompatible and biodegradable, its chemical versatility permits further functionalization strategies, and it has a strong ability to adsorb drugs via π–π stacking or hydrogen bond interactions. In addition, PDA NPs are capable of releasing drugs in a pH-responsive manner and [19–21], most importantly, they have proven to have intrinsic antitumor activity [17,22,23].

So far, no studies were found in the literature in which PTX has been loaded to PDA NPs, and since these NPs are capable of charging drugs with high loading rates, this fact was used to directly load PTX to them. Thus, the employment of additional compounds necessary to improve the taxane solubility, like β-cyclodextrins, was avoided by using these NPs, which made the conjugation process more profitable. Furthermore, since PDA NPs have antitumor activity themselves, especially when they are synthesized with 2-propanol [23], synergy between them and PTX was expected.

Otherwise, Tmab was also directly adsorbed in PDA NPs for the first time. In addition, since PDA can be easily functionalized, the mAb was bound by means of the car-

bodiimide chemistry to try to enhance the receptor-mediated endocytosis and selectivity of the resulting loaded PDA NPs.

Thereby, two different nanosystems were obtained, whose antitumor activity and neoplastic selectivity were validated by conventional viability assays. These assays were performed with two human HER2+ BC cell lines and with stromal cells. Based on the results obtained, since PDA NPs covalently charged with Tmab had slightly better antitumor effect and reduced the viability of normal cells less, they were chosen to perform further studies. Herein, their cytotoxicity was analyzed by alive/death confocal microscopy (CLSM) assays and, to verify that PTX pharmacological activity did not change upon loading to PDA NPs, NP ability to induce apoptosis in HER2+ cancer cells was verified by flow cytometry. Furthermore, the effectiveness of the loaded PDA NPs was also validated in HER2+ tumor spheroids to prove that it was maintained in these 3D histostructures. For this purpose, the interaction between the spheroids and the loaded PDA NPs was studied by scanning electron microscopy (SEM). Moreover, additional alive/death CLSM assays and cell counting experiments were carried out. As a result, it was proven that PDA NPs loaded with both PTX and Tmab, were able to significantly reduce the survival rate of HER2+ malignant cells cultured in both 2D and 3D, to a similar or even greater extent than equivalent concentrations of free PTX. Moreover, loaded PDA NPs were notably less toxic to stromal cells than the parent drug. Therefore, their employment may constitute a good strategy to improve PTX bioavailability, while reducing its effective dose and its adverse effects. Likewise, avoiding the apparition of treatment resistances may be possible with the administration of these targeted PDA NPs, which proved to be more advantageous than the previous, similarly reported paclitaxel and trastuzumab DDS.

## 2. Results

### 2.1. Synthesis and Characterization of PDA NPs

Initially, PDA NPs were prepared by the oxidation and self-polymerization of dopamine in a basic, aqueous medium containing 2-propanol (2-PrOH) and $NH_4OH$. Even though ethanol is the alcohol normally used in this synthesis procedure [17,23,24], 2-PrOH was chosen because it had been found in a previous work that its employment also allowed PDA NPs to be obtained, and that it conferred them greater antitumor activity in comparison to other alcohols [23]. Otherwise, the $NH_4OH$ concentration was adjusted in order to prepare NPs with a diameter smaller than 200 nm, since PDA NPs with that size had been observed to have greater inherent antineoplastic effect than bigger ones [22].

Once obtained, PDA NP hydrodynamic diameter was determined by dynamic light scattering (DLS). It was found to be 179.3 ± 41 nm (PDI = 0.07) (Figure 1(a)). In addition, PDA NP surface charge (zeta potential), which was −27.4 ± 1.5 mV, was also determined, and PDA NPs were characterized by transmission electron microscopy (TEM) to analyze their morphology and to obtain a size-range histogram (Figure 1(b)). According to this, NPs had an average diameter of 124.3 ± 19.2 nm, which was a lower value than that observed by DLS possibly due to the dehydration suffered by the NPs when preparing TEM samples [25].

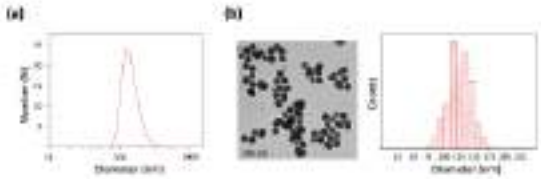

**Figure 1.** (a) DLS number distribution of the PDA NPs synthesized, suspended in Trizma base solution (pH 10.0); (b) TEM image and size-range histogram of the PDA NPs obtained.

### 2.2. PDA NP Loading With PTX and Tmab

Next, synthesized PDA NPs were washed through five centrifugation–redispersion cycles in phosphate buffer saline (PBS) and charged with PTX and Tmab following two different methods (Figure 2). First, the drug and the antibody were loaded to PDA NPs through a simple chemisorption process (PDA NPs@Tmab@(PTX) by adding solutions of both compounds to PDA NP suspensions. Secondly, the carbodiimide coupling strategy was used to covalently bind Tmab to PDA NPs with the aim of verifying whether this type of conjugation improved the antineoplastic activity and selectivity of the resulting NPs (PDA NPs•Tmab@(PTX). To do this, in order for the carbodiimide chemistry to be more efficient, the pH of the NP suspensions was acidified [26], and carboxyl groups of PDA NP surface were activated with EDC and NHS solutions [5]. Later, in two sequential steps, Tmab and PTX solutions with a similar concentration to those used in the adsorption process were incorporated into NP suspensions.

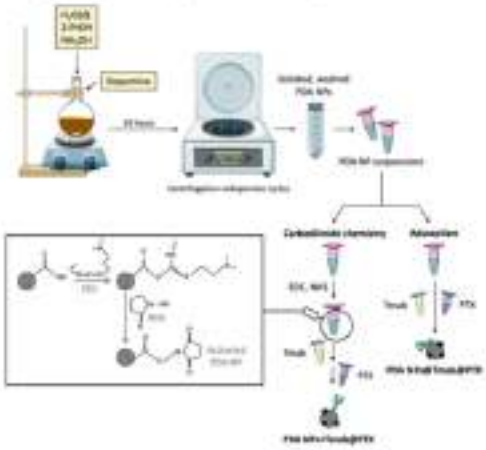

**Figure 2.** Schematic representation of PDA NPs synthesis and loading with PTX and Tmab by following two different methods in the latter case: adsorption and the carbodiimide coupling chemistry (H$_2$O(d) – Deionized water; EDC - N-(3-Dimethylaminopropyl)-N′-ethylcarbodiimide hydrochloride; NHS - N-hydroxysuccinimide); PDA - Polydopamine.

Charged PDA NPs were isolated by centrifugation, and Tmab and PTX loading efficiencies were both determined by difference, measuring the absorbance of the supernatants obtained by UV-Vis spectrophotometry. Results were obtained according to the

two different Tmab conjugation strategies followed and are summarized in Table 1. As can be seen, there were no very significant differences between PTX loading efficiency values, but Tmab conjugation efficiency was greater when the carbodiimide chemistry was employed.

Moreover, zeta potential of PDA NPs@Tmab@PTX and PDA NPs•Tmab@PTX was also analyzed after the conjugation processes. It can be consulted in the Supplementary Material (Table S1).

**Table 1.** Conjugation efficiencies (%) and Tmab (Trastuzumab) and PTX (Paclitaxel) content in PDA NPs (µg/mg) after adsorbing the drug and loading the antibody by adsorption or by means of the carbodiimide chemistry.

| | Adsorption | | Carbodiimide chemistry | |
|---|---|---|---|---|
| | Conjugation efficiency | Drug/Antibody content | Conjugation efficiency | Drug/Antibody content |
| **Tmab** | 37.4% | 1.4 µg/mg NPs | 37.8% | 1.9 µg/mg NPs |
| **PTX** | 18.0% | 2.3 µg/mg NPs | 19.1% | 2.44 µg/mg NPs |

### 2.3. *In Vitro Evaluation of the Antitumor Activity and Selectivity of PDA NPs Charged With Tmab and PTX*

In order to evaluate and compare the antitumor activity and selectivity of the two types of loaded PDA NPs obtained, MTT assays were carried out with two breast carcinoma cell lines overexpressing HER2 (BT474 and SKBR3) and with stromal cells (HS5 cell line) [16].

For such assays, all cells were treated with 0.035 and 0.042 mg/mL PDA NP concentrations. As already mentioned, these NPs have intrinsic antineoplastic activity, and it had been proven that these two concentrations were able to reduce tumor cell viability in a remarkable manner in previous studies [23]. Likewise, the same concentrations of PDA NPs charged only with PTX or/and Tmab were administered, and cells were also treated with concentrations of the drug and antibody equivalent to those loaded to PDA NPs. To perform the viability assays, a previously developed protocol that avoids overestimating cell viability by subtracting PDA contribution to the absorbance values of the samples was followed [17]. Results obtained after cell treatment with PDA NPs in which Tmab was adsorbed can be found in Figure S1, while those obtained after the administration of PDA NPs covalently conjugated with Tmab are summarized in Figure 3.

As can be seen in both figures, bare PDA NPs were not excessively toxic to normal cells, but they notably reduced BC cell survival rate. These results were in line with those obtained in prior research, in which it had been hypothesized that the great affinity of PDA NPs for the iron (III) existing in the lysosomes could be responsible for their cytotoxicity, which could be thus potentially related to a ferroptosis-mediated excessive production of reactive oxygen species (ROS) in tumor cells [22–24].

Otherwise, both PDA NPs•Tmab@PTX and PDA NPs@Tmab@PTX were found to be highly effective, since they reduced the viability of HER2+ BC cells to a slightly greater extent than free PTX concentrations equivalent to those adsorbed in most of the conditions studied ($p < 0.05$) (Tables S2–S4). In this manner, when BT474 cells were treated with PDA NPs•Tmab@PTX, only 10–17% of them survived after 72 hours, while this percentage was 13–19% when PDA NPs@Tmab@PTX were employed. Regarding the viability of the SKBR3 cell line, it was 10–14% 72 hours after treatment with PDA NPs•Tmab@PTX while, when PDA NPs@Tmab@PTX were administered, SKBR3 survival rate was close to 15–23%. Furthermore, it was noticed in both cases that Tmab covalent conjugation or adsorption to PDA NPs enhanced their antineoplastic activity, since it was greater when NPs were simultaneously charged with the antibody and the drug than when they were only loaded with PTX. Thus, PDA NPs•Tmab@PTX and PDA NPs@Tmab@PTX reduced BT474 and SKBR3 cell viability rates between 5–15% more than PDA NPs@PTX (depending on the NP concentration and treatment time), a fact that revealed that Tmab loading could enhance NP endocytosis in HER2+ tumor cells.

On the contrary, Tmab loading to PDA NPs made them less toxic to stromal cells than PDA NPs charged only with PTX. Thereby, when HS5 cells were treated with PDA NPs•Tmab@PTX and PDA NPs@Tmab@PTX, their survival rate was 23–30% higher than when the different concentrations of PDA NPs@PTX were used. With respect to the free parent drug, this gap was 25–34% and, compared to BC cells, about 26–36% more stromal cells survived after the same treatment. In fact, Tmab loading even slightly improved the intrinsic toxicity of bare PDA NPs to normal cells.

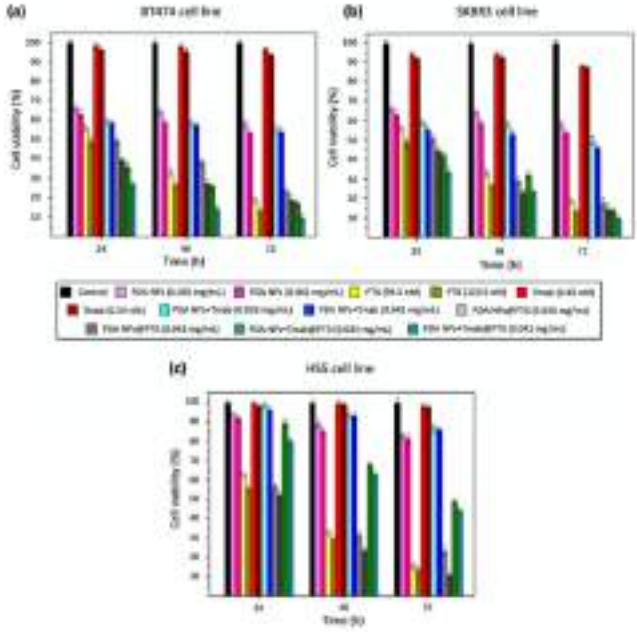


**Figure 3.** Survival rates of BT474 (**a**), SKBR3 (**b**) and HS5 (**c**) cells after treatment with 0.035 and 0.042 mg/mL bare PDA NPs, PDA NPs•Tmab, PDA NPs@PTX and PDA NPs•Tmab@PTX, as well as with concentrations of free Tmab and PTX similar to those loaded in PDA NPs.

Even though the differences in terms of efficacy and selectivity between PDA NPs@Tmab@PTX and PDA NPs•Tmab@PTX were not considered statistically significant ($p > 0.05$) (Table S5–S7), those NPs that had the antibody covalently bound decreased BT474 and SKBR3 viability by 1.2–13.5% more (depending on concentration and time) than PDA NPs@Tmab@PTX. Likewise, PDA NPs•Tmab@PTX affected HS5 survival rate by 2.2–15.9% less than PDA NPs@Tmab@PTX. For this reason, PDA NPs•Tmab@PTX were chosen to perform further studies.

Herein, their antineoplastic activity was also validated by alive/death CLSM assays, which were performed with the BT474 cell line. These HER2-overexpressing cells were treated with 0.035 mg/mL PDA NPs•Tmab@PTX and with a concentration of free PTX equivalent to that adsorbed to compare the results. Different CLSM images were acquired once 48 and 72 hours elapsed. These images have been included in Figure 4(a)

and, from them, the average percentage of living and dead cells was determined for each treatment condition. While 48 and 72 hours after treatment with free PTX 36.1% and 16.7% of BT474 cells remained alive, 36.3% and 14.3% of them survived when treated with 0.035 mg/mL PDA NPs•Tmab@PTX for 48 and 72 hours, respectively. Thereby, results of these CLSM assays proved that PDA NPs•Tmab@PTX were highly effective.

Finally, given that PTX exerts its pharmacological activity by inducing apoptosis of tumor cells [14], the number of early and late apoptotic BT474 cells was determined by flow cytometry 48 hours after treatment with PDA NPs•Tmab@PTX (0.035 mg/mL) and free PTX (99.5 nM). The aim was to verify that the taxane was mainly responsible for the antineoplastic effect of the loaded PDA NPs, and that its adsorption and the later Tmab conjugation to PDA NPs had not altered its antitumor activity. A FITC Annexin V apoptosis detection kit with 7AAD was used [27]. It was observed that treatment with PDA NPs•Tmab@PTX increased the number of early apoptotic HER2+ breast tumor cells (7AAD-/Annexin V+) in a similar manner than treatment with an equivalent concentration of free PTX (Figure 4(b)). Therefore, PTX pharmacological activity was not significantly reduced upon loading to PDA NPs.

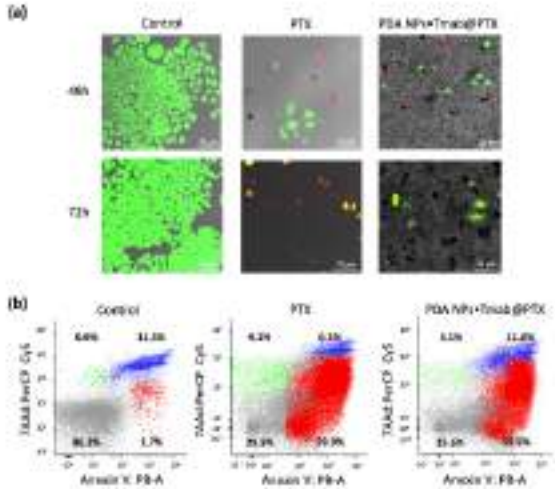


**Figure 4.** (a) CLSM images of BT474 cells 48 and 72 hours after treatment with PTX (99.5 nM) and PDA NPs•Tmab@PTX (0.035 mg/mL). Cell viability and death were assessed by using calcein AM (green) and propidium iodide (red), respectively; (b) flow cytometry analysis showing the percentage of apoptotic and necrotic BT474 cells 48 hours after treatment with PTX (99.5 nM) and PDA NPs•Tmab@PTX (0.035 mg/mL). The vertical axis indicates the cells labeled with 7AAD (PerCP) and the horizontal axis indicates those stained by Annexin V (FITC) (early apoptosis: right lower, late apoptosis/necrosis: right upper).

### 2.4. Assessment of the Antitumor Effect of PDA NPs Loaded With Tmab and PTX in 3D Cell Cultures

Since in vitro 3D culture systems mimic the in vivo growth conditions of solid tumors better than conventional monolayer cells cultures [28], they have been largely adopted as a model for drug and nanomedicine screening [29,30]. Among the numerous spherical cancer models that can be developed, multicellular tumor spheroids (MCTS), which are obtained by growing cancer cell lines under non-adherent conditions, have been reported to accurately mimic the drug sensitivity behavior of in vivo tumors [29,31]. For this reason, in the current work, developing MCTS derived from the BT474 cell line was decided to further evaluate the antitumor efficacy of the PDA NPs•Tmab@PTX.

Thus, BT474 cells were assembled in a 3D architecture after seeding them in U-shaped-bottom microplates. By day 3 of growth, they had formed compact multicellular spheres about 1 mm in diameter. At that time, they were treated with PDA NPs•Tmab@PTX (0.035 mg/mL) and with free PTX in an equivalent concentration to that adsorbed to PDA NPs. Three different types of studies were performed.

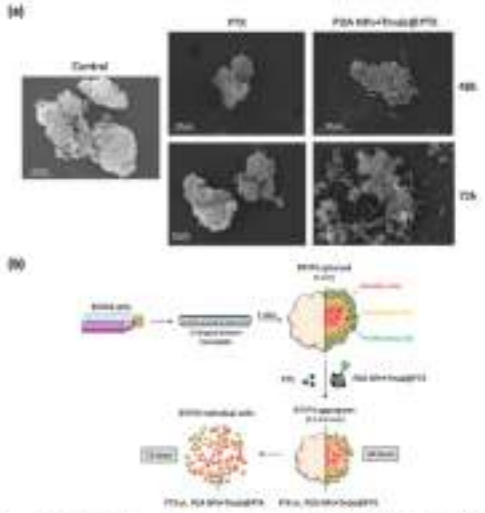


**Figure 5.** (a) SEM characterization of sections of BT474 spheroids 48 and 72 hours after treatment with PTX (99.5 nM) and PDA NPs•Tmab@PTX (0.035 mg/mL); (b) schematic representation of how BT747 spheroids were developed and the effect that PTX vs. PDA NPs•Tmab@PTX treatment had on their structure and morphology.

First, with the aim of analyzing the interaction between the loaded PDA NPs and the 3D cell biostructures, SEM was employed to acquire images of spheroid sections in a secondary electron mode after critical point drying [30]. These images were taken 48 and 72 hours after treatment. Morphological differences between the control spheroids and the spheroids treated with both free PTX and loaded PDA NPs could be observed, especially when 72 hours had elapsed. In this way, after treatment with the taxane, BT474 spheroids became smaller and disaggregated. This reduction in size and the structural disorganization with loss of integrity could already be detected after exposure to PDA

NPs•Tmab@PTX, with which spheroids acquired a grape bunch-shape in which individual cells could be better distinguished (Figure 5). Moreover, in both the images obtained from the spheroids treated with free PTX and with PDA NPs•Tmab@PTX, filamentous-like structures were observed that might correspond to PTX crystals formed in solution [32].

Second, additional live/death CLSM assays were also carried out with the 3D cell cultures (Figure 6(a)). Again, confocal images were taken 48 and 72 hours after spheroid treatment, just as with the monolayer cell cultures. Control images allowed an appreciation of how BT474 MCTS had a necrotic core surrounded by a viable rim, with an inner layer of quiescent cells and an outer layer of proliferating cells. This phenomenon occurs in large tumor spheroids (> 500 µm) [29]. Otherwise, the results obtained by SEM were corroborated with these assays, since it could be noticed that both free PTX and PDA NPs•Tmab@PTX were able to reduce the size of the spheroids developed and to disaggregate them, especially after 72 hours.

Likewise, the effect of PDA NPs•Tmab@PTX treatment on spheroid morphology was borne out by phase-contrast images, which can be found in the Supplementary Material (Figure S2). From them, it could be observed how after 48 hours, loaded PDA NPs made the spheroids smaller and decreased their density. In addition, their margins were less marked, an indication of the cellular disassemble that was beginning to take place.

Lastly, the viability of the BT474 cells that made up the spheroids was determined by cell-counting 48 hours after treating them with free PTX and PDA NPs•Tmab@PTX, as well as with 0.035 mg/mL bare PDA NPs. Results obtained can be found in Figure 6(b). As can be seen, the viability of the control spheroids was close to 71 ± 4% due to the existence of the necrotic core described in the previous paragraph, caused by the diffusion gradient of oxygen and nutrients [29]. The mean survival rate of the spheroids treated with unloaded PDA NPs was about 65 ± 5% while, when free PTX and PDA NPs•Tmab@PTX were administered, their viability was reduced to 58 ± 5% and 59 ± 6%, respectively. Therefore, it was proven that loaded PDA NPs were not only effective in inducing apoptosis of monolayer HER2+ BC cells. When these cells were forming 3D structures, they also showed a cytotoxicity similar to that of the parent drug, even spreading worse [33].

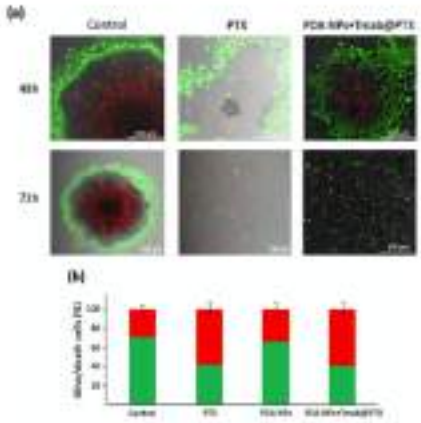


**Figure 6.** (a) CLSM images of BT474 MCTS 48 and 72 hours after treatment with PTX (99.5 nM) and PDA NPs•Tmab@PTX (0.035 mg/mL). Cell viability and death were again assessed by using calcein

AM (green) and propidium iodide (red); (b) percentage of living (green) and dead (red) BT474 cells cultured in 3D spheres, determined by cell-counting, 48 hours after treatment with PTX (99.5 nM), PDA NPs (0.035 mg/mL) and PDA NPs+Tmab@PTX (0.035 mg/mL).

## 3. Discussion

In the last couple of decades, nanotechnology, taking advantage of the deeper knowledge that the scientific community has acquired about cancer biology, has become essential for the development of DDS that seek to overcome the drawbacks of conventional chemotherapy [10–11,15]. Thus, for instance, with the aim of reducing Tmab and PTX side effects while potentially avoiding the apparition of resistances to these agents, we had already designed alginate and piperazine NPs as a targeted nanovehicle for the anti-HER2 mAb and the taxane [16]. In a similar manner, other authors developed targeted micelles to transport Tmab and PTX to improve HER2+ BC treatment [33]. In both cases, the polymeric NPs and the micelles were inactive, so they did not show cytotoxicity. Moreover, including PTX into β-cyclodextrins was necessary before loading it to alginate-piperazine nanoparticles, and encapsuling the taxane into the micelles took a two -day procedure [16,34]. Thus, in order to make the PTX loading process easier and more profitable, and further reduce the effective doses and the side effects of this drug, a novel PTX-Tmab targeted DDS was developed in the current study to improve HER2+ BC treatment.

This novel nanovehicle was made up of PDA NPs, which have specific antineoplastic activity themselves [17,22,23], can directly adsorb drugs with great loading rates [19], and can release these drugs in a pH-sensitive manner [35,36]. Thanks to these three properties, it was expected that the taxane could be directly loaded to the aforementioned NPs, that synergy could occur between PDA NPs and PTX, and that PDA pH-sensitivity could improve the selectivity of the DDS obtained, enhancing that provided by Tmab binding.

Herein, PDA NPs (approximately 180 nm in size) were prepared and easily loaded with PTX for the first time. Likewise, the nanosystem was novelty decorated by Tmab, which was both adsorbed and covalently bound by means of the carbodiimide chemistry. Two types of loaded PDA NPs were obtained, PDA NPs+Tmab@PTX and PDA NPs@Tmab@PTX, which were shown to be highly effective in vitro, reducing the viability rate of HER2+ BC cells similarly or further than PTX concentrations equivalent to those adsorbed. In addition, compared to the other Tmab-PTX-transporting nanosystems mentioned previously [16,34], loaded PDA NPs were found to have more remarkable antitumor activity, perhaps because their inherent toxicity was added to PTX pharmacological activity. In this manner, PDA NPs loaded with both Tmab and PTX reduced the viability of HER2+ breast tumor cells to a greater or equal extent than the similar reported nanomedicines [16,34], but transporting a smaller amount of PTX and having been administered in a lower concentration to the cells. In addition, loaded PDA NPs were not only effective when validated in monolayer cell cultures, but they were also capable of disintegrating and reducing the viability survival rate of HER2+ breast tumor spheroids.

Otherwise, apart from being effective, charged PDA NPs, which were proven to induce apoptosis in target HER2+ BC cells, reduced stromal cell viability to a lesser extent than similar PTX concentrations. Thus, stromal cell survival rate was notably less affected than that of breast tumor cells upon treatment with loaded PDA NPs, while equivalent PTX concentrations reduced the viability of both types of cells in a similar way.

Therefore, PTX loading to PDA NPs also carrying Tmab could constitute a good strategy to improve the bioavailability of the drug in an efficient manner while reducing its adverse effects. Furthermore, their administration may even avoid the apparition of potential resistances by targeting HER2+ tumor cells thanks to Tmab presence, as well as by releasing PTX in a pH-responsive way in neoplastic tissues.

## 4. Materials and Methods

### 4.1. Chemicals

Dopamine hydrochloride, $NH_4OH$ (28–30%), PBS (0.01M, pH 7.4), N-hydroxysuccinimide (NHS), N-(3-Dimethylaminopropyl)-N'-ethylcarbodiimide hydrochloride (EDC), PTX (from semisynthetic, >97%), Dulbecco's modified Eagle's medium (DMEM), fetal bovine serum (FBS, USA origin), thiazolyl blue tetrazolium bromide (MTT reagent) and dimethyl sulfoxide (DMSO) were all supplied by Sigma–Aldrich (Darmstadt, Germany). Penicillin-streptomycin (5000 U/mL), calcein AM, propidium iodide ReadyProbes™ reagent, Gibco™ Trypsin-EDTA (0.25%) and trypan blue stain (0.4%) were obtained from Thermo Fisher Scientific (Eugene, OR, USA). 2-PrOH and HCl (37%) were purchased from PanReac Química S.L.U. (Castellar del Vallès, Barcelona, Spain). Tmab was gifted from the Instituto de Biología Molecular y Celular del Cáncer (Salamanca, Spain) and the FITC Annexin V apoptosis detection kit with 7AAD was obtained from Immunostep (Salamanca, Spain).

### 4.2. Synthesis and Characterization of PDA NPs

PDA NPs about 180 nm in size were prepared by dopamine oxidation and self-polymerization in an alkaline medium. Briefly, an ammonia aqueous solution (2.5 mL) was mixed with 2-PrOH (40 mL) and $H_2O$(d) (90 mL) under magnetic stirring at room temperature for 30 minutes. Dopamine hydrochloride (0.5 g) was dissolved in $H_2O$(d) (10 mL) and added to the above solution [23]. The resulting mixture was left to react for 24 hours and PDA NPs obtained were isolated by centrifugation. Four centrifugation-redispersion cycles in $H_2O$(d) were performed to eliminate any residue, and PDA NPs were finally resuspended in $H_2O$(d) in a 2 mg/mL concentration once washed.

Next, to characterize PDA NPs, their hydrodynamic diameter was determined by DLS on the basis of their intensity–average size distribution, along with their zeta potential (Zetasizer Nano ZS90, Malvern Instruments Inc., Royston, Hertfordshire, UK). For such a purpose, PDA NPs were dispersed in Trizma base solution (pH 10.0) in a concentration lower than 0.01% (WT). Moreover, PDA NP size and morphology were also characterized by TEM (Tecnai Spirit Twin, Fei Company, Hillsboro, OR, USA). PDA NPs were again resuspended in $H_2O$(d) in a concentration inferior to 0.01% (WT) to prepare the samples and drops of this dispersion were deposited on copper grids with a collodion membrane. NPs were allowed to dry for 24 hours and TEM images of at least 300 different PDA NPs were taken with a 120 kV voltage acceleration. To conclude, these images were analyzed (ImageJ software, NIH, Bethesda, MD, USA) to make a NP size–range histogram.

### 4.3. PDA NP Loading With Tmab and/or PTX

In order to subsequently carry out in vitro studies, PDA NPs were washed through five more centrifugation-redispersion cycles in PBS before being loaded with Tmab and PTX. Next, this loading process was performed following two different methods. On one hand, to adsorb both Tmab and PTX, solutions of the antibody (1.35 μM, 17.5 μL) and the drug (0.52 μM, 20.2 μL, 2:1 $H_2O$(d)/DMSO) were incorporated to suspensions of PDA NPs (2 mg/mL, 350 μL). The resulting mixtures were kept under orbital shaking (100 rpm) in dark conditions, and loaded PDA NPs were isolated the next day by centrifugation [37].

On the other hand, to covalently attach Tmab and adsorb PTX to PDA NPs, the pH of the NP suspensions (2 mg/mL, 1 mL) was adjusted to 4.7–4.8 by dropping HCl (37%). Then, solutions of EDC (193 mg/mL, 10 μL) and NHS (58 mg/mL, 10 μL) were added. NPs were kept under orbital shaking (100 rpm) for 40 minutes and, after that time, a Tmab solution (1.35 μM, 50 μL) was incorporated into the suspensions. Mixtures were kept under agitation for 3 additional hours and, finally, a PTX solution (0.52 μM, 58 μL,

2:1 $H_2O$(d)/DMSO) was also added. Final mixtures were left shaking overnight in dark conditions, and charged PDA NPs were isolated by centrifugation, too [16].

The same procedures were carried out to prepare PDA NPs@Tmab, PDA NPs•Tmab and PDA NPs@PTX but, in these cases, only the solution of the antibody or the drug were incorporated to the NP suspensions. All supernatants were preserved to determine Tmab and PTX loading efficiencies and content in PDA NPs.

*4.4. Determination of Tmab and PTX Loading Efficiencies and Content*

While quantification of PTX in PDA NP supernatants was achieved via spectrophotometry at 227 nm (UV-1800, Shimadzu Corporation, Kioto, Japan), Tmab concentration in them was determined using the Pierce™ BCA Protein Assay Kit (Thermo Fisher Scientific, Eugene, OR, USA) following the instructions detailed by the manufacturer. The amount of Tmab and PTX charged in the NPs was determined by difference, and the different loading efficiencies (%) and the antibody and drug content in the charged PDA NPs were found by applying the following equations [38]:

$$Loading\ efficiency\ (\%) = \frac{Weight\ of\ antibody\ or\ drug\ found\ loaded}{Weight\ of\ total\ antibody\ or\ drug\ used} \times 100 \quad (1)$$

$$Antibody\ or\ drug\ content\ (W/W) = \frac{Weight\ of\ antibody\ or\ drug\ found\ loaded}{Weight\ of\ loaded\ PDA\ NPs} \quad (2)$$

*4.5. Cell Culture*

BT474, SKBR3 and HS5 cell lines (ATCC, Wesel, Germany) were cultured as instructed. They were grown in DMEM, supplemented with FBS (10% V/V) and antibiotics (100 U/mL penicillin and 100 mg/mL streptomycin) at 37°C in a 95:5 air/$CO_2$ humidified atmosphere.

*4.6. MTT Assays Performance*

Once grown, BT474, SKBR3 and HS5 cells were used to carry out MTT assays. For this purpose, they were seeded into 24-well plates (12,000 cells/well) and incubated to allow attachment. The next day, culture medium in the wells of some plates was replaced by supplemented DMEM containing PBS (for the control), PDA NPs (0.035 and 0.042 mg/mL), PTX (99.5 and 119.5 nM), Tmab (0.45 and 0.54 nM), PDA NPs•Tmab (0.035 and 0.042 mg/mL), PDA NPs@PTX (0.035 and 0.042 mg/mL) and PDA NPs•Tmab@PTX (0.035 and 0.042 mg/mL). Culture medium in the wells of other plates was otherwise replaced by supplemented DMEM containing PBS, PDA NPs (0.035 and 0.042 mg/mL), PTX (94.9 and 113.6 nM), Tmab (0.33 and 0.42 nM), PDA NPs@Tmab (0.035 and 0.042 mg/mL), PDA NPs@PTX (0.035 and 0.042 mg/mL) and PDA NPs@Tmab@PTX (0.035 and 0.042 mg/mL). In both cases, cells were later incubated for 24, 48 and 72 hours and, after those times, a MTT solution (5 mg/mL, 110 µL) was added to each well. Cell incubation was performed for an additional hour and formazan crystals were dissolved by adding DMSO (500 µl/well). The optical density value of each well was determined by applying a procedure that was previously set up to subtract PDA contribution to absorbance [17], which was measured in a microplate reader (Zetasizer Nano ZS90, Malvern Instruments Inc., Royston, UK). All data were obtained in triplicate.

*4.7. Live/Death Fluorescence Staining of BT474 Cells*

In order to perform the first alive/death CLSM assays, BT474 cells were seeded (12,000 cells/mL) in glass-bottom dishes (Ibidi, Gräfelfing, Germany) and incubated for 24 hours. Subsequently, they were treated with or without PTX (99.5 nM) or PDA NPs•Tmab@PTX (0.035 mg/mL) and incubated again. After 48 and 72 hours, cells were incubated with calcein AM (1 µM) and propidium iodide (1 drop/mL) fluorescent dyes for 15 minutes. BT474 stained cells were imaged by CLSM (Leica TCS SP5, Leica Mi-

crosystems, L'Hospitalet de Llobregat, Barcelona, Spain) with an excitation/detection of 494/517 and 535/617 nm, respectively. The average number of living and dead cells after each type of treatment was determined from at least 5 different CLSM images.

### 4.8. Flow Cytometry Analysis

Flow cytometry data were obtained by an annexin V apoptosis detection kit with 7AAD according to the manufacturer's instructions (Immunostep, Salamanca, Spain). Briefly, BT474 cells were cultured in dishes (12,000 cells/mL), treated with or without PTX (99.5 nM) and PDA NPs•Tmab@PTX (0.035 mg/mL) and incubated for 48 hours. After this time, cells were collected, centrifuged and resuspended in warm PBS. Then, they were washed by warm PBS twice and resuspended in annexin binding buffer (1×) at a concentration of $10^6$ cells/mL. Annexin V (5 µL) and 7AAD (5 µL) were added to the cell samples ($10^6$ cells/mL, 100 µL), and these were incubated at room temperature and in dark conditions for 15 minutes. Stained cells were analyzed by flow cytometry (FACSAria™ III cytometer, BD Biosciences, San José, CA, USA), using FITC (green) for annexin V and PerCP (red) for 7AAD.

### 4.9. Development of BT474 Spheroids and SEM Characterization

BT474 MCTS were obtained by seeding the mentioned cells in Nunclon™ Sphera™ 96-well, U-shaped bottom microplates (Thermo Fisher Scientific, Eugene, OR, USA) (10,000 cells/mL) and allowing them to grow for 3 days. Then, they were treated with or without PTX (99.5 nM) or PDA NPs•Tmab@PTX (0.035 mg/mL), and 48 and 72 hours later spheroids were characterized by SEM (JSM-IT500, Jeol, Tokio, Japan). To prepare the samples, MCTS were carefully collected and sectioned, deposited on filter paper with poly-L-lysine acid fixed overnight at 8°C in PBS with glutaraldehyde (25%). The next day, they were washed by PBS three times and after that, PBS with osmium (1%) was added to the samples. One hour later, spheroids were washed by $H_2O$(d) three times and were progressively dehydrated by a gradient concentration of acetone series. Critical point drying was achieved with $CO_2$ and samples were observed by SEM after gold coating.

### 4.10. Live/dead® Fluorescence Staining and Cell-Counting of BT474 Spheroids

Live/dead® CLSM assays with BT474 spheroids were performed in the same way as those with the monolayer cell cultures, simply developing them on the microplates mentioned in the previous point and depositing them once grown in glass-bottom dishes.

Otherwise, to assess BT474 spheroid viability by cell-counting, these grown 3D cellular spheres were kept on the U-shaped bottom microplates, where they were treated with or without PTX (99.5 nM), bare PDA NPs (0.035 mg/mL) or PDA NPs•Tmab@PTX (0.035 mg/mL). After 48 hours, MCTS were washed by warm PBS, disaggregated with trypsin, collected in DMEM and centrifuged. Cells were resuspended in supplemented DMEM and their viability was determined (InvitrogenCountess II FL Automated Cell Counter, ThermoFisher Scientific) after mixing them with trypan blue. Data were again obtained in triplicate.

### 4.11. Statistical Analysis

Data regarding the size (DLS) and zeta potential values of PDA NPs were the average ± SEM of three different measurements. Data concerning MTT assays were analyzed using an unpaired two-tailed Student t-test. P-values less than 0.05 were considered to be statistically significant. Displayed viability results were the average ± SEM of three replicates per treatment condition.

## 5. Conclusions

In conclusion, this report has presented the synthesis of PDA NPs that could act as targeted nanocarriers for PTX and Tmab for the treatment of HER2+ breast tumors. The combination of this taxane and this anti-HER2 antibody is extensively used in the clinical setting as adjuvant therapy and, given its great results, several DDS transporting PTX and Tmab have already been developed. However, neither the taxane or the anti-HER2 antibody have been loaded to PDA NPs to date, and the resulting drug delivery NPs have been shown to reduce normal cell viability rate to a lower extent than the parent drug and to have a very remarkable antitumor activity in vitro, not only in HER2+ conventional cell cultures, but also in breast tumor spheroids.

Thus, if Tmab-PTX loaded PDA NPs would also yield good results in vivo in the future, they may constitute an excellent approach to overcome the many disadvantages that the current adjuvant treatment of Tmab and PTX entails, mainly related to their toxicity and the apparition of resistances.

**Supplementary Materials:** The following are available online at www.mdpi.com/2072-6694/13/11/2526/s1, Figure S1: survival rates of BT474, SKBR3 and HS5 cells after treatment bare PDA NPs, PDA NPs-Tmab, PDA NPsetPTX and PDA NPs-TmabetPTX, as well as with concentrations of free Tmab and PTX similar to those loaded to PDA NPs; Figure S2: phase-contrast images of BT474 spheroids 48 hours after treatment with or without PDA NPs•TmabetPTX.

**Author Contributions:** Conceptualization, C.N., M.A.V. and E.M.d.V.; methodology, C.N. and M.A.V.; software, C.N. and M.A.V.; validation, C.N. and M.A.V.; investigation, C.N., M.A.V. and E.M.d.V; writing—original draft preparation, C.N.; writing—review and editing, C.N., M.A.V. and E.M.d.V.; supervision, M.A.V. and E.M.d.V.; project administration, E.M.d.V.; funding acquisition, E.M.d.V. All authors have read and agreed to the published version of the manuscript.

**Funding:** This research was funded by the Spanish Ministry of Sciences, Innovation and Universities, grant number PID2019-108899RB-I00.

**Institutional Review Board Statement:** Not applicable.

**Informed Consent Statement:** Not applicable.

**Data Availability Statement:** The data that support the findings of this study are available from the corresponding authors upon reasonable request.

**Acknowledgments:** C.N. thanks Junta de Castilla y León for her predoctoral fellowship, and all the authors thank the Electron Microscopy Facilities (NUCLEUS) of the University of Salamanca for the SEM images.

**Conflicts of Interest:** The authors declare no conflict of interest.

## Abbreviations

| | |
|---|---|
| BC | Breast cancer |
| CLSM | Confocal laser scanning microscopy |
| DDS | Drug delivery system |
| DLS | Dynamic light scattering |
| HER2 | Human epidermal growth factor receptor 2 |
| HER2+ | Human epidermal growth factor receptor 2-positive |
| mAb | Monoclonal antibody |
| MCTS | Multicellular tumor spheroid |
| NPs | Nanoparticles |
| PDA | Polydopamine |
| PDA NPsetPTX | Polydopamine nanoparticles loaded with paclitaxel through adsorption |
| PDA NPs•Tmab | Polydopamine nanoparticles covalently loaded with trastuzumab |
| PDA NPsetTmab | Polydopamine nanoparticles loaded with trastuzumab through adsorption |
| PDA NPs•TmabetPTX | Polydopamine nanoparticles covalently loaded with trastuzumab and with adsorbed paclitaxel |

| | |
|---|---|
| PDA | Polydopamine nanoparticles loaded with both trastuzumab and paclitaxel through adsorption |
| NPs@Tmab@PTX | |
| PTX | Paclitaxel |
| ROS | Reactive oxygen species |
| SEM | Scanning electron microscopy |
| TEM | Transmission electron microscopy |
| TK | Tyrosine kinase |
| Tmab | Trastuzumab |
| 2-PrOH | 2-propanol |

## References


1. Global Cancer Observatory. Available online: https://gco.iarc.fr/today/data/factsheets/cancers/20-Breast-fact-sheet.pdf (accessed on 8 April 2021).
2. Dieci, M.V.; Miglietta, F.; Griguolo, G.; Guarneri, V. Biomarkers for HER2-positive metastatic breast cancer: Beyond hormone receptors. *Cancer Treat. Rev.* **2020**, *88*, 102064.
3. Elsaginy, S.A.; Hamdy, R.; Moraes, Y.; Almahdi, A.M.; El-Awady, R.; Soliman, S.S.M. Design, synthesis, and computational validation of novel compounds selectively targeting HER2-expressing breast cancer. *Bioorg. Med. Chem. Lett.* **2020**, *30*, 127658.
4. Dhritlahre, R.K.; Saneja, A. Recent advances in HER2-targeted delivery for cancer therapy. *Drug Discov. Today* **2020**, in press.
5. Nieto, C.; Vega, M.A.; Martín del Valle, E.M. Trastuzumab: More than a guide in HER2-positive cancer nanomedicine. *Nanomaterials* **2020**, *10*, 1674.
6. Stewart, F.; Blanchette, P.; Shah, P.S.; Yu, X.Y.; Boldt, R.G.; Fernandes, R.; Vandenberg, T.; Rhapsel, J. Do all patients with HER2 positive breast cancer require one year of adjuvant trastuzumab? A systematic review and meta-analysis. *Breast* **2020**, *54*, 203–210.
7. De Sanctis, R.; Giordano, L.; D'Antonio, F.; Agostinetto, E.; Marinello, A.; Gaiducci, D.; Masci, G.; Losurdo, A.; Zuradelli, M.; Torrisi, R.; et al. Clinical predictors of cardiac toxicity in HER2-positive early breast cancer patients treated with adjuvant s.c. versus i.v. trastuzumab. *Breast* **2021**, *57*, 80–85.
8. Plosker, G.L.; Keam, S.J. Trastuzumab. *Drugs* **2006**, *66*, 449–475.
9. Nahta, R.; Esteva, F.J. HER2 therapy: Molecular mechanisms of trastuzumab resistance. *Breast Cancer Res.* **2006**, *8*, 215.
10. Marques, A.C.; Costa, P.J.; Velho, S.; Amaral, M.H. Functionalizing nanoparticles with cancer-targeting antibodies: A comparison of strategies. *J. Control. Release* **2020**, *320*, 180–200.
11. Wicki, A.; Witzigmann, D.; Balasubramanian, V.; Huwyler, J. Nanomedicine in cancer therapy: Challenges, opportunities and clinical applications. *J. Control. Release* **2015**, *200*, 138–157.
12. Slamon, D.; Eiermann, W.; Robert, N.; Pienkowski, T.; Martin, M.; Press, M.; Mackey, J.; Glaspy, J.; Chan, A.; Pawlicki, M.; et al. Adjuvant trastuzumab in HER2-positive breast cancer. *N. Engl. J. Med.* **2011**, *365*, 1273–1283.
13. Zhao, L.; Bi, D.; Qi, X.; Guo, Y.; Yue, F.; Wang, X.; Han, M. Polydopamine based surface modification of paclitaxel nanoparticles for osteosarcoma targeted therapy. *Nanotechnology* **2019**, *30*, 255101.
14. Samuni, T.M.A.; Samec, M.; Liskova, A.; Kubatka, P.; Büsselberg, D. Paclitaxel's mechanistic and clinical effects on breast cancer. *Biomolecules* **2019**, *9*, 789.
15. Raj, S.; Khurana, S.; Choudhari, R.; Kesari, K.K.; Kamal, M.A.; Garg, N.; Ruokolainen, J.; Das, B.C.; Kumar, D. Specific targeting cancer cells with nanoparticles and drug delivery in cancer therapy. *Semin. Cancer Biol.* **2019**, in press.
16. Nieto, C.; Cenis, A.; Rodríguez-Rodríguez, J.A.; Pandiella, A.; Martín del Valle, E.M. Paclitaxel-trastuzumab mixed nanovehicle to target HER2-overexpressing tumors. *Nanomaterials* **2019**, *9*, 948.
17. Nieto, C.; Vega, M.A.; Marcelo, G.; Martín del Valle, E.M. Polydopamine nanoparticles kill cancer cells. *RSC Adv.* **2018**, *8*, 36203–36208.
18. Ambekar, R.S.; Kandasubramanian, B. A polydopamine-based platform for anti-cancer drug delivery. *Biomater. Sci.* **2019**, *7*, 1776–1792.
19. Wang, W.; Tang, Z.; Zhang, Y.; Wang, Q.; Liang, Z.; Zeng, X. Mussel-inspired polydopamine: The bridge for targeting drug delivery system and synergistic cancer treatment. *Macromol. Biosci.* **2020**, *20*, 200022.
20. Wu, H.; Hu, H.; Wan, J.; Li, Y.; Wu, Y.; Tang, Y.; Xiao, C.; Xu, H.; Yang, X.; Li, Z. Hydroxyethyl starch stabilized polydopamine nanoparticles for cancer chemotherapy. *Chem. Eng. J.* **2018**, *349*, 129–145.
21. Han, Y.-N.; Zhang, A.-Q.; Guo, T.-T.; Shu, Y.; Wang, J.-H.; Johnson, O.; Chen, W. Glutathione triggered degradation of polydopamine to facilitate controlled drug release for synergic combinational cancer treatment. *J. Mater. Chem. B* **2019**, *7*, 6742–6750.
22. Nieto, C.; Vega, M.A.; Enrique, J.; Marcelo, G.; Martín del Valle, E.M. Size matters in the cytotoxicity of polydopamine nanoparticles in different types of tumors. *Cancers* **2019**, *11*, 1679.
23. Nieto, C.; Marcelo, G.; Vega, M.; Martín del Valle, E.M. Antineoplastic behaviour of polydopamine nanoparticles prepared in different water/alcohol media. *Colloid. Surf. B Biointerfaces* **2021**, *199*, 111506.
24. Vega, M.A.; Nieto, C.; Marcelo, G.; Martín del Valle, E.M. Cytotoxicity of paramagnetic cations-loaded polydopamine nanoparticles. *Colloid. Surf. B Biointerfaces* **2018**, *167*, 284–290.

25. Lizunova, A.A.; Loshkarev, A.A.; Tokunov, Y.M.; Ivanov, U.V. Comparison of the results of measurements of the sizes of nanoparticles in stable colloidal solutions by the methods of acoustic spectroscopy, dynamic light scattering, and transmission electron microscopy. *Meas. Teach.* **2017**, *35*, 1131–1135.
26. Madkour, S.A.; Carnali, J.O. pH optimization of amidation via carbodiimides. *Ind. Eng. Chem. Res.* **2013**, *52*, 13547–13555.
27. Park, J.; Kim, H.-D.; Lee, S.-H.; Kwak, C.-H.; Chang, Y.-C.; Lee, Y.-C.; Chang, T.-W.; Magae, J.; Kim, C.-H. Ascochlorin induces caspase-independent necroptosis in LSP-stimulated RAW 264.7 macrophages. *J. Ethnopharmacol.* **2018**, *59*, 111898.
28. Ishiguro, T.; Ohata, H.; Sato, A.; Yamawaki, K.; Enomoto, T.; Okamoto, K. Tumor-derived spheroids: Relevance to cancer stem cells and clinical applications. *Cancer Sci.* **2017**, *108*, 283–289.
29. Weiswald, L.-B.; Bellet, D.; Dangles-Marie, V. Spherical cancer models in tumor biology. *Neoplasia* **2015**, *17*, 1–15.
30. Mollo, V.; Scognamiglio, P.; Marino, A.; Ciofani, G.; Santoro, F. Probing the ultrastructure of spheroids and their uptake of magnetic nanoparticles by FIB-SEM. *Adv. Mater. Technol.* **2020**, *5*, 1900887.
31. Nath, S.; Devi, G.R. Three-dimensional culture systems in cancer research: Focus on tumor spheroid model. *Pharmacol. Ther.* **2016**, *163*, 94–108.
32. Castro, J.I.; Tapia, L.Y.; Silveyra, R.A.; Martinez, C.A.; Deyanire, P.A. Negative impact of paclitaxel crystallization in hydrogels and novel approaches for anticancer drug delivery systems. In *Current Cancer Treatment: Novel Beyond Conventional Approaches*; Ozdemir, O., Ed.; IntechOpen Limited: Rijeka, Croatia, 2011; pp. 767–782.
33. Tchoryk, A.; Taresco, V.; Argent, R.H.; Ashford, M.; Gellert, P.R.; Stolnik, S.; Grabowska, A.; Garnett, M.C. Penetration and uptake of nanoparticles in 3D tumor spheroids. *Bioconjug. Chem.* **2019**, *30*, 1371–1384.
34. Lee, A.L.Z.; Wang, Y.; Cheng, H.Y.; Pervaiz, S.; Yang, Y.Y. The co-delivery of paclitaxel and Herceptin using cationic micellar nanoparticles. *Biomaterials* **2009**, *30*, 919–927.
35. Chang, D.; Gao, Y.; Wang, L.; Liu, G.; Chen, Y.; Wang, T.; Tao, W.; Mei, L.; Huang, L.; Zeng, X. Polydopamine-based surface modification of mesoporous silica nanoparticles as pH-sensitive drug delivery vehicles for cancer therapy. *J. Colloid. Interface Sci.* **2016**, *463*, 279–287.
36. Bi, D.; Zhao, L.; Yu, R.; Li, H.; Gao, Y.; Wang, X.; Han, M. Surface modification doxorubicin-loaded nanoparticles based on polydopamine with pH-sensitive property for tumor targeting therapy. *Drug Deliv.* **2018**, *25*, 564–575.
37. Nieto, C.; Vega, M.A.; Martín del Valle, E.M. Tailored-made polydopamine nanoparticles to induce ferroptosis in breast cancer cells in combination with chemotherapy. *Int. J. Mol. Sci.* **2021**, *22*, 3661.
38. Yousefpour, P.; Atyabi, F.; Vasheghani-Farahani, E.; Movahedi, A.-A.M.; Dinarvand, R. Targeted delivery of doxorubicin-containing chitosan nanoparticles surface functionalized with anti-HER2 trastuzumab. *Int. J. Nanomed.* **2011**, *6*, 1977–1990.

# CHAPTER 7

## GELLAN GUM HYDROGELS LOADED WITH PACLITAXEL FOR BREAST LOCAL CHEMOTHERAPY

# CHAPTER 8

## GENERAL CONCLUSION

In this doctoral thesis, three different strategies, summarized in **Figure 8.1**, were developed to improve HER2-overexpressing breast cancer treatment. The first two, thought to be potentially administered by the systemic route, consisted of the design of particle nanosystems. By contrast, the third strategy, developed to complement the treatment with the previously synthesized NPs, consisted of macroscopic, implantable hydrogels for local therapy.

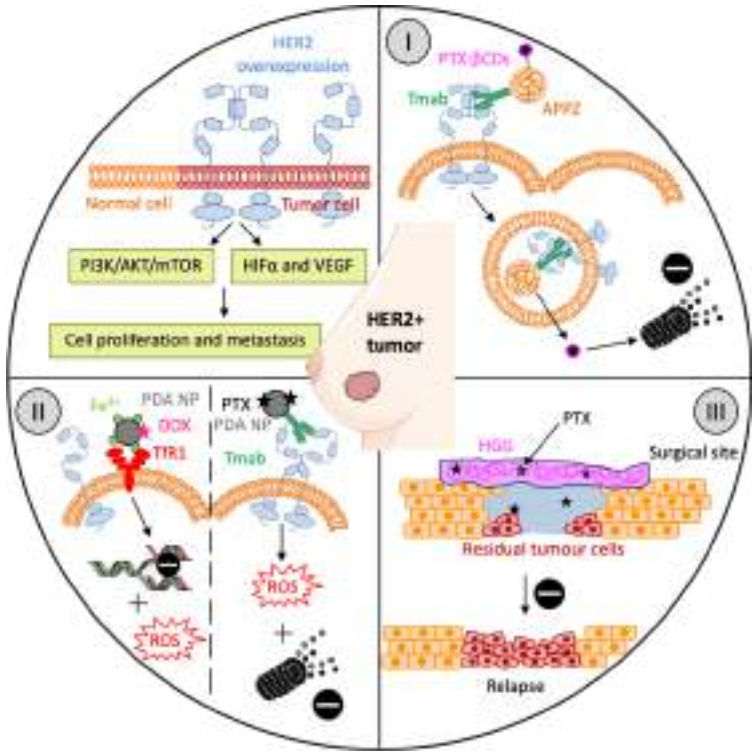


**Figure 8.1.** Major strategies developed in this thesis to improve current treatment of HER2+ breast cancer.

***First strategy***

The first NPs developed (**APPZ**) were obtained thanks to the electrostatic interactions that occur between alginate and piperazine at acidic pH. They were used as a targeted vehicle for Tmab and PTX, which was included into β-CDs to improve its aqueous solubility. Compared to PTX, conjugated APPZ proved to have greater anti-tumour activity *in vitro*.

Thus, these NPs showed an antineoplastic effect similar to that of equivalent concentrations of PTX:βCDs complexes. Nevertheless, they had a clear advantage: conjugated APPZ were not as toxic to normal cells as these drug complexes. Therefore, the potential use of this Tmab-PTX nanovehicle may help to improve PTX bioavailability and biodistribution. Likewise, it could reduce the side toxicity and the probability of resistance emerge that usually accompany PTX treatment, mainly due to its lack of selectivity.

***Second strategy***

Otherwise, **PDA NPs** were prepared by dopamine solution oxidation in this project to develop a second anti-tumour strategy for being more advantageous than APPZ in some respects. First of all, for instance, it should be noted that despite the fact that APPZ size could be modulated by modifying the alginate/piperazine ratio, obtaining polymeric NPs with a diameter less than 160 nm and acceptable polydispersity was not achieved. However, the synthesis of much less polydisperse PDA NPs with a size between 100 and 450 nm could be controlled simply by varying the $NH_4OH$ concentration and the type of ROH used in their preparation. Furthermore, what is more relevant, by modifying the ROH employed, it was possible to tailor the $Fe^{3+}$ adsorption capacity and, consequently, the intrinsic, selective anti-tumour activity that PDA NPs were shown to have.

Secondly and in relation to the latter, PDA NP ability to chelate different metal cations was used to develop a nanosystem in which their inherent cytotoxicity was enhanced. Thereby, PDA NPs were loaded with both $Fe^{3+}$ and DOX to target HER2+ breast cancer cells and induce two types of regulated cell death in them: ferroptosis and apoptosis. As the molecular mechanisms of these two processes are different, by inducing both, it was sought to decrease the potential appearance of possible resistances, which is frequent when pro-apoptotic agents are administered in isolation. Moreover, DOX side toxicity was reduced when loaded to PDA NPs. In this way, since the anti-tumour activity and selectivity of the PDA NPs charged with this anthracycline and with $Fe^{3+}$ could be adjusted depending on the concentration of DOX used in the

adsorption process and the pH at which $Fe^{3+}$ loading was performed, this DDS could be potentially tuned to fulfil different clinical needs.

Third and last, the ability of PDA NPs to directly load drugs was exploited to develop a new targeted nanovehicle for Tmab and PTX. On this occasion, the use of β-CDs to improve PTX solubility and transport it was not necessary, so the synthesis of the nanosystem was simpler and more profitable. These charged PDA NPs were found to be equal to or more effective than equivalent concentrations of PTX in reducing the viability of HER2+ breast cancer cells *in vitro* but, like conjugated APPZ, they proved to be significantly more selective, so their administration would entail fewer side effects. In addition, PDA NPs, despite transporting an inferior amount of the taxane and being administered in a much lower concentration, reduced the viability rate of tumour cells in a very similar way to APPZ. Thus, PDA NPs loaded with Tmab and PTX proved to be more effective than the latter, possibly because their cytotoxicity was added to PTX pharmacological action. In this way, they may constitute a great strategy to improve PTX pharmacokinetics and reduce its adverse effects.

***Third strategy***

Finally, given that systemic treatments are normally administered in the clinical setting a few weeks after surgery, and that during that time residual cancer cells can keep proliferating, **HGGs** loaded with PTX were developed for local, post-surgery treatment of HER2+ breast cancer. The advantage of HGG use, thought as a potential complement to a subsequent systemic chemotherapy, was that PTX release could be better controlled depending on the medium employed to prepare them and on their crosslinking degree. Moreover, since PTX was released locally and non-specific drug distribution in normal tissues could be avoided, HGGs could be loaded with higher drug concentrations that those employed in the nanoparticulate systems. Thereby, these hydrogels could represent a good strategy to achieve a future, sustained release of the taxane prior systemic chemotherapy.

# APPENDIX

# Appendix I

## Reagents and equipment

| Reagent trade name | Trade firm and location |
|---|---|
| Alginic sodium salt, from brown algae | Sigma Aldrich (St. Louis, MO, USA) |
| Ammonium hydroxide solution, 28-30% | Sigma Aldrich (St. Louis, MO, USA) |
| ANXVKF7-100T kit | Immunostep (Salamanca, Spain) |
| B-cyclodextrin, minimum 98% | Sigma Aldrich (St. Louis, MO, USA) |
| Bradford Reagent | Sigma Aldrich (St. Louis, MO, USA) |
| Calcein AM | Invitrogen (Eugene, OR, USA) |
| Calcium chloride anhydrous | Panreac (Castellar del Vallès, Barcelona, Spain) |
| CellROX™ Deep Red Flow Cytometry Assay Kit | Sigma Aldrich (St. Louis, MO, USA) |
| CellTracker™ Green CMFDA | Invitrogen (Carlsbad, CA, USA) |
| CellTracker™ Red CMPTX | Invitrogen (Carlsbad, CA, USA) |
| Citric acid anhydrous | Panreac (Castellar del Vallès, Barcelona, Spain) |
| Countes™ cell counting chamber slides | Invitrogen (Carlsbad, CA, USA) |
| Deferoxamine mesylate CRS | Sigma Aldrich (St. Louis, MO, USA) |
| Dimethyl sulfoxide, >99% | Fisher Scientific (Loughborough, UK) |
| Dopamine hydrochloride | Sigma Aldrich (St. Louis, MO, USA) |
| Doxorubicin hydrochloride | Sigma Aldrich (St. Louis, MO, USA) |
| Dulbecco's modified Eagle's medium (1x) | Gibco (Gaithersburg, MD, USA) |
| Ethanol absolute pure | Panreac (Castellar del Vallès, Barcelona, Spain) |
| Foetal bovine serum, qualified, HI | Gibco (Gaithersburg, MD, USA) |
| Gelzan™ CM | Sigma Aldrich (St. Louis, MO, USA) |
| Glass bottom dishes (35 mm) | Ibidi (Gräfelfing, Germany) |
| Hydrochloric acid (37%) | Panreac (Castellar del Vallès, Barcelona, Spain) |
| Iron(II) chloride anhydrous (97%) | Panreac (Castellar del Vallès, Barcelona, Spain) |
| Iron(III) chloride anhydrous (97%) | Panreac (Castellar del Vallès, Barcelona, Spain) |
| L-Cysteine (97%) | Sigma Aldrich (St. Louis, MO, USA) |
| L-Glutathione reduced | Sigma Aldrich (St. Louis, MO, USA) |
| Lysozyme human | Sigma Aldrich (St. Louis, MO, USA) |
| Lysotracker™ Red DND-99 | Invitrogen (Carlsbad, CA, USA) |
| Methanol | Panreac (Castellar del Vallès, Barcelona, Spain) |
| N-hydroxysulfosuccinimide | Sigma Aldrich (St. Louis, MO, USA) |
| N-(3-dimethyl(aminopropyl)-N'-ethylcarbodiimide hydrochloride | Sigma Aldrich (St. Louis, MO, USA) |

| | |
|---|---|
| Nunclon™ Sphera™ 96-well, U-shape bottom plates | Sigma Aldrich (St. Louis, MO, USA) |
| Paclitaxel, from semisynthetic, >97% | Sigma Aldrich (St. Louis, MO, USA) |
| Penicillin streptomycin solution (100x) | Corning (Manassas, VA, USA) |
| Phosphate buffered saline, powder, pH 7.4 | Sigma Aldrich (St. Louis, MO, USA) |
| Pierce™ BCA Protein Assay kit | Sigma Aldrich (St. Louis, MO, USA) |
| Piperazine, 99% | Sigma Aldrich (St. Louis, MO, USA) |
| Potassium bromide for IR | Panreac (Castellar del Vallès, Barcelona, Spain) |
| Propidium iodide ReadyProbes™ | Invitrogen (Carlsbad, CA, USA) |
| Sodium hydroxide | Panreac (Castellar del Vallès, Barcelona, Spain) |
| Thiazolyl blue tetrazolium bromide BioChemica | Panreac (Castellar del Vallès, Barcelona, Spain) |
| Trypan blue stain, 0.4% | Invitrogen (Carlsbad, CA, USA) |
| Trypsin EDTA (1x), 0.05% | Gibco (Gaithersburg, MD, USA) |
| 1-propanol | Panreac (Castellar del Vallès, Barcelona, Spain) |
| 2'-7'-Dichlorofluorescein | Sigma Aldrich (St. Louis, MO, USA) |
| 2-methyl-2-propanol | Panreac (Castellar del Vallès, Barcelona, Spain) |
| 2-propanol | Panreac (Castellar del Vallès, Barcelona, Spain) |

| **Equipment** | **Trade firm and location** |
|---|---|
| AR 1500 Ex (Rheometer) | Waters Corporation (Milford, MA, USA) |
| Countess™ II FL Automated Cell Counter | Invitrogen (Carlsbad, CA, USA) |
| ESEM QUANTA 200 FEG (SEM) | FEI (Hillsboro, OR, USA) |
| EZ Microplate Reader 2000 | Biochrom (Cambridge, UK) |
| DSC Q100 calorimeter | Waters Corporation (Milford, MA, USA) |
| FACSAria™ III cytometer | BD Biosciences (San José, CA, USA) |
| FEI TECNAI G2 F30 (STEM) | FEI (Hillsboro, OR, USA) |
| JSM-IT500 (SEM) | JEOL (Tokyo, Japan) |
| LC-2795 chromatograph | Waters Corporation (Milford, MA, USA) |
| Leica DM1000 (Optical microscope) | Leica Microsystems (Wetzlar, Germany) |
| sensION™ PH3 phmeter | Hach (Loveland, CO, USA) |
| Spectrum Two™ spectrometer (IR) | Perkin Elmer (Waltham, MA, USA) |
| TCS SPS (CLSM) | Leica Microsystems (Wetzlar, Germany) |
| Telstar LyoQuest lyophilizer | Telstar (Lisbon, Portugal) |
| ULTIMA 2 (ICP-OES) | HORIBA Jobin Yvon (Haching, Germany) |
| UV-1800 spectrophotometer | Shimadzu Corporation (Kioto, Japan) |
| Zetasizer Nano ZS90 | Malvern Instruments (Malvern, UK) |
| ZQ-4000 mass spectrometer | Waters Corporation (Milford, MA, USA) |
| FEI Tecnai Spirit Twin (TEM) | FEI (Hillsboro, OR, USA) |

# Appendix II

## Estimation of the ionic strength of the media used in the study of the swelling behaviour of gellan gum hydrogels

The ionic strength (μ) of the media that were used to analyse the swelling kinetics of the different HGGs prepared in Chapter 7 was determined according to the following equation:

$$\mu = \frac{1}{2}\sum Z_i^2 C_y = \frac{1}{2}[Z_1^2 C_1 + Z_2^2 C_2 + Z_3^2 C_3 + \cdots]$$

Where $Z_i$ is the charge of the ions existing in the media and $C_y$ is their concentration.

Calculations corresponding to the determination of the ionic strength of the different media can be seen below.

**PBS (1x)**

| Compound | $C_y$ | $Z_i$ | | $Z_i^2 C_y$ |
|---|---|---|---|---|
| $Na_2HPO_4$ | 0.01 | $2Na^+$ | $HPO_4^{2-}$ | 0.06 |
| $KH_2PO_4$ | 0.0018 | $K^+ + H^+$ | $HPO_4^{2-}$ (negligible) | 0.0036 |
| $NaCl$ | 0.137 | $Na^+$ | $Cl^-$ | 0.274 |
| $KCl$ | 0.027 | $K^+$ | $Cl^-$ | 0.0054 |
| **μ (M)** | | | | **0.17** |

**DMEM**

| Compound | $C_y$ | $Z_i$ | | $Z_i^2 C_y$ |
|---|---|---|---|---|
| $NaCl$ | 0.116 | $Na^+$ | $Cl^-$ | 0.232 |
| $KCl$ | 0.054 | $K^+$ | $Cl^-$ | 0.0108 |
| $MgSO_4$ | 0.00075 | $Mg^{2+}$ | $SO_4^{2-}$ | 0.006 |
| $CaCl_2$ | 0.0018 | $Ca^{2+}$ | $2Cl^-$ | 0.0108 |
| **μ (M)** | | | | **0.13** |

**NaCl solution (0.15 M)**

| Compound | $C_y$ | $Z_i$ | | $Z_i^2 C_y$ |
|---|---|---|---|---|
| $NaCl$ | 0.15 | $Na^+$ | $Cl^-$ | 0.30 |
| **μ (M)** | | | | **0.15** |

**Citrate buffer (0.1 M)**

| Compound | $C_y$ | $Z_i$ | | $Z_i^2 C_y$ |
|---|---|---|---|---|
| $HOC(COOH)(CH_2COOH)_2$ | 0.1 | $HOC(COO^-)(CH_2COOH)_2$ | $H^+$ | 0.2 |
| $NaOH$ | 1.0 | $Na^+$ | $OH^-$ | 2 |
| $HCl$ | 0.1 | $H^+$ | $Cl^-$ | 0.2 |
| **μ (M)** | | | | **1.20** |

**Acetate buffer (0.04 M)**

| Compound | $C_y$ | $Z_i$ | | $Z_i^2 C_y$ |
|---|---|---|---|---|
| $CH_3COONa$ | 0.4 | $CH_3COO^- + H^+$ (negligible) | $Na^+$ | 0.4 |
| **μ (M)** | | | | **0.2** |

**Trizma base solution (0.05 M)**

| Compound | $C_y$ | $Z_i$ | | $Z_i^2 C_y$ |
|---|---|---|---|---|
| $NH_2C(CH_2OH)_3$ | 0.05 | $R_3 - C - NH^-$ | $H^+$ | 0.1 |
| **μ (M)** | | | | **0.05** |